

---

# THE COMPUTER SIMULATION OF DISPERSED TWO-PHASE FLOWS

DAVID PAUL HILL

Thesis submitted for the degree of  
Doctor of Philosophy  
of the University of London

IMPERIAL COLLEGE OF SCIENCE, TECHNOLOGY AND MEDICINE  
Department of Mechanical Engineering  
Exhibition Road  
London SW7 2BX.

**July 1998**

---



*For Lesley, Peter and Eleanor...*



## Abstract

This study describes the development of a two-phase mathematical model for the prediction of dispersed solid-liquid, liquid-liquid and gas-liquid two-phase flows. The model is based on the two-fluid approach where Eulerian conservation equations for mass and momentum are employed for each phase. These equations are derived using a conditional-averaging technique using a single ensemble average.

Closure is effected by assembling models for the interfacial forces applicable to dispersed two-phase systems and include drag, virtual mass and lift forces. The effects of turbulence are modelled using a two-equation  $k$ - $\epsilon$  turbulence model. The conditional-averaged transport equations for  $k$  and  $\epsilon$  are rigorously derived and include terms accounting for the effects of the dispersed phase on the turbulence. The dispersed phase Reynolds stresses are modelled by relating them to those of the continuous phase via an algebraic response equation.

The effects of break-up and coalescence are accounted for using a presumed PDF approach where transport equations are derived for intensive properties related to the PDF moments. Models for the source and sink terms in these equations, which account for the effects of break-up and coalescence on the PDF, and applicable to systems involving surfactants, are described.

To obtain a solution to the resulting set of non-linear partial differential equations, a finite volume discretisation technique is employed coupled with a specially developed solution algorithm based loosely on the SIMPLE algorithm but with an additional sub-iterative update stage to improve the stability of the algorithm in the case of high inter-phase drag forces.

The performance of the complete model is assessed by applying it to three validation cases involving gas-liquid bubbly flow in a plane shear layer, the break-up of oil droplets in a co-axial pipe-mixer device in the presence of surfactants and the gas-liquid bubbly flow in a stirred vessel. Good agreement is obtained with regard to the phase distribution in all cases. The break-up of the oil droplets is generally well captured, although it is under-predicted at high droplet viscosities.

## Acknowledgements

I would like to express my sincere gratitude to my supervisors Professor David Gosman and Dr. Raad Issa for their continuous support, guidance, constructive criticism and patience. Without their help and encouragement, this study would not have been possible.

Very special thanks are also due to my ‘unofficial’ supervisors Henry Weller and Fred Marquis whose constant support and friendship have been invaluable. Many thanks are also due to Dr. Gavin Tabor for his advice during the preparation of this thesis and for his help in running the stirred vessel simulations, and to Dr. Hrovje Jasak for his encouragement and for many, many helpful discussions. Thanks are also due to Dr. DeMing Wang for his much appreciated support in the early stages.

I would also like to thank Dr. Jo Janssen, Prof. Wim Agterof and Prof. Allan Chesters for their assistance with the break-up and coalescence modelling aspects of this study. Their help and encouragement was very much appreciated. I would also like to express my appreciation to the Unilever Research Laboratory, Imperial Chemical Industries and to the EEC for the financial support which made this study possible.

Finally, I would like to thank my family, especially my wife Lesley and my children Peter and Eleanor for their support, encouragement and patience over the last 6 years.

David Hill

June 1998

# Contents

<b>1</b>	<b>Introduction</b>	<b>25</b>
1.1	Two-phase Flow . . . . .	25
1.2	Objectives Of The Present Research . . . . .	30
1.3	Present Contribution . . . . .	31
1.4	Thesis Outline . . . . .	32
1.5	Review Of Two-Phase Flow Analysis Techniques . . . . .	33
1.5.1	Lagrangian Approaches . . . . .	35
1.5.2	Eulerian Approaches . . . . .	38
1.5.3	Averaging . . . . .	40
1.6	Conditional-Averaged Two-Phase Flow Equations . . . . .	47
1.6.1	Conservation of Mass . . . . .	48
1.6.2	Conservation of Linear Momentum . . . . .	50
1.7	Closure . . . . .	53
<b>2</b>	<b>Two-phase Flow Equation Closure</b>	<b>55</b>
2.1	Introduction . . . . .	55
2.2	Interfacial Momentum Transfer . . . . .	56
2.2.1	The Drag Force . . . . .	57
2.2.2	The Virtual Mass Force . . . . .	67
2.2.3	The Lift Force . . . . .	68
2.2.4	The Interfacial Pressure Force . . . . .	69
2.2.5	The Basset Force . . . . .	71

2.2.6	Interfacial Closure Summary . . . . .	71
2.3	Turbulence Closure . . . . .	72
2.3.1	Previous Work . . . . .	72
2.3.2	Continuous Phase Reynolds Stress Modelling . . . . .	83
2.3.3	Dispersed Phase Reynolds Stress Modelling . . . . .	94
2.4	Two-Phase Flow Equation Summary . . . . .	100
2.5	Closure . . . . .	102
<b>3</b>	<b>Break-up and Coalescence</b>	<b>105</b>
3.1	Introduction . . . . .	105
3.2	The Presumed PDF Approach . . . . .	109
3.2.1	The Adopted Droplet Size PDF . . . . .	110
3.2.2	The Intensity Of Dispersion - $\mathbf{S}_\gamma$ . . . . .	111
3.2.3	The $\mathbf{S}_\gamma$ Transport Equation . . . . .	113
3.2.4	Evaluation Of The Interfacial Drag Term . . . . .	115
3.3	Break-up And Coalescence Models . . . . .	117
3.3.1	Generic Break-up Model . . . . .	117
3.3.2	Break-up Models For Clean Systems . . . . .	119
3.3.3	Break-up Models For Systems With Surfactants . . . . .	126
3.3.4	Generic Coalescence Model . . . . .	138
3.4	Concentration Transport Equations . . . . .	140
3.4.1	Bulk Concentration Transport Equation . . . . .	141
3.4.2	Interfacial Concentration Transport Equation . . . . .	143
3.4.3	Interface Mass Transfer Rate Model . . . . .	143
3.5	Closure . . . . .	145
<b>4</b>	<b>Numerical Solution Procedure</b>	<b>147</b>
4.1	Introduction . . . . .	147
4.2	Discretisation Of The Solution Domain . . . . .	148
4.3	Discretisation Of The Governing Differential Equations . . . . .	150
4.3.1	Convection Terms . . . . .	153



4.3.2	Diffusion Terms . . . . .	155
4.3.3	Source Terms . . . . .	155
4.3.4	Final Form Of The Discretised Equations . . . . .	156
4.3.5	Under-Relaxation . . . . .	157
4.3.6	Convergence . . . . .	158
4.4	Boundary Conditions . . . . .	159
4.4.1	Fixed Value Boundary Condition . . . . .	159
4.4.2	Fixed Gradient Boundary Condition . . . . .	160
4.4.3	Wall boundary conditions . . . . .	161
4.5	Numerical Solution Algorithm . . . . .	163
4.5.1	Previous Studies . . . . .	165
4.5.2	An Improved Two-phase Solution Algorithm . . . . .	177
4.5.3	Overview of the final algorithm . . . . .	187
4.6	Closure . . . . .	189
<b>5</b>	<b>Two-Phase Flow In A Plane Ducted Shear Layer</b>	<b>191</b>
5.1	Introduction . . . . .	191
5.1.1	Previous Experimental Studies Into Plane Free Shear Layers . . . . .	193
5.2	INPT Two-phase Shear Layer Experiments . . . . .	195
5.2.1	Experimental Set-up . . . . .	195
5.2.2	Mass Balance Check . . . . .	197
5.3	Numerical Simulations . . . . .	198
5.3.1	Inlet Conditions . . . . .	199
5.3.2	Calculations . . . . .	203
5.4	Results - Single-phase Cases . . . . .	205
5.4.1	Case 1.1 . . . . .	205
5.4.2	Case 2.1 . . . . .	207
5.4.3	Case 3.1 . . . . .	209
5.5	Results - Two-phase Cases . . . . .	211
5.5.1	Case 1.2 . . . . .	211

5.5.2	Case 2.2 . . . . .	214
5.5.3	Case 2.3 . . . . .	221
5.5.4	Case 2.4 . . . . .	228
5.5.5	Case 3.2 . . . . .	234
5.5.6	Mesh Sensitivity Tests . . . . .	237
5.6	Two-Phase Turbulence Model Performance . . . . .	238
5.7	Solution Algorithm Performance . . . . .	241
5.8	Discussion And Conclusions . . . . .	244
<b>6</b>	<b>Droplet Break-up In A Co-axial Pipemixer Device</b>	<b>249</b>
6.1	Introduction . . . . .	249
6.2	The Unilever Experiments . . . . .	251
6.2.1	The Coaxial Pipe-Mixer Device . . . . .	251
6.2.2	Single-Phase Experiments . . . . .	253
6.2.3	Two-Phase Experiments . . . . .	254
6.3	Numerical Simulations . . . . .	256
6.3.1	Single-Phase Cases . . . . .	256
6.3.2	Two-Phase Cases . . . . .	257
6.3.3	Break-up Model Coefficients . . . . .	258
6.4	Results . . . . .	261
6.4.1	Single-Phase Cases . . . . .	261
6.4.2	Two-Phase Cases . . . . .	265
6.5	Discussion And Conclusions . . . . .	280
<b>7</b>	<b>Two-Phase Flow In A Stirred Vessel</b>	<b>295</b>
7.1	Introduction . . . . .	295
7.2	Previous Stirred Vessel Studies . . . . .	297
7.2.1	Single-Phase Studies . . . . .	297
7.2.2	Two-Phase Studies . . . . .	298
7.2.3	Impeller Modelling . . . . .	299
7.3	The Experiment of Fischer <i>et al.</i> . . . . .	300

7.4	Numerical Simulations . . . . .	301
7.5	Results . . . . .	303
7.6	Discussion And Conclusions . . . . .	305
<b>8</b>	<b>Summary And Conclusions</b>	<b>319</b>
8.1	Summary Of Achievements And Main Findings . . . . .	319
8.1.1	Basic Mathematical Model . . . . .	319
8.1.2	Physical Modelling . . . . .	321
8.1.3	Break-up and Coalescence Modelling . . . . .	322
8.1.4	Numerical Solution Procedure . . . . .	323
8.1.5	Experimental Validation Studies . . . . .	324
8.2	Suggestions For Further Work . . . . .	326
8.2.1	Turbulence And Physical Effect Modelling . . . . .	327
8.2.2	Numerical Solution Algorithm . . . . .	328
8.2.3	Further Model Validation . . . . .	329
<b>A</b>	<b>Conditional Averaging</b>	<b>331</b>
A.1	Introduction and Basic Definitions . . . . .	331
A.2	Conditional-Averaged Quantities . . . . .	334
A.3	Spatial and Temporal Derivatives . . . . .	335
A.4	Surface Average Notation . . . . .	336
A.5	Interface Transport Equation . . . . .	337
<b>B</b>	<b>Derivation of the <math>C_t</math> model of Issa</b>	<b>339</b>
<b>C</b>	<b>Turbulence Transport Equations</b>	<b>341</b>
C.1	Introduction . . . . .	341
C.2	Fluctuating Velocity Transport Equation . . . . .	342
C.3	Conditional-Averaged Reynolds Stress Equation . . . . .	344
C.4	Conditional-Averaged T.K.E Equation . . . . .	345
C.5	Conditional-Averaged Dissipation Rate Equation . . . . .	346

---

<b>D Overview Of The Single-Phase SIMPLE Algorithm</b>	<b>349</b>
<b>E Break-up Source Term Evaluation</b>	<b>353</b>
<b>F Pseudo Turbulence Due To Bubble Size Variation</b>	<b>355</b>
F.1 Bubble Size Distribution Effects . . . . .	355
F.2 Mean Terminal Velocity . . . . .	357
F.3 Apparent RMS Velocity . . . . .	358

# List of Figures

1.1	Topological classification of two-phase flows . . . . .	26
1.2	Flow patterns for gas-liquid flow in a tube . . . . .	27
1.3	The Baker and Hewitt-Roberts flow maps. . . . .	27
1.4	Influence of the averaging domain on averaged values. . . . .	42
1.5	Decomposition of the interface velocity. . . . .	50
2.1	Drag coefficients for smooth, axially symmetric solid bodies. . . . .	59
2.2	Drag coefficient as a function of Reynolds number. . . . .	63
2.3	Influence of turbulence intensity on the drag coefficient. . . . .	65
2.4	Fluctuating velocity definition. . . . .	85
3.1	Droplet size PDF in the ensemble averaged framework. . . . .	106
3.2	Characterisation of 2D linear flows. . . . .	120
3.3	Critical capillary number curves for various flow types and viscosity ratios. . . . .	123
3.4	Damping factor as a function of droplet diameter and viscosity ratio. . . . .	138
3.5	Components of damping factor. . . . .	139
4.1	Typical computational cell arrangement. . . . .	149
4.2	Schematic of the one-dimensional test case. . . . .	183
4.3	Residual history comparison between Oliveira's and the new algorithm. . . . .	185
5.1	Schematic layout of the INPT shear layer experiment. . . . .	196
5.2	Schematic arrangement of the computational mesh. . . . .	204
5.3	Case 1.1 - Mean axial velocity. . . . .	205
5.4	Case 1.1 - Axial RMS velocity. . . . .	206

5.5	Case 2.1 - Mean axial velocity. . . . .	207
5.6	Case 2.1 - Axial RMS velocity. . . . .	208
5.7	Case 3.1 - Mean axial velocity. . . . .	209
5.8	Case 3.1 - Axial RMS velocity. . . . .	210
5.9	Case 1.2 - Dispersed phase fraction. . . . .	211
5.10	Case 1.2 - Continuous phase mean axial velocity. . . . .	212
5.11	Case 1.2 - Continuous phase axial RMS velocity. . . . .	213
5.12	Case 2.2 - Dispersed phase fraction. . . . .	214
5.13	Case 2.2 - Continuous phase mean axial velocity. . . . .	215
5.14	Case 2.2 - Dispersed phase mean axial velocity. . . . .	216
5.15	Case 2.2 - Continuous phase axial RMS velocity. . . . .	217
5.16	Case 2.2 - Dispersed phase axial RMS velocity. . . . .	218
5.17	Case 2.2 - Axial RMS velocity ratio $C_t$ . . . . .	219
5.18	Case 2.2 - Dispersed phase lateral force balance at $x = 30$ cm. . . . .	220
5.19	Case 2.3 - Dispersed phase fraction. . . . .	221
5.20	Case 2.3 - Continuous phase mean axial velocity. . . . .	222
5.21	Case 2.3 - Dispersed phase mean axial velocity. . . . .	223
5.22	Case 2.3 - Continuous phase streamlines showing recirculation zone. . . . .	224
5.23	Case 2.3 - Continuous phase axial RMS velocity. . . . .	225
5.24	Case 2.3 - Dispersed phase axial RMS velocity. . . . .	226
5.25	Case 2.3 - Axial RMS velocity ratio $C_t$ . . . . .	227
5.26	Case 2.4 - Dispersed phase fraction. . . . .	228
5.27	Case 2.4 - Continuous phase mean axial velocity. . . . .	229
5.28	Case 2.4 - Dispersed phase mean axial velocity. . . . .	230
5.29	Case 2.4 - Continuous phase axial RMS velocity. . . . .	231
5.30	Case 2.4 - Dispersed Phase axial RMS velocity. . . . .	232
5.31	Case 2.4 - Axial RMS velocity ratio $C_t$ . . . . .	233
5.32	Case 3.2 - Dispersed phase fraction. . . . .	234
5.33	Case 3.2 - Continuous phase mean axial velocity. . . . .	235
5.34	Case 3.2 - Continuous phase axial RMS velocity. . . . .	236

5.35	Effect of mesh size on $\alpha_d$ and $U_c$ predictions at $x = 60$ cm (Case 1.2).	237
5.36	Turbulence model comparison for continuous phase RMS velocity predictions (Case 1.2).	238
5.37	Turbulence model comparison for dispersed phase RMS velocity predictions (Case 1.2).	239
5.38	Turbulence model comparison for $C_t$ predictions (Case 1.2).	240
5.39	Residual history without using the sub-iterative technique (Case 1.2C).	242
5.40	Residual history using the sub-iterative technique (Case 1.2C).	243
6.1	Schematic arrangement of the pipe-mixer device.	252
6.2	Pipe-mixer measurement plane positions.	253
6.3	Mean velocity profiles for the single-phase 6/2.5 m/s case.	261
6.4	Turbulent kinetic energy profiles for the single-phase 6/2.5 m/s case.	262
6.5	Mean velocity profiles for the single-phase 15/2.5 m/s case.	263
6.6	Turbulent kinetic energy profiles for the single-phase 15/2.5 m/s case.	264
6.7	Mesh sensitivity results for the single-phase 6/2.5 m/s case.	265
6.8	Mean diameter profiles for 15/2.5 m/s cases.	267
6.9	Surfactant concentration along centreline (Case 2)	268
6.10	Surface tension and mean diameter along centreline (Case 2)	269
6.11	Mean diameter profiles for 6/2.5 m/s cases.	270
6.12	Surfactant concentration along centreline (Case 7)	271
6.13	Surface tension and mean diameter along centreline (Case 7)	272
6.14	Effect of surfactant transport on the mean diameter predictions (Case 7).	273
6.15	Mean diameter profiles for Bayol 35 and Marcol 82.	275
6.16	Damping factor and critical diameter as a function of viscosity ratio.	276
6.17	Mesh sensitivity results for Case 6 (6/2.5 m/s, surfactant-free).	278
6.18	Turbulence model performance for Case 1 (15/2.5 m/s, surfactant-free).	279
6.19	Turbulence model performance for Case 6 (6/2.5 m/s, surfactant-free).	280
6.20	Case 1 (15/2.5 m/s) - Mean diameter profiles.	282
6.21	Case 1 (15/2.5 m/s) - Phase fraction profiles.	282
6.22	Case 2 (15/2.5 m/s) - Mean diameter profiles.	283

6.23	Case 2 (15/2.5 m/s) - Phase fraction profiles. . . . .	283
6.24	Case 3 (15/2.5 m/s) - Mean diameter profiles. . . . .	284
6.25	Case 3 (15/2.5 m/s) - Phase fraction profiles. . . . .	284
6.26	Case 4 (15/2.5 m/s) - Mean diameter profiles. . . . .	285
6.27	Case 4 (15/2.5 m/s) - Phase fraction profiles. . . . .	285
6.28	Case 5 (15/2.5 m/s) - Mean diameter profiles. . . . .	286
6.29	Case 5 (15/2.5 m/s) - Phase fraction profiles. . . . .	286
6.30	Case 6 (6/2.5 m/s) - Mean diameter profiles. . . . .	287
6.31	Case 6 (6/2.5 m/s) - Phase fraction profiles. . . . .	287
6.32	Case 7 (6/2.5 m/s) - Mean diameter profiles. . . . .	288
6.33	Case 7 (6/2.5 m/s) - Phase fraction profiles. . . . .	288
6.34	Case 8 (6/2.5 m/s) - Mean diameter profiles. . . . .	289
6.35	Case 8 (6/2.5 m/s) - Phase fraction profiles. . . . .	289
6.36	Case 9 (6/2.5 m/s) - Mean diameter profiles. . . . .	290
6.37	Case 9 (6/2.5 m/s) - Phase fraction profiles. . . . .	290
6.38	Case 10 (6/2.5 m/s) - Mean diameter profiles. . . . .	291
6.39	Case 10 (6/2.5 m/s) - Phase fraction profiles. . . . .	291
6.40	Case 11 (Bayol 35) - Mean diameter and phase fraction profiles. . . . .	292
6.41	Case 12 (Marcol 82) - Mean diameter and phase fraction profiles. . . . .	292
6.42	Case 13 (Marcol 172) - Mean diameter and phase fraction profiles. . . . .	293
7.1	Trailing vortices behind the Rushton impeller blades. . . . .	298
7.2	Multiple reference frames and moving mesh impeller model approaches. . .	307
7.3	Details of the stirred tank employed by Fischer. . . . .	308
7.4	Layout of the stirred vessel computational mesh. . . . .	309
7.5	Location of the rotating reference frame section of the mesh. . . . .	310
7.6	Predicted and measured dispersed phase fraction profiles. . . . .	311
7.7	Predicted and measured bubble mean velocity profiles. . . . .	312
7.8	Predicted and measured bubble mean velocity vectors. . . . .	313
7.9	Phase fraction contours and continuous phase mean velocity vectors. . . .	314



7.10	Phase fraction contours on a plane 10 mm above the impeller plane. . . . .	315
7.11	Phase fraction isosurface at $\alpha_d = 0.05$ in the impeller region. . . . .	316
7.12	Phase fraction contours on a plane -35 mm below the impeller plane. . . . .	317
A.1	Unconditioned and conditioned measurements. . . . .	332
A.2	Phase distribution function and surface normal definition. . . . .	338



# List of Tables

2.1	$k - \epsilon$ turbulence model coefficients. . . . .	94
3.1	Distribution variance as a function of viscosity ratio . . . . .	111
3.2	Coefficients for critical capillary number correlations . . . . .	122
3.3	Coefficients in $f(\lambda)$ model - Eqn (3.40). . . . .	124
4.1	Generic form of the two-phase flow equations. . . . .	152
4.1	Generic form of the two-phase flow equations. . . . .	153
4.2	Normalisation factors for the two-phase flow equations. . . . .	158
4.3	Boundary conditions applied to each equation by boundary type. . . . .	159
4.4	Comparison between Oliveira's and the new algorithm. . . . .	185
4.5	No. of sub-iterations required in the calculation of $U_r$ . . . . .	186
5.1	INPT shear layer experiment summary. . . . .	197
5.2	INPT shear layer experiment mass balance check. . . . .	198
5.3	Computational mesh details. . . . .	203
5.4	Computational mesh details for mesh sensitivity tests. . . . .	203
5.5	Iterations to convergence with and without sub-iterative correction to drag factor (Case 1.2). . . . .	241
6.1	Ryoto SE surfactant properties. . . . .	255
6.2	Summary of the pipe-mixer experimental cases. . . . .	256
6.3	Mesh sizes for pipe-mixer calculations. . . . .	257
E.1	Coefficients for the error function approximation. . . . .	354



# Nomenclature

## Greek

$\alpha$	Phase Fraction.
$\beta$	Parameter in $C_t$ model.
$\dot{\gamma}$	Local shear rate.
$\Gamma$	Interfacial surfactant concentration.
$\Gamma_\infty$	Fully saturated interfacial surfactant concentration.
$\epsilon$	Turbulent kinetic energy dissipation rate; Elasticity modulus.
$\eta$	Drag function in $C_t$ model; Flow type parameter.
$\kappa_v$	Von Karman's constant.
$\lambda$	Viscosity ratio; Under-relaxation factor.
$\lambda_k$	Kolmogorov eddy size.
$\mu$	Dynamic viscosity.
$\mu^t$	Turbulent dynamic viscosity.
$\nu$	Kinematic viscosity.
$\nu_t$	Turbulent kinematic viscosity.
$\sigma$	Turbulent Prandtl number; Surface tension.
$\Sigma$	Mean surface area per unit volume.
$\hat{\sigma}^2$	Distribution variance.
$\boldsymbol{\sigma}$	Total stress tensor.
$\boldsymbol{\sigma}^t$	Reynolds stress tensor.
$\tau_b$	Droplet break-up time-scale.
$\tau_w$	Wall shear stress.
$\boldsymbol{\tau}$	Viscous shear stress tensor.
$\Phi$	Surface dilatational elasticity.
$\chi_k$	Phase indicator function.

---

$\psi$	Largest droplet diameter subject to break-up.
$\Psi$	Departure of surface concentration from equilibrium.
$\omega$	Oscillation frequency.
$\omega^*$	Resonance frequency.
$\Omega$	Capillary number.
$\Omega_c$	Critical Capillary number.

## Roman

$a$	Bulk half-saturation surfactant concentration.
$A$	Area.
$A_d$	Drag force coefficient - Equation (2.8).
$\mathbb{A}$	Central or neighbour coefficient.
$C, c$	Bulk surfactant concentration.
$C_d$	Dimensionless drag coefficient.
$C_l$	Dimensionless lift coefficient.
$C_t$	Response coefficient.
$C_{vm}$	Dimensionless virtual mass coefficient.
$d$	Diameter.
$d_c$	Critical droplet diameter.
$\mathbf{d}_n$	Relative position of neighbouring node.
$D$	Surfactant laminar diffusion coefficient.
$\frac{D_k}{Dt}$	Phasic substantive derivative.
$F$	Damping factor; Drag force coefficient.
$\mathbb{F}$	Cell face flux.
$\mathbf{F}$	Total force vector.
$\mathbf{F}_b$	Basset force.
$\mathbf{F}_d$	Drag force.
$\mathbf{F}_l$	Lift force.
$\mathbf{F}_p$	Interfacial pressure force.
$\mathbf{F}_{vm}$	Virtual mass force.
$\Delta F$	Additional damping factor due to surfactant.
$\mathbf{g}$	Gravity vector.
$G$	Turbulent kinetic energy generation rate.
$H$	Parameter in Frumkin isotherm.
$\mathbb{H}()$	Neighbour coefficients plus explicit sources.

$\mathbf{I}$	Unit tensor.
$I$	Turbulence intensity.
$k$	Turbulent kinetic energy.
$K$	Critical amplitude parameter.
$M_\gamma$	$\gamma$ 'th distribution moment.
$n$	Droplet number density.
$\mathbf{n}_k$	Surface normal interior to phase k.
$N$	Number of realisations; Number of fragments after droplet break-up.
$p$	Pressure.
$P(d)$	Probability density function.
$P_e$	Peclet number.
$r, R$	Bubble/particle Radius.
$R$	Universal gas constant.
$\rho$	Density.
$Re$	Reynolds number.
$R_p$	Residual for node 'p'.
$Re_b, Re_p$	Bubble/particle Reynolds number.
$Re_t$	Turbulence Reynolds number.
$Sh$	Sherwood number.
$S_k$	Two-phase source terms in turbulent kinetic energy equation; Surface propagation speed.
$S_p$	Implicit part of source term.
$S_u$	Explicit part of source term.
$S_\epsilon$	Two-phase source terms in T.K.E. dissipation rate equation.
$\mathbf{S}_f$	Cell face area vector.
$S_\gamma$	Intensity of dispersion.
$t, T$	Time; Temperature.
$t_p$	Particle response time.
$\mathbf{u}$	Velocity vector.
$\mathbf{u}_r$	Relative velocity vector = $\mathbf{u}_c - \mathbf{u}_d$ .
$\mathbf{v}_i$	Interface velocity vector.
$V, \Delta V$	Volume.
$We$	Weber number.
$We_c$	Critical Weber number.
$y$	Parameter in Frumkin isotherm = $\Gamma/\Gamma_\infty$ .
$y^+$	Normalised distance to the wall.
$Z_\phi$	Normalised residual sum for equation $\phi$ .

## Subscripts

$k$	Pertaining to phase $k$ .
$c$	Pertaining to the continuous phase.
$d$	Pertaining to the dispersed phase.
$s$	Pertaining to the solid dispersed phase.
$l$	Pertaining to the liquid continuous phase.
$i$	Pertaining to the phase interface.
$m$	Pertaining to the mixture.
$\phi$	Pertaining to equation $\phi$ .
$\alpha$	Pertaining to the phase fraction.
eq	Equilibrium value.
eff	Effective value.

## Superscripts

'	Phasic fluctuation.
"	Surface fluctuation.
$t$	Turbulent.
$T$	Transpose.
$o$	Old or previously calculated value.
$n$	Newly calculated value.
*	Intermediate value.

## Averaging Operators

$\overline{\phi}$	Ensemble averaged quantity.
$\overbrace{\phi}^{\Sigma}$	Surface average quantity.



# Chapter 1

## Introduction

### 1.1 Two-phase Flow

Multi-phase flows are the rule rather than the exception in both natural and industrial fluid flow processes. Many diverse industries, including the chemical, aerospace, nuclear, water and transport, frequently encounter flows with more than one phase<sup>1</sup>. The analysis and understanding of these flows is of paramount importance if these processes are to be optimally and safely designed and controlled.

The term ‘multi-phase flow’ covers an extremely wide range of flow patterns and regimes. It is useful to subdivide these into a small number of readily identifiable classes. Multi-phase flows are generally categorised first by the physical states of the constituent components and then by the topology of the interfaces [1]. Thus, a two-phase flow can be classified as gas-solid, gas-liquid, liquid-solid or, in the case of two immiscible liquids, liquid-liquid. Similarly, the flow can be broadly classified topologically as separated, dispersed or mixed. Separated flows include free surface flows, such as stratified flows in ducts, where both phases are separated by one continuous interface. Dispersed flows are characterised by the fact that one of the constituent phases exists in the form of particles, droplets or bubbles, each of which is suspended within a continuous phase. Transitional flows, as the name suggests, represent flows which come somewhere between separated and dispersed. Figure 1.1 shows these regimes and some of the sub-regimes which can be identified within each.

The classification of the flow according to the topology of the interfaces is considerably more difficult than classification by the physical states of the constituents since the transformation between broadly identifiable states is continuous and identification of intermediate

---

<sup>1</sup>The term ‘phase’ is used generically in this work to denote one discrete component of a flow involving substances in different physical states (i.e. gas, liquid or solid) or two or more immiscible liquids.





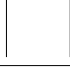
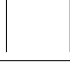
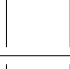
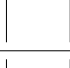

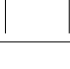
Class	Typical Regimes	Geomery	Configuration
Separated Flows	Film Flow		Liquid film in gas Gas film in liquid
	Annular Flow		Liquid core and gas film Gas core and liquid film
	Jet Flow		Liquid jet in gas Gas jet in liquid
Mixed or Transitional Flows	Slug or Plug Flow		Gas pocket in liquid
	Bubbly annular Flow		Gas bubbles in liquid film with gas core
	Droplet Annular Flow		Gas core with droplets and liquid film
	Bubbly Droplet Annular Flow		Gas core with droplets and liquid film with gas bubbles
Dispersed Flows	Bubbly Flow		Gas bubbles in liquid
	Droplet Flow		Liquid droplets in gas
	Particulate Flow		Solid particles in gas or liquid

Figure 1.1: Topological classification of two-phase flows : Ishii (1975).

states is largely subjective. The transition between states may be heavily dependent on many factors including geometry, flow rate, flow direction, surface tension, etc. In addition, more than one flow pattern may exist in different regions within a given apparatus. For example, in the case of gas-liquid flows, many workers have tried to define the entire range of flow patterns encountered in vertical and horizontal tubes. Nearly one hundred different flow patterns have been identified for this situation [2], although many of these merely delineate minor differences between the most common flow patterns, which are illustrated in Figure 1.2.

In an attempt to quantify the main flow patterns and the transitions between them, many workers have used experimental observations to infer two-dimensional ‘flow pattern maps’ which relate the flow pattern most likely to be encountered to specific properties of the flow. The simplest of these, such as the Baker map for horizontal flow [3] or the Hewitt and

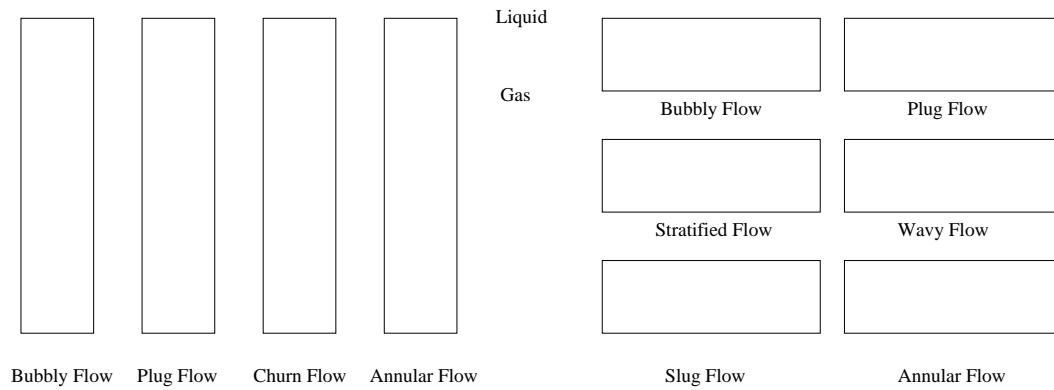


Figure 1.2: Flow patterns for gas-liquid flow in a tube : Whalley (1996).

Roberts map for vertical upflow [4], use the same axes for all flow patterns and transitions and involve a single map, as shown in Figure 1.3. More complex maps, such as the Taitel and Dukler map for horizontal flow [5], involve multiple maps, each using different flow parameters as axes, for different transitions.

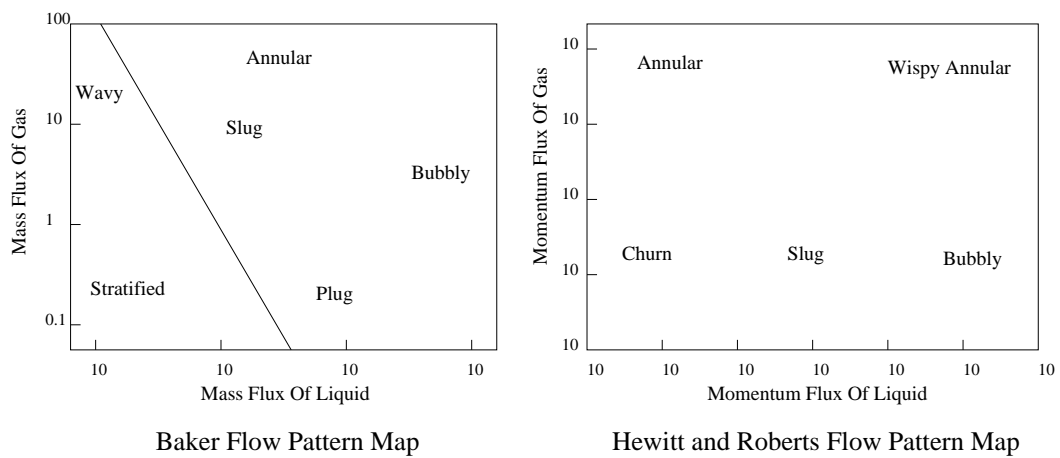


Figure 1.3: The Baker and Hewitt-Roberts flow maps.

The main drawback with flow pattern maps is that they are only useful for the exact situation for which they have been derived and cannot be used to accurately predict the flow pattern for situations outside of the studied range. Also, it should be noted that although the maps show the different flow patterns as discrete and separated by a thin line, the transition between them actually occurs gradually over a range of flow rates thus

reducing their utility.

Despite the wide variety of combinations of phases and flow regimes encountered in multi-phase flows, they are all in fact governed by the same fundamental conservation laws of mass, momentum and energy. The development of predictive techniques for fluid flow processes based on these fundamental laws is part of a general trend in the move away from empirical correlations based on experimental data to more generally applicable and accurate mathematical models of engineering systems. Such techniques can be used with more confidence in regions outside those studied experimentally and can be used to predict dynamic as well as static behaviour.

Research into multi-phase flow predictive methods has really only been undertaken in earnest in the last 20 years with the advent of the digital computer and CFD (Computational Fluid Dynamics) techniques for the numerical prediction of fluid flow. In many ways the field can still be said to be in its infancy. Progress is hampered by the wide variety of flow patterns and the lack of a detailed understanding of the micro- and macroscopic physical processes underlying them. The wide variety of flow patterns has necessitated the development of techniques applicable to a limited subset of the many possible configurations. A completely general procedure for the calculation of multi-phase flows is still some way off.

The dispersed two-phase flow regime is perhaps the most important regime to industry, especially for industrial chemical processes. For example, this regime is encountered in liquid-liquid extraction, polymer and paint production, emulsification and water purification processes. Since the development of a completely general two-phase flow predictive method is currently not practical, the present work focuses on the development of a technique applicable to dispersed two-phase flows.

A previous study [6] was successful in providing a method for the prediction of dispersed solid-liquid flows in industrial stirred tank reactors. The present work modifies and extends that technique considerably to make it generally applicable to dispersed solid-liquid, liquid-liquid and gas-liquid systems. The extension of a method originally developed for solid-liquid flows is not trivial due to the considerable increase in the complexity of the system.

In particular, turbulent liquid-liquid and gas-liquid flows are characterised by the fact that the individual droplets or bubbles are often broken up into smaller entities due to high shear rates in the continuous phase or due to impaction with a solid surface or with other bubbles or droplets. Similarly, coalescence can occur when two droplets or bubbles collide with each other forming a larger entity. Such effects can lead to a wide variation of droplet or bubble sizes, which can in turn have a significant effect on the behaviour of the dispersed phase. Such effects can be heavily influenced by the presence of impurities

or surface-active agents ('surfactants') or by the rheology of the dispersed and continuous phases.

Indeed, it is the fact that such systems exhibit break-up and coalescence that causes them to be used so widely in the chemical process industries. Emulsification processes, for example, where two immiscible liquids are mixed to produce an emulsion of very fine droplets are very common in the food, paint and chemical industries. A predictive technique which did not predict the droplet or bubble size distribution would be of limited use in these cases.

In addition, the flexibility or mobility of the interface in gas-liquid and liquid-liquid systems, coupled with the fact that the overall shape of the droplet or bubble can change, means that the forces governing the interaction between the dispersed phase and continuous phase are highly non-linear. Most notably, the drag force experienced by the droplet or bubble due to the relative motion of the continuous phase varies considerably from that for solid particles. Such non-linear effects introduce considerable complexities into the development of a stable and accurate computational solution method for such flows.

The present research encompasses the development of the mathematical model for dispersed two-phase systems, the assembly of suitable sub-models which are required in order to provide a closed equation set and the development of a computational solution algorithm for these equations. The research also includes the integration of an advanced technique for the modelling of break-up and coalescence processes into the overall method and the development of a two-phase flow turbulence model. The resulting method represents a powerful predictive technique which is applicable to a wide range of dispersed two-phase situations.

In order to validate the procedure, it is applied to three cases which have been studied experimentally. These cases provide a stringent test of the physical modelling and computational algorithm parts of the method. First, the method is applied to the bubbly two-phase gas-liquid flow in a ducted plane shear layer. Here, bubbles are introduced into one or both of two upward flowing inlet streams, one of which has a higher velocity than the other. The resulting shear layer and turbulence generation produce a distinctive phase distribution profile due to the existence of strong lateral forces on the bubbles.

Second, the method is applied to the turbulent oil-water flow in an co-axial pipe-mixer device where the oil droplets undergo break-up due to the high turbulence levels. Such devices are common in the chemical industry and consists of a central high-speed jet and an outer annular inlet flow within a tube. The effects of surfactants in the continuous phase and the effects of the viscosity of the dispersed phase are investigated.

Finally, the method is applied to the air-water bubbly flow in a stirred tank reactor of the

type commonly used for fermentation in the biochemical industry. This cases utilises a commercial CFD program which allows the simulation of flows in a completely arbitrary geometry. A novel technique using multiple inertial reference frames is used to accurately model the impeller.

## 1.2 Objectives Of The Present Research

The research presented in this thesis formed part of a large research project<sup>2</sup> carried out under the auspices of the EEC BRITE/EURAM programme. This project involved several companies in the chemical industry, several academic institutions and a commercial CFD software company. The overall aim of this project was to produce validated predictive methods, eventually to be embodied in a commercial CFD code, for the design of two-phase chemical processes.

There were many aspects to this project, including theoretical studies into local physical effects and experimental studies to provide suitable data for validation purposes. The present research was aimed at the formulation of a general purpose predictive procedure for two-phase flows into which models of the local physical effects, developed by other participants in the project, could be integrated.

The theoretical studies undertaken by the other participants were principally aimed at investigating the many different break-up and coalescence mechanisms frequently encountered in two-phase flows of engineering interest. Notably, the effects of surfactants and dispersed phase viscosity on the break-up process were studied extensively. These investigations culminated in the formulation of suitable mathematical models which could be integrated into the general purpose two-phase flow predictive procedure outlined in this thesis.

The principle objectives of the present research are summarised as follows:-

- The derivation of the appropriate mathematical representation of the dispersed two-phase flow conservation equations.
- The assembly of suitable physical models required to complete the two-phase flow equation set. Such models included those describing drag, lift, virtual mass and turbulence effects for solid-liquid, liquid-liquid and gas-liquid systems.
- The integration into the two-phase framework of a novel technique for taking into

---

<sup>2</sup>Project number BE 4098—‘The development of validated predictive models for the optimal design of multi-phase chemical processes’.

account droplet break-up and coalescence in two-phase flows, including the effects of surfactants and dispersed phase viscosity.

- The development and implementation of a robust and efficient numerical solution algorithm to yield accurate solutions to the assembled equations.
- The extensive validation of the method against a wide variety of experimental data.

### 1.3 Present Contribution

The present work contains contributions towards all of the above objectives:-

- A review and analysis of the available two-phase mathematical model formulation techniques, including an extensive investigation into the implications of the various averaging techniques available.
- The derivation of the two-fluid mass and momentum conservation equations using a conditioned ensemble-averaging technique.
- A review of the current models for the interfacial momentum transfer terms appearing in the two-phase momentum equations, and the evaluation and selection of appropriate models for dispersed solid-liquid, gas-liquid and liquid-liquid systems.
- The derivation of the fundamental conditional-averaged Reynolds stress, turbulent kinetic energy and turbulent kinetic energy dissipation rate equations.
- The formulation of a two-equation two-phase turbulence model based on the conditional averaged equations for the turbulent kinetic energy and its dissipation rate.
- The development of a novel solution technique involving the sub-iterative updating of the drag coefficient to cope with the highly non-linear effects of the drag force in gas-liquid systems.
- The extensive validation of the final model against diverse experimental data for gas-liquid and liquid-liquid systems, including air-water bubbly flow in a ducted shear layer, the break-up of oil droplets in an in-line mixer device under the influence of surface-active agents and varying droplet viscosity, and the air-water bubbly flow in a stirred tank reactor using an advanced impeller modelling technique.

## 1.4 Thesis Outline

The remainder of this chapter contains a overview of the available techniques which may be used to analyse two-phase flow systems. The relative merits of each approach are discussed and reasons given for the final adoption of the ‘multi-fluid’ approach in which averaged Eulerian transport equations for mass, momentum and energy for each phase are employed. The need for, and the nature of, the averaging process applied to the local conservation equations to yield the final averaged equations is discussed. Finally, the two-phase conservation equations for mass and momentum which form the basis of this work are then derived using a conditioned ensemble averaging technique.

The first part of Chapter 2 then goes on to discuss the models for the interfacial transfer terms which appear in the momentum conservation equations for each phase. These terms represent the coupling between the phases due to the transfer of momentum. Models for the drag, lift and virtual mass forces and for the interfacial pressure on the surface of the dispersed phase are presented.

The effects of turbulence are then considered in the latter part of Chapter 2. An extensive review of previous work in the area of two-phase turbulence modelling is given, followed by the derivation of the fundamental conditional-averaged turbulence transport equations which form the basis of the turbulence modelling adopted in this work. Next, the modelling of the various correlation terms in the turbulence transport equations and the Reynolds stress term in the continuous phase momentum equation is described. Finally, the modelling of the Reynolds stress terms in the dispersed phase momentum equations is discussed.

Chapter 3 describes the framework used to integrate the effects of droplet/bubble break-up and coalescence into the overall method. The basis of the framework and the modifications required to make it as widely applicable as possible are described. Finally, the sub-models used for the break-up and coalescence of droplets for various flow regimes and the effects of surfactants and droplet viscosity are described in detail.

Chapter 4 presents the numerical solution techniques developed to solve the two-phase flow equations. An detailed description of the finite volume discretisation technique adopted in this work is given followed by an extensive review of previous work in the field of two-phase solution algorithms. The derivation of a solution algorithm which relies on the sub-iterative updating of the drag coefficient is then described in detail.

The next three chapters present validation studies where detailed comparisons between the predictions and experimental data are made and the overall performance of the model is assessed. The first of these studies, in Chapter 5, concerns the air-water bubbly flow



in a plane ducted shear layer. Chapter 6 is concerned with the break-up of oil droplets in an co-axial pipe-mixer device under the influence of surfactants and different droplet viscosities. Chapter 7 presents the results for the air-water bubbly flow in a stirred tank reactor stirred by a Rushton (flat blade) turbine.

Finally, Chapter 8 summarises the main findings of this research and various outstanding issues are identified which could form the basis for further work in this area.

## 1.5 Review Of Two-Phase Flow Analysis Techniques

The equations governing single-phase flows, the so-called Navier-Stokes equations, have been known for more than a century. Despite intensive research, direct analytical solutions to these equations are not available, except for a very limited number of special cases. Since digital computers first became widely available in the 1960's, the analysis of single-phase flows have increasingly been carried out numerically using a range of techniques which together form the field known as Computational Fluid Dynamics (CFD). Here, the Navier-Stokes equations are solved numerically to yield values for the flow variables of interest, such as velocity, pressure, temperature, etc, at discrete points within the region of interest; the so-called 'flow domain'.

Typically, a CFD analysis starts with the definition of the geometry of the flow domain. This stage consists of specifying the overall boundaries of the domain and then sub-dividing it into many non-overlapping control volumes or cells. Each cell defines the position of the point at which the flow variables will be calculated. Next, the equations governing the fluid flow within the flow domain are selected and initial and boundary conditions are specified. These equations are then discretised using the previously defined control volumes to yield a series of non-linear algebraic equations relating to the discrete points within the flow domain. These equations are then solved using a suitable procedure to yield the numerical solution to the governing Navier-Stokes equations. The final stage of a CFD analysis consists of extracting the relevant information from the solution.

CFD techniques are constantly being refined and extended and significant progress has been made in the last 10 years. Present techniques allow the simulation of a wide variety of fluid flow situations including subsonic, trans-sonic and supersonic flows, laminar and turbulent regimes, and with additional phenomenon such as combustion and chemical reaction. Further, and of particular importance for engineering applications, the methods are now applicable to arbitrarily complicated geometries. Current CFD software packages provide a powerful and easy-to-use environment in which the CFD simulations may be prepared, run and analysed. The wider availability of such packages, and their increasing

range of applicability and ease of use, has meant that CFD simulations have become commonplace in industry, especially in the early stages of the design process where the cost benefits are greatest.

The ability to simulate multi-phase flows is an important addition to the arsenal of CFD techniques and increases its range of applicability to flows of engineering interest considerably. The first problem in the CFD analysis of two-phase flow systems is how to represent the multi-phase nature of the flow in a suitable mathematical form which embodies the principles of conservation of mass, momentum and energy.

At the most fundamental level, a multi-phase flow is a combination of many single-phase flow regions, each region delimited by the interface between the constituent phases or by the physical boundaries enclosing the flow. In principle it is possible to simulate the flow by the numerical solution of the local conservation equations of mass and momentum within each phase, taking into account the instantaneous position of the phase interfaces and the smallest length and time scales of the flow. However, since the interfaces between phases are mobile, often highly distorted and tightly coupled with the local flow conditions, this approach requires detailed calculations of the flow within each phase, and the dynamic calculation of the phase interface motion based on the local flow conditions.

In the past, this ‘direct simulation’ approach has not been adopted because it poses significant numerical problems and requires substantial computing resources. Recent advances have started to address some of these issues and, while this technique is still in its infancy, it has now started to be applied to the study of free surface flows [7], droplet break-up and coalescence and the motion of large bubbles [8]. For the turbulent flows usually encountered in industry, the direct simulation of the turbulent flow within a single phase region is currently too expensive due to the wide range of velocity and length scales typically found in such flows. It has only recently become possible to calculate simple turbulent flows with a transitional Reynolds number [9], and even then such calculations require excessively large computing resources.

It is doubtful that these direct simulation techniques will become widespread in industrial applications in the near future; the utility of these approaches at the moment lies in the validation and development of simpler, general models of turbulence and two-phase interaction models.

In any case, the level of detail produced by such calculations is not necessary, or even desired, in general engineering situations. The engineer is generally only interested in the ‘average’ properties of the flow, such as the mean velocity, mean pressure or phase fraction. For most purposes of equipment or process design, the average or macroscopic flow information is sufficient; turbulent fluctuations, or the two-phase details of the flow

need be accounted for only to the extent that they affect the mean flow properties [10]. Practical simulations of turbulent or two-phase flows are therefore most frequently carried out using conservation equations which describe the mean properties of the flow. These equations are derived from the fundamental microscopic (Navier-Stokes) equations by applying a suitable averaging procedure [1, 11].

The process of averaging the microscopic equations results in the introduction of statistical correlation terms into the averaged equations. These terms represent the effects of the turbulence or two-phase details on the mean properties. These terms have to be modelled so that they can be calculated from known quantities. For single-phase turbulent flows, this process is well established [9, 11]. In the two-phase case, however, the matter is more complicated because there are several ways in which the mathematical description of the flow can be formulated, and the exact form chosen depends on the physical nature of the flow situation under consideration and the nature of the information required.

For dispersed two-phase flows it is possible to formulate a mathematical description of two-phase flow by either treating each discrete particle separately, where the motion of each is governed by its own equation of motion—the so-called Lagrangian approach—or by averaging the microscopic equations governing each phase to obtain macroscopic conservation equations which are valid throughout the entire flow domain—the Eulerian approach [1, 12, 13]. In the next two sections, each approach is briefly described and the advantages and disadvantages of each are discussed.

### 1.5.1 Lagrangian Approaches

In the Lagrangian approach, individual dispersed phase ‘elements’ (i.e. particles, droplets or bubbles) are tracked through the flow domain. The conservation equations of momentum and energy for each element are expressed in a co-ordinate frame of reference which follows its trajectory. The conservation equation of momentum for a particle is called the particle equation of motion. This equation simply relates the rate of change of the particle’s velocity to the sum of forces acting upon it.

$$\rho_d \frac{d\mathbf{u}_d}{dt} = \sum \mathbf{F} \quad (1.1)$$

where  $\mathbf{u}_d$  = Velocity of dispersed phase element.

$\rho_d$  = Dispersed phase density.

$\mathbf{F}$  = Individual forces acting on the particle.

Despite the apparent simplicity of this equation, the nature of the forces acting on indi-

vidual particles in a complicated flow are still not fully understood and have received the attention of many workers, including Stokes [1851], Basset [1888], Oseen [1927], Tchen [14], Maxey and Riley [15] and Auton [16]. The commonly accepted Lagrangian equation governing the motion of a particle at low Reynolds numbers reads [17]

$$\begin{aligned}
m_p \frac{d\mathbf{u}_d}{dt} = & m_p F_d(\mathbf{u}_c - \mathbf{u}_d) + \\
& m_f \frac{D\mathbf{u}_c}{Dt} + \\
& \frac{1}{2} m_f \left( \frac{D\mathbf{u}_c}{Dt} - \frac{d\mathbf{u}_d}{dt} \right) + \\
& 6r^2 (\pi \rho_c \mu)^{\frac{1}{2}} \int_{t_{po}}^{t_p} \frac{d/dt(\mathbf{u}_c - \mathbf{u}_d)}{(t_p - \tau)^{\frac{1}{2}}} d\tau + \\
& \mathbf{g}(m_p - m_f)
\end{aligned} \tag{1.2}$$

- where
- $d/dt$  = Derivative with respect to time following the moving particle.
  - $D/Dt$  = Total acceleration of the continuous phase as seen by the particle.
  - $\mathbf{u}_d$  = Velocity of dispersed phase particle.
  - $\mathbf{u}_c$  = Velocity of continuous phase.
  - $\mathbf{g}$  = Gravity.
  - $m_p$  = Mass of particle.
  - $m_f$  = Mass of fluid displaced by particle =  $m_p(\rho_c/\rho_d)$ .
  - $r$  = Particle radius.
  - $F_d$  = Drag force exerted on particle due to relative motion.
  - $\mu$  = Dynamic viscosity of the continuous phase.
  - $\rho_d$  = Density of the dispersed phase.
  - $\rho_c$  = Density of the continuous phase.
  - $t_p$  = Particle response time.

The terms on the right hand side of the above equation represent the viscous and pressure drag forces, the force due to the fluid pressure gradient and viscous stresses, the inertia force of added mass, the viscous force due to unsteady relative motion (the Basset force) and the buoyancy force respectively. One of the main advantages of the Lagrangian approach lies in the direct physical interpretation of these inter-phase forces on the motion of the dispersed phase.

Another significant advantage of the Lagrangian approach is that since there is one equation of motion for each particle, it is relatively easy to account for a distribution of particle sizes. Also, in gas-liquid and liquid-liquid systems, where the bubbles or droplets can break up into two or more smaller fragments or coalesce into a larger entity, the Lagrangian ap-

proach can be easily applied.

The strategy of a Lagrangian analysis of two-phase flow is usually to follow a sufficient number of particles individually through the flow domain by solving the above equation for each one. The calculated trajectories of the particles are then used to obtain information regarding the average nature of the flow, such as the dispersion coefficient, the deposition rate of droplets on a surface or the local volume fraction.

The matter is complicated somewhat by the fact that the continuous and dispersed phases are closely coupled; the continuous phase flow influences the motion of the individual particles and the particles in turn influence the flow of the continuous phase. The motion of the continuous phase is invariably described using an Eulerian framework, where the flow parameters are related to a fixed co-ordinate reference frame (i.e. one that does not move with the flow), yielding descriptions of the flow parameter ‘fields’ throughout the entire flow domain (e.g. the pressure field  $p(x, y, z, t)$ ).

For turbulent flows, the wide range of length and time scales precludes the direct numerical solution of the governing equations for the continuous phase, at least for flows of engineering interest [11]. In such cases a suitable averaging procedure is applied to the continuous phase flow equations, resulting in equations describing the average nature of the flow and the statistical nature of the turbulence. The averaging of the continuous phase removes some of the detail of the flow field surrounding each element which has to be reintroduced via modelling. In particular, the random effects of continuous phase turbulence have to be taken into account in the trajectory of the individual elements although only statistical data is available describing the local turbulence structure. In these situations, use is made of random number (Monte-Carlo) methods [18, 19, 20].

The coupling between the continuous phase and the dispersed phase is often tackled in the solution procedure by using a two-step iterative approach. Here, the continuous phase flow is determined at a particular instant in time after which the motion and position of the individual dispersed phase elements are updated according to the newly calculated continuous phase flow. The exchange of momentum between phases is evaluated between steps so that it can be included as sources or sinks in the subsequently solved equations for the other phase. The sequence is repeated until sufficient data on the motion of the dispersed phase has been gathered [20].

For sufficiently dilute suspensions, where the particle size is small, the influence of the dispersed phase on the motion of the continuous phase can be neglected, so the coupling is then one-way. The continuous phase flow may then be calculated separately and the motion of the dispersed phase superimposed onto it.

In any case, the Lagrangian equation of motion for each particle is formulated and solved

yielding the trajectory of that particle through the flow domain. The initial conditions of each particle are, in general, not well known and have to be specified statistically using Monte-Carlo methods. The solution yields detailed information for each element, such as its position at any point in time and its velocity and acceleration.

However, problems arise with the Lagrangian approach when the system of interest contains many particles. The first problem is that since there is one equation of motion for each particle the problem may become computationally too large to allow the trajectory of every particle to be calculated. Many particle trajectories are required in order to obtain meaningful information on the average nature of the flow. For example, a typical stirred vessel (say with a volume of  $6 \text{ m}^3$ ) with particles of 1mm diameter at a volume fraction of 1% contains approximately  $10^8$  particles. In such cases, a representative sample of particles trajectories are calculated and the overall flow properties inferred from these. Secondly, for high to moderate phase fractions, the increased coupling between the particles and the continuous phase can introduce numerical stability problems [20].

The Lagrangian approach has successfully been applied to low volume fraction solid-gas dispersed flows such as particle laden jets (see for example Durst, Milojevic and Schonung [18]) or fuel injection systems (see for example Gosman and Ioannides [19] and Kralj [20]).

### 1.5.2 Eulerian Approaches

In the Eulerian approach, both the continuous and dispersed phases are described using Eulerian conservation equations written in fixed co-ordinates. Each phase is treated as a continuous medium, each inter-penetrating the other, and is represented by macroscopic conservation equations, one set for each phase, which are valid throughout the entire flow domain. This approach is commonly known as the ‘Two-Fluid’ approach, or when more than two phases are considered, the ‘Multi-Fluid’ approach [1].

The two-fluid conservation equations are derived from the fundamental conservation equations for mass, momentum and energy which govern the behaviour of each phase and which are valid within each phase up to the interface between the phases—the familiar Navier-Stokes equations. The two-fluid conservation equations are obtained by applying a suitable averaging procedure to the entire two-phase system. The resulting mathematical form of the two-fluid equations is similar to the single-phase Navier-Stokes equations but contain extra terms which account for the transfer of mass and momentum between phases.

The two-fluid approach is more general than the Lagrangian approach since the topology and nature of the flow is not explicit in the form of the equations. The effects of individual particles (including their size, shape, velocity, etc) and the inter-phase forces acting on

them are accounted for collectively in the extra inter-phase transfer terms. The two-fluid approach realises the mutual interaction between phases in averaged form and this requires the prescription of the ‘average’ effects of all the particles at a particular point through the introduction of suitable models.

In principle, the two-fluid approach is applicable to the entire range of flow regimes encountered in multi-phase flows, including the separated, dispersed and intermediate regimes. The physical character of the extra inter-phase mass and momentum transfer terms depends heavily on the exact nature of the flow, but the Eulerian approach is only limited by the ability to accurately model these terms, and is not inherently limited to dispersed systems.

The generality of this approach comes at a cost, however, and it’s main disadvantage is the difficulty in prescribing suitable inter-phase models for the flow regime under consideration. The identification of relevant inter-phase forces, such as drag or lift, is not as obvious as in the Lagrangian approach where each is represented by its own term and modelling the effects of many particles in averaged form can add considerable complexity to the modelling process. Similarly, the derivation of models which are applicable to flows which are between well defined regimes, or where the regime varies in different parts of the flow, can be extremely complex and the physical understanding of these situations may not be sufficiently well developed.

However, the two-fluid approach is frequently more efficient than the Lagrangian approach, since individual dispersed phase elements are not tracked and the calculations are not restricted to the transient case. The two-fluid equations for both phases are discretised using the same computational mesh and are often solved using similar techniques to those employed for single-phase flow but suitably extended to account for the coupled nature of the flow. Importantly, this approach allows the numerical problems arising from the coupling between phases to be more easily handled. For these reasons, the two-fluid approach has proven to be popular in the study of two-phase systems and has been adopted as the basis for the present work.

Various simplifications to the generic two-fluid method are possible. One of the most popular is the so-called ‘Drift-Flux’ method where the relative motion between phases is accounted by the use of an empirically specified ‘drift’ velocity. This allows the individual phase conservation equations to be combined to yield a single set of equations written in terms of mixture properties. These models usually have limited applicability.

Some workers have applied the drift-flux model to gas-liquid flows, in particular Wallis [2, 21], but these studies have been one dimensional and are therefore not general enough to be of interest here. For other examples of the use of the drift-flux approach see Zhang,

Rao and Fukuda [22], Alhanati and Shirazi [23] and Hermann, Issler and Keller [24].

Since it is the intention that this work results in a generally applicable two-phase flow prediction method, this work is based on the more general two-fluid approach where the conservation equations for each phase are not combined but are solved individually. However, even within this framework, different two-fluid formulations have been proposed leading to a wide variety in the models reported in the literature. These differences stem from the different approaches to the initial derivation of the two-phase equations and from the subsequent modelling of the extra terms.

There are many choices which can be made in the initial derivation of the two-fluid equations with regard to the averaging of the microscopic equations. As well as the choice of averaging method (for example, time, volume or ensemble averaging) there is also a choice in the number of times that the averaging process is applied. Some workers use a single average while others apply a double average in an attempt to separate the two-phase and turbulence effects [6, 25].

There are also many differences in the modelling of the extra terms resulting from the averaging process. These differences can be due to the specific case under consideration but often are due to the fact that the physical processes involved are not well understood, resulting in a wide variety of interpretations. Significantly, the nature of the averaging procedure itself may strongly affect the form and meaning of the extra terms, which then influences the way in which they are modelled.

Because of the wide variety of practices, a commonly accepted set of fundamental two-fluid equations (i.e. before any modelling is introduced) does not exist. These equations are required before the final model can be assembled by appropriately modelling the extra terms introduced by the averaging process. The following section discusses the choices available in the derivation of the fundamental two-fluid equations with regard to the averaging procedure and reasons are given for the adoption of a single ensemble averaging technique in the present work.

### 1.5.3 Averaging

The microscopic equations may be averaged using volume, time or ensemble averaging. For any scalar or vector quantity  $q$ , these are defined respectively as



$$\bar{q} = \frac{1}{V} \int_V q \, dV \quad (1.3)$$

$$\bar{q} = \frac{1}{T} \int_T q \, dt \quad (1.4)$$

$$\bar{q} = \frac{1}{N} \sum_N q_r \quad (1.5)$$

Here,  $V$  and  $T$  are the volume and time averaging domains,  $N$  is the total number of realisations in the ensemble ( $N \rightarrow \infty$ ) and  $q_r$  is the value of  $q$  for a particular realisation. The time and volume averages have been the most commonly adopted averages in the past due to their direct physical interpretation [26, 27, 6, 25], although later workers have tended to adopt the more fundamental ensemble average [28, 10, 29, 30, 13, 12].

Time and volume averages are subject to certain constraints which must be observed in order that the resulting equations are rigorous and meaningful. The precise definitions of these averages requires that the averaging domains are clearly defined. When applied to two-phase flow, this means that special care must be taken to ensure that the time and length scales of the particles are taken into account as well as the time and length scales of the turbulence [13]. For a meaningful average, the averaging time/volume domain adopted must be larger than the time/length scale of the particles but smaller than the ‘macroscopic’ time/length scales which pertain to the large scale flow features. In some systems, notably gas-liquid flows, the time and length scales associated with the bubbles may become large and approach the macroscopic scale.

For example, for an air-water flow with a typical bubble size of 5 mm and a typical velocity of 1 m/s, the corresponding transit time scale across a point probe is 5 ms. For a meaningful time average, the averaging period should be of the order of several hundred milliseconds, and the macroscopic time scale should therefore be of the order of several seconds. The resulting equations could only strictly be used to model systems displaying relatively slow transient behaviour [13].

Similarly, the adoption of volume averaging introduces restrictions on the spatial resolution of the final equations. These equations, however, would be valid for the analysis of highly transient phenomena since they are ‘instantaneous’ in that they do not involve any time averaging. The adoption of both time and volume averaging, as proposed by some workers to account for two-phase and turbulent effects independently, essentially means that restrictions exist on both the temporal and spatial resolution of the resulting equations.

Following Serizawa and Kataoka [13], if the macroscopic time/length scales are denoted

as  $T_M$  and  $L_M$ , and the averaging time/length scales as  $T$  and  $L$ , and the time/length scales of the dispersed phase particles as  $T_m$  and  $L_m$ , then the following relations must be obeyed.

$$T_M \gg T \gg T_m \quad (1.6)$$

$$L_M \gg L \gg L_m \quad (1.7)$$

This situation is depicted graphically in Figure 1.4. If too small an averaging domain is chosen then the average value is subject to microscopic uncertainty. If the averaging domain is too large, then macroscopic uncertainty is introduced. Only equations derived under the above constraints can be used to predict phenomena of the order of  $T_M$  and/or  $L_M$ .

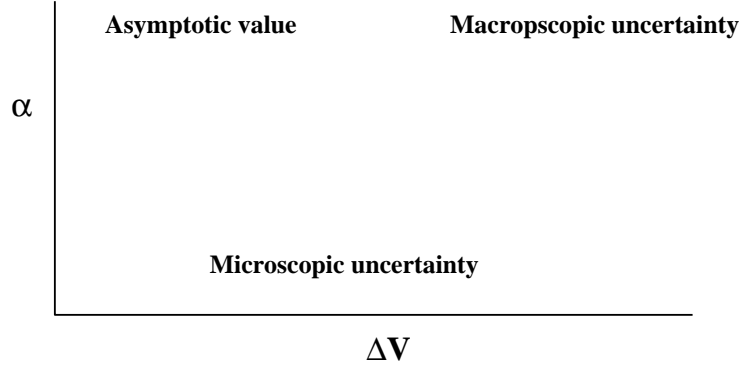


Figure 1.4: Influence of the averaging domain on averaged values.

It is widely recognised that ensemble, or statistical, averaging is more fundamental than time and volume averaging [13]. Indeed, time and volume averages are special cases of ensemble averaging. Ensemble averaging is mathematically rigorous and the resulting equations are valid in infinitesimal time and space domains; there are no restrictions on the temporal or spatial resolution of the final equations.

Despite the mathematical and physical rigour of such an averaging procedure, ensemble averaging has only been adopted by a few workers, although in recent years it has become more popular (in particular see Drew [28, 10], Kataoka [29], Kataoka and Serizawa [30, 13] and Drew and Wallis [12]). Since the ensemble average is regarded as the most general and does not impose any time or space resolution restrictions on the final equations, it is adopted here.

As well as the choice of average, previous derivations of the two-fluid equations differ in the number of times that the equations are averaged. Many workers derived the two-fluid equations by averaging the microscopic equations twice. The first average, usually a volume average, is applied to obtain the ‘instantaneous’ volume-averaged two-phase equations. Since these equations are instantaneous, they are believed to exhibit fluctuations in time due to the effects of turbulence. To obtain a set of equations which are smooth in both space and time, a second average, usually a time average, is applied. Workers who have adopted this approach include Drew [31, 32], Politis [6] and Oliveira [25].

The volume averaging stage introduces the phase volume fractions and correlations between the phase velocity fluctuations into the phase momentum equations. The second average introduces a large number of correlations between the fluctuating volume fraction and the fluctuating phase velocities and other flow quantities such as the pressure. In order to avoid the proliferation of these complex terms, which would be difficult if not impossible to model, many workers define ‘phase weighted’ quantities such as velocity and pressure in a manner akin to that of the Favré density weighted decomposition employed in compressible flows [33] which itself is an extension to the so-called Reynolds, or unweighted, decomposition.

For example, Politis [6] derives the two-fluid equations by applying volume and then time averaging to the microscopic equations. The volume average produces ‘instantaneous volume averaged’ equations involving the volume fraction,  $\alpha_l$  and  $\alpha_s$ , and volume-averaged phase velocities,  $\overline{\mathbf{u}}_l$  and  $\overline{\mathbf{u}}_s$ , where the subscripts  $l$  and  $s$  denote the liquid and solid phases respectively.

To illustrate, the Reynolds decomposition of a fluctuating scalar or vector quantity  $q$  takes the form

$$q = \overline{q} + q' \quad (1.8)$$

where  $\overline{q}$  is the average value of  $q$  and  $\overline{q'} = 0$ . The averaging of terms which contain the product of two fluctuating quantities, say  $\alpha$  and  $q$ , which may similarly be decomposed using Reynolds decomposition, yields

$$\overline{\alpha q} = \overline{\alpha q} + \overline{\alpha' q'} \quad (1.9)$$

The final term represents the correlation between  $\alpha'$  and  $q'$  which would require modelling to obtain a closed equation set. It is possible to avoid the additional correlation term

using a phase fraction weighted decomposition for  $q$  which incorporates the phase fraction fluctuations within the averaging definition itself. Phase fraction weighted decomposition for  $q$  takes the form

$$q = \tilde{q} + q'' \quad (1.10)$$

where, in general,  $\overline{q''} \neq 0$  and

$$\tilde{q} = \frac{\overline{\alpha q}}{\overline{\alpha}} \quad (1.11)$$

The following relationships between weighted and unweighted quantities frequently prove useful (see Politis [6], Appendix A).

$$\tilde{q} = \bar{q} + \frac{\overline{\alpha' q'}}{\overline{\alpha}} \quad (1.12)$$

$$\overline{q''} = -\frac{\overline{\alpha' q'}}{\overline{\alpha}} \quad (1.13)$$

Therefore, the average of the product  $\alpha q$  using Reynolds decomposition on  $\alpha$  and phase fraction weighted decomposition on  $q$  yields, in view of Eqn (1.10),

$$\overline{\alpha q} = \overline{\alpha} \tilde{q} \quad (1.14)$$

which avoids the additional correlation term.

Politis introduced the phase fraction weighted decomposition for the phase velocities after the first volume average. The subsequent time average produced equations in terms of the time averaged volume fraction  $\overline{\alpha}$  and the phase fraction weighted phase velocities  $\tilde{\mathbf{u}}$ . Although many of the possible extra correlation terms were avoided by using this technique, numerous other correlation terms were unavoidably introduced, many of which involved correlations between the fluctuating phase fraction, fluctuating pressure gradient and fluctuating velocities. These terms proved to be difficult to model since the physical difference between unweighted and weighted quantities has to be accounted for during the modelling phase.

Even though the use of a phase fraction weighted decomposition leads to a reduction in the number of extra correlation terms, it could be argued that this benefit is outweighed

by the difficulties in the accurate modelling and physical interpretation of the terms which are introduced. In addition, to maintain consistency, any additional turbulence transport equations (for example, the transport equation for the turbulent kinetic energy) also have to be defined in terms of the phase fraction weighted velocities. Strictly, the derivation of such equations requires the definition of phase weighted turbulence properties and again, while there may be a reduction in the number of terms introduced in the turbulence equations, the physical interpretation and modelling of the phase weighted terms is more complex.

Also, since the behaviour of any model is judged by comparing the results to experimental data, it is important to ensure that the quantities being compared are equivalent [34]. Experimental data may be weighted or unweighted according to the instrumentation used. For example, LDA techniques produce unweighted values while slow response thermocouples or sampling probes produce weighted values. The results from a two-fluid model derived using phase fraction weighted decomposition can only be compared directly with suitable phase fraction weighted experimental data.

Lately, other workers have voiced more fundamental concerns over the validity of the double averaging approach [13, 12]. In general, the dispersed phase particle time and length scales may be of the order of, or greater than, those of the turbulence. Therefore, the definition of suitable averaging domains which are to capture the effects of the two-phase nature of the flow will inevitably capture the effects of the turbulence also. That is, the definition of a volume averaging domain suitable for general turbulent dispersed two-phase flow cannot help but include contributions from the turbulence in the individual phases. It is therefore impossible to separate basic two-phase unsteadiness from turbulence.

It can thus be seen that two-phase and turbulence effects cannot be cleanly separated with valid time or volume averaging domains. It follows that the modelling of the extra terms introduced into the equations becomes more complicated because now we are dealing with correlations between volume averaged and time averaged values which both contain elements of the turbulence.

The essence of the problem is that, in the general case, the volume average and time average domains overlap. To cleanly separate the effects of turbulence from the two-phase effects the averaging domains for the first and second averages must be widely separated so that each does not capture significant effects intended to be captured by the other average. This can only be achieved in the limiting case when the dispersed phase particle size is very much smaller than the turbulent eddy size, so that the volume averaging domain does not contain any significant turbulent velocity fluctuations.

Frequently, workers who have adopted a double averaging procedure neglect the turbulent

stress term resulting from the first volume average and only consider the time average turbulent stress term [6, 25]. Alternatively, they propose that the combination of the two terms may be modelled by assuming that the turbulence due to the particles and the “true” turbulence due to shear may be accounted for by separate models superimposed on each other [35, 36, 37]. Other workers have shown that this approach is only valid in a limiting number of cases [12, 13].

In the more recent past, workers have abandoned double averaging in favour of a single, usually ensemble, average. These include Drew [28, 10], Kataoka [29], Kataoka and Serizawa [30, 13] and Drew and Wallis [12]. They argue that the ensemble average is more fundamental than both the time and volume average and does not introduce any spatial or temporal restrictions into the final equations.

They also argue that a single averaging process suffices because it will capture both the two-phase and the turbulence effects at the same time. The resulting extra terms in the conservation equations represent both effects but, they argue, so do the terms resulting from double averaging. In addition, the number of extra terms introduced is smaller and their physical significance is more apparent which in turn makes their modelling easier.

The basis for the argument that a single ensemble average is sufficient is usually centred around the definition of the phase fraction. In the double averaging technique, a *volume* fraction is first defined which is subsequently decomposed into mean and fluctuating components and time averaged. The resulting terms in the conservation equations contain correlations between the fluctuating volume fraction and other quantities. Usually, proponents of double averaging state that these terms are essential for the prediction of phase dispersion and that their existence in the double averaged equations is an indication of the correctness of the approach; without them the equations would not predict any phase dispersion and would therefore not be physically valid. However, as will be shown in subsequent chapters, this is not the case and dispersion is adequately predicted without the explicit presence of fluctuating volume fraction terms in the conservation equations.

Workers in favour of a single average argue that the correct definition of the phase fraction is one that does *not* fluctuate since, by definition, it is an average quantity. The correct definition of an averaging domain (be it volume, time or ensemble) requires that the averaged quantities are not prone to fluctuations in the domain size or its content. This is equivalent to satisfying the situation shown in Figure 1.4.

To illustrate the point, consider the definition of the phase fraction defined using an ensemble average. The phase fraction  $\alpha$  is defined as the number of times a particular phase is present at a certain point in time and space divided by the total number of realisations.

$$\alpha = \frac{1}{N} \sum \chi_k = \frac{N_k}{N} \quad (1.15)$$

where  $N$  is the total number of realisations,  $\chi_k$  is a phase indicator function which is one when phase  $k$  is present and zero otherwise.  $N_k$  is the resulting number of times phase  $k$  was present at the particular point in time and space. The ensemble average requires that  $N \rightarrow \infty$ . Thus, the resulting phase fraction can be viewed as the *probability* that a certain phase is present at a certain point in space and time. It can be seen that, as such, the phase fraction does not fluctuate.

In view of the above discussion, this work employs a single averaging process whereby the effects of the discontinuities and turbulence are treated at the same time and broadly follows the approach of Dopazo [38], Drew and Wallis [12] and Serizawa and Kataoka [13]. In this approach, not only is the derivation of the conservation equations easier, but the basic flow quantities retain their physical significance and their redefinition in terms of phase fraction weighting is not necessary. The next section describes in detail the derivation of the basic two-phase flow equations used in this work.

## 1.6 Conditional-Averaged Two-Phase Flow Equations

In order to derive conservation equations for each phase valid throughout the flow domain we need to distinguish between the individual phases as we average the local conservation equations. This is achieved by ‘conditioning’ the local equations so that contributions to the averaged conservation equation of one phase come only from regions (in space and time) which contain that particular phase.

Conditioning is provided by multiplying each conservation equation by a phase indicator function,  $\chi_k$ , defined as follows

$$\chi_k(\mathbf{x}, t) = \begin{cases} 1 & \text{Phase } k \text{ present at } (\mathbf{x}, t). \\ 0 & \text{Otherwise.} \end{cases} \quad (1.16)$$

Mathematically, the phase indicator function may be defined in terms of the Heaviside unit step function operating on an imaginary scalar phase distribution function  $f(\mathbf{x}, t)$  which is defined to be zero at the phase interfaces. This enables spatial and temporal derivatives of the indicator function to be clearly defined in terms of the Dirac delta function. Full details are given in Appendix A.

Once the local conservation equations have been conditioned, they are ensemble averaged to yield the final conservation equations. This process is applied to the conservation equations for mass and momentum in the following sections.

### 1.6.1 Conservation of Mass

The local continuity equation reads

$$\frac{\partial \rho}{\partial t} + \nabla \cdot (\rho \mathbf{u}) = 0 \quad (1.17)$$

Conditioning the continuity equation and taking the ensemble average, denoted by an overbar, gives

$$\overline{\chi_k \frac{\partial \rho}{\partial t}} + \overline{\chi_k \nabla \cdot (\rho \mathbf{u})} = 0 \quad (1.18)$$

This may be rearranged to give,

$$\frac{\partial \overline{\chi_k \rho}}{\partial t} + \nabla \cdot (\overline{\chi_k \rho \mathbf{u}}) = \overline{\rho \frac{\partial \chi_k}{\partial t}} + \overline{\rho \mathbf{u} \cdot \nabla \chi_k} \quad (1.19)$$

The temporal derivative of the phase indicator function is directly related to the motion of the interface, via

$$\frac{\partial \chi_k}{\partial t} = -\mathbf{v}_i \cdot \nabla \chi_k \quad (1.20)$$

where  $\mathbf{v}_i$  is the velocity of the interface (see Appendix A). Eqn (1.19) may therefore be rewritten as

$$\frac{\partial \overline{\chi_k \rho}}{\partial t} + \nabla \cdot (\overline{\chi_k \rho \mathbf{u}}) = \overline{\rho (\mathbf{u} - \mathbf{v}_i) \cdot \nabla \chi_k} \quad (1.21)$$

The term on the right hand side is non-zero only on the interface between phases. This term represents the averaged effects of the local interfacial conditions on the mass continuity.

The conditional-averaged phase quantities (that is, the average quantities relating to one particular phase only, sometimes called the ‘phasic’ average) are defined as



$$\overline{\phi} = \frac{\overline{\chi_k \phi}}{\alpha_k} \quad (1.22)$$

where the subscript  $k$  denotes the phase to which the quantity relates<sup>3</sup>,  $\alpha_k$  is the phase fraction and  $\phi$  is the quantity under consideration.

Rewriting Eqn (1.21) in terms of the conditional-averaged quantities, we have

$$\frac{\partial \alpha_k \overline{\rho}_k}{\partial t} + \nabla \cdot \alpha_k \overline{\rho}_k \mathbf{u}_k = \overbrace{\rho_{k_i} (\mathbf{u}_{k_i} - \mathbf{v}_i) \cdot \mathbf{n}_k} \Sigma \quad (1.23)$$

- where
- $\alpha_k$  = Phase fraction of phase  $k$ .
  - $\mathbf{u}_{k_i}$  = Limiting value of velocity of phase  $k$  at the interface.
  - $\rho_{k_i}$  = Limiting value of density of phase  $k$  at the interface.
  - $\Sigma$  = Local average interfacial area density.
  - $\mathbf{n}_k$  = Unit normal vector *interior* to phase  $k$ .

and  $\frown$  represents a surface average (see Appendix A). The quantities  $\mathbf{u}_{k_i}$  and  $\rho_{k_i}$  relate to the values of velocity and density immediately adjacent to the phase interface; the delta function acts to ‘pick out’ these values on the phase  $k$  side of the interface.

The term on the right hand side of Eqn (1.23) represents the effects of the interface behaviour on the local mass balance. For combusting or reacting systems, or those which involve inter-phase mass transfer or phase change, this term represents the surface averaged rate of mass introduction or removal into phase  $k$ . This term may be simplified considerably by decomposing the interface velocity  $\mathbf{v}_i$  into the vectorial sum of the velocity of phase  $k$  at the interface and the surface propagation velocity acting in the direction normal to the interface  $S_k \mathbf{n}_k$  as shown schematically in Figure 1.5.

$$\mathbf{v}_i = \mathbf{u}_{k_i} + S_k \mathbf{n}_k \quad (1.24)$$

Physically, this decomposition shows that the motion parallel to the interface has no effect on the local mass balance; only motion normal to the interface affects the rate of mass transfer between phase. Eqn (1.23) becomes

$$\frac{\partial \alpha_k \overline{\rho}_k}{\partial t} + \nabla \cdot \alpha_k \overline{\rho}_k \mathbf{u}_k = - \overbrace{\rho_{k_i} S_k} \Sigma \quad (1.25)$$

---

<sup>3</sup>Later, when we differentiate between the continuous and dispersed phases, the subscript will become  $c$  or  $d$  as appropriate.

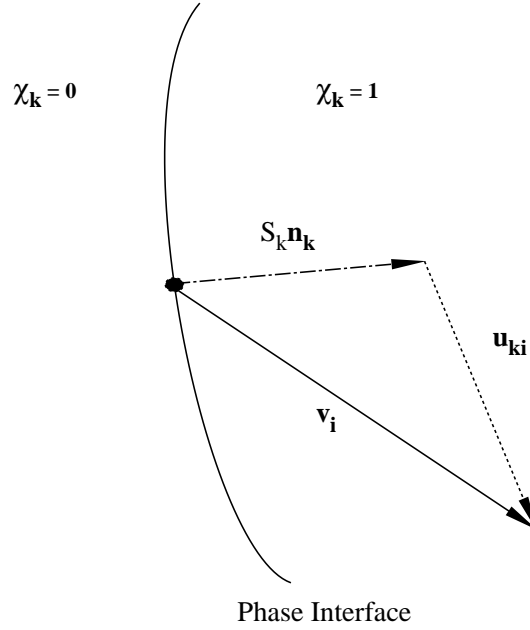


Figure 1.5: Decomposition of the interface velocity.

For flows with passive (i.e. non reacting) interfaces, such as those considered in this work, the velocity of the interface is equal to the velocity of phase  $k$  at the interface and therefore the surface propagation speed  $S_k$  is zero. Similarly, restricting our attention to incompressible phases, Eqn (1.25) becomes

$$\frac{\partial \alpha_k \rho_k}{\partial t} + \nabla \cdot \alpha_k \rho_k \bar{\mathbf{u}}_k = 0 \quad (1.26)$$

Note that if the phases were to be considered compressible, then the phasic velocity  $\mathbf{u}_k$  could be decomposed into a density weighted mean plus a fluctuation as in Favré averaging [33].

### 1.6.2 Conservation of Linear Momentum

The local conservation equation for linear momentum reads

$$\frac{\partial \rho \mathbf{u}}{\partial t} + \nabla \cdot (\rho \mathbf{u} \mathbf{u}) = \nabla \cdot \boldsymbol{\sigma} + \rho \mathbf{g} \quad (1.27)$$

where  $\rho$  = Fluid density.  
 $\mathbf{u}$  = Fluid velocity vector.  
 $\boldsymbol{\sigma}$  = Total stress tensor.

Applying the conditioning and averaging procedure to this equation gives its conditional-averaged form:

$$\begin{aligned} \frac{\partial}{\partial t} \overline{\chi_k \rho \mathbf{u}} + \nabla \cdot (\overline{\chi_k \rho \mathbf{u} \mathbf{u}}) &= \nabla \cdot (\overline{\chi_k \boldsymbol{\sigma}}) + \overline{\mathbf{g} \chi_k \rho} \\ &+ \overline{\rho \mathbf{u} \mathbf{u} \cdot \nabla \chi_k} - \overline{\rho \mathbf{u} \mathbf{v}_i \cdot \nabla \chi_k} - \overline{\boldsymbol{\sigma} \cdot \nabla \chi_k} \end{aligned} \quad (1.28)$$

The last three terms are non-zero only at the interface and represent the transfer of momentum between phases. Introducing the phase conditional averages and the surface average notation, we now have

$$\begin{aligned} \frac{\partial}{\partial t} \alpha_k \overline{\rho_k \mathbf{u}_k} + \nabla \cdot \alpha_k \overline{\rho_k \mathbf{u}_k \mathbf{u}_k} &= \nabla \cdot \alpha_k \overline{\boldsymbol{\sigma}_k} + \alpha_k \overline{\rho_k} \mathbf{g} \\ &+ \overbrace{\rho_{k_i} \mathbf{u}_{k_i} \mathbf{u}_{k_i} \cdot \mathbf{n}_k} \Sigma - \overbrace{\rho_{k_i} \mathbf{u}_{k_i} \mathbf{v}_i \cdot \mathbf{n}_k} \Sigma - \\ &\overbrace{\boldsymbol{\sigma}_{k_i} \cdot \mathbf{n}_k} \Sigma \end{aligned} \quad (1.29)$$

Decomposing the interfacial velocity as in Eqn (1.24), and rearranging gives

$$\begin{aligned} \frac{\partial}{\partial t} \alpha_k \overline{\rho_k \mathbf{u}_k} + \nabla \cdot \alpha_k \overline{\rho_k \mathbf{u}_k \mathbf{u}_k} &= \nabla \cdot \alpha_k \overline{\boldsymbol{\sigma}_k} + \alpha_k \overline{\rho_k} \mathbf{g} - \\ &\overbrace{\rho_{k_i} \mathbf{u}_{k_i} S_k} \Sigma - \overbrace{\boldsymbol{\sigma}_{k_i} \cdot \mathbf{n}_k} \Sigma \end{aligned} \quad (1.30)$$

The phasic velocities may be decomposed into an unweighted mean plus a fluctuation part (i.e. Reynolds decomposition — see Section 1.5.3) whereupon the inertial term on the left hand side gives rise to the so-called turbulent Reynolds stresses. The decomposition is such that the fluctuating velocity is relative to the phase mean velocity  $\overline{\mathbf{u}_k}$ . Assuming incompressible phases with no mass transfer, and denoting the turbulent Reynolds stresses as  $\boldsymbol{\sigma}_k^t$  we have

$$\begin{aligned} \frac{\partial}{\partial t} \alpha_k \rho_k \overline{\mathbf{u}_k} + \nabla \cdot \alpha_k \rho_k \overline{\mathbf{u}_k \mathbf{u}_k} &= \nabla \cdot \alpha_k (\overline{\boldsymbol{\sigma}_k} + \boldsymbol{\sigma}_k^t) + \alpha_k \rho_k \mathbf{g} - \\ &\overbrace{\boldsymbol{\sigma}_{k_i} \cdot \mathbf{n}_k} \Sigma \end{aligned} \quad (1.31)$$

where  $\sigma_k^t = -\rho_k \overline{\mathbf{u}'_k \mathbf{u}'_k}$ .

The total viscous stress  $\overline{\sigma}_k$  may be decomposed into pressure plus deviatoric components

$$\sigma_k = -p_k \mathbf{I} + \tau_k \quad (1.32)$$

where  $\mathbf{I}$  is the unit tensor. Substitution into Eqn (1.31), this gives

$$\begin{aligned} \frac{\partial}{\partial t} \alpha_k \rho_k \overline{\mathbf{u}}_k + \nabla \cdot \alpha_k \rho_k \overline{\mathbf{u}}_k \overline{\mathbf{u}}_k &= -\nabla \alpha_k \overline{p}_k + \nabla \cdot \alpha_k (\overline{\tau}_k + \sigma_k^t) + \\ &\quad \alpha_k \rho_k \mathbf{g} + \overbrace{p_{k_i} \mathbf{n}_k} \Sigma - \overbrace{\tau_{k_i} \cdot \mathbf{n}_k} \Sigma \end{aligned} \quad (1.33)$$

To aid the modelling process in later chapters, it is useful to decompose the interfacial pressure  $p_{k_i}$  into a mean and fluctuating component.

$$\overbrace{p_{k_i} \mathbf{n}_k} \Sigma = \overbrace{p_{k_i}} \overbrace{\mathbf{n}_k} \Sigma + \overbrace{p''_{k_i} \mathbf{n}_k} \Sigma \quad (1.34)$$

Noting that  $\overbrace{\mathbf{n}_k} \Sigma = \nabla \alpha_k$  we obtain

$$\overbrace{p_{k_i} \mathbf{n}_k} \Sigma = \overbrace{p_{k_i}} \Sigma \nabla \alpha_k + \overbrace{p''_{k_i} \mathbf{n}_k} \Sigma \quad (1.35)$$

Substitution into Eqn (1.33) and rearranging yields

$$\begin{aligned} \frac{\partial}{\partial t} \alpha_k \rho_k \overline{\mathbf{u}}_k + \nabla \cdot \alpha_k \rho_k \overline{\mathbf{u}}_k \overline{\mathbf{u}}_k &= -\alpha_k \nabla \overline{p}_k + \nabla \cdot \alpha_k \overline{\tau}_k + \\ &\quad \nabla \cdot \alpha_k \sigma_k^t + \alpha_k \rho_k \mathbf{g} + \\ &\quad (\overbrace{p_{k_i}} - \overline{p_k}) \nabla \alpha_k + \overbrace{p''_{k_i} \mathbf{n}_k} \Sigma - \overbrace{\tau_{k_i} \cdot \mathbf{n}_k} \Sigma \end{aligned} \quad (1.36)$$

Equations (1.26) and (1.36) constitute the basic conditional-averaged two-fluid equation set which are in principle applicable to any two-phase flow with incompressible phases and no mass transfer. The last five terms on the right hand side of Eqn (1.36) represent the transfer of momentum from one phase to the other from phenomena such as drag, virtual mass or lift. These terms, along with the Reynolds stresses which represent the effects of velocity fluctuations, require rewriting in terms of known quantities in order to obtain a closed equation system. The following chapter deals with this issue in detail.

## 1.7 Closure

A mathematical model which could be used to analyse and predict industrial two-phase flows is highly desirable and would represent a significant improvement over previous empirical approaches. A review of available techniques for the derivation of such a model has shown that the Eulerian two-fluid approach is the most appropriate for general engineering flow studies. The two-fluid approach can encompass a wide variety of two-phase flow regimes, is more computationally efficient than the Lagrangian alternative and is more adept at handling numerical problems arising during the solution of the coupled two-phase flow equations.

However, despite research over more than 20 years, a definitive form of this model is not available from the literature. Many differences between workers still exist, especially with regard to the application of the averaging procedure which is required to obtain equations pertaining to individual phases but which are valid throughout the flow domain of interest. Earlier researchers have favoured the application of multiple averages, such as volume averaging followed by time averaging. Excessive and complex correlation terms are avoided by resorting to phase fraction weighted decomposition of the phase velocities. Later studies have tended to adopt a single ensemble average with unweighted velocity decomposition.

In either case, the averaging process introduces extra terms into the phase equations which need to be rewritten in terms of known quantities so that they can be computed. The extra terms are related to the transfer of momentum between phases and to the effects of velocity fluctuations.

This work is based on a conditioned-ensemble technique where the equations are first conditioned by a phase indicator function and then ensemble averaged, once only. It has been shown that such an approach is without the conceptual limitations on applicability that beset other approaches. The extra terms in the resulting equations are more amenable to physical interpretation, which makes their modelling and mathematical form a little less complex.



## Chapter 2

# Two-phase Flow Equation Closure

In the previous chapter, the basic conditional-averaged two-phase flow equations for mass and momentum were presented. These equations contain extra terms representing the effects of inter-phase momentum transfer and the effects of turbulent velocity fluctuations. These need to be modelled in terms of known quantities before a closed equation set can be obtained. In this chapter, the significance of these terms in the context of a dispersed two-phase flow system is evaluated and models for drag, virtual mass and lift effects are described in detail. The effects of turbulence are accounted for using a two-phase turbulence model based on the formal derivation of the conditional averaged  $k - \epsilon$  equations.

### 2.1 Introduction

The conditional averaging process used to derive the two-phase flow equations necessarily results in a loss of detailed information about the local flow conditions and the introduction of additional unknown correlation terms. These extra terms represent the effects of the local flow details on the averaged properties of the flow. The lost information must be restored by the appropriate modelling of these terms so that they can be calculated from known or previously calculated quantities. In the phase momentum equations, two extra terms are introduced which represent the effects of inter-phase momentum transfer and the effects of turbulence.

A generally applicable two-phase flow model which would be valid for any two-phase flow situation, regardless of the flow type or regime, could be formulated if these additional terms could be modelled appropriately. The wide variety of two-phase flow regimes which may be encountered, however, means that general models for these terms are, at present,

virtually impossible to formulate. The lack of detailed experimental data for many of the different flow regimes means that the level of understanding required to formulate generally applicable models does not yet exist.

In this work we are specifically interested in dispersed two-phase flows where one phase exists in discrete regions of space, each completely surrounded by the continuous phase. As discussed in the previous chapter, the dispersed two-phase flow regime can be subdivided into bubbly, droplet and particulate sub-regimes which correspond to gas-liquid, liquid-liquid and solid-liquid flows respectively [1]. Fortunately, each of these sub-regimes has been studied extensively in the past and the resulting data allows models applicable to these regimes to be formulated.

The additional terms resulting from the conditional averaging process comprise the interfacial momentum transfer terms and the phase Reynolds stresses. The phase Reynolds stress terms relate to the effects of velocity fluctuations on the mean transport of the phases. Generally, these velocity fluctuations are as a result of shear induced turbulence, although in two-phase flow factors other than turbulence can also induce velocity fluctuations. These terms are discussed in detail in Section 2.3 when the effects of turbulence on the continuous and dispersed phases are considered.

On the other hand, the interfacial terms relate to the transfer of momentum between one phase and the other due to their relative motion. These terms are not directly related to turbulence, although they may be affected by it. The modelling of these terms is considered in the next section.

## 2.2 Interfacial Momentum Transfer

The basic conditional averaged two-phase flow equations, in the absence of mass transfer and for incompressible phases, read

### Conservation of Mass

$$\frac{\partial \alpha_k \rho_k}{\partial t} + \nabla \cdot \alpha_k \rho_k \bar{\mathbf{u}}_k = 0 \quad (2.1)$$

### Conservation of Linear Momentum

$$\begin{aligned} \frac{\partial}{\partial t} \alpha_k \rho_k \bar{\mathbf{u}}_k + \nabla \cdot \alpha_k \rho_k \bar{\mathbf{u}}_k \bar{\mathbf{u}}_k &= -\alpha_k \nabla \bar{p}_k + \nabla \cdot \alpha_k \bar{\boldsymbol{\tau}}_k + \nabla \cdot \alpha_k \boldsymbol{\sigma}_k^t + \alpha_k \rho_k \mathbf{g} \\ &+ (\overbrace{(p_{k_i}'' - \bar{p}_k)} \nabla \alpha_k + \overbrace{p_{k_i}'' \mathbf{n}_k} \Sigma - \overbrace{\boldsymbol{\tau}_{k_i} \cdot \mathbf{n}_k} \Sigma \end{aligned} \quad (2.2)$$



Grouping the interfacial terms on the right hand side of Eqn (2.2), we have

$$\mathbf{M}_k = (\overbrace{p_{k_i}} - \overline{p_k}) \nabla \alpha_k + \overbrace{p''_{k_i} \mathbf{n}_k} \Sigma - \overbrace{\boldsymbol{\tau}_{k_i} \cdot \mathbf{n}_k} \Sigma \quad (2.3)$$

Where  $\mathbf{M}_k$  is the total momentum transfer from or to phase k. Neglecting the surface tension terms, which are expected to be small in comparison with other forces, the momentum jump conditions over the interface imply that  $\mathbf{M}_c = -\mathbf{M}_d$ , where the subscripts d and c denote the dispersed and continuous phases respectively [12, 25].

This is a restatement of Newton's third law and provides a convenient basis for the formulation of the interfacial momentum transfer models since we need only consider the forces acting on one of the phases. It is convenient to consider the forces acting on the dispersed phase since the total force on the dispersed phase may be naturally decomposed into its components, since Newton's second law implies

$$\mathbf{M}_d = \sum \mathbf{F} \quad (2.4)$$

The forces acting on the dispersed phase usually comprise the drag force, the virtual mass force, the lift force and the Basset force [6, 25]. In this work an additional force is considered which arises from the consideration of the difference between the pressure in the bulk and the local averaged pressure at the phase interface and is represented by the first term in Eqn (2.3) above. This additional contribution arises from the averaged nature of the flow equations and has no counterpart in the analysis of single droplets or particles.

Hence, symbolically we have

$$\mathbf{M}_d = \mathbf{F}_d + \mathbf{F}_{vm} + \mathbf{F}_l + \mathbf{F}_b + \mathbf{F}_p \quad (2.5)$$

where  $\mathbf{F}_d$  represents the drag force,  $\mathbf{F}_{vm}$  the virtual mass force,  $\mathbf{F}_l$  the lift force,  $\mathbf{F}_b$  the Basset force and  $\mathbf{F}_p$  the interfacial pressure force. Each of these constituent forces is considered separately below.

### 2.2.1 The Drag Force

The relative motion between a submerged body and the surrounding fluid gives rise to the so-called drag force. The drag force has two components; skin friction and form drag.

The former is related to the shear stress at the surface of the submerged body while the latter arises due to the non-uniform surface pressure distribution caused by the relative motion.

It is usual to consider the total drag force (ie, the skin friction and the form drag) together rather than the individual components since it is the total drag which is usually of interest. It is noteworthy, however, that the form drag and the skin friction components are separately represented by the last two terms respectively in Eqn (2.3) above.

The drag force on a single droplet is usually expressed in terms of its projected area, the relative velocity and a dimensionless drag coefficient  $C_d$  as

$$\mathbf{F}_d = \frac{1}{2} \rho_c A C_d |\mathbf{u}_r| \mathbf{u}_r \quad (2.6)$$

where  $A$  is the projected area of the droplet and  $\mathbf{u}_r$  is the relative velocity between it and the surrounding fluid. The total average drag force per unit volume of the dispersed phase follows from consideration of the average number of droplets per unit volume, given in terms of the phase fraction, and the corresponding average projected area and relative velocity. For spherical dispersed phase particles we have

$$\mathbf{F}_d = A_d \bar{\mathbf{u}}_r \quad (2.7)$$

where

$$A_d = \frac{3}{4} \frac{\alpha_d \rho_c C_d}{d} |\bar{\mathbf{u}}_r| \quad (2.8)$$

Here  $d$  is the droplet or particle diameter<sup>1</sup> and  $\bar{\mathbf{u}}_r$  is the mean relative velocity  $\bar{\mathbf{u}}_c - \bar{\mathbf{u}}_d$ . The drag coefficient depends on the characteristics of the flow surrounding the body and is a function of the droplet Reynolds number [40] defined as

$$Re = \frac{\rho_d |\bar{\mathbf{u}}_r| d}{\mu_c} \quad (2.9)$$

where  $\mu_c$  and  $\rho_c$  are the viscosity and density of the continuous phase respectively. For non-spherical particles, the diameter in the above expression can be taken as the ‘equivalent’ diameter.

---

<sup>1</sup>For a mono-dispersed system with droplets all of the same size, the droplet diameter  $d$  in Eqn (2.8) is clearly defined. Cases involving a distribution of droplet sizes, however, require special consideration as discussed in Chapter 3.

Theoretical studies into the functional dependence of the drag coefficient on the droplet Reynolds number have not progressed much since the early work of Stokes due to the complexity of the flow surrounding the droplet in all but the simplest flow regimes. Consequently, the determination of the drag coefficient relies heavily on experimental studies of the flow under consideration, which usually focus on single, non-rotating, spherical particles in an infinite fluid moving at a constant relative velocity. The result of such studies usually takes the form of a graph of the drag coefficient against the Reynolds number called the ‘drag curve’, an example of which is shown in Figure 2.1 for axially symmetric solid bodies [40].

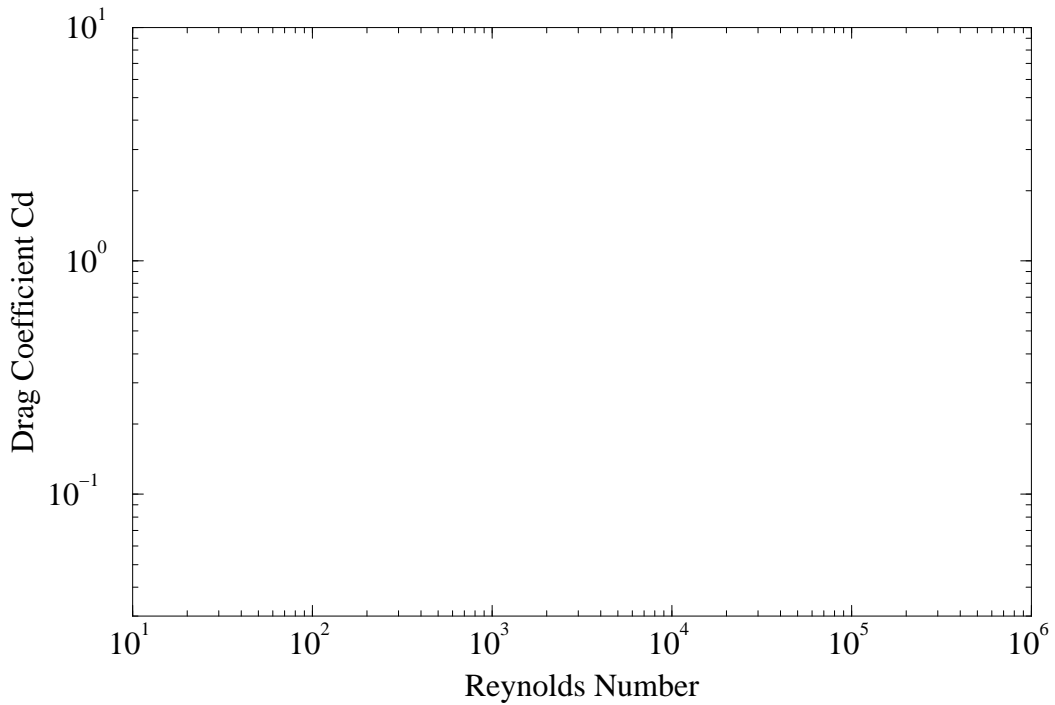


Figure 2.1: Drag coefficients for smooth, axially symmetric solid bodies.

For the purposes of analysis, many empirical relationships between the drag coefficient and the Reynolds number have been proposed. Many of these are based on detailed studies of the experimental data resulting in expressions obtained by curve-fitting. The most relevant of these studies are described below.

### 2.2.1.1 Solid Particles

For solid particles, the most commonly quoted correlation is that of Wallis [21] which reads

$$C_d = \frac{24}{Re} \left(1 + 0.15Re^{0.687}\right) \quad Re \leq 10^3 \quad (2.10)$$

$$C_d = 0.44 \quad Re > 10^3 \quad (2.11)$$

For  $Re \leq 10^3$ , Eqn (2.10) is accurate to within  $\pm 5\%$  of the experimental data. Clift and Gauvin [41] have extended this correlation for Reynolds numbers up to the ‘critical value’ where turbulence effects dominate (see Figure 2.1). For turbulent freeflows, the critical Reynolds number for a solid spherical particle is approximately  $3.65 \times 10^5$ . At this point the drag force on the particle reduces dramatically as the boundary layer becomes turbulent and the separation point moves further behind the body [40]. The effects of turbulence on the drag coefficient are discussed further in Section 2.2.1.3. The Clift and Gauvin correlation reads

$$C_d = \frac{24}{Re} \left(1 + 0.15Re^{0.687}\right) + 0.42 \left(1 + \frac{4.25 \times 10^4}{Re^{1.16}}\right)^{-1} \quad Re \leq 3 \times 10^5 \quad (2.12)$$

### 2.2.1.2 Bubbles

Several workers have proposed correlations for the drag coefficient for bubbles and droplets. The most notable of these are the studies of Peebles and Garber [42] and Ishii and Zuber [43].

Peebles and Garber [42] studied the motion of single air bubbles in various liquids to determine the steady-state terminal rise velocity and the drag coefficient. The liquid phases considered were chosen to highlight the effects of differences in density, viscosity and surface tension and included water, oils and alcohol. Their correlations read

$$C_d = \frac{24}{Re} \quad Re \leq 2 \quad (2.13)$$

$$C_d = 18.7Re^{-0.68} \quad 2 < Re \leq 4.02G^{-0.214} \quad (2.14)$$

$$C_d = 0.0275GRe^4 \quad 4.02G^{-0.214} < Re \leq 3.1G^{-0.25} \quad (2.15)$$

$$C_d = 0.82G^{0.25}Re \quad 3.1G^{-0.25} < Re \quad (2.16)$$

where

$$G = \frac{g\mu_c^4}{\rho_c\sigma^3} \quad (2.17)$$

and  $\sigma$  is the surface tension.

On the other hand, Ishii and Zuber [43] studied bubbles, droplets and solid particles to determine the drag coefficients for a wide range of phase fraction and Reynolds number values. One of their principle aims was to quantify the effect of neighbouring bubbles on the drag coefficient. For this they proposed a ‘mixture viscosity’ approach where the mixture viscosity incorporates a modification to the true continuous phase viscosity which attempts to take into account the added resistance to the droplet motion due to the crowding effect of neighbouring droplets. Other studies into this effect are described in Section 2.2.1.4.

Various regimes which characterise the drag behaviour of bubbles and droplets were identified. Correlations were formulated for each of these regimes, as were the criteria governing the transition between them. The Ishii and Zuber correlations for bubbles and droplets read

$$C_d = \frac{24}{Re_m} \quad \text{Stokes Regime} \quad (2.18)$$

$$C_d = \frac{24}{Re_m} \left(1 + 0.1Re_m^{0.75}\right) \quad \text{Undistorted Particle Regime} \quad (2.19)$$

$$C_d = \frac{4d}{6} f(\alpha_d) \sqrt{\frac{g(\rho_c - \rho_d)}{\sigma}} \quad \text{Distorted Particle Regime} \quad (2.20)$$

$$C_d = \frac{8}{3}(1 - \alpha_d)^2 \quad \text{Churn Turbulent Regime} \quad (2.21)$$

where

$$Re_m = \frac{d\rho_c u_r}{\mu_m} \quad (2.22)$$

is the droplet Reynolds number based on the mixture viscosity  $\mu_m$ . The function  $f(\alpha_d)$  depends on the relative viscosity of the continuous and dispersed phases and is given by

$$\begin{aligned}
f(\alpha_d) &= (1 - \alpha_d)^{-0.5} && \text{For } \mu_c \gg \mu_d \\
&= (1 - \alpha_d)^{-1.0} && \text{For } \mu_c \approx \mu_d \\
&= (1 - \alpha_d)^{-1.5} && \text{For } \mu_c \ll \mu_d
\end{aligned}$$

An alternative to the general empirical correlation functions proposed above is to make direct use of experimental data for the particular system under investigation. For instance, Haberman and Morton [1953] (reported in Wallis [21]) measured the terminal velocities of single air bubbles in distilled water. Distilled water was used because the presence of contaminants in the continuous phase is known to effect the drag characteristic of the bubbles. By considering the balance of forces on a single bubble rising in a infinite medium the following expression for the drag coefficient can be derived

$$C_d = \frac{4}{3} \frac{(\rho_c - \rho_d)}{\rho_c} \frac{dg}{u_t^2} \quad (2.23)$$

where  $u_t$  is the measured terminal rise velocity of the bubble. By substituting the measured values of  $d$  and  $u_t$  into Eqn (2.23) the drag coefficient may be calculated and the resulting curve plotted as a function of the Reynolds number, as shown in Figure 2.2. Wang [44] derived expressions to fit this experimental data using a least squares curve-fit method. Since the experimental data indicates a sharp rise in the drag coefficient at a Reynolds number of approximately 450 where the onset of bubble distortion occurs, Wang split the curve into two sections, appropriately matched at the  $Re = 450$  point. Wang's expression for the drag coefficient reads

$$\log_e C_d = a + b \log_e Re + c(\log_e Re)^2 \quad (2.24)$$

where, for  $Re < 450$ ,

$$\begin{aligned}
a &= 2.699467 \\
b &= -0.335816 \\
c &= -7.135617 \times 10^{-2}
\end{aligned}$$

and, for  $Re \geq 450$ ,

$$a = -51.77171$$

$$b = 13.16707$$

$$c = -0.82356$$

It is instructive to compare the drag models of Peebles and Garber [42] and Ishii and Zuber [43] by applying them to the case of air bubbles rising in water and comparing their predictions for the drag coefficient against that calculated directly from the experimental data of Haberman and Morton and the least-squares curve fit of Wang.

### Drag Coefficient–Reynold’s No. Relationship Clean Air–Water System

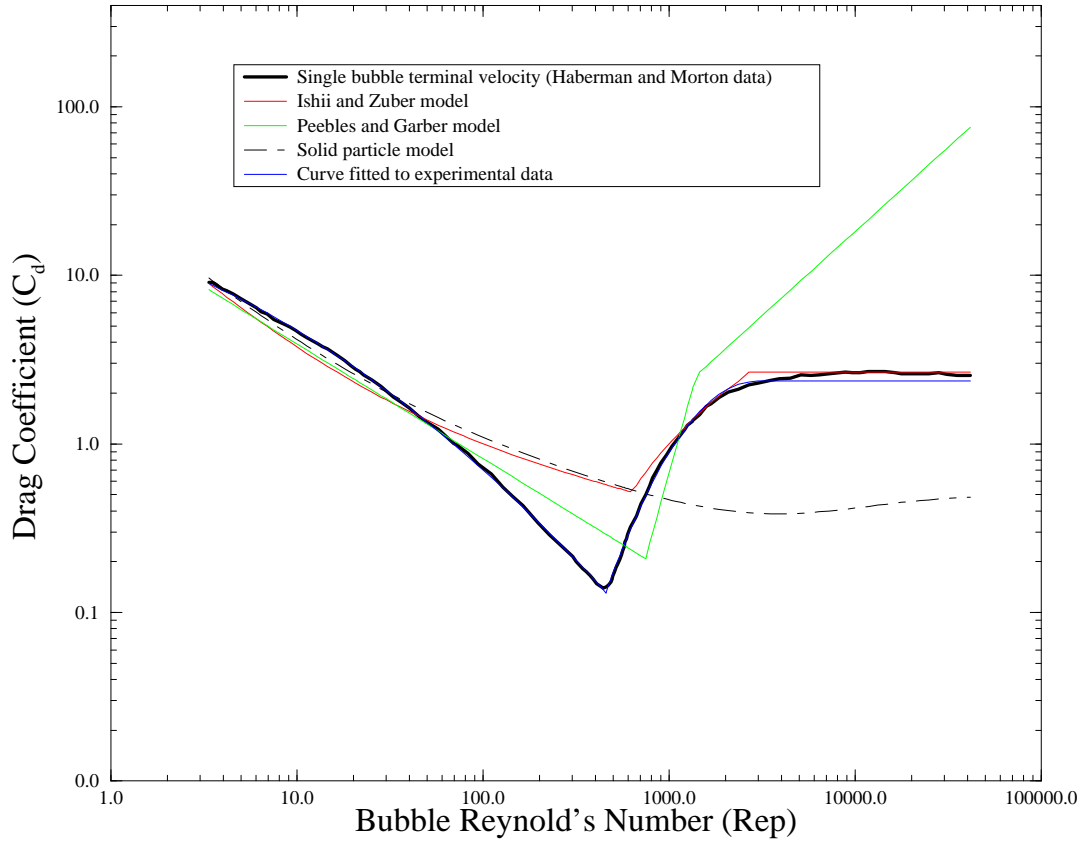


Figure 2.2: Drag coefficient as a function of Reynolds number.

Figure 2.2 shows the resulting drag coefficient curves. The solid black line indicates the

drag coefficient calculated from the experimental data. The red and green lines indicate the drag coefficient predictions of the Ishii and Zuber and Peebles and Garber models respectively. The drag coefficient for solid particles, as calculated from Eqn (2.12), is shown to illustrate the difference in drag behaviour between bubbles and solid particles. The blue line indicates the predicted drag coefficient using the curve fit expression.

It can be seen that both the Peebles and Garber and Ishii and Zuber models predict a drag coefficient which deviates significantly from the curve obtained from the experimental data at higher Reynolds number. The application of these correlation to air-water flows under these conditions may lead to the incorrect prediction of the drag coefficient at high Reynolds number.

Of course, since the curve fit drag model is strictly only valid for a clean air-water system it is not generally applicable. Further, it may not be possible to obtain experimental data relating to the exact system under investigation and so an exact curve-fitted model may not be possible. In this situation, the Ishii and Zuber may be preferred on the grounds that it embodies a wealth of data concerning many different fluids and density ratios (including liquid-liquid and gas-liquid systems) and modifications which account for high phase fraction systems.

It should be noted that some form of surface active contamination or impurities in the dispersed or continuous phase may significantly alter the drag characteristics of the system. Very little data exists in the literature concerning this phenomena and there are no analytical models with which to predict the drag coefficient for such systems. If the determination of a curve-fitted expression for the drag coefficient by direct experimental investigation of the system is not possible, then an acceptable alternative approach may be to use the solid particle drag model to determine the drag coefficient. Even small concentrations of surface active contaminants are known to immobilise the interface in liquid-liquid and gas-liquid systems; under these conditions the drag characteristics become more like that of a solid particle [45].

One possible alternative approach would be to modify the mixture viscosity framework, as used by Ishii and Zuber, to account for the immobilisation of the interface. However, insufficient experimental data exists at the moment with which to formulate and validate such a model making the solid particle drag model the only viable alternative.

### 2.2.1.3 The Effects of Turbulence on the Drag Coefficient

The effects of turbulence on the drag coefficient of solid particles has been studied extensively [46, 47, 41, 45]. For particles which are larger than the typical turbulent length



scales, the effect of the turbulence is to modify the size and origin of the boundary layers on the particle surface thus influencing the drag force [45].

The effects of turbulence are commonly characterised by the free stream turbulence intensity  $I$ , defined as the ratio of the turbulent RMS velocity fluctuations to the mean velocity, and the so-called critical Reynolds number  $Re_{crit}$ , defined as the Reynolds number at which the drag coefficient falls to a value of 0.3. Typically, at this point the boundary layer becomes turbulent and the separation point moves further behind the body leading to a sharp reduction in the drag coefficient [40]. These effects are shown in Figure 2.3.

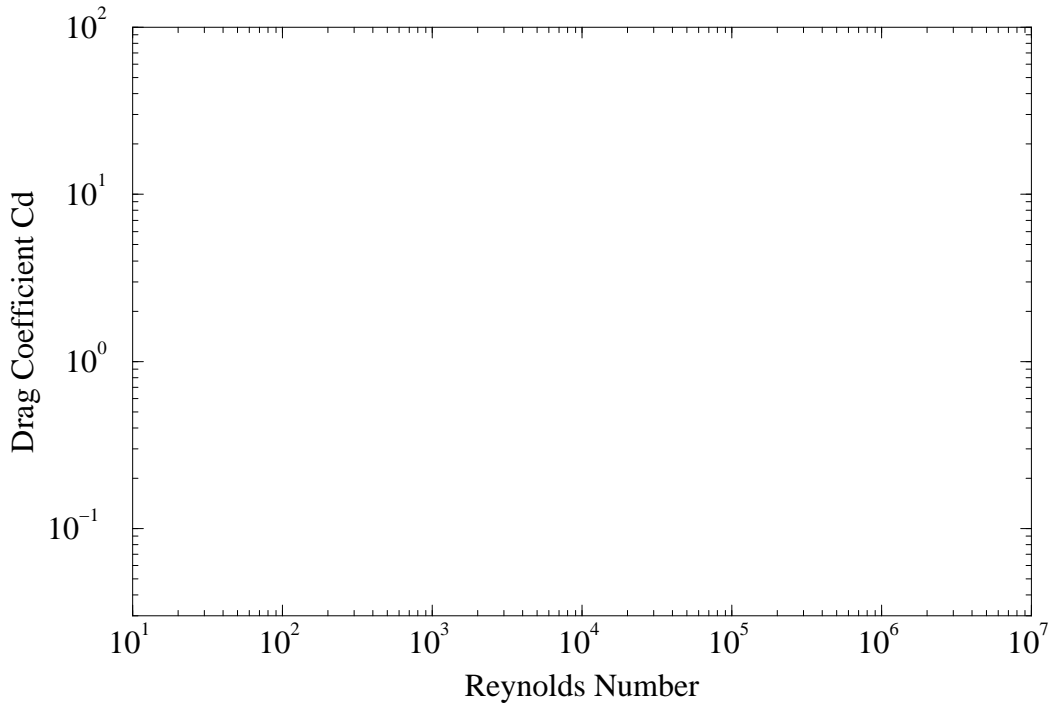


Figure 2.3: Influence of turbulence intensity on the drag coefficient.

For solid particles in a laminar flow (ie.  $I = 0$ ), the value of the critical Reynolds number is approximately  $3.65 \times 10^5$ . Studies performed by Torobin and Gauvin [46, 47] indicate that  $Re_{crit}$  falls as  $I$  increases due to the promotion of turbulence transition in the boundary layers on the particle surface. Beyond the critical Reynolds number, the drag coefficient increases again, probably due to an increase in form drag, before tending towards a constant value. The value at which the drag coefficient reaches a value of 0.3 again is termed

the meta-critical Reynolds number  $Re_M$ .

Clift *et al.* [45] provide empirical correlations for the drag coefficient which take account of the turbulence intensity in the sub-critical, critical and super-critical regimes. These correlations are given in Table 2.2.1.3, where  $Re_{min}$  is the value at which  $C_d$  is a minimum and  $Re_M$  is the meta-critical Reynolds number. Clift and Gauvin [41] provide correlations for  $Re_{crit}$  in terms of the turbulence intensity. These correlation read

$$\log_{10} Re_{crit} = 5.562 - 16.4I \quad I \leq 0.15 \quad (2.25)$$

$$\log_{10} Re_{crit} = 3.371 - 1.75I \quad I > 0.15 \quad (2.26)$$

Regime	$Re$	$I$	$C_d$
Sub-critical	$< 50$	$0.05 < I < 0.5$	$\frac{162I^{1/3}}{Re}$
	$50 < Re < 500$	$0.07 < I < 0.5$	$4I + 0.133(1 + \frac{150}{Re})^{1.565}$
Critical	$0.9Re_{crit} < Re < Re_{min}$		$0.3(\frac{Re_{crit}}{Re})^3$
Super-critical	$Re_{min} < Re < Re_M$	$I > 0.07$	$0.3(\frac{Re}{Re_M^{(0.45+20I)}})$
	$Re_M < Re < 3 \times 10^4$		$\frac{3990}{\log(Re)^{6.1}} - \frac{4.47 \times 10^5}{I^{0.97} Re^{1.8}}$

In the case of liquid-liquid and gas-liquid systems, the effects of turbulence on the drag coefficient are not clear and little data can be found in the literature. With gas-liquid systems especially, the low inertia of the dispersed phase and the mobility of the interface allows the turbulence to distort the interface, thus modifying the drag force by changing the projected area. Large-scale turbulent structures cause the translation of the entire bubble causing an oscillating motion.

In the present work, the effects of turbulence on solid particles is accounted for using the Clift, Grace and Weber [45] correlations above. For liquid-liquid and gas-liquid systems the effects of turbulence on the drag coefficient are neglected due to lack of data.

#### 2.2.1.4 The Effects of Phase Fraction on the Drag Coefficient

The majority of experimental studies into the drag coefficient are based on a single particle in an infinite medium. However, in practical situations there will be neighbouring particles, whose proximity can be approximated by the phase fraction, which will effect the drag force experienced by the particle.

Most correlations of this effect are based on modifications to the drag coefficient for single particles. Wallis [21], using fluidised bed data, proposed that the drag coefficient for a particle surrounded by other particles, denoted  $C_d(\alpha_d)$ , could be expressed as

$$C_d(\alpha_d) = C_d(1 - \alpha_d)^{-2.7} \quad (2.27)$$

Ishii and Zuber [43] adopted an alternative approach where the particle Reynolds number is defined using a mixture viscosity, which is purported to account for the confinement effect of the surrounding particles on the flow surrounding the particle. Their expression for the mixture viscosity reads

$$\mu_m = \mu_c \left\{ 1 - \frac{\alpha_d}{\alpha^*} \right\}^{\frac{-2.5\alpha^*(\mu_d + 0.4\mu_c)}{(\mu_d + \mu_c)}} \quad (2.28)$$

where  $\alpha_k < \alpha^*$  and  $\alpha^*$  takes a value of approximately 0.62 for solid particles (maximum packing limit) and 1.0 for liquid droplets and gas bubbles (so as to include foaming systems).

### 2.2.2 The Virtual Mass Force

The virtual mass or added mass force  $\mathbf{F}_{vm}$  is the additional force required to accelerate a particle due to the mass of the fluid in its vicinity, which also needs to be accelerated. The virtual mass force is especially important in gas-liquid flows where the low inertia of the dispersed phase allows the bubbles to experience rapid (temporal or spatial) acceleration. If the virtual mass force is not taken into account, the bubble accelerates too rapidly thus leading to a loss of accuracy, and in numerical solution procedures, numerical instabilities [48].

Drew, Cheng and Lahey Jr. [49] and Drew and Lahey Jr. [50, 51] have analysed the virtual mass force by considering a single sphere accelerating relative to an inviscid fluid undergoing pure strain and rotation far from the sphere. For low phase fraction  $\mathbf{F}_{vm}$  is given as

$$\mathbf{F}_{vm} = C_{vm}\alpha_d\rho_c \left( \frac{D_c}{Dt}\bar{\mathbf{u}}_c - \frac{D_d}{Dt}\bar{\mathbf{u}}_d \right) \quad (2.29)$$

where  $\frac{D_k}{Dt}$  is the phasic material derivative (ie. the material derivative relating to one phase only) and  $C_{vm}$  is a dimensionless coefficient. For a single non-deformable sphere in an inviscid fluid the theoretical value of  $C_{vm}$  is 0.5 [50, 12].

Little data exists in the literature as to the appropriate value of the virtual mass coefficient when the phase fraction is high. Milne-Thomson [52] considered the effects of a particle cloud on the virtual mass coefficient and obtained the expression

$$C_{vm} = \frac{1}{2}(1 + 3\alpha_d) + O(\alpha_d^2) \quad (2.30)$$

As  $\alpha_d \rightarrow 0$  the above equation yields  $C_{vm} \rightarrow 0.5$ . Similar expressions have been derived by Van Wijngaarden [53] and Mokeyev [54] which read

$$C_{vm} = \frac{1}{2}(1 + 2.78\alpha_d) + O(\alpha_d^2) \quad (2.31)$$

and

$$C_{vm} = \frac{1}{2}(1 + 4.2\alpha_d) \quad (2.32)$$

respectively.

### 2.2.3 The Lift Force

The ‘lift force’  $\mathbf{F}_l$  describes the lateral force experienced by a particle subjected to a shearing flow field or due to the rotation of the particle itself. For solid-liquid flows, the lift force is negligible compared with other forces [6]. However, it is important for gas-liquid flows in which regions of high shear exist and it can have a large effect on phase distribution. For example, the lift force is known to largely account for the lateral phase fraction variation in pipeline and duct flows [55, 25, 56]. This phenomenon is also clearly demonstrated in the validation study concerning the air-water bubbly flow in a plane ducted shear layer described in Chapter 5.

Drew, Cheng and Lahey Jr. [49] and Drew and Lahey Jr. [50, 51] have derived an expression for the lift force. For low phase fraction and low vorticity (strictly laminar) flow it reads

$$\mathbf{F}_l = C_l \alpha_d \rho_c (\mathbf{\bar{u}}_c - \mathbf{\bar{u}}_d) \times (\nabla \times \mathbf{\bar{u}}_c) \quad (2.33)$$

where  $C_l$  is a dimensionless coefficient. For a non-deformable sphere in an inviscid fluid, the value of  $C_l$  can be calculated analytically to be 0.5 [50, 12].

Wang, Lee, Jones Jr. and Lahey Jr. [55], in a study into the phase distribution in upward and downward flowing air-water two-phase flow in a vertical pipe, discuss the magnitude of  $C_l$  for high Reynolds number turbulent flows. By simplifying the two-fluid momentum equations they obtained an equation for the phase distribution across the pipe for fully developed pipe flow. Using measured values of the phase fraction and Reynolds stress distributions they were able to infer the value of  $C_l$ . Correlating the data for a number of cases, they found that the  $C_l$  is a function of the local phase fraction, bubble Reynolds number, velocity gradient, bubble diameter and relative velocity. The lift coefficient for the cases considered was found to range between 0.01 and 0.1, which is far from the ‘classical’ value of 0.5.

Conversely, Lance and de Bertodano [35] have measured the lift force on a single bubble in a rotating turbulent flow and obtained a value for the lift coefficient of approximately 0.25.

Clearly, the value of  $C_l$  in turbulent flows is subject to some uncertainty. It is likely, in view of the work of Wang *et al.* [55], that  $C_l$  is a local function of the flow properties in much the same way as the drag coefficient. However, until more experimental data concerning the lift force exerted on droplet and bubbles in practical flows becomes available, a generally applicable model for the lift coefficient cannot be obtained. In view of the uncertainty surrounding the appropriate value of  $C_l$  a globally constant value is adopted in this work. The value adopted for gas-liquid systems is 0.25 while for liquid-liquid and solid-liquid systems the ‘classical’ value of 0.5 is used.

#### 2.2.4 The Interfacial Pressure Force

The first term on the right hand side of Eqn (2.3) involves the difference between the ‘mean interfacial’ pressure  $\widehat{p_{k_i}}$  and the ‘mean bulk’ pressure  $\overline{p_k}$ . In general, these two pressures are not equal since there is usually a reduction in the mean pressure local to the particle associated with the relative motion between phases [48]. The net force caused by this pressure difference is denoted  $\mathbf{F}_p$ .

$$\mathbf{F}_p = (\widehat{p_{k_i}} - \overline{p_k}) \nabla \alpha_d \quad (2.34)$$

It is important to note that this pressure force is in addition to the form drag component of the drag force considered previously. Statistical variations in the mean interfacial pressure do not affect the form drag component of the drag force. The form drag force on a single body is calculated by integrating the local pressure multiplied by the local surface normal over the surface of the body.

$$\mathbf{F}_d^f = \oint p_i \mathbf{n} dA \quad (2.35)$$

where  $\mathbf{F}_d^f$  represents the form drag component. The local pressure on the surface  $p_i$  is composed of a mean value  $\widehat{p_i}$  (ie. the mean value over the surface of the sphere) and a fluctuating component  $p_i''$ . Clearly, a change in the mean value will not affect the total form drag over the sphere's surface since the change will be cancelled out by the diametrically opposite point on the sphere's closed surface.

$$\mathbf{F}_d^f = \oint (\widehat{p_i} + p_i'') \mathbf{n} dA = \oint p_i'' \mathbf{n} dA \quad (2.36)$$

By considering the flow around a sphere it is possible, in some circumstances, to derive an analytical expression for the pressure distribution over its surface relative to the bulk pressure. Then, by averaging over the surface, an expression for  $\widehat{p_i}$  can be obtained. Stuhmiller [48] used an approximate expression for the pressure distribution over a bubble based on an inviscid flow solution, but relevant to bubble Reynolds numbers outside the inviscid limit. The average pressure at the surface is given by

$$\widehat{p_i} = \bar{p} - 0.37 \rho_c C_d |\overline{\mathbf{u}_r}|^2 \quad (2.37)$$

The drag coefficient is as calculated using the appropriate model from Section 2.2.1. Substituting the above expression into Eqn (2.34) yields

$$\mathbf{F}_p = -0.37 \rho_c C_d |\overline{\mathbf{u}_r}|^2 \nabla \alpha_d \quad (2.38)$$

Examination of Eqn (2.38) shows that this term is dispersive since it contains the phase fraction gradient. Physically, this behaviour can be understood by envisioning a situation where a cloud of particles causes a reduction in the local pressure due to the relative motion. This local pressure reduction then causes the dispersion of the particle cloud due to the local pressure gradient influence in the continuous phase momentum equation.

It is shown in Chapters 5 and 6, during the validation of the model against experimental data, that the interfacial pressure force, as modelled above, yields good results with regard to the dispersion rate.

### 2.2.5 The Basset Force

The Basset force represents the influence of the time dependent development of the boundary layer on the particle surface in accelerating flows. In essence, it takes into account the fact the drag on the particle depends on the previous history of the particle motion. The Basset force is given by

$$\mathbf{F}_b = \frac{3}{2}d^2\sqrt{\pi\rho_c\mu_c}\int_{t_0}^t \frac{d}{dt}(|\mathbf{u}_d - \mathbf{u}_c|_{t=t'}) \frac{dt'}{\sqrt{t-t'}} \quad (2.39)$$

It can be shown [6] that in solid-liquid flows the Basset force is very small when compared to the drag force and is usually neglected. Similarly, in gas-liquid and liquid-liquid flows, where the boundary layer is very small or non-existent due to the mobility of the interface, the Basset force is very much smaller than the form drag and can be neglected.

### 2.2.6 Interfacial Closure Summary

Collecting the models for the various interfacial forces described above and substituting them into Eqn (2.5) we have

$$\begin{aligned} \mathbf{M}_d = & \frac{3}{4}\frac{\alpha_d\rho_c C_d}{d}|\overline{\mathbf{u}}_r|\overline{\mathbf{u}}_r + \\ & C_{vm}\alpha_d\rho_c\left(\frac{D_c}{Dt}\overline{\mathbf{u}}_c - \frac{D_d}{Dt}\overline{\mathbf{u}}_d\right) + \\ & C_l\alpha_d\rho_c(\overline{\mathbf{u}}_c - \overline{\mathbf{u}}_d) \times (\nabla \times \overline{\mathbf{u}}_c) - \\ & 0.37\rho_c C_d |\overline{\mathbf{u}}_r|^2 \nabla \alpha_d \end{aligned} \quad (2.40)$$

In this work, the drag coefficient  $C_d$  is given by Equations (2.10) and (2.11) for solid-liquid flows, Equations (2.18) to (2.21) for liquid-liquid flows and non air-water gas-liquid flows, and Eqn (2.24) for clean air-water systems. Phase fraction effects are accounted for using Eqn (2.27) for solid-liquid and gas-liquid flows. Liquid-liquid flows make use of the Ishii and Zuber mixture viscosity correction as given by Eqn (2.28).

The virtual mass coefficient is calculated using Eqn (2.30). A globally constant value for the lift coefficient is adopted. For gas-liquid systems a value of 0.25 is used. For liquid-liquid and solid-liquid systems a value of 0.5 is used.

Eqn (2.40) is assumed to be valid in both laminar and turbulent flows. Turbulent effects may be taken into account through modifications to the dimensionless coefficients where

the effects of turbulence on the interfacial force in question is understood. In practical terms, turbulence effects have only been studied in relation to the drag coefficient and can be accounted for using the correlations described in Section 2.2.1.3 if necessary, although they are not applied in this work.

## 2.3 Turbulence Closure

In this section we examine in detail the Reynolds stress terms which appear in each of the phase momentum equations as a result of the averaging process. These unknown terms represent the effects of turbulence on the average phase momentum and need to be modelled in terms of known quantities to obtain a closed equation set. The models adopted for each of these need not be the same and so the continuous and dispersed phase Reynolds stress modelling strategies can be considered separately.

In what follows, Section 2.3.1 contains a summary of previous work on two-phase turbulence and discusses the commonly adopted modelling strategies for the phase Reynolds stresses. Following this, Section 2.3.2 goes on to discuss the continuous phase Reynolds stress models adopted in this work. This is based on the eddy viscosity concept and utilises a two-equation  $k - \epsilon$  conditional averaged turbulence model. The derivation of the conditional averaged phase Reynolds stress equation is first described in Section 2.3.2.2, followed by the derivation of the conditional averaged  $k - \epsilon$  equations themselves in Section 2.3.2.3. Section 2.3.2.4 describes the models adopted for the additional terms in the  $k - \epsilon$  equations which represent the two-phase effects on the turbulence structure.

Section 2.3.3 discusses the modelling of the dispersed phase Reynolds stresses which is based on the response coefficient concept of Politis [6]. Particular emphasis is given in Section 2.3.3.1 to the exact definition of the response coefficient and how it relates to the conditional averaged framework adopted in this work. The modelling of the response coefficient is discussed in detail in Section 2.3.3.2.

### 2.3.1 Previous Work

Two-phase turbulence modelling approaches vary considerably between workers, principally due to the many different ways in which the equations may be derived. Further, the approaches tend to be influenced by the specific turbulence effects in which the authors are interested, and the simplifying assumptions introduced along the way can yield significantly different final results. This section attempts to identify and evaluate the different modelling strategies proposed by previous workers. Emphasis is given to the overall ap-



proach rather than to the detailed modelling of individual terms. Where relevant, these details are discussed in Section 2.3.2.4 where the development of the present two-phase  $k - \epsilon$  turbulence model is discussed.

The majority of workers who have attempted to derive generally applicable multi-phase flow turbulence models have tried to extend the popular two-equation  $k - \epsilon$  model of Jones and Launder [57] for single-phase flows to the two-phase situation. The dominance of the  $k - \epsilon$  turbulence model in single-phase flows is attributed to its effective balance between accuracy and computational cost. Since this model is in widespread use and its behaviour and limitations are well understood, it is a natural choice as the basis for a two-phase turbulence model.

Workers who have developed two-phase  $k - \epsilon$  turbulence models include Buckingham [58], Buckingham and Siekhaus [59, 60], Pourahmadi [61], Pourahmadi and Humphrey [62], Elghobashi and Abou-Arab [63, 64], Chen and Wood [65, 66], Politis [6], Kataoka and Serizawa [30] and Lahey [67]. In this framework, the continuous phase Reynolds stresses are modelled using the ‘eddy viscosity’ concept of Boussinesq [1877]. Here, the Reynolds stress is related to the mean shear rate using an eddy viscosity  $\nu^t$ .

$$-\overline{u'_c u'_c} = \nu_c^t \left\{ \nabla \bar{u}_c + \nabla \bar{u}_c^T - \frac{2}{3}(\nabla \cdot \bar{u}_c) \mathbf{I} \right\} - \frac{2}{3} k \mathbf{I} \quad (2.41)$$

where  $k$  is the turbulent kinetic energy in the continuous phase and  $\nu_c^t$  is the continuous phase eddy viscosity which is usually evaluated from the following relation

$$\nu_c^t = C_\mu \frac{k^2}{\epsilon} \quad (2.42)$$

where  $\epsilon$  is the continuous phase turbulent energy dissipation rate and  $C_\mu$  is a coefficient which usually takes the value 0.09. Some workers (notably Elghobashi and Abou-Arab [63, 64]) have attempted to determine alternate values for the other coefficients in the  $k - \epsilon$  equations which are applicable to the two-phase situation. The  $C_\mu$  coefficient however tends to remain unmodified.

The modelling of the dispersed phase Reynolds stresses again differs considerably between workers. While some workers neglect them entirely (for example, Lance and de Bertodano [35] and Wang *et al.* [55]) many workers adopt the eddy viscosity approach for both the dispersed and continuous phases. For the dispersed phase, the eddy viscosity relationship reads

$$-\overline{\mathbf{u}'_d \mathbf{u}'_d} = \nu_d^t \left\{ \nabla \overline{\mathbf{u}}_d + \nabla \overline{\mathbf{u}}_d^T - \frac{2}{3} (\nabla \cdot \overline{\mathbf{u}}_d) \mathbf{I} \right\} - \frac{2}{3} k_d \mathbf{I} \quad (2.43)$$

The disadvantage with this approach is the need to formulate and solve the dispersed phase  $k$ - $\epsilon$  equations which are required to calculate the dispersed phase eddy viscosity. To avoid this, some workers relate the dispersed phase eddy viscosity to the continuous phase eddy viscosity. One such approach, adopted by Pourahmadi [61], Pourahmadi and Humphrey [62] and Elghobashi and Abou-Arab [63, 64] is to relate the dispersed phase eddy viscosity using Peskin's [68] formula.

$$\frac{\nu_d^t}{\nu_c^t} = 1 - \frac{\tau_L^2 \epsilon}{15 \nu_c} \frac{3B^2}{B+2} \quad (2.44)$$

where  $\tau_L$  is the Lagrangian integral time scale and  $B = 2\tau_p/\tau_L$  where  $\tau_p$  is the particle response time. The dispersed phase turbulent kinetic energy  $k_d$  is related to that of the continuous phase via

$$k_d = k \frac{\tau_L}{\tau_p + \tau_L} \quad (2.45)$$

Elghobashi and Abou-Arab found, by applying it to the case of a particle laden axis-symmetric jet, that Peskin's formula yielded poor results since it predicted negative diffusivities for the dispersed phase. In order to remedy the situation, they proposed a modified relationship which reads

$$\frac{\nu_d^t}{\nu_c^t} = 1 - \frac{3}{2} \left( \frac{L_\epsilon}{R} \right)^2 \frac{B^2}{B+2} \quad (2.46)$$

where  $L_\epsilon$  is the dissipation length scale given by  $C_\mu k^{1.5}/\epsilon$ .

In the same vein, Chen and Wood [65, 66] adopted a simple relationship between the two phase viscosities which reads

$$\frac{\nu_d^t}{\nu_c^t} = \frac{\tau_e}{\tau_p + \tau_e} \quad (2.47)$$

where  $\tau_e$  is the time scale of the energetic eddies given by  $0.165k/\epsilon$ .

Other workers have adopted different approaches to the modelling of the dispersed phase Reynolds stresses. For example, by analysing the dispersed phase Reynolds stress transport equation and making certain local equilibrium assumptions, Lahey [67] replaces the dispersed phase Reynolds stress term with an algebraic stress law. His model is completed by solving for the dispersed phase  $k$  and  $\epsilon$  equations. Politis [6] adopted a different approach by relating the dispersed phase velocity fluctuations to those of the continuous phase via a ‘response coefficient’  $C_t$  defined as

$$C_t = \frac{u'_s}{u'_l} \quad (2.48)$$

where  $u'_s$  and  $u'_l$  are the (unweighted) velocity fluctuations of the solid dispersed phase and liquid continuous phase respectively. The response coefficient  $C_t$  allows the dispersed phase Reynolds stresses to be rewritten in terms of the continuous phase Reynolds stresses and  $C_t$ . Politis’ final model for the dispersed phase Reynolds stress reads

$$\overline{\alpha_s \mathbf{u}''_s \mathbf{u}''_s} = \frac{C_t^2 \alpha_s}{\alpha_l} \overline{\alpha_l \mathbf{u}''_l \mathbf{u}''_l} + \frac{C_p^2}{\alpha_s \rho_d^2} \nabla \alpha_l \nabla \alpha_l (2\alpha_s - 1) \quad (2.49)$$

where  $\mathbf{u}''$  are the phase weighted velocity fluctuations, and

$$C_p = \frac{C_t \mu^t \alpha_l \rho_d}{(\alpha_l \rho_l)^2 \sigma_\alpha} \quad (2.50)$$

Note that Politis’ two-phase equations were derived in terms of phase weighted velocities  $\mathbf{u}''$  and  $C_t$  is defined in terms of unweighted phase velocities  $\mathbf{u}'$ . This difference introduces considerable complication into the modelling.

The response coefficient approach is attractive in that it relies on the definition of a function for  $C_t$  which, in principle, is physically easier to formulate and understand than relationships between the phase turbulent viscosities. In addition, independent validation of  $C_t$  models is likely to be much easier and reliable than models describing the relationship between phase turbulent viscosities. For these reasons, this approach has been adopted in the current work and is studied in more depth in Section 2.3.3.1.

Even though many workers have adopted the  $k - \epsilon$  framework coupled with one of the above approaches for the modelling of the dispersed phase Reynolds stresses, considerable differences are still evident between their proposals. The details of the modelling are closely related to the exact nature of the derivation of the  $k - \epsilon$  equations. In particular,

the adoption of different decomposition and averaging techniques during the derivation can lead to significantly different forms of the correlations terms within the equations. The rigorous derivation of the two-phase  $k-\epsilon$  equations requires the averaged and un-averaged forms of the momentum equations and the nature of the averaging process used to derive these equations therefore has a direct influence on the final form of the equations. Furthermore, the subsequent modelling of these terms can give rise to a final model which differs considerably from those of other workers.

The adoption of a single or double averaging technique is of fundamental importance since the two-phase equation derivation procedure yields equations for different physical quantities. For example, double averaging may produce  $k-\epsilon$  equations in terms of phase weighted average quantities, whereas a single conditioned average yields equations in terms of conditional averaged quantities. This has implications when trying to validate the final model. Predictions for phase weighted quantities should be compared to phase weighted experimental data [34].

Early workers derived the two-phase flow equations, including the  $k-\epsilon$  equations, using a double average procedure (for example, volume-time, time-time, etc) [61, 62, 63, 64, 6]. In general, this results in the appearance of many terms in the resulting equations which involve correlations between the ‘fluctuating’ phase fraction and the phase velocities and pressure. The modelling of these terms is problematical since their mathematical and physical nature is not well understood, a situation exacerbated by the lack of suitable experimental data. The most relevant of the previous studies using this approach is that of Politis [6] which is studied in depth in the next section.

Later workers have tended to adopt a single averaging technique similar to the one adopted in the present work [69, 30, 67]. This approach does not produce terms involving fluctuating phase fraction correlations but still generates many other terms which require modelling. The work of Kataoka and Serizawa [30] and Lahey and Alajbegovic [69, 67] are studied in detail in Sections 2.3.1.2 and 2.3.1.3.

### 2.3.1.1 The Work of Politis

Politis [6] proposed a new  $k-\epsilon$  turbulence model applicable to solid-liquid flows based on a rigorous derivation of the two-phase  $k-\epsilon$  equations based on a double (volume-time) averaging technique. The double average basis of Politis’ derivation has many implications on the form and nature of the final turbulence model.

Politis avoids the proliferation of correlation terms usually introduced by the double averaging processes by redefining the phase velocities using the phase-fraction-weighted de-

composition before the time averaging process. The first volume averaging process yields conservation equations for mass and momentum which are based on the volume fraction and the volume averaged phase velocities. These are denoted as  $\alpha_l$ ,  $\alpha_s$ ,  $\bar{\mathbf{u}}_l$  and  $\bar{\mathbf{u}}_s$  respectively, where the subscripts  $l$  and  $s$  denote the liquid and solid phases.

Using phase fraction weighted decomposition for the phase velocities, Politis applied the time averaging process to the volume averaged equation set and obtained conservation equations for mass and momentum in terms of the time averaged volume fraction  $\bar{\alpha}$  and the phase fraction weighted phase velocities, denoted  $\tilde{\mathbf{u}}$ , and the corresponding fluctuating variables, denoted  $\alpha'$  and  $\mathbf{u}''$  (see Section 1.5.3). The phase Reynolds stress terms introduced by this process read

$$\overline{\alpha_s \mathbf{u}_s'' \mathbf{u}_s''} \quad (2.51)$$

$$\overline{\alpha_l \mathbf{u}_l'' \mathbf{u}_l''} \quad (2.52)$$

The modelling of the continuous phase Reynolds stress term was accomplished using the eddy viscosity concept which was assumed to be applicable to the phase weighted velocities. Thus,

$$-\overline{\alpha_l \mathbf{u}_l'' \mathbf{u}_l''} = \alpha_l \nu_l^t \left\{ \nabla \tilde{\mathbf{u}}_l + \nabla \tilde{\mathbf{u}}_l^T - \frac{2}{3} (\nabla \cdot \tilde{\mathbf{u}}_l) \mathbf{I} \right\} - \frac{2}{3} k \mathbf{I} \quad (2.53)$$

Politis' rigorous derivation of the  $k - \epsilon$  transport equations for the two-phase system was accomplished by first deriving the two-phase Reynolds stress transport equation (RSTE) by extending the single-phase RSTE derivation procedure to the two-phase case.

The single phase RSTE derivation starts with the derivation of the transport equation for the fluctuating velocity. This is obtained by subtracting the averaged momentum equation from the instantaneous momentum equation. In tensor notation, this process yields a transport equation for a particular velocity component, say  $u'_i$ . This equation is then multiplied by the velocity component  $u'_k$  and added to the same equation written in terms of  $u'_k$  but multiplied by  $u'_i$ . The resulting equation is then averaged and rearranged to yield the final single-phase Reynolds stress transport equation. McComb [70] gives a clear description of the above procedure.

In the two-phase case, the derivation similarly begins with the transport equation for the phase fluctuating velocity. Politis defines this as

$$\mathbf{u}'' = \bar{\mathbf{u}} - \tilde{\mathbf{u}} \quad (2.54)$$

where  $\bar{\mathbf{u}}$  is the volume averaged velocity. Note that Politis defines the ‘fluctuating’ velocity as the difference between the double averaged phase weighted velocity and the volume averaged velocity. This definition raises some questions concerning the exact nature of the velocity fluctuations since it is clearly defined as the difference between two averaged values.

As noted previously, the volume averaged velocity contains information concerning the spatial distribution of the turbulent velocity fluctuations since the averaging volume must be significantly larger than the dispersed phase droplets whose size is likely to be of the same order, or bigger than, the turbulent eddy sizes. Politis calls the velocity fluctuations relative to the volume averaged velocity ‘pseudo turbulence’ and subsequently neglects the resulting Reynolds stress term which is introduced into the volume averaged momentum equation.

While the definition given by Eqn (2.54) is mathematically valid, the physical nature of the velocity fluctuations, and the likely cause of them, is not clear. Furthermore, since Politis elects to define the phase velocities as phase weighted quantities,  $k$  and  $\epsilon$  must also be similarly defined; Politis defines the phase weighted (PW) turbulent kinetic energy as

$$k = \frac{1}{2} \frac{\overline{\alpha_l u_i'' u_i''}}{\alpha_l} \quad (2.55)$$

and the PW turbulent energy dissipation rate  $\epsilon$  as

$$\epsilon = \frac{\nu_l}{\alpha_l} \overline{\alpha_l \frac{\partial u_i''}{\partial x_j} \frac{\partial u_i''}{\partial x_j}} \quad (2.56)$$

The transport equation for the phase fluctuation velocity  $u_i''$  is derived by subtracting the volume-time averaged momentum equation from the ‘instantaneous’ volume averaged momentum equation. This equation is manipulated as outlined above to yield the Reynolds stress transport equation. The resulting equation contains 4 additional terms with respect to the corresponding single phase equation which arise from the interfacial terms appearing in the volume averaged and double averaged momentum equations.

The turbulent kinetic energy equation for the continuous phase is derived by simply contracting the Reynolds stress transport equation. The resulting equation, given below, contains an additional two terms with respect to the single-phase  $k$  equation.

The derivation of the  $\epsilon$  equation is carried out by differentiating the fluctuating velocity transport equation for  $u_i''$  with respect to  $x_k$ , multiplying by  $\frac{\partial u_i''}{\partial x_k}$  and averaging. The final

$\epsilon$  equation contains many correlation terms, many of which are neglected by Politis. The resulting equation, also given below, retains just one of these additional terms with respect to the single-phase  $\epsilon$  equation.

The additional two-phase terms in the  $k$  and  $\epsilon$  equations are modelled by Politis using the gradient diffusion assumption. Terms involving the dispersed phase fluctuation velocity are modelled by relating the (unweighted) dispersed phase velocity fluctuations to those of the continuous phase via a response coefficient  $C_t$  defined as

$$C_t = \frac{u'_s}{u'_l} \quad (2.57)$$

The terms common to the single-phase  $k - \epsilon$  equations are modelled the same way as their corresponding single-phase counterparts. The coefficients introduced are assumed to take their appropriate single-phase values. In vector notation, the final form of the Politis  $k - \epsilon$  equations reads

$$\nabla \cdot \rho_l \bar{\alpha}_l k \tilde{\mathbf{u}}_c = \nabla \cdot \left\{ \bar{\alpha}_l \left( \mu_l + \frac{\mu_l^t}{\sigma_k} \right) \nabla k \right\} + \bar{\alpha}_l G - \rho_l \bar{\alpha}_l \epsilon + S_k \quad (2.58)$$

$$\frac{\partial \alpha_l \rho_l \epsilon}{\partial t} + \nabla \cdot \alpha_l \rho_l \bar{\mathbf{u}}_l \epsilon = \nabla \cdot \left( \alpha_l \left( \mu_l + \frac{\mu_l^t}{\sigma_k} \right) \nabla \epsilon \right) + C_1 \alpha_l \frac{\epsilon}{k} G - C_2 \alpha_l \rho_l \frac{\epsilon^2}{k} + S_\epsilon \quad (2.59)$$

where

$$G = \mu_l^t \left\{ \nabla \tilde{\mathbf{u}}_c + \nabla \tilde{\mathbf{u}}_c^T - \frac{2}{3} (\nabla \cdot \tilde{\mathbf{u}}_c) \mathbf{I} \right\} : \nabla \tilde{\mathbf{u}}_c - \frac{2}{3} \rho_l k \mathbf{I} : \nabla \tilde{\mathbf{u}}_c \quad (2.60)$$

$$S_k = A_d \left\{ \frac{\nu_l^t}{\bar{\alpha}_l \bar{\alpha}_d \sigma_k} (\tilde{\mathbf{u}}_d - \tilde{\mathbf{u}}_c) \cdot \nabla \bar{\alpha}_l + 2k(C_t - 1) \right\} + A_d \left\{ \left( 2C_t - 2 - \frac{C_t}{\bar{\alpha}_s} \right) \frac{C_p^2}{C_t^2 \alpha_s \rho_s^2} \nabla \bar{\alpha}_l : \nabla \bar{\alpha}_l \right\} \quad (2.61)$$

$$S_\epsilon = 2A_d \epsilon (C_t - 1) \quad (2.62)$$

$$C_p = \frac{C_t \mu^t \alpha_l \rho_d}{(\alpha_l \rho_l)^2 \sigma_\alpha} \quad (2.63)$$

The terms  $S_k$  and  $S_\epsilon$  in the above equations are the two-phase terms which are additional to the single-phase  $k - \epsilon$  equations. The first term in  $S_k$  represents the generation or dissipation of turbulence according to the relative directions of the slip velocity and the phase fraction gradient. The second term in  $S_k$  and  $S_\epsilon$  represents the additional dissipation of  $k$  due to the presence of the dispersed phase.

### 2.3.1.2 The Work of Kataoka and Serizawa

Kataoka and Serizawa [30] attempted to rigorously derive the two-phase  $k$ - $\epsilon$  equations by using their ‘local instant’ formulation of two-phase flow. This approach is broadly similar to the conditional averaging technique used in this work. Kataoka and Serizawa define the fluctuating velocity for phase  $k$  as

$$\mathbf{u}'_k = \mathbf{u}_k - \overline{\mathbf{u}_k} \quad (2.64)$$

where  $\mathbf{u}_k$  and  $\overline{\mathbf{u}_k}$  are the instantaneous and mean velocities respectively. The derivation of the transport equation for the phase fluctuation velocity is achieved by subtracting the mean momentum equation from the instantaneous momentum equation which is in terms of  $\mathbf{u}_k$ .

The conditioning process adopted by Kataoka and Serizawa is sufficiently similar to the one used in this work to allow meaningful comparison between their equations and the equations derived in Section 2.3.2.3. To facilitate this comparison, Kataoka and Serizawa’s equations are reproduced here in surface average notation. Their turbulent kinetic energy equation reads

$$\begin{aligned} \frac{\partial \alpha k}{\partial t} + \frac{\partial}{\partial x_j}(\alpha \overline{u_j k}) &= -\alpha \overline{u'_i u'_j} \frac{\partial \overline{u_i}}{\partial x_j} - \frac{\partial}{\partial x_j} \left\{ \alpha \frac{\overline{u'_i u'_i}}{2} \overline{u'_j} + \frac{\alpha}{\rho} \overline{p' u'_j} \right\} - \alpha \epsilon + \\ &\quad \frac{\partial}{\partial x_j}(\alpha \overline{u'_i \tau'_{ij}}) + \frac{1}{\rho} \overbrace{p'' u''_i n_i} \Sigma - \overbrace{\tau''_{ij} u''_i n_j} \Sigma \end{aligned} \quad (2.65)$$

where  $k''$  is defined as

$$k'' = \frac{u''_i u''_i}{2} \quad (2.66)$$

Here,  $p''$ ,  $u''$  and  $\tau''$  are surface fluctuations (ie, relative to the surface average) and  $n_i$  is the surface normal pointing *into* the continuous phase.

The derivation of the  $\epsilon$  equation is carried out by differentiating the fluctuating velocity transport equation for  $u'_i$  with respect to  $x_k$ , multiplying by  $\frac{\partial u'_i}{\partial x_k}$  and averaging, to yield



$$\begin{aligned}
\frac{\partial \alpha \epsilon}{\partial t} + \frac{\partial \bar{u}_j \alpha \epsilon}{\partial x_j} = & -2\nu \alpha \left\{ \overline{\frac{\partial u'_i}{\partial x_k} \frac{\partial u'_i}{\partial x_j} \frac{\partial u'_j}{\partial x_k}} + \frac{\partial \bar{u}_j}{\partial x_k} \overline{\frac{\partial u'_i}{\partial x_k} \frac{\partial u'_i}{\partial x_j}} + \frac{\partial \bar{u}_i}{\partial x_k} \overline{\frac{\partial u'_i}{\partial x_k} \frac{\partial u'_j}{\partial x_k}} + \frac{\partial^2 \bar{u}_i}{\partial x_j \partial x_k} \overline{u'_j \frac{\partial u'_i}{\partial x_k}} \right\} \\
& - \frac{\partial \alpha \epsilon \bar{u}_j}{\partial x_j} - \frac{2\nu}{\rho} \frac{\partial}{\partial x_i} \left( \alpha \overline{\frac{\partial p'}{\partial x_k} \frac{\partial u'_i}{\partial x_k}} \right) + \nu \frac{\partial^2 \alpha \epsilon}{\partial x_j^2} - \nu^2 \alpha \overline{\left( \frac{\partial^2 u'_i}{\partial x_j \partial x_k} \right)^2} \\
& + \frac{2\nu}{\rho} \overbrace{\frac{\partial p''}{\partial x_k} \frac{\partial u'_i}{\partial x_k} n_i} \Sigma - \frac{2\nu}{\rho} \overbrace{p'' n_i} \Sigma \frac{\partial}{\partial x_k} \left( \frac{1}{\alpha} \overbrace{u'_i n_i} \Sigma \right) \\
& - \frac{2\nu}{\rho} \overbrace{u'_i n_k} \Sigma \frac{\partial}{\partial x_k} \left\{ \frac{1}{\alpha} \overbrace{\tau''_{ij} n_j} \Sigma + \frac{1}{\alpha} \overbrace{u'_i u'_j} \overbrace{n_j} \Sigma - \frac{1}{\alpha} \overbrace{p'' n_i} \Sigma \right\} \\
& - 2\nu^2 \overbrace{u'_i n_k} \Sigma \frac{\partial^2}{\partial x_k \partial x_i} \left( \frac{1}{\alpha} \overbrace{u'_j n_j} \Sigma \right) + 2\nu^2 \overbrace{u'_i n_k} \Sigma \frac{\partial^2}{\partial x_j \partial x_k} \left( \frac{1}{\alpha} \overbrace{u'_i n_j} \Sigma \right) \\
& + 2\nu^2 \overbrace{u'_i n_k} \Sigma \frac{\partial^2}{\partial x_j \partial x_k} \left( \frac{1}{\alpha} \overbrace{u'_j n_i} \Sigma \right) \\
& + \nu^2 \frac{\partial}{\partial x_j} \left( \overbrace{\frac{\partial u'_i}{\partial x_k} n_j} \Sigma \right) + 2\nu^2 \overbrace{\frac{\partial u'_i}{\partial x_k} \frac{\partial^2 u'_i}{\partial x_k \partial x_j}} \Sigma
\end{aligned} \tag{2.67}$$

Kataoka and Serizawa proposed models for the correlation terms in Equations (2.65) and (2.67) and obtained a final set of modelled equations applicable to gas-liquid two-phase flow. These models are examined closely in Section 2.3.2.4 where the present two-phase  $k$ - $\epsilon$  is developed.

### 2.3.1.3 The Work of Alajbegovic and Lahey

Alajbegovic [69], reported in Lahey [67], derived the conditional averaged Reynolds stress equation as well as the conditional averaged  $k$ - $\epsilon$  equations. The conditional averaging technique used by Alajbegovic is essentially the same as the one adopted in this work and his equations may also be compared directly with those obtained by the author in Section 2.3.2.3. The turbulent kinetic energy equation reads,

$$\begin{aligned}
\frac{\partial \alpha k}{\partial t} + \frac{\partial}{\partial x_j} (\alpha \bar{u}_j k) = & -\alpha \overline{u'_i u'_j} \frac{\partial \bar{u}_i}{\partial x_j} - \frac{\partial}{\partial x_j} \left\{ \alpha \overline{\frac{u'_i u'_i}{2} u'_j} + \frac{\alpha}{\rho} \overline{p' u'_j} \right\} - \alpha \epsilon + \\
& \frac{\partial}{\partial x_j} (\alpha \overline{u'_i \tau''_{ij}}) + \frac{1}{\rho} \overbrace{p'' u''_i n_i} \Sigma - \overbrace{\tau''_{ij} u''_i n_j} \Sigma
\end{aligned} \tag{2.68}$$

while the turbulent kinetic energy dissipation rate equation reads,

$$\begin{aligned}
\frac{\partial \alpha \epsilon}{\partial t} + \frac{\partial}{\partial x_j} (\alpha \bar{u}_j \epsilon) = & \\
& -2\nu\alpha \left\{ \overline{\frac{\partial u'_i}{\partial x_k} \frac{\partial u'_i}{\partial x_j} \frac{\partial u'_j}{\partial x_k}} + \frac{\partial \bar{u}_j}{\partial x_k} \overline{\frac{\partial u'_i}{\partial x_k} \frac{\partial u'_i}{\partial x_j}} + \frac{\partial \bar{u}_i}{\partial x_k} \overline{\frac{\partial u'_i}{\partial x_k} \frac{\partial u'_j}{\partial x_k}} + \frac{\partial^2 \bar{u}_i}{\partial x_j \partial x_k} \overline{u'_j \frac{\partial u'_i}{\partial x_k}} \right\} \\
& -2\nu^2 \alpha \left( \overline{\frac{\partial^2 u'_i}{\partial x_j \partial x_k}} \right)^2 - \frac{2\nu}{\rho} \frac{\partial}{\partial x_i} \left( \alpha \overline{\frac{\partial p'}{\partial x_k} \frac{\partial u'_i}{\partial x_k}} \right) - \frac{\partial \alpha \epsilon \bar{u}'_j}{\partial x_j} + \nu \frac{\partial^2 \alpha \epsilon}{\partial x_j^2} \\
& + \frac{2\nu}{\rho} \overbrace{\frac{\partial p''}{\partial x_k} \frac{\partial u'_i}{\partial x_k} n_i} \Sigma - \nu \frac{\partial}{\partial x_j} (\overbrace{\epsilon n_j} \Sigma) - \nu \overbrace{\frac{\partial \epsilon}{\partial x_j} n_j} \Sigma \\
& + 2\nu \overbrace{u'_i n_k} \Sigma \left\{ \frac{\partial \bar{u}_i}{\partial t} + \bar{u}_j \frac{\partial \bar{u}_i}{\partial x_j} + \frac{1}{\rho} \frac{\partial \bar{p}}{\partial x_i} - \frac{\partial^2 \bar{u}_i}{\partial x_i^2} \right\} \\
& + \frac{2\nu}{\rho} \overbrace{p'' n_k} \Sigma \frac{\partial^2 \bar{u}_i}{\partial x_k \partial x_i}
\end{aligned} \tag{2.69}$$

Note that while the  $k$  equation is the same as that derived by Kataoka and Serizawa [30], the  $\epsilon$  equations differs significantly. One curious feature of Alajbegovic's result is the complete mean momentum equation which appears as a source term on the right hand side.

It is interesting to note that Lahey has assumed that the continuous phase Reynolds stress is composed of the superposition of the shear induced (SI) and bubble or particle induced (BI) components. Thus, the continuous phase Reynolds stress is given by

$$\mathbb{R}_c = \mathbb{R}_c^{SI} + \mathbb{R}_c^{BI} \tag{2.70}$$

The model adopted for the bubble-induced Reynolds stress is that of de Bertodano [71] which reads

$$\alpha_c \mathbb{R}_c^{SI} = -\alpha_d \rho_c (a_c \bar{\mathbf{u}}_r \bar{\mathbf{u}}_r + b_c \bar{\mathbf{u}}_r \cdot \bar{\mathbf{u}}_r \mathbf{I}) \tag{2.71}$$

where  $a_c$  and  $b_c$  are empirical coefficients.

The shear-induced Reynolds stress terms in the phase momentum equations are represented by an algebraic stress model, in which the phase Reynolds stresses are replaced by algebraic expressions written in terms of the phase  $k$  and  $\epsilon$  values. It appears that the  $k$

and  $\epsilon$  equations adopted by Lahey for the actual calculations presented in their paper are the single-phase versions despite the presentation of the two-phase equations containing the extra two-phase terms as shown above.

### 2.3.2 Continuous Phase Reynolds Stress Modelling

In this section, the models adopted in the present work for the continuous phase Reynolds stresses are discussed. It is clear from the previous section that many previous workers have adopted the Boussinesq eddy viscosity concept in conjunction with the  $k$ - $\epsilon$  model for the modelling of the continuous phase Reynolds stresses [61, 62, 63, 64, 65, 66, 6]. The  $k$ - $\epsilon$  turbulence model has served single-phase flow prediction methods well due to its reasonable accuracy over a wide range of flow conditions and its computational efficiency. In addition, in view of the complexity of the two-phase flow equations and the corresponding uncertainty associated with the many models and approximations which have to be introduced into other parts of the model, the adoption of a more complicated turbulence model (such as a full Reynolds Stress or Algebraic Stress model) cannot be justified at this time. Consequently, the present work also adopts the eddy viscosity approach coupled with a specially formulated two-phase  $k$ - $\epsilon$  turbulence model.

The turbulent Reynolds stresses  $\sigma_k^t$  for the continuous phase are therefore assumed to given by

$$\sigma_c^t = -\rho_c \overline{u'_c u'_c} = \mu_c^t \left\{ \nabla \overline{u}_c + \nabla \overline{u}_c^T - \frac{2}{3} (\nabla \cdot \overline{u}_c) \mathbf{I} \right\} - \frac{2}{3} \rho_c k \mathbf{I}, \quad (2.72)$$

where the turbulent viscosity is given by

$$\mu_c^t = C_\mu \rho_c \frac{k^2}{\epsilon}. \quad (2.73)$$

and where  $k$  and  $\epsilon$  relate to the continuous phase.  $C_\mu$  is a dimensionless coefficient which is assumed to have the same value as in single-phase flow, namely 0.09. The turbulent kinetic energy and its dissipation rate are calculated from their own transport equations.

The conditional-averaged form of the  $k$  and  $\epsilon$  equations are required in order to maintain consistency with the rest of this work. Kataoka and Serizawa [30] and Alajbegovic [69] have both attempted to derive these equations but their equations differ considerably. To try to resolve this inconsistency, the conditional averaged Reynolds stress, turbulent kinetic energy and dissipation rate equations are rigorously derived here.

The derivation starts by formally defining the phase fluctuating velocity and the quantities  $k$  and  $\epsilon$ . The transport equation for the fluctuating velocity is then derived as a precursor to the derivation of the conditional averaged phase Reynolds stress equation in Section 2.3.2.2. Following this, the  $k$  and  $\epsilon$  equations are derived in Section 2.3.2.3. The modelling of the correlation terms in the  $k$ - $\epsilon$  equations is then addressed in Section 2.3.2.4.

### 2.3.2.1 Fluctuating Velocity Definition

In the derivation of the conditional averaged momentum equations in the previous chapter, the velocity was decomposed into mean and a fluctuating components, thus

$$\mathbf{u}_k = \overline{\mathbf{u}}_k + \mathbf{u}'_k \quad (2.74)$$

This allows  $\overline{\mathbf{u}_k \mathbf{u}_k}$  to be decomposed into

$$\overline{\mathbf{u}_k \mathbf{u}_k} = \overline{\mathbf{u}}_k \overline{\mathbf{u}}_k + \overline{\mathbf{u}'_k \mathbf{u}'_k} \quad (2.75)$$

Thus, the velocity fluctuation for phase  $k$  may be defined as

$$\mathbf{u}'_k = \mathbf{u} - \overline{\mathbf{u}}_k \quad (2.76)$$

$$= \mathbf{u} - \frac{\overline{\chi_k \mathbf{u}}}{\overline{\chi_k}} \quad (2.77)$$

This definition is illustrated graphically in Figure 2.4. Note that the instantaneous velocity fluctuation is defined in all space and time domains, even when the other phase is present, relative to the conditional average velocity of phase  $k$ .

This definition for the fluctuating velocity is not the only one possible. One alternative is

$$\mathbf{u}^\sharp_k = \overline{\mathbf{U}} - \overline{\mathbf{u}}_k \quad (2.78)$$

where  $\overline{\mathbf{U}}$  is the mean of the unconditioned velocity. This definition, however, would not allow the conditional-averaged convection term to be rewritten in terms of the phase mean velocities  $\overline{\mathbf{u}}_k$ , and is of little use in the two-fluid model. This definition is more suited to the mixture model of two-phase flow as discussed in Section 1.5.

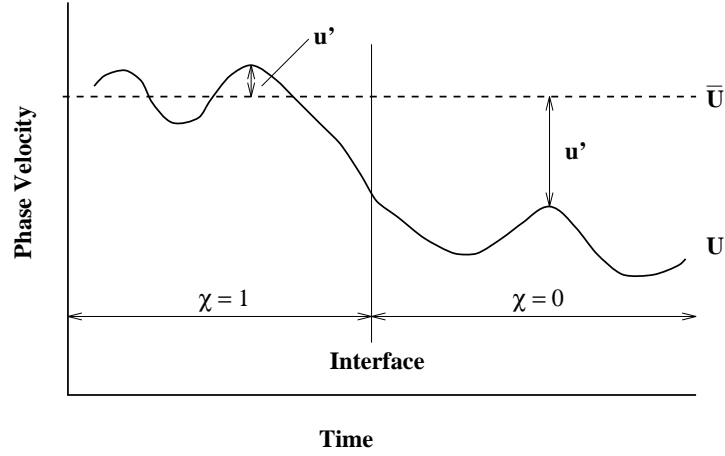


Figure 2.4: Fluctuating velocity definition.

Following from the definition of the velocity fluctuation by Eqn (2.76), the turbulent kinetic energy and its dissipation rate for phase  $k$  are defined, in tensor notation, by

$$k = \frac{1}{2} \overline{u'_i u'_i} \quad (2.79)$$

$$\epsilon = \nu \overline{\frac{\partial u'_i}{\partial x_j} \frac{\partial u'_i}{\partial x_j}} \quad (2.80)$$

The derivation of the turbulence transport equations requires the transport equation for the fluctuation velocity defined by Eqn (2.76). This is obtained by subtracting the conditional averaged momentum equation from the instantaneous momentum equation. Therefore, subtraction of Eqn (1.36) from Eqn (1.27) yields

$$\begin{aligned} \frac{\partial u'_i}{\partial t} + \frac{\partial}{\partial x_j} \left\{ \bar{u}_i u'_j + u'_i \bar{u}_j + u'_i u'_j \right\} + \bar{u}_i \frac{\partial \bar{u}_j}{\partial x_j} = \\ \frac{\partial \tau'_{ij}}{\partial x_j} - \frac{1}{\rho_k} \frac{\partial p' \delta_{ij}}{\partial x_j} + \\ \frac{\partial \overline{u'_i u'_j}}{\partial x_j} + \frac{1}{\alpha_k \rho_k} \frac{\partial \alpha_k}{\partial x_j} \left\{ \rho_k \overline{u'_i u'_j} - \bar{\tau}_{ij} + \bar{p} \delta_{ij} \right\} \\ + \frac{1}{\alpha_k} \overbrace{\tau''_{ij} n_j}^{\Sigma} - \frac{1}{\alpha_k \rho_k} \overbrace{p'' \delta_{ij} n_j}^{\Sigma} \end{aligned} \quad (2.81)$$

where  $\tau''$  and  $p''$  are surface fluctuations of the stress and pressure in phase  $k$ . The above equation forms the basis of the derivation of the conditional averaged Reynolds stress,  $k$

and  $\epsilon$  equations. It is interesting to note that the above equation compares directly with the corresponding equation of Kataoka and Serizawa [30].

### 2.3.2.2 Conditional Averaged Reynolds Stress Transport Equation

Although the derivation of the conditional-averaged Reynolds stress equations is not strictly required in order to derive the  $k$ - $\epsilon$  equation (they can be derived directly from Eqn (2.81)), it is presented here for completeness. The derivation proceeds by multiplying Eqn (2.81), written in terms of  $u'_i$ , by  $u'_k$  and adding the result to Eqn (2.81) in terms of  $u'_k$  multiplied by  $u'_i$ . The resulting equation is then conditional averaged rearranged to yield the required equation. Appendix C contains the detailed derivation. The resulting equation reads

$$\begin{aligned}
\frac{\partial \overline{\alpha u'_i u'_k}}{\partial t} + \frac{\partial}{\partial x_j} (\alpha \overline{u_j u'_i u'_k}) &= -\overline{\alpha u'_k u'_j} \frac{\partial \overline{u_i}}{\partial x_j} - \overline{\alpha u'_i u'_j} \frac{\partial \overline{u_k}}{\partial x_j} - \\
&\quad \frac{\partial}{\partial x_j} (\overline{\alpha u'_i u'_j u'_k}) - 2\alpha \epsilon_{ik} + \\
&\quad \frac{\partial}{\partial x_j} (\overline{\alpha u'_k \tau'_{ij}} + \overline{\alpha u'_i \tau'_{kj}}) - \\
&\quad \frac{1}{\rho} \left\{ \frac{\partial \overline{\alpha u'_i p'}}{\partial x_k} - \frac{\partial \overline{\alpha u'_k p'}}{\partial x_i} \right\} - \frac{1}{\rho} \left\{ \overline{\alpha p' \left( \frac{\partial u'_i}{\partial x_k} + \frac{\partial u'_k}{\partial x_i} \right)} \right\} + \\
&\quad \frac{1}{\rho} \left\{ \overline{u''_k p'' n_i} \Sigma + \overline{u''_i p'' n_j} \Sigma \right\} - \overline{u''_k \tau''_{ij} n_j} \Sigma + \overline{u''_i \tau''_{kj} n_j} \Sigma + \\
&\quad \overline{u_j u''_i u''_k n_j} \Sigma + \overline{u''_i u''_j u''_k n_j} \Sigma - \overline{u''_i u''_k U_j n_j} \Sigma \quad (2.82)
\end{aligned}$$

The terms on the left-hand side of Eqn (2.82) represent the rate of change and convective transport of the Reynolds stress tensor. The first two terms on the right-hand side represent stress production, while the third, fifth and sixth terms represent diffusive transport. The fourth term represents the viscous dissipation of the Reynolds stresses. The seventh term represents the pressure-strain effect and the last seven terms represent the additional effects of the dispersed phase on the Reynolds stresses.

Eqn (2.82) is similar to that of Alajbegovic [69] (as reported in Lahey [67]) except for the last three of the two-phase terms which do not appear in his equation. The origin of these terms lies in the conditioning of the derivatives of fluctuating quantities which results in derivatives containing the phase fraction and surface average terms (see Appendix C). It may be that these additional terms have been neglected by Alajbegovic, or that they have been inadvertently omitted. This inconsistency will be further discussed below.

### 2.3.2.3 Conditional Averaged $k$ - $\epsilon$ Equations

Contraction of Eqn (2.82) yields

$$\begin{aligned}
\frac{\partial \alpha k}{\partial t} + \frac{\partial}{\partial x_j} (\alpha \bar{u}_j k) &= -\alpha \overline{u'_i u'_j} \frac{\partial \bar{u}_i}{\partial x_j} - \frac{\partial}{\partial x_j} \left\{ \alpha \frac{\overline{u'_i u'_i}}{2} \bar{u}_j + \frac{1}{\rho} \overline{p' u'_j} \right\} + \\
&\quad \frac{\partial}{\partial x_j} \left( \alpha \nu \frac{\partial k}{\partial x_j} \right) - \alpha \epsilon \\
&\quad \frac{1}{\rho} \overbrace{p'' u''_i n_i} \Sigma - \overbrace{\tau''_{ij} u''_i n_j} \Sigma + \\
&\quad (\bar{u}_j - \overbrace{u_j}) \overbrace{k'' n_j} \Sigma
\end{aligned} \tag{2.83}$$

where  $k''$  is the turbulent kinetic energy of the velocity fluctuations at the interface.

The first term on the right hand side represents the production of turbulent kinetic energy by the interaction between the Reynolds stresses and the mean velocity gradients. The second and third terms represent the turbulent and viscous diffusive transport of  $k$  respectively while the fourth term represents the viscous dissipation of  $k$  into heat.

The last three terms are in addition to the single phase turbulent kinetic energy transport equation and represent the effects of the dispersed phase on  $k$ . The first two terms represent the interaction between the pressure and shear stresses with the phase interface. Kataoka and Serizawa [30] have shown that these terms account for the additional generation and dissipation of turbulence due to surface tension and drag forces. The third term is associated with turbulence generation due to non-isotropic disturbances of the interface.

Comparison of Eqn (2.83) with the corresponding equations of Kataoka and Serizawa (Eqn (2.65)) and Alajbegovic (Eqn (2.68)) shows that the last term in Eqn (2.83) does not appear in the other equations. This term originates from the last three terms in the conditional averaged Reynolds stress equation which were found to be missing from the equation derived by Alajbegovic. Close examination of Kataoka and Serizawa's derivation indicates that the missing three terms should in fact be present. Since Kataoka and Serizawa do not explicitly state that these terms have been purposefully omitted (for example, by order of magnitude arguments) it has to be assumed that they have been accidentally missed.

The detailed derivation of the conditional averaged  $\epsilon$  equation is given in appendix C. The result reads

$$\begin{aligned}
\frac{\partial \alpha \epsilon}{\partial t} + \frac{\partial \bar{u}_j}{\partial x_j} \alpha \epsilon &= -2\nu\alpha \left\{ \frac{\partial \bar{u}_j}{\partial x_k} \overline{\frac{\partial u'_i}{\partial x_k} \frac{\partial u'_j}{\partial x_j}} + \frac{\partial \bar{u}_i}{\partial x_k} \overline{\frac{\partial u'_i}{\partial x_k} \frac{\partial u'_j}{\partial x_j}} + \frac{\partial^2 \bar{u}_i}{\partial x_j \partial x_k} \overline{u'_j \frac{\partial u'_i}{\partial x_k}} \right\} - \\
&\quad \frac{2\nu\alpha}{\rho} \frac{\partial}{\partial x_i} \left( \overline{\frac{\partial p'}{\partial x_k} \frac{\partial u'_i}{\partial x_k}} \right) - \nu \frac{\partial}{\partial x_j} \left( \overline{u'_j \frac{\partial u'_i}{\partial x_k} \frac{\partial u'_i}{\partial x_k}} \right) + \\
&\quad \nu\alpha \frac{\partial^2 \epsilon}{\partial x_j \partial x_j} - 2\nu\alpha \overline{\frac{\partial u'_i}{\partial x_k} \frac{\partial u'_i}{\partial x_j} \frac{\partial u'_j}{\partial x_k}} - 2\alpha \left\{ \nu \overline{\frac{\partial^2 u'_i}{\partial x_j \partial x_k}} \right\}^2 + \\
&\quad (\bar{u}_j - \overbrace{u_j}) \overbrace{\epsilon'' n_j} \Sigma - \overbrace{\epsilon'' \bar{u}_j}'' n_j \Sigma
\end{aligned} \tag{2.84}$$

The first three terms on the right side of the above equation are responsible for the generation of  $\epsilon$  by the mean motion. The next three terms are responsible for the diffusive transport of  $\epsilon$ . The seventh term represents the generation of  $\epsilon$  due to the self-stretching of the turbulence vortex tubes while the eighth term represents the viscous destruction of  $\epsilon$ . The last two terms represent the additional dissipation of energy due to the presence of the dispersed phase.

Comparison of Eqn (2.84) with the  $\epsilon$  equations of Kataoka and Serizawa (Eqn (2.67)) and Alajbegovic (Eqn (2.69)) reveals considerable differences. Unfortunately, insufficient details are given by Kataoka and Serizawa and Alajbegovic to attempt a full re-derivation of their equations. It is likely that the differences in the  $\epsilon$  equation arise from the conditioning of terms involving more than one derivative. When a term contains the product of two or more derivatives it is not immediately obvious into which derivative the conditioning function should be placed. There are numerous possibilities and the method chosen strongly affects the resulting form of the equation.

The derivation of Eqn (2.84) presented here is based on the assumption that such terms may be written as simple conditional averages, for example,

$$\overline{\chi_k \frac{\partial u'_i}{\partial x_k} \frac{\partial u'_i}{\partial x_j}} = \alpha \overline{\frac{\partial u'_i}{\partial x_k} \frac{\partial u'_i}{\partial x_j}} \tag{2.85}$$

This is consistent with the definition of  $\epsilon$  given by Eqn (2.80).

Complicated alternative definitions of the indicator function, such as conditioning with  $\chi_k^2$  or  $\chi_k^3$  for example, have not been pursued here since such methods introduce other problems when applied to terms involving a single derivative. Furthermore, the adoption of such conditioning functions requires that the definition of  $\epsilon$  be changed to suit leading to a cumbersome and physically obscure  $\epsilon$  definition.



In any case, the resulting complexity in the derivation process is not necessarily accompanied by an increase in the accuracy of the final  $\epsilon$  equation since rather drastic modelling assumptions have to be applied to obtain a practical  $\epsilon$  equation [72]. Consequently, the current work is based on the  $\epsilon$  equation as shown above.

#### 2.3.2.4 Modelled Form of the $k - \epsilon$ Equations

This section describes the closure of the  $k$  and  $\epsilon$  equations derived in the previous section by the introduction of models to represent the unknown terms. The modelling of the terms which are common to both the single and two-phase  $k$ - $\epsilon$  equations is accomplished by adopting the single-phase counterparts. These are well established and are known to produce good results in a wide variety of flow conditions; see for example, Rodi [73, 72], Launder and Spalding [11] and McComb [70]. It is assumed that these models, along with the corresponding values for the coefficients within them, are applicable to two-phase flow. Since the present derivation of the  $k$ - $\epsilon$  equations is similar to that of Kataoka and Serizawa [30], it is instructive to consider in detail their practices before the final models adopted in this work are presented.

Kataoka and Serizawa have derived models for the first two two-phase terms in the  $k$  equation (Eqn (2.83)) by writing the fluctuating quantities of velocity, pressure and stress at the interface in terms of the phase averages and the values at the interface.

$$\begin{aligned} u'' &= u_i - \bar{u} \\ p'' &= p_i - \bar{p} \\ \tau'' &= \tau_i - \bar{\tau} \end{aligned}$$

where  $u_i$ ,  $p_i$  and  $\tau_i$  are the value at the interface and  $\bar{u}$ ,  $\bar{p}$  and  $\bar{\tau}$  are the conditional averages. Substitution of the above into the two-phase terms yields

$$\begin{aligned} \overbrace{p'' u_i'' n_i} \Sigma - \overbrace{\tau_{ij}'' u_i'' n_j} \Sigma &= \overbrace{p u_i n_i} \Sigma - \overbrace{\tau_{ij} u_i n_j} \Sigma - \\ &\quad \overline{u_i} \overbrace{(p - \bar{p}) n_i} \Sigma + \overline{u_i} \overbrace{\tau_{ij} n_j} \Sigma - \\ &\quad \overbrace{p u_i n_i} \Sigma + \overline{\tau_{ij}} \overbrace{u_i'' n_j} \Sigma \end{aligned} \quad (2.86)$$

The first two terms on the right hand side are shown to be related to the surface tension force due to the momentum balance at the interface. These two terms can be written as

$\overbrace{F_\sigma u_i} \Sigma$  which represents the work done by the surface tension force  $F_\sigma$ . Kataoka and Serizawa relate this to the reduction in the surface energy and write it as

$$\overbrace{F_\sigma u_i} \Sigma = -U_s \Gamma_s \Sigma \quad (2.87)$$

where  $U_s$  is the surface energy per unit area and  $\Gamma_s$  is the rate of increase in the surface area. The next two terms in Eqn (2.86) are shown to be related to the drag force. The interfacial drag term is written as

$$F_{d_i} = \overbrace{p'' n_i} \Sigma - \overbrace{\tau_{ij} n_j} \Sigma \quad (2.88)$$

These two terms are modelled in terms of the drag coefficient and the relative velocity

$$-F_{d_i} u_i^r = A_d u_i^r u_i^r = A_d |u^r|^2 \quad (2.89)$$

where  $u^r$  is the relative velocity between phases and  $A_d$  is the drag coefficient (for example, as given by Eqn (2.8)). This term is always positive, since the drag force always acts to reduce the relative velocity and so has a sign opposite to it. This term is therefore held to be responsible to the drag-induced turbulence generation.

The next term in Eqn (2.86) is related to the temporal derivative of the phase fraction since

$$\overbrace{u_i n_i} \Sigma = -\frac{\partial \alpha}{\partial t} \quad (2.90)$$

(see Appendix A). The physical significance of this term is related to the turbulence generated by void wave propagation. The final term in Eqn (2.86) is assumed by Kataoka and Serizawa to be zero because the velocity fluctuations at the interface are assumed to be isotropic and not correlated with the surface normal. Thus, the final modelled form of the two-phase terms reads

$$\begin{aligned} \overbrace{p'' u_i'' n_i} \Sigma - \overbrace{\tau_{ij}'' u_i'' n_j} \Sigma = \\ -U_s \Gamma_s \Sigma - F_{d_i} u_i^r - (p_1 - p_2) \frac{\partial \alpha}{\partial t} \end{aligned} \quad (2.91)$$

The closure of the Kataoka and Serizawa  $\epsilon$  equation is accomplished by first simplifying the equation by applying the same assumptions as for the  $k$  equation and then neglecting terms involving higher-order derivatives. In this way, the ten or so two-phase terms in the  $\epsilon$  equation are reduced to two which involve the surface averaged derivatives of the pressure and velocity at the interface. These terms are modelled by simply assuming that the surface average of these terms is the same as the phase average, thus allowing their direct computation.

The modelling strategy of Kataoka and Serizawa is adopted in the present work but with some modifications to maintain consistency with the rest of the present two-phase framework. First, the interfacial pressure, velocity and stress fluctuations in Eqn (2.83) are defined to be relative to their surface averaged values, not the phase average values. Thus, we have

$$\begin{aligned} u'' &= u_i - \overbrace{u} \\ p'' &= p_i - \overbrace{p} \\ \tau'' &= \tau_i - \overbrace{\tau} \end{aligned}$$

where  $\overbrace{u}$ ,  $\overbrace{p}$  and  $\overbrace{\tau}$  are the surface average values of velocity, pressure and shear stress. Substitution of the above into the first two two-phase terms in Eqn (2.83) yields

$$\begin{aligned} \overbrace{p'' u_i'' n_i} \Sigma - \overbrace{\tau_{ij}'' u_i'' n_j} \Sigma &= \overbrace{p u_i n_i} \Sigma - \overbrace{\tau_{ij} u_i n_j} \Sigma - \\ &\quad \overbrace{u_i} \overbrace{(p - \bar{p}) n_i} \Sigma + \overbrace{u_i} \overbrace{\tau_{ij} n_j} \Sigma - \\ &\quad \overbrace{p} \overbrace{u_i n_i} \Sigma + (\overbrace{p} - \bar{p}) \overbrace{u_i} \Sigma \frac{\partial \alpha_k}{\partial x_i} + \\ &\quad \overbrace{\tau_{ij}} \overbrace{u_i'' n_j} \Sigma + (\overline{u_i} - \overbrace{u_i}) \overbrace{k n_i} \Sigma \end{aligned} \quad (2.92)$$

The sixth and eighth terms in Eqn (2.92) are additional to Kataoka and Serizawa's Eqn (2.86) and involve the difference between the phase average and surface average values of pressure and velocity. All the other terms are taken to have the same meaning ascribed by Kataoka and Serizawa.

An expression for the surface average pressure was derived in Section 2.2.4 which reads

$$\overbrace{p_i} = \bar{p} - 0.37 \rho_c C_d |\overline{\mathbf{u}_r}|^2 \quad (2.93)$$

Substitution of this expression into the final term on the right hand side of Eqn (2.92), along with the assumption that  $\overbrace{u_i} \approx \overline{u_i}$  yields

$$(\overbrace{p} - \overline{p}) \overbrace{u_i} \Sigma \frac{\partial \alpha_k}{\partial x_i} = -0.37 \rho_c C_d |\overline{\mathbf{u}_r}|^2 \overline{u_i} \frac{\partial \alpha_k}{\partial x_i} \quad (2.94)$$

The final term in Eqn (2.92) is associated with turbulence generation by non-isotropic disturbances at the interface. This mechanism of turbulence generation is assumed to be small and this term will therefore be neglected. This is consistent with the assumption that  $\overbrace{u_i} \approx \overline{u_i}$ .

Adopting Kataoka and Serizawa's model for the drag-induced turbulence generation (Eqn (2.89)) and neglecting the effects of surface tension and void wave propagation, Eqn (2.94) becomes

$$\overbrace{p'' u_i'' n_i} \Sigma - \overbrace{\tau_{ij}'' u_i'' n_j} \Sigma = -F_{d_i} u_i^r - 0.37 \rho_c C_d |\overline{\mathbf{u}_r}|^2 \overline{u_i} \frac{\partial \alpha_k}{\partial x_i} \quad (2.95)$$

Turning to the  $\epsilon$  equation, the two-phase terms in the conditional averaged two-phase  $\epsilon$  equation (Eqn (2.84)) are

$$(\overline{u_j} - \overbrace{u_j'}) \overbrace{\epsilon'' n_j} \Sigma - \overbrace{\epsilon'' u_j'' n_j} \Sigma \quad (2.96)$$

As noted above, the present  $\epsilon$  equation differs considerably from that of Kataoka and Serizawa due to the conditional average derivation procedure and the adoption of a consistent definition for  $\epsilon$  as given by Eqn (2.80).

In Kataoka and Serizawa's model, the higher-order terms in the  $\epsilon$  equation are neglected and the terms containing derivatives of surface averaged properties are modelled by assuming that the surface averaged properties are equal to the phase averaged properties. Because of the large differences between the Kataoka and Serizawa equation and the conditional averaged equation, this strategy is not relevant and an alternative approach must be sought.

The first of the two-phase terms in Eqn (2.96) represents the additional dissipation of  $k$  through non-isotropic disturbances in the interface. This term is neglected in the present work. The last term is held to be responsible for the dissipation of  $k$  due to the presence of the dispersed phase. In order to determine a suitable modelled form for this term, it is useful to consider the case of a homogeneous swarm of bubbles rising in a stagnant fluid within a large tank. Under these conditions, the  $k$  and  $\epsilon$  equations reduce to [74]

$$0 = -\alpha_c \epsilon + S_k \quad (2.97)$$

$$0 = -\alpha_c C_2 \frac{\epsilon^2}{k} + S_\epsilon \quad (2.98)$$

where  $S_k$  and  $S_\epsilon$  represent the additional two-phase terms. These two equations together imply that

$$S_\epsilon = C_2 \frac{\epsilon}{k} S_k \quad (2.99)$$

which yields an approximate model for the additional two-phase source terms in the  $\epsilon$  equation.

It should be noted that the above heuristic arguments are entirely in keeping with the modelling of the other (single-phase) terms in the  $\epsilon$  equation. The complicated form of the  $\epsilon$  equation, and the lack of a detailed knowledge of the behaviour of the many complex correlations it contains means that some fairly drastic modelling assumptions are required in order to produce a practical result [72].

### 2.3.2.5 Summary Of The Two-phase $k - \epsilon$ Equations

The final two-phase turbulent kinetic energy equation reads

$$\begin{aligned} \frac{\partial \rho_c \alpha_c k}{\partial t} + \nabla \cdot \rho_c \alpha_c k \bar{\mathbf{u}}_c &= \nabla \cdot \left\{ \alpha_c \left( \mu_c + \frac{\mu_c^t}{\sigma_k} \right) \nabla k \right\} + \\ &\alpha_c G - \rho_c \alpha_c \epsilon - \mathbf{F}_d \cdot \bar{\mathbf{u}}_r - \\ &0.37 \rho_c C_d |\bar{\mathbf{u}}_r|^2 \bar{\mathbf{u}}_r \cdot \nabla \alpha_c \end{aligned} \quad (2.100)$$

where  $\mathbf{F}_d$  is given by Eqn (2.7) and  $G$  represents the turbulence generation due to the mean shear and is given by

$$G = \mu_c^t \left\{ \nabla \bar{\mathbf{u}}_c + \nabla \bar{\mathbf{u}}_c^T - \frac{2}{3} (\nabla \cdot \bar{\mathbf{u}}_c) \mathbf{I} \right\} : \nabla \bar{\mathbf{u}}_c - \frac{2}{3} \rho_c k \mathbf{I} : \nabla \bar{\mathbf{u}}_c \quad (2.101)$$

Similarly, the modelled form of the two-phase  $\epsilon$  equation reads

$$\begin{aligned}
\frac{\partial \alpha_c \rho_c \epsilon}{\partial t} + \nabla \cdot \alpha_c \rho_c \overline{\mathbf{u}}_c \epsilon &= \nabla \cdot \left( \alpha_c \left( \mu_c + \frac{\mu_c^t}{\sigma_\epsilon} \right) \nabla \epsilon \right) + \\
&C_1 \alpha_c \frac{\epsilon}{k} G - C_2 \alpha_c \rho_c \frac{\epsilon^2}{k} - \\
&C_2 \frac{\epsilon}{k} \mathbf{F}_d \cdot \overline{\mathbf{u}}_r - 0.37 C_2 \frac{\epsilon}{k} \rho_c C_d |\overline{\mathbf{u}}_r|^2 \overline{\mathbf{u}}_r \cdot \nabla \alpha_c \quad (2.102)
\end{aligned}$$

The values adopted for the coefficients are the same as for the single-phase case and are summarised in Table 2.1.

$C_\mu$	$C_1$	$C_2$	$\sigma_\epsilon$	$\sigma_k$
0.09	1.44	1.92	1.0	1.3

Table 2.1:  $k - \epsilon$  turbulence model coefficients.

### 2.3.3 Dispersed Phase Reynolds Stress Modelling

In this work, the modelling of the dispersed phase Reynolds stresses broadly follows the response coefficient approach of Politis [6]. However, before this approach can be confidently incorporated into the current conditional averaging framework, certain conceptual questions need to be resolved. In particular, consideration must be given to the exact definition of the response coefficient  $C_t$  with respect to the definition of the phase velocity fluctuations since the original definition proposed by Politis does not fit well with the current conditional averaged framework. Following this, suitable models for  $C_t$  must be found which are applicable to liquid-liquid and gas-liquid flows.

#### 2.3.3.1 Response Coefficient Definition

Politis [6] originally defined the response coefficient as

$$C_t = \frac{u'_d}{u'_c} \quad (2.103)$$

where  $u'_c$  and  $u'_d$  are the unweighted phase velocity fluctuations. This deceptively simple definition requires careful consideration. Firstly, the scalar relationship in Eqn (2.103) implies that the velocity fluctuations in each co-ordinate direction are related by the same coefficient,

$$C_t = \frac{u'_d}{u'_c} = \frac{v'_d}{v'_c} = \frac{w'_d}{w'_c} \quad (2.104)$$

where  $u$ ,  $v$  and  $w$  represent the velocity components in the  $x$ ,  $y$  and  $z$  directions respectively. This, in turn, implies that the response time of the particle or bubble is always small compared to the eddy lifetime and the particle responds to changes in the surrounding fluid direction quickly so that the phase velocities are always co-linear.

Secondly, since, in the instantaneous sense, the velocity fluctuations  $u'_c$  and  $u'_d$  are not strictly defined at the same point in time and space, it is not clear exactly which fluctuating velocities are implied by Eqn (2.103). Since Politis was concerned with solid particles, the velocity fluctuation of the dispersed phase can be taken as being the velocity fluctuation of the entire particle. The continuous phase fluctuating velocity, however, is not so clearly defined. Presumably, Politis intended  $u'_c$  to be interpreted as some ‘characteristic’ velocity fluctuation.

Also, in the derivation of the dispersed phase Reynolds stresses, Politis has implicitly assumed that the response coefficient is constant with respect to time averaging, thus allowing  $C_t$  to be taken out of the averaging process. Hence

$$\overline{C_t^2 u''_c u''_c} = C_t^2 \overline{u''_c u''_c} \quad (2.105)$$

This allows the dispersed phase Reynolds stresses to be related directly to the continuous phase Reynolds stresses without any additional correlation terms involving  $C_t$  fluctuations.

Finally, experimental validation of any proposed  $C_t$  model clearly depends on the experimental determination of the appropriate quantities. Hence, the fluctuating velocities in Eqn (2.103) must be clearly defined if accurate and independently validated  $C_t$  models are to be produced.

Clearly, the definition of  $C_t$  as proposed by Politis suffers from some conceptual difficulties. In order to remedy the situation, the  $C_t$  concept is here generalised and extended in order to address the issues raised above.

The ultimate aim of the response coefficient approach is to be able to write the dispersed phase Reynolds stresses in terms of the continuous phase Reynolds stresses. In this respect, the approach may be generalised via the definition of a tensorial response coefficient, denoted  $C_{ij}^t$ , which relates the Reynolds stress components of the two phase Reynolds stress terms rather than the individual velocity component. Hence, in tensor notation, we have

$$\overline{u'_{d_i} u'_{d_j}} = C_{ij}^t \overline{u'_{c_i} u'_{c_j}} \quad \text{No summation over } i \text{ or } j \quad (2.106)$$

Thus, the individual dispersed phase normal stresses are given by

$$\overline{u'^2_{d_i}} = C_{ii}^t \overline{u'^2_{c_i}} \quad (2.107)$$

The dispersed phase turbulent kinetic energy is therefore defined as

$$k_d = \frac{1}{2}(\overline{u'^2_{d_1}} + \overline{u'^2_{d_2}} + \overline{u'^2_{d_3}}) = \frac{1}{2}(C_{11}^t \overline{u'^2_{c_1}} + C_{22}^t \overline{u'^2_{c_2}} + C_{33}^t \overline{u'^2_{c_3}}) \quad (2.108)$$

Similarly, the off-diagonal stress terms then take the form

$$\overline{u'_{d_i} u'_{d_j}} = C_{ij}^t \overline{u'_{c_i} u'_{c_j}} \quad (2.109)$$

The most general of models would need to provide all six independent values for the  $C^t$  tensor. Simplifications are possible by modelling the off-diagonal components of the  $C_{ij}^t$  in terms of the diagonal components, for example by assuming that the dispersed phase Reynolds stress correlation coefficients have a constant value. The correlation coefficient  $C_{ij}$  is defined as

$$C_{ij} = \frac{\overline{u'_{d_i} u'_{d_j}}}{\sqrt{\overline{u'^2_{d_i}}} \sqrt{\overline{u'^2_{d_j}}}} \quad (2.110)$$

Hence, the off diagonal terms could be written in terms of the diagonal components of the  $C_{ij}^t$  tensor

$$\overline{u'_{d_i} u'_{d_j}} = C_{ij} C_{ii}^t C_{jj}^t \sqrt{\overline{u'^2_{c_i}}} \sqrt{\overline{u'^2_{c_j}}} \quad (2.111)$$

where  $C_{ij}$  is the value of the correlation coefficient. This would reduce the number of models required to three,  $C_{11}^t$ ,  $C_{22}^t$  and  $C_{33}^t$  which relate the three dispersed and continuous phase normal stresses.



A further simplification may be obtained by assuming that the three normal stresses are related by the same coefficient, as would be the case in isotropic turbulence where the bubble or particle response is also isotropic, and that the correlation coefficient is one. In this case we would have

$$\overline{u'_{d_i} u'_{d_j}} = C_t^2 \overline{u'_{c_i} u'_{c_j}} \quad (2.112)$$

It can be seen from this that the definition of  $C_t$  proposed by Politis is a limiting form of the more general definition proposed above. Note that Eqn (2.112) implies that  $C_t$  is defined as the ratio of the two phase RMS velocities.

$$C_t = \frac{\sqrt{\overline{u_{d_i}^2}}}{\sqrt{\overline{u_{c_i}^2}}} \quad (2.113)$$

In the simple form given by Eqn (2.113), it can be seen that the new definition of  $C_t$  relates the conditional averaged normal stresses of the phases. This has a number of advantages. Firstly, the conceptual difficulties associated with the original definition are avoided since the conditional averaged phase normal stresses exist at all points in time and space. Secondly, since the phase normal stresses may be measured experimentally, the independent validation of proposed  $C_t$  models can now be achieved. Finally, the assumption that the response coefficient is constant with respect to time averaging is now no longer required since it is defined in terms of averaged quantities.

The response coefficient concept clearly relies on the fact that the individual components of the dispersed phase Reynolds stress tensor may be directly linked to those of the continuous phase Reynolds stress tensor via a scalar function. At the moment, there is insufficient experimental evidence to prove or disprove this hypothesis. The inherent difficulty in obtaining accurate LDA measurements of the off-diagonal terms of the Reynolds stress tensor is exacerbated by the presence of the dispersed phase. In addition, the accurate measurement of any of the components of the dispersed phase Reynolds stress tensor is exceedingly difficult.

Hereafter, in the present work it will be assumed that the individual components of the response coefficient tensor are all equal to the single value  $C_t$ . The adopted definition of  $C_t$  is based on the relationship between the phase normal stresses as shown above, and not on the ‘instantaneous’ velocity fluctuations of Politis.

### 2.3.3.2 Response Coefficient Modelling

Various models for  $C_t$  have been proposed, both for solid-liquid and gas-liquid flows. Politis derived a relatively simple  $C_t$  model applicable to solid/liquid flows by considering the response of a solid particle subjected to a suddenly accelerating flow. By working with a linearised form of the Lagrangian equation of motion for a particle, Politis was able to obtain an expression for the fluctuating velocity of the particle as a function of the continuous phase fluctuating velocity and the particle response time  $\tau_p$ , as follows

$$u'_s = u'_f(1 - \exp^{-\tau_f/\tau_p}) \quad (2.114)$$

where  $\tau_f$  is the Lagrangian time scale, assumed by Politis to be given by

$$\tau_f = \frac{15}{12} \frac{k}{\epsilon} \quad (2.115)$$

The particle response time-scale  $\tau_p$  is given in terms of the particle drag coefficient  $A_d$  as

$$\tau_p = \frac{1}{A_d} \quad (2.116)$$

where  $A_d$  relates to the drag on the particle and is given in terms of its particular mean relative velocity as given, for example, by Eqn (2.8).

For  $\tau_p \ll \tau_f$ , Politis' model predicts  $C_t \rightarrow 1$  which indicates that the particle will follow the continuous phase velocity fluctuations exactly. For  $\tau_p \gg \tau_f$ , on the other hand,  $C_t \rightarrow 0$  which indicates that the particles do not respond at all to the continuous phase velocity fluctuations.

Other authors have attempted to derived  $C_t$  models by a similar route which are applicable to bubbly flows, notably Chesters [75] and Issa [76]. Issa's model reads

$$C_t = \frac{3 + \beta}{1 + \beta + 2\rho_d/\rho_c} \quad (2.117)$$

where

$$\beta = \frac{12A_d}{\pi d \mu_c} \left( \frac{l_e}{d} \right) \frac{1}{Re_t} \quad (2.118)$$

and  $l_e$  is the turbulence length scale, given by  $C_\mu k^{1.5}/\epsilon$ , and  $Re_t$  is the turbulence Reynolds number given by  $u'_c l_e/\nu_c$ . The derivation of the above equation is given in Appendix B.

For large density ratios, this model yields values for  $C_t$  which vary between 3 (as  $\beta \rightarrow 0$ ) and 1 (as  $\beta \rightarrow \infty$ ). The large  $C_t$  values are due to the low inertia of the dispersed phase with respect to the continuous phase leading to high acceleration of the bubble. As  $\rho_d/\rho_c \rightarrow 1$  the model predicts that  $C_t \rightarrow 1$ , which is consistent with the model of Politis.

In the present work, the  $C_t$  models of Politis and Issa are used for solid-liquid and gas-liquid flows respectively. In order to satisfy the present requirement for a model for  $C_t$  in terms of averaged quantities, rather than instantaneous quantities, it is assumed here that the models of Politis and Issa presented above are applicable when they are calculated with suitably averaged quantities.

For example, in Politis'  $C_t$  model, the particle response time is based on the average drag force which is in terms of the mean relative velocity between the two phases as a whole rather than the specific particle's relative velocity. In Issa's  $C_t$  model, the drag force is similarly taken to be the same as the average drag force while the continuous phase fluctuating velocity is taken to be RMS value as determined from the continuous phase turbulent kinetic energy via  $\sqrt{\frac{3k}{2}}$ .

The assumption that these models remain valid is based on the assumption that the response of a particular particle or bubble to a particular eddy is essentially the same regardless of the relative sizes or motion between the particle or bubble and the eddy. Clearly, this assumption may not always be valid.

As discussed extensively in the next chapter, two-phase flows of engineering interest are frequently associated with a distribution of bubble, droplet or particle sizes due to break-up, coalescence or separation effects. Similarly, the continuous phase turbulence itself contains a very large number of length scales. It is easy to imagine situations where the response of a bubble or particle to an eddy is highly dependent on the relative size.

For instance, bubbles much larger than the energy containing eddy sizes will probably not respond much to the turbulence but would rather exhibit oscillations in its surface structure. Conversely, bubbles or particles much smaller than the Kolmogorov eddy size will experience a transient viscous flow and their response will approach that predicted by classical dispersion theory [77].

In order to capture such effects, it may be necessary to formulate a 'spectral'  $C_t$  model which takes into account the different response of bubbles or particles of a particular size to turbulent eddies of a particular size. A requirement of this approach is that the response of individual bubbles is known for a wide range of bubble and eddy sizes. The final  $C_t$

value would then be obtained by integrating the response function over all bubble and eddy sizes.

The next chapter describes a general method for the inclusion of a distribution of bubble or particle sizes within the two-fluid model. This method gives access to the local bubble or particle size distribution which would, in principle, enable the spectral  $C_t$  approach to be incorporated within the two-fluid model. Unfortunately, the response behaviour of bubbles and particles over a wide range of relative sizes is not well understood at present.

Furthermore, the bubbles perception of the turbulence structure changes with its relative velocity; the so-called ‘crossing trajectories’ effect. This complicates the formulation of a general response function since the response would now depend on the relative velocity as well as the exact nature of the turbulence structure. Again, the behaviour of bubbles in this situation is not well understood.

In any case, the considerable effort expended in the formulation of a spectral  $C_t$  model would have to be accompanied by a suitable improvement in the overall accuracy of the two-fluid model. It is demonstrated in Chapter 5, where the air-water bubbly flow in a plane shear layer is considered, that the dispersed phase Reynolds stresses may be less important than forces such as drag and lift which may dominate the dispersed phase behaviour. Consequently, the adoption of the fairly simple  $C_t$  models proposed above can be justified in terms of extending the accuracy and applicability of other parts of the model.

## 2.4 Two-Phase Flow Equation Summary

For convenience, the complete set of modelled two-phase flow equations are summarised below.

### Phase Continuity Equations

$$\frac{\partial \alpha_c \rho_c}{\partial t} + \nabla \cdot \alpha_c \rho_c \bar{\mathbf{u}}_c = 0 \quad (2.119)$$

$$\frac{\partial \alpha_d \rho_d}{\partial t} + \nabla \cdot \alpha_d \rho_d \bar{\mathbf{u}}_d = 0 \quad (2.120)$$

### Continuous Phase Momentum Equation

$$\begin{aligned}
\frac{\partial}{\partial t} \alpha_c \rho_c \bar{\mathbf{u}}_c + \nabla \cdot \alpha_c \rho_c \bar{\mathbf{u}}_c \bar{\mathbf{u}}_c = & -\alpha_c \nabla \bar{p} + \\
& \nabla \cdot \alpha_c \left( \mu_c + \mu_c^t \right) \left\{ \nabla \bar{\mathbf{u}}_c + \nabla \bar{\mathbf{u}}_c^T - \frac{2}{3} (\nabla \cdot \bar{\mathbf{u}}_c) \mathbf{I} \right\} - \\
& \nabla \cdot \frac{2}{3} k \mathbf{I} + \alpha_c \rho_c \mathbf{g} + \mathbf{M}_c
\end{aligned} \tag{2.121}$$

### Dispersed Phase Momentum Equation

$$\begin{aligned}
\frac{\partial}{\partial t} \alpha_d \rho_d \bar{\mathbf{u}}_d + \nabla \cdot \alpha_d \rho_d \bar{\mathbf{u}}_d \bar{\mathbf{u}}_d = & -\alpha_d \nabla \bar{p} + \\
& \nabla \cdot \alpha_d \mu_d \left\{ \nabla \bar{\mathbf{u}}_d + \nabla \bar{\mathbf{u}}_d^T - \frac{2}{3} (\nabla \cdot \bar{\mathbf{u}}_d) \mathbf{I} \right\} + \\
& \nabla \cdot \alpha_d C_t^2 \frac{\rho_d}{\rho_c} \mu_c^t \left\{ \nabla \bar{\mathbf{u}}_c + \nabla \bar{\mathbf{u}}_c^T - \frac{2}{3} (\nabla \cdot \bar{\mathbf{u}}_c) \mathbf{I} \right\} - \\
& \nabla \cdot \frac{2}{3} C_t^2 \rho_d k \mathbf{I} + \alpha_d \rho_d \mathbf{g} + \mathbf{M}_d
\end{aligned} \tag{2.122}$$

where

$$\begin{aligned}
\mathbf{M}_d = -\mathbf{M}_c = & \frac{3}{4} \frac{\alpha_d \rho_c C_d}{d} |\bar{\mathbf{u}}_r| \bar{\mathbf{u}}_r + \\
& C_{vm} \alpha_d \rho_c \left( \frac{D_c}{Dt} \bar{\mathbf{u}}_c - \frac{D_d}{Dt} \bar{\mathbf{u}}_d \right) + \\
& C_l \alpha_d \rho_c (\bar{\mathbf{u}}_c - \bar{\mathbf{u}}_d) \times (\nabla \times \bar{\mathbf{u}}_c) - \\
& 0.37 \rho_c C_d |\bar{\mathbf{u}}_r|^2 \nabla \alpha_d
\end{aligned} \tag{2.123}$$

and  $\bar{\mathbf{u}}_r = \bar{\mathbf{u}}_c - \bar{\mathbf{u}}_d$ .

### Turbulent Kinetic Energy Equation

$$\begin{aligned}
\frac{\partial \rho_c \alpha_c k}{\partial t} + \nabla \cdot \rho_c \alpha_c k \bar{\mathbf{u}}_c = & \nabla \cdot \left\{ \alpha_c \left( \mu_c + \frac{\mu_c^t}{\sigma_k} \right) \nabla k \right\} + \\
& \alpha_c G - \rho_c \alpha_c \epsilon - \mathbf{F}_d \cdot \bar{\mathbf{u}}_r - \\
& 0.37 \rho_c C_d |\bar{\mathbf{u}}_r|^2 \bar{\mathbf{u}}_r \cdot \nabla \alpha_c
\end{aligned} \tag{2.124}$$

where  $\mathbf{F}_d$  is given by Eqn (2.7) and

$$G = \mu_c^t \left\{ \nabla \bar{\mathbf{u}}_c + \nabla \bar{\mathbf{u}}_c^T - \frac{2}{3} (\nabla \cdot \bar{\mathbf{u}}_c) \mathbf{I} \right\} : \nabla \bar{\mathbf{u}}_c - \frac{2}{3} \rho_c k \mathbf{I} : \nabla \bar{\mathbf{u}}_c \quad (2.125)$$

### Turbulent Kinetic Energy Dissipation Rate Equation

$$\begin{aligned} \frac{\partial \alpha_c \rho_c \epsilon}{\partial t} + \nabla \cdot \alpha_c \rho_c \bar{\mathbf{u}}_c \epsilon &= \nabla \cdot \left( \alpha_c \left( \mu_c + \frac{\mu_c^t}{\sigma_\epsilon} \right) \nabla \epsilon \right) + \\ &C_1 \alpha_c \frac{\epsilon}{k} G - C_2 \alpha_c \rho_c \frac{\epsilon^2}{k} + C_2 \frac{\epsilon}{k} S_k \end{aligned} \quad (2.126)$$

where  $C_\mu, C_1, C_2, \sigma_\epsilon, \sigma_k$  are given in Table 2.1.

## 2.5 Closure

The basic conditional-averaged two-fluid equations contain extra terms which represent the effects of inter-phase momentum transfer and velocity fluctuations on the mean properties of the flow. The issues surrounding the modelling of these terms so that a closed equation set applicable to dispersed two-phase flow can be obtained have been extensively discussed. Models have been assembled which cover the effects of drag, virtual mass, lift forces and the so-called interfacial pressure force for solid-liquid, gas-liquid and liquid-liquid systems. The effects of turbulence and phase fraction effects on these forces can be accounted for when appropriate.

The effects of velocity fluctuations on the continuous phase momentum equation are accounted for using the eddy-viscosity concept where the Reynolds stresses are related to the mean shear rate using a turbulent viscosity. The turbulent viscosity is calculated from local values for the turbulent kinetic energy  $k$  and its dissipation rate  $\epsilon$  which are in turn calculated from their own transport equations. The conditional-averaged form of these transport equations have been rigorously derived, along with the fundamental Reynolds stress transport equation. The extra terms in the  $k$  and  $\epsilon$  equations relating to two-phase effects have been modelled and include the effects of turbulence generation due to the relative motion between the phases.

The Reynolds stresses in the dispersed phase momentum equation have been modelled using the response coefficient approach of Politis [6]. Here, the dispersed phase Reynolds stresses are related to those of the continuous phase by a scalar response coefficient  $C_t$ .

The continuous phase Reynolds stresses, which now appear in the dispersed phase momentum equation, are modelled using the eddy viscosity concept as in the continuous phase momentum equation.

The original approach of Politis suffers from certain conceptual difficulties which have been resolved in the present work and the approach has now been placed on a firm conceptual footing. Models for  $C_t$  for solid-liquid and gas-liquid systems have been presented.





## Chapter 3

# Break-up and Coalescence

This chapter describes a general technique which allows the effects of droplet size variations, typically due to break-up and coalescence, to be accounted for within the two-fluid framework. The approach is based on a presumed droplet size probability density function (PDF) parameterised in terms of a series of conserved scalar quantities related to its moments. Eulerian transport equations are derived for these quantities, which include source and sink terms accounting for the effects of break-up and coalescence on the PDF. Sub-models for the turbulent break-up of droplets in systems with and without surfactants are described in detail. Finally, auxiliary conservation equations for the surfactant concentration within the bulk and at the interface, which are required to complete the modelling of surfactant effects, are derived.

### 3.1 Introduction

The two-fluid equations developed in the previous two chapters represent a significant advance in the modelling of dispersed two-phase systems over simpler one dimensional or drift-flux approaches. The fundamental nature of the approach and the many important physical effects which may be accounted for make it applicable to many important two-phase flow situations.

However, the equations as they stand are based implicitly on a uniform droplet<sup>1</sup> size which severely limits their applicability to industrial two-phase processes, the vast majority of which involve significant spatial or temporal changes in droplet diameter, typically because

---

<sup>1</sup>The term droplet is used throughout this chapter to signify a single dispersed phase ‘entity’. The approach described in this chapter has been mainly developed with droplets in mind, although the principles apply equally to bubbles or solid particles which may break-up or flocculate.

of droplet break-up or coalescence effects. Indeed, the primary aim of many industrial processes is to control the droplet size characteristics in some way (for example, in stirred vessels or in-line mixing devices).

Spatial or temporal variations in droplet size may be a feature of the system under consideration even when break-up and coalescence effects are absent. For example, the mixing together of two different droplet size distributions to produce a third size distribution is a common requirement. If such a system were to be analysed using a two-fluid model based on a uniform droplet size, the existence of significant variations in droplet size may have an adverse effect on the accuracy of the predictions. The accurate prediction of these types of processes therefore requires that droplet size variations, and the physical processes which bring them about, are accounted for.

In the context of the ensemble averaging framework adopted in this work, the local droplet size generally varies from realisation to realisation, as well as spatially and temporally. Associated with each point in space and time, therefore, is a droplet size distribution, which is described using a droplet size probability distribution function (PDF). The situation is depicted graphically in Figure 3.1.

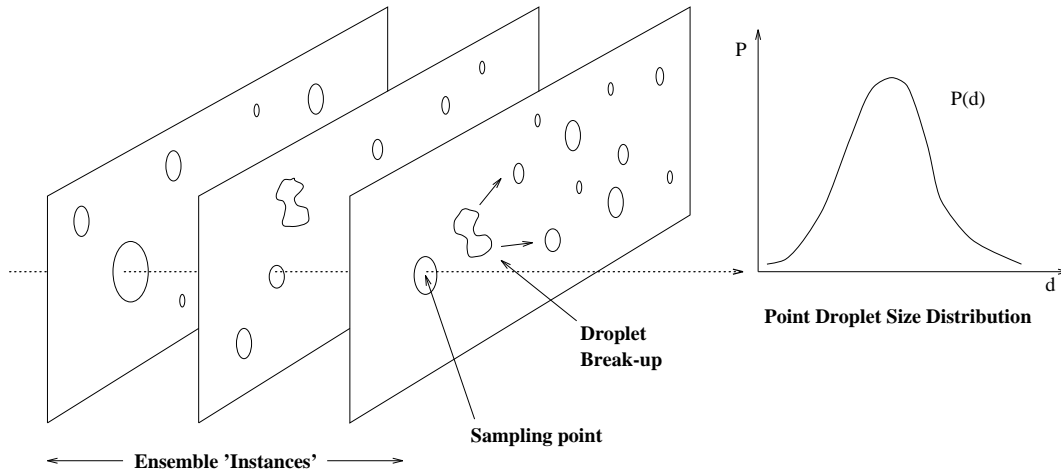


Figure 3.1: Droplet size PDF in the ensemble averaged framework.

The PDF provides a convenient mechanism for describing the state of the local size distribution. Analytical PDF forms exist which describe a very wide variety of possible distribution characteristics. Many of the PDFs important to industrial processes (for example, the Log-Normal and Gaussian forms) are two parameter PDFs, usually parameterised in terms of a local mean diameter and the distribution variance.

Ziman [80] studied various ways in which a variable droplet size may be incorporated into a computational model of multi-phase fluid flow. Ziman's principle aim was to find a method suitable for the calculation of turbulent emulsifying flow in stirred vessels. The methods he studied varied considerably in complexity and generality.

The simpler methods are based on zero dimensional models which infer the local mean droplet size from the local flow conditions (for example, the local turbulence intensity, etc). Ziman rejected these models as too simplistic since they do not account for droplet history effects and local process time scales. For example, in an in-line mixer, the highly turbulent region within the mixing layer would infer small droplet sizes whilst the low turbulence at the outlet would infer large droplet sizes regardless of the upstream conditions. Physically, this downstream increase in droplet size may only occur as a result of coalescence or mass transfer which depends strongly on the initial droplet size and the local time scales. The opportunities for the accurate modelling of such effects in this framework are very limited.

More complex methods are based on the discretisation of the local droplet size distribution into a number of size ranges. Here, Eulerian transport equations for the droplet number density in each size range are employed with droplet break-up and coalescence being accounted for by source terms which describe the increase or decrease in the number density as droplets transfer from one size category to another. Each size range is assumed to move with the same mean velocity. The local size distribution (or PDF) is reconstructed from the discrete size range information, from which the local mean diameter information may then be derived.

This approach does account for droplet history effects since each size range is governed by its own Eulerian transport equation. The drawbacks with this approach, however, lie mainly in the number of additional transport equations which need to be solved in order to provide an accurate discretisation of the droplet size PDF, and the difficulty in the modelling of the break-up and coalescence effects.

Finally, Ziman studied the 'presumed PDF' approach, where the form of the droplet size PDF is presumed beforehand and is described by a continuous function. The droplet size PDF is parameterised by a number of properties, usually an appropriate mean diameter and the distribution variance. Eulerian transport equations can be rigorously derived for a generalised form of each of these parameters which include the effects of break-up and coalescence [81]. The solution of these transport equations then allows the entire local droplet size PDF to be reconstructed at each point using the local values of the PDF parameters. The PDF may then be used to derive any further diameter related information required.

Although this approach relies on a presumed form for the droplet size PDF, experimental

evidence suggests [82] that the vast majority of emulsification processes are adequately approximated by a two parameter Log-Normal PDF. Furthermore, the approach requires only the same number of transport equations as parameters in the PDF. The complexity and accuracy of the presumed PDF form may be increased significantly without incurring a significant computational overhead. This allows the method to be extended to more complex systems including those involving a bi-modal size distribution.

Ziman [83] and Chesters [81, 84, 85, 86] further developed this approach and successfully integrated it into a pseudo single-phase CFD code for the prediction of the break-up and coalescence of droplets within stirred vessels. Here, the effects of droplet break-up and coalescence were superimposed onto a single-phase flow solution which was obtained from a special CFD code which incorporated a momentum-source type (averaged) model for the tank impeller. This code yielded the velocity, pressure and  $k$ - $\epsilon$  turbulence fields which formed the input to the separate ‘effects’ code which then calculated the scalar phase fraction and PDF parameter fields.

The main assumption of the pseudo single-phase approach is that the two phases do not have an appreciable slip velocity and that the dispersed phase does not affect the continuous phase flow and turbulence structure. As such, the pseudo single-phase approach is only applicable to low phase fraction systems in which the density difference between phases and the droplet diameter is small.

The presumed PDF approach is very attractive in that it allows for many important effects to be incorporated into a consistent and elegant framework. The sub-models which account for the actual break-up and coalescence effects form the heart of the method and embody the appropriate physical processes. This modularity eases the implementation of the method and allows the sub-models to be independently validated outside of the CFD code. In addition, this approach provides the user with the information most often required in a concise form and at a reasonable computational cost.

For these reasons, the presumed PDF approach is adopted in the current work and extended to take advantage of the two-fluid framework. In this way, the restrictions on the phase fraction and droplet size imposed by the pseudo single-phase approach are removed allowing the approach to be applied to a wider range of problems. As employed by Ziman, however, the presumed PDF approach is not immediately suitable for inclusion into the current two-phase flow model and requires some modification.

Firstly, the derivation of the required transport equations needs to be reassessed with regard to the current conditional averaged two-fluid framework. Secondly, since we are now in a position to account for the relative velocity between phases, we need to ensure that the local droplet size information is used appropriately in the calculation of the interfacial

closure terms involving the droplet diameter, such as the drag force. Lastly, since the numerical solution of the droplet size equations is to be integrated into the numerical solution of the flow field itself, some numerical issues have to be resolved if an efficient solution algorithm is to be obtained.

The next section describes in detail the presumed PDF approach and the modifications necessary to incorporate it into the current two-fluid model. Section 3.3 then describes a generic model for droplet break-up. Specific models for the turbulent break-up of droplets in systems with and without surface active agents (surfactants) are described in Sections 3.3.2 and 3.3.3. Although coalescence effects are not considered in this work, for completeness, Section 3.3.4 contains a brief summary of the generic model for coalescence effects. Finally, Section 3.4 describes a further extension to the framework which allows the calculation of the interfacial surfactant concentration which is required to complete the modelling of droplet break-up when surfactants are present.

## 3.2 The Presumed PDF Approach

In summary, the basis of the presumed PDF approach is to first adopt a particular parameterised form of the droplet size PDF and then to solve a series of related scalar transport equations, one for each PDF parameter required. The local values of these parameters are calculated and used to reconstruct the local droplet size PDF from which other information may then be derived. Break-up and coalescence, and other effects which have an effect on the local state of the droplet size distribution, are modelled within the scalar transport equations for the PDF parameters.

This procedure thus yields the PDF itself and the parameters which are used to calculate it. In many cases, it is the parameters themselves which are most useful to the engineer and the PDF will be ignored. In other cases, however, the PDF is used to derive more useful information concerning the local state of the droplet size distribution. Associated with the droplet size PDF, denoted  $P(d)$ , are a family of mean droplet diameters which are derived from the various moments of the PDF [82, 87].

$$d_{ab} = \left\{ \frac{\int_0^\infty P(d) d^a d(d)}{\int_0^\infty P(d) d^b d(d)} \right\}^{\frac{1}{a-b}} \quad \text{for } a \neq b \quad (3.1)$$

$$d_{aa} = \exp \left\{ \frac{\int_0^\infty P(d) d^a \ln(d) d(d)}{\int_0^\infty P(d) d^a d(d)} \right\} \quad (3.2)$$

The values of  $a$  and  $b$  are chosen to select a particular mean diameter, each of which

has a different physical meaning. For example,  $d_{00}$  is the geometric mean diameter and  $d_{32}$  is the Sauter, or surface area weighted, mean diameter. Thus, given the droplet size PDF, many different mean diameters may be derived and the local state of the droplet size distribution may be presented in a convenient and physically meaningful manner according to the process under investigation.

The derivation of the various mean diameters from the PDF may be carried out as a post-processing exercise or within the calculation itself if some part of the modelling requires a particular local mean diameter value. As we shall see, the determination of an appropriate local mean diameter within the two-phase calculation allows us to account for local droplet size variations within the dispersed phase transport equations themselves, instead of having to rely on a globally constant diameter, leading to a corresponding increase in accuracy.

It should be noted that the two-phase momentum equations are now written in terms of integrals over the entire droplet size PDF and not just a single droplet diameter. The solution of these equations yields an average velocity which takes into account contributions from all droplet sizes. This average velocity is used in the auxiliary equations governing the transport of the PDF parameters. This approach therefore assumes that all PDF parameters are transported with the same velocity.

### 3.2.1 The Adopted Droplet Size PDF

It is clear that the approach relies on the adoption of an appropriate form of the PDF in the first place. de Bruijn [82] performed an extensive survey of the droplet size distributions produced by many experimentally studied emulsification processes. He found that the vast majority of size distributions resulting from emulsification processes displayed a slightly asymmetric shape biased towards the larger droplet sizes and that such a distribution may be accurately described using a ‘Log-Normal’ form of a PDF which is given by

$$P(d) = \frac{1}{d\sqrt{\hat{\sigma}^2 2\pi}} \exp \left\{ -\frac{(\ln(d) - \ln(d_{00}))^2}{2\hat{\sigma}^2} \right\} \quad (3.3)$$

This PDF has two parameters; the distribution variance  $\hat{\sigma}^2$  and the geometric mean diameter  $d_{00}$ .

At this point, de Bruijn identified two possibilities for the simulation of break-up and coalescence effects; the calculation of the two individual parameters as normal, or a simplified approach which reduces the number of parameters to one.

The data available in the literature relating to liquid-liquid turbulent emulsification suggests that it is possible to adopt a globally uniform distribution variance which is chosen

Viscosity Ratio $\lambda = \mu_d/\mu_c$	Distribution Variance $\hat{\sigma}^2$
$\lambda \leq 10^2$	0.25
$10^2 < \lambda < 10^4$	$0.175 \log(\lambda) - 0.1$
$\lambda \geq 10^4$	0.6

Table 3.1: Distribution variance as a function of viscosity ratio

according to the viscosity ratio of the two phases, whence Eqn (3.3) becomes a single parameter PDF. The solution of a single scalar equation for this parameter, as oppose to two, may yield a reduction in the calculation time without a significant reduction in accuracy. Appropriate values for the distribution variance as a function of the viscosity ratio  $\lambda$  is shown in Table 3.2.1 [82].

### 3.2.2 The Intensity Of Dispersion - $S_\gamma$

The derivation of transport equations for the various PDF parameters such as the droplet diameter and the distribution variance poses something of a problem since they are not usually conserved quantities. In order to solve this problem, and also to generalise the modelling of the break-up and coalescence effects, Chesters [81] proposed that a family of conserved scalars known as the ‘intensity of dispersion’, denoted  $S_\gamma$ , which are related to the  $\gamma$ ’th moment of the droplet size PDF, be used to form the basis of the PDF parameters. Each of the PDF parameters may be then be deduced from the local value of  $S_\gamma$  which is governed by its own transport equation. Since the quantity  $S_\gamma$  is conserved, the derivation of its transport equation is relatively straightforward and the form of the modelling of the break-up and coalescence source terms becomes the same for all of the PDF parameters. The local intensity of dispersion  $S_\gamma$  is defined in terms of the  $\gamma$ ’th moment of the droplet size PDF as follows

$$S_\gamma = n \int_0^\infty P(d) d^\gamma d(d) = n M_\gamma \quad (3.4)$$

where  $n$  = Droplet number density  
 $d$  = Droplet diameter  
 $P(d)$  = Droplet size PDF  
 $M_\gamma$  =  $\gamma$ ’th distribution moment

The value of  $\gamma$  may take any positive or negative value. For example, for the particular case when  $\gamma$  is zero we have  $S_0 = n$ , the number of droplets per unit volume and for  $\gamma = 2$ ,  $S_2$  is a measure of the interfacial area per unit volume.

Using Eqn (3.1) we see that the family of mean diameters may be defined in terms of  $S_\gamma$ .

$$d_{ab} = \left(\frac{S_a}{S_b}\right)^{\frac{1}{a-b}} \quad \text{for } a \neq b \quad (3.5)$$

It should be noted at this stage that the value  $S_3$  is related to the local volume fraction of the dispersed phase via the equation

$$S_3 = \frac{6}{\pi} \alpha_d \quad (3.6)$$

and therefore, diameters of the form  $d_{3a}$  may be derived from

$$d_{3a}^{3-a} = \frac{6}{\pi} \frac{\alpha_d}{S_a} \quad (3.7)$$

Conversely, the value of  $S_a$  may be determined from the local mean diameter and the volume fraction.

$$S_a = \frac{6}{\pi} \alpha_d d_{3a}^{a-3} \quad (3.8)$$

Hence, given the local value of the volume fraction and  $S_\gamma$  we may immediately derive the local mean diameter  $d_{3\gamma}$ . It is most likely that the value of  $\gamma$  is chosen to give the desired mean diameter  $d_{3\gamma}$  since this has more physical significance than  $S_\gamma$  most (but not necessarily all) of the time.

In addition, for the Log-Normal PDF described above the following useful relationship may be derived [82].

$$d_{ab} = d_{cd} \exp \left( 0.5 \hat{\sigma}^2 (a + b - c - d) \right) \quad (3.9)$$

whence

$$\hat{\sigma}^2 = \ln \left( \frac{d_{ab}}{d_{cd}} \right) \frac{2}{(a + b - c - d)} \quad (3.10)$$



Thus, the adoption of a globally uniform distribution variance and the solution of a single  $S_\gamma$  equation yields a mean diameter  $d_{3\gamma}$  via Eqn (3.7) which may be used to obtain  $d_{00}$  via Eqn (3.9). Alternatively, the solution of two  $S_\gamma$  equations,  $S_a$  and  $S_b$ , yields two mean diameters  $d_{3a}$  and  $d_{3b}$  which may then be used to calculate the local distribution variance via Eqn (3.10).

### 3.2.3 The $S_\gamma$ Transport Equation

In order to account for history effects on the break-up and coalescence processes (associated with the convective and diffusive transport of droplet populations) an appropriate transport equation for  $S_\gamma$  is required. For consistency with the conditional averaged framework adopted in the rest of this work, the transport equation for  $S_\gamma$  should also be derived using conditional averaging techniques.

It should be noted that the quantity  $S_\gamma$  is, in some sense, an already averaged quantity since it relates to a large number of individual droplets which form a meaningful PDF. Thus, the quantity  $S_\gamma$  needs to be redefined in terms of its fundamental quantities which can then be conditionally averaged to form the required transport equation. The approach adopted here relies on the definition of a suitable indicator function which is used to condition the local instantaneous conservation equations in the same way as the phase indicator function in Chapter 1.

Noting that we require a the transport equation for the  $\gamma$ 'th moment of the droplet size distribution function, and that the transport equation for the third moment reduces to the phase fraction transport equation (ie, the dispersed phase continuity equation), a suitable indicator function may be defined in terms of a specific droplet diameter as follows

$$\chi_\gamma(\mathbf{x}, t, d) = \begin{cases} d^{\gamma-3} & \text{Droplet of diameter } d \text{ present at } (\mathbf{x}, t). \\ 0 & \text{Otherwise.} \end{cases} \quad (3.11)$$

Thus, the value of the indicator function within droplets of a particular diameter  $d$  is  $d^{\gamma-3}$  and zero elsewhere. For the third moment ( $\gamma = 3$ ), the indicator function reduces to unity within droplets of diameter  $d$ , the average of which naturally yields the 'phase fraction' of droplets of diameter  $d$ . Hence, for the third moment, we have

$$\alpha(d) = \overline{\chi_3} \quad (3.12)$$

at  $(\mathbf{x}, t)$ . The total dispersed phase fraction  $\alpha$  (ie, the phase fraction for all droplet sizes)

may now be redefined in terms of the sum of the phase fraction for each individual droplet size,

$$\alpha = \int_0^\infty \alpha(d) d(d) = \frac{\pi n}{6} \int_0^\infty P(d) d^3 d(d) = \frac{\pi}{6} S_3 \quad (3.13)$$

where Equations (3.4) and (3.6) have been used to relate the phase fraction to the number density  $n$  and the droplet diameter  $d$ .

Now, conditional averaging of the local dispersed phase continuity equation using the conditioning function as defined above leads naturally to a transport equation for  $\alpha(d)d^{\gamma-3}$ .

$$\frac{\partial}{\partial t} \alpha(d) d^{\gamma-3} + \nabla \cdot (\alpha(d) \bar{\mathbf{u}}(d) d^{\gamma-3}) = \Gamma(d) \quad (3.14)$$

Integration over the entire droplet size PDF then yields

$$\frac{\partial}{\partial t} \int_0^\infty \alpha(d) d^{\gamma-3} d(d) + \nabla \cdot \left( \int_0^\infty \alpha(d) \bar{\mathbf{u}}(d) d^{\gamma-3} d(d) \right) = \int_0^\infty \Gamma(d) d(d) \quad (3.15)$$

Rearranging the divergence term yields

$$\begin{aligned} \frac{\partial}{\partial t} \int_0^\infty \alpha(d) d^{\gamma-3} d(d) + \nabla \cdot \left( \bar{\mathbf{u}} \int_0^\infty \alpha(d) d^{\gamma-3} d(d) \right) = \\ \nabla \cdot \left( \int_0^\infty \alpha(d) d^{\gamma-3} (\bar{\mathbf{u}} - \bar{\mathbf{u}}(d)) d(d) \right) + \int_0^\infty \Gamma(d) d(d) \end{aligned} \quad (3.16)$$

where  $\bar{\mathbf{u}}$  is the dispersed phase conditional averaged velocity. The first term on the right hand side accounts for the distribution of droplet velocities around the conditional averaged mean; the so-called ‘drift’ term. The final term accounts for the changes in  $S_\gamma$  due to bulk changes, for example due to break-up and coalescence. Use of Eqn (3.4), noting that  $\alpha(d) = nP(d)d^3\pi/6$ , yields the required transport equation for  $S_\gamma$ .

$$\frac{\partial S_\gamma}{\partial t} + \nabla \cdot \bar{\mathbf{u}} S_\gamma = \nabla \cdot \left( \int_0^\infty \alpha(d) d^{\gamma-3} (\bar{\mathbf{u}} - \bar{\mathbf{u}}(d)) d(d) \right) + \int_0^\infty \Gamma(d) d^{\gamma-3} d(d) \quad (3.17)$$

Note that for  $\gamma = 3$ , the above equation reduces to the dispersed phase continuity equation since both the drift and break-up and coalescence source terms disappear; the former because the sum of the implied fluxes is equal to the true flux, hence

$$\int_0^\infty \alpha(d) \overline{\mathbf{u}}(d) d(d) = \alpha \overline{\mathbf{u}} \quad (3.18)$$

and the latter since there is no change in the dispersed phase mass since mass is conserved during droplet break-up and coalescence. For brevity, we write the final  $S_\gamma$  transport equation as

$$\frac{\partial}{\partial t} S_\gamma + \nabla \cdot S_\gamma \overline{\mathbf{u}} = S_b + S_c + S_{drift} \quad (3.19)$$

Where the terms  $S_b$  and  $S_c$  represent the contributions to the change in  $S_\gamma$  from droplet break-up and coalescence respectively, and  $S_{drift}$  represents the drift term as defined above. Note that the velocity in Eqn (3.19) is the dispersed phase mean velocity.

Chesters [86] has derived a preliminary expression for the drift term in Eqn (3.20) by assuming that the differences in the individual droplet velocities to be predominantly determined by the drag force. His expression reads

$$S_{drift} = \nabla \cdot \left\{ S_\gamma \hat{\sigma}^2 \beta (\gamma - 3) \overline{\mathbf{u}}_r \right\} \quad (3.20)$$

where  $\beta$  is a function of the drag law used ( $\beta = 0.5$  for a quadratic drag law, 2 for a linear drag law) and  $\overline{\mathbf{u}}_r$  is the mean relative velocity  $\overline{\mathbf{u}}_d - \overline{\mathbf{u}}_d$ .

The drift contribution to the transport of  $S_\gamma$  is expected to be negligible except in situations where there are large variations in the relative velocity or in  $S_\gamma$  itself. The former situation is representative of a swirling flow such as that encountered in a cyclone, or perhaps within a stirred tank. In most situations the effect of drift will be minor compared to that of break-up and coalescence which will typically be an order of magnitude larger [86]. Consequently, the drift term is neglected in the remainder of this work.

The terms  $S_b$  and  $S_c$  represent the total contribution to the transport of  $S_\gamma$  due to break-up and coalescence. Models for these terms can be formulated in a generic way by summing all the contribution from the break-up of a single droplet and the coalescence of two droplets. These terms are considered in detail in Sections 3.3.1 and 3.3.4.

### 3.2.4 Evaluation Of The Interfacial Drag Term

The presence of a local droplet size distribution implies that the interfacial terms in the conditional averaged momentum equation which depend on the droplet diameter should

be calculated by summing the contributions from all droplet sizes in the distribution. In the present framework, however, only the interfacial drag force depends on the droplet diameter so attention will be limited to this term.

Formally, the drag term should be written as

$$\mathbf{F}_d = \int_0^\infty \alpha(d) \mathbf{F}_d(d) d(d) \quad (3.21)$$

where  $F_d(d)$  is the drag force at diameter  $d$ . The general evaluation of such a term within a numerical solution is likely to prove rather expensive since it would probably have to be carried out using some form of numerical integration technique.

However, Chesters [81] has shown that when the dependence of the drag force on the diameter is known (and constant over the entire droplet size range) it is possible to avoid the integral in the above equation and to evaluate the drag force using an effective droplet diameter.

We can determine this effective diameter  $d_{eff}$  by expressing the drag force in the above equation as the product of a constant part  $\mathbf{k}$  and a diameter-dependent part  $d^a$  where  $a$  is to be determined. Hence, we have

$$\alpha_k \mathbf{F}_d(d_{eff}) = \mathbf{k} \int_0^\infty \alpha(d) d^a d(d) \quad (3.22)$$

Noting Eqn (3.6) and Eqn (3.13), the above equation may be rewritten in terms of  $S_\gamma$  as

$$\mathbf{F}_d(d_{eff}) = \mathbf{k} \frac{S_{3+a}}{S_3} \quad (3.23)$$

Finally, the ratio of  $S_{3+a}$  to  $S_3$  may be recast as a function of a mean diameter  $d_{3(3+a)}$  via Eqn (3.7). Thus, we have

$$\mathbf{F}_d(d_{eff}) = \mathbf{k} d_{3(3+a)}^a \quad (3.24)$$

Now, for a linear drag law  $a = -2$  yielding

$$\mathbf{F}_d(d_{eff}) = \mathbf{k} d_{31}^{-2} \quad (3.25)$$

Note that when the drag law is not linear then the above procedure cannot formally be used. However, for clean air-water cases, as considered in Section 2.2.1, the drag law may be decomposed into two sections, each yielding a different effective diameter. In this case, the efficiency of the above technique may be retained with minimal loss of accuracy by using an effective diameter in-between the two formally required.

### 3.3 Break-up And Coalescence Models

#### 3.3.1 Generic Break-up Model

The term  $S_b$  in Eqn (3.20) represents the total contribution to the rate of change of  $S_\gamma$  due to droplet break-up. Chesters [81] has derived a generic form for the break-up source term by considering the break-up of one droplet into  $N$  equi-sized fragments and calculating the corresponding change in  $S_\gamma$ . The final source term is therefore the sum of all such droplet break-up events.

By noting that the volume of the dispersed phase must be conserved during droplet break-up, it is easy to show that the change in  $S_\gamma$  due to the break-up of a single droplet into  $N$  equi-sized fragments is given by

$$\Delta S_\gamma(d) = d^\gamma \left\{ N^{1-\gamma/3} - 1 \right\} \quad (3.26)$$

Representing the time-scale of this break-up event as  $\tau_b$ , defined as the time between the drop deformation becoming supercritical and break-up occurring [88], and summing all such contributions for the portion of the droplet size distribution which undergoes break-up, we obtain the generic break-up source term which reads

$$\begin{aligned} S_b = \frac{dS_\gamma}{dt} &= \int_{d_c}^{\psi} nP(d) \frac{\Delta S_\gamma(d)}{\tau_b(d)} d(d) \\ &= \int_{d_c}^{\psi} nP(d) \frac{(N^{1-\gamma/3} - 1)}{\tau_b} d^\gamma d(d) \end{aligned} \quad (3.27)$$

Note that, in general, both the number of fragments and the break-up time-scale are functions of the initial droplet diameter. The parameter  $\psi$  and the critical droplet diameter  $d_c$  represent the upper and lower droplet diameter above or below which droplet break-up does not physically occur by a particular mechanism.

In order to complete the break-up source term we now require sub-models for the critical diameter  $d_c$ , the break-up time scale  $\tau_b$ , the number of fragments  $N$  and the upper limit

of the integral  $\psi$  for each particular break-up mechanism we wish to consider. Multiple break-up mechanisms may be considered simultaneously by summing contributions from all mechanisms.

It should be noted that for some break-up mechanisms, the assumption that the droplet breaks into a number of equi-sized fragments may not be appropriate. In particular, it is known that in surfactant induced ‘end-pinching’ and high capillary number break-up the droplet may break into a series of equi-sized fragments plus a few smaller satellites [88]. If these effects need to be accounted for, the above expression would need to be reformulated to take into account the corresponding change in  $S_\gamma$  resulting from the non-uniform droplet break-up. In this work, however, we assume that these effects are not dominant and that, while the number of fragments may be a function of the initial droplet diameter, the fragments are all the same size.

Furthermore, in order to maintain the efficiency of the overall numerical solution algorithm, the integral in the above expression needs to be evaluated in the most computationally efficient way possible. To achieve this we can take advantage of some of the properties of the Log-Normal PDF and recast the integral in terms of the Standard Error Function, as outlined in Appendix E. In order to use this technique, however, the integral has to be simplified and some restrictions on the modelling of the number of fragments and the break-up time-scale have to be imposed.

To use the technique outlined in Appendix E, we require integrals of the form

$$\int_{d_c}^{\psi} nP(d)d^{\delta} d(d) \quad (3.28)$$

where  $\delta$  is a constant. To this end we adopt models for  $N$  and  $\tau_b$  of the form

$$\tau_b(d) = \tau'_b d^a \quad (3.29)$$

and

$$N(d) = N' d^b \quad (3.30)$$

where the coefficients  $\tau'_b, N', a$  and  $b$  are supposed independent of the droplet diameter. Thus, the break-up source term may be written as

$$S_b = \frac{N'^{1-\gamma/3}}{\tau'_b} \int_{d_c}^{\psi} nP(d)d^{\delta_1} d(d) - \frac{1}{\tau'_b} \int_{d_c}^{\psi} nP(d)d^{\delta_2} d(d) \quad (3.31)$$

where

$$\delta_1 = \gamma + b - \frac{b\gamma}{3} - a \quad (3.32)$$

$$\delta_2 = \gamma - a \quad (3.33)$$

This enables the integrals in Eqn (3.31) to be evaluated quickly whilst retaining some measure of generality in the form of the available expressions for  $N$  and  $\tau_b$ .

De Bruijn [82] has performed an extensive study of the break-up of droplets in turbulent emulsifying flow and discerned two distinct regimes in which break-up occurs; the so-called inertial regime where the droplet is larger than the Kolmogorov eddy size, and the viscous regime where the droplet is smaller than this size. Chesters and co-workers [89, 82, 81, 90] have developed sub-models for the required parameters in the generic break-up model for each of these two basic regimes. Recently, sub-models for the break-up of droplets in laminar flow and in flows with surfactants and inter-phase mass transfer have been developed [91, 92, 93, 88, 94] thus increasing the range of applicability of the models.

In this work we are primarily interested in the turbulent break-up of droplets. Chapter 6 describes a detailed validation study concerning the turbulent break-up of oil droplets within an in-line pipe-mixer device. In this case, the break-up of the oil droplets is strongly affected by the presence of surface active agents (surfactants) in the continuous phase. The sub-models which have been developed to capture these effects are described in detail in the following sections.

### 3.3.2 Break-up Models For Clean Systems

#### 3.3.2.1 Viscous Break-up

The viscous break-up regime refers both to break-up in laminar flow and in turbulent flows in which the viscous forces dominate, such as when the droplet diameter is smaller than the smallest (Kolmogorov) turbulent eddies. In this section, the ‘turbulent’ viscous break-up model is described in detail. Differences between the turbulent and laminar models are indicated where necessary.

The Kolmogorov eddy size  $\lambda_k$  is given by

$$\lambda_k = \left( \frac{\nu^3}{\epsilon} \right)^{1/4} \quad (3.34)$$

where  $\nu$  is the kinematic viscosity of the continuous phase and  $\epsilon$  is the turbulent kinetic energy dissipation rate. This size forms the upper limit of the applicability of the model; droplets larger than this do not break up due to the viscous break-up regime. The parameter  $\psi$  in the generic break-up model is therefore  $\lambda_k$ . For the laminar flow break-up case, the upper limit is essentially infinite since all droplets are likely to be smaller than the scale of the macroscopic flow features.

For droplets smaller than  $\lambda_k$  the flow surrounding the droplet is essentially laminar. Furthermore, when the eddy lifetime is much larger than the droplet break-up time-scale, then the laminar flow around the droplet can be taken as stationary. The relative simplicity of this flow has enabled the situation to be extensively studied, both experimentally and theoretically (see [95, 82] and references therein).

Studies have shown that the most relevant flow conditions for break-up are those classed as two-dimensional linear creeping flows [89]. Such flows may be mathematically characterised by two parameters; the shear rate  $\dot{\gamma}$  and the flow type parameter  $\eta$  which varies between -1 and 1. Both  $\dot{\gamma}$  and  $\eta$  may be determined from the local two-dimensional velocity gradient tensor. Figure 3.2 shows the flow conditions relevant to various values of  $\eta$ . Note that droplet break-up only occurs for  $\eta \geq 0$  since rotational flow hardly induce any deformation.

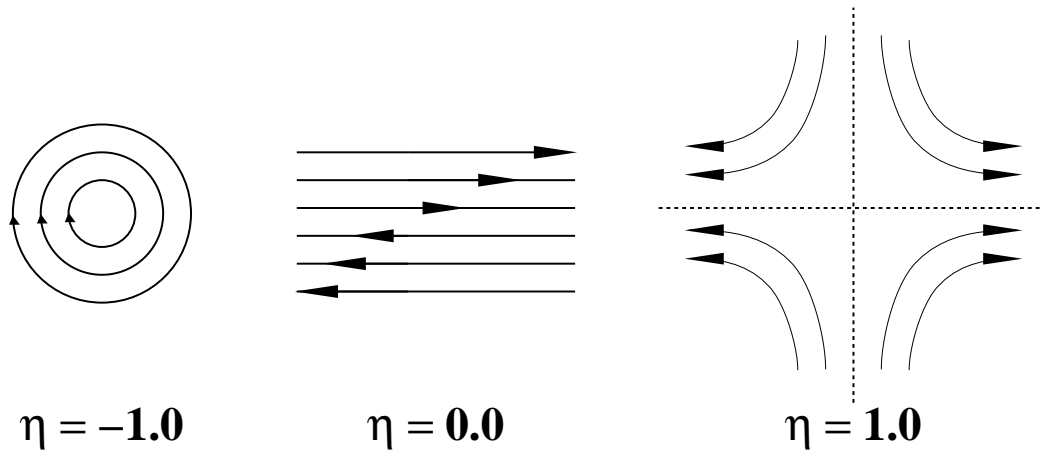


Figure 3.2: Characterisation of 2D linear flows.

The utility of such a flow characterisation lies in the fact that, in general, the sub-models for the viscous break-up regime model parameters are a function of the local flow type [88]. For turbulent flow, Chesters has argued [90] that the flow within a turbulent eddy



may be adequately approximated by a two-dimensional linear flow with  $\eta \approx 0.2$  with the shear rate given by

$$\dot{\gamma} = \sqrt{\frac{\epsilon}{\nu}} \quad (3.35)$$

which is the inverse of the Kolmogorov eddy lifetime. For laminar break-up, the shear rate is simply the local velocity gradient magnitude and an appropriate local flow type parameter can be determined from the local velocity gradient tensor [89].

Furthermore, de Bruijn [82] has shown that there are only two dimensionless parameters relevant to the viscous break-up regime; the viscosity ratio  $\lambda = \mu_d/\mu_c$  and the capillary number  $\Omega$  given by

$$\Omega = \frac{\mu_c \dot{\gamma} d}{2\sigma} \quad (3.36)$$

where  $\dot{\gamma}$  is the shear rate, as given by Eqn (3.35), and  $\sigma$  is the surface tension. Experiments have shown that for each value of the viscosity ratio there exists a critical value of the capillary number beyond which no stable deformation exists and break-up occurs [82].

Based on the available experimental data, de Bruijn has constructed a family of analytical correlations for the critical capillary number as a function of the viscosity ratio and the flow type parameter for  $\eta = 0.0, 0.2, 0.4, 0.6, 0.8$  and  $1.0$  [89]. These correlations are of the form

$$\log(\Omega) = \left\{ \left( \frac{c_2}{c_3} \log(\lambda) + \frac{c_5}{c_3} \right)^2 - \frac{c_1}{c_3} \log(\lambda)^2 - 2 \frac{c_4}{c_3} \log(\lambda) - \frac{1}{c_3} \right\}^{\frac{1}{2}} - \frac{c_2}{c_3} \log(\lambda) - \frac{c_5}{c_3} - 1 \quad (3.37)$$

The values of the coefficients  $c_1$  to  $c_5$  for the various flow type values are given in Table 3.3.2.1 and the resulting curves are shown in Figure 3.3.

The critical capillary number forms the basis of the model for the critical diameter. Eqn (3.38) is rearranged to give

$$d_c = \frac{2\sigma\Omega_c}{\mu_c \dot{\gamma}} \quad (3.38)$$

Coeff	Flow Type $\eta$					
	0.0	0.2	0.4	0.6	0.8	1.0
$c_1$	0.9353264	0.3273221	0.2858330	0.2443439	0.3102020	0.4653474
$c_2$	0.5570426	0.4726207	0.3795495	0.2864782	0.2732713	0.4538783
$c_3$	-0.0000215	-0.0091768	-0.0171332	-0.0250896	-0.3524792	-0.5259108
$c_4$	-0.0019007	-0.2481238	-0.2919881	-0.3358528	-0.4351167	-0.6653536
$c_5$	-0.7542608	-1.3686552	-1.9388083	-2.5089614	-3.5251310	-5.2591139

Table 3.2: Coefficients for critical capillary number correlations

where the critical capillary number  $\Omega_c$  is determined from the local flow type parameter  $\eta$  and the viscosity ratio  $\lambda$  as detailed above. For the turbulent viscous regime the flow type parameter is taken as 0.2.

The viscous break-up model is completed with a sub-model for the break-up time-scale  $\tau_b$ . It can be shown that any such model for  $\tau_b$  must have the following form [88]

$$\tau_b(d) = \frac{\mu_c d}{\sigma} f(\lambda) \quad (3.39)$$

The experimental evidence of Grace [96] indicates that the break-up time scale for simple shear ( $\eta = 0$ ) and hyperbolic flows ( $\eta = 1$ ) are very similar. The function  $f(\lambda)$  has been deduced by Janssen *et al.* [88] by deriving a least-squares analytical fit to the data of Grace for these two flow types. The final function  $f(\lambda)$  reads

$$\log(f) = p_0 + p_1 \log(\lambda) + p_2 \log(\lambda)^2 \quad (3.40)$$

where the coefficients take the value as shown in Table 3.3.2.1. For intermediate flow types, where  $0 < \eta < 1$ , the value of  $f(\lambda)$  is linearly interpolated.

Finally, we note that in barely critical steady shear flows, experimental evidence shows that the droplets breaks-up into two equi-sized fragments regardless of their initial size [82]. For this regime, therefore, the parameter  $N$  takes the constant value 2. When the shear rate greatly exceeds the critical value, however, the droplet may become very elongated before breaking into a series of equi-sized fragments plus a few small satellites [97]. In this case, the assumption of a binary cascade (ie, taking  $N$  to be a constant value of 2 resulting a series of binary break-up events) may result in the break-up rate being

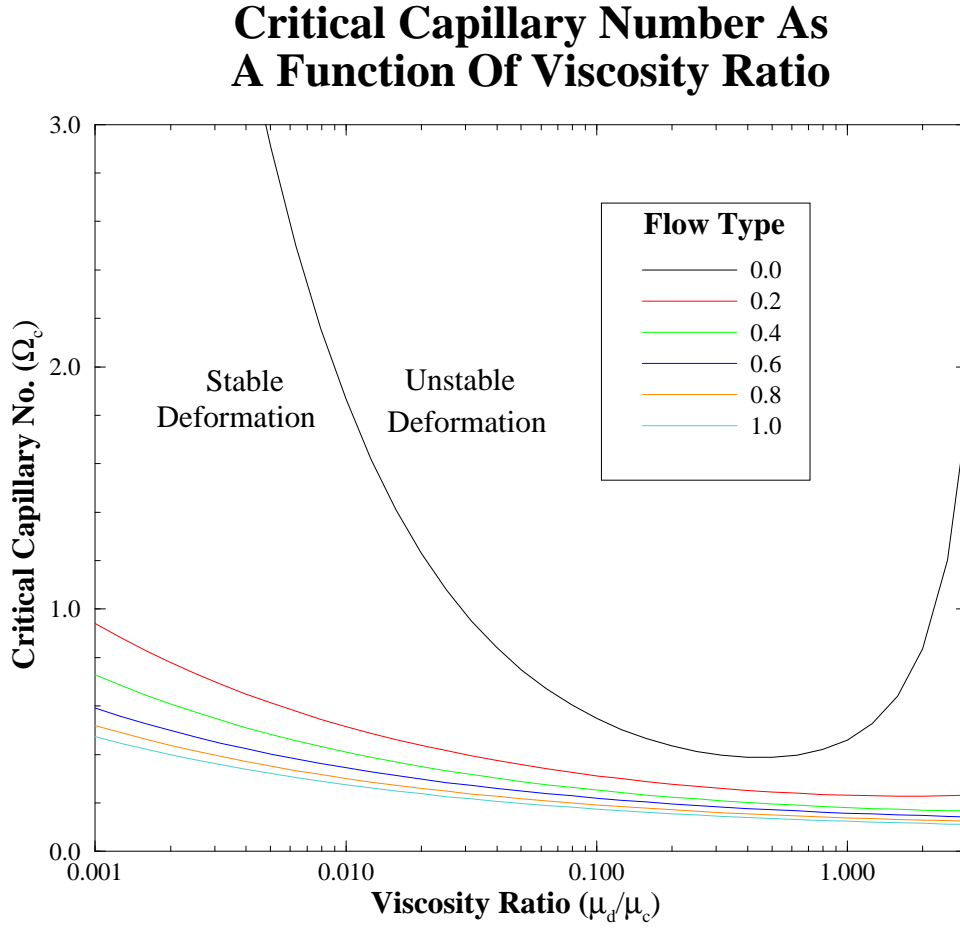


Figure 3.3: Critical capillary number curves for various flow types and viscosity ratios.

under-predicted. Unfortunately, no general models for this regime exist at present, and the binary cascade has to be used as an approximation.

#### 3.3.2.2 Inertial Break-up

The physical modelling underlying the inertial break-up of droplets larger than the Kolmogorov eddies is based on the destructive oscillations of the droplet induced by the turbulent pressure fluctuations [82, 81, 88]. The relative strength of the inertial forces in the turbulent continuous phase are characterised by the Weber number defined as

Coefficient	Flow Type $\eta$	
	Simple Shear ( $\eta = 0$ )	Hyperbolic Flow ( $\eta = 1$ )
$p_0$	1.43	1.852
$p_1$	0.267	0.362
$p_2$	-0.026	-0.013

Table 3.3: Coefficients in  $f(\lambda)$  model - Eqn (3.40).

$$We = \frac{\rho_c u_c'^2 d}{2\sigma} \quad (3.41)$$

where  $u_c'$  is a characteristic velocity fluctuation.

The Weber number represents the ratio of turbulent inertial stresses ( $\rho_c u_c'^2$ ) to the stabilising surface tension forces ( $2\sigma/d$ ). For low phase fraction dispersions at the length scale of the droplet, which is much larger than the Kolmogorov length scale in this case, the relevant fluctuation velocity scale may be written [81]

$$u_c'^2 = (\epsilon d)^{2/3} \quad (3.42)$$

The criterion for the break-up of the droplet is when the Weber number exceeds some pre-defined critical value  $We_c$ . This forms the basis of the model for the critical droplet diameter. Equating Eqn (3.41) to the critical Weber number value and rearranging to give an expression for  $d_c$  yields

$$d_c = \left\{ \frac{2\sigma We_c}{\rho_c} \epsilon^{-2/3} \right\}^{3/5} \quad (3.43)$$

Unfortunately, little is known about the behaviour of the critical Weber number parameter. In principle, it is a function of the viscosity and density ratio. In the present work a constant value for  $We_c$  is assumed for particular dispersed phases; for liquid-liquid systems a value of about 0.5 is used, while for gas-liquid systems the value is taken as 1.2 [88].

The above relations are valid when the droplet viscosity is small enough to not damp the oscillations of the droplet by the turbulence. If the droplet viscosity is of influence, then the critical diameter is corrected as follows

$$d_c = \frac{0.3}{Re_{crit}} d_{c,0} \quad (3.44)$$

where  $d_{c,0}$  is the calculated value for the high droplet Reynolds number case (ie, using Eqn (3.43) above) and  $Re_{crit}$  is the critical droplet Reynolds number defined by

$$Re_{crit} = \frac{\rho_d u'_d d_c}{\mu_d} \quad (3.45)$$

The characteristic dispersed phase fluctuating velocity  $u'_d$  is taken to be equal to that of the continuous phase  $u'_c$  as above. The final expression for the critical diameter when the droplet viscosity is of influence is

$$d_c = \left\{ \frac{0.3 \mu_d d_{c,0}}{\rho_d \epsilon^{1/3}} \right\}^{3/7} \quad (3.46)$$

For higher phase fraction dispersions, the velocity fluctuations in the continuous phase are damped due to the presence of the dispersed phase. In this case, the critical diameter is determined by correcting the low phase fraction critical diameter, as given above, via

$$d_c = d_c(\alpha \rightarrow 0) \{1 + k\alpha\} \quad (3.47)$$

where  $k$  is a parameter which takes the value of about 4.5 [82].

The break-up time-scale for the inertial break-up of droplets follows from consideration of the lowest-mode free oscillation period of the droplet [98] as given by

$$T = 2\pi \sqrt{\frac{(3\rho_d + 2\rho_c)d^3}{192\sigma}} \quad (3.48)$$

Dimensional reasoning implies that the break-up time-scale is related to the free oscillation time-scale via a coefficient which is a function of the viscosity ratio.

$$\tau_b = f(\lambda)T \quad (3.49)$$

Due to a lack of experimental information, the best estimate for the function  $f(\lambda)$  is a constant value of approximately 0.2 [81].

The inertial break-up model is completed by noting that the number of fragments resulting from the destructive oscillation of a droplet is taken to be 2. The upper limit on the droplet diameter is taken to be effectively infinity since all droplets will be substantially smaller than the size of the flow domain.

### 3.3.3 Break-up Models For Systems With Surfactants

This section discusses the influence of surfactants on the break-up of droplets. Much of the information presented in this section is based on the studies of Janssen [91, 92] and Chesters [94] who studied the effects of surfactants on the viscous and inertial break-up of droplets respectively, eventually arriving at suitable models for each regime. The details of these models are discussed in Sections 3.3.3.1 and 3.3.3.2 while the rest of this section is given over to a general discussion on the nature of surfactants.

Surfactant molecules are ‘amphiphilic’ which means that part of the molecule, typically a polar head group, prefers to be in a polar solvent like water while the remainder, typically a hydrocarbon chain, prefers to be in an apolar environment such as oil. The surfactant thus has an affinity for the interface formed between a polar phase and an apolar phase since this represents the energetically most favoured position for the molecules. Surfactant molecules that diffuse towards the interface are trapped there temporarily by the potential energy well. Subsequent fluctuations in the kinetic energy of the surfactant molecule may result in the molecule being ejected from the interface.

The diffusion of surfactant molecules towards the interface decreases as the interfacial concentration increases and the area available for adsorption is reduced. On the other hand, the desorption from the interface increases with the interfacial concentration. The result is a dynamic equilibrium between the adsorption of the molecules to the interface due to diffusion and their desorption from the interface due to thermal motion.

The relationship between the surfactant concentration within the bulk and at the interface when they are in equilibrium is called an ‘adsorption isotherm’. Perhaps the simplest of the adsorption isotherms is the Langmuir isotherm which is written

$$\Gamma(c) = \Gamma_{\infty} \frac{c}{c + a} \quad (3.50)$$

where  $c$  is the bulk surfactant concentration,  $a$  is the bulk half-saturation concentration,  $\Gamma_{\infty}$  is the fully-saturated interfacial concentration and  $\Gamma(c)$  is the resulting interfacial concentration. The half-saturation concentration is the concentration in the bulk at which the interfacial concentration is half the fully-saturated interfacial concentration.

The main influence of the surfactants on the break-up of droplets lies in the modification of the interfacial surface tension. A relationship between the interfacial surface tension  $\sigma$  and the local interfacial concentration  $\Gamma$  is given by the Gibbs adsorption equation which, for ideal solutions, reads

$$\Gamma = -\frac{1}{RT} \frac{d\sigma}{d \ln(c)} \quad (3.51)$$

where  $R$  is the universal gas constant and  $T$  is the absolute temperature. Combination of the Gibbs equation and the Langmuir isotherm results in the so-called Szyszkowski equation which reads

$$\sigma(c) = \sigma(0) - \Gamma_{\infty} RT \ln\left(1 + \frac{c}{a}\right) \quad (3.52)$$

where  $\sigma(0)$  is the interfacial surface tension at zero surfactant concentration. Eqn (3.52) shows that the equilibrium interfacial surface tension reduces as the bulk surfactant concentration increases. However, when the bulk surfactant concentration exceeds a certain value known as the ‘critical micelle concentration’ (CMC) then the surfactant molecules begin to cluster amongst themselves forming so-called micelles. Above the CMC the interfacial surface tension remains constant. Eqn (3.52) is valid up to the CMC after which the surface tension is taken as a constant value corresponding to  $\sigma(\Gamma_{\text{CMC}})$ .

The strict validity of the Langmuir isotherm is limited. An alternative isotherm frequently used to described systems which are not adequately described by the Langmuir isotherm is the so-called Frumkin isotherm which describes non-ideal interfacial adsorption. The Frumkin isotherm reads

$$\frac{c}{a} = \frac{y}{1-y} \exp\left(\frac{2Hy}{RT}\right) \quad (3.53)$$

where  $y = \Gamma/\Gamma_{\infty}$  and  $H$  is an additional parameter which describes the deviation of the system from ideal adsorption. The Frumkin equivalent of the Szyszkowski equation reads

$$\frac{\sigma(0) - \sigma(c)}{-RT\Gamma_{\infty}} = \ln(1-y) + \frac{y^2 H}{RT} \quad (3.54)$$

Note that when  $H = 0$ , the above two equations reduce to the Langmuir isotherm and the Szyszkowski equation.

In a dynamic situation when the interface is disturbed by a sudden dilation or contraction, the interfacial concentration, and hence the surface tension, will deviate from the equilibrium value until equilibrium can be restored by interface-bulk exchange processes some time later. This relaxation time can range from millisecond to hours. In the context of droplet break-up when the droplet deformation time-scale are of the order of the relaxation time-scale this effect needs to be accounted for.

Break-up models which use the equilibrium surface tension only and do not take into account the instantaneous deviations of the surface tension due to local deformation have been shown to be adequate only when the relaxation time-scale is very fast (as may be case at very high surfactant concentrations) or when the surfactant concentration is small [91, 92]. Experiments using the Langmuir trough apparatus have shown that when the surfactant concentration is very small, the dynamic dependence of the surface tension on the deformation rate is also small since the surface tension is insensitive to the surfactant at low concentrations. Similarly, when the bulk surfactant concentration is high, the relaxation time is so short that equilibrium is attained faster than the deformation time-scale.

At intermediate concentrations, the non-uniform deformation of droplet will result in a dynamic surface tension which varies from one part of the surface to another according to whether that part is dilated or contracted. Furthermore, the presence of surfactants is known to affect the stress balance at the interface causing the droplet to rotate when subjected to a shear flow. The rotation period is approximately that of a solid body rotation. The rotation causes the local deformation to become both non-uniform and time dependent as each interfacial element is compressed and then dilated in turn.

The effect of surfactants on the break-up of droplets may thus be summarised as follows [92]

- At very low surfactant concentration, there will be no significant deviation from the clean system since there is insufficient surfactant present to form appreciable deviations from the equilibrium surface tension.
- At high surfactant concentration the fast relaxation time ensures that the equilibrium interfacial concentration and surface tension is maintained throughout the droplet deformation process.
- At intermediate surfactant concentrations, the dynamic behaviour of the surfactant and the interface have to be accounted for since there may be significant variations in the break-up behaviour of droplets compared to the clean system.



### 3.3.3.1 Surfactant Influenced Viscous Break-up

Janssen *et al.* [92] studied the effects of surfactants on droplet break-up in simple shear flow and found that the deformation and break-up process differs significantly from that observed in systems with a uniform and constant surface tension. In general, the presence of surfactants was found to hamper break-up in simple shear flow although, intuitively, one may have expected the reduction in surface tension to have aided break-up. Janssen *et al.* ascribe this behaviour to the dynamic nature of the interfacial rheology.

As discussed above, the dynamic deformation of the interface may cause significant local variations in the interfacial surface tension, the magnitude of which depends on the ratio of the deformation time-scale and the relaxation time-scale required for adsorption equilibrium to be obtained.

However, Janssen found that the behaviour of the critical capillary number could not be explained solely by the reduction in the interfacial surface tension caused by the enlargement of the interface as a whole during break-up. Rather, experimental results indicate that the continual local interfacial deformation, caused by the rotation of the droplet in the shear flow field, correlates well with the visco-elastic behaviour of a harmonically deforming planar interface; the so-called Langmuir trough.

Consequently, Janssen *et al.* proposed a model based the viscous break-up model for clean systems, as described in Section 3.3.2.1, but using an ‘effective’ surface tension which accounts for the visco-elastic nature of the deformation process. The criterion for droplet break-up is therefore based on a capillary number defined in terms of the effective surface tension instead of the clean surface tension.

The effective surface tension is given in terms of the equilibrium surface tension by

$$\sigma_{\text{eff}}(c) = \sigma_{\text{eq}}(c) + \beta|\epsilon(c)| \quad (3.55)$$

where  $\epsilon(c)$  is the elasticity modulus, which relates the changes in surface tension to the interface deformation, and  $\beta$  is a fit parameter which is a function of the viscosity ratio. The elasticity modulus is determined from

$$|\epsilon(c)| = \frac{\epsilon_0}{\sqrt{1 + 2\zeta + 2\zeta^2}} \quad (3.56)$$

where  $\epsilon_0$  is the limiting value of the elasticity modulus when the relaxation time-scale is very high and is given by

$$\epsilon_0 = -\Gamma \frac{d\sigma}{d\Gamma} \quad (3.57)$$

and  $\zeta^2$  is the ratio of the deformation and the relaxation time-scale

$$\zeta^2 = \frac{\tau_{\text{def}}}{\tau_{\text{rel}}} \quad (3.58)$$

where

$$\tau_{\text{def}} = \frac{1}{\omega} \quad (3.59)$$

$$\tau_{\text{rel}} = \frac{2}{D} \left( \frac{d\Gamma}{dc} \right)^2 \quad (3.60)$$

The rotation frequency  $\omega$  is taken to be of the order of the shear rate  $\dot{\gamma}$ . The derivatives  $\frac{d\sigma}{d\Gamma}$  and  $\frac{d\Gamma}{dc}$  need to be determined according to the chosen isotherm. For the Langmuir isotherm it can be shown that

$$\frac{d\Gamma}{dc} = \Gamma_{\infty} \frac{a}{(c+a)^2} \quad (3.61)$$

$$\frac{d\sigma}{d\Gamma} = -\frac{a\Gamma_{\infty}^2 RT}{(a+c)(\Gamma_{\infty}-\Gamma)^2} \quad (3.62)$$

while for the Frumkin isotherm we have

$$\frac{d\Gamma}{dc} = \frac{\Gamma_{\infty}}{a} \left\{ \frac{1}{(1-y)^2} - \frac{2H}{RT} \frac{y}{(1-y)} \exp\left(-\frac{2H}{RT}y\right) \right\}^{-1} \quad (3.63)$$

$$\frac{d\sigma}{d\Gamma} = \left\{ \frac{2H\Gamma}{\Gamma_{\infty}} - \frac{RT}{1-\Gamma/\Gamma_{\infty}} \right\} \frac{d\Gamma}{dc} \quad (3.64)$$

The fit parameter  $\beta$  is given as

$$\beta = 0.165 - 0.033 \log(\lambda) \quad (3.65)$$

which for  $0.001 < \lambda < 1$  is approximately constant at 0.23.

Once the effective surface tension has been calculated, the critical droplet diameter is calculated from

$$d_c = \frac{2\sigma_{\text{eff}}\Omega_c}{\mu_c\dot{\gamma}} \quad (3.66)$$

where the critical capillary number is as for the clean laminar break-up case and  $\dot{\gamma}$  is taken to be the velocity gradient magnitude, in the laminar case, or the turbulent shear rate in the turbulent case, as given by Eqn (3.37).

### 3.3.3.2 Surfactant Influenced Inertial Break-up

The inertial break-up model for clean systems, described in Section 3.3.2.2, has been extended by Chesters [94] to take account of the presence of surfactants and the viscosity of the dispersed phase. The basic premise of the model remains the same with droplet break-up resulting from destructive oscillations in the droplet shape induced by the turbulent pressure fluctuations. The effect of the dispersed phase viscosity is to damp the induced oscillations resulting in a reduction in the break-up rate. The influence of surfactants, however, is shown to be more complex; while the reduction in the surface tension facilitates break-up, in general, the transient behaviour of the surfactant at the oscillating interface may cause a net damping effect.

The modifications introduced by Chesters are based on the work of Lu and Apfel [99] who analysed the free oscillations of droplets in the small amplitude limit, for which the governing equations are linear, when surfactant and viscosity induced damping is present. The result of this analysis was approximate expressions for the complex oscillation frequency  $\omega_c$  for a droplet in a number of limiting cases.

Chesters built upon this basic analysis to arrive at the sub-models required to complete the  $S_\gamma$  break-up source term for this case. The basis of the modelling approach adopted by Chesters is briefly outlined below, followed by a discussion of the numerical issues which have to be addressed to allow the model to be implemented into the CFD code itself.

It can be shown that for a free linear oscillator with moderate damping, the oscillation displacement  $x$ , in complex form, is given by

$$x = x_0 \exp(-i\omega_i t) \cos(\omega_r t) \quad (3.67)$$

where

$$\omega_c = \omega_i + i\omega_r \quad (3.68)$$

$$\Omega_i = \frac{\omega_i}{\omega^*} = \frac{F}{2} \quad (3.69)$$

$$\Omega_r = \frac{\omega_r}{\omega^*} = \left(1 - \frac{F^2}{4}\right)^{1/2} \quad (3.70)$$

and  $\omega^*$  is the resonance frequency (ie, the oscillation frequency with no damping), as given by the reciprocal of Eqn (3.48), for the prolate-oblate ellipsoid droplet oscillation mode, and  $F$  is the dimensionless damping factor. Note that  $F = 2$  corresponds to critical damping for which the oscillation frequency is zero. Lu and Apfel expressed  $\Omega_c$ , the ratio of the complex frequency and the resonance frequency as

$$-\Omega_c = -\frac{\omega_c}{\omega^*} = 1 + \epsilon_1 + \epsilon_2 + \dots \quad (3.71)$$

where  $\epsilon_1$  and  $\epsilon_2$  denote the first and second order perturbations from the resonance frequency due to viscous damping.  $\epsilon_1$  and  $\epsilon_2$  are expressed in terms of a Reynolds number based on the characteristic velocity  $R\omega^*$  and are given by

$$\epsilon_1 = -\frac{5(i+1)}{4\sqrt{2}Re}g(m, r) \quad (3.72)$$

$$\epsilon_2 = -\frac{25i}{16Re}h(m, r) \quad (3.73)$$

where

$$Re = \frac{\rho_c R^2 \omega^*}{\mu_c} \quad (3.74)$$

$$g(m, r) = \frac{10}{(2 + 3/r)(1 + \sqrt{rm})} \quad (3.75)$$

$$h(m, r) = g(m, r)^2 \left\{ \frac{2}{125}(2 + 3/r)(6/m + 4 - r + 16rm) - 1 \right\} \quad (3.76)$$

and  $m = \mu_c/\mu_d$  and  $r = \rho_c/\rho_d$ . The damping factor may now be written, via Eqn (3.69), as

$$F = \frac{5}{2\sqrt{2}Re}g(m, r) + \frac{25}{8Re}h(m, r) \quad (3.77)$$

If surfactants are present in the continuous phase then there is an additional contribution to the damping factor due to the effects of diffusional exchange of the surfactant between the interface and the bulk fluid. The alternating contraction and dilation of the interface during oscillations coupled with the finite rate of diffusional exchange means that the surface tension of contracted parts of the interface will be lower than the equilibrium value due to the higher surfactant concentration. Similarly, in dilating parts of the interface, the surface tension will be higher than equilibrium due to the reduced surfactant concentration there. The net result is that more energy is expended during the expansion phase than is recovered in the contraction phase leading to a net damping factor.

To account for such effects, two dimensionless parameters are introduced;  $\Phi$  which is the surface dilational elasticity number and  $\Psi$  which indicates the departure of the surface concentration from equilibrium.

$$\Phi = \frac{\Gamma}{\sigma} \frac{d\sigma}{d\Gamma} \quad (3.78)$$

$$\Psi = \sqrt{\frac{D}{\omega^*}} \left( \frac{d\Gamma}{dC} \right)^{-1} \quad (3.79)$$

where  $\Gamma$  is the equilibrium interfacial surfactant concentration, as given by the appropriate isotherm,  $\sigma$  is the surface tension,  $D$  is the surfactant bulk diffusion coefficient and  $C$  is the bulk surfactant concentration. For moderate values of  $\Phi$  and  $\Psi$  the resulting increase in the damping factor is given by

$$\Delta F = \frac{\Phi \Psi}{4(\sqrt{2} + 2\Psi + \sqrt{2}\Psi^2)} \left\{ \frac{1 - 4\sqrt{rm}}{1 + \sqrt{rm}} \right\}^2 \quad (3.80)$$

Eqn (3.80) shows that  $\Delta F \rightarrow 0$  as  $\Psi \rightarrow 0$  or  $\Psi \rightarrow \infty$ . For  $\Psi \rightarrow 0$  this behaviour is due to the fact that the surfactant is essentially confined to the interface since the distance associated with diffusional exchange compared with the distance required to maintain equilibrium is small. Conversely, for  $\Phi \rightarrow 0$  the tendency for  $\Delta F \rightarrow 0$  is due to the fact that equilibrium between the interface and the bulk is maintained at all times and the interfacial surface tension is essentially constant.

Having arrived at the above expressions for the damping factor which take account of the droplet viscosity and the influence of surfactants, Chesters then went on to derive appropriate expression for the sub-models required to form the  $S_\gamma$  break-up source term. Chesters first obtains an expression for the Weber number in terms of the oscillation

frequency and the resonant frequency by equating the oscillation frequency given by the reciprocal of Eqn (3.48) with the turbulent forcing frequency which is of the order

$$\omega^* \approx \left\{ 2\pi \left( \frac{\epsilon^*}{d^2} \right)^{1/3} \right\}^2 \quad (3.81)$$

where  $\epsilon^*$  is the turbulent dissipation rate corresponding to the resonance frequency  $\omega^*$ . The resulting expression for the resonance Weber number is therefore

$$We^* = \frac{\rho_c d^{5/3} \epsilon^{2/3}}{2\sigma} \quad (3.82)$$

We can now obtain an expression for the Weber number in terms of  $\Omega$  as defined by Eqn (3.71).

$$We = \Omega^2 \frac{\rho_c d^{5/3} \epsilon^{2/3}}{\sigma} = \Omega^2 We^* \quad (3.83)$$

As in the inertial break-up case for clean systems, as described in Section 3.3.2.2, break-up is expected to occur when the Weber number exceeds a certain critical value  $We_c$ . An expression for the critical Weber number may be derived based on the expectation that droplet break-up will occur when the distortion of the interface exceeds some critical value. It can be shown [100] that the maximum radial perturbation,  $a_o$ , of the droplet interface in the low frequency limit may be expressed in terms of the Weber number via

$$a_o = \kappa R We = \kappa R We^* \Omega^2 \quad (3.84)$$

where  $\kappa$  is a constant with a value of  $1/6$  and  $R$  is the droplet radius. For a linear forced oscillator, it can also be shown that the oscillation amplitude  $a$  may be expressed in terms of  $\Omega$  and  $F$  as

$$\frac{a}{a_o} = \frac{1}{\sqrt{\Omega^2 F^2 + (1 - \Omega^2)^2}} \quad (3.85)$$

Combining Equations (3.84) and (3.85) we obtain

$$\frac{a}{R We^* \kappa} = \frac{\Omega^2}{\sqrt{\Omega^2 F^2 + (1 - \Omega^2)^2}} \quad (3.86)$$

The left hand side of the above equation forms a dimensionless distortion amplitude. Break-up is supposed to occur when this amplitude exceeds some pre-defined critical limit which we term the ‘critical amplitude parameter’,  $K$ . At the critical amplitude, the frequency ratio attains its critical value  $\Omega_c$ . At critical conditions, Eqn (3.86) reads

$$K = \frac{\Omega_c^2}{\sqrt{\Omega_c^2 F^2 + (1 - \Omega_c^2)^2}} \quad (3.87)$$

Eqn (3.87) provides a quadratic equation for  $\Omega^2$  the solution of which is given by

$$\Omega_c^2 = \frac{-B \pm \sqrt{B^2 - 4A}}{2A} \quad (3.88)$$

where

$$\begin{aligned} A &= 1 - K^{-2} \\ B &= F^2 - 2 \end{aligned}$$

Chesters notes that the behaviour of Eqn (3.88) depends strongly on the value of the critical amplitude parameter  $K$ . For  $K < 1$  a solution exists for all values of  $F$  with the minus sign applying in Eqn (3.88). For  $K > 1$ , however, a solution only exists when

$$F^2 \leq 2 - 2\sqrt{1 - K^{-2}} \quad (3.89)$$

Chesters analysed the experimental data of Janssen *et al.* [101] and determined that for those cases  $K$  had an approximate value of 1.2 implying that break-up will only occur when Eqn (3.89) is satisfied. Chesters ascribes this behaviour to the imperfect modelling of turbulence as a harmonic disturbance whose frequency is directly coupled with its intensity. The net result is that large disturbances have a short duration and will not result in break-up, although in reality break-up will be possible at damping factors above the limit imposed by Eqn (3.89), although improbable.

The calculation of the  $\Omega_c$  from Eqn (3.87) allows the critical Weber number to be calculated using Eqn (3.83) via

$$We_c = \Omega_c^2 We^* \quad (3.90)$$

The critical droplet diameter, which is required to calculate the break-up source term in the  $S_\gamma$  equation, is determined from the critical Weber number via

$$d_c = \left\{ \frac{2\sigma W e_c}{\rho_c} \right\}^{3/5} \epsilon^{-2/3} \quad (3.91)$$

Finally, Chesters arrived at an expression for the break-up time-scale in the presence of surfactants by noting that the break-up time scales with the reciprocal of the droplets resonance frequency given by the reciprocal of Eqn (3.48). Thus, we have

$$\tau_b = \frac{2\pi k_b}{\omega^* \sqrt{1 - \frac{F^2}{4}}} \quad (3.92)$$

where  $k_b$  is a constant coefficient of order unity.

### 3.3.3.3 Implementation Issues

The implementation of the inertial break-up model for systems involving surfactants as outlined in the previous section is not straightforward. The main complication lies in the fact that the critical droplet diameter is a function of the critical Weber number which, in turn, is a function of the critical droplet diameter. This inter-dependence necessitates an iterative solution procedure.

Examining of Equations (3.88) and (3.90) shows that the dependence of the Weber number on the droplet diameter comes through the damping factor  $F$ . At critical conditions, the critical Weber number is based on the critical value of the oscillation frequency ratio  $\Omega_c$  which is based on the value of the damping factor at that critical diameter.

In order to determine the critical diameter, Chesters [94] suggested the following iterative procedure.

- 1 First, estimate a value for the critical Weber number by calculating  $\Omega_c$  using a damping factor of zero.
- 2 Obtain the corresponding value of the critical diameter  $d_c$  from Eqn (3.91) and calculate the appropriate value for the damping factor from Equations (3.77) and (3.80).
- 3 Recalculate the value for  $\Omega_c$  using the latest value for the damping factor.



4 Repeat the above procedure from 1 until convergence is obtained.

However, the determination of the critical droplet diameter is complicated by the fact that the damping factor cannot rise beyond a certain limit (the value of which depends on the adopted value for the critical amplitude parameter because of Eqn (3.89)). Physically, this means that there is a corresponding droplet diameter below which break-up does not occur,  $d_{min}$ . The dependence of the critical droplet diameter on the Weber number represents another, related, limit below which break-up does not occur. The task is to determine which of these lower bounds is the more restrictive in an efficient and stable way.

In order to study the situation more closely, it is instructive to consider the behaviour of the damping factor as a function of the droplet diameter. Figure 3.4 shows the damping factor against droplet diameter for a variety of viscosity ratios between 1 and 100 for an oil-water system without surfactants.

It can be seen that the damping factor rises steeply with a reduction in the droplet diameter for the higher viscosity ratios. For these conditions, a critical amplitude parameter value of 1.2, as proposed by Chesters, implies a limiting value of the damping factor of 0.95 (as given by Eqn (3.89)) which means that for viscosity ratios above about 20 break-up will not occur at any diameter. For a viscosity ratio of 10, the diameter corresponding to the limiting damping factor,  $d_{min}$  is about  $66 \mu m$ .

If we now consider the damping factor taking into account the effects of surfactants we see that the situation becomes more complex. Figure 3.5 shows the total damping factor (ie, the clean component plus the surfactant component) for a viscosity ratio of 3.5 for a sucrose monolaureate surfactant (Ryoto SE). It can be seen that the damping factor may exhibit a local peak due to the fact that the additional contribution due to the surfactant, as given by Eqn (3.80), exhibits a maximum at  $\Psi = 1$ .

If the local minimum reduces the damping factor to below the limit imposed by Eqn (3.89), then there may be a small range of droplet diameters which can undergo break-up. In principle, it is possible to account for this additional range by calculating the critical droplet diameter within this region, which then forms the lower limit of the integral in the break-up term, and using the diameter at which the damping factor rises to the maximum allowable value as the upper limit. However, the determination of the appropriate upper and lower limits would be expensive since it has to be carried out iteratively. In any case, the contribution to the total break-up from this small region is likely to be relatively small and can be neglected without too much loss of accuracy [102].

Therefore, the final critical droplet diameter is taken to be the maximum between the

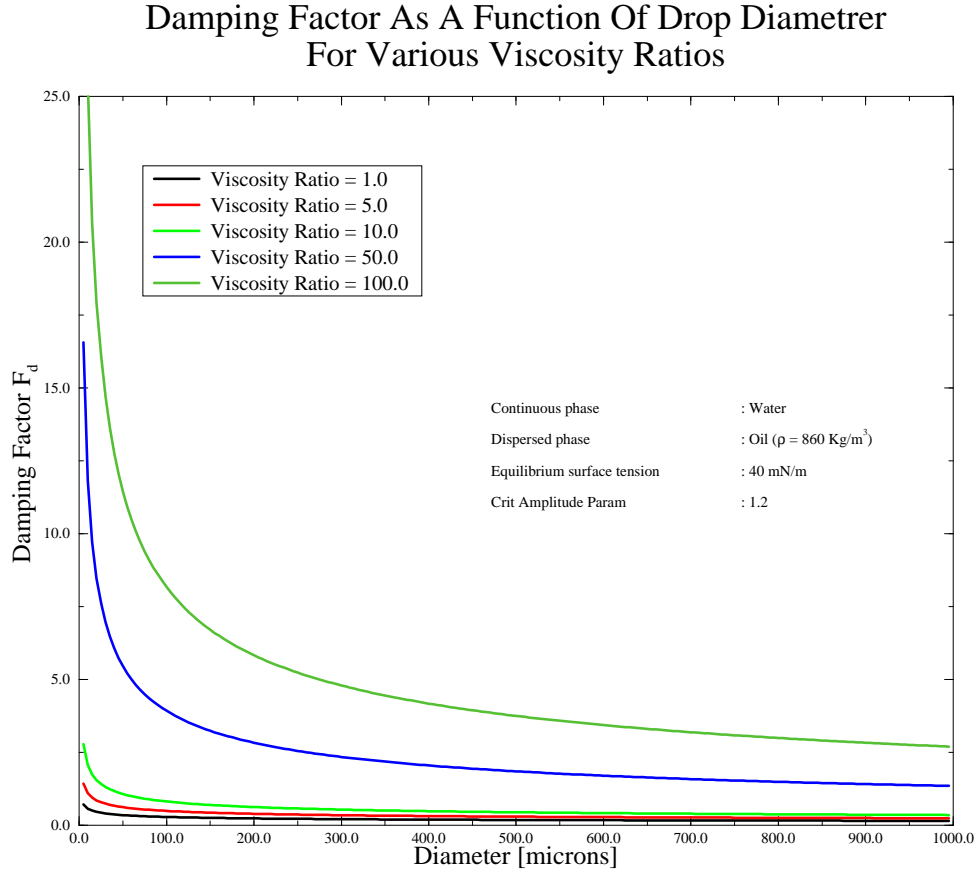


Figure 3.4: Damping factor as a function of droplet diameter and viscosity ratio.

diameter at the limiting value of the damping factor  $d_{min}$  and the critical droplet diameter as determined from the critical Weber number. For the surfactant case,  $d_{min}$  is taken as the highest diameter at which the damping factor reaches the limiting value.

### 3.3.4 Generic Coalescence Model

For completeness, the generic coalescence model is briefly described here, although coalescence effects are not considered in any of the validation cases undertaken as part of the present study. In general, the sub-models required to complete the coalescence modelling are less well developed than those for break-up due to the fact that coalescence effects are of less importance in industry than break-up effects. This fact is reflected by the dearth of suitable experimental data which are required to accurately formulate the

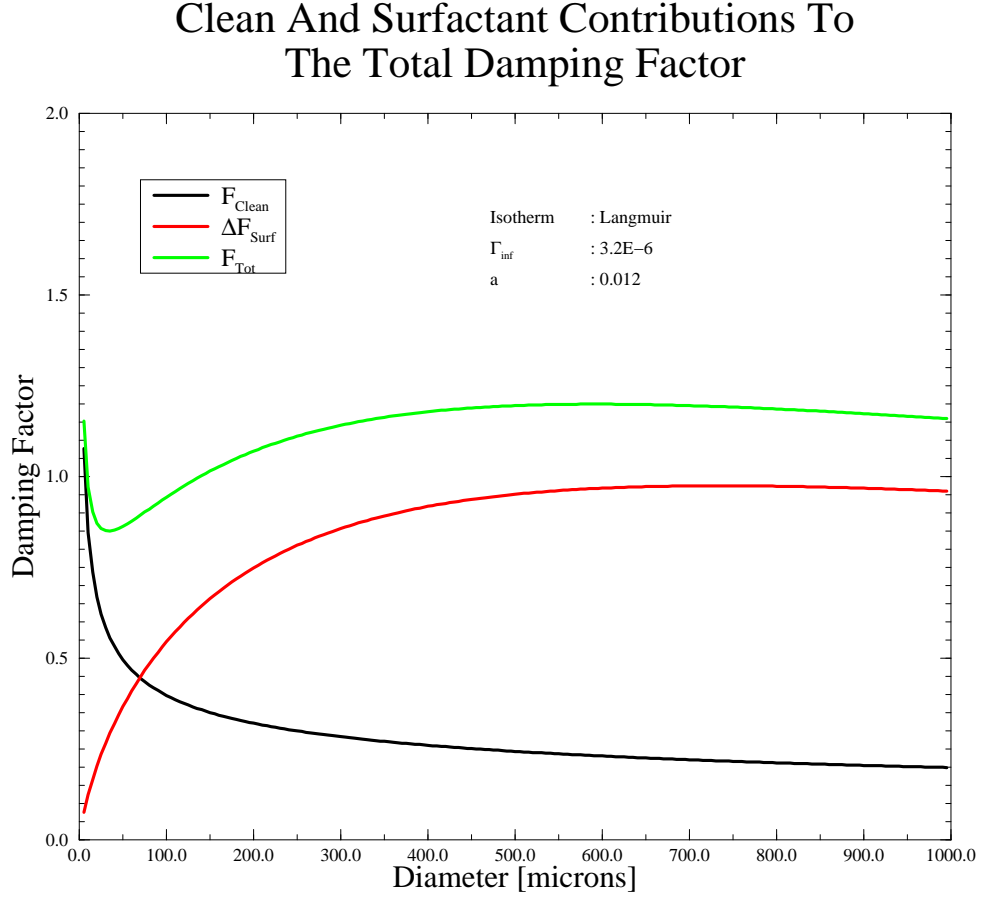


Figure 3.5: Components of damping factor.

required sub-models.

By considering the contribution of a single coalescence event, the rate of change of  $S_\gamma$  may be determined by summing all such contributions. The generic coalescence source term therefore reads [81]

$$S_c = \int_0^\infty \int_0^\infty C(d, d') P_{\text{coal}}(d, d') \Delta S_\gamma(d, d') d(d) d(d') \quad (3.93)$$

- where  $C(d, d')$  = Collision rate per unit volume between droplets  
 = of diameter  $d$  and  $d'$ .  
 $P_{coal}(d, d')$  = Probability that collision leads to coalescence.  
 $\Delta S_\gamma(d, d')$  = Change in  $S_\gamma$  due to single coalescence event  
 = between droplets of diameter  $d$  and  $d'$ .

The coalescence source term therefore requires the specification of the various sub-models for the collision rate, the coalescence probability and the corresponding change in  $S_\gamma$  for a single coalescence event. Chesters [81] has derived an expression for the change in  $S_\gamma$  which reads

$$\Delta S_\gamma(d) = d^\gamma \left\{ \left( 1 + \left( \frac{d}{d'} \right)^3 \right)^{\gamma/3} - \left( 1 + \left( \frac{d}{d'} \right)^\gamma \right) \right\} \quad (3.94)$$

If it is assumed that only droplets of the same diameter coalesce, the coalescence source term reduces to

$$S_c = \int_0^\infty C(d) P_{coal}(d) \Delta S_\gamma(d) d(d) \quad (3.95)$$

with

$$\Delta S_\gamma(d) = d^\gamma (2^{\gamma/3} - 2) \quad (3.96)$$

A further simplification may be made if the integral in the term is removed by using mean or averaged values for the collision rate, coalescence probability and the droplet diameter. The coalescence source term may then be written as

$$S_c = (2^{\frac{\gamma}{3}} - 2) d^\gamma C P_{coal} \quad (3.97)$$

Chesters has derived preliminary models for these quantities [81].

### 3.4 Concentration Transport Equations

The models outlined in Sections 3.3.3.1 and 3.3.3.2 account for the effects of surfactants on the break-up of droplets in the viscous and inertial regimes. These models yield the

local break-up rate given the bulk and interfacial surfactant concentration. The bulk and interfacial surfactant concentrations, however, are strongly coupled to the flow field of the phase containing the surfactant and the droplet break-up and coalescence rate itself.

For instance, the break-up or coalescence of droplets results in a corresponding increase or decrease in the interfacial surface area which subsequently affects the rate at which the surfactant is adsorbed or desorbed from the interface to the bulk. Convective and diffusive transport of the surfactant within the bulk affects the amount of surfactant available at a particular point in space and time which subsequently influences the break-up and coalescence rate.

The result is a tightly coupled system where the break-up, coalescence and the transport processes all have to be accounted for simultaneously. The current break-up and coalescence framework can be easily extended to allow all of these effects and their coupling to be taken into account by introducing transport equations for the bulk and interfacial surfactant concentration. These transport equations, derived below, naturally contain the convective and diffusive transport terms and the source and sink terms which account for the effects of droplet break-up and coalescence.

The derivation of these equations is carried out in the next section using the conditional averaging technique used throughout the rest of this work. The modelling of the interfacial transport terms which arise from the conditional averaging is discussed in Section 3.4.3.

### 3.4.1 Bulk Concentration Transport Equation

The conservation equation for the mean bulk surfactant concentration is derived by simply conditionally averaging the local surfactant concentration conservation equation. The local conservation equation for the concentration of a solute within phase  $k$  reads

$$\frac{\partial C_k}{\partial t} + \nabla \cdot \mathbf{u}_k C_k = \nabla \cdot D_k \nabla C_k + S_{ck} \quad (3.98)$$

where  $C_k$  is the local concentration,  $\mathbf{u}_k$  is the local fluid velocity,  $D_k$  is the laminar diffusivity of the solute and  $S_{ck}$  is the bulk source of the solute due to chemical reactions, etc. Since we are not considering chemical reactions in this work the bulk source term will henceforth be neglected. This equation is valid within each phase up to the interfaces between phases.

Multiplication of the above equation with the phase indicator function,  $\chi_k$ , and ensemble averaging yields

$$\frac{\partial \alpha_k \overline{C_k}}{\partial t} + \nabla \cdot \overline{\mathbf{u}_k C_k} = \nabla \cdot \alpha_k D_k \nabla \overline{C_k} - \nabla \cdot \alpha_k \overline{\mathbf{u}_{\mathbf{k}}' C_k'} + \overline{C_{k_i} (\mathbf{u}_{\mathbf{k}_i} - \mathbf{u}_i) \cdot \nabla \chi_k} - \overline{D_k \nabla C_{k_i} \cdot \nabla \chi_k} \quad (3.99)$$

where  $\mathbf{u}_{\mathbf{k}_i}$  is the limiting value of the velocity adjacent to the interface and  $\mathbf{u}_i$  is the velocity of the interface itself. For flows with a passive (ie, non-propagating) interface,  $\mathbf{u}_{\mathbf{k}_i} = \mathbf{u}_i$  and Eqn (3.99) reduces to

$$\frac{\partial \alpha_k \overline{C_k}}{\partial t} + \nabla \cdot \overline{\mathbf{u}_k C_k} = \nabla \cdot \alpha_k D_k \nabla \overline{C_k} - \nabla \cdot \alpha_k \overline{\mathbf{u}_{\mathbf{k}}' C_k'} - \overline{D_k \nabla C_{k_i} \cdot \nabla \chi_k} \quad (3.100)$$

The term  $\nabla \cdot \alpha_k \overline{\mathbf{u}_{\mathbf{k}}' C_k'}$  represents the turbulent diffusion of the concentration and is modelled in this work using the gradient diffusion assumption,

$$\overline{\mathbf{u}_{\mathbf{k}}' C_k'} = -D_k^t \nabla \overline{C_k} = -\frac{\mu_k^t}{\sigma_{ck}} \nabla \overline{C_k} \quad (3.101)$$

where  $D_k^t$  is the turbulent diffusion coefficient which is written in terms of the turbulent viscosity  $\mu_k^t$  and the turbulent Schmidt number  $\sigma_{ck}$ .

The last term in Eqn (3.100) represents the source in the mean concentration due to the transfer of solute between the interface and the bulk. Denoting this term as  $-M_k$ , Eqn (3.100) becomes

$$\frac{\partial \alpha_k \overline{C_k}}{\partial t} + \nabla \cdot \overline{\mathbf{u}_k C_k} = \nabla \cdot \alpha_k (D_k + D_k^t) \nabla \overline{C_k} + M_k \quad (3.102)$$

In surface average notation, the mass transfer term reads

$$M_k = - \overbrace{D_k \nabla C_k \cdot \mathbf{n}_k} \Sigma \quad (3.103)$$

where  $\mathbf{n}_k$  represents the interface unit normal vector interior to phase  $k$ . This mass transfer term requires modelling in terms of known values before Eqn (3.102) can be solved to yield the mean concentration  $\overline{C_k}$ .

### 3.4.2 Interfacial Concentration Transport Equation

The interfacial concentration transport equation follows directly from the consideration of mass conservation in a material volume of the dispersed phase [103]. The balance equation for the total amount of surfactant present within the material volume may be written in terms of the bulk concentration and the interfacial concentration. For a surfactant in the continuous phase, this equation reads

$$\frac{D_d \phi_c}{Dt} + \phi \nabla \cdot \bar{\mathbf{u}}_d = \nabla \cdot \alpha_c (D_c + D_c^t) \nabla \bar{C}_c - \nabla \cdot \alpha_c \bar{C}_c (\bar{\mathbf{u}}_c - \bar{\mathbf{u}}_d) \quad (3.104)$$

where  $\phi_c = \Gamma A + \alpha_c \bar{C}_c$  is the total amount of surfactant in the continuous phase per unit volume and  $A$  is the interfacial area per unit volume which is related to  $S_2$  via  $A = \pi S_2$ . The first term on the right hand side accounts for the diffusion through the material volume surface while the second term accounts for the flux of continuous phase through the surface of the material volume.

When the surfactant is in the dispersed phase, we have

$$\frac{D_d \phi_d}{Dt} + \phi \nabla \cdot \bar{\mathbf{u}}_d = \nabla \cdot \alpha_d (D_d + D_d^t) \nabla \bar{C}_d \quad (3.105)$$

where  $\phi_d = \Gamma A + \alpha_d \bar{C}_d$ .

Combining Equations (3.105) and (3.104) and (3.102) we find that

$$\frac{D_d}{Dt} (\Gamma A) + \Gamma A \nabla \cdot \bar{\mathbf{u}}_d = -M_k \quad (3.106)$$

which is the required interfacial surfactant concentration transport equation. The solution of Eqn (3.106) yields the product  $\Gamma A$ . The interfacial surfactant concentration  $\Gamma$  may then be deduced by calculating  $S_2$  via its own transport equation (Eqn (3.19)) which accounts for the local changes in interfacial surface area changes due to break-up and coalescence.

### 3.4.3 Interface Mass Transfer Rate Model

The mass transfer term  $M_k$  in Eqn (3.103) above represents both the transfer of a solute from one phase *to* the interface, and the transfer of a solute *through* the interface to the other phase. The former process is dominant in the case of surface active agents and is the one considered here.

Ziman [104] and Chesters [84] have proposed a first order model for this process, taking into account the effects of turbulence and the existence of a droplet size distribution. Their expression reads

$$M_k = \frac{6\alpha_k D_k S_h}{d^2} (C_o - \overline{C_k}) \quad (3.107)$$

where  $S_h$  is the Sherwood number (the ratio of the convective and diffusive mass transfer rates) based on the droplet diameter,  $C_o$  is the concentration adjacent to the interface,  $D$  is the solute diffusion coefficient in phase  $k$  and  $d$  is an appropriate mean diameter.  $\overline{C_k}$  is the local mean solute concentration. The concentration of the surfactant immediately adjacent to the interface  $C_o$  is related to the interfacial concentration by the appropriate isotherm; see Equations (3.50) and (3.53).

For droplets smaller than the Kolmogorov eddies, mass transfer is found to be dominated by the velocity variations associated with the turbulence [85]; velocity variations due to mean velocity gradients and the mean and fluctuating relative velocity are found to be negligible. The corresponding Sherwood number is given by

$$S_h = 1 + 0.55 P_e^{1/3} \quad (3.108)$$

where  $P_e$  is the Peclet number given by

$$P_e = \left( \frac{\epsilon}{\nu} \right)^{1/2} \frac{d^2}{4D_k} \quad (3.109)$$

where  $\nu$  is the phase kinematic viscosity and  $\epsilon$  is the turbulent energy dissipation rate. Eqn (3.108) is valid for high Peclet numbers.

For droplets larger than the Kolmogorov eddies, velocity variations due to the mean relative velocity are found to be important in addition to those due to the turbulence [85]. In this case the Sherwood number is given by

$$S_h = 1 + 0.69 P_e^{1/3} \quad (3.110)$$

In order to account for the presence of a droplet size distribution, the appropriate mean droplet diameter  $d$  in the above equations is shown to be  $d_{3, \frac{3}{5}}$  [85]. This diameter can be obtained from the local PDF via Eqn (3.9) given one other mean diameter (obtained from the local value of  $S_\gamma$  and the phase fraction) and the distribution variance.



### 3.5 Closure

In this chapter, a general approach for the inclusion of a variable droplet size within the two-fluid framework has been described. The approach is able to account for the temporal and spatial variations in droplet sizes which frequently occur in many important engineering processes due to the break-up and coalescence of droplets. Less complex approaches have been reviewed and have been discarded on the basis of a lack of generality or computational cost.

The adopted approach is based on a presumed PDF and employs transport equations for a series of conserved quantities ( $S_\gamma$ ) which are related to the moments of the PDF. The Log-Normal PDF has been found to adequately represent the droplet size variations found in engineering emulsification processes. The effects of a distribution of droplet sizes on the drag term in the phase momentum equations has been discussed. The need to fully evaluate the drag force over the entire range of droplet sizes has been avoided by the use of an appropriate mean droplet diameter which effectively takes into account the existence of a distribution of sizes on the mean drag force.

Transport equations for the  $S_\gamma$  quantities have been derived using the conditional averaging technique consistent with the derivation of the two-fluid equations in Chapter 1. These transport equations contains source and sink terms which account for the effects of break-up and coalescence on the local state of the PDF. Generalised models for these source and sink terms have been described and are written in terms of a well-defined set of parameters which need to be specified according to the particular break-up or coalescence mechanism of interest.

The physical mechanisms underlying the break-up of droplets in turbulent flows has been discussed and two important break-up regimes have been identified, according to whether the droplet size is smaller or larger than the Kolmogorov eddy size. For droplets smaller than the Kolmogorov eddies, the break-up mechanism is essentially that of stationary laminar break-up and is dominated by viscous forces. Break-up is brought about by the deformation of the droplet by the localised shearing flow and is a function of the viscosity ratio and local capillary number. For droplets larger than the Kolmogorov eddies, break-up is dominated by inertial forces which incite destructive oscillations in the droplet eventually bringing about break-up.

The effects of surface active agents on these break-up regimes has been discussed and appropriate sub-models described for when the droplets are smaller or larger than the Kolmogorov eddies. Although the presence of surfactants at the interface nominally reduces the surface tension, which should increase the break-up rate, it has been found that

the dynamic nature of the interface has to be accounted for.

For the viscous break-up regime, the rotation and deformation of the droplet in the shear flow field introduces a visco-elastic behaviour due to the non-uniform surfactant concentration on the interface. This effect has been modelled by the introduction of an effective surface tension which take into account the deformation and relaxation time-scale at the interface.

Similarly, the oscillations of the interface in the inertial break-up regime has been found to introduce a non-uniform surfactant concentration which introduces additional damping over and above that due to the viscosity of the droplet. This effect has been modelled by considering the free oscillations of droplets in the small amplitude limit resulting in an expression for the critical Weber number.

The modelling of surfactant effects has been completed by the derivation of the conditionally averaged conservation equations for the bulk surfactant concentration and the concentration at the interface. Surfactant is transferred between the bulk and the interface due to concentration differences brought about by the changes in surface area due to break-up and coalescence.

Although the approach described in this chapter can be used independently, it is especially powerful when coupled with the two-fluid framework since the coupled physical processes affecting each phase are accounted for simultaneously. For example, in the case of surfactant influenced break-up, the bulk transport of the surfactant has to be accounted for at the same time as the break-up itself since the break-up rate and the transfer rate of surfactant between the bulk and interface are highly dependent on each other. The local changes in mean diameter can have a significant effect on the transport of the droplets due to the changes in the drag behaviour. Coupling the variable droplet size framework and the two-fluid framework together allows such effects to be readily accounted for.

The application of the approach presented in this chapter to a system involving the break-up of droplets in an in-line mixing device is described in detail in Chapter 6. This study is based on a series of experiments which were designed to determine the effects of surfactants and the droplet viscosity on the break-up rate. Systems with and without surfactants, and a number of different viscosity ratios were considered resulting in a wealth of good quality experimental data which was used to gauge the performance of the coupled two-fluid and variable droplet size approach.

## Chapter 4

# Numerical Solution Procedure

This chapter describes in detail a procedure which enables the two-phase equations derived in the previous chapters to be solved numerically. The procedure is an implicit iterative method based on the finite volume discretisation technique and uses a solution algorithm specially developed for two-phase flow which is based loosely on the SIMPLE algorithm. Special consideration is given to the coupling between the phase momentum equations due to drag and to the imposition of continuity constraints and their effect on the overall stability of the solution algorithm. Details of all boundary conditions and auxiliary techniques required to facilitate implementation of the procedure are also given.

### 4.1 Introduction

The two-phase model developed in the Chapters 1 and 2 comprises differential conservation equations for the mass and momentum of each phase and the turbulent kinetic energy and dissipation rate for the continuous phase. In Chapter 3, a number of additional scalar conservation equations were added to allow break-up and coalescence effects to be included. The direct analytical solution to the entire equation set is presently impossible due to their highly non-linear and coupled nature and so we need to turn to the digital computer to provide a numerical solution.

Many different techniques enabling the numerical solution of the single-phase Navier-Stokes equations over a wide variety of flow conditions have been developed and refined in recent years and this has led to the considerable expansion of the field known as Computational Fluid Dynamics (CFD). Perhaps the most common technique applied to engineering flows is that based on the Finite Volume discretisation technique coupled with an

implicit, iterative pressure correction solution algorithm, such as the SIMPLE algorithm of Patankar [105] or the PISO algorithm of Issa [106].

A wealth of experience in the application of these techniques to single-phase and, to a much lesser extent, two-phase engineering flows over a wide variety of geometries and flow conditions already exists. This experience has been drawn upon as much as possible to guide the development of a general solution procedure applicable to dispersed two-phase flows. The proposed two-phase numerical solution procedure is based on the finite volume discretisation technique coupled with a fully implicit pressure correction algorithm similar to the SIMPLE algorithm, but with suitable modifications due to the two-phase nature of the flow.

The solution procedure is split into two stages. The first stage involves the discretisation of the solution domain and the governing differential equations using the finite volume technique. This involves subdividing the solution domain into a number of tessellating polyhedral cells over which each of the governing equations are integrated, resulting in a set of linear algebraic equations which are then solved using an appropriate solver. The discretisation of the solution domain and governing equations is discussed in Sections 4.2 and 4.3 respectively. The application of the boundary conditions is discussed in Section 4.4.

The second stage concerns the two-phase numerical solution algorithm itself, whose purpose is to maintain the coupling between all of the equations and impose any continuity and boundedness constraints on the system as a whole. It is at this stage in particular that we need to consider the special features of the two-phase system. These include the coupling between the two phase momentum equations, due to drag and pressure, etc, and the imposition of the individual and total phase continuity constraints. These issues are discussed in detail in Section 4.5.

## 4.2 Discretisation Of The Solution Domain

The discretisation of the solution domain is achieved by subdividing it into many tessellating polyhedral sub-volumes or cells. Associated with each cell are a number of flat faces, which make up the boundary of the cell, and a point situated at the cell centre at which the values of the primitive variables, such as pressure, velocity, etc, are sought. Each cell face is shared between two adjacent cells but, in the general case, each cell may contain any number of faces [107]. The resulting arrangement of the cells forms a ‘mesh’ upon which the governing differential equations are discretised.

Figure 4.1 illustrates a typical cell and shows the positions of the cell node, denoted ‘p’,

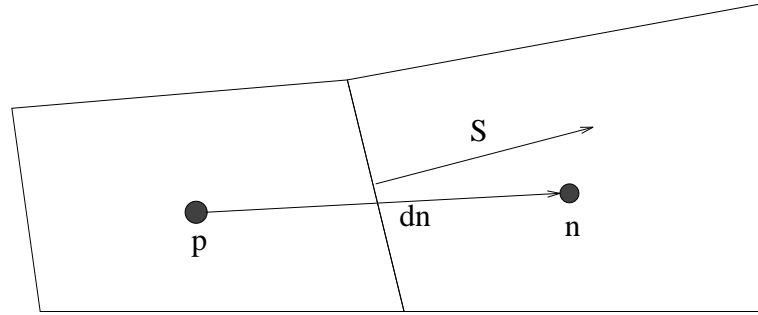


Figure 4.1: Typical computational cell arrangement.

and a neighbour cell node, denoted ‘n’. The face area vector  $\mathbf{S}$  is defined to point outward from the cell containing cell node  $p$ . The vector  $\mathbf{d}_n$  represents the relative position of node  $n$  with respect to node  $p$ .

The subdivision of the solution domain may be accomplished in many different ways depending on the exact nature of the geometry being discretised and the solution algorithm being used. All of the different methods may be broadly categorised according to whether the cells are arranged in a structured or unstructured manner and whether the same cell arrangement is used for all of the discretised equations.

Structured meshes are those in which the location of any neighbouring cell may be inferred solely from the adopted cell numbering scheme, which implies that the cells are arranged in previously defined structure, usually comprising a three dimensional block of cells with a known number of cells along each side. Complicated geometrical features, which aren’t directly amenable to the structured nature of the mesh, are treated by creating dummy cells within the solid part of the geometry, which are subsequently ignored during the solution, or by combining multiple block sections together.

Conversely, in an unstructured mesh arrangement, the cells may be arranged in any convenient manner. Neighbouring cell labels are determined by the use of indirect addressing where the label of the neighbouring cell is stored for each cell face in a lookup table. The use of unstructured meshes in general engineering calculations is almost essential. The internal geometry of the equipment in which the flow solution is sought is rarely simple enough to allow the use of a structured mesh unless efficiency and/or accuracy is sacrificed. The use of an unstructured mesh allows a great deal of freedom in the generation of the mesh and allows a greater solution accuracy to be obtained for the same number of cells. Complicated geometrical features on the boundary may be resolved easily without compromising the arrangement of the cells within the solution domain itself.

Since the numerical discretisation of each equation is effectively performed in isolation, there is no strict requirement for the same mesh arrangement to be used for each equation. In particular, the discretisation of the momentum equations is frequently performed on a different cell arrangement than the scalar transport equations (in particular, the pressure) to avoid the classic ‘checkerboard’ pressure-velocity de-coupling problem [105]. This approach is called the ‘staggered’ cell approach since the cells associated with the momentum equations are staggered relative to the cells associated with the scalar equations.

Due to the considerable complication in implementation introduced by using different meshes for some or all of the equations, special techniques have recently been developed which allow the same cell arrangement to be used for all of the equations without introducing pressure-velocity de-coupling or sacrificing solution accuracy. The use of these techniques considerably simplifies the implementation of the solution algorithm. Such an approach is called a ‘co-located’ approach since all variables are associated with the same point within the cell.

The simple physical geometry of two of the three validation studies performed as part of this work allowed a two-dimensional structured mesh to be used. For the third case, where the two-phase flow in a stirred vessel was analysed, the use of an arbitrary unstructured mesh was essential. In all cases, a co-located mesh was used.

### 4.3 Discretisation Of The Governing Differential Equations

Once the solution domain mesh has been defined, the governing equations are discretised by integrating them over each cell and applying Gauss’ theorem which translates the volume integral into a surface integral. The values of the primitive variables on the cell faces are then rewritten in term of neighbouring cell centre values yielding an algebraic equation for that cell. The result is a set of linear algebraic equations, one for each discretised equation, written in terms of the mesh cell centre values.

The procedure is well defined and its application to the equations comprising the present two-phase model is straightforward. To aid the process, the equations are first written in a generic form by grouping the individual terms into convection, diffusion and ‘source’ terms. The discretisation of each group of terms is the same for all equations.

For the two-phase system under consideration, the generic form of the steady state transport equation for any scalar or vector quantity  $\phi$  is written as

$$\nabla \cdot \rho \alpha \bar{\mathbf{u}} \phi = \nabla \cdot \rho \alpha \Gamma_{\phi} \nabla \phi + S_{\phi} \quad (4.1)$$

---

where  $\rho$  is the phase density,  $\alpha$  is the phase fraction,  $\overline{\mathbf{u}}$  is the phase velocity,  $\Gamma_\phi$  is the diffusion coefficient and  $S_\phi$  represents the remaining source terms which may include additional fluxes or stress components. The corresponding values for  $\phi$ ,  $\Gamma_\phi$  and  $S_\phi$  for the mass, momentum, turbulent kinetic energy and dissipation rate equations are summarised in Table 4.1.

Table 4.1: Generic form of the two-phase flow equations.

Equation	$\phi$	$\Gamma_\phi$	$S_\phi$
Cont Eqn.	1	0	0
$\bar{\mathbf{u}}_c$ Eqn.	$\bar{\mathbf{u}}_c$	$\nu_c + \nu_c^t$	$ \begin{aligned} & -\alpha_c \nabla \bar{p} + \nabla \cdot \alpha_c (\mu_c + \mu_c^t) \left\{ \nabla \bar{\mathbf{u}}_c^T - \frac{2}{3} (\nabla \cdot \bar{\mathbf{u}}_c) \mathbf{I} \right\} - \\ & \nabla \cdot \frac{2}{3} k \mathbf{I} + \alpha_c \rho_c \mathbf{g} + \frac{3}{4} \frac{\alpha_d \rho_c C_d}{d}  \bar{\mathbf{u}}_r  (\bar{\mathbf{u}}_d - \bar{\mathbf{u}}_c) - \\ & C_{vm} \alpha_d \rho_c \left( \frac{D_c}{Dt} \bar{\mathbf{u}}_c - \frac{D_d}{Dt} \bar{\mathbf{u}}_d \right) - \\ & C_l \alpha_d \rho_c (\bar{\mathbf{u}}_c - \bar{\mathbf{u}}_d) \times (\nabla \times \bar{\mathbf{u}}_c) + 0.37 \rho_c C_d  \bar{\mathbf{u}}_r ^2 \nabla \alpha_d \end{aligned} $
$\bar{\mathbf{u}}_d$ Eqn.	$\bar{\mathbf{u}}_d$	$\nu_d$	$ \begin{aligned} & -\alpha_d \nabla \bar{p} + \nabla \cdot \alpha_d \mu_d \left\{ \nabla \bar{\mathbf{u}}_d^T - \frac{2}{3} (\nabla \cdot \bar{\mathbf{u}}_d) \mathbf{I} \right\} + \\ & \nabla \cdot \alpha_d C_t^2 \frac{\rho_d}{\rho_c} \mu_c^t \left\{ \nabla \bar{\mathbf{u}}_c + \nabla \bar{\mathbf{u}}_c^T - \frac{2}{3} (\nabla \cdot \bar{\mathbf{u}}_c) \mathbf{I} \right\} - \\ & \nabla \cdot \frac{2}{3} C_t^2 \rho_d k \mathbf{I} + \alpha_d \rho_d \mathbf{g} + \frac{3}{4} \frac{\alpha_d \rho_c C_d}{d}  \bar{\mathbf{u}}_r  (\bar{\mathbf{u}}_c - \bar{\mathbf{u}}_d) + \\ & C_{vm} \alpha_d \rho_c \left( \frac{D_c}{Dt} \bar{\mathbf{u}}_c - \frac{D_d}{Dt} \bar{\mathbf{u}}_d \right) + \\ & C_l \alpha_d \rho_c (\bar{\mathbf{u}}_c - \bar{\mathbf{u}}_d) \times (\nabla \times \bar{\mathbf{u}}_c) - 0.37 \rho_c C_d  \bar{\mathbf{u}}_r ^2 \nabla \alpha_d \end{aligned} $
$k$ Eqn.	$k$	$\nu_c + \frac{\nu_c^t}{\sigma_k}$	$ \begin{aligned} & \alpha_c G - \rho_c \alpha_c \epsilon - \mathbf{F}_d \cdot \bar{\mathbf{u}}_r - 0.37 \rho_c C_d  \bar{\mathbf{u}}_r ^2 \bar{\mathbf{u}}_r \cdot \nabla \alpha_c \\ & G = \mu_c^t \left\{ \nabla \bar{\mathbf{u}}_c + \nabla \bar{\mathbf{u}}_c^T - \frac{2}{3} (\nabla \cdot \bar{\mathbf{u}}_c) \mathbf{I} \right\} : \nabla \bar{\mathbf{u}}_c - \\ & \frac{2}{3} \rho_c k \mathbf{I} : \nabla \bar{\mathbf{u}}_c \end{aligned} $



Table 4.1: Generic form of the two-phase flow equations.

Equation	$\phi$	$\Gamma_\phi$	$S_\phi$
$\epsilon$ Eqn.	$\epsilon$	$\nu_c + \frac{\nu_c^t}{\sigma_\epsilon}$	$C_1 \alpha_c \frac{\epsilon}{k} G - C_2 \alpha_c \rho_c \frac{\epsilon^2}{k} + C_2 \frac{\epsilon}{k} \mathbf{F}_d \cdot \bar{\mathbf{u}}_r -$ $0.37 C_2 \frac{\epsilon}{k} \rho_c C_d  \bar{\mathbf{u}}_r ^2 \bar{\mathbf{u}}_r \cdot \nabla \alpha_c$

The discretisation of the convection, diffusion and source terms in Eqn (4.1) will be considered in detail in the following sections. Repeated use of the generalised form of Gauss' theorem will be made which, when applied to the various spatial derivatives of a scalar or vector property  $Q$ , yields the following results

$$\int_{\delta V} \nabla Q \, dV = \oint_{\delta S} Q \, d\mathbf{S} \quad (4.2)$$

$$\int_{\delta V} \nabla \cdot \mathbf{Q} \, dV = \oint_{\delta S} \mathbf{Q} \cdot d\mathbf{S} \quad (4.3)$$

$$\int_{\delta V} \nabla \mathbf{Q} \, dV = \oint_{\delta S} \mathbf{Q} \, d\mathbf{S} \quad (4.4)$$

where  $\Delta V$  is the volume of the cell and  $\delta S$  is the closed bounding surface of the cell.

Since the cell volumes are bounded by flat faces, the surface integrals in the above equations may be written in terms of a sum of integrals over each face. For example,

$$\begin{aligned}
\int_{\delta V} \nabla Q \, dV &= \oint_{\delta S} Q \, d\mathbf{S} \\
&= \sum_{\text{faces}} \left( \int_{\text{face}} Q \, d\mathbf{S} \right) \\
&= \sum_{\text{faces}} Q_f \mathbf{S}_f
\end{aligned} \quad (4.5)$$

where  $Q_f$  is the cell face-average value of  $Q$  over the face and  $\mathbf{S}_f$  is the cell face area vector.

#### 4.3.1 Convection Terms

Application of the above discretisation procedure to the convection term yields

$$\begin{aligned}
\int_{\Delta V} \nabla \cdot \rho \alpha_k \bar{\mathbf{u}} \phi \, dV &= \sum_f \mathbf{S}_f \cdot (\rho \alpha_k \bar{\mathbf{u}} \phi)_f \\
&= \sum_f \mathbf{S}_f \cdot (\rho \alpha_k \bar{\mathbf{u}})_f \phi_f \\
&= \sum_f \mathbb{F}_f \phi_f
\end{aligned} \tag{4.6}$$

where  $\mathbb{F}_f$  represents the face mass flux<sup>1</sup> given by

$$\mathbb{F}_f = \mathbf{S}_f \cdot (\rho \alpha_k \bar{\mathbf{u}}_k)_f \tag{4.7}$$

The discretisation of the convection term is completed when the face average value  $\phi_f$  is recast in terms of the cell nodal values; a task ascribed to the chosen ‘differencing scheme’. There exist many possibilities in the choice of differencing scheme, with each scheme having its own advantages and disadvantages. The main issues surrounding the choice of differencing scheme are the boundedness of the solution, the stability and the overall accuracy of the scheme. Jasak [107] and Muzaferija [108] have reviewed many of the available schemes and provide a detailed discussion on all of the above considerations.

The differencing scheme adopted in this work is upwind-differencing. Although this scheme is known to have drawbacks in terms of accuracy, it does have the highly desirable property of providing unconditionally bound face values and is simple to implement. Other schemes which also obey the boundedness criterion have recently been formulated, such as the Gamma scheme of Jasak [107], and are known to provide more accurate solutions. However, since the intention here is to test the basic validity of the two-phase model and the stability of the solution algorithm; issues of accuracy in the convection term are somewhat secondary compared with the uncertainties in the modelling of two-phase flow and turbulence.

The upwind-differencing scheme determines the value of  $\phi$  at the cell face by considering the direction of the flow normal to the cell face. The value at the face is set equal to the value of the cell node from the upwind direction. The flow direction normal to the face is determined from the face flux value  $\mathbb{F}_f$  so that the face value of the product  $\mathbb{F}_f \phi_f$  may be written in compact form as

---

<sup>1</sup>The cell face flux is an important quantity and is calculated directly by the solution algorithm rather than from cell face values for the velocity, density, phase fraction, etc, which will, in general, not be calculated directly.

$$\mathbb{F}_f \phi_f = \phi_p \max[\mathbb{F}, 0] - \phi_n \max[-\mathbb{F}, 0] \quad (4.8)$$

where the subscripts  $p$  and  $n$  indicate the current and neighbouring cell values respectively, and the operator  $\max[a, b]$  indicates the maximum value of  $a$  and  $b$ .

#### 4.3.2 Diffusion Terms

The integration of the diffusion term over the control volume followed by the application of Gauss' theorem yields

$$\begin{aligned} \int_{\Delta V} \nabla \cdot \rho \alpha_k \Gamma \nabla \phi &= \sum_f \mathbf{S}_f \cdot (\rho \alpha_k \Gamma \nabla \phi)_f \\ &= \sum_f (\rho \alpha_k \Gamma)_f \mathbf{S}_f \cdot (\nabla \phi)_f \end{aligned} \quad (4.9)$$

If the mesh is orthogonal, i.e. the cell faces are at right angles to the line connecting the two cell nodes on either side of the face, then we have

$$\mathbf{S}_f \cdot (\nabla \phi)_f = |\mathbf{S}_f| \frac{\phi_n - \phi_p}{|\mathbf{d}_n|} \quad (4.10)$$

where the vector  $\mathbf{d}_n$  connects the current and neighbouring cell centres as shown in Figure 4.1. When the mesh is not orthogonal, then an additional correction term is added to Eqn (4.10) to account for the fact that the face area vector is no longer co-linear with the vector  $\mathbf{d}$  connecting the two cell nodes. The numerical treatment of this extra term requires considerable care and attention [107]. Since the calculations presented in this work do not employ any non-orthogonal meshes, this term is not considered in detail here.

#### 4.3.3 Source Terms

The terms in the original transport equation which may not be written as convection or diffusion terms are grouped together as 'source' terms. These terms may be any general function of  $\phi$ . The treatment of the source terms follows that of Patankar [105] where the source terms are linearised to be of the form

$$S = S_u + S_p \phi_p \quad (4.11)$$

where  $S_u$  and  $S_p$  may also depend on  $\phi$ .

Integration of Eqn (4.11) over the control volume yields

$$\int_{\delta V} S_\phi dV = S_u \Delta V + S_p \phi_p \Delta V \quad (4.12)$$

In an iterative sequence, the coefficients  $S_u$  and  $S_p$  are calculated using the currently available values for  $\phi$  and therefore their values may be calculated explicitly. Ideally, the coefficient  $S_p$  should be negative which allows the contribution  $S_p \phi$  to be specially treated, as shown in Section 4.3.4, which increases the stability of the solution [105].

For the momentum equations in the present two-phase model, the source terms involve complicated spatial derivatives of the velocities and the phase fraction, as shown in Table 4.1. Consideration of the linearisation of these terms will be deferred until the solution algorithm is discussed in Section 4.5, because these terms have a large influence on the final form of the solution algorithm itself.

#### 4.3.4 Final Form Of The Discretised Equations

The discretisation of the individual terms in the generic transport equation yields an equation for  $\phi$  in each cell written in terms of the values of  $\phi$  in neighbouring cells. By grouping all coefficients relating to the current and neighbouring cell values, the resulting equation may be written in compact form as

$$\mathbb{A}_p \phi_p = \sum_n \mathbb{A}_n \phi_n + S_u \quad (4.13)$$

where the sum is over all neighbouring cells and  $A_p$  and  $A_n$  represent the central and neighbour coefficients respectively. The central coefficient  $\mathbb{A}_p$  is given by

$$\mathbb{A}_p = \sum_n \mathbb{A}_n - S_p \quad (4.14)$$

Note that the  $S_p \phi_p$  part of the linearised source term has been moved over to the left hand side of Eqn (4.13). When  $S_p$  is negative, as it should be when the source term is properly linearised, its contribution acts to increase the diagonal dominance of the central coefficient which increases the stability of the solution.  $S_u$  is the explicit part of the source term which is calculated using currently known values of  $\phi$ .

In the fully implicit discretisation scheme employed here, the neighbouring values of  $\phi$  are also governed by a similar equation involving the neighbouring values of  $\phi$ . This leads to a set of coupled linear equations, one for each cell, of the form given by Eqn (4.13). In this work, the system of equations is solved using an iterative solution technique based on the Conjugate Gradient Solution Method [109].

For brevity we denote the term involving the sum of the neighbour coefficients and the explicit part of the source in the above equation as  $\mathbb{H}(\phi)$ . Eqn (4.13) becomes

$$\mathbb{A}_p \phi_p = \mathbb{H}(\phi) \quad (4.15)$$

where

$$\mathbb{H}(\phi) = \sum_n \mathbb{A}_n \phi_n + S_u \quad (4.16)$$

#### 4.3.5 Under-Relaxation

Under-relaxation of the discretised transport equations is required to improve the stability of the solution due to the non-linear coupling between the equations. An implicit global under-relaxation is used where the value at the next iteration level is calculated according to

$$\phi_p = \lambda \phi_p^n + (1 - \lambda) \phi_p^o \quad (4.17)$$

where  $\phi^n$  is the value which would have been obtained if under-relaxation was not used,  $\phi_p^o$  is the ‘old’ value of  $\phi_p$  and  $\lambda$  is the under-relaxation factor [6]. When the under-relaxation is introduced into Eqn (4.15) we obtain

$$\frac{\mathbb{A}_p \phi_p}{\lambda_{\phi_p}} = \mathbb{H}(\phi_n) + \frac{1 - \lambda}{\lambda} \mathbb{A}_p \phi_p^o \quad (4.18)$$

Since all equations apart from the pressure are under-relaxed, the under-relaxation terms will henceforth be absorbed into the central coefficient and the  $\mathbb{H}()$  term so that all equations will still be of the form given by Eqn (4.15).

### 4.3.6 Convergence

The overall iterative process is assumed to be converged when the normalised sum of the absolute residuals for each equation has been reduced below a pre-specified value. The residual for equation  $\phi$  is denoted  $R_\phi$  and is a measure of how well the discretised equation is satisfied at a particular cell node. From Eqn (4.15),  $R_\phi$  is defined as

$$R_\phi = |\mathbb{H}((\phi)_n) - \mathbb{A}_p \phi_p| \quad (4.19)$$

The residuals are summed over the solution domain and then normalised using an appropriate normalisation factor  $N_\phi$ . Thus, the normalised residual sum for equation  $\phi$  is given as

$$Z_\phi = \frac{\sum_1^{N_c} R_\phi}{N_\phi} \quad (4.20)$$

where  $N_c$  is the total number of computational cells.

The normalisation factor for each equation are given in Table 4.3.6. Here,  $\sum_i$  is the sum over all ‘inlet’ cells to the domain,  $\mathbf{A}_f$  is the cell face area vector for the inlet cell,  $N_k$  is the normalisation factor for the  $k$  equation.  $L_{\text{nom}}$  and  $V_{\text{nom}}$  are nominal length and velocity scales respectively. For pipe flow, for example, these are taken as the radius of the pipe and the centreline velocity.

Equation	Normalisation factor $N$
Continuous phase momentum	$\sum_i \alpha_c \rho_c  \mathbf{u}_c  \mathbf{A}_f \cdot \mathbf{u}_c$
Dispersed phase momentum	$\sum_i \alpha_d \rho_d  \mathbf{u}_d  \mathbf{A}_f \cdot \mathbf{u}_d$
Overall continuity (pressure)	$\sum_i (\alpha_c \mathbf{A}_f \cdot \mathbf{u}_c + \alpha_d \mathbf{A}_f \cdot \mathbf{u}_d)$
Phase fraction	$\sum_i \alpha_d \mathbf{A}_f \cdot \mathbf{u}_d$
Turbulence kinetic energy $k$	$\sum_i \alpha_c \rho_c  \mathbf{u}_c ^2 \mathbf{A}_f \cdot \mathbf{u}_c$
Dissipation rate $\epsilon$	$\frac{N_k V_{\text{nom}}}{L_{\text{nom}}}$
General scalar $\phi$	$\sum_i \alpha_d \rho_d \phi \mathbf{A}_f \cdot \mathbf{u}_c$

Table 4.2: Normalisation factors for the two-phase flow equations.

The ‘general scalar’ equation in Table 4.3.6 relates to any additional scalar equations which are solved as part of the system to account for droplet size effects (i.e. the  $S_\gamma$  equations), and any surfactant concentration transport equations.

In addition to monitoring the normalised residuals, the values of the flow variables at a position in the flow domain which is considered sensitive are also monitored. At convergence, these values are checked to see that no appreciable changes in their values are taking place.

## 4.4 Boundary Conditions

The majority of engineering calculations rely on a few well defined physical boundary ‘types’ which translate into the necessary boundary conditions which are applied to each of the equations. In this work, the boundary types treated are walls, inlets, outlets and symmetry planes. The corresponding boundary conditions for each of the variables are shown in Table 4.4.

Variable	Wall	Inlet	Outlet	Symmetry Plane
$\bar{u}_c$	Fixed Value	Fixed Value	Zero Gradient	Zero Gradient
$\bar{u}_d$	Fixed Value	Fixed Value	Zero Gradient	Zero Gradient
$\alpha_d$	Zero Gradient	Fixed Value	Zero Gradient	Zero Gradient
$p$	Zero Gradient	Zero Gradient	Fixed Value	Zero Gradient
$k$	Fixed Value	Fixed Value	Zero Gradient	Zero Gradient
$\epsilon$	Fixed Value	Fixed Value	Zero Gradient	Zero Gradient

Table 4.3: Boundary conditions applied to each equation by boundary type.

The following sections discusses in detail how each of these boundary conditions are implemented.

### 4.4.1 Fixed Value Boundary Condition

The fixed value boundary condition prescribes the value of  $\phi$  on the boundary faces to be some known value  $\phi_b$ . The discretised form of the terms involving spatial derivatives, notably the convection and diffusion terms, involve the values of  $\phi$  at the cell faces. For the fixed value boundary faces  $\phi_f = \phi_b$  allowing the term involving  $\phi_b$  to be calculated directly.

For example, the discretised convection term in a cell adjacent to a fixed value boundary reads

$$\int_{\Delta V} \nabla \cdot \rho \alpha_k \bar{\mathbf{u}}_k \phi \, dV = \sum_{f \neq b} \mathbb{F} \phi_f + \mathbb{F}_b \phi_b \quad (4.21)$$

where the subscript  $b$  denotes the values on the boundary. Since the values of  $\phi_f$  and the face flux  $\mathbb{F}$  is known on the boundary, the last term in the above equation may be calculated explicitly and added to the source term of the algebraic system.

Similarly, the diffusion term is discretised as

$$\int_{\Delta V} \nabla \cdot \rho \alpha_k \Gamma \nabla \phi \, dV = \sum_f (\rho \Gamma)_f \mathbf{S}_f \cdot (\nabla \phi)_f \quad (4.22)$$

For the boundary face, the face gradient is calculated from

$$\mathbf{S}_f \cdot (\nabla \phi)_f = |\mathbf{S}_f| \frac{\phi_b - \phi_p}{|\mathbf{d}_n|} \quad (4.23)$$

which may be split into an implicit and explicit part

$$|\mathbf{S}_f| \frac{\phi_b - \phi_p}{|\mathbf{d}_n|} = |\mathbf{S}_f| \frac{\phi_b}{|\mathbf{d}_n|} - |\mathbf{S}_f| \frac{\phi_p}{|\mathbf{d}_n|} \quad (4.24)$$

#### 4.4.2 Fixed Gradient Boundary Condition

In the case of the fixed gradient boundary condition, the component of the gradient of  $\phi$  normal to the boundary is known. Thus, we have

$$(\mathbf{n} \cdot \nabla \phi)_b = g_b \quad (4.25)$$

where  $\mathbf{n}$  is the outward pointing unit normal. Where a value of  $\phi$  at the boundary face is required, this may be determined via

$$\phi_b = \phi_p + \mathbf{d}_n \cdot (\nabla \phi)_f \quad (4.26)$$

so that



$$\phi_b = \phi_p + |\mathbf{d}_n|g_b \quad (4.27)$$

The resulting contribution to the convection term, for example, is

$$\mathbb{F}_b \phi_b = \mathbb{F}_b \phi_p + \mathbb{F}_b |\mathbf{d}_n|g_b \quad (4.28)$$

Similarly, for the diffusion term, the face gradient at the boundary face is known and we simply have

$$\mathbf{S}_f \cdot (\nabla \phi)_f = |\mathbf{S}_f|g_b \quad (4.29)$$

For the special case of a zero-gradient boundary condition, there is no contribution since  $g_b$  is zero.

#### 4.4.3 Wall boundary conditions

The actual treatment of the no-slip condition at wall boundaries depends on whether or not the flow is laminar or turbulent. In a laminar flow, the velocities are simply set to zero. In turbulent flow, however, a special treatment is additionally required to capture the effects of the turbulent boundary layer without having to fully resolve the region with a fine mesh.

In this work, this is achieved using the so-called ‘wall function’ approach [11, 110] where the effects of the turbulent boundary layer are accounted for by special algebraic formulae which represent the distribution of velocity, turbulence energy and its dissipation rate adjacent to the wall. The use of wall functions implies the following assumptions

- Variations in velocity are predominantly normal to the wall so that the flow is essentially one dimensional.
- There is an exact balance between turbulence production and dissipation in the boundary layer.
- The turbulence length scale varies linearly with distance from the wall.
- The shear stress across the layer is constant and co-linear with the velocity.

The wall function approach treats the cells adjacent to the wall according to whether the cell centre is in the laminar or turbulent region. This is determined from the local value of the dimensionless distance from the wall  $y^+$  which is defined as

$$y^+ = \frac{\Delta y_p \rho}{\mu} \sqrt{\frac{\tau_w}{\rho}} \quad (4.30)$$

where  $\Delta y_p$  is the normal distance of the cell node from the wall,  $\mu$  is the fluid dynamic viscosity and where  $\tau_w$  is the wall shear stress. The transition between laminar and turbulent flow is given by the solution to the equation

$$y^+ = \frac{1}{\kappa_v} \ln E y^+ \quad (4.31)$$

where  $\kappa_v$  is Von Karman's constant (of value 0.4187) and  $E$  is an integration constant that depends on the roughness of the wall. For smooth walls it has a value of 9.793. The solution to Eqn (4.31) is the intersection between the linear shear stress profile and the turbulent log-law region which, for the values quoted, is 11.63.

Therefore, if  $y^+ \leq 11.63$ , then the near wall flow is taken to be laminar and the shear stress is calculated from

$$\tau_w = \frac{\mu u_p}{\Delta y_p} \quad (4.32)$$

where  $u_p$  is the velocity at the cell node. The shear force on the fluid is therefore given by

$$F_s = -\alpha_c \tau_w A_b \quad (4.33)$$

which is included directly in the momentum equations as a source term. If  $y^+ > 11.63$ , then the point is in the turbulent region and the shear stress is given by

$$\tau_w = \frac{C_\mu^{1/4} \sqrt{k_p} u_p \kappa_v}{\ln E y^+} \quad (4.34)$$

where  $k_p$  is the turbulent kinetic energy at the cell node.

Wall boundary conditions are also applied to the  $k$  and  $\epsilon$  equations. For the  $k$  equation, the sink term  $\alpha_c \rho \epsilon$  is replaced by

$$\alpha_c C_\mu^{3/4} \rho \frac{k_p^{3/2} \ln Ey^+}{\kappa_v \Delta y_p} \quad (4.35)$$

for  $y^+ \leq 11.63$ , and by

$$C_\mu^{3/4} \rho k_p^{3/2} \frac{y^+}{\Delta y_p} \quad (4.36)$$

for  $y^+ > 11.63$ .

The wall boundary condition for  $\epsilon$  follows from the assumption that turbulence production equals dissipation which implies that the value of  $\epsilon$  at the near wall cell node is given by

$$\epsilon = \frac{C_\mu^{3/4} k_p^{3/2}}{\kappa_v \Delta y_p} \quad (4.37)$$

In the case of two-phase flow very little information exists as to the nature of the turbulent boundary layer in two-phase flow, so the strict validity of the wall function approach is not known. This work assumes that the effects of the second phase on the turbulent boundary layer are adequately accounted for by the inclusion of the phase fraction in the above equations which represents an effective reduction in the wall surface area in contact with the liquid phase [6].

Given the lack of experimental data, alternative approaches for accounting for the influence of the wall, such as those based on low Reynolds number modelling, would introduce more uncertainties in the turbulence modelling and cannot be applied with any confidence at this time.

## 4.5 Numerical Solution Algorithm

The discretisation process discussed in Section 4.3 is applied to each equation, yielding a set of non-linear algebraic equations for each of the conservation equations to be solved. The complete system of equations is solved using an iterative, or segregated, technique where, within an iterative cycle, each set of algebraic equations is solved in turn using an appropriate solver. The cycle is repeated until some pre-specified convergence criteria has been satisfied by the complete system of equations.

The solution process necessarily introduces some linearisation and lagging of information into the equations, either through the explicit linearisation of the terms involving the

dependent variable, or through the calculation of the terms involving other variables. It is the task of the solution algorithm to ensure that the iterative cycle finally converges to yield a solution and that the coupling between all of the equations is maintained and any system wide continuity constraints are properly imposed.

Solution algorithms for single-phase flows are fairly well developed. General engineering flow calculations based on the finite volume discretisation technique usually adopt the SIMPLE algorithm of Patankar [105], or the PISO algorithm of Issa [106]. Unfortunately, two-phase flow solution algorithms are not as well developed as their single-phase counterparts and it is not yet possible to use an ‘off the shelf’ algorithm which will suit every need.

A reasonable starting point for the development of a two-phase flow algorithm is an existing single-phase flow algorithm. The issue surrounding the coupling between the velocities and pressure, the imposition of global continuity and the general form of the algorithm are then fairly well resolved, leaving only the two-phase specific problems to be dealt with. Specifically, the following points have to be addressed during the development of a two-phase algorithm.

- The coupling between the phase momentum equations due to the interfacial forces such as drag, virtual mass and lift forces, and their effect on the stability of the solution algorithm.
- The coupling between the pressure field, which is common to both phases in this case, and the phase momentum equations, and its impact on phase continuity and the overall stability of the algorithm.
- The determination of the phase fraction from the phase continuity equation and its effect on individual phase continuity.

A considerable amount of work has already been done by workers in the field to try to resolve some of these issues. Two of the most relevant studies, due to Politis [6] and Oliveira [25], have been based on the SIMPLE algorithm (or on a variant of it) and these are discussed in detail in Section 4.5.1.

Section 4.5.2 then analyses the good and bad points of these two algorithms. Section 4.5.2.1 first discusses the coupling between the two phase momentum equations due to drag. It is known that one of the main causes of instability in a two-phase gas-liquid system is due to the highly non-linear nature of the drag force. Methods are proposed to improve the stability of the solution algorithm by improving the numerical treatment of the drag terms. Section 4.5.2.2 then goes on to discuss the phase continuity constraints

which are to be imposed on the system. Here, it is shown that the solution of the phase fraction and pressure equations have to be carefully sequenced if the phase continuity constraints and the stability of the algorithm are to be maintained. The analysis of these two issues allows an improved algorithm to be developed.

The stability and robustness of the proposed algorithm is then tested using a one dimensional test case comprising the air-water bubbly flow in a vertical duct with the highly non-linear drag model appropriate to air-water systems. The performance of the improved algorithm is compared to the algorithm of Oliveira. Several variants of the algorithm are identified and tested before the final form of the algorithm is determined. The final algorithm is then summarised in Section 4.5.3.

#### 4.5.1 Previous Studies

The SIMPLE algorithm of Patankar and Spalding [111] has proven very successful in the calculation of a wide variety of single-phase engineering fluid flows [105, 9]. Because of its successful track record, many workers have also sought to apply it to two-phase flows. Two such workers, Politis [6] and Oliveira [25], have proposed solution algorithms which are based on the SIMPLE algorithm, but with suitable modifications for the two-phase case. These two algorithms are studied in detail in this section.

Since both of these algorithms are based on the SIMPLE algorithm, it is useful at this stage to briefly review its main features. Essentially, the SIMPLE algorithm consists of the following steps carried out in sequence.

- 1 Velocity prediction.
- 2 Pressure prediction.
- 3 Velocity and face flux correction to satisfy continuity.
- 4 Solution of auxiliary scalar transport equations.

The velocity prediction stage uses the momentum equations to calculate ‘predictor’ velocities. These velocities, in general, do not satisfy the continuity equation. An equation is formulated for an updated pressure field which produces updated velocities which do satisfy continuity. Once this pressure field has been calculated, the updated velocities are calculated and used to update the cell face flux values. Any additional scalar equations are solved at this point using the new values of pressure, velocities and cell face fluxes. The sequence is repeated until the solution convergence criterion has been met, such as that

described in Section 4.3.6. Appendix D contains a more detailed overview of the single-phase SIMPLE algorithm applicable to co-located meshes where each of these stages is explained in more detail.

Within the iterative procedure it is necessary to differentiate between variables calculated at different stages of the sequence. In the following discussion, variables calculated in the previous iteration have a superscript ‘o’ while variables calculated in the present iteration have a superscript ‘n’. Intermediate values of variables have one or more ‘\*’ superscripts.

#### 4.5.1.1 The PISO-2P Algorithm Of Politis

As part of his study into two-phase solid-liquid flow in stirred vessels Politis [6] performed an extensive survey of previous studies into two-phase solution algorithms. He concluded that all had deficiencies in terms of convergence rate or stability. To resolve these problems he proposed a new algorithm, PISO-2P, which was based on the PISO (Pressure Implicit with Splitting of Operators) single-phase solution algorithm of Issa [106]. PISO is a variant of SIMPLE but uses multiple pressure correction stages to enable a non-iterative solution applicable to unsteady as well as steady flow problems.

The PISO-2P algorithm attempts to integrate the momentum equations and the pressure solution closely together within the iterative sequence. The multiple pressure correction stages allows the drag related terms to be updated within the sequence rather than at the end or beginning of every iteration.

Politis’ algorithm consists of 5 stages:

- 1 Velocity prediction.
- 2 First pressure correction stage.
- 3 Second pressure correction stage.
- 4 Phase fraction prediction.
- 5 Turbulence equation solution.

Each of these stages is described below. It is necessary in the following discussion to differentiate between variables calculated at different stages of the sequence and between variables relating to the two phases. The convention of indicating old, current and intermediate values using ‘o’, ‘n’ and ‘\*’ superscripts will be retained. Properties pertaining to individual phases will be indicated using the subscripts ‘c’ or ‘d’ for the continuous

and dispersed phases respectively. The subscript ‘p’ and ‘n’ indicating the position of the variable relative to the computational cell will be dropped to avoid confusion.

### Velocity Prediction

The discretised phase momentum equations are first written in the following form in which the drag and pressure gradient terms are not calculated as part of the source term  $S_u$  but are shown as additional terms in the discretised equation.

$$\mathbf{A}_c \mathbf{u}_d = \mathbb{H}(\mathbf{u}_c) - \alpha_c \Delta p + F(\mathbf{u}_d - \mathbf{u}_c) \quad (4.38)$$

$$\mathbf{A}_d \mathbf{u}_d = \mathbb{H}(\mathbf{u}_d) - \alpha_d \Delta p + F(\mathbf{u}_c - \mathbf{u}_d) \quad (4.39)$$

where  $F$  is the drag force coefficient given by Eqn (2.8) and the operator  $\mathbb{H}()$  contains the sum over the neighbouring cells and the source terms which are not pressure or drag related.

The main feature of the above equations is that both phase velocities appear within the drag term in each equation. The key issue is whether to treat these velocities ‘explicitly’, that is, to use the velocities from the previous iteration, or ‘implicitly’ by using the velocity to be calculated in this iteration.

In an attempt to promote stability, Politis tried to treat the drag term as implicitly as possible by treating one of the phase velocities on the right hand side of the above equations implicitly. The equations for the predictor phase velocities then become

$$(\mathbf{A}_c + F) \mathbf{u}_c^* = \mathbb{H}(\mathbf{u}_c^*) - \alpha_c^o \Delta p^o + F \mathbf{u}_d^o \quad (4.40)$$

$$(\mathbf{A}_d + F) \mathbf{u}_d^* = \mathbb{H}(\mathbf{u}_d^*) - \alpha_d^o \Delta p^o + F \mathbf{u}_c^o \quad (4.41)$$

It was found that this practice leads to slow convergence rates for high values of  $F$ , as encountered, for example, when there are high relative velocities between phases, or when the dispersed phase droplet or bubble size is large. The convergence rate is slow due to the fact that when  $F \gg \mathbf{A}$  the two equations predict  $\mathbf{u}_c^* \rightarrow \mathbf{u}_d^o$  and  $\mathbf{u}_d^* \rightarrow \mathbf{u}_c^o$ . The tendency for the predicted phase velocities to ‘flip’ leads to oscillatory behaviour which has to be attenuated using heavy under-relaxation, leading to a corresponding slow convergence rate [112].

Following Looney *et al.* [112], Politis tried to break the dominance of the drag term by treating it fully explicitly in the continuous phase momentum equation. The implicit treatment of the dispersed phase equation is retained but now uses the predicted velocity for the continuous phase instead of the previous iteration value. The equations then read

$$\mathbb{A}_c \mathbf{u}_c^* = \mathbb{H}(\mathbf{u}_c^*) - \alpha_c^o \Delta p^o + F(\mathbf{u}_d^o - \mathbf{u}_c^o) \quad (4.42)$$

$$(\mathbb{A}_d + F) \mathbf{u}_d^* = \mathbb{H}(\mathbf{u}_d^*) - \alpha_d^o \Delta p^o + F \mathbf{u}_c^* \quad (4.43)$$

After under-relaxation has been applied these equations are then solved in sequence to yield the predicted phase velocities  $\mathbf{u}_c^*$  and  $\mathbf{u}_d^*$ .

### First corrector stage

Since these predicted velocities will not in general satisfy continuity, new phase velocities  $\mathbf{u}_c^{**}$  and  $\mathbf{u}_d^{**}$  and an updated pressure  $p^*$  are sought such that the overall continuity equation

$$\nabla \cdot (\alpha_c^o \mathbf{u}_c^{**} + \alpha_d^o \mathbf{u}_d^{**}) = 0 \quad (4.44)$$

is satisfied. Equations for  $\mathbf{u}_c^{**}$  and  $\mathbf{u}_d^{**}$  are derived by writing Equations (4.42) and (4.43) as

$$\mathbb{A}_c \mathbf{u}_c^{**} = \mathbb{H}(\mathbf{u}_c^*) - \alpha_c^o \Delta p^* + F(\mathbf{u}_d^* - \mathbf{u}_c^*) \quad (4.45)$$

$$(\mathbb{A}_d + F) \mathbf{u}_d^{**} = \mathbb{H}(\mathbf{u}_d^*) - \alpha_d^o \Delta p^* + F \mathbf{u}_c^{**} \quad (4.46)$$

where the  $\mathbb{H}()$  term is written in terms of the predicted velocities  $\mathbf{u}_c^*$  and  $\mathbf{u}_d^*$  and can be calculated explicitly. Note that the relative velocity on the right hand side of the continuous phase momentum equation (4.45) is now written in terms of the predictor velocities  $\mathbf{u}_d^*$  and  $\mathbf{u}_c^*$ , and the continuous phase velocity on the right hand side of the dispersed phase momentum equation (4.46) is now written in terms of  $\mathbf{u}_c^{**}$ .

Equations (4.45) and (4.46) are subtracted from Equations (4.42) and (4.43) to yield velocity and pressure increments  $\mathbf{u}_c'$ ,  $\mathbf{u}_d'$  and  $p'$ .

$$\mathbb{A}_c \mathbf{u}_c' = -\alpha_c^o \Delta p' + F(\mathbf{u}_d^* - \mathbf{u}_c^* - \mathbf{u}_d^o + \mathbf{u}_c^o) \quad (4.47)$$

$$(\mathbb{A}_d + F) \mathbf{u}_d' = -\alpha_d^o \Delta p' + F \mathbf{u}_c' \quad (4.48)$$

where  $\mathbf{u}_c' = \mathbf{u}_c^{**} - \mathbf{u}_c^*$  and  $\mathbf{u}_d' = \mathbf{u}_d^{**} - \mathbf{u}_d^*$  and  $p' = p^* - p^o$ . Eqn (4.48) may now be substituted into Eqn (4.47) to yield



$$(\mathbb{A}_d + F)\mathbf{u}'_d = -\alpha_d^o \Delta p' - \frac{F\alpha_c^o}{\mathbb{A}_c} \Delta p' + \frac{F^2}{\mathbb{A}_c} (\mathbf{u}_d^* - \mathbf{u}_c^* - \mathbf{u}_d^o + \mathbf{u}_c^o) \quad (4.49)$$

Equations (4.45) and (4.46) are now rearranged to yield equations for  $\mathbf{u}_c^{**}$  and  $\mathbf{u}_d^{**}$  and substituted into the total continuity equation (4.44) to yield

$$\begin{aligned} \nabla \cdot \left( \frac{\bar{\alpha}_c^o \alpha_c^o}{\mathbb{A}_c} + \frac{\bar{\alpha}_d^o \alpha_d^o}{\mathbb{A}_d + F} + \frac{\bar{\alpha}_d^o \alpha_c^o}{\mathbb{A}_c (\mathbb{A}_d + F)} \right) \Delta p' = \\ \nabla \cdot \bar{\alpha}_c^o \mathbf{u}_c^* + \bar{\alpha}_d^o \mathbf{u}_d^* + \\ \nabla \cdot \left( \frac{\bar{\alpha}_c^o F}{\mathbb{A}_c} + \frac{\bar{\alpha}_d^o F^2}{\mathbb{A}_c (\mathbb{A}_d + F)} \right) (\mathbf{u}_d^* - \mathbf{u}_c^* - \mathbf{u}_d^o + \mathbf{u}_c^o) \end{aligned} \quad (4.50)$$

where  $\bar{\alpha}_k^o$  denotes an upwind value of the phase fraction at the cell face.

This equation is a Laplacian in  $p'$  and its solution yields the updated velocities  $\mathbf{u}_c^{**}$  and  $\mathbf{u}_d^{**}$ , via equations (4.47) and (4.49), and the updated pressure  $p^*$ . Similarly, the phase face fluxes are recalculated by writing equations (4.45) and (4.46) in terms of the face values of the velocities and interpolating all necessary terms on the right hand side to the cell face.

There are several points to note here. Firstly, phase fraction values in the total continuity equation (4.44) at the cell face are calculated by using the upwind values according to the direction of the phase flux across that face. Politis states that this is to ensure consistency with the upwind convective differencing scheme used in the dispersed phase continuity equation which is used to calculate the dispersed phase fraction.

Secondly, updating the drag term using the predictor velocities  $\mathbf{u}_c^*$  and  $\mathbf{u}_d^*$  and the corrected velocities  $\mathbf{u}_c^{**}$  and  $\mathbf{u}_d^{**}$  in equations (4.45) and (4.46) respectively, is meant to improve the coupling between the phase momentum equations by increasing the implicitness of the relative velocity. In practice, the updating of the drag term before the first corrector has to be under-relaxed to promote convergence.

Although total continuity is satisfied at this stage, the pressure  $p^*$  is dominated by mass errors due to the explicit form of equations (4.45) and (4.46). Hence, a second corrector is employed to yield new phase velocities  $\mathbf{u}_c^{***}$  and  $\mathbf{u}_d^{***}$  and a new pressure  $p^{**}$  which can be taken as the next iteration values  $\mathbf{u}_c^n$ ,  $\mathbf{u}_d^n$  and  $p^n$ , as follows.

### Second corrector stage

The next stage then is to obtain the next iteration velocities  $\mathbf{u}_c^n$  and  $\mathbf{u}_d^n$  and pressure  $p^n$  such that the total continuity equation is again satisfied,

$$\nabla \cdot \alpha_c^o \mathbf{u}_c^n + \alpha_d^o \mathbf{d}_c^n = 0 \quad (4.51)$$

Again, we start by writing the momentum equations in updated form as

$$\mathbb{A}_c \mathbf{u}_c^n = \mathbb{H}(\mathbf{u}_c^{**}) - \alpha_c^o \Delta p^{**} + F(\mathbf{u}_d^{**} - \mathbf{u}_c^{**}) \quad (4.52)$$

$$(\mathbb{A}_d + F) \mathbf{u}_d^n = \mathbb{H}(\mathbf{u}_d^{**}) - \alpha_d^o \Delta p^{**} + F \mathbf{u}_c^n \quad (4.53)$$

Note that again the drag terms have been updated with the latest known phase velocities. The procedure for obtaining an equation for the pressure correction  $p''$  is the same as the previous corrector stage. The final equation reads

$$\begin{aligned} & \nabla \cdot \left( \frac{\vec{\alpha}_c^o \alpha_c^o}{\mathbb{A}_c} + \frac{\vec{\alpha}_d^o \alpha_d^o}{\mathbb{A}_d + F} + \frac{\vec{\alpha}_d^o \alpha_c^o}{\mathbb{A}_c(\mathbb{A}_d + F)} \right) \Delta p'' = \\ & \nabla \cdot \left( \frac{\vec{\alpha}_c^o \mathbb{H}(\mathbf{u}_c')}{\mathbb{A}_c} + \frac{\vec{\alpha}_d^o F}{\mathbb{A}_c(\mathbb{A}_d + F)} \right) \mathbb{H}(\mathbf{u}_c') + \frac{\vec{\alpha}_d^o F}{\mathbb{A}_d + F} \mathbb{H}(\mathbf{u}_d') + \\ & \nabla \cdot \left( \frac{\vec{\alpha}_c^o F}{\mathbb{A}_c} + \frac{\vec{\alpha}_d^o F^2}{\mathbb{A}_c(\mathbb{A}_d + F)} \right) (\mathbf{u}_d^{**} - \mathbf{u}_c^{**} - \mathbf{u}_d^* + \mathbf{u}_c^*) \end{aligned} \quad (4.54)$$

Again, Eqn (4.54) is solved for  $p''$  which is then used to obtain the next iteration values for the phase velocities, pressure and face fluxes. At this stage the total continuity equation is satisfied.

### Phase fraction prediction

All previous equations have been constructed with the old value of the phase fraction  $\alpha_k^o$ . The next step is to obtain updated values for the phase fraction  $\alpha_k^n$ . This is achieved in PISO-2P by solving the dispersed phase continuity equation using the newly obtained values for the dispersed phase velocities so that

$$\nabla \cdot \alpha_d^n \mathbf{u}_d^n = 0 \quad (4.55)$$

Unless special care is taken, the solution to this equation does not guarantee that the predicted phase fraction value obeys the constraint  $0 \leq \alpha_d^n \leq 1$ . The principle difficulties are concerned with the boundedness properties of the adopted convective differencing scheme and the treatment of the terms arising from the discretisation process.

The boundedness criterion for a convective differencing scheme states that, in the absence of internal sources, the calculated internal nodal value of the dependent variable are bound by the values of the neighbouring nodes. It can be shown [105, 9] that when a differencing scheme obeys the boundedness criterion, all  $\mathbf{A}$  coefficients in the discretised equation will have the same sign. Physically, this implies that an increase in the value at one node results in an increase in the value at neighbouring nodes.

It is known that the upwind differencing scheme unconditionally obeys the boundedness criterion [105] and for this reason, Politis adopts this scheme for the discretisation of the above equation. Unfortunately, the adoption of a bounded differencing scheme by itself does not guarantee that Eqn (4.55) yields phase fraction values which obey the required constraint.

Discretisation of Eqn (4.55) yields

$$\mathbf{A}_d \alpha_d = \mathbb{H}(\alpha_d) \quad (4.56)$$

where

$$\mathbf{A}_d = \Sigma \mathbf{A}_n - S_p \quad (4.57)$$

$$\mathbb{H}(\alpha_d) = \Sigma_n \mathbf{A}_n \alpha_{dn} + S_u \quad (4.58)$$

and  $\mathbf{A}_n$  represents the neighbour coefficients.

The source terms in the above equation contain the discretised form of  $\alpha_d \nabla \cdot \mathbf{u}_d^n$  which, in general, is finite. Politis adopts the technique whereby this term is placed into  $S_p$  if it is negative, and is therefore treated implicitly so as to increase the diagonal dominance of the matrix and increase the stability of the solution [9]. In this case

$$S_p = \sum_f (\mathbf{u}_d^n)_f \cdot \mathbf{A}_f \quad (4.59)$$

$$S_u = 0 \quad (4.60)$$

where  $\mathbf{A}_f$  is the face area vector and  $(\mathbf{u}_d^n)_f$  is the dispersed phase velocity at the cell face. If the term is positive, then it is placed into  $S_u$  and treated explicitly giving

$$S_p = 0 \quad (4.61)$$

$$S_u = \alpha_d^o \sum_f (\mathbf{u}_d^n)_f \cdot \mathbf{A}_f \quad (4.62)$$

This practice ensures that the solution to Eqn (4.55) produces values for the predicted phase fraction  $\alpha_d^n$  which obeys the lower constraint  $\alpha_d^n \geq 0$  since the negative source term responsible for driving down the phase fraction is treated implicitly [6]. The upper constraint  $\alpha_d^n \leq 1$  cannot be guaranteed since a positive source term is treated explicitly and, within the overall iterative sequence before convergence is obtained, its magnitude may lead to an unbounded phase fraction value. Under-relaxation can be used in this case to prevent high intermediate values of phase fraction.

Once Eqn (4.55) has been solved for  $\alpha_d^n$ ,  $\alpha_c^n$  is calculated from the relationship  $\alpha_d^n + \alpha_c^n = 1$ . The cell face fluxes are then updated using Equations (4.52) and (4.53) using the latest  $\mathbf{u}^n$  and  $\alpha_k^n$  values.

The final stage in the PISO-2P sequence is the solution of the remaining scalar transport equations for the turbulence properties  $k$  and  $\epsilon$ . Once these equations have been solved, and the turbulent viscosity has been updated, the iterative cycle is repeated until convergence is obtained.

#### 4.5.1.2 The algorithm of Oliveira

Oliveira [25] presented a new two-phase flow algorithm based on the SIMPLE algorithm which was especially designed to be able to calculate gas-liquid flows within tee junctions. For gas-liquid systems the drag term may be highly non-linear, which may induce unstable behaviour in the solution unless special care is taken. The numerical treatment of the drag terms has a large effect on the stability of the algorithm, and Oliveira's algorithm is essentially centred around the treatment of these terms.

Oliveira identified four different drag term treatment variants and analysed the performance of each using a one-dimensional test case. The four variations studied are

- 1 The drag term is treated fully explicitly in the continuous phase momentum equation, while in the dispersed phase momentum equation it is treated semi-implicitly. This treatment is the same as that used by Politis; see Equations (4.42) and (4.43).
- 2 The drag terms are treated semi-implicitly in both phase momentum equations to give

$$(\mathbb{A}_c + F)\mathbf{u}_c = \mathbb{H}(\mathbf{u}_c) + F\mathbf{u}_d^o \quad (4.63)$$

$$(\mathbb{A}_d + F)\mathbf{u}_d = \mathbb{H}(\mathbf{u}_d) + F\mathbf{u}_c^o \quad (4.64)$$

- 3 A ‘partial elimination’ method, where the discretised momentum equations are used to partially eliminate the phase velocities from the drag terms. This method is described in detail more below.
- 4 An alternative partial elimination method, where the drag term linearisation is modified in the dispersed phase momentum equation in an attempt to improve the overall linearisation.

The key element to Oliveira’s algorithm lies in form of the discretised phase momentum equations used to calculate the predictor velocities  $\mathbf{u}_c^*$  and  $\mathbf{u}_d^*$ . The remainder of Oliveira’s algorithm is similar in form to the single-phase SIMPLE algorithm and consists of the following steps.

- The discretised phase momentum equations are solved in turn to yield predictor phase velocities  $\mathbf{u}_c^*$  and  $\mathbf{u}_d^*$ .
- The pressure equation is formulated based on the total continuity equation, written in terms of the corrected velocities  $\mathbf{u}_c^{**}$  and  $\mathbf{u}_d^{**}$ , which reads

$$\nabla \cdot (\alpha_c^o \mathbf{u}_c^{**} + \alpha_d^o \mathbf{u}_d^{**}) = 0 \quad (4.65)$$

- The updated pressure field is used to correct the phase velocities and cell face fluxes using the equivalents of Equations (4.45) and (4.46).
- The dispersed phase fraction field is calculated using the dispersed phase continuity equation using the same techniques as those described in Section 4.5.1.1.
- The turbulence equations for  $k$  and  $\epsilon$  are solved.

The above sequence is repeated until convergence is obtained.

Of the four variants studied by Oliveira, the third, the so-called ‘partial elimination’ method, was found to be the most promising and is discussed in detail more below.

### The Partial Elimination Method (Variant 3)

The partial elimination method attempts to treat the drag terms in a more implicit way by eliminating completely one of the phase velocities from each of the phase momentum equations. Variations of this method were originally developed by Harlow and Amsden [113, 114] and by Spalding [115].

The elimination begins by writing the discretised momentum equations for ‘partially updated’ phase velocities  $\mathbf{u}_c^\sharp$  and  $\mathbf{u}_d^\sharp$  as

$$(\mathbb{A}_c + F)\mathbf{u}_c^\sharp = \mathbb{H}(\mathbf{u}_c^\circ) + F\mathbf{u}_d^* \quad (4.66)$$

$$(\mathbb{A}_d + F)\mathbf{u}_d^\sharp = \mathbb{H}(\mathbf{u}_d^\circ) + F\mathbf{u}_c^* \quad (4.67)$$

Where the  $\mathbb{H}()$  term has been written in terms of the previous values of the velocities, and so can be calculated directly. These equations are rearranged to give explicit expressions for  $\mathbf{u}_c^\sharp$  and  $\mathbf{u}_d^\sharp$ .

$$\mathbf{u}_c^\sharp = \frac{\mathbb{H}(\mathbf{u}_c^\circ) + F\mathbf{u}_d^*}{(\mathbb{A}_c + F)} \quad (4.68)$$

$$\mathbf{u}_d^\sharp = \frac{\mathbb{H}(\mathbf{u}_d^\circ) + F\mathbf{u}_c^*}{(\mathbb{A}_d + F)} \quad (4.69)$$

The discretised momentum equations for the predictor velocities  $\mathbf{u}_c^*$  and  $\mathbf{u}_d^*$  are now written as

$$(\mathbb{A}_c + F)\mathbf{u}_c^* = \mathbb{H}(\mathbf{u}_c^*) + F\mathbf{u}_d^\sharp \quad (4.70)$$

$$(\mathbb{A}_d + F)\mathbf{u}_d^* = \mathbb{H}(\mathbf{u}_d^*) + F\mathbf{u}_c^\sharp \quad (4.71)$$

where the velocities on the right hand side have been taken as the ‘partially updated’ velocities defined in Equations (4.68) and (4.69) above. Substitution for these velocities into Equations (4.70) and (4.71) gives, after some rearrangement,

$$(\mathbb{A}_c + \mathbb{B}_d \mathbb{A}_d)\mathbf{u}_c^* = \mathbb{H}(\mathbf{u}_c^*) + \mathbb{B}_d \mathbb{H}(\mathbf{u}_d^\circ) \quad (4.72)$$

$$(\mathbb{A}_d + \mathbb{B}_c \mathbb{A}_c)\mathbf{u}_d^* = \mathbb{H}(\mathbf{u}_d^*) + \mathbb{B}_c \mathbb{H}(\mathbf{u}_c^\circ) \quad (4.73)$$

where

$$\mathbb{B}_c = \frac{F}{F + \mathbb{A}_c}$$

$$\mathbb{B}_d = \frac{F}{F + \mathbb{A}_d}$$

### Oliveira's one-dimensional test case results

Oliveira used a simple one-dimensional test case to determine the relative performance of the four alternatives. This case consisted of air-water bubbly flow within a circular pipe 50 mm in diameter and 0.5 m in length. Inlet velocities for both phase were set to 1.0 m/s with an inlet dispersed phase fraction of 10%. Two drag models were tested; a linear model using a prescribed drag coefficient  $C_d$ , and a non-linear drag model of the form

$$C_d = 1.0 + 0.15R_e^{0.687} \quad (4.74)$$

where  $R_e$  is the bubble Reynolds number.

The use of a prescribed drag coefficient  $C_d$  renders the drag force linearly proportional to the relative velocity. Oliveira varied the drag coefficient between  $10^3$  and  $10^{10} \text{ kg/m}^3\text{s}$ . Oliveira showed that for a high prescribed drag coefficient using the linear drag model, the partial elimination method (variant 3 above) out-performed the other three variants, essentially leading to a converged solution in the same number of iterations regardless of the magnitude of the drag coefficient. The three other alternatives performed well for low values of the drag coefficient (below  $10^5$ ) but failed at higher values due to their less implicit treatment of the drag terms.

As noted by Oliveira, a drag coefficient of  $10^5$  is somewhat higher than that experienced by a 1 mm bubble rising at its terminal velocity in water. Thus, for the vast majority of cases, all variants would perform adequately and lead to a converged solution. Oliveira argues for the use of artificially high drag coefficients to test the algorithms because, in complex flow situations, forces other than gravity may be present leading to strong segregation of the phases which could induce high drag.

For the non-linear drag model, Oliveira reported that the partial elimination method could obtain solutions for a wide range of bubble diameters (0.2 to 5.0 mm). The number of iterations to convergence varied only slightly with the bubble diameter (ranging between 42 and 56 iterations) which represented an order of magnitude difference in the drag coefficient value, illustrating the advantages of the more implicit treatment of the drag terms.

Oliveira reports that alternative 1 (where the drag term is treated implicitly in the dispersed phase momentum equation) also performs well for the values of the drag coefficient encountered in typical gas-liquid flows. However, he states that this method breaks down in complicated three dimensional flows where other forces are exerted on the bubble, for instance due to a locally high phase fraction or lift or virtual mass forces. On this basis, Oliveira discards alternatives 1, 2 and 4 and finally adopts the partial elimination method.

#### 4.5.1.3 Summary Of Previous Studies

The algorithms of Politis and Oliveira share many common features. The principle differences relate to the treatment of the drag terms in the discretised phase momentum equations and, in Politis' case, the presence of additional pressure corrector stages which included interim updates to the relative velocity (Equations (4.45) and (4.46)). The drag term treatment adopted by Politis in the predictor momentum equations corresponds to Oliveira's variant 1.

The Politis' algorithm was designed to tackle solid-liquid flows and was apparently successful in that role. When applied to gas-liquid systems it was found that this algorithm suffered severe stability problems and convergence could only be obtained when large under-relaxation was introduced in the momentum equations and in the relative velocity update between corrector stages.

This behaviour was found to be due to the high degree of non-linearity in the drag models appropriate to gas-liquid systems combined with the implicit treatment of the drag term in only one of the phase momentum equations. The heavy under-relaxation required in the update of the relative velocity between corrector stages effectively cancels out any benefit obtained from this update, leaving an algorithm very similar to that of Oliveira's variant 1, which he discards on the basis of poor performance when applied to gas-liquid systems.

In addition, in Politis' algorithm, the drag term is only updated with respect to the corrections in the phase relative velocity due to continuity constraints and not with respect to the non-linearity of the drag term itself (ie, the drag coefficients  $C_d$  and  $F$  are not updated). Since the pressure equation derivation is based on the total continuity equation (4.51), individual phase continuity will not be exactly satisfied, leading to small phase continuity errors until convergence is obtained. The updating of the relative velocity with these intermediate phase velocities was found to be problematical unless under-relaxation was introduced.

The determination of the phase fraction fields using the dispersed phase continuity equation after the pressure-velocity prediction stage is a common feature of both algorithms.



Unfortunately, the calculation of the phase fraction in this way proved to be troublesome. The techniques required to ensure that the solution of the phase fraction equation yields a bounded solution may cause the dispersed phase continuity to be violated. The practices of treating part of the equation explicitly (see Eqn (4.62)) and the introduction of under-relaxation means that dispersed phase continuity is not exactly satisfied when the equation is solved.

Consequently, the calculation of the cell face fluxes using the new phase fraction fields can result in non-conservative flux fields for both the continuous and dispersed phases. Total continuity is also destroyed by this process so that, at the end of each iteration, errors exist both in the total and individual phase continuity equations. In a converged solution these continuity errors disappear but in the intermediate stages of the calculation the existence of these errors may cause significant problems due to the complicated coupling between the phase fraction, pressure and phase velocity equations. The overall stability of the solution proved to be sensitive to the maintenance of the phase continuity constraints.

The algorithm of Oliveira improves upon Politis' algorithm in the treatment of the drag term for gas-liquid systems. Of the four variants studied by Oliveira, the partial elimination method was demonstrably superior due to the more implicit treatment of the drag terms. The first of Oliveira variants may be discarded due to its failure in general three dimensional flows, while Politis discards the second due to its poor convergence rate in high drag systems, which reduces its generality.

It should be noted that the one dimensional test case performed by Oliveira was not a full test of the algorithms' performance since the drag model he adopted was only really appropriate for solid particles or viscous droplets. As noted in Section 2.2.1, a drag law appropriate to bubbles may be significantly different to that of solid particles and involve a higher degree of non-linearity. It was found that the partial elimination method itself was not sufficient to guarantee convergence of the solution when a highly non-linear drag model is used.

#### 4.5.2 An Improved Two-phase Solution Algorithm

The algorithms of Politis and Oliveira are not entirely suitable for general engineering applications due to the problems discussed in the previous section. They do, however, represent a good starting point for the development of such an algorithm. The two main issues to be resolved can be summarised as follows.

- The coupling between the phase momentum equations due to the (possibly highly non-linear) drag force and its effect on the stability and efficiency of the solution

algorithm.

- The manner in which the continuity constraints are imposed on the system.

This section describes in detail a number of improvements to Oliveira's algorithm designed to deal with the above issues. The coupling between the phase momentum equations is improved by using a 'point iteration' method to improve the handling of the drag term. The partial elimination method is retained in the implicit solution phase. Section 4.5.2.1 contains a detailed discussion on the origin of the instabilities caused by the non-linearity of the drag force and the basis of the point iteration method.

The imposition of continuity constraints requires careful consideration of the order in which the equations are solved within the overall iterative scheme. The present algorithm provides some improvement in this area by arranging the order in which the equations are solved so as to properly maintain the continuity constraints. An extensive discussion of these matters is given in Section 4.5.2.2.

In Section 4.5.2.3 the superiority of the new algorithm is illustrated by applying it to a one dimensional test case comprising air-water bubbly flow in a vertical duct. For this case the drag model appropriate to air-water systems (as described in Section 2.2.1) is used, demonstrating the effects of a highly non-linear drag force. A wide variety of bubble sizes are calculated in order to illustrate the wide range of applicability and stability of the algorithm. Finally, in Section 4.5.3, the final form of the algorithm is summarised.

#### 4.5.2.1 Drag Related Instabilities

The drag term appearing in the phase momentum equations has to be linearised with respect to the phase velocities during the discretisation phase. The drag force expression in the phase momentum equation reads

$$\mathbf{F}_d = \frac{3}{4} \frac{\alpha_d \rho_c C_d(|\mathbf{u}_r|)}{d} |\mathbf{u}_r| \mathbf{u}_r \quad (4.75)$$

which is linearised by calculating the velocity magnitude using known velocities from the previous iteration,  $\mathbf{u}_c^o$  and  $\mathbf{u}_d^o$  Eq4.Instab.eq1 becomes

$$\mathbf{F}_d = \frac{3}{4} \frac{\alpha_d \rho_c C_d(|\mathbf{u}_r^o|)}{d} |\mathbf{u}_r^o| \mathbf{u}_r \quad (4.76)$$

$$= F(\mathbf{u}_d - \mathbf{u}_c) \quad (4.77)$$

where  $\mathbf{u}_r^o = \mathbf{u}_d^o - \mathbf{u}_c^o$ .

The various ways of treating the drag term in the discretised momentum equations, as studied by Politis and Oliveira, are concerned with the way that the phase velocities  $\mathbf{u}_d$  and  $\mathbf{u}_c$  in Eqn (4.77) are handled. In all the variations studied,  $F$  is calculated using the previously calculated velocities and is treated as a constant coefficient. The partial elimination method is effective in handling the coupling between these phase velocities by using ‘updated’ velocities instead of those from the previous iteration but still relies on lagged velocity information through  $F$  and  $C_d$ .

For highly non-linear drag situations, the dependence of  $F$  on  $|\mathbf{u}_r^o|$  can introduce substantial instabilities into the solution which have to be damped using under-relaxation. For example, for air bubbles of diameter about 1.4 mm and less in water, the drag coefficient varies with  $\mathbf{u}_r^{-1}$  (see Figure 2.2) rendering Eqn (4.76) linear with respect to  $\mathbf{u}_r$ . In this situation, the solution of the momentum equations using the partial elimination method poses no problems. For bubbles larger than about 1.4 mm, however,  $C_d$  varies with  $\mathbf{u}_r^{1.7}$  so that  $F$  varies with  $\mathbf{u}_r^{2.7}$ . This high degree of non-linearity is the cause of instability which requires heavy under-relaxation in order to obtain a solution.

A new method of calculating the drag coefficient  $F$  is now proposed which reduces the effects of a non-linear drag and obviates the need for heavy under-relaxation in these cases. The proposed method uses the discretised momentum equations to yield an expression for the relative velocity. This expression is then solved using a point-wise iterative cycle to yield an updated relative velocity which is used to update  $C_d$  and  $F$ . The use of the updated values for  $C_d$  and  $F$  reduces any instabilities caused by the drag non-linearities and results in faster convergence.

In order to derive an expression for the relative velocity, we start with the discretised phase momentum equations. It is not entirely clear at this stage which form of equations is appropriate. We are faced with two alternatives; the semi-implicit form or the partial elimination form. The ‘semi-implicit’ form of the phase momentum equations are written as

$$(\mathbb{A}_c + F)\mathbf{u}_c = \mathbb{H}(\mathbf{u}_c) + F\mathbf{u}_d^o \quad (4.78)$$

$$(\mathbb{A}_d + F)\mathbf{u}_d = \mathbb{H}(\mathbf{u}_d) + F\mathbf{u}_c^o \quad (4.79)$$

while the ‘partial elimination’ form are written as

$$\left\{ \mathbb{A}_c + \frac{F \mathbb{A}_d}{F + \mathbb{A}_d} \right\} \mathbf{u}_c = \mathbb{H}(\mathbf{u}_c) + \frac{F}{F + \mathbb{A}_d} \mathbb{H}(\mathbf{u}_d^o) \quad (4.80)$$

$$\left\{ \mathbb{A}_d + \frac{F \mathbb{A}_c}{F + \mathbb{A}_c} \right\} \mathbf{u}_d = \mathbb{H}(\mathbf{u}_d) + \frac{F}{F + \mathbb{A}_c} \mathbb{H}(\mathbf{u}_c^o) \quad (4.81)$$

where the  $\mathbb{H}()$  operator contains all the source terms which are not drag related.

An explicit expression for the phase velocities can be obtained by writing the above equations in operator split form. These explicit velocities are denoted as  $\mathbf{u}_c^\sharp$  and  $\mathbf{u}_d^\sharp$ . Equations (4.80) and (4.81) then read

$$\left\{ \mathbb{A}_c + \frac{F \mathbb{A}_d}{F + \mathbb{A}_d} \right\} \mathbf{u}_c^\sharp = \mathbb{H}(\mathbf{u}_c^o) + \frac{F}{F + \mathbb{A}_d} \mathbb{H}(\mathbf{u}_d^o) \quad (4.82)$$

$$\left\{ \mathbb{A}_d + \frac{F \mathbb{A}_c}{F + \mathbb{A}_c} \right\} \mathbf{u}_d^\sharp = \mathbb{H}(\mathbf{u}_d^o) + \frac{F}{F + \mathbb{A}_c} \mathbb{H}(\mathbf{u}_c^o) \quad (4.83)$$

Here, the splitting is similar to that employed in the single-phase PISO algorithm of Issa [106]. Equations (4.82) and (4.83) are now combined algebraically to yield an explicit equation for the relative velocity  $\mathbf{u}_r^\sharp = \mathbf{u}_c^\sharp - \mathbf{u}_d^\sharp$  for each cell node.

$$\begin{aligned} \mathbf{u}_r^\sharp = & \frac{\mathbb{H}(\mathbf{u}_c^o)}{\mathbb{A}_c + \frac{F \mathbb{A}_d}{F + \mathbb{A}_d}} + \frac{F \mathbb{H}(\mathbf{u}_d^o)}{(\mathbb{A}_c + F) \left\{ \mathbb{A}_c + \frac{F \mathbb{A}_d}{F + \mathbb{A}_d} \right\}} - \\ & \frac{\mathbb{H}(\mathbf{u}_d^o)}{\mathbb{A}_d + \frac{F \mathbb{A}_c}{F + \mathbb{A}_c}} - \frac{F \mathbb{H}(\mathbf{u}_c^o)}{(\mathbb{A}_d + F) \left\{ \mathbb{A}_d + \frac{F \mathbb{A}_c}{F + \mathbb{A}_c} \right\}} \end{aligned} \quad (4.84)$$

The same process for the semi-implicit form of the momentum equations yields

$$\begin{aligned} \mathbf{u}_r^\sharp = & \frac{\mathbb{H}(\mathbf{u}_c^o)}{\mathbb{A}_c + F} + \frac{F}{(\mathbb{A}_c + F)} \mathbf{u}_d^o - \\ & \frac{\mathbb{H}(\mathbf{u}_d^o)}{\mathbb{A}_d + F} - \frac{F}{(\mathbb{A}_d + F)} \mathbf{u}_c^o \end{aligned} \quad (4.85)$$

The relative merits of using Eqn (4.84) or Eqn (4.85) are discussed in Section 4.5.2.3 when the present algorithm is applied to a simple test problem.

Since Equations (4.84) and (4.85) are functions of  $F$ , which in turn depends on the relative velocity, they have to be solved for  $\mathbf{u}_r^\sharp$ . One way of solving equations such as Eqn (4.85) is through successive substitution, although other techniques such as Newton-Raphson

could be employed if the necessary derivatives can be efficiently calculated. The solution of Equations (4.84) or (4.85) proceeds by calculating  $C_d$  and  $F$  using  $\mathbf{u}_d^o$  and  $\mathbf{u}_c^o$ .  $\mathbf{u}_r^\sharp$  is then recalculated.  $C_d$  and  $F$  are then recalculated using  $\mathbf{u}_r^\sharp$  and the process is repeated as required. Some under-relaxation may be necessary to procure convergence when the drag is highly non-linear [116].

$\mathbf{u}_r^\sharp$  is calculated on a point by point basis for each node and is used to obtain updated values for  $C_d$  and  $F$ . The implicit solution of the partial elimination momentum equations (Equations (4.80) and (4.80)) is then carried out using these updated values. The updating of  $F$  in this way results in a net decrease in the total computer time required since the under-relaxation factors for the phase momentum equation may be increased without incurring instabilities in the solution. As the overall solution progresses, the initial ‘guess’ for the relative velocity improves reducing the number of sub-iterations required. At convergence  $\mathbf{u}_c^o \rightarrow \mathbf{u}_c^*$  and the calculation of  $F$  need not be carried out at all.

The performance and stability benefits of using this technique compared with the algorithm of Oliveira are examined in detail in Section 4.5.2.3 where it is applied to a one-dimensional test case of air-water flow in a vertical expanding tube.

#### 4.5.2.2 Continuity constraints

The algorithms of Politis and Oliveira both have deficiencies in imposing continuity constraints since both total continuity and individual phase continuity may not be satisfied at the end of each iteration. By closely examining the relevant equations it can be seen that the basic approach adopted by these algorithms is flawed.

The solution of the pressure equation ensures that total continuity

$$\nabla \cdot \alpha_c^o \mathbf{u}_c^n + \alpha_d^o \mathbf{u}_d^n = 0 \quad (4.86)$$

is satisfied. The subsequent solution to the dispersed phase continuity equation

$$\nabla \cdot \alpha_d^n \mathbf{u}_d^n = 0 \quad (4.87)$$

is meant to ensure that dispersed phase continuity is also satisfied. The idea is that, since total and dispersed phase continuity is satisfied, continuous phase continuity is satisfied also. This is not the case. Firstly, since Eqn (4.86) is based on  $\alpha_c^o$  and  $\alpha_d^o$ , and given Eqn (4.87), it does not automatically follow that

$$\nabla \cdot \alpha_c^n \mathbf{u}_c^n = 0 \quad (4.88)$$

except at convergence when  $\alpha_d^n = \alpha_d^o$  and  $\alpha_c^n = \alpha_c^o$ . Secondly, the techniques employed to ensure that Eqn (4.87) yields bounded values for  $\alpha_d^n$  mean that Eqn (4.86) it is not exactly satisfied anyway, again except at convergence. The resulting errors in individual phase and total continuity have been found to produce instabilities which may prevent a converged solution from being obtained.

The essence of the problem is that the solution of the phase fraction works against the solution of the pressure by corrupting total continuity. Regardless of the nature of the pressure equation solution, the determination of the dispersed phase fraction, and the subsequent updating of the cell face fluxes, introduces continuity errors into the system.

The task then is to find a way to calculate the phase fraction in such a way that continuity is not compromised. It is proposed here that total continuity be maintained by solving for the phase fraction at the beginning of the iterative sequence rather than after the pressure equation solution. Importantly, the phase fluxes are not updated with the new phase fraction values immediately (since this would compromise continuity) but are instead only recalculated after the pressure solution, thus ensuring that total continuity is satisfied at the end of each iteration. The dispersed phase continuity equation is therefore written as

$$\nabla \cdot \alpha_d^n \mathbf{u}_d^o = 0 \quad (4.89)$$

The repositioning of the phase fraction calculation means that the phase momentum equations are constructed with the new phase fraction values as is the total phase continuity equation which used to calculate the pressure.

$$\nabla \cdot \alpha_c^n \mathbf{u}_c^n + \nabla \cdot \alpha_d^n \mathbf{u}_d^n = 0 \quad (4.90)$$

Thus, the new values of the phase fraction are naturally incorporated into the face fluxes without having to explicitly recalculate them after the phase fraction equation solution. This simple alteration makes a large improvement in the stability of the algorithm as illustrated in Section 4.5.2.3.

This change does not address the problem of individual phase continuity which will, in general, not be satisfied until convergence when the effects of under-relaxation will have disappeared. Given the requirement that the solution to Eqn (4.87) obeys the constraint

$0 \leq \alpha_d^n \leq 1$ , there is no way to guarantee that the dispersed phase continuity is maintained throughout the solution. This, in turn, implies that the continuous phase continuity is not maintained.

#### 4.5.2.3 One dimensional test case

In order to determine the relative merits of the two different algorithmic variants identified in Section 4.5.1, and to gauge the performance of these against the basic Oliveira algorithm (variant 3), a series of simple one dimensional test calculations was performed. The case involved the air-water bubbly upward flow in a vertical expanding channel as shown schematically in Figure 4.2. It was designed to provide a challenging and realistic test of the various algorithms, which are gauged according to the number of iterations to convergence and their stability.

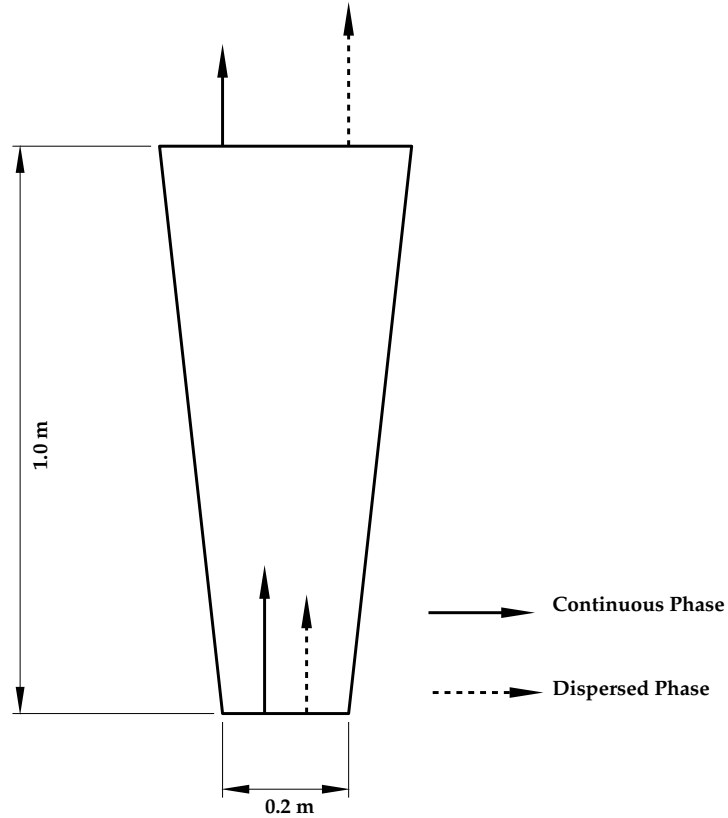


Figure 4.2: Schematic of the one-dimensional test case.

The drag model used was that appropriate to a clean air-water system as described in Section 2.2.1. The bubble size was uniformly set to  $2\text{mm}$  which implies that the drag will be firmly in the non-linear region at the terminal velocity. The channel expansion yields a decelerating flow so that virtual mass forces will be present thus providing an additional complication.

The inlet and initial velocities of the dispersed and continuous phases were arbitrarily set to 0.9 and 1.2 m/s respectively. Note that these initial velocities are somewhat ‘unreasonable’ in that the final solution should yield a dispersed phase velocity greater than that of the continuous phase since the flow is vertically upward; it is a requirement of the algorithm that it should be able to cope with a diverse range of initial conditions. The inlet dispersed phase fraction was set to 10% with an initial field value of 1%. The inlet turbulence quantities  $k$  and  $\epsilon$  were set to values corresponding to a turbulence intensity of approximately 7% of the continuous phase inlet velocity with a turbulent length scale of the width of the base of the duct.

The calculations were performed on a small mesh of 20 cells uniformly spaced axially. Symmetry plane boundary conditions were imposed on the sides of the duct with a constant pressure condition at the outlet.

Various calculations were performed with each algorithm with varying under-relaxation factors for the momentum and phase fraction equations. For each calculation, the number of iterations to convergence, if convergence could be obtained at all, was noted.

Initially, a series of calculations was performed to ascertain the impact of varying the momentum equation under-relaxation factors. For these calculations, the phase fraction under-relaxation factor was set to 0.3, while the under-relaxation factors for the pressure and  $k - \epsilon$  equations were 0.2 and 0.7 respectively. The under-relaxation factor used in the iterative calculation of the relative velocity was set to 0.2 for the ‘semi-implicit’ and ‘partial elimination’ algorithms. Table 4.5.2.3 shows the number of iterations to convergence for the three algorithms.

As can be seen from the table, the new algorithm outperforms the previous one in two respects. Firstly, it is evident that with the new algorithms, convergence can be obtained without difficulty for a wide range of momentum under-relaxation factor values. Oliveira’s algorithm only converges for low values of the momentum under-relaxation factor. Secondly, when all three algorithms do yield a converged solution, the new ones do so with an approximately a two-fold reduction in the number of iterations required.

Table 4.5.2.3 also shows that the number of iterations to convergence for the new algorithms is a weak function of the momentum under-relaxation factor for this case. The reason for this behaviour can be seen when one examines the magnitude of the residuals



Momentum under-relaxation factor	Algorithm		
	Oliveira	Semi-implicit $U_r$ calculation	Partial elimination $U_r$ calculation
0.3	173	83	83
0.5	$\infty$	82	81
0.7	$\infty$	81	81

Table 4.4: Comparison between Oliveira's and the new algorithm.

for the various equations as a function of iteration number. Figure 4.3 shows the residuals for the momentum, pressure and phase fraction equations for both the Oliveira algorithm and the semi-implicit form of the new algorithm for the first of the cases shown above.

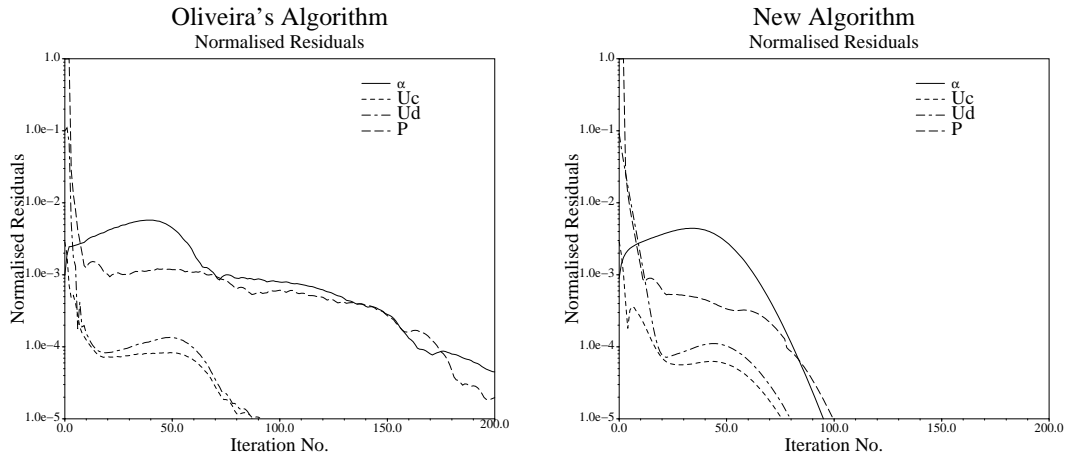


Figure 4.3: Residual history comparison between Oliveira's and the new algorithm.

It can be seen that the phase fraction and pressure equations are the last to converge for both cases. The phase fraction under-relaxation factor was set to a fairly low value for these cases and a reduction in the number of iterations required can be obtained by increasing its value, although the same relative performance of the two algorithms will be maintained.

It is important to note that the residuals of the new algorithm tend to reduce more smoothly than those from Oliveira's method. This feature is primarily due to the improved treatment of the phase fraction equation in relation to phase continuity. The phase fraction and pressure equations are now more appropriately coupled so that the solution of the phase fraction equation does not violate the total continuity constraint which forms the

basis of the pressure equation. This clearly results in a smoother and more stable solution. Comparison of the phase momentum residuals between the two algorithms shows that the new algorithm gives only a small improvement in the convergence rate for this case. It should be noted that, in this case, the use of a low momentum under-relaxation factor, which is required by Oliveira's algorithm, reduces the benefit gained from the sub-iterative updating of the drag coefficient. The momentum under-relaxation factor may be increased substantially with the present method yielding a corresponding increase in the momentum equation convergence rate without incurring instabilities, as indicated by Table 4.5.2.3.

Table 4.5.2.3 also shows that the performance of the semi-implicit and partial elimination versions of the relative velocity calculation are virtually indistinguishable in terms of the number of iterations to convergence. The partial elimination form only gives a small improvement in one case. However, when the actual computer calculation time is taken into account it is found that the semi-implicit version requires approximately 30% less calculation time than the partial elimination version. This is due to the more complicated form of the momentum equations used to calculate the relative velocity. This added complication reduces the efficiency of the algorithm.

It should be noted that both forms of the new algorithm perform approximately the same number of sub-iterations through the relative velocity calculation at each stage in the solution. Table 4.5.2.3 shows the number of sub-iterations required as a function of the (outer) iteration number.

Outer Iteration No.	No. of sub-iterations in $U_r$ calculation	
	Semi-implicit form	Partial elimination form
1	11	10
5	8	8
10	6	6
20	4	5
40	4	5
80	3	4

Table 4.5: No. of sub-iterations required in the calculation of  $U_r$ .

Since the partial elimination form of the relative velocity calculation imposes a significant computational cost with no additional benefit over the semi-implicit treatment, it is discarded in favour of the simpler and easier to implement semi-implicit form.

In conclusion, the new algorithm represents a significant improvement over the algorithm of

Oliveira. The improvements in the phase continuity and the drag term treatment together combine to give a stable and efficient solution algorithm which is applicable to gas-liquid systems with highly non-linear drag. The improved phase continuity treatment allows the pressure and phase fraction equations to converge easily whilst the sub-iterative relative velocity calculation effectively removes a major source of instability in the two phase momentum equations allowing higher under-relaxation factors to be used.

### 4.5.3 Overview of the final algorithm

The final algorithm is summarised below. At the start of each iteration we have the previously calculated values for the phase fraction, phase velocities, pressure and cell face fluxes. These are denoted  $\alpha_c^o, \alpha_d^o, \mathbf{u}_c^o, \mathbf{u}_d^o, p^o, \mathbb{F}_c^o$  and  $\mathbb{F}_d^o$  respectively.

#### 4.5.3.1 Step 1 : Phase Fraction Prediction

The dispersed phase fraction is first calculated using the dispersed phase continuity equation based on the previous values of the dispersed phase velocity. The techniques discussed in Section 4.5.1.1 are applied to ensure that  $0 \leq \alpha_d^n \leq 1$ .

$$\nabla \cdot \alpha_d^n \mathbf{u}_d^o = 0 \quad (4.91)$$

The continuous phase fraction is calculated via  $\alpha_c^n = 1 - \alpha_d^n$ .

#### 4.5.3.2 Step 2 : Calculation Of The Updated Drag Coefficients

An equation for the relative velocity is formed from the discretised momentum equation written in semi-implicit form (Equations (4.78) and (4.79)). This equation reads

$$\begin{aligned} \mathbf{u}_r^n = & \frac{\mathbb{H}(\mathbf{u}_c^o)}{\mathbb{A}_c + F} + \frac{F}{(\mathbb{A}_c + F)} \mathbf{u}_d^o - \\ & \frac{\mathbb{H}(\mathbf{u}_d^o)}{\mathbb{A}_d + F} - \frac{F}{(\mathbb{A}_d + F)} \mathbf{u}_c^o \end{aligned} \quad (4.92)$$

where  $\mathbb{H}()$  contains all the sources which are not drag related. The central coefficients  $\mathbb{A}_c$  and  $\mathbb{A}_d$  and the neighbour coefficients are calculated and stored for each phase. Eqn (4.92) is solved on a point-by-point basis to yield updated values for the relative velocity which is used to update the drag coefficients  $C_d$  and  $F$ .

#### 4.5.3.3 Step 3 : Phase Velocity Prediction

The phase momentum equations in partial elimination form based on the old pressure field  $p^o$  are written

$$\left\{ \mathbb{A}_c + \frac{F \mathbb{A}_d}{F + \mathbb{A}_d} \right\} \mathbf{u}_c^* = \mathbb{H}(\mathbf{u}_c^*) - \alpha_c^n \Delta p^o + \frac{F}{F + \mathbb{A}_d} \{ \mathbb{H}(\mathbf{u}_d^o) - \alpha_d^n \Delta p^o \} \quad (4.93)$$

$$\left\{ \mathbb{A}_d + \frac{F \mathbb{A}_c}{F + \mathbb{A}_c} \right\} \mathbf{u}_d^* = \mathbb{H}(\mathbf{u}_d^*) - \alpha_d^n \Delta p^o + \frac{F}{F + \mathbb{A}_c} \{ \mathbb{H}(\mathbf{u}_c^o) - \alpha_c^n \Delta p^o \} \quad (4.94)$$

where the  $\mathbb{H}()$  operators contain all the sources which are not drag or pressure related. Equations (4.93) and (4.93) are solved to yield the predictor velocities  $\mathbf{u}_c^*$  and  $\mathbf{u}_d^*$ .

#### 4.5.3.4 Step 3 : Pressure Prediction

Updated phase velocities  $\mathbf{u}_c^n$  and  $\mathbf{u}_d^n$  and an updated pressure  $p^*$  are now sought such that the overall continuity equation

$$\nabla \cdot (\alpha_c^n \mathbf{u}_c^n + \alpha_d^n \mathbf{u}_d^n) = 0 \quad (4.95)$$

is satisfied.

Equations for  $\mathbf{u}_c^n$  and  $\mathbf{u}_d^n$  are derived by writing Equations (4.93) and (4.94) as

$$\left\{ \mathbb{A}_c + \frac{F \mathbb{A}_d}{F + \mathbb{A}_d} \right\} \mathbf{u}_c^n = \mathbb{H}(\mathbf{u}_c^*) - \alpha_c^n \Delta p^* + \frac{F}{F + \mathbb{A}_d} \{ \mathbb{H}(\mathbf{u}_d^o) - \alpha_d^n \Delta p^o \} \quad (4.96)$$

$$\left\{ \mathbb{A}_d + \frac{F \mathbb{A}_c}{F + \mathbb{A}_c} \right\} \mathbf{u}_d^n = \mathbb{H}(\mathbf{u}_d^*) - \alpha_d^n \Delta p^* + \frac{F}{F + \mathbb{A}_c} \{ \mathbb{H}(\mathbf{u}_c^o) - \alpha_c^n \Delta p^o \} \quad (4.97)$$

Substitution of Equations (4.96) and (4.97) into Eqn (4.95) yields the pressure equation

$$\begin{aligned} \nabla \cdot \left\{ \frac{(\alpha_c^n + \alpha_d^n \mathbb{B}_d) \alpha_c^n}{(\mathbb{A}_c + \mathbb{B}_d \mathbb{A}_d)} + \frac{(\alpha_d^n + \alpha_c^n \mathbb{B}_c) \alpha_d^n}{(\mathbb{A}_d + \mathbb{B}_c \mathbb{A}_c)} \right\} \nabla p^* = \\ \nabla \cdot \left\{ \frac{\alpha_c^n \mathbb{H}(\mathbf{u}_c^*)}{\mathbb{A}_c + \mathbb{B}_d \mathbb{A}_d} + \frac{\alpha_c^n \mathbb{B}_d \mathbb{H}(\mathbf{u}_d^o)}{\mathbb{A}_c + \mathbb{B}_d \mathbb{A}_d} \right\} + \\ \nabla \cdot \left\{ \frac{\alpha_d^n \mathbb{H}(\mathbf{u}_d^*)}{\mathbb{A}_d + \mathbb{B}_c \mathbb{A}_c} + \frac{\alpha_d^n \mathbb{B}_c \mathbb{H}(\mathbf{u}_c^o)}{\mathbb{A}_d + \mathbb{B}_c \mathbb{A}_c} \right\} \end{aligned} \quad (4.98)$$

where

$$\mathbb{B}_c = \frac{F}{F + \mathbb{A}_c}$$

$$\mathbb{B}_d = \frac{F}{F + \mathbb{A}_d}$$

The solution of Eqn (4.98) yields  $p^*$  which is used to calculate  $\mathbf{u}_c^n$  and  $\mathbf{u}_d^n$  using Equations (4.96) and (4.97). The cell face fluxes are updated using  $\mathbf{u}_c^n$  and  $\mathbf{u}_d^n$ .

The new pressure field  $p^n$  is obtained via

$$p^n = p^o + \lambda(p^* - p^o) \quad (4.99)$$

where  $\lambda \approx 0.2$ .

#### 4.5.3.5 Step 4 : Auxiliary Scalar Equation Solution

If the flow being considered is turbulent, the discretised equations for  $k$  and  $\epsilon$ —Equations (2.100) and (2.102)—are solved and the updated turbulent viscosity field  $\mu_t^n$  is calculated using Eqn (2.42). The response coefficient  $C_t$  is updated.

If droplet or bubble break-up or coalescence effects are being considered, then the relevant equations are solved at this point. If surfactant are present, the discretised transport equations for the bulk and interfacial concentration—Equations (3.102) and (3.104) or (3.105)—are solved to yield  $C^n$  and  $\Gamma^n$ . The discretised  $S_\gamma$  equations—Eqn (3.17)—are then solved to give  $S_\gamma^n$ . The droplet/bubble diameter field is updated using Eqn (3.7). If two  $S_\gamma$  equations are being solved, the updated distribution variance field is then calculated using Eqn (3.10).

The above sequence is repeated until the sum of the normalised residuals for each equation falls below a pre-specified limit as described in Section 4. Convergence.

## 4.6 Closure

The partial differential equations comprising the present two-phase flow model cannot be solved analytically due to their coupled and highly non-linear nature and so we need to

turn to numerical solution methods to provide a solution. Applicable methods are usually based on the finite volume discretisation technique coupled with an implicit, pressure-correction solution algorithm.

The discretisation of the solution domain and the governing differential equations is fairly straightforward and has been described in detail. This process yields a set of non-linear algebraic equations for each equation to be solved. The task of the solution algorithm is to orchestrate the solution of these equations so as to maintain the appropriate coupling between all of the equations and to impose any boundedness and continuity constraints on the system as a whole.

The two-phase nature of the problem introduces particular demands on the solution algorithm. In particular, the coupling between the phase momentum equations due to the, often highly non-linear, drag forces and the imposition of phase continuity constraints within the iterative cycle are issues which need careful consideration.

Two previous studies have gone some way to resolving these issues but have fallen short of providing a general purpose solution algorithm applicable to gas-liquid as well as liquid-liquid and solid-liquid flows. Modifications to these algorithms have been proposed which result in a much improved algorithm capable of handling the highly non-linear coupling between the phase momentum equations and which is better at imposing the global continuity constraint used as the basis of the pressure solution.

The new algorithm relies on the sub-iterative solution to the phase relative velocity equation which then yields improved values for the drag coefficients in the phase momentum equations. The updating of the drag coefficients in this way reduces the instabilities due to the drag related coupling between the phase momentum equations.

The superiority of the new algorithm over previous algorithms was demonstrated using a simple one-dimensional test case based on the air-water bubbly flow in a vertical channel using an appropriate but highly non-linear drag model. The generality of the algorithm is demonstrated further in the following chapters which describe extensive validation studies for a wide range of flow conditions and geometries.

## Chapter 5

# Two-Phase Flow In A Plane Ducted Shear Layer

The performance of the two-phase flow model developed in Chapters 1 to 3 is evaluated in this chapter by comparing its predictions against experimental data for air-water bubbly flow in a vertical ducted shear layer. This data includes local phase fraction and mean and RMS phase velocity measurements for both phases. Good agreement between the predictions and experimental data is obtained, especially for the dispersed phase fraction distribution within the shear layer. It is shown that in this region the dispersed phase motion is dominated by lateral lift forces which are well captured by the model.

### 5.1 Introduction

The plane shear layer (PSL) is one of the most widely studied single-phase flow configurations in fluid dynamics. This is partly due to the simplicity of the geometry and the ability to precisely control the flow parameters, but also because of its ubiquitous nature; the characteristics of the PSL are found in the developing region of both the plane and round jets, in the separated boundary layer in the wake of an object, and in many other complex flows. The two-phase PSL represents one of the most basic two-phase flows encountered and serves as a good validation test of general two-phase predictive methods. However, the apparent simplicity of the PSL is deceptive. In particular, the PSL clearly exhibits the existence of the large scale ‘coherent’ vortical structures which characterise free turbulent shear flows. Early studies into single-phase PSL flows, using mainly visual rather than quantitative techniques, have shown the importance of these structures on the

development of the shear layer [117, 118].

Studies into dispersed two-phase flows in the presence of these coherent structures have revealed their large effect on the transport of bubbles or particles [119, 120, 121]. The entrainment of bubbles during the interaction of the structures with each other, and subsequent bubble/vortex interaction means that there is a tendency for the bubbles to travel in distinct clusters within the centre of the vortex. Very high local phase fraction values in this region may be experienced, which may consequently have a significant influence on the turbulence structure, phase distribution and coalescence rate of bubbles. The complicated and inter-related effects of inter-phase momentum transfer and continuous phase turbulence combine to make the two-phase PSL a challenging case.

Validation of the present two-phase model against suitable experimental data for this problem would be highly desirable. A recent experimental study has been performed by Roig [56] at L'Institut National Polytechnique De Toulouse (INPT). Roig studied the bubbly two-phase flow in a plane shear layer formed via the mixing of two upward co-flowing streams of water within a square duct. Both single and two-phase experiments were performed for a variety of velocity ratios and phase distributions.

Importantly, for the two-phase cases, Roig measured the individual phase mean velocities, the RMS velocities of both phases, the mean bubble size and the local phase fraction. The wealth of two-phase experimental data makes this case ideal for validation purposes and allows certain important aspects of the two-phase model to be closely examined. In particular, information regarding the  $C_t$  parameter, which is central to the adopted two-phase turbulence modelling approach, may be derived from Roig's continuous and dispersed phase RMS velocity measurements.

Similarly, the models adopted for the inter-phase momentum transfer effects, such as drag, virtual mass and lift forces, may be assessed using Roig's data. In particular, it is desirable to determine the accuracy of the default lift and virtual mass coefficients and the model for the drag coefficient by comparing the numerical prediction against the phase fraction and slip velocity measurements respectively. The single-phase experimental data will also prove useful in order to give an indication of the underlying performance of the  $k-\epsilon$  turbulence model.

The following section summarises previous single and two-phase experimental studies into plane shear layers while Section 5.2 describes in detail the experiments performed by Roig. Section 5.3 describes the numerical simulation of Roig's experiments using the current two-phase model in detail. Particular attention is given to the determination of the inlet conditions for the simulation since incomplete experimental data in the inlet region meant that certain assumptions had to be made. Sections 5.4 and 5.5 respectively compare the



single and two-phase experimental data to the numerical predictions. The performance of the turbulence model proposed in Chapter 2 and the solution algorithm proposed in Chapter 4 are assessed in relation to this case in Sections 5.6 and 5.7. Finally, some conclusions as to the overall performance of the two-fluid model for this case are drawn in Section 5.8.

### 5.1.1 Previous Experimental Studies Into Plane Free Shear Layers

The plane free shear layer has been extensively studied in the past, mainly for single-phase flow. Most experimental studies have concentrated on the effect of the velocity ratio, density ratio and Mach number on the development of the shear layer formed between a half jet and a quiescent fluid or between two co-flowing streams. The shear layer's development is usually described in terms of its spreading rate and the distribution of normal and shear stresses within the layer (see Murthy [122] for a review of early investigations). Some workers have additionally performed flow visualisation studies which have indicated the existence of large scale coherent structures within the shear layer [117].

The next two sub-sections summarise the main findings of studies into single and two-phase free shear layer flows.

#### 5.1.1.1 Single-Phase Studies

Many workers have investigated the turbulence structure of the plane shear layer. Perhaps the first extensive work was that of Liepmann and Laufer [123] (see also the review by Murthy [122]) who studied the shear layer formed by a half jet of air into still surroundings. Their main findings indicate that the axial fluctuating velocity ( $u'$ ) is significantly higher than the lateral fluctuating velocity ( $v'$ ) within the shear layer, with the peak in  $v'$  off-centre. This finding was confirmed by Wygnanski and Fiedler [124] who found that the peak in  $v'$  was offset towards the high speed side of the shear layer. Fiedler [125] reported that the axial RMS velocity was of the order of twice the transverse and lateral RMS velocities.

Although the above investigations provide detailed information on the average properties of the shear layer, the existence of the large scale elements implied by the measurements was not fully appreciated until flow visualisation studies were carried out. Brown and Roshko [117] photographed the large scale coherent structures formed during the mixing of two gases with different densities and velocity ratios using a shadowgraph technique. The resulting photographs indicate the existence of large scale two-dimensional vortical structures within the shear layer formed by the initial laminar instability between the two

streams.

Similarly, Winant and Browand [118] used dye injected into the shear layer formed between two co-flowing streams to observe the interaction of the coherent structures with the surrounding flow and with each other. With the camera following the motion of individual vortices, they found that they would intermittently combine with their neighbours to form larger vortices, thus causing the shear layer to spread. The entrainment of the surrounding fluid, and the fluid from between the vortical structures, takes place as the vortices combine in a process known as ‘pairing’. In this process the two-dimensional vortices roll around each other before amalgamating into one large vortical structure.

Thus, the development and growth of the shear layer can be summarised as follows :

- The initial laminar instability at the origin of the shear layer causes small waves, of some wavelength and amplitude, to be formed.
- These waves grow in amplitude and initiate the periodic formation of the two-dimensional vortical structures with nearly uniform spacing.
- Due to small difference in the strength and spacing of the vortices they intermittently combine, in a random manner, via the pairing process.

If the free stream turbulence, or end effects from walls or boundaries, produce secondary spanwise instabilities, then the essentially two-dimensional vortices may become significantly non-parallel thus initiating a local pairing process. This situation leads to a double helix pairing process which traverses the flow in a spanwise direction and is followed by a rapid increase in small scale turbulence [126].

Early questions about the existence of the coherent structures in flows with high Reynolds number seem to have been resolved. Free stream turbulence, or other forms of perturbation, may limit the spanwise extent of the vortex structures due to induced instabilities. The structures breakdown locally, thus rendering the flow fully three-dimensional, but the coherent structures still exist [126, 70, 127].

#### 5.1.1.2 Two-Phase Studies

Studies into two-phase free shear layers have not been extensive due to the difficulty in obtaining accurate measurements. Most studies have been numerical, using direct numerical simulation (DNS) or discrete vortex methods (DVM) to create the flow field within a free shear layer and then performing Lagrangian tracking of individual bubbles or particles.

Chein and Chung [120] analysed the motion of particles within the large scale structures in a plane shear layer. In particular, they studied the effect of vortex pairing on the dispersion of the particles. Using a DVM to calculate the flow field, and performing Lagrangian tracking of particles with varying Stokes number, they found that particles with low Stokes number (i.e. particles with a low aerodynamic response time, such as bubbles) were mainly entrained into the vortex structures during pairing. Subsequent dispersion of the particles depended on the ability of particles to escape the vortex structure.

Hulin, Fierfort and Coudol [119] performed an experimental study into the motion of bubbles in the wake of a bluff body. They found that the bubbles travelled in discrete clusters in the centre of the large scale vortices shed from a bluff body. The generation of these coherent structures was not significantly affected by the presence of the bubbles for phase fractions less than 10%. They found that the peak phase fraction within the vortex may be as high as 7 times the upstream phase fraction. For phase fractions greater than 10%, the generation of vortices becomes much more irregular due to the interference of the bubbles and the emission process.

## 5.2 INPT Two-phase Shear Layer Experiments

### 5.2.1 Experimental Set-up

The study by Roig [56] into the two-phase air-water flow in a ducted PSL was designed to provide detailed experimental data on the effects of turbulence on the bubbles distribution within the duct, and on the interactions between the bubbles and the developing shear layer. The simple geometry and wealth of experimental data provided make this case ideal for the validation of two-phase predictive techniques.

The experimental set-up of Roig [56] is shown schematically in Figure 5.1. The experiment employs the vertical upward flow of two separate inlet streams brought together to form a plane shear layer within a square test section. Provision is made for independent control of both continuous and dispersed phase flow rates in each stream, allowing a wide range of flow conditions.

The water phase is pumped from the settling tank into a settling chamber via a perforated plate consisting of 4 mm holes spaced 8 mm apart. This plate serves to eliminate large scale eddies and disturbances. Free stream turbulence intensity at the entrance to the test section varied from approximately 3 to 9%. The inlet streams are separated by a 2 mm thick splitter plate which is tapered at its trailing edge to reduce the influence of the wake. Air is introduced into the flow via three injection tubes positioned normal to the splitter

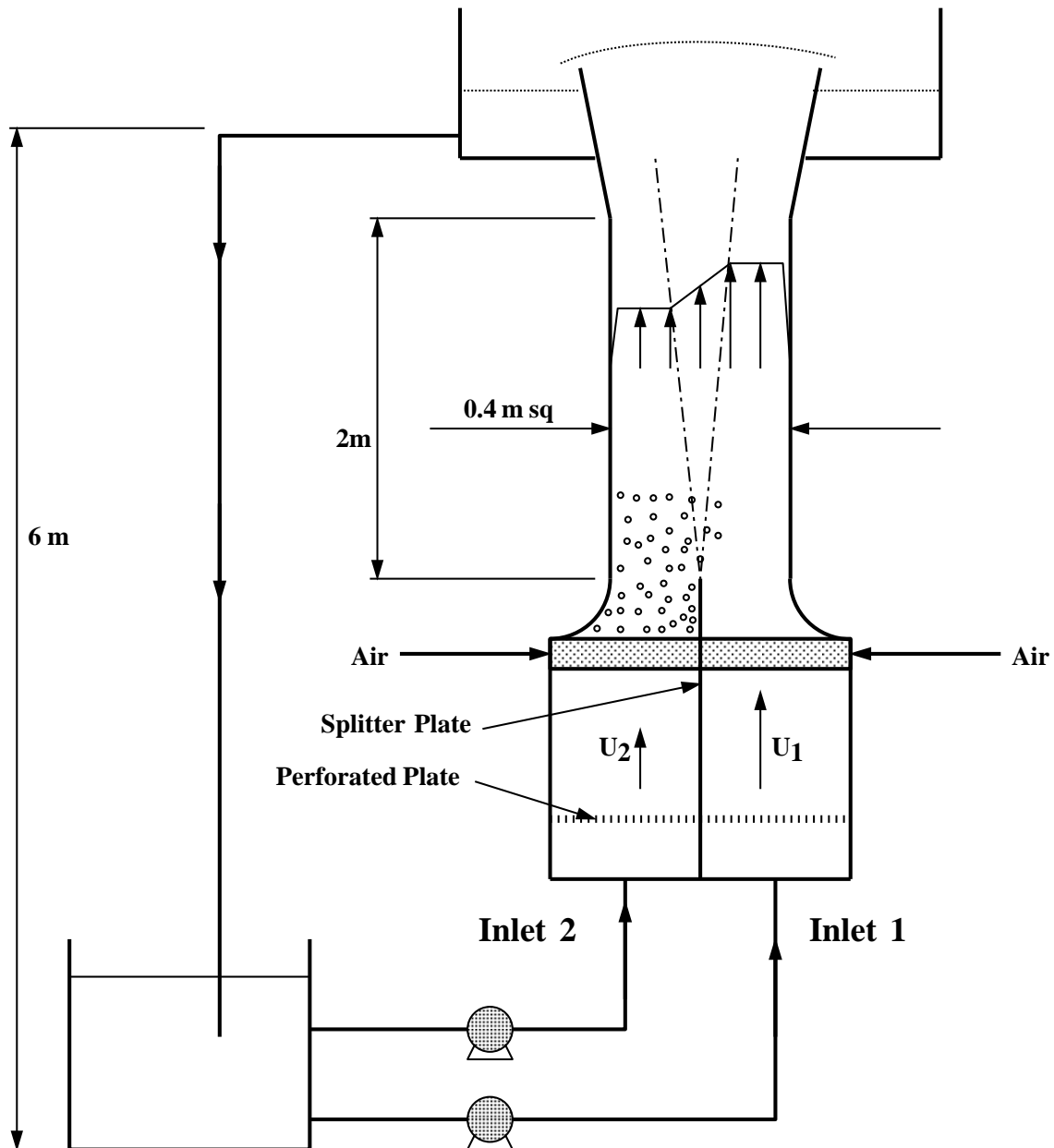


Figure 5.1: Schematic layout of the INPT shear layer experiment.

Experiment No.	$U_1$ [m/s]	$U_2$ [m/s]	Velocity Ratio [ $U_2/U_1$ ]	$\alpha_1$ [%]	$\alpha_2$ [%]	$x_{max}$ [m]	Dispersed Phase Velocity Measured
1.1	0.87	0.55	0.63	0	0	1.0	-
1.2	0.94	0.60	0.64	1.9	1.9	0.6	-
2.1	0.61	0.26	0.43	0	0	1.38	-
2.2	0.54	0.22	0.41	1.9	1.9	0.5	✓
2.3	0.51	0.18	0.35	1.9	0	1.0	✓
2.4	0.58	0.20	0.34	0	1.5	0.4	✓
3.1	0.59	0.59	1.0	0	0	0.6	-
3.2	0.60	0.58	0.97	1.8	1.8	0.6	-

Table 5.1: INPT shear layer experiment summary.

plate. The injection tubes produce bubbles of approximately 1.5 to 2.5 mm diameter. The flow is then subjected to a contraction which ensures that the velocity profile and phase distribution are as uniform as possible at the end of the splitter plate.

The axial mean and fluctuating velocity for both continuous and dispersed phases were measured using an LDV technique. The local phase fraction was measured using a fibre-optic probe.

A series of 8 experiments were carried out by Roig. These included both single and two-phase flows with different phase fraction and inlet velocity ratios, producing both shear layer and wake flows with bubbles distributed in one or both streams. Table 5.1 summarises the conditions for each experiment. The  $x_{max}$  column indicates the distance downstream from the inlet at which the last measurements were taken and the last column indicates whether the dispersed phase (air) mean and fluctuating velocities were measured.

Note that the first case in each series is a single-phase experiment. The subscripts on the average inlet velocity and phase fraction refer to the inlet stream; inlet streams 1 and 2 are indicated in Figure 5.1, region 1 always being the faster of the two streams in the shear layer cases.

### 5.2.2 Mass Balance Check

In order to gauge the consistency of the measurements provided by Roig, the author performed a simple mass balance check on the data. The mass flux of each phase at one

Experiment No.	$x_1$ [cm]	$x_2$ [cm]	Continuous Phase Mass Imbalance [%]	Dispersed Phase Mass Imbalance [%]
1.1	-1	100	0.9	-
1.2	-1	60	2.6	$\Gamma$
2.1	-1	138	2.4	-
2.2	6	50	13.2	19.1
2.3	6	70	9.3	12.7
2.4	6	40	-0.02	14.3
3.1	-1	60	-0.6	-
3.2	-1	60	6.1	$\Gamma$

Table 5.2: INPT shear layer experiment mass balance check.

upstream location,  $x_1$ , was compared with the mass flux at the furthest measured downstream axial location,  $x_2$ . The mass flux was calculated by interpolating the experimental data for the phase velocity and phase fraction onto the computational mesh employed for the CFD analysis and integrating numerically. Since the measurements do not extend to the outer wall region the values in this region were assumed to be the same as the nearest measured value.

The two axial locations were chosen to be as far apart as possible with the restriction that phase velocity and phase fraction measurements were available at both. The mass balance for Cases 1.2 and 3.2 could not be calculated since the dispersed phase velocity was not measured. Table 5.2 shows the calculated imbalance for the remaining cases.

The relatively high mass imbalance values for the two-phase cases may be indicative of the presence of three-dimensional effects due to, or exacerbated by, the presence of the bubbles. Alternatively, they may be due to the difficulty of obtaining accurate measurements in two-phase flows, especially for the dispersed phase. These issues have to be kept in mind when comparing the data against numerical predictions.

### 5.3 Numerical Simulations

The accurate simulation of Roig's experiments requires that accurate boundary and initial conditions are applied. Despite the large amount of data provided by Roig, certain measurements relating to the inlet region were not provided and had to be inferred or cal-

culated from the data available. In the next section, the estimation of the inlet conditions, and the assumptions which were necessarily introduced, are discussed. Section 5.3.2 then discusses the other issues surrounding the calculations, such as the computational mesh employed for each case. The results of the simulations are presented in Sections 5.4 and 5.5 and compared with the experimental data.

### 5.3.1 Inlet Conditions

The two-phase simulations require both phase velocities, the phase fraction and the turbulence quantities  $k$  and  $\epsilon$  to be specified at the simulation inlet. Since Roig provided measurements for some of these quantities at the  $x = -1$  mm position (i.e. just upstream of the splitter plate end), and since this position represents a convenient and well defined inlet position, it was chosen as the start of the solution domain. For the quantities directly measured by Roig at this position (i.e. the phase fraction and continuous phase mean velocity), determination of the inlet profiles was achieved by simply interpolating the experimental data onto the computational mesh. Where the lack of experimental data made this impossible, other techniques had to be adopted.

Since Roig's emphasis was on the shear layer region, the data does not span the entire width of the duct. Specifically, a region of the flow within approximately 5cm of the outer walls at the inlet region was not measured and assumptions were therefore required concerning the distribution of flow quantities in this area. The profiles within the boundary layers at the splitter plate were measured.

For the majority of cases, Roig did not measure the dispersed phase mean velocities at this position, the first available data being at  $x = 6$  cm, usually. Some cases (i.e. Cases 1.2 and 3.2) do not contain any dispersed phase mean velocity data at all. Suitable values for the dispersed phase mean velocity at the inlet plane, therefore, had to be derived from the available data for all of the two-phase cases. The techniques adopted are discussed in the next section.

The inlet profiles of  $k$  and  $\epsilon$  had to be estimated from the available information which consisted solely of the continuous phase axial RMS velocity measurements. This data provides a basis for estimating the turbulent kinetic energy in the inlet region, but the derivation of the dissipation rate profile required a number of assumptions and approximations, as described in Sections 5.3.1.2 and 5.3.1.3.

### 5.3.1.1 Dispersed Phase Mean Velocity

The dispersed phase velocity at the inlet plane was inferred from the available downstream data for the slip velocity between phases. On the assumption that this slip velocity was approximately constant down the length of the duct, the dispersed phase mean velocity was determined by combining it with the measured continuous phase mean velocity at the inlet plane.

Thus, the continuous and dispersed phase velocity profiles at the  $x = 6$  cm measuring position were linearly interpolated to yield the relative velocity profile at the  $x = 6$  cm position. This slip velocity profile was then applied to the inlet velocity profile for the continuous phase to yield a dispersed phase inlet velocity profile with the same slip velocity profile as at the  $x = 6$  cm measuring position.

This procedure obviated the need to extrapolate the dispersed phase velocity from the experimental values downstream of the inlet plane which could have lead to erroneous values due to the strong development of the velocity profile downstream.

The measurements for the slip velocity at various axial positions down the duct indicated that the assumption of a constant slip velocity was justified; the measured slip velocity profiles were found to be essentially the same at all measuring positions. The slip velocity was found to be very close to the terminal rise velocity of the bubbles in an infinite medium indicating that the turbulence did not much affect the slip velocity.

Since no dispersed phase velocity measurements were reported for Cases 1.2 and 3.2, a uniform slip velocity of 0.3 m/s, corresponding to the terminal rise velocity for bubbles of 2mm diameter was assumed at the inlet.

### 5.3.1.2 Turbulent Kinetic Energy

The axial RMS velocity measurements for the liquid phase allow estimation of the inlet turbulent kinetic energy if assumptions are made regarding the relative magnitudes of the fluctuating velocities in each direction. Near the splitter plate, and within the shear layer itself, the turbulence is expected to be anisotropic, with the axial RMS velocity significantly higher than the lateral and transverse components. Based on earlier investigations [125, 128], it is assumed that

$$\frac{1}{2}u'^2 = v'^2 = w'^2 \quad (5.1)$$

where  $u'^2$ ,  $v'^2$  and  $w'^2$  are the axial, transverse and lateral RMS velocities respectively,



and applies at both the inlet region and within the shear layer itself. Roig [56] reported that the same assumption was adopted in another two-phase CFD code validation study [129] of this case.

Thus, the turbulent kinetic energy at the inlet was calculated as

$$k = \frac{1}{2}(u'^2 + v'^2 + w'^2) = u'^2 \quad (5.2)$$

The axial RMS velocities were linearly interpolated from the experimental data onto the computational mesh.

### 5.3.1.3 Turbulent Kinetic Energy Dissipation Rate

A common method [11, 72] used to estimate the  $\epsilon$  profile at an inlet is to assume a mixing length  $l_m$  distribution and calculate  $\epsilon$  from

$$\epsilon = C_\mu \frac{k^{1.5}}{l_m} \quad (5.3)$$

The mixing length distribution across the inlet region is composed of the distribution across the boundary layers adjacent to the splitter plate and the outer walls, and the distribution across the remainder of the inlet region which is assumed to correspond to fully developed duct flow. In this work, it is assumed that the continuous phase boundary layers are similar in structure to the single phase boundary layer and the corresponding velocity and turbulence profiles are the same.

By way of justification for this practice, it is noted that Lance and de Bertodano's [35] experimental study into two-phase bubbly flow adjacent to a flat plate found that, while the Von Kármán constant and the constants in the logarithmic law are functions of the phase fraction, the logarithmic velocity profile and the classical structure of the boundary layer prevails. Since no information on the phase fraction dependence of these constants is available, it is assumed here that the values for single-phase flow apply.

The mixing length distribution within the boundary layer, which, in this case may have significant width due to the migration of bubbles towards the wall, is therefore given by a ramp function [72]

$$l_m = \begin{cases} \kappa y & \text{for } y/\delta < \lambda/\kappa \\ \lambda\delta & \text{for } y/\delta > \lambda/\kappa \end{cases} \quad (5.4)$$

where  $\lambda$  and  $\kappa$  take the values 0.09 and 0.435 respectively. For the remainder of the inlet region the mixing length distribution was assumed to be that given by Nikuradse's formula for fully developed duct flow [11].

$$l_m = R \left\{ 0.14 - 0.08(1 - y/R)^2 - 0.06(1 - y/R)^4 \right\} \quad (5.5)$$

While it may be argued that the flow is not fully developed in the outer wall region because of the contracting section, the influence of any error in the prescription of the mixing length in this region is expected to be small. Conversely, the boundary layers on the splitter plate will have a significant effect on the development of the shear layer [130]. Since the flow is parallel to the splitter plate for a significant distance before entering the test section (see Figure 5.1) it is reasonable to assume that these boundary layers, and the flow adjacent to the splitter plate, are fully developed so that the above equations are valid.

#### 5.3.1.4 Bubble Diameter

Although the measured variation in bubble diameter throughout the duct is small (approximately  $\pm 0.5$  mm about a mean of about 2 mm) the corresponding variation in drag coefficient with respect to the bubble Reynolds number may be quite large. Examination of the typical slip velocity and mean bubble diameter measurements reveals a Reynolds number of approximately 600. Figure 2.2 shows that the onset of bubble distortion is likely at around a Reynolds number of 450. Small changes in local bubble diameter and/or slip velocity in this region may produce variations in the terminal rise velocity of approximately  $\pm 10\%$ .

In order to account for these effects, the calculations were performed by solving for the local bubble size using a single  $S_\gamma$  equation (see Section 3.2.3) which takes into account the transport of the dispersed phase and the effect this has on the local mean bubble size. Bubble break-up and coalescence effects were not included. The  $S_\gamma$  equation requires the specification of the mean bubble size and the phase fraction at the inlet, both of which were measured by Roig. The experimental mean diameter was taken to be the mean volume diameter, so that  $\gamma = 0$ .

### 5.3.2 Calculations

The inlet of the computational domain is taken to coincide with the first measuring station at  $x = -1$  cm and extends beyond the final measuring station, as given by the  $x_{max}$  column in Table 5.1, according to the case being considered. The 1 cm length of splitter plate which intrudes into the computational domain is simulated using a zero thickness wall (i.e. a wall boundary condition is applied to the cell faces coinciding with the position of the splitter plate).

Case	No. Axial Nodes	No. Lateral Nodes	$x_{max}$ [m]	Expansion Ratio	
				Axial	Lateral
1.1	100	80	1.1	1.022	0.96
1.2	100	80	1.1	1.022	0.96
2.1	100	80	1.5	1.015	0.96
2.2	80	80	0.6	1.010	0.94
2.3	100	80	2.0	1.022	0.96
2.4	70	60	0.6	1.016	0.97
3.1	100	80	1.1	1.022	0.96

Table 5.3: Computational mesh details.

Due to the high gradients in phase fraction and the continuous phase mean velocity in the region of the splitter plate, and since we are most interested in the development of the shear layer in the centre of the duct, the computational mesh was refined considerably in this region by gradually increasing the mesh density between the outer part of the mesh and the centre of the duct.

This was achieved using a ‘geometric progression’ where the cell sizes in a single direction are calculated using a geometric series. The cell size at the start of the series is fixed and subsequent cell sizes are increased by multiplying the previous cell size by common factor

Mesh	No. Axial Nodes	No. Lateral Nodes	Total
Coarse	60	40	2400
Intermediate	100	80	8000
Fine	150	120	18000

Table 5.4: Computational mesh details for mesh sensitivity tests.

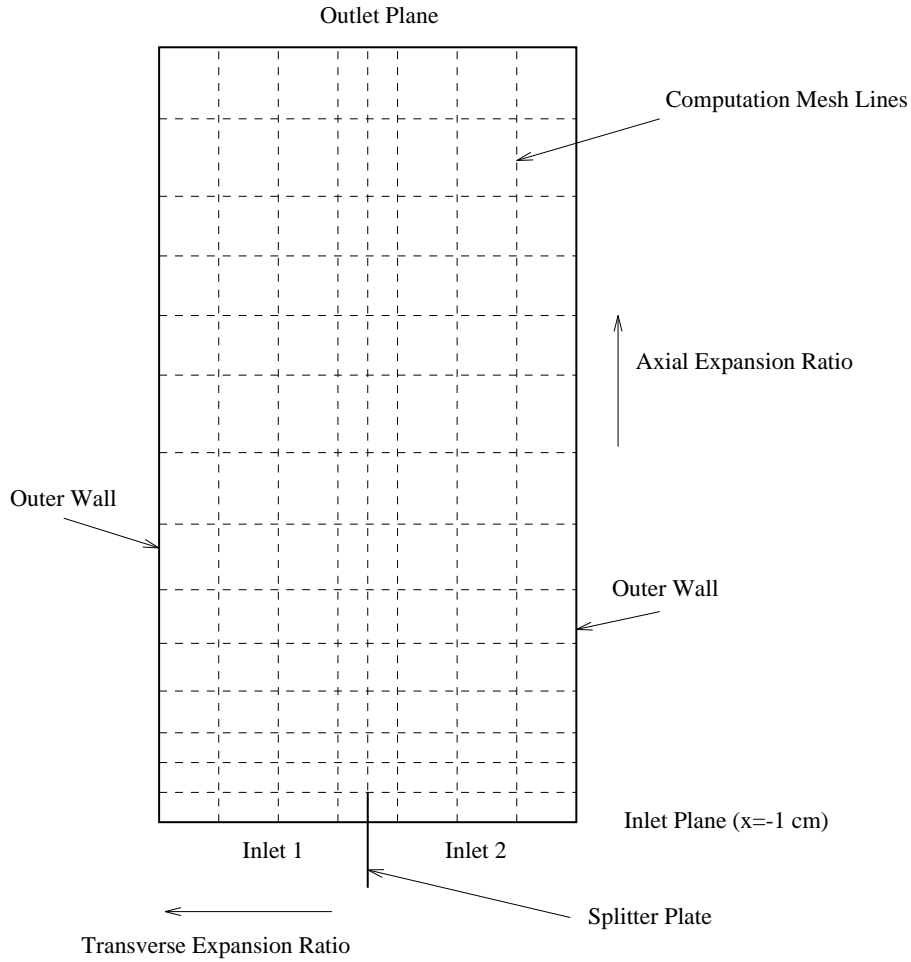


Figure 5.2: Schematic arrangement of the computational mesh.

or expansion ratio [131].

The degree of refinement, and the length of the calculation domain, differed slightly for each case. Figure 5.2 shows a simplified schematic arrangement of a typical mesh. Table 5.3 shows the details of the mesh employed for each case. The convergence tolerance (see Section 4.3.6) for all calculations was taken to be  $10^{-4}$ .

In order to assess the sensitivity of the solution on the mesh size, additional calculations for Case 1.2 were performed using a coarser and finer mesh size. Tables 5.4 shows the details of the meshes employed. The predictions resulting from the calculations using these meshes are compared in Section 5.5.6.

The following section describes the simulation results and compares them against the ex-

perimental data. Section 5.4 considers the single-phase cases. These cases give a good indication of the underlying performance of the  $k-\epsilon$  turbulence model. Section 5.5 considers the two-phase cases which make up the bulk of this study.

## 5.4 Results - Single-phase Cases

### 5.4.1 Case 1.1

The inlet stream velocities for Case 1.1 were 0.87 and 0.55 m/s yielding a velocity ratio of 0.63.

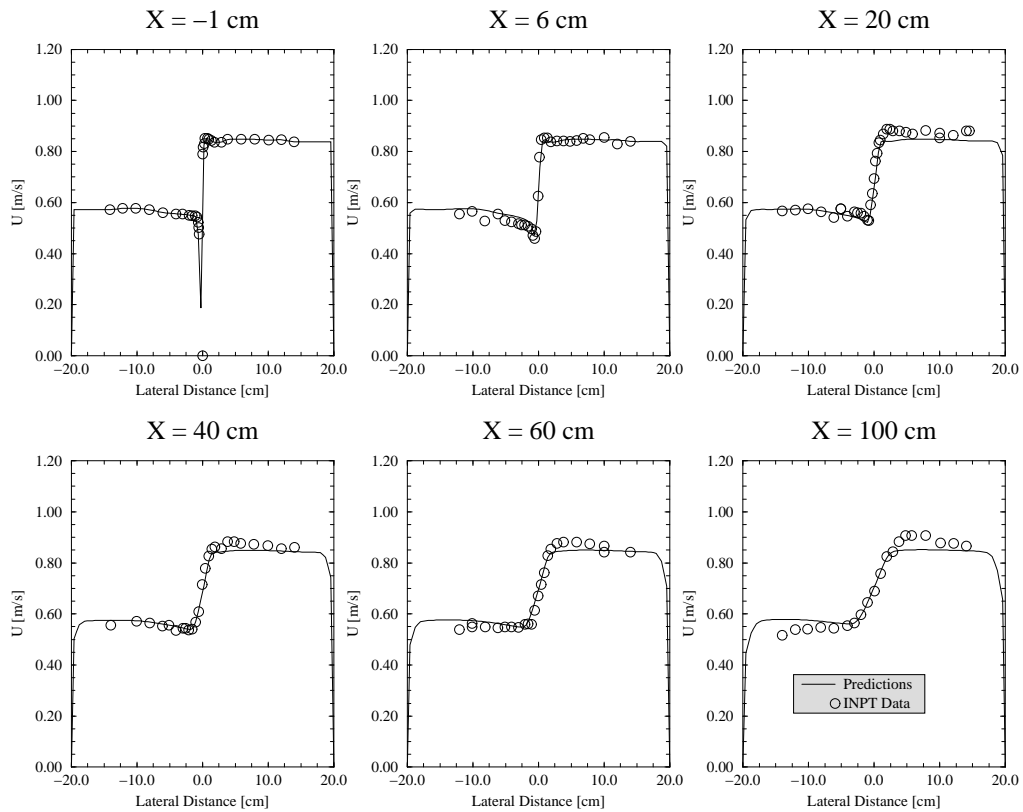


Figure 5.3: Case 1.1 - Mean axial velocity.

Figures 5.3 and 5.4 show the mean axial velocity and axial RMS velocity predictions for each of the 6 axial measuring stations. Considering first the mean velocity profiles, it can be seen that the spreading rate of the shear layer is well predicted. The experimental data shows some anomalies at the high speed edge of the shear layer; the velocity seems to increase in this area for  $x > 20$  cm. The present predictions do not exhibit this behaviour.

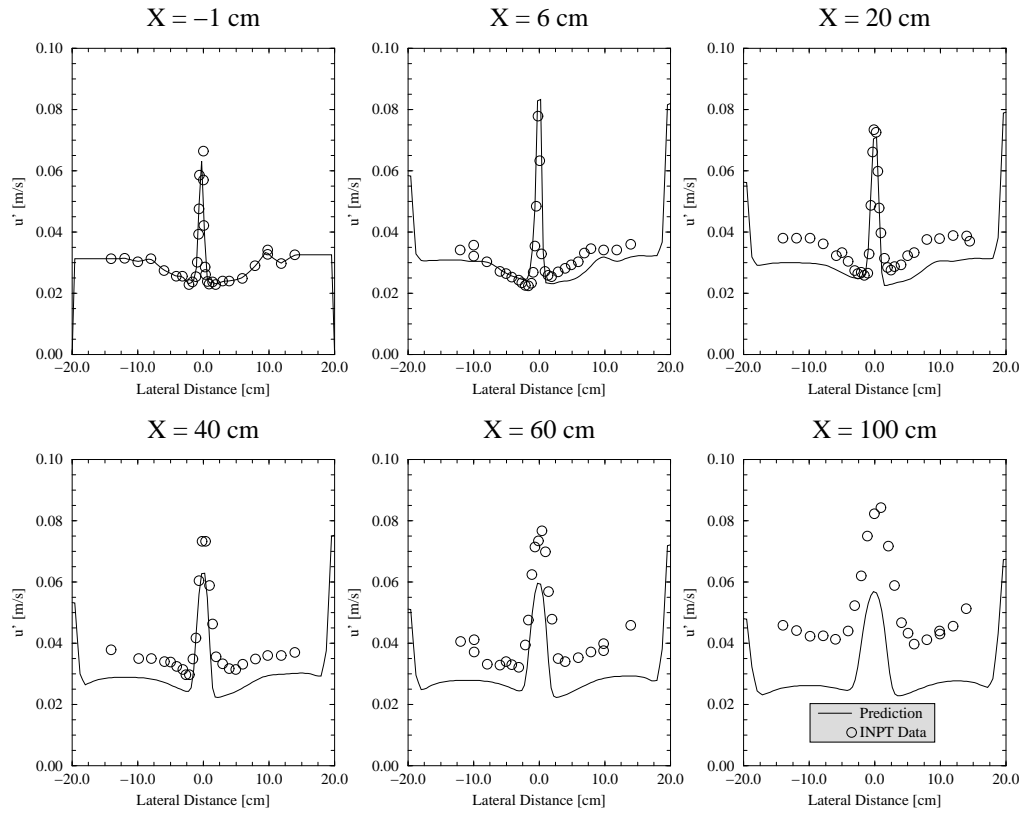


Figure 5.4: Case 1.1 - Axial RMS velocity.

Turning to the axial RMS velocity predictions, Figure 5.4 shows significant deviations (approximately 50%) between measured and predicted values at the downstream measuring stations ( $x > 60$  cm). It appears that the predicted peak axial RMS velocity decays more rapidly than the experimental data indicates. Indeed, the experimental data show a steady increase in the peak axial RMS velocity beyond  $x = 40$  cm. The free stream RMS velocity well outside the shear layer region also show this behaviour and seems to increase steadily from the origin of the shear layer in relative proportion to the peak value. This is a feature not shown by other studies.

### 5.4.2 Case 2.1

The inlet stream velocities for Case 1.1 were 0.61 and 0.26 m/s yielding a velocity ratio of 0.43.

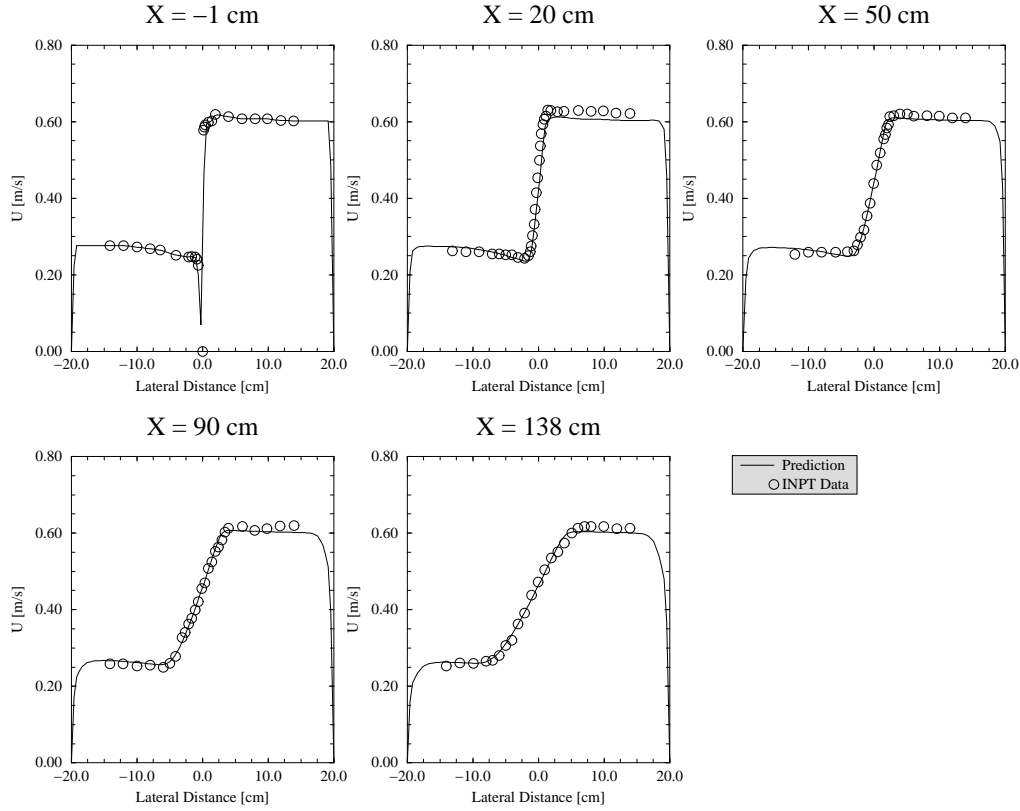


Figure 5.5: Case 2.1 - Mean axial velocity.

Figures 5.5 and 5.6 show the mean axial velocity and axial RMS velocity predictions for Case 2.1. Again, it can be seen that the shear layer spreading rate is very well predicted. This case does not show any of the anomalies at the high speed edge of the shear layer that Case 1.1 does, and so the comparison over the entire duct width is acceptable. The calculated mass imbalance for this case is approximately 2.4%.

The axial RMS velocity predictions for this case are rather better than those of Case 1.1. This may be because the velocity ratio is lower than Case 1.1 yielding a higher shear layer Reynolds number; the  $k-\epsilon$  turbulence model is known to be more accurate in situations with high shear, and would require some modification to be accurate in low shear rate situations [72]. It should be noted that the experimental data show that the peak in the axial RMS velocity is maintained after  $x = 20$  cm, as opposed to the steady increases shown in Case 1.1.

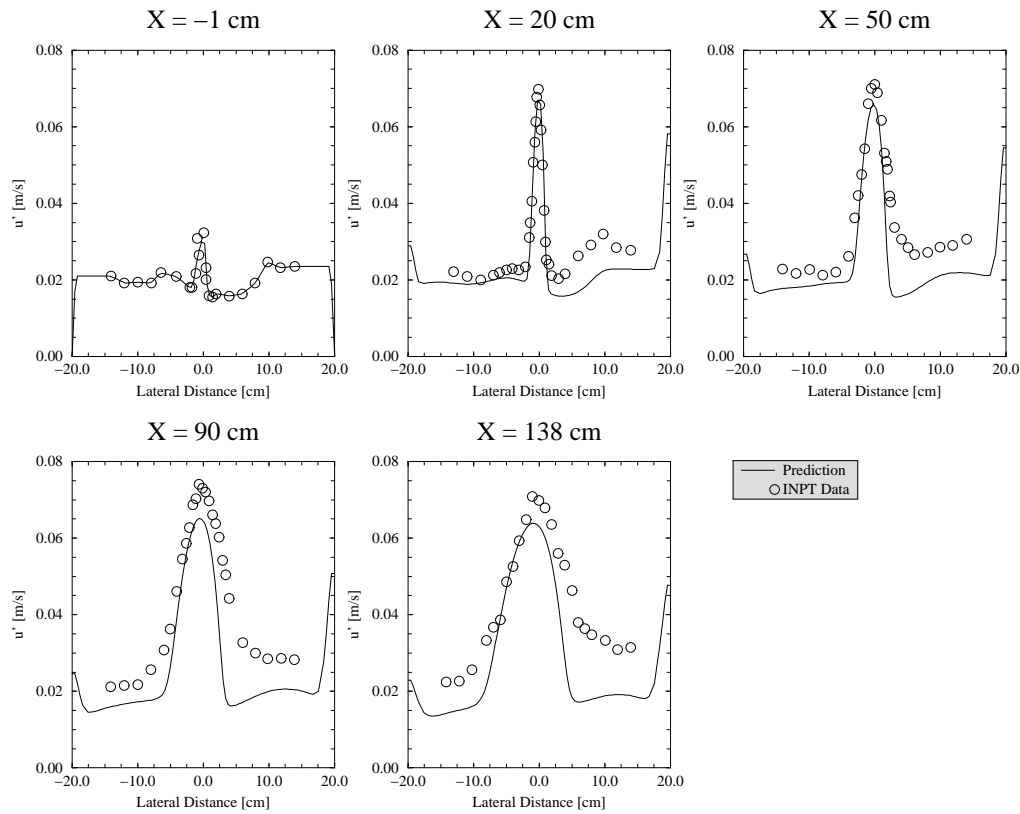


Figure 5.6: Case 2.1 - Axial RMS velocity.

The free stream axial RMS values are seen to increase slightly in the high speed side of the layer. The width of the peak increases, preferentially into the high speed side also, at a slightly faster rate than the predictions show.

In general, the predictions of the axial RMS velocity for this case are more acceptable than those of Case 1.1. If we are to attribute this to the higher shear rate, with the corresponding improvement in accuracy of the  $k-\epsilon$  model, then we should expect the turbulence predictions for the other high shear rate cases to be reasonable also.



### 5.4.3 Case 3.1

The inlet stream velocities for this case are both the same at 0.59 m/s, essentially leading to a trailing wake behind the splitter plate.

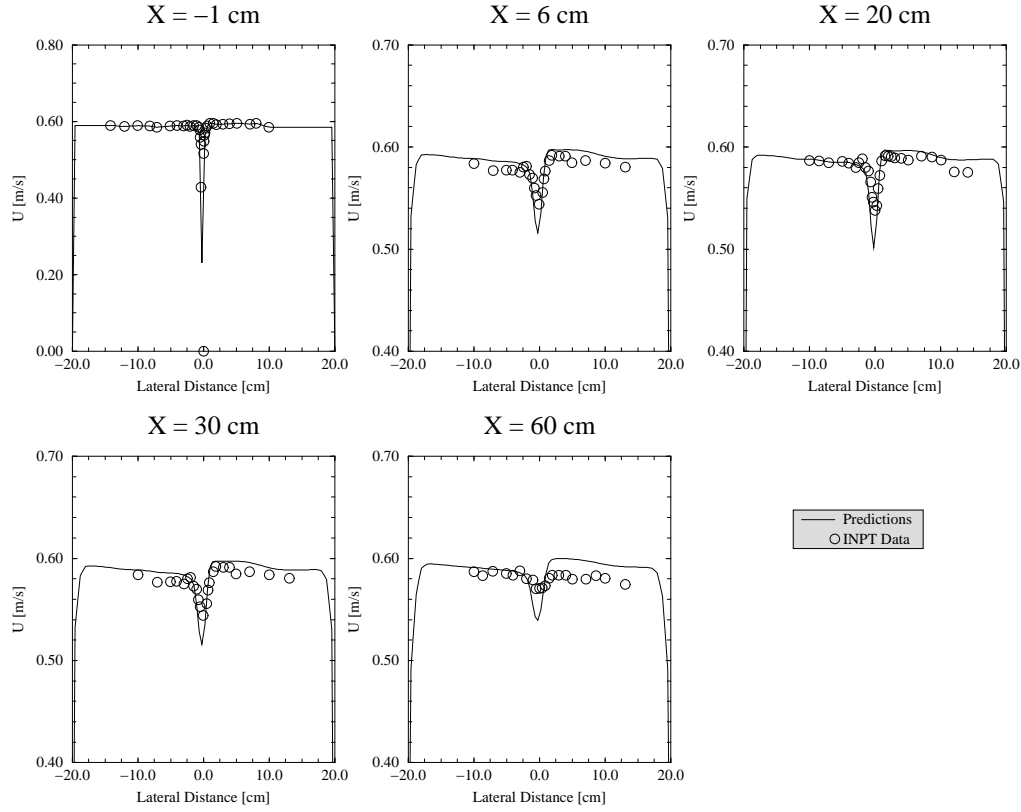


Figure 5.7: Case 3.1 - Mean axial velocity.

Figures 5.7 and 5.8 show the predicted and measured mean and RMS axial velocities. Comparing the axial mean velocities in Figure 5.7 we see adequate agreement for all measuring stations, although the experimental data indicate that the flow recovery is somewhat faster than that predicted.

Turning to Figure 5.8 we see that simulations under-predict the decay of the peak in the RMS velocity within the shear layer. Consequently, the RMS velocity outside the shear layer is under-predicted. This is consistent with the hypothesis that RMS velocity development discrepancies are due to the low shear rate.

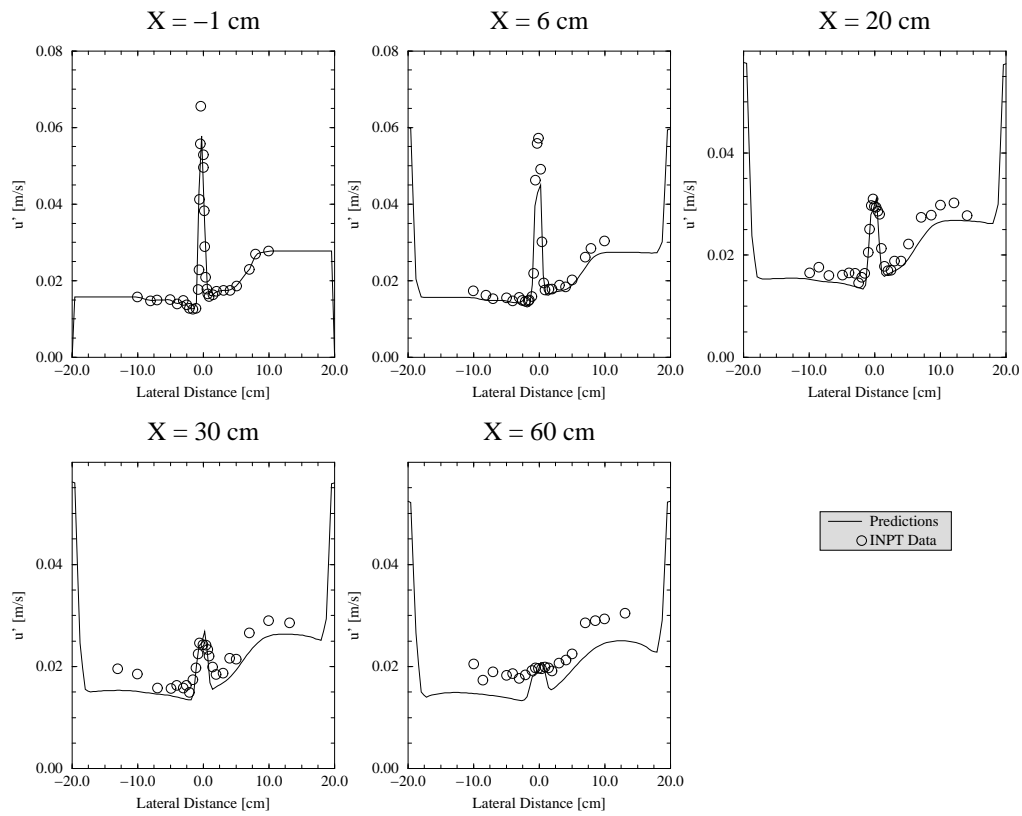


Figure 5.8: Case 3.1 - Axial RMS velocity.

## 5.5 Results - Two-phase Cases

### 5.5.1 Case 1.2

The inlet stream velocities for Case 1.2 were 0.94 and 0.6 m/s yielding a velocity ratio of 0.6. Air was introduced into both streams at the same phase fraction of 1.9%. As the shear layer develops, the experimental data shows distinct regions of high and low phase fraction across the shear layer. These peaks and troughs are a result of the lateral shift of bubbles within the shear layer due to lift forces with a peak at the low velocity side of the shear layer and a trough in the centre.

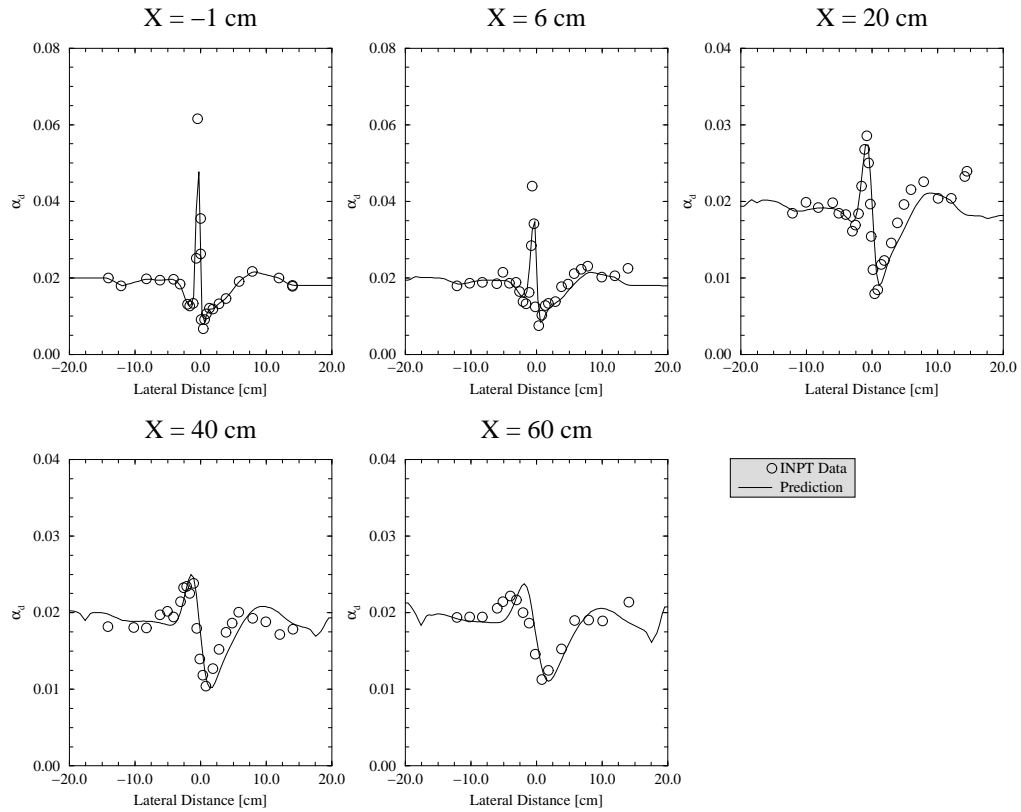


Figure 5.9: Case 1.2 - Dispersed phase fraction.

Figure 5.9 shows the measured and predicted dispersed phase fraction for this case. It can be seen that good agreement is obtained between the measurements and predictions for  $x > 20$  cm. The lateral phase distribution is well predicted, both in terms of the magnitude and width of the peaks and troughs. Some discrepancy is evident at  $x = 20$  cm in that the lateral dispersion rate of the bubbles is slightly over-predicted.

Figure 5.10 shows the mean axial velocity for the continuous phase. It can be seen that

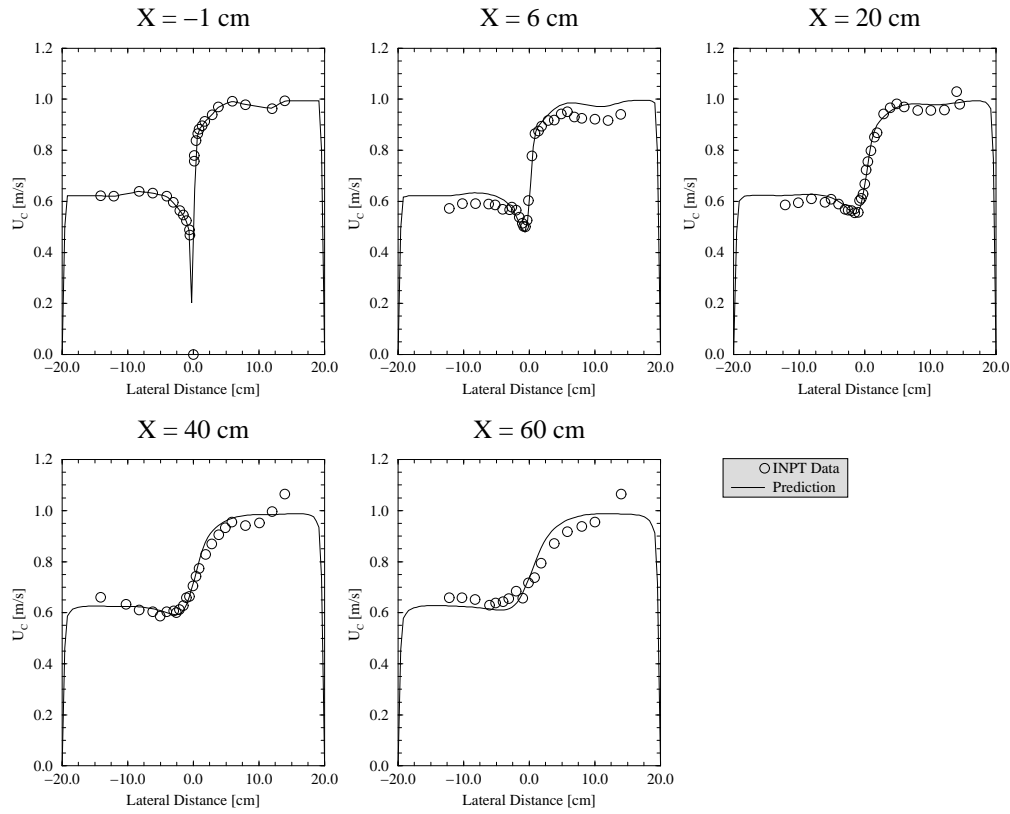


Figure 5.10: Case 1.2 - Continuous phase mean axial velocity.

the spreading rate of the shear layer is reasonably well predicted. Some discrepancy near the wall on the high speed side is evident at  $x = 40$  cm and  $x = 60$  cm where the data seems to indicate some unexplained local acceleration. Note that the mass imbalance for this case is approximately 2.6% for the continuous phase (Table 5.2).

Figure 5.11 shows the measured and predicted axial RMS velocity. The predictions are calculated from the turbulent kinetic energy via Equations (5.1) and (5.2). It can be seen that they are somewhat lower than the experimental data, especially for  $x > 40$  cm, although the overall shape of the profiles are in good agreement with the relative magnitude of the peak in the centre of the shear layer.

The experimental data displays some anomalous behaviour near the wall on the high speed side at  $x = 40$  and 60 cm where high RMS velocity values are reported. The predictions do not show any significant increase in the turbulence level in this region over and above the turbulence generated by the shear layer associated with the wall.

The RMS peak within the shear layer at  $x = 6$  cm seems to be over-predicted since the measurements indicate that it has dissipated. The measurements at subsequent stations,

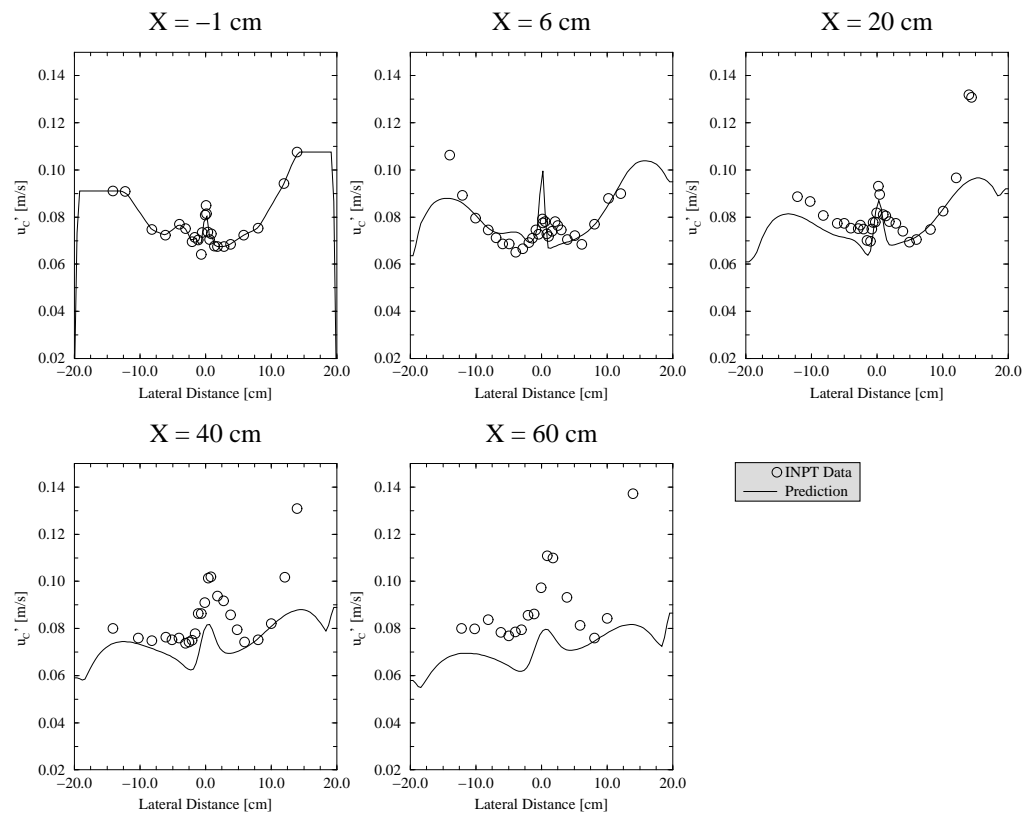


Figure 5.11: Case 1.2 - Continuous phase axial RMS velocity.

however, shows reappearance of the peak.

No measurements were reported for the dispersed phase mean velocity and the axial RMS velocity for this case.

### 5.5.2 Case 2.2

Case 2.2 is similar to Case 1.2 in that air is introduced into both streams with the same phase fraction (1.9%), but the stream velocities are 0.54 and 0.22 m/s giving a smaller velocity ratio of 0.4.

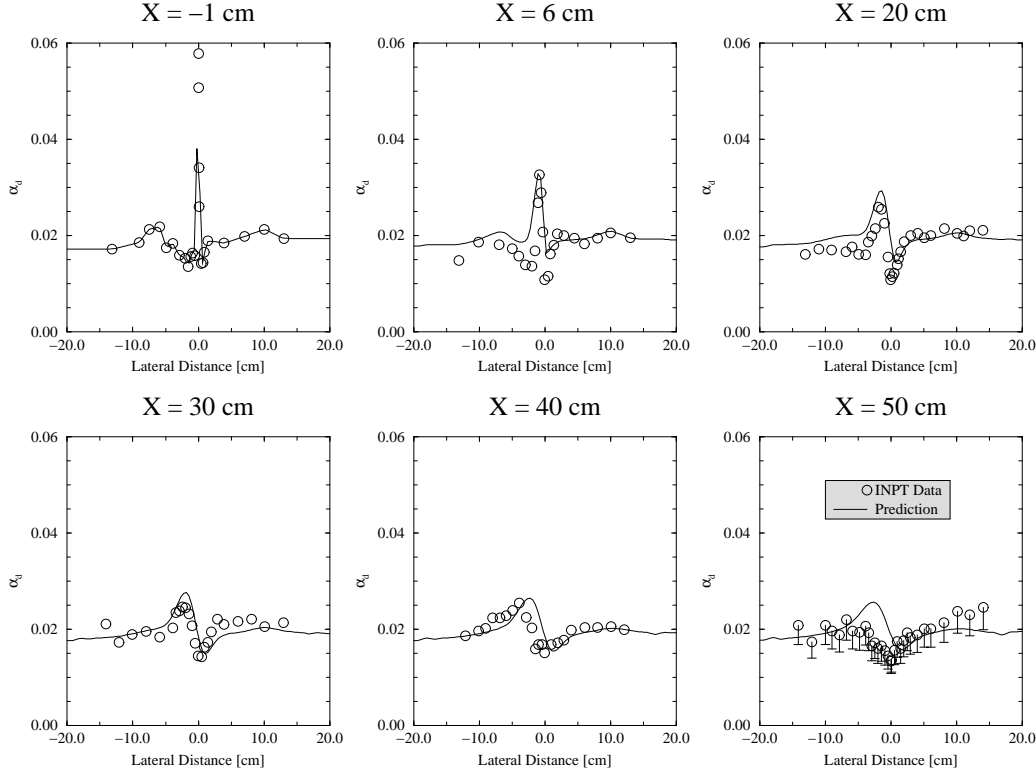


Figure 5.12: Case 2.2 - Dispersed phase fraction.

Figure 5.12 shows the measured and predicted dispersed phase fractions for each of the six measuring stations. It can be seen that the distribution of  $\alpha_d$  is reasonably well predicted although at the last station ( $x = 50\text{cm}$ ) the predictions deviate somewhat from the measurements. Here the trend in the measured phase fraction distribution seems to differ from the previous stations and the peak on the left hand side of the shear layer is lost. This may be due to some flow disturbance, possibly helical vortex pairing [126], or to some other flow anomaly or experimental error, as discussed below.

The mass imbalance for this case is relatively high, at approximately 13.2% for the continuous phase and 19.1% for the dispersed phase. The error bars on the phase fraction measurements at the final measuring station show the magnitude of the reduction in the phase fraction measurements required to account for the mass imbalance of the dispersed

phase.

Again, note that the peak in phase fraction is associated with the edge of the shear layer on the low speed side. This is consistent with the bubbles being trapped in the coherent structures towards the down-flowing side (relative to the mean motion) as shown by Sene, Hunt and Thomas [121] in their discrete vortex calculations for bubbles in a vertical shear layer.

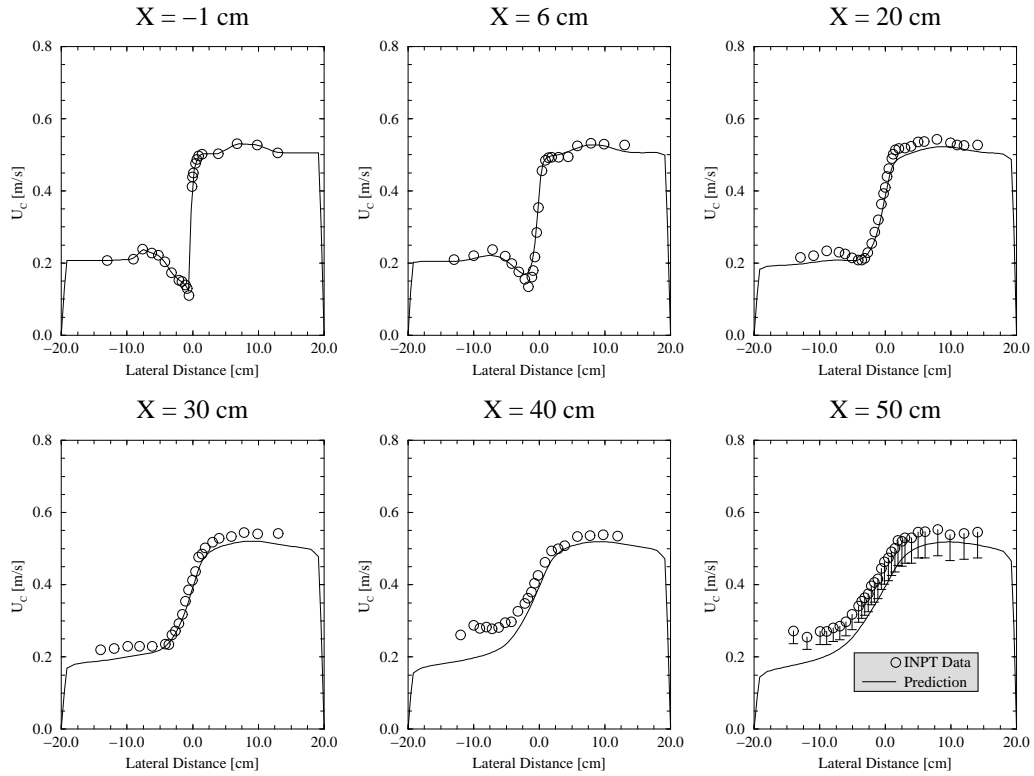


Figure 5.13: Case 2.2 - Continuous phase mean axial velocity.

Figures 5.13 and 5.14 show the measured and predicted mean axial velocities for the continuous and dispersed phases respectively. Again, the error bars on the last measuring station indicate the relative error in the phase velocity measurements needed to account for the calculated mass imbalance. It can be seen that while the spreading rate of the shear layer is reasonably well predicted, there are some discrepancies between the absolute magnitude of the phase velocities on the low velocity side at the downstream locations ( $x > 30$  cm), especially for the dispersed phase. The predictions fall within these error bars for the majority of the duct width.

Examination of the measured and predicted dispersed phase fraction in Figure 5.12 shows

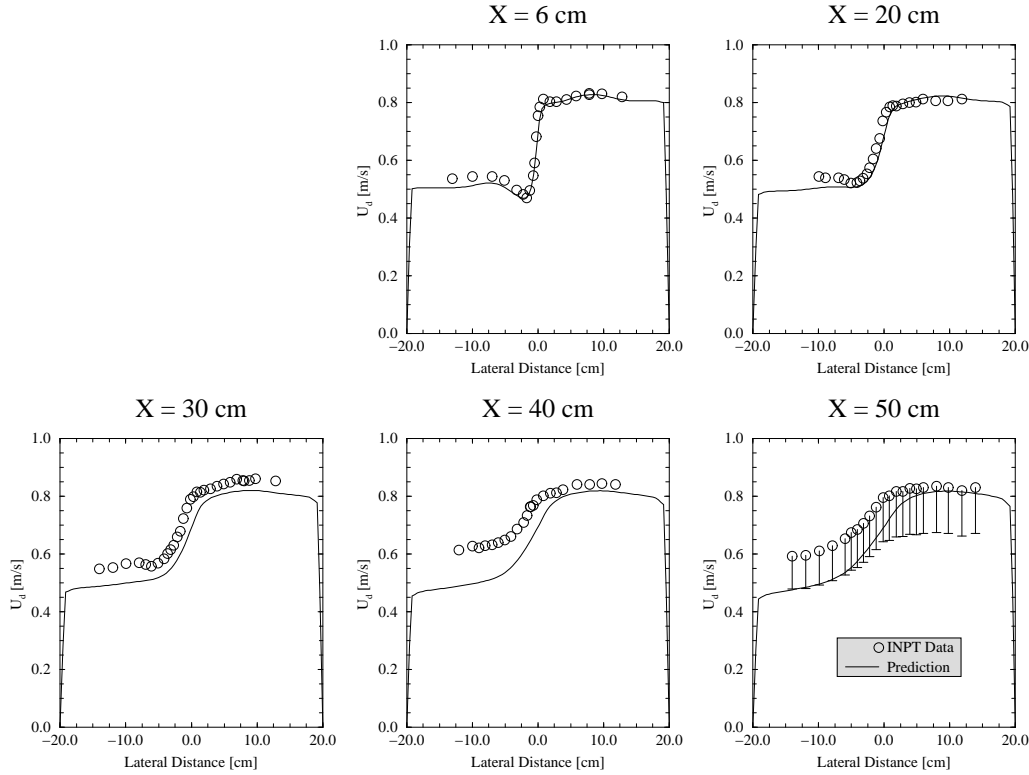


Figure 5.14: Case 2.2 - Dispersed phase mean axial velocity.

that the calculated phase fraction is approximately the same as the measured values everywhere. Since the calculation conserves mass, this implies that the mass imbalance in the experimental data (approximately 19%) will likely be due to errors in the measurement of the phase velocities.

It can be seen that the discrepancy in the dispersed phase velocity in Figure 5.14 is higher than that for the continuous phase, which is consistent with the fact that the mass imbalance is higher for the dispersed phase.

Figures 5.15 and 5.16 show the axial RMS velocities for the continuous and dispersed phases respectively. The predicted RMS velocities are calculated from the turbulent kinetic energy via Equations (5.1) and (5.2) while the dispersed phase RMS velocities are calculated from Eqn (2.113). The axial RMS for the continuous phase is well predicted, although for  $x > 30$  cm the RMS velocity is under-predicted somewhat. Again, the shape of the profile is well captured but the experimental data shows an unexpected increase in turbulence level downstream.

It can be seen from Figure 5.16 that the dispersed phase RMS velocity predictions are



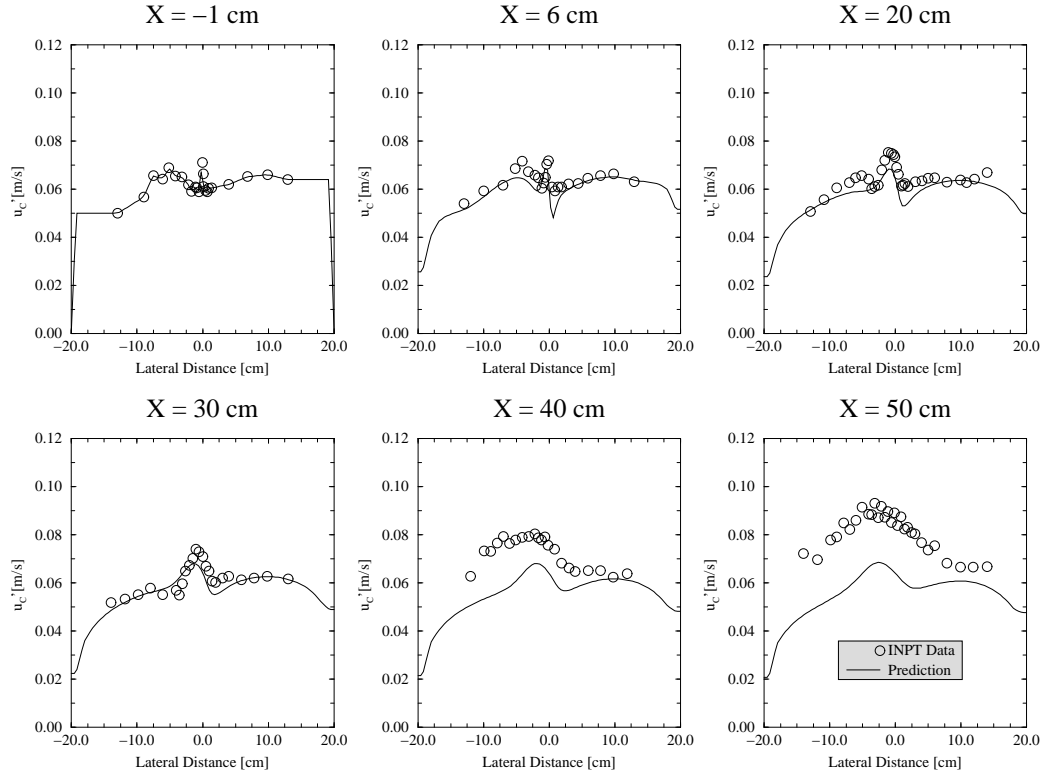


Figure 5.15: Case 2.2 - Continuous phase axial RMS velocity.

generally lower than the experimental data, especially at the downstream locations. This is a consequence of the under-prediction of  $C_t$ , as discussed below. Again, the data shows an unexpected increase in the RMS velocity downstream. Note also that the experimental data shows significant dispersed phase RMS velocity magnitudes outside the shear layer for all measuring stations, in contrast with the continuous phase RMS velocity, which are difficult to explain. This feature is not reproduced by the predictions since both the continuous phase RMS velocity and the  $C_t$  profiles show a peak within the shear layer.

It is possible to compare directly the predicted values for  $C_t$  with measured values by deriving  $C_t$  values from the continuous and dispersed phase axial RMS velocity measurements. Figure 5.17 shows the resulting predicted and measured axial RMS velocity ratio,  $C_t$ . The predictions are seen to peak in the shear layer region and to steadily decrease downstream — a tendency not displayed by the experimental values which are scattered around the 1.5 value at each measuring station. The peak in the predicted  $C_t$ , and its subsequent decrease downstream, is due to the increasing eddy length scale,  $l_e$ , and the decreasing axial RMS velocity for the continuous phase (Eqn (2.117) and Eqn (2.118)). Furthermore, there is no discernible pattern to the experimental  $C_t$  distribution.

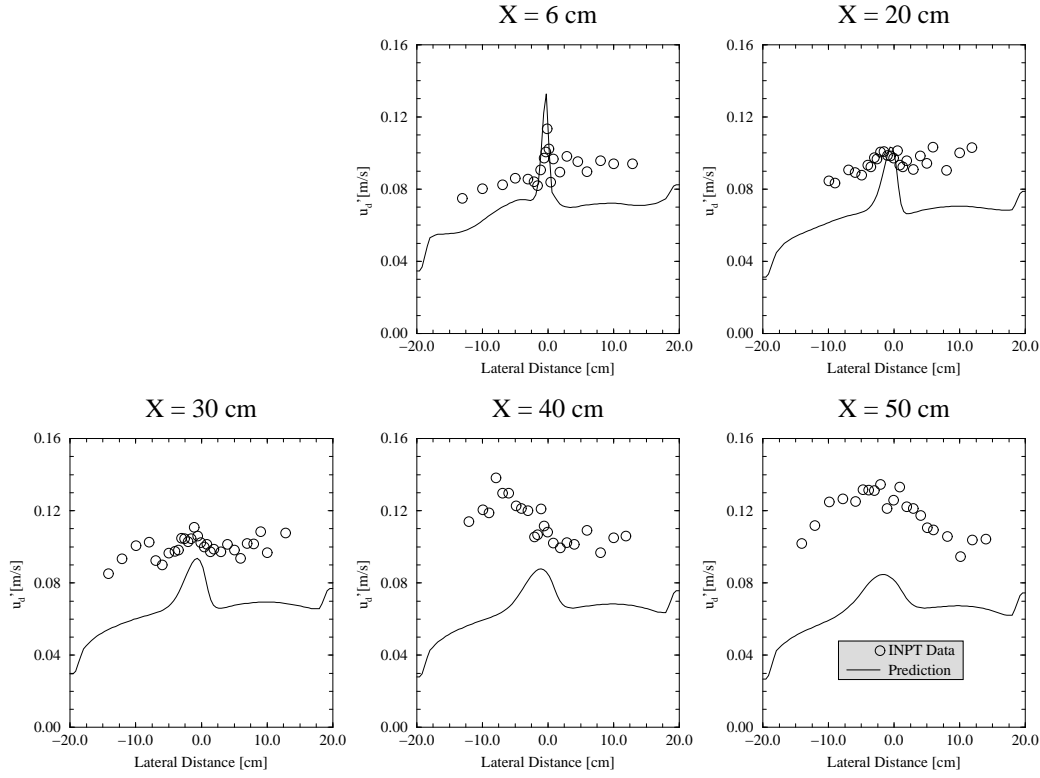
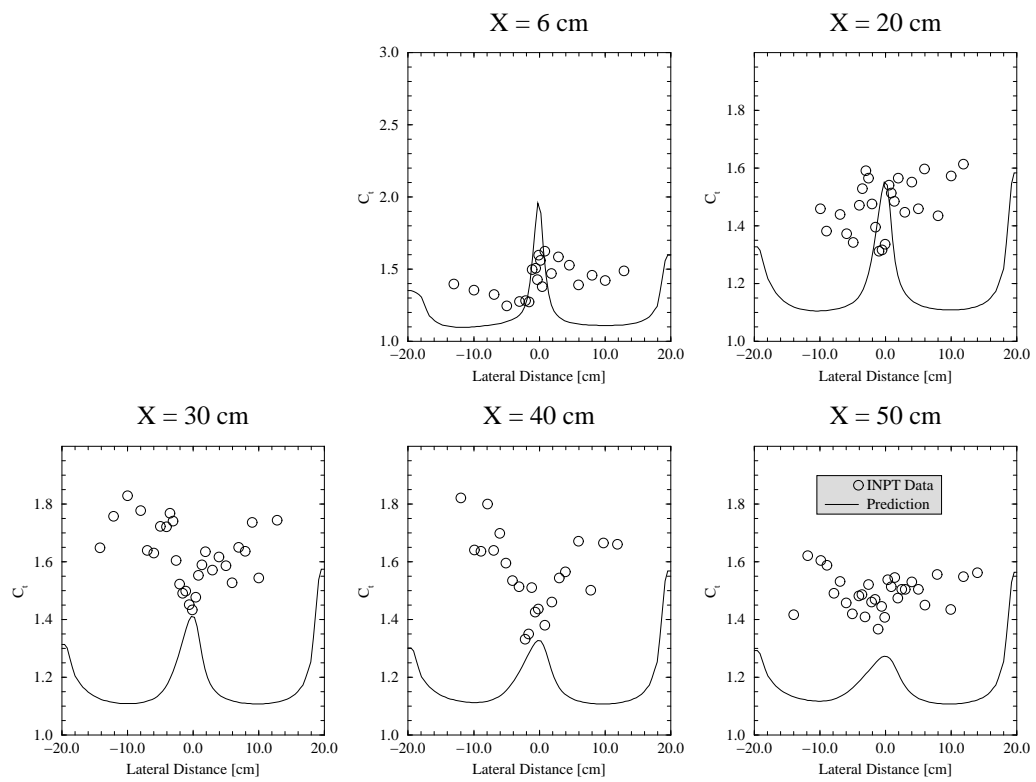


Figure 5.16: Case 2.2 - Dispersed phase axial RMS velocity.

In order to uncover the major influences in the dispersed phase lateral motion, the relative magnitudes of each of the terms in the momentum equation (Eqn (2.122)) at the  $x = 30$  cm position are shown in Figure 5.18. It can be seen that the dominant forces are lift, mean drag and interfacial pressure.

The peak in the interfacial pressure force coincides with the maximum gradient in the phase fraction. The mean drag is seen to oppose the combined effects of the interfacial pressure and lift forces on the edges of the shear layer at  $x \approx -5.0$  and  $x \approx 2.5$  cm. In the centre of the shear layer ( $x \approx 0$ ), the dominant forces are the lift and interfacial pressure forces while the drag force reduces to zero.

Figure 5.18 also shows why the magnitude of  $C_t$  has a very small effect on the lateral distribution of the phase fraction. The normal stress gradients and the dispersed phase Reynolds stresses are negligible compared to the drag and lift forces.

Figure 5.17: Case 2.2 - Axial RMS velocity ratio  $C_t$ .

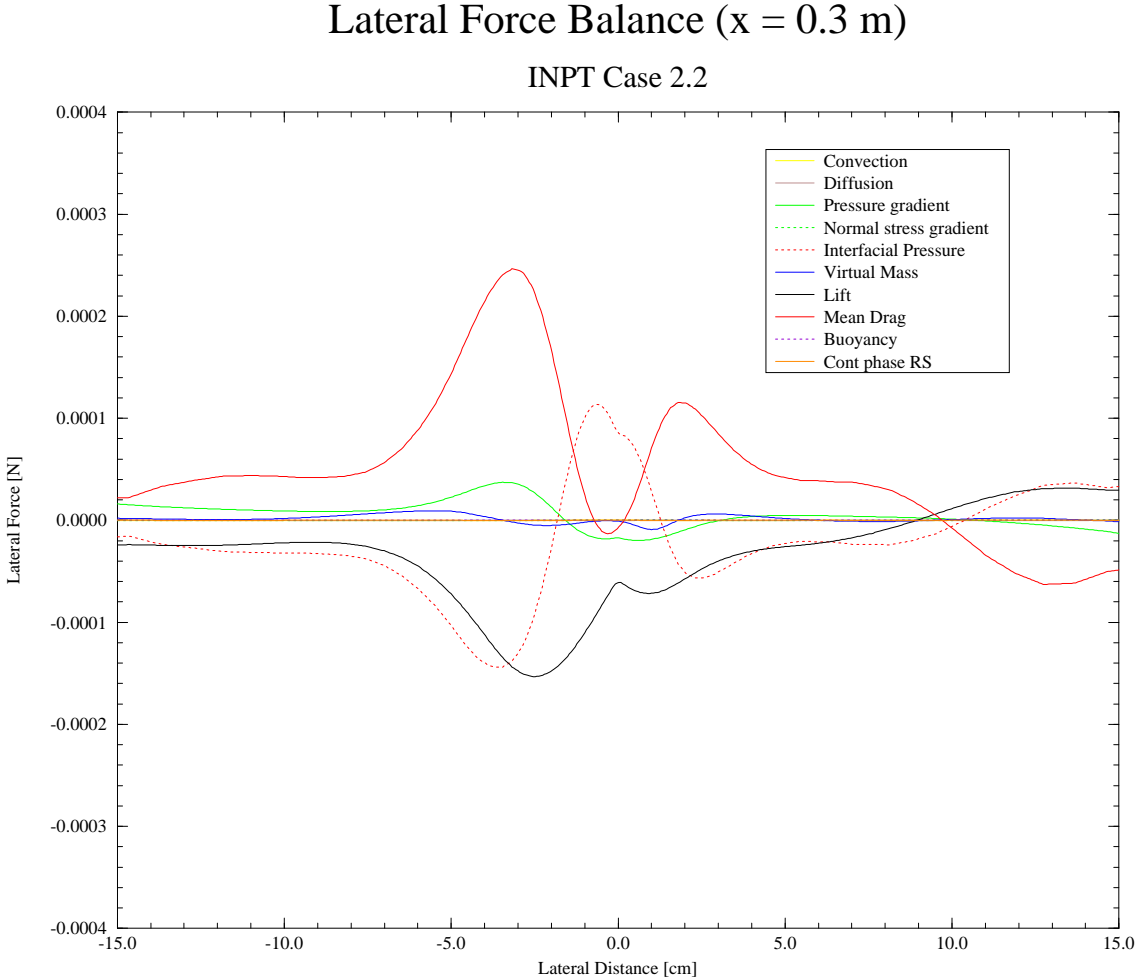


Figure 5.18: Case 2.2 - Dispersed phase lateral force balance at  $x = 30$  cm.

### 5.5.3 Case 2.3

The inlet stream velocities for Case 2.3 are 0.51 and 0.18 m/s yielding a velocity ratio of 0.35. In contrast to the previous case, air bubble are introduced into the high speed stream only.

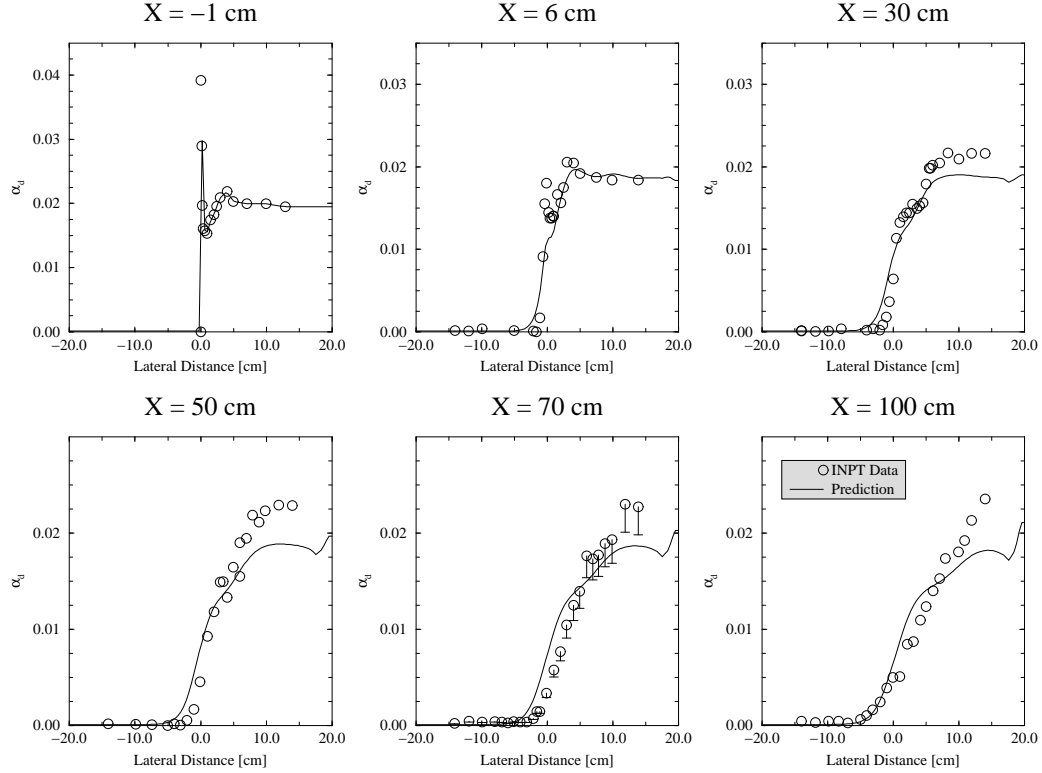


Figure 5.19: Case 2.3 - Dispersed phase fraction.

Figure 5.19 shows the predicted dispersed phase fraction distribution for this case. It can be seen that the agreement is generally acceptable, although discrepancies on the high speed side are apparent for  $x > 50$  cm. In this area the phase fraction seems to be steadily increasing towards the wall. Peaks in phase fraction at the wall are predicted due to lift forces, but this effect is local to the wall and does not extend very far into the centre of the duct.

Note that the experimental mass imbalances for this case are approximately 9.3% for the continuous phase and 12.7% for the dispersed phase. The error bars at the  $x = 60$  cm position in Figure 5.19 show the relative error in the phase fraction measurements required to account for the imbalance in the dispersed phase.

Examination of the mean velocity predictions for the continuous phase (Figure 5.20) show

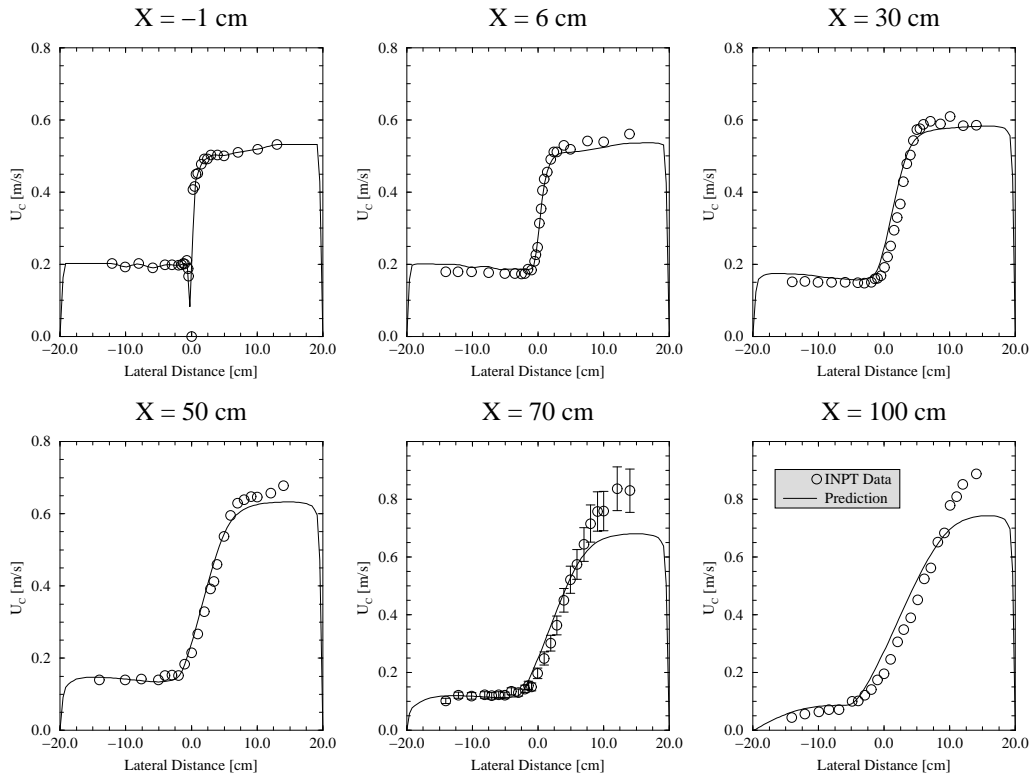


Figure 5.20: Case 2.3 - Continuous phase mean axial velocity.

a similar discrepancy in the high speed region. The data indicates that the flow is accelerating on the high speed side but decelerating on the low speed side. Such a flow configuration could indicate the presence of a recirculation zone within the low speed side beyond the last measuring station.

In order to determine whether or not such a flow feature existed, the solution domain was extended well beyond the final measuring station to cover the entire 2m length of the duct. The subsequent simulations did indeed reveal the presence of a recirculation zone with its centre approximately 1.5 m downstream from the end of the splitter plate. Figure 5.22 shows the resulting continuous phase stream lines.

The recirculation zone was found to be due to the combined effects of the low velocity ratio and the presence of the rising air bubbles within the high speed side of the shear layer which tend to accelerate the continuous phase in this region, eventually leading to the formation of a recirculation zone. Interestingly, the recirculation zone revealed by the calculations only appears in the two-phase flow case; a similar single-phase calculation, with the same velocity ratio and inlet conditions for the continuous phase, shows no recirculation zone.

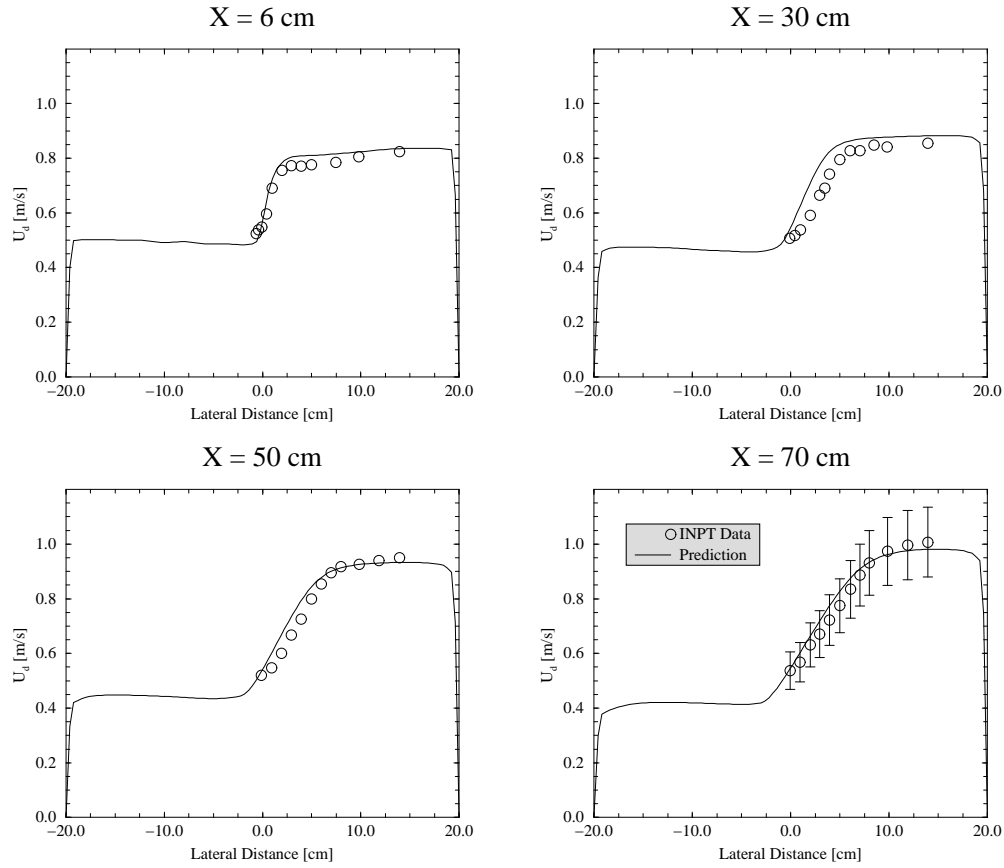


Figure 5.21: Case 2.3 - Dispersed phase mean axial velocity.

The leading edge of the recirculation zone was found to coincide with the  $x = 1.1\text{m}$  position. Consequently, at the  $x = 1.0\text{ m}$  measuring station, both phases are found to accelerate, especially near the wall, as they enter the high speed side of the recirculation zone.

However, while the increase in the dispersed phase velocity is well predicted (see Figure 5.21) the continuous phase velocity and phase fraction are under-predicted. The continuous phase flow is accelerating towards the wall on the high speed side so that the phase fraction profile becomes stretched towards the high speed side wall as the bubbles are carried with it. The extent of this stretching is seemingly under-predicted, although the mass imbalance in the measurements could explain some of the discrepancy.

The axial RMS velocities for both phases are shown in Figures 5.23 and 5.24. The continuous phase RMS velocity predictions are acceptable for  $x \leq 30\text{cm}$ . Beyond this point, although the magnitude of the peak is adequately predicted, the data indicate that this peak shifts towards the wall, probably due to the influence of the recirculation zone.

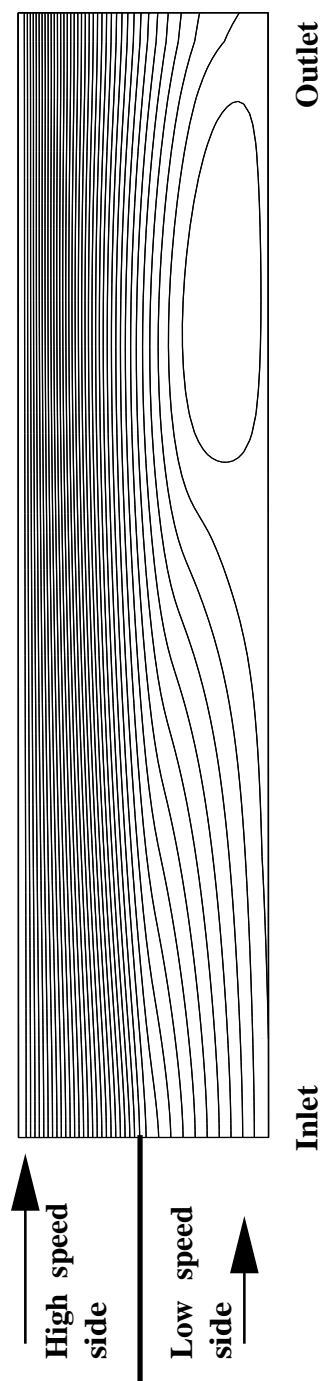


Figure 5.22: Case 2.3 - Continuous phase streamlines showing recirculation zone.



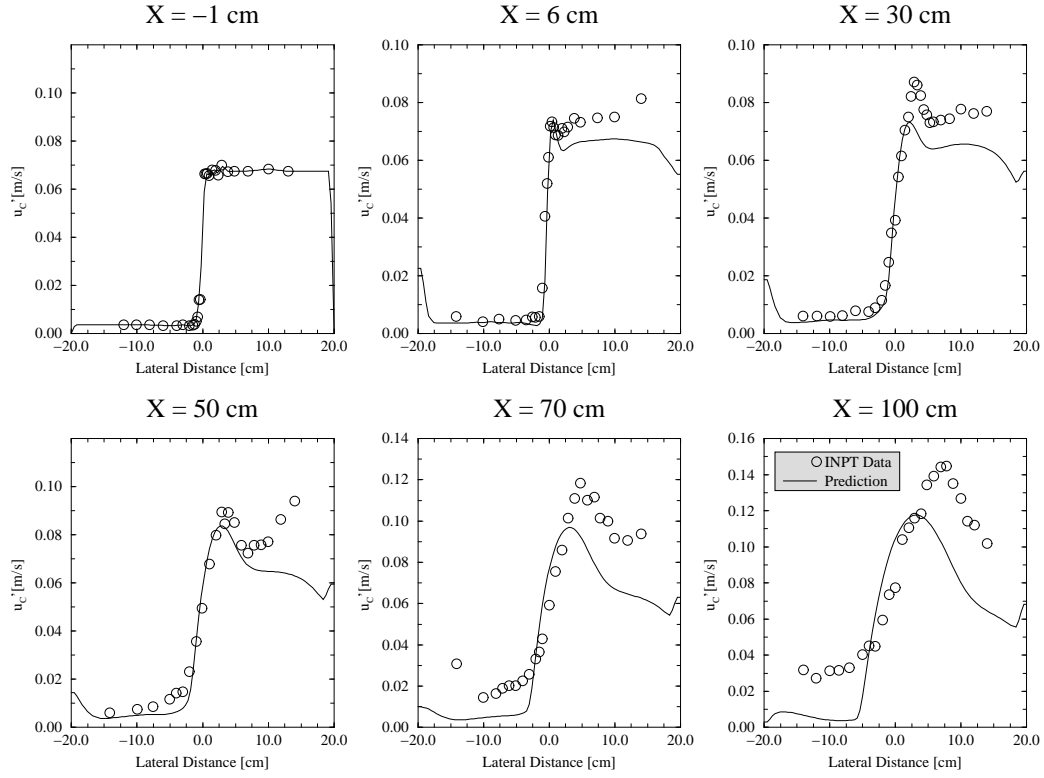


Figure 5.23: Case 2.3 - Continuous phase axial RMS velocity.

The dispersed phase RMS velocities are well predicted within the shear layer but the data indicate that the free stream RMS velocity is high within the high speed side. The simulations under-predict the RMS velocities in this region. This is due to the under-prediction of the continuous phase RMS velocity and the  $C_t$  values in this area.

Figure 5.25 shows the predicted and measured axial  $C_t$  profiles. The calculation shows qualitative agreement with the data in terms of magnitude but there is a significant difference in distribution.

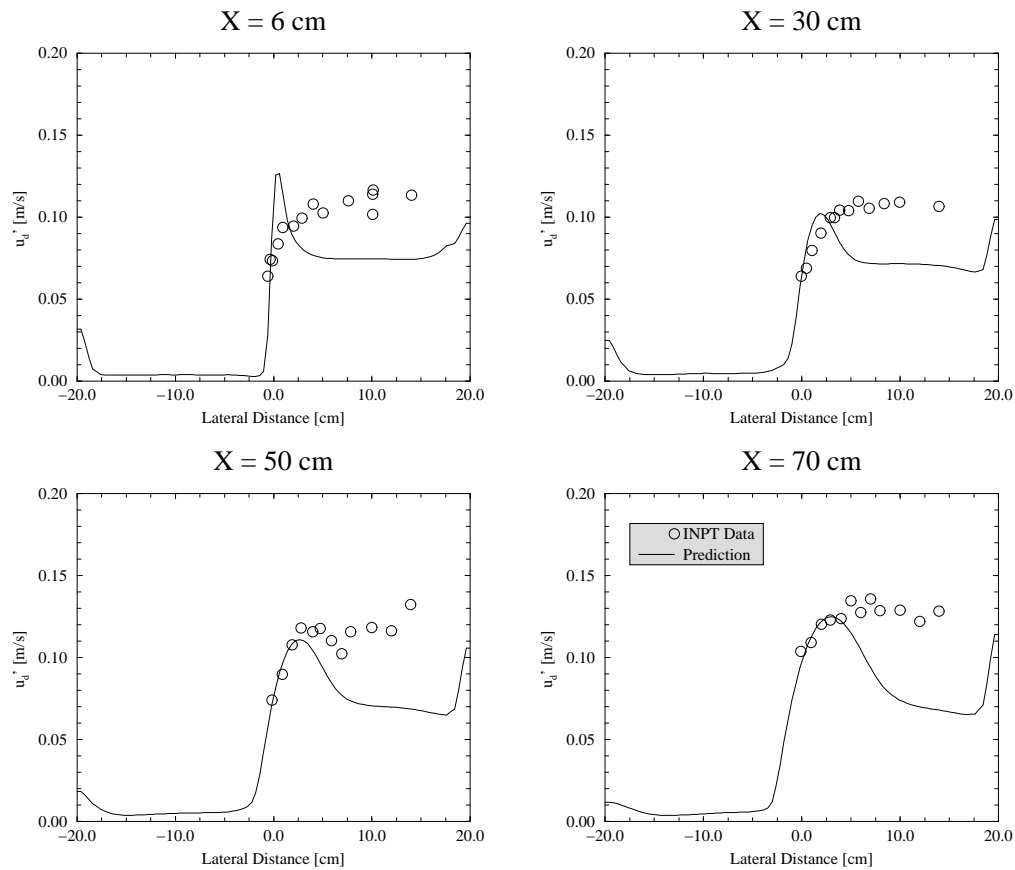
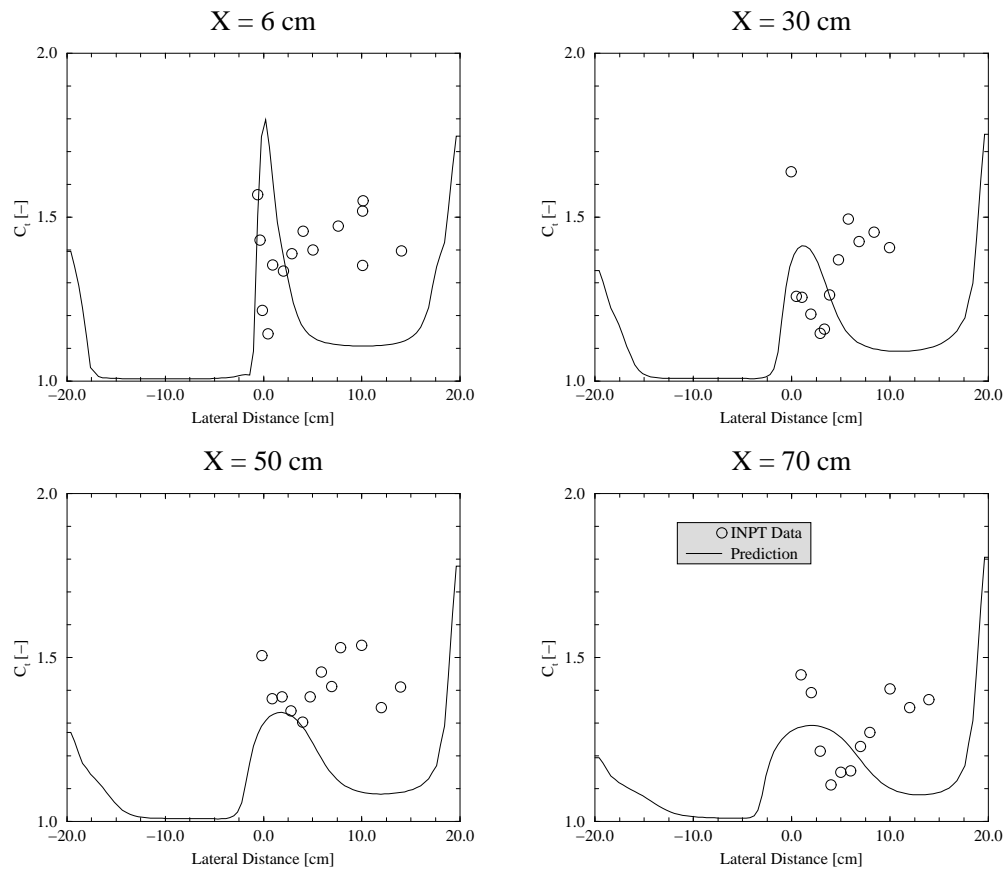


Figure 5.24: Case 2.3 - Dispersed phase axial RMS velocity.

Figure 5.25: Case 2.3 - Axial RMS velocity ratio  $C_t$ .

#### 5.5.4 Case 2.4

The Case 2.4 inlet velocities are 0.58 and 0.2 m/s giving a velocity ratio of 0.34. In this case, air was introduced into the slower stream only at a phase fraction of 1.5%.

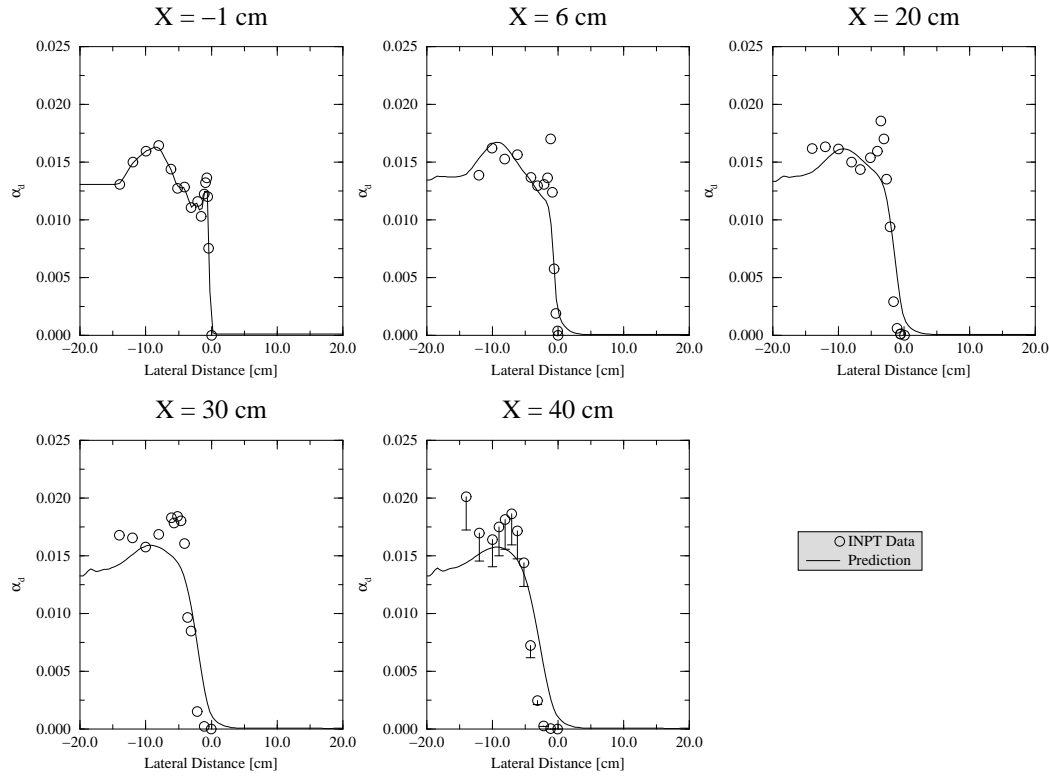


Figure 5.26: Case 2.4 - Dispersed phase fraction.

Figure 5.26 shows the measured and predicted phase fraction distribution for this case. From the latter data it can be seen that there is little lateral dispersion into the high speed side; to the contrary, the bubbles are driven further into the low speed side of the flow as the high speed fluid spreads into this region. This effect is well captured by the predictions.

The experimental data shows some scatter at the slow speed edge of the shear layer but the predictions are in general agreement with the data. The error bars on the phase fraction measurements for the last measuring position indicate the relative magnitude of the reductions required to correct the mass imbalance of the dispersed phase, which is approximately 14.3%. It is only -0.02% for the continuous phase for this case.

Figures 5.27 and 5.28 show the measured and predicted phase mean velocities. Again, the shear layer spreading rate is reasonably well predicted, but some discrepancies in

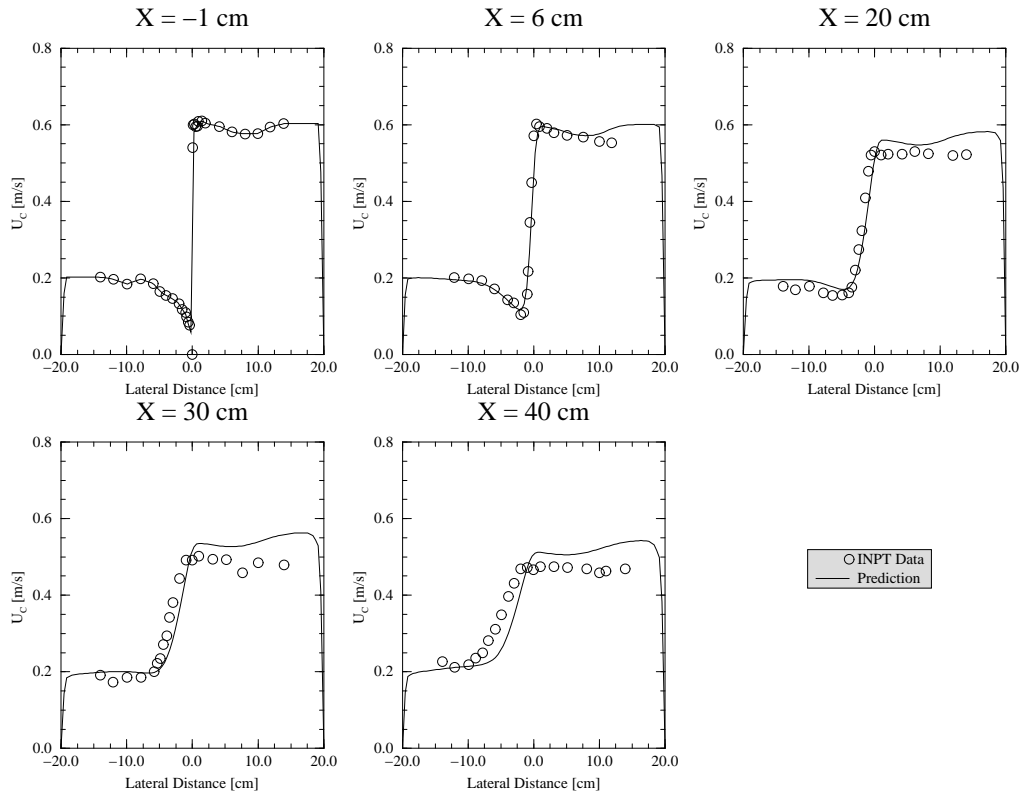


Figure 5.27: Case 2.4 - Continuous phase mean axial velocity.

magnitude are apparent on the high speed side of the flow. The predicted dispersed phase velocities are also reasonably well predicted, although some discrepancy is evident at the  $x = 40$  cm station. The error bars introduced due to the calculated mass imbalance for this case can be seen to extend to beyond the predicted velocity profile. No measurements are available for the dispersed phase in the high speed region since no bubbles are to be found there.

The axial RMS velocity predictions for the continuous phase, shown in Figure 5.29, are very close to the measured values except at the later measuring stations and only then on the low speed side of the flow. The peak in the RMS velocity and its decay rate are well predicted for all stations.

It can be seen from Figure 5.30 that the dispersed phase RMS velocities in the shear layer region are well predicted. This is due to the accurate prediction of the continuous phase RMS velocity and the approximate  $C_t$  magnitude in this region.

Figure 5.31 shows the measured and predicted axial  $C_t$  profiles. Again, there is no strongly defined pattern to the measured values for  $C_t$  with the values scattered somewhat randomly

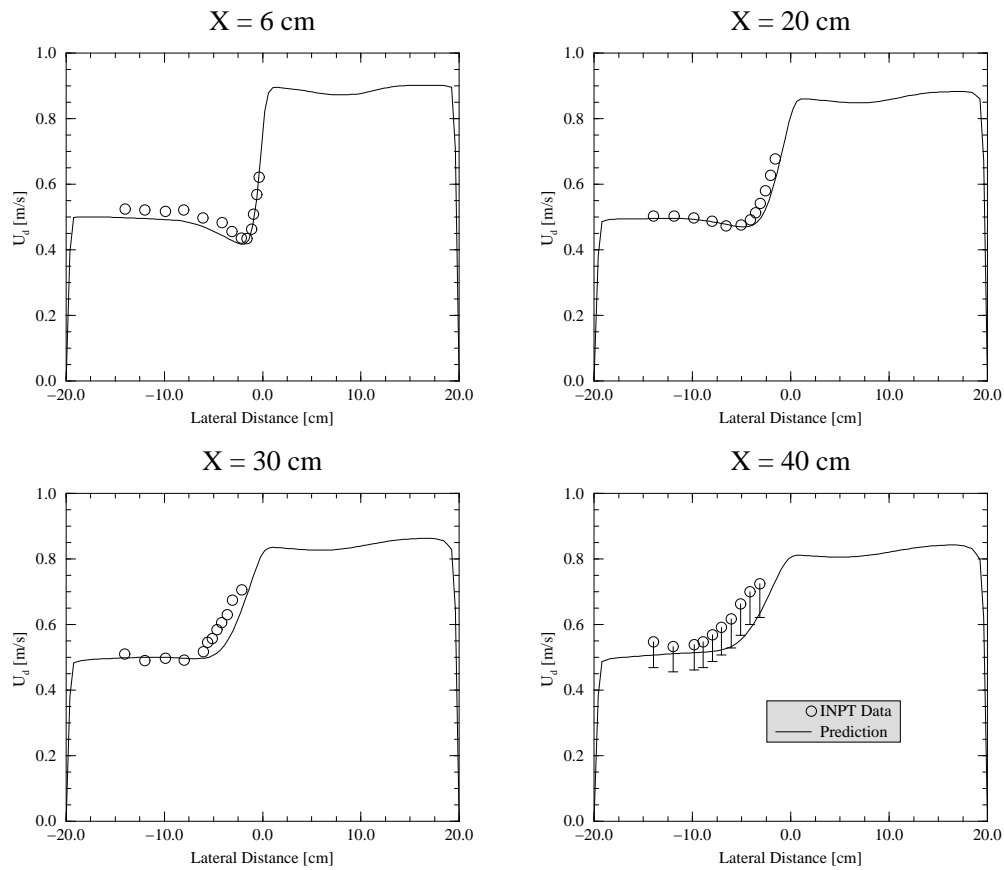


Figure 5.28: Case 2.4 - Dispersed phase mean axial velocity.

around the 1.5 value. The predicted  $C_t$  profiles exhibit a peak within the shear layer which diminishes gradually downstream. The peak value of  $C_t$ , however, has the correct order of magnitude and is in approximate agreement with the mean measured  $C_t$  value of 1.5.

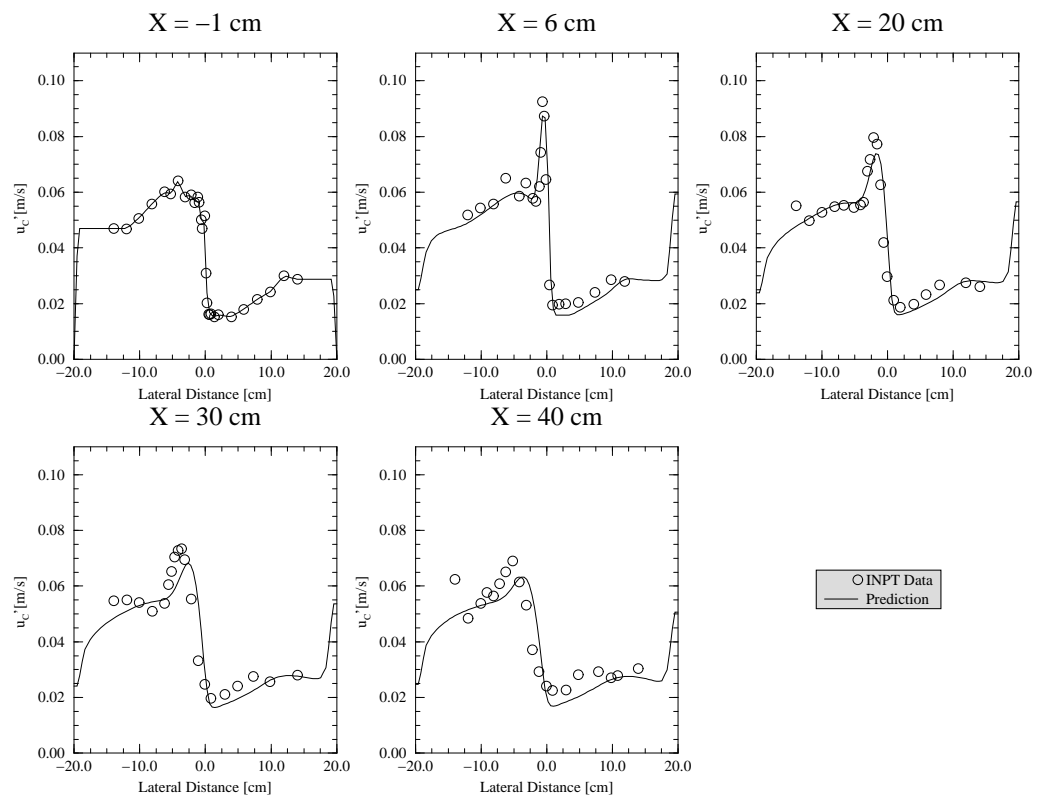


Figure 5.29: Case 2.4 - Continuous phase axial RMS velocity.

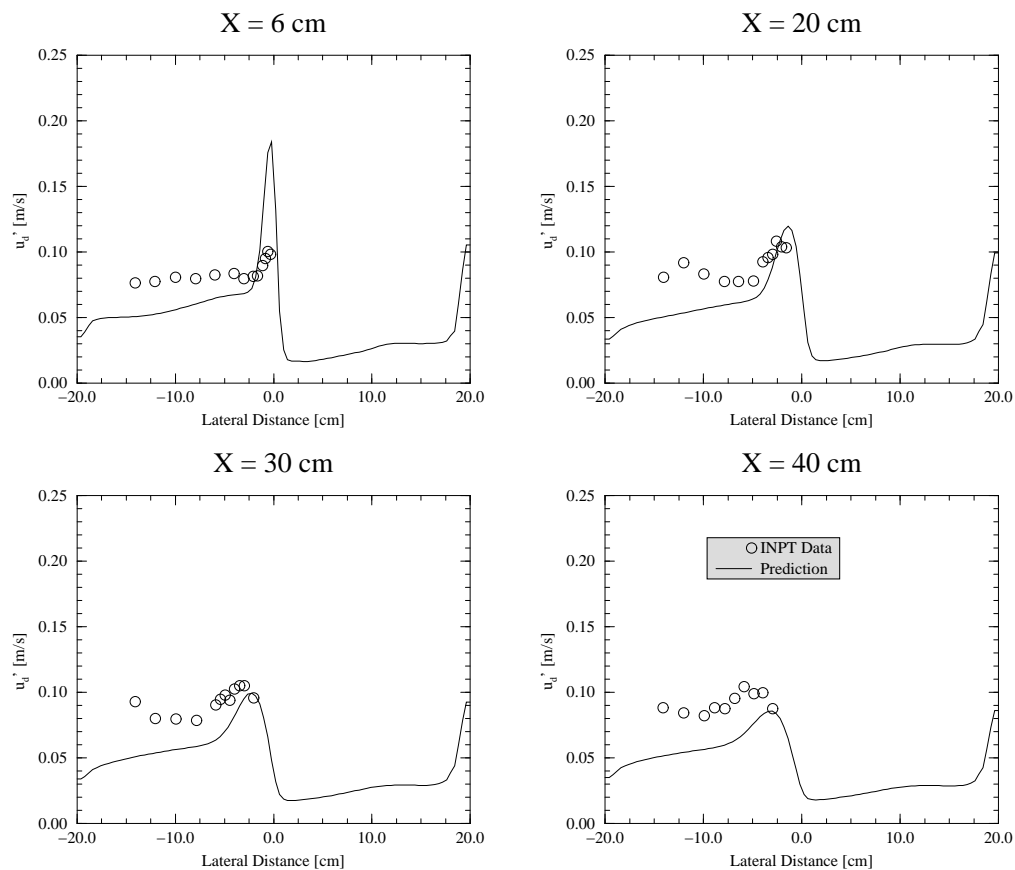
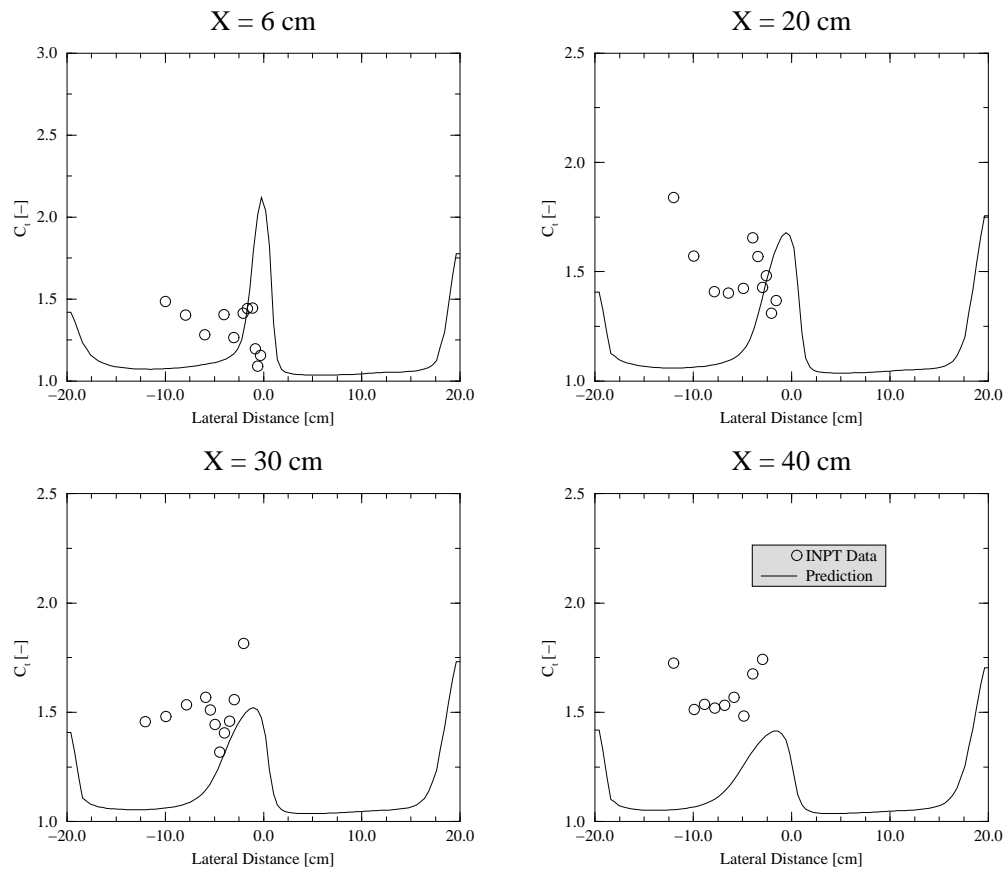


Figure 5.30: Case 2.4 - Dispersed Phase axial RMS velocity.



Figure 5.31: Case 2.4 - Axial RMS velocity ratio  $C_t$ .

### 5.5.5 Case 3.2

The inlet velocities for Case 3.2 were the same in each stream at approximately 0.6 m/s. Since the inlet velocities were equal, no shear layer was generated within the duct, but a trailing wake was produced behind the splitter plate due to the boundary layers formed on it. The air bubbles were introduced into both streams at a phase fraction of 1.8%.

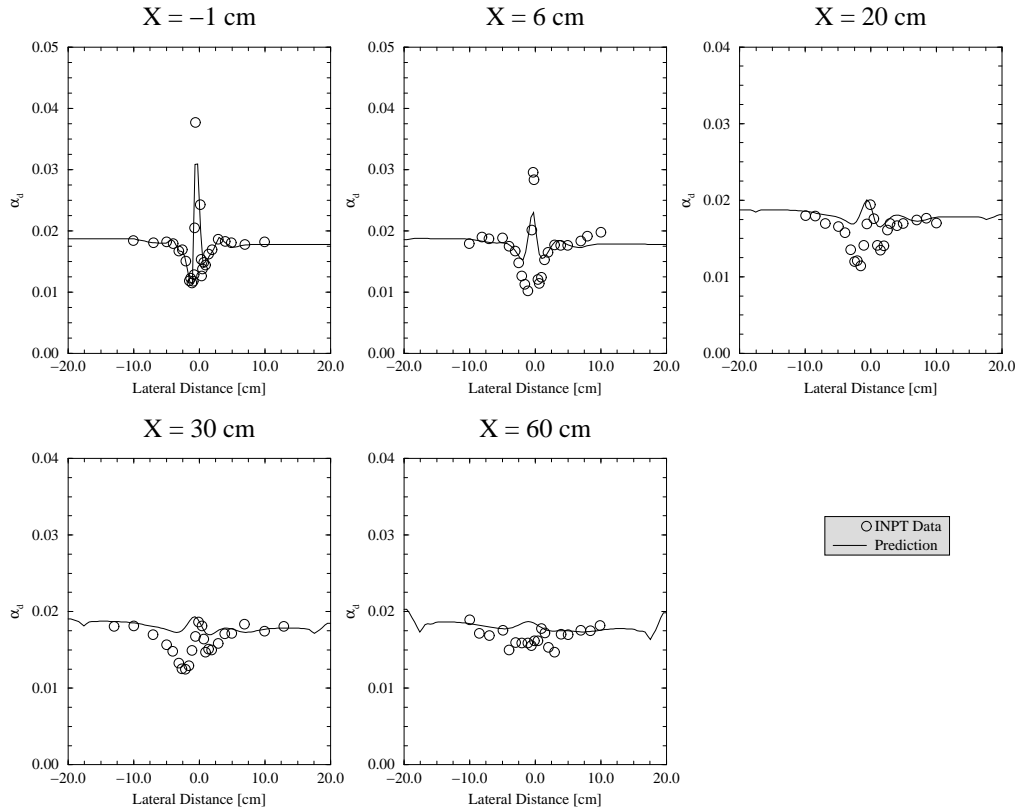


Figure 5.32: Case 3.2 - Dispersed phase fraction.

Figures 5.32, 5.33 and 5.34 shows the dispersed phase fraction, mean axial velocity and axial RMS velocity respectively. The predicted dispersed phase fraction profile is in quite good agreement with the data. The peaks in phase fraction are less pronounced in this case due to the lack of a strong shear layer. The positions and magnitudes of these small peaks are generally well captured by the predictions.

The mean axial velocity is reasonably well predicted except at the last station, where the measured velocity nearest the wall seems to increase. The mass imbalance for the continuous phase is approximately 6.1%. The corresponding error bars bracket the predicted profile except at the outer edges.

The RMS velocity is under-predicted at the later stations. This is consistent with the limi-

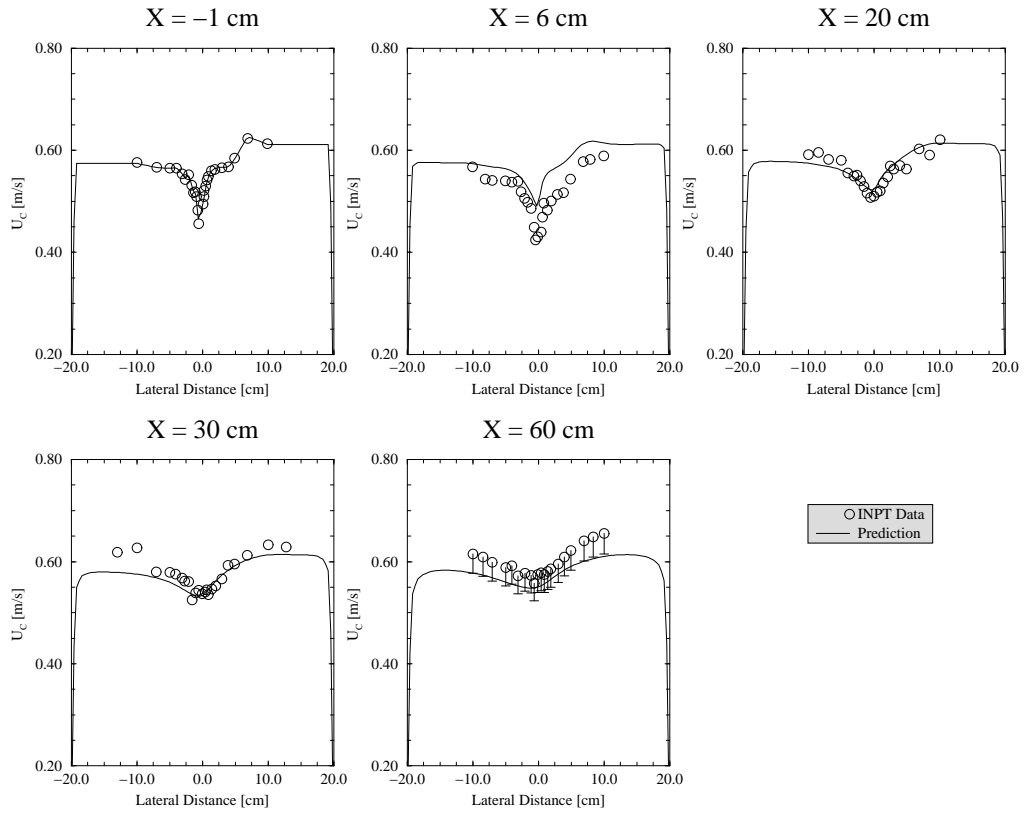


Figure 5.33: Case 3.2 - Continuous phase mean axial velocity.

tations of the  $k-\epsilon$  model which are known to exist in wake flows such as this [72]. However, the experimental data shows an unexpected rise in the turbulence level downstream. The predicted RMS velocity values do not exhibit this behaviour.

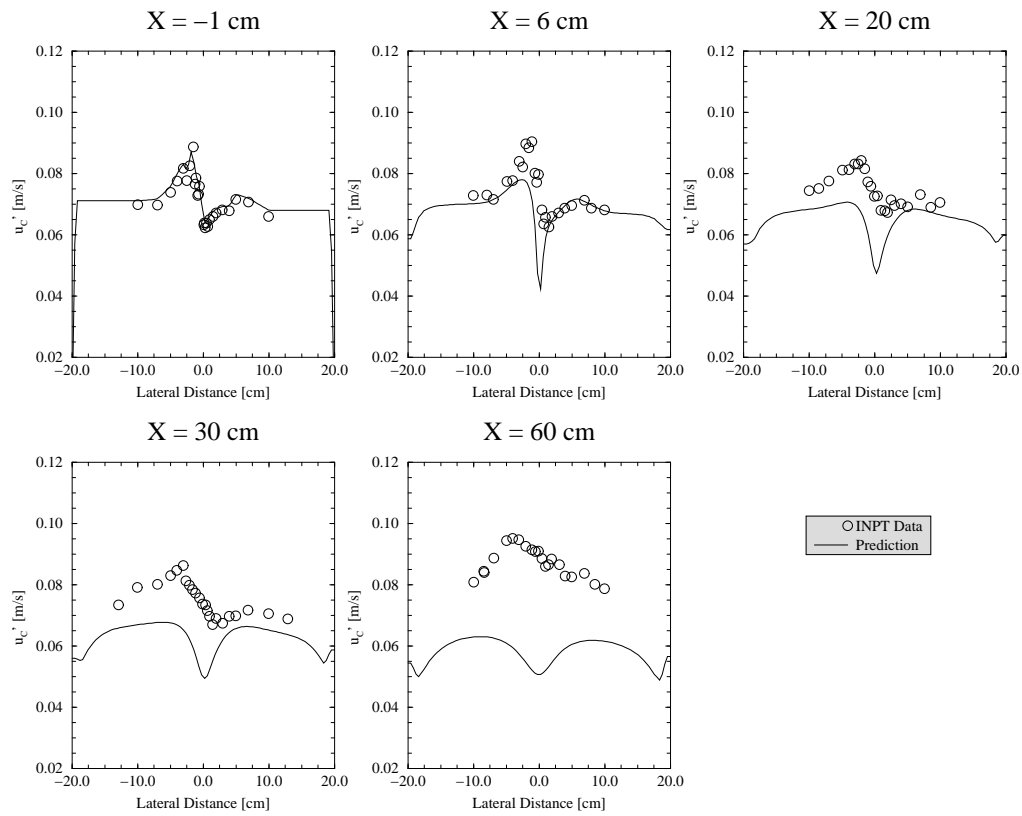


Figure 5.34: Case 3.2 - Continuous phase axial RMS velocity.

### 5.5.6 Mesh Sensitivity Tests

To assess the sensitivity of the results on the computational mesh size, the two-phase calculations were repeated on meshes of three different sizes as shown in Table 5.3. Figure 5.35 shows the resulting profiles of dispersed phase fraction and continuous phase velocity at the  $x = 60$  cm position for Case 1.2.

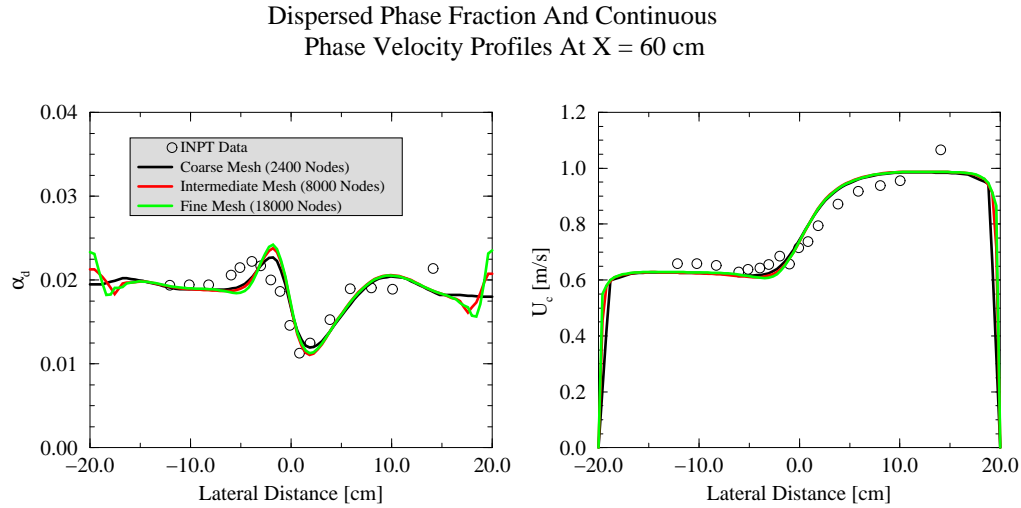


Figure 5.35: Effect of mesh size on  $\alpha_d$  and  $U_c$  predictions at  $x = 60$  cm (Case 1.2).

It is readily apparent that, despite the large differences in the total number of cells in each mesh, the results are very similar. The dispersed phase fraction profile shows some discrepancy in the centre of the duct, especially at the apex of the peak. Here, a maximum difference of approximately 10 % between the coarse and fine meshes is apparent. The predictions for the mean continuous phase velocity in this region show negligible differences.

Larger discrepancies are apparent near the wall in both the phase fraction and mean velocity profiles. The coarse mesh does not resolve any of the details of the boundary layer adjacent to the wall; the zero-gradient boundary condition applied to the phase fraction leads to the flat profile in this region while the no-slip condition applied to the phase velocity results in the steep linear profile from the node nearest to the wall to the wall itself.

As the finer meshes start to resolve the boundary layer, the differences between the profiles become more apparent. The finer meshes show an increase in the phase fraction adjacent

to the wall which is due to the influence of lift forces in this region forcing the bubbles towards the wall [132, 133, 55]. The increase in phase fraction at the wall results in a depletion of bubbles in the adjacent region. The mean velocity profiles in the near-wall region show some differences as the finer meshes start to resolve the boundary layer.

## 5.6 Two-Phase Turbulence Model Performance

In order to assess the performance of the two-phase turbulence model, the simulation of Case 1.2 was repeated without the extra two-phase terms in the  $k$  and  $\epsilon$  equations, reducing the turbulence model to (essentially) the single-phase form. The resulting profiles for the continuous and dispersed phase RMS velocities, and the resulting value of  $C_t$ , are shown in Figures 5.36, 5.37 and 5.38. In these figures, the single-phase model predictions are shown by the dotted lines while the full two-phase model predictions are depicted by the solid lines.

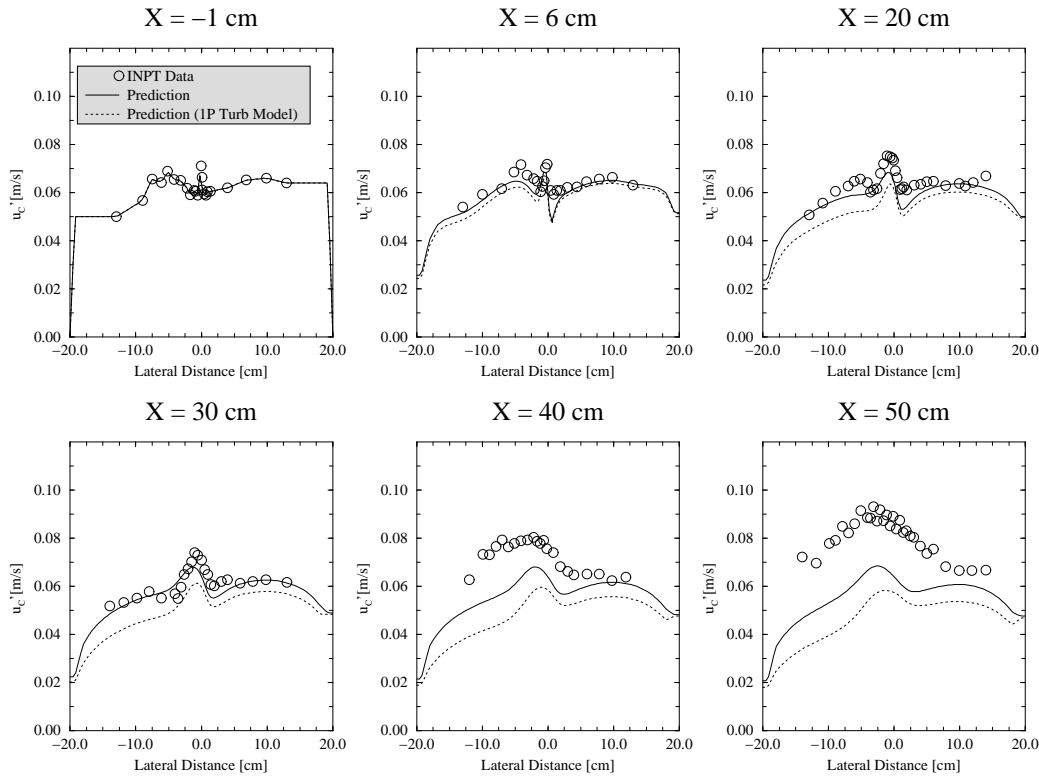


Figure 5.36: Turbulence model comparison for continuous phase RMS velocity predictions (Case 1.2).

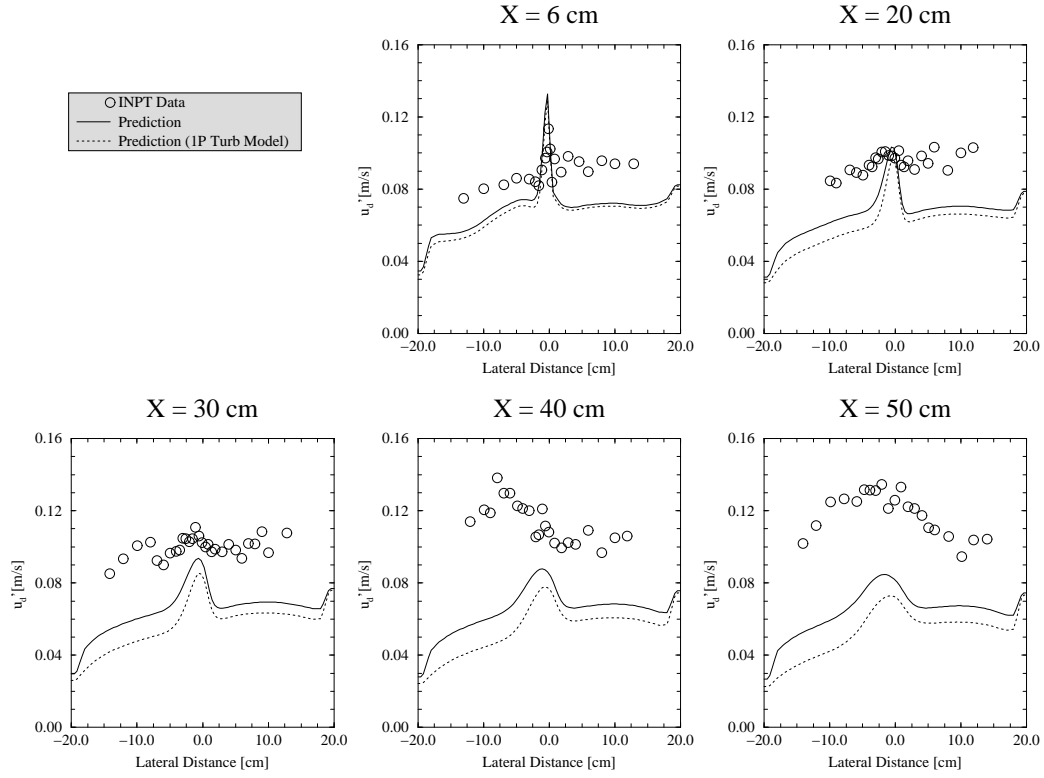


Figure 5.37: Turbulence model comparison for dispersed phase RMS velocity predictions (Case 1.2).

From Figure 5.36 it is obvious that the single-phase model predicts lower turbulence levels than the two-phase version. At the  $x = 50$  cm position, the RMS velocity predicted by the single-phase model is about 20% lower than the two-phase model across the width of the duct. The root of this behaviour lies in the drag related turbulence generation term in the  $k$  equation (Eqn (2.89)). This term represents the generation of turbulence due to the relative motion of the dispersed phase. For the present case, where there is a large relative velocity, caused by the large density difference between the phases, and a relatively high bubble size, the drag induced turbulence is significant. Despite the increased turbulence levels predicted by the two-phase model, the experimental data shows an even larger turbulence level.

The predicted response coefficient  $C_t$ , as shown in Figure 5.38, shows that the lower RMS velocity predicted by the single-phase model leads to lower values for  $C_t$ , which lead to correspondingly lower values for the dispersed phase RMS velocity, as shown in Figure 5.37. Again, despite the two-phase model predictions being significantly higher than those of the single-phase model, the experimental data shows higher RMS velocity values than

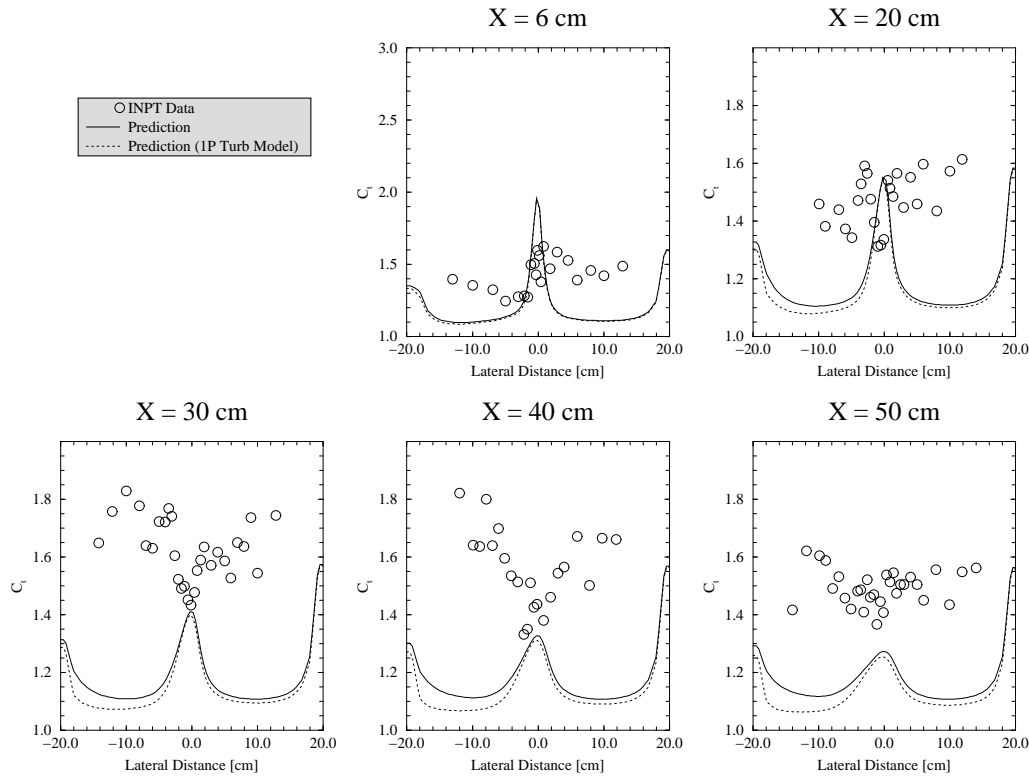


Figure 5.38: Turbulence model comparison for  $C_t$  predictions (Case 1.2).

those predicted.

It is clear that the drag-induced turbulence generation term in the two-phase turbulence model represents an important mechanism for the generation of turbulence in this case. The under-prediction of the turbulence level may imply that there is another turbulence generation mechanism at play which is not captured by the model, or that the drag-induced effect is under-predicted by the present model and needs to be modified to increase its relative effect.

In the present case, the prediction of the lateral phase distribution across the duct is not sensitive to the turbulence predictions, the dominant mechanism for lateral phase distribution being the lift forces. The effects of the different turbulence predictions on the phase fraction predictions are therefore negligible.



Calculation	Under-relaxation Factors		Iterations to Convergence	
	$\lambda_U$	$\lambda_{F_d}$	Without Sub-Iter.	With Sub-Iter.
A	0.5	0.7	426	426
B	0.6	0.7	$\infty$	314
C	0.7	0.7	$\infty$	300
D	0.7	0.3	-	$\infty$
E	0.7	0.5	-	$\infty$
F	0.7	0.7	-	300
G	0.7	0.8	-	300
H	0.7 (0.5)	0.7	311	310
I	0.7 (0.6)	0.7	$\infty$	305

Table 5.5: Iterations to convergence with and without sub-iterative correction to drag factor (Case 1.2).

## 5.7 Solution Algorithm Performance

The present case, involving large phase density differences and relatively large bubble sizes, provides a challenging case with which to analyse the performance of the solution algorithm described in Section 4.5.2. Of particular interest is the effect of the sub-iterative calculation of the drag coefficient (Section 4.5.2.1) on the stability of the solution. To this end, the calculations for Case 1.2 were repeated at various under-relaxation factors with and without the sub-iterative calculation of the drag coefficient. Table 5.5 shows the under-relaxation factors used in the phase momentum equations  $\lambda_U$  and the drag factor in the sub-iterative solution  $\lambda_{F_d}$  and the number of iterations to convergence for each case. The symbol  $\infty$  denotes solution divergence or no convergence.

Cases A, B and C examine the effect of the sub-iterative technique on the stability of the solution at increasing values of phase momentum equation under-relaxation factors. It can be seen that, while convergence can be obtained using relatively low under-relaxation factors without the sub-iterative technique, at higher under-relaxation factors its effect is marked and its use is essential if convergence is to be obtained. Furthermore, at higher under-relaxation factors, convergence is obtained in fewer iterations.

For example, for  $\lambda_{F_d} = 0.7$ , the required number of iterations is reduced by more than 30% compared to the solution at  $\lambda_{F_d} = 0.5$ . It should be noted, however, that using the sub-iterative technique makes each iteration more computationally expensive, so that the

net reduction in the computing time is reduced by only about 10%. Figures 5.39 and 5.40 show the history of the normalised residuals for calculation C both with and without the sub-iterative solution.

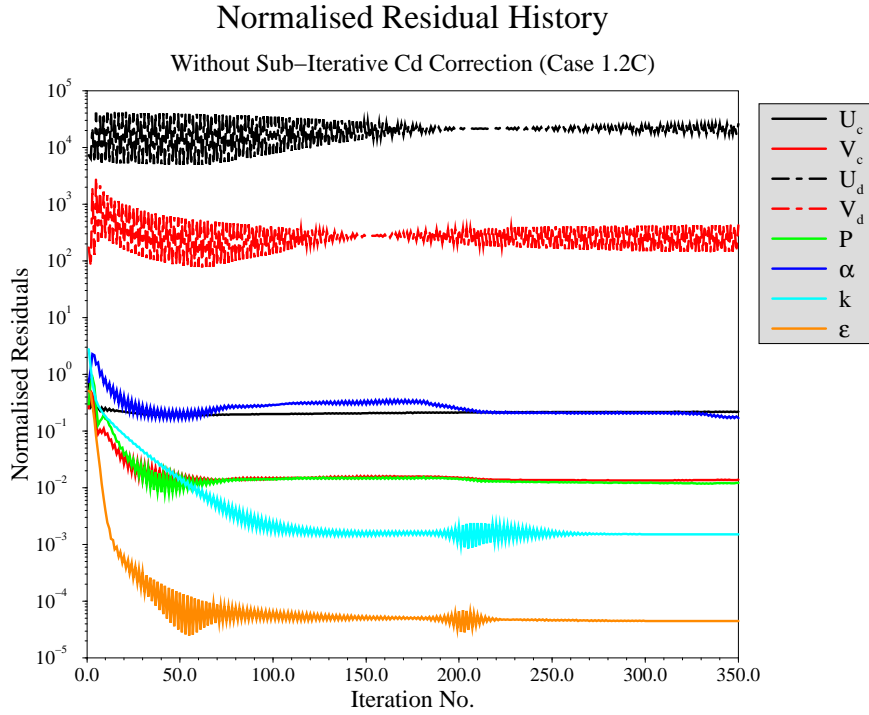


Figure 5.39: Residual history without using the sub-iterative technique (Case 1.2C).

The third column in Table 5.5 gives the values for  $\lambda_{F_d}$ ; the under-relaxation factor applied to the calculated drag force after its sub-iterative calculation (see Section 4.5.2.1). Calculations D to G show the affect of this parameter on the solution for fixed values of  $\lambda_U$ . Too low a value negates the effectiveness of the technique, effectively throwing away the improvements to the calculated drag coefficient, leading to the instability evident in the cases which do not use the sub-iterative technique. Values above about 0.7 do not produce any improvement in the stability or rate of convergence, although values too close to unity start to produce instability for the reasons discussed in Section 4.5.2.1.

Since the present case is a steady-state flow, the proposal of Wang [134] to use separate under-relaxation factors for the continuous and dispersed phase momentum equations may be employed. Cases H and I examine the use of a lower under-relaxation factor for the dispersed phase. The under-relaxation factor used for the dispersed phase is shown in

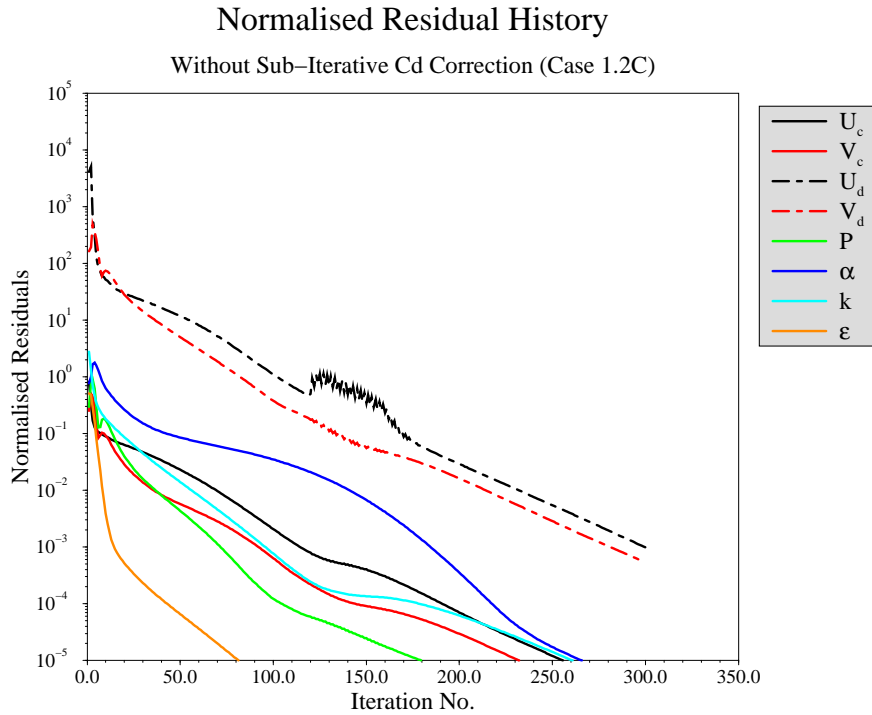


Figure 5.40: Residual history using the sub-iterative technique (Case 1.2C).

parentheses. The continuous phase under-relaxation factor is 0.7 in both cases. It can be seen that this technique is very effective in this case and solutions can be obtained at higher continuous phase under-relaxation factors. For case H, the use of the sub-iterative technique produces negligible benefit in relation to the number of iterations, and is actually more expensive computationally.

It is apparent that the sub-iterative technique is effective in increasing the stability of the solution at higher under-relaxation factors. In the present case, however, where convergence may be obtained by using lower under-relaxation factors (at least for the dispersed phase) its use may produce a reduction in the efficiency of the solution and its usefulness is questionable. The main benefit of the technique lies in the fact that it is applicable to the transient case and that it can be employed to reduce the sensitivity to the under-relaxation factors specified by the user.

## 5.8 Discussion And Conclusions

The predictions of the single- and two-phase bubbly flow in a plane shear layer have been found to be in generally good agreement with the experimental data of Roig [56]. In particular, the phase fraction distribution, phasic mean velocities and shear layer spreading rate have been found to be well predicted.

The two-phase shear layer spreading rate is found to be much higher than that of the corresponding single-phase flow at the same velocity ratio due to the influence of inter-phase momentum transfer and phase redistribution. For example, Cases 2.1 and 2.2, both with a velocity ratio  $U_2/U_1$  of approximately 0.42, show that the two-phase shear layer spreads twice as fast as the single-phase shear layer. The predictions of the shear layer spreading rate for both single and two-phase flows are in good agreement with the data despite the different mechanisms involved.

Continuous phase RMS velocity predictions have been found to be somewhat lower than the measurements indicate for both the single and two-phase cases. Maximum discrepancies are of the order of 10% for the majority of cases (i.e. those involving higher shear rates). Exceptions are the wake flows, Cases 3.1 and 3.2, and Case 1.1 which show discrepancies of up to 60%.

The reasons for these large discrepancies may be due to one of the following reasons.

- Inappropriate inlet conditions for the  $k$  or  $\epsilon$  equations.
- The standard  $k - \epsilon$  turbulence model (i.e. with the standard coefficients) may not be suitable for the accurate prediction of the turbulent kinetic energy or its dissipation rate in free shear layers with low shear rates [72].
- The assumption required for the extraction of the axial RMS velocity component from the turbulent kinetic energy is incorrect.
- Experimental uncertainties.

Assuming that the measurements for the liquid phase axial RMS velocity are accurate, it is likely that any discrepancies attributable to inappropriate inlet profiles for  $k$  and  $\epsilon$  would stem from the assumptions which were made in their estimation. To test the sensitivity of the solutions to the inlet condition for  $\epsilon$ , the  $\kappa y$  distribution (Eqn (5.4)) and the Nikuradse formula (Eqn (5.5)) were tested individually. These two equations produce quite different mixing length profiles across the inlet region. In particular, using a  $\kappa y$  distribution over the entire inlet region leads to flat mixing length profile in the central fully developed region, leading to a higher  $\epsilon$  in this region.

It was found that adopting either of these two profiles for  $l_m$  did not make any significant difference to the axial RMS velocity predictions. The higher  $\epsilon$  given by the  $\kappa y$  distribution increases the axial RMS velocity discrepancies slightly, implying that the use of Nikuradse's mixing length formula is more appropriate in this region.

On the other hand, adoption of Nikuradse's mixing length formula across the whole inlet plane (i.e. within the boundary layers as well as across the central region) lead to discrepancies in the shear layer spreading rate. It is known that the boundary layers at the origin of the shear layer affect the spreading rate significantly [130] so it is important that the mixing length distribution in this region is taken into account, especially since the boundary layers have a significant thickness due to the concentration of bubbles near the wall.

In any case, it was found that the turbulent energy dissipation rate within the shear layer becomes essentially independent of the inlet conditions after a short axial distance. Axial RMS velocity predictions beyond this distance are therefore insensitive to the  $\epsilon$  inlet condition even though the initial development of the shear layer is sensitive. For these reasons it was concluded that the  $k$  and  $\epsilon$  inlet conditions applied (i.e. a combination of Nikuradse in the free stream region and  $\kappa - y$  within the boundary layers) are appropriate and lead to the correct prediction of the shear layer spreading rate.

Turning to the second point, it is known that the performance of the standard  $k\epsilon$  turbulence model is poor in flows with weak shear (i.e. wake flows and far-field shear flows) [72]. In this case, the  $C_\mu$  coefficient (Eqn (2.73)) is not constant and is a function of the local average turbulence production/dissipation ratio, so that  $C_\mu = f(\overline{P}/\epsilon)$ . Although a function has been proposed which takes into account this dependence, it has not been applied here due to its lack of generality.

In addition, it is likely that the assumption that the axial RMS velocity is twice that of the lateral and transverse components (Eqn (5.2)) is not universal. In the predictions, this assumption has been adopted both for the estimation of the inlet  $k$  profile (using the measured values of the axial RMS velocities) and the extraction of the axial RMS velocity from the predicted  $k$  profiles at the downstream measuring positions. It is open to question whether the same ratio applies along the entire length of the duct.

Single-phase experimental shear layer data by Wygnanski and Fiedler [124] indicate that the axial component is only approximately 30-40% higher than the other components within the shear layer itself. In fully developed single-phase boundary layers, such as those on the splitter plate, the axial component is found to be approximately 25% higher than the transverse component and approximately 50% higher than the lateral component [135].

Similarly, Leuchter [136] performed a turbulent free shear layer calculation using the  $k - \epsilon$  turbulence model but had to resort to a ‘pseudo’ Reynolds stress turbulence model to get reasonable comparisons with the measured RMS velocity values. In his work, a Reynolds stress turbulence model, de-coupled from the flow, was used to calculate the local normal stress components which were then used to extract the RMS velocity components from  $k$ . Presumably this technique was successful due to the prediction of the local variations in the RMS velocity component ratio.

The presence of local changes in the proportionality between the RMS velocity components of the turbulent kinetic energy has not been taken into account. Further, since the effects of a dispersed phase on the anisotropy of the turbulence in the boundary layers and within the shear layer is unknown, it may not be appropriate to adopt data relating to single-phase flows for different parts of the flow. The adoption of Wygnanski and Fiedler’s ratio of 30-40% higher axial RMS velocities, for instance, would result in larger discrepancies than those shown in the predictions based on 50% higher velocities.

The steady increase in the measured axial RMS velocity component along the shear layer seen in the majority of cases (both single and two-phase) implies either that the flow is becoming increasingly anisotropic or that some other turbulence generation mechanism is at play. Given the complicated nature of the flow within the shear layer and the possibility of wall effects, vortex pairing, etc. , and the inherent difficulty in performing accurate measurements in bubbly two-phase flow, it is difficult to be certain as to the cause of this increase.

In conclusion, it may be that the discrepancies in the RMS velocity predictions are due to the combined effects of the inapplicability of the standard  $k - \epsilon$  model in weakly shearing flow regions, and the assumptions needed to extract and derive the axial RMS velocity data from  $k$ . To draw definitive conclusions, one would need experimental measurements for all normal stress components and their variation along the shear layer.

Turning to two-phase flow specific issues, it is clear that the accurate prediction of the phasic mean velocities and the phase fraction distribution for this case depends largely on the modelling of the drag and lift forces. It is apparent that the use of the drag coefficient derived from single bubble terminal velocity data has enabled the accurate prediction, within experimental uncertainty, of the dispersed phase mean velocity. The validity of this practice is probably restricted to the low phase fraction case but could be indicative of the unimportance of the continuous phase turbulence on the drag force.

Similarly, the incorporation of the lateral lift forces is important for the accurate prediction of the phase distribution. Assuming a lift coefficient  $C_l$  of 0.25 has been shown to lead to reasonable results for this case. However, as shown in the two-phase backward-facing

step flow studied by Wang [134], the assumption of a global lift coefficient may not always give an accurate representation of the lift forces. The findings of Wang *et al.* [55] that the lift force coefficient is a function of local parameters such as the phase fraction, velocity gradient, etc. , needs to be examined further if a general lift force model is to be obtained and empirical input to the model is to be minimised. Also, the general validity of the presently-used lift and virtual mass models in turbulent flows needs to be verified by application to a wide variety of flow configurations.

An order of magnitude analysis reveals that the dispersed phase Reynolds stresses are of secondary importance compared to the inter-phase drag and lift forces for this case. Consequently the  $C_t$  parameter does not have any significant influence, except in the extraction of the dispersed phase RMS velocity component. The adopted  $C_t$  model displayed a peak within the shear layer due to the high RMS velocity and small turbulence length scale there. Despite the fact that the experimental  $C_t$  data shows a large amount of scatter, the predicted value for  $C_t$  within the shear layer (i.e. at the peak) was of the correct order of magnitude, with an approximate value of 1.5.

Importantly, it should be also be noted that all cases display significant experimental RMS velocity values for the dispersed phase outside the shear layer which leads to relatively high  $C_t$  values in this region. It is proposed here that one reason for the scatter in the  $C_t$  distribution may be due to the existence of a distribution of bubble sizes within the flow. The measurement of the bubble RMS velocity will include bubble velocity differences due to their different sizes and hence velocities. This ‘apparent’ RMS velocity is *not* due to the turbulence in the continuous phase.

In these experiments, the bubble size measurements indicate that the bubbles have a diameter of approximately  $2 \pm 0.5$  mm and it has been shown that the mean slip velocity of the bubbles is essentially the same as that of a single bubble in a quiescent fluid. The apparent RMS velocity from such a distribution may be quantified by considering the apparent RMS velocity displayed by a distribution of bubbles rising at their terminal velocity in a quiescent fluid. By using an expression for the terminal velocity as a function of bubble size it is possible to calculate the apparent RMS and mean velocity due to the range of bubble sizes — see Appendix F. In particular, Section F.1 shows that this apparent RMS velocity is approximately 0.085 m/s which implies a turbulence intensity of 24% (!) based on the mean terminal velocity, and between 9 and 19% based on the absolute velocity of the dispersed phase in the INPT shear layer case.

Examination of the INPT data shows that the dispersed phase RMS velocity is between 0.085 and 0.15 m/s. This implies that the RMS velocity measurements are dominated by the apparent RMS velocity due to the bubble size distribution. This may also explain why

the dispersed phase RMS velocity is large outside the shear layer since the bubble size distribution is essentially uniform across the duct.

It is evident that this case is not suitable for the validation of the proposed two-phase turbulence model alone, and in particular, the  $C_t$  model, due to the dominant influence of the lift force, the bubble size distribution effects and the lack of lateral and transverse RMS velocity measurements. Despite these limitations, however, it is evident that the two-phase model in its current form is able to predict some of the important features of the flow, such as the lateral phase distribution and the shear layer spreading rate with a reasonable degree of accuracy.



## Chapter 6

# Droplet Break-up In A Co-axial Pipemixer Device

The second of the validation cases applies the two-phase flow model coupled with the variable droplet size framework to the inertial break-up of oil droplets within an in-line pipe-mixer device. The influence of surfactants and droplet viscosity on the droplet break-up characteristics are examined closely. Predictions for the mean droplet size and dispersed phase fraction at various positions within the pipe-mixer are compared against the experimental data of Janssen *et al.* [137, 138, 139] and shows that the model captures the essential features of the flow and gives good agreement with the data.

### 6.1 Introduction

The variable droplet size framework described in Chapter 3, when coupled with the two-phase flow model, represents a powerful tool for the prediction and simulation of engineering two-phase flows involving break-up and coalescence effects. However, the system requires extensive validation before it can be applied with confidence to the many engineering problems of interest.

The validation of such a complex system is best accomplished where possible by the independent validation of each of the component parts. In reality this means choosing validation cases which depend heavily on the component of interest while minimising the influence of the rest of the system.

The previous chapter dealt with the basic transport and turbulence properties of the two-phase system; break-up and coalescence effects did not feature in that case because of the

relatively low turbulence levels and the low phase fraction. In this case, we consider the break-up of oil droplets within an in-line pipe-mixer device. The simple geometry of this device, and the relatively high density of the dispersed phase, means that transport effects due to interfacial forces like drag and lift do not dominate. This allows us to concentrate on the behaviour of the variable droplet size framework and, in particular, the inertial break-up model as described in Sections 3.3.2.2 and 3.3.3.2.

The pipe-mixer device essentially consists of two co-axial fluid streams with different velocities which are brought together within a tube. A region of high turbulence is formed at the confluence of the streams due to the high shear rate. Typically, one of the streams is carrying a dispersed droplet phase. The high turbulence level causes the droplets to break-up and disperse forming a two-phase emulsion. Figure 6.1 shows a schematic view of the pipe-mixer device.

The co-axial pipe-mixer has many advantages in the study of the break-up of droplets. Apart from being a widely-used piece of process equipment in its own right, the pipe-mixer has the advantages of being physically small, with a relatively simple and well defined geometry. Importantly, the geometry is axisymmetric, allowing the simulation to be carried out in two dimensions giving faster model development/validation cycles.

The advantages of the pipe-mixer have long been recognised by workers trying to provide quality two-phase data specifically for the validation of two-phase CFD codes. In particular, a series of experiments using a co-axial pipe-mixer device has been performed by researchers at Unilever under the auspices of BRITE/EURAM project BE 4098 (of which the research in this thesis forms a part). These experiments were based on the emulsification of oil droplets within a vertical pipe-mixer device constructed from Perspex. These experiments were intended to yield measurements for the local mean droplet size and the local dispersed phase fraction at various positions downstream of the pipe-mixer inlet region.

One of the most detailed of these studies, and the one most relevant to the present research, was performed by Janssen, Boon and Agterof [137, 138, 139]. The experiments of Janssen *et al.* were focused on the inertial break-up of a dispersed oil phase within a continuous water phase. Of particular interest to them was the influence of different surfactant concentrations and different droplet viscosities on the break-up characteristics.

In all, Janssen *et al.* performed a series of thirteen experiments, involving five different surfactant concentrations (including surfactant-free ‘clean’ cases), with two outer stream velocities, and three different droplet viscosities. LDA techniques were used to measure the velocity and turbulence characteristics of the flow, while an isokinetic sampling technique was used to measure the local mean droplet diameter and the dispersed phase fraction.

This chapter contains detailed comparison between the data of Janssen, Boon and Agterof [138] and the predictions of the two-phase flow model coupled with the variable droplet size framework as described in Chapters 2 and 3. This validation exercise is essentially the first full test of the surfactant influenced inertial break-up model of Chesters [94], and the first detailed test of the variable droplet size framework coupled directly to a two-fluid model.

The next section describes in some detail the experiments performed by Janssen *et al.* The properties of the pipe-mixer device and the experimental techniques used are first discussed followed by a summary of all of the flow conditions considered.

Section 6.3 then goes on to describe the calculations themselves. This is followed in Section 6.4 by a detailed comparison between the predictions and the experimental data. Finally, in Section 6.5, the overall performance of the model is assessed.

## 6.2 The Unilever Experiments

### 6.2.1 The Coaxial Pipe-Mixer Device

The Unilever pipe-mixer device, shown in Figure 6.1, brings two coaxial streams with differing velocities together within a long vertical perspex tube. The higher velocity stream enters through a central nozzle while the slower stream enters via the annular region between the nozzle and the pipe wall. Because of the appreciable difference in the velocities of the two streams, a region of high turbulence is produced when they stream meet due to the high shear rate. The transparent pipe-mixer body allows the flow characteristics to be studied via Laser Doppler Anemometry (LDA) and by local sampling.

An inlet assembly houses the central nozzle and the annular inlet region. This assembly sits atop the main pipe-mixer tube which has a inside diameter of 10 mm and is approximately 1 m in length. The pipe-mixer tube is constructed from multiple perspex sections approximately 8 cm in length, clamped together. The annulus stream is fed by two 4.6 mm diameter pipes positioned diametrically with respect to the pipe-mixer axis. The inner diameter of the nozzle at exit is 2.75 mm.

The flow rates of the central nozzle and annular inlet streams may be independently controlled to introduce a specific velocity difference between the two streams at the inlet to the pipe-mixer tube. For the cases relevant to this validation study, the mean velocity of the annulus stream at the entrance to the tube was 2.5 m/s while the mean velocity of the central nozzle stream at the nozzle exit was 6 m/s or 15 m/s, according to the case.

For the two-phase cases, a dispersed phase was introduced into the central nozzle inlet

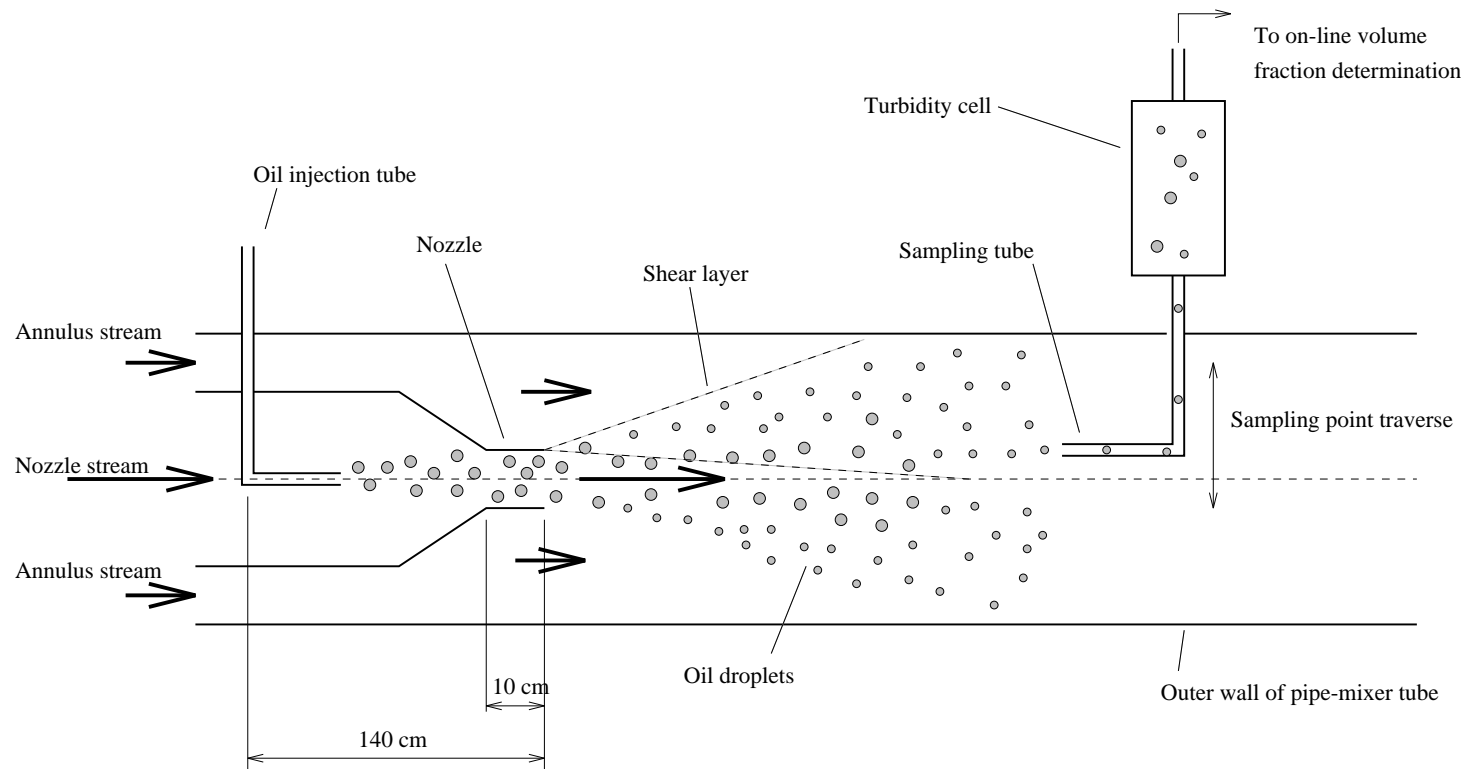


Figure 6.1: Schematic arrangement of the Unilever co-axial pipe-mixer device.

stream via an injection tube 1.35 mm in diameter. Local sampling of the two-phase flow was accomplished via a 1 mm sampling tube positioned at various axial and radial positions. A modified Fraunhofer technique and a centrifugal technique were used to determine the local mean diameter and phase fraction within the flow. More details of these techniques are discussed below when the two-phase cases studied by Janssen *et al.* are described.

### 6.2.2 Single-Phase Experiments

In order to fully understand the fundamental flow characteristics of the pipe-mixer device, Janssen, Boon and Agterof performed a series of single-phase experiments for a range of velocity ratios and for two nozzle sizes to provide detailed Laser Doppler Anemometry (LDA) mean velocity and turbulent kinetic energy data within the pipe-mixer [137, 139]. These data are extremely useful for the validation of the two-phase model since they can be used to provide important information on the underlying performance of the single-phase flow and turbulence predictions. In addition, since the two-phase experiments of Janssen *et al.* provide only local phase fraction and mean droplet diameter data, the single-phase data are used, after making some assumptions, to infer the required inlet conditions for the two-phase calculations.

For each velocity ratio, two sets of data are provided, each relating to a particular measurement plane as shown in Figure 6.2. The orientation of the two planes were defined with respect to the two feed tubes which feed the annulus inlet region. These measurements were made to check for any asymmetry introduced into the flow by the inlet tubes.

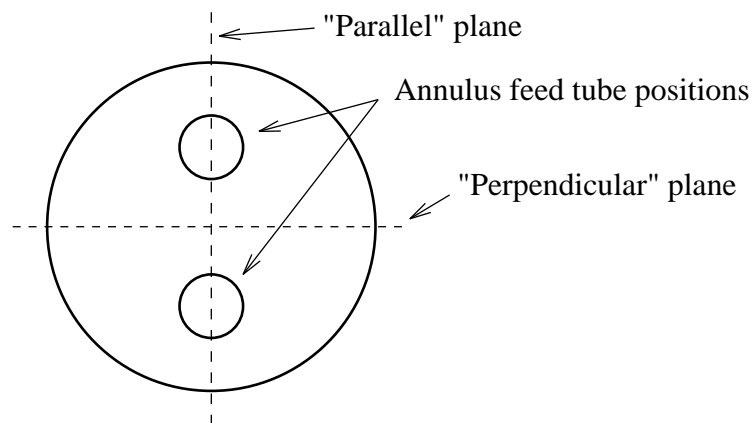


Figure 6.2: Pipe-mixer measurement plane positions.

For each plane, LDA measurements were made at two axial positions :  $z=0.5$  mm and  $z=20.0$  mm measured from the end of the nozzle. Radial measurements were made at approximately 0.15 mm intervals across the radius of the pipe-mixer. Janssen *et al.* state that, while the distance *between* measuring points is determined with some accuracy, the *initial* positioning of the first point adjacent to the pipe wall has an uncertainty of  $\pm 0.5$  mm. Janssen *et al.* quote the experimental accuracy of the velocity and turbulent kinetic energy measurements to be approximately 2%.

### 6.2.3 Two-Phase Experiments

For the two-phase cases the dispersed oil phase was continuously injected into the nozzle channel approximately 140 cm upstream of the nozzle exit via a small tube of diameter 1.35 mm. The oil was injected at a rate of 14.5 litres/hour. Small oil droplets, approximately 1 mm in diameter, were formed at or soon after the injection pipe due to jet break-up. The nozzle stream then underwent a contraction down from 8 mm to 2.75 mm in diameter approximately 10 cm upstream from the nozzle exit. The dispersed phase fraction produced at the exit of the nozzle channel was typically about 15%, giving a phase fraction of approximately 1% at the exit plane of the pipe-mixer.

For the majority of cases the droplet phase was a paraffin oil (trade name Bayol 35) with a density of  $860 \text{ Kg/m}^3$  and a dynamic viscosity of 3.5 mPas. For the cases examining the influence of the droplet viscosity, the droplet phase was a paraffin oil with viscosities of 30 mPas and 72 mPas (trade names Marcol 82 and Marcol 172 respectively). Both of these oils have a density of  $886 \text{ Kg/m}^3$ . No additional purification was performed on the continuous or dispersed phase fluids.

Measurements of the local phase fraction and mean diameter were made using a small sampling tube introduced through the pipe-mixer wall at various axial positions. The sample tube could be moved radially across the whole diameter of the tube. Radial positioning of the sample tube was made via a micrometer screw mechanism. Samples were taken from the flow isokinetically in order to cause minimum disturbance to the flow. The sample tube was 1mm in diameter and fed straight into a flat glass turbidity cell for in-line mean droplet size determination. The turbidity cell was mounted close to the actual sample point to reduce the likelihood of coalescence effects.

The technique used to determine the mean droplet size was based on a modified Fraunhofer technique; see Janssen *et al.* [138] and references therein for precise details. This technique essentially involves passing a monochromatic light with a known intensity through the turbidity cell which contains the two-phase fluid sample. Part of the light is absorbed

by the droplets or is deviated from its original course by scattering and diffraction. The mean droplet size is determined by measuring the intensity of the light reaching the other side. Corrections are applied to the measurements to account for the fact that some of the diffracted or scattered light may pass into the detector. The accuracy of the mean droplet diameter measurements was estimated by Janssen *et al.* to be better than 10%.

After the turbidity cell, the sample was collected in a cuvette for subsequent volume fraction determination. This was achieved by weighing the sample using a precision balance and then placing it in a centrifuge and spinning at 2000 RPM for approximately 30 minutes. The water phase was then extracted and weighed and the volume fraction subsequently determined. For volume fractions between 1% and 4%, the accuracy of this technique was stated to be about 2%. However, Janssen *et al.* state that for volume fractions below 1%, the inaccuracy becomes somewhat larger.

It should be noted that the calculation of the mean droplet size from the light intensity at the detector depends on the local phase fraction measurements. Therefore, the final accuracy of the mean droplet size will be correspondingly reduced for phase fraction values below 1%.

The surfactant used in the surfactant influenced cases was a Ryoto sucrose ester dissolved in the continuous water phase at concentrations between 0.001 and 0.05% by weight. The adsorption properties of this surfactant have been studied by Janssen, Wieringa, Groeneweg, Boon and Agterof [101] who found it to be best described using the so-called Frumkin adsorption isotherm (Eqn (3.53)). Table 6.1 shows the values adopted for the isotherm parameters.

Property	Value
Molar Weight	524g
$\Gamma_{\infty}$	$3.2 \times 10^{-6} \text{ mol/m}^2$
a	$0.012 \text{ mol/m}^3$
H/RT	0.6

Table 6.1: Ryoto SE surfactant properties.

In all, Janssen *et al.* [138] performed a total of thirteen experiments. These thirteen cases may be split into three series, the first of which comprised five experiments with a nozzle velocity of 6 m/s with surfactant concentrations of 0, 0.001, 0.004, 0.01 and 0.5%. The second series was performed with the same surfactant concentrations but with a nozzle velocity of 15 m/s. Finally, the third series was performed with a nozzle velocity of 15 m/s

with three different droplet phase viscosities. Table 6.2 summarises the cases considered.

Case No.	Nozzle Vel. [m/s]	Dispersed Phase	Surf. Conc. [%]	Axial Measurement Locations [mm]
1	15	Bayol 35 (3.5 mPas)	0.0	7.5, 10, 20, 40, 60, 200
2			0.001	
3			0.004	
4			0.01	
5			0.05	
6	6	Bayol 35 (3.5 mPas)	0.0	7.5, 10, 20, 40, 60, 200
7			0.001	
8			0.004	
9			0.01	
10			0.05	
11	15	Bayol 35 (3.5 mPas)	0.0	60, 200
12	15	Marcol 82 (30 mPas)	0.0	
13	15	Marcol 172 (72 mPas)	0.0	

Table 6.2: Summary of the pipe-mixer experimental cases.

## 6.3 Numerical Simulations

### 6.3.1 Single-Phase Cases

The single-phase calculations were performed using three different sized meshes in order to gauge the effect of the mesh size on the accuracy of the solution. The mesh sizes used are shown in Table 6.3. In all cases, the computational domain extended from the  $z=0.5$  mm position to the  $z=60$  mm position downstream of the nozzle exit. All meshes were refined in the inlet region to provide more accuracy there. The SIMPLE algorithm and standard single-phase  $k-\epsilon$  turbulence model were used.

The inlet conditions at the  $z=0.5$  mm plane were determined from the LDA measurements by assuming fully developed flow in the inlet region. The inlet profiles for the mean velocity and turbulent kinetic energy were obtained by interpolating the measurements directly onto the computational mesh. The inlet profile for the turbulent kinetic energy dissipation rate  $\epsilon$  was estimated from Nikuradse's mixing length formula [11] for fully developed pipe flow which reads



Mesh	Axial Cells	Radial Cells	Total No. of Cells
Coarse	60	20	1200
Intermediate	80	35	2800
Fine	120	60	7200

Table 6.3: Mesh sizes for pipe-mixer calculations.

$$l_m = R \left( 0.14 - 0.08 \left( 1 - \frac{y}{R} \right)^2 - 0.06 \left( 1 - \frac{y}{R} \right)^4 \right) \quad (6.1)$$

where  $R$  is the pipe radius,  $y$  is the distance from the pipe wall and  $l_m$  is the mixing length. This mixing length, when combined with the turbulent kinetic energy measurements, yielded the appropriate turbulent kinetic energy dissipation rate via

$$\epsilon = \frac{C_\mu k^{\frac{3}{2}}}{l_m} \quad (6.2)$$

Convergence for both velocity ratios was obtained in approximately 580 iterations for the 15/2.5 m/s cases and approximately 300 iterations for the 6/2.5 m/s cases on the intermediate mesh size.

### 6.3.2 Two-Phase Cases

The two-phase calculations require both phase velocities, the continuous phase turbulence properties, the dispersed phase fraction and the mean droplet diameter to be specified at the calculation inlet plane. Due to the experimental techniques used, measurements in the vicinity of the nozzle exit were restricted to the  $z=7.5$  mm position. Janssen *et al.* measured the dispersed phase fraction and the mean droplet size at this plane but did not measure any of the other required quantities. For the two-phase calculations, therefore, the  $z=7.5$  mm position has been taken as the calculation inlet plane allowing the inlet profiles for the phase fraction and mean droplet diameter to be obtained via direct interpolation of the measurements onto the computational mesh.

Since the two-phase cases involved low phase fractions, and the fact that the outer annulus flow is single-phase, the continuous phase inlet profiles at the  $z=7.5$  mm position were assumed to be the same as the corresponding single phase profiles. Therefore, the inlet profiles for the continuous phase mean velocity (both axial and radial components) and

the turbulent kinetic energy and its dissipation rate were obtained by interpolating the results from the single-phase calculations performed in the previous section directly onto the computational mesh at the  $z=7.5$  mm position. The single-phase results obtained using the fine mesh were used for this purpose.

The estimation of the dispersed phase mean velocity at the  $z=7.5$  mm plane was accomplished by inferring the slip velocity between phases from the measured mass flow rate of the dispersed phase and the measured phase fraction at this plane. The dispersed phase was injected into the central nozzle stream at a rate of 14.5 litres/hour. By assuming that the relative velocity was uniform across the radius of the pipe-mixer, the dispersed phase mean velocity could be calculated.

This procedure implied that the dispersed phase velocity was approximately 40 % lower than that of the continuous phase at the inlet plane. Such a large difference cannot be ascribed to buoyancy effects since, for droplets of the size encountered in the present case with a density ratio close to unity, such effects are negligible. Janssen [140] explored the possibility of errors in the phase fraction measurements due to the inadequate sampling of small droplets. Such a situation may occur due to non-isokinetic sampling where the sampling flow-rate is too small compared to the local fluid flow-rate. This situation allows the small droplets to be carried away from the sampling tube by the flow while the larger droplets pass into the sample tube due to their higher inertia. However, work by Pal [141] taking into account droplet inertia and non-isokinetic sampling concluded that this effect was minor for oil-water emulsions. Moreover, Janssen [140] found that altering the sampling flow-rate did not overly affect the results.

Janssen [140] also analysed the response of the droplet to the acceleration of the continuous phase in the contracting section upstream of the nozzle exit. He concluded that droplets larger than about  $200\text{ }\mu\text{m}$  would not accelerate as strongly as the continuous phase and would have a substantially lower velocity at the nozzle exit.

The majority of the two-phase simulations were carried out using the intermediate mesh size as described in Table 6.3. To allow the accuracy of the solutions to be assessed, some cases were recalculated using all three mesh sizes. For the two-phase calculations, the computational domain extended from the  $z=7.5$  mm position to the  $z=60$  mm position.

### 6.3.3 Break-up Model Coefficients

The pipe-mixer flow conditions were designed so that droplet break-up would be dominated by the inertial break-up regime. The calculation of the Kolmogorov length scale at a position approximately 20 mm downstream of the nozzle exit, where the majority of the

droplet break-up takes place, yields values of approximately  $7 \mu\text{m}$  for the  $6/2.5 \text{ m/s}$  cases, and  $3 \mu\text{m}$  for the  $15/2.5 \text{ m/s}$  cases. All measured droplet sizes at the inlet to the pipe-mixer are significantly greater than this size confirming that break-up is dominated by the inertial mechanism. The simulations employ the inertial break-up model as described in detail in Section 3.3.3.2 which has the ability to take into account the effects of surfactants and the droplet phase viscosity on the break-up characteristics. No coalescence of droplets was observed in the experiments and no account is taken in the simulations.

There are two empirical coefficients which have to be specified in the break-up model; one is in the inertial break-up time scale expression (Eqn (3.49)), and the other is the critical amplitude parameter,  $K$ , which characterises the amplitude required to cause break-up with respect to the low frequency limit (Eqn (3.87)). The break-up time-scale coefficient,  $k_b$ , has been assigned a value of unity in accordance with the estimate of Chesters [94].

However, the critical amplitude parameter could not be so readily estimated. Chesters [94] obtained an initial estimate for  $K$  by analysing data relating to the break-up of oil droplets of two different viscosities in a stirred vessel, with a low surfactant concentration. The critical Weber number ratio  $We_r$  was inferred for each case by assuming that the final droplet size is a result of inertial break-up only and that differences in turbulent energy dissipation rate, surface tension and droplet phase densities were negligible. Thus, from Equations (3.41) and (3.42), under the above assumptions, we obtain

$$We_r = \frac{We_2}{We_1} = \left(\frac{d_2}{d_1}\right)^{5/3} \quad (6.3)$$

where  $We_r$  is the critical Weber number ratio and  $d_1$  and  $d_2$  are the final mean droplet diameters in the first and second cases respectively. The damping factor may be calculated for each case using Eqn (3.77). Using Equations (3.83) and (3.88) and substituting for the known critical Weber number ratio above we obtain an expression for the parameter  $A$

$$A = We_r \left\{ \frac{B_1 B_2 - We_r (B_1^2 + B_2^2) + B_1 B_2 We_r^2}{1 - 2We_r^2 + We_r^4} \right\} \quad (6.4)$$

where the  $B$  coefficients are calculated from  $B = F^2 - 2$  (Eqn (3.88)). The critical amplitude parameter  $K$  is then given via

$$K = \sqrt{\frac{1}{1 - A}} \quad (6.5)$$

For the cases studied by Chesters,  $K$  was determined to have a value of 1.2. Application of the above procedure to the present study, using the data from the surfactant-free cases involving three different droplet viscosities, gave a value for  $K$  of 0.54 which was the value adopted for the simulations presented here.

The value for  $K$  derived above differs significantly from the value obtained by Chesters. This difference may be due to the violation of some of the assumptions which are required in order to infer the critical amplitude parameter from the final droplet diameter in the cases used by Chesters to determine his value. In particular, it is well known that the flow characteristics of a stirred vessel are extremely complex and droplet break-up within such devices may be due to a wide variety of mechanisms and not purely the inertial mechanism.

## 6.4 Results

### 6.4.1 Single-Phase Cases

#### 6.4.1.1 6/2.5 m/s Case

Figure 6.3 shows the predicted and measured mean velocity profiles for the single-phase 6/2.5 m/s case at the  $z=20$  mm measuring position. The two graphs depict the predicted and measured data corresponding to the two measuring planes as shown in Figure 6.2. The predictions shown were calculated using the fine mesh as described in Table 6.3.

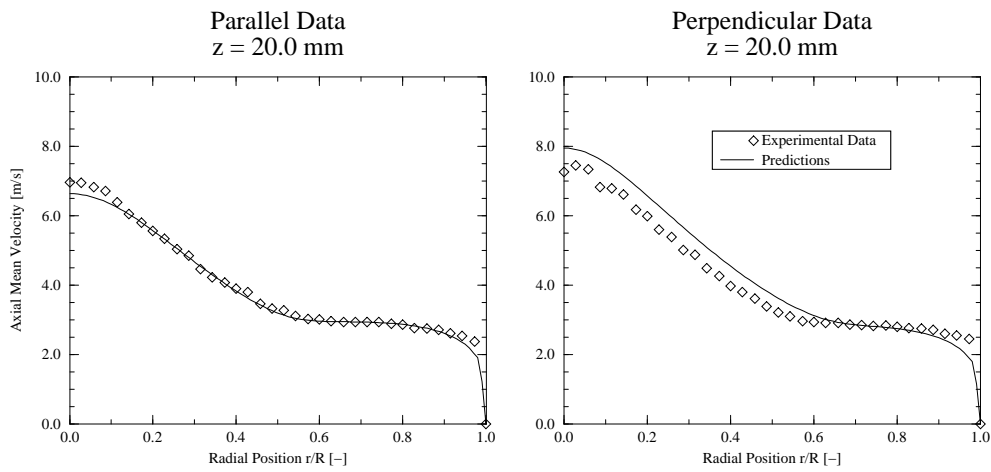


Figure 6.3: Mean velocity profiles for the single-phase 6/2.5 m/s case.

Examination of the experimental data in Figure 6.3 reveals distinct differences in the velocity magnitude at the centreline for the parallel and perpendicular cases. These discrepancies could imply a non-symmetric flow with respect to the inlet pipes. A mass balance check on the consistency of the experimental data (achieved by integrating the velocity measurements across the pipe radius at the  $z=0.5$  mm and  $z=20.0$  mm positions) shows that the parallel data case has an imbalance of about -0.12% while the perpendicular data case has an imbalance of 4.5% with respect to the inlet mass flow rate. Again, this could be indicative of an asymmetric flow.

However, Janssen [142] studied these discrepancies and could find no systematic asymmetry in the flows studied. Instead, he ascribes them to experimental inaccuracies in the radial positioning of the LDA measuring volume. The uncertainty in the initial radial positioning was of the order of  $\pm 0.5$  mm (i.e. 10% of the pipe radius), although the

incremental positioning of the volume with respect to the initial position was much more accurate. The application of a small radial offset (of approximately 0.25 mm) to the experimental data yields very good agreement with the predictions and reduces the mass conservation errors.

Comparing the predictions to the data as it stands, it can be seen that fairly good agreement is obtained over most of the pipe radius for both cases. In particular, the jet spreading rate, as indicated by the velocity gradients at the edge of the mixing layer, is well predicted in both cases, although the perpendicular data case does show some discrepancy in the velocity magnitude in this region. Some discrepancy is also apparent on the centreline in both cases where the predicted mean velocity deviates from the experimental data by approximately 5%. These discrepancies could well be due to the experimental inaccuracies noted above, or to small inaccuracies in the predicted jet spreading rate, or to errors in the measurements themselves. Janssen states that the accuracy of the LDA measurements is of the order of 2%.

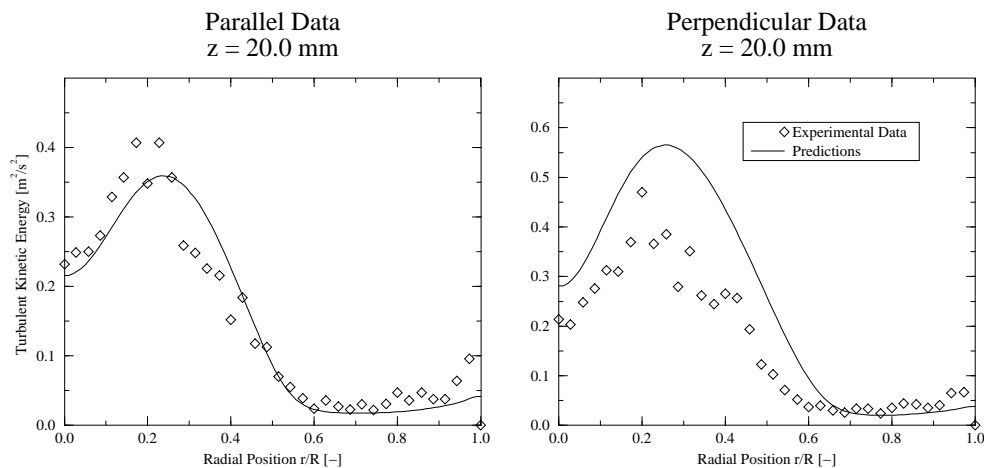


Figure 6.4: Turbulent kinetic energy profiles for the single-phase 6/2.5 m/s case.

Figure 6.4 shows the prediction and measured turbulent kinetic energy profiles at the  $z=20.0$  mm position. Again, the two graphs depict the predicted and measured data corresponding to the parallel and perpendicular measuring planes. It can be seen that reasonably good agreement is obtained for the parallel plane case but the perpendicular case shows some discrepancy in the magnitude of the turbulent kinetic energy peak, over-predicting it by approximately 15%.

It should be noted that the radial positioning of the experimental data may account for

a large proportion of the apparent discrepancies in the parallel plane case. Again, the application of a small offset to the experimental data yields very good agreement. The predicted profile then lie within the scatter of the measured points.

Since the parallel data case yields the best comparison between the experimental data and the predictions, this case will be used to derive the inlet conditions for the 6/2.5 m/s two-phase calculations as described above.

#### 6.4.1.2 15/2.5 m/s Case

Figure 6.5 shows the predicted and measured axial mean velocity profiles for the 15-2.5 m/s case. Again, the predictions shown were calculated using the fine mesh as described in Table 6.3. It can be seen that in both measurement planes the centreline velocity is under-predicted by approximately 10%. These discrepancies appear to be mainly as a consequence of the over-prediction of the jet spreading rate as evidenced by the velocity gradients at the edge of the shear layer. A mass balance consistency check for this case reveals that in both planes there is a mass imbalance of approximately 15%, which could also explain some of the discrepancies at the pipe centreline.

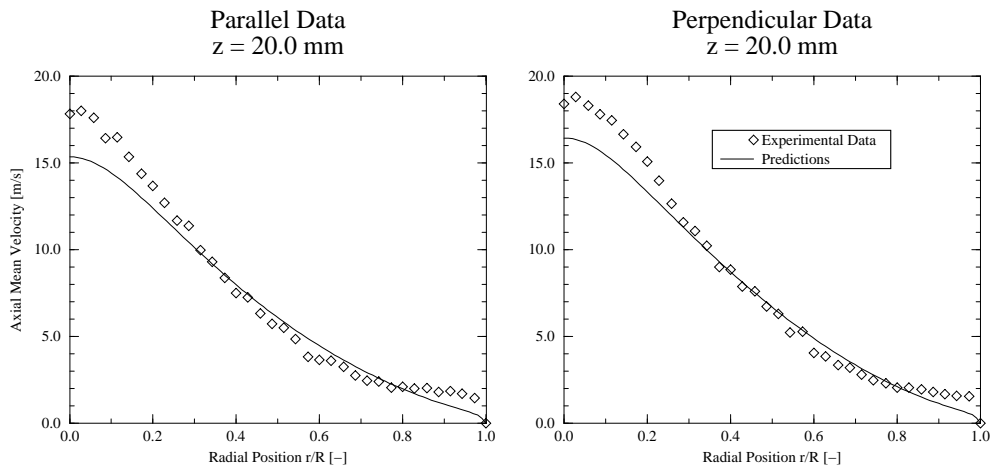


Figure 6.5: Mean velocity profiles for the single-phase 15/2.5 m/s case.

Figure 6.6 shows the turbulent kinetic energy profile comparisons. It can be seen that the agreement is reasonable, especially with respect to the magnitude and position of the peak associated with the shear layer. Radial inaccuracies in the data could explain many of the discrepancies in the parallel plane case. However, there are some discrepancies in the outer edge of the pipe for the perpendicular case, with the turbulent kinetic energy

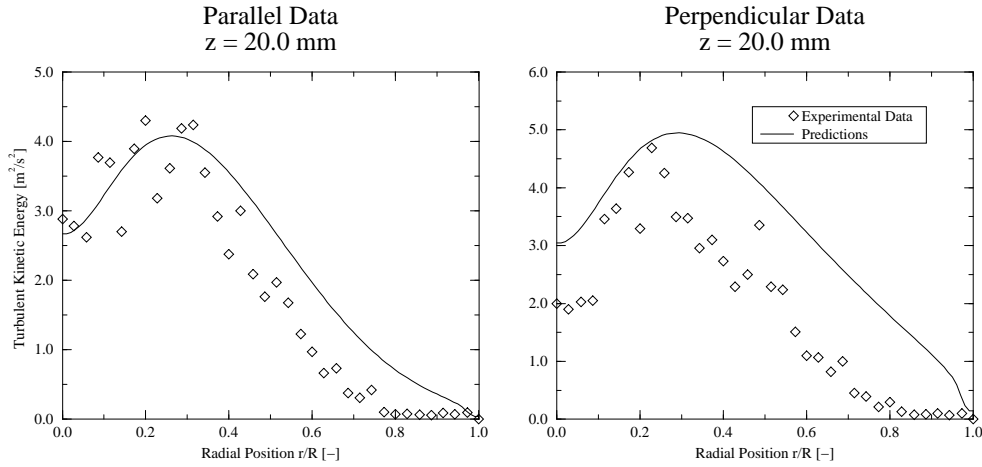


Figure 6.6: Turbulent kinetic energy profiles for the single-phase 15/2.5 m/s case.

being over-predicted significantly in that region.

Again, the parallel data case yields the best predictions and will be likewise adopted to derive the inlet conditions for the 15/2.5 m/s two-phase cases.

#### 6.4.1.3 Mesh Sensitivity Tests

In order to gauge the effect of the mesh size on the accuracy of the results, the 6/2.5 m/s calculations were carried out on three different meshes sizes. Figure 6.7 shows the resulting profiles for mean velocity and turbulent kinetic energy at the  $z=20$  mm measuring position.

The results for all three meshes are very similar. The difference in the centreline velocity between the coarse mesh and the fine mesh is approximately 3.6%. The difference between the fine and intermediate meshes is approximately 1.6%.

The differences between the meshes for the turbulent kinetic energy are larger since the turbulent kinetic energy is more sensitive to mesh size since it depends on the square of the velocity gradients. The difference at the centreline between the coarse and fine meshes is approximately 13%. Between the fine and intermediate meshes, the difference is approximately 8%.



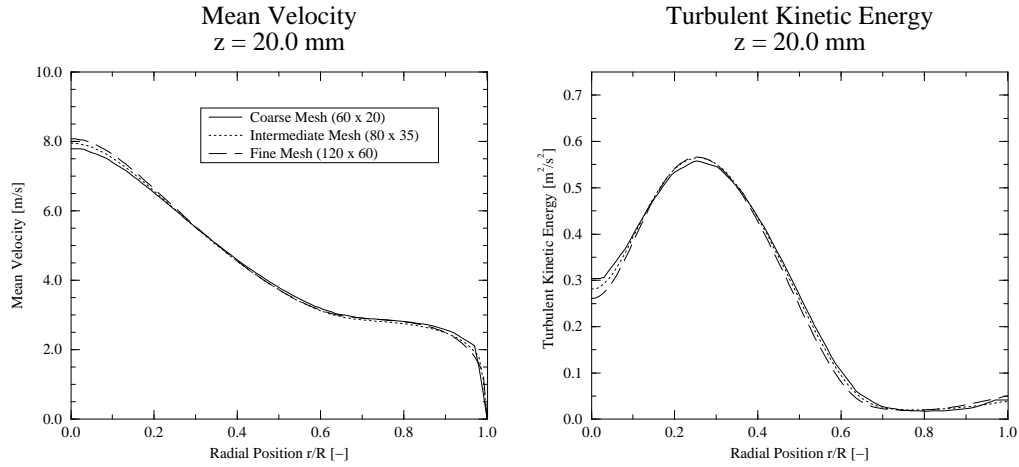


Figure 6.7: Mesh sensitivity results for the single-phase 6/2.5 m/s case.

## 6.4.2 Two-Phase Cases

### 6.4.2.1 15/2.5 m/s Cases

These five cases have surfactant concentrations ranging from 0% to 0.05%, as shown in Table 6.2. The predictions and experimental data are shown in Figures 6.20 to 6.29. Each figure shows the predicted and measured mean droplet diameter or the dispersed phase fraction for the  $z=10$ , 20, 40 and 60 mm measuring positions.

The experimental measurements performed by Janssen *et al.* [138] for the mean diameter and the phase fraction were across the entire diameter of the pipe-mixer. Consequently, the figures show the mean diameter and phase fraction data at a particular radius as two data points, one on either side of the pipe axis. This give some indication on the amount of scatter in the data.

Close examination of the predicted mean diameters for these cases shows quite reasonable agreement, especially at the last measuring station where the final droplet size is generally within about 15% of the data at the centreline. Good agreement is obtained in the development of the mean droplet diameter down the length of the pipe-mixer, again especially at the centreline. The centreline value at the  $z=7.5$  mm position is approximately  $70 \mu\text{m}$  while at the  $z=60$  mm position it is reduced to approximately  $38 \mu\text{m}$  for all cases

Figure 6.22 shows the mean diameter for Case 2, which has a surfactant concentration of 0.001%. It can be seen that very good agreement is obtained for all the measuring stations, especially at  $z=10$  and 20 mm. There are some discrepancies at the  $z=60$  mm

position where the predicted value is below the measured data in the outer region of the pipe. However, comparison between the experimental data at  $z=40$  mm and  $z=60$  mm positions indicates that the mean droplet diameter seems to be increasing. Whether this is due to coalescence effects, which are unlikely in these flow conditions, or some anomaly with the data is not clear.

The dip in the mean diameter at the mid radial position at  $z=10$  mm is due to the break-up of droplets within the shear layer. This region has a high turbulence level which is generated as the fast and slow streams come together. Further down the pipe, the turbulence decreases and the droplets are dispersed across the entire pipe radius. Finally, at about the  $z=60$  mm position, the radial profile is fairly flat indicating that the flow has become fully mixed as indicated by the phase fraction profiles shown in Figure 6.21.

Figure 6.24 shows the mean diameter for Case 3, which has a surfactant concentration of 0.004%. Again, good agreement is obtained for all measuring stations with the development of the mean droplet diameter down the pipe length being quite well captured.

There are discrepancies in the mean diameter profiles at the  $z=10$  mm station in the outer part of the pipe where the experimental data indicates relatively large droplets adjacent to the wall. These large droplets are absent from the  $z=7.5$  mm and the  $z=20$  mm data. Given the low phase fraction in this area, this anomaly may be due to inaccuracies in the droplet diameter measurements since the accuracy of the mean diameter measurements is reduced for phase fractions below 1%.

Figure 6.26 relates to Case 4, with a surfactant concentration of 0.01%. Good agreement is once again obtained for most measuring stations, although there are some discrepancies at the  $z=20$  mm station, where the experimental data seems to indicate a sharp increase in the mean diameter in the outer part of the pipe, and at the  $z=60$  mm station, where the predicted mean diameter profile is not uniform and shows smaller mean droplet sizes in the outer part of the pipe.

Examination of the phase fraction profiles in Figure 6.27 show that the predicted flow has become fully mixed at the  $z=60$  mm station. This implies that the predicted droplet break-up cascade has not quite been completed by the  $z=60$  mm station resulting in a non-uniform droplet diameter profile.

Figure 6.28 shows the results for Case 5, which has a surfactant concentration of 0.05%. Here, although the development of the mean diameter profiles down the pipe is quite well predicted, the final droplet size is under-predicted by approximately 30%. Also, there are discrepancies at the  $z=10$  mm station in the outer part of the pipe where the data indicates large droplets. Again, large droplets in this area are absent at the  $z=7.5$  mm and the  $z=20$  mm data implying that these anomalous points may be a result of inaccuracies

in the data caused by a low phase fraction in this area.

In order to see clearly the effects of the surfactants on the droplet break-up characteristics, Figure 6.8 assembles the predicted and measured mean diameter profiles for each surfactant concentration at the  $z=60$  mm position.

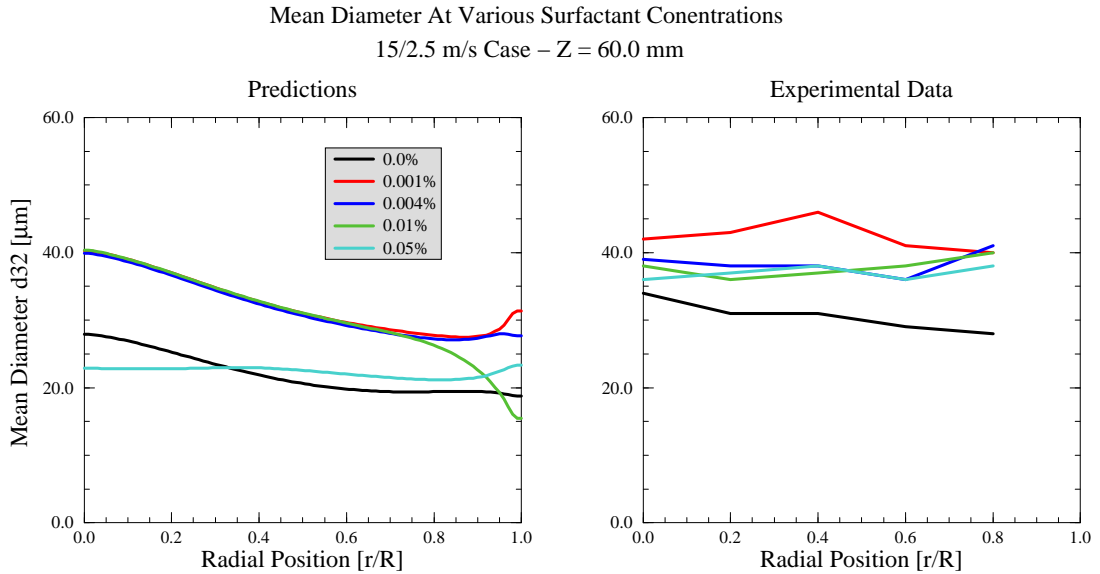


Figure 6.8: Mean diameter profiles for all surfactant concentrations, 15/2.5 m/s cases.

Close examination of these plots shows that the general trends indicated by the experimental data have been captured by the predictions. In particular, the surfactant-free clean case, perhaps somewhat surprisingly, shows the smallest mean diameter, while Case 2, with a surfactant concentration of 0.001% shows the largest mean diameter. The predicted diameter profiles for the intermediate concentrations (ie, 0.004 and 0.01%) show little change in behaviour compared to the 0.001% cases, although the 0.05% cases does display a clear reduction in mean diameter. The reasons why the surfactant-free case has resulted in the smallest mean droplet diameter are examined more closely in the next section.

Figure 6.8 shows that, while the presence of surfactants can have a marked effect on the final droplet diameter, it is not simply a function of the surfactant concentration. Furthermore, when one considers that the surface tension (at equilibrium) has been reduced by up to a factor of 6.5 in these cases, the effects of the surfactant is less pronounced than expected. Janssen *et al.* concluded that this was primarily due to the fact that adsorption equilibrium is in fact not reached at the droplet interface due to the rapid increase in the

surface area caused by the initial droplet break-up outstripping the ability of the surfactant to adsorb to the interface [138]. As the droplets break up within the pipe-mixer, their surface area increases rapidly causing a sharp reduction in the interfacial surfactant concentration. Re-adsorption of the surfactant to the interface will take place, but at a finite rate. In the 15/2.5 m/s cases, the droplets are apparently transported out of the turbulent break-up zone before full re-adsorption is complete. Since the interfacial concentration is reduced to something significantly below equilibrium, the droplet surface tension tends to its higher surfactant-free value.

This phenomenon is illustrated by the plots in Figure 6.9 of the predicted bulk and interfacial surfactant concentration profiles along the centreline of the pipe-mixer for the 0.001% surfactant concentration case (Case 2).

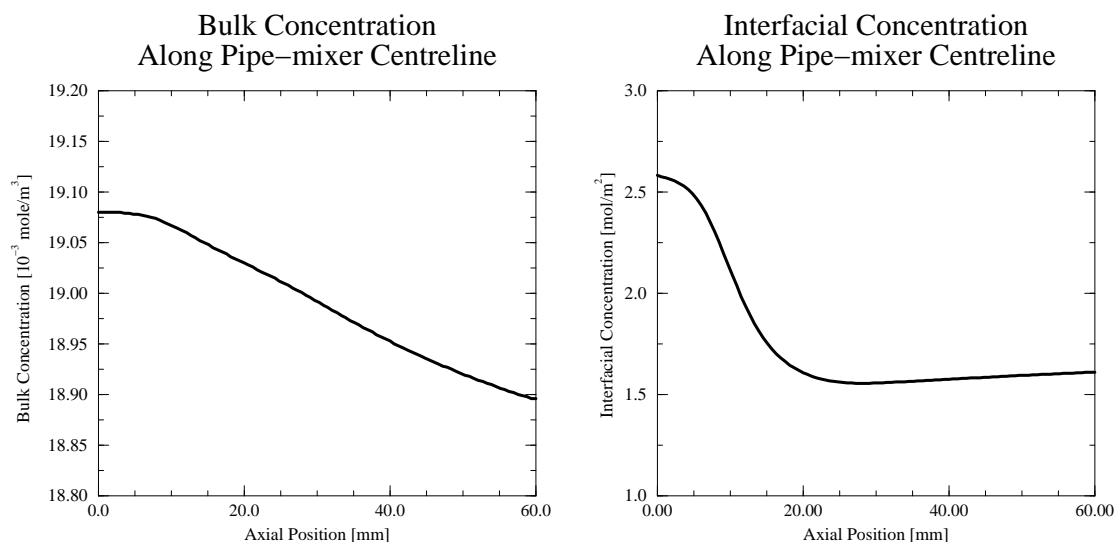


Figure 6.9: Bulk and interfacial surfactant concentration along centreline (Case 2).

The graph on the left shows the bulk surfactant concentration between  $z=7.5$  mm and  $z=60$  mm. It can be seen that the surfactant concentration shows a steady reduction along the pipe length as the surfactant adsorbs to the newly created surface area caused by the droplet break-up. However, as shown in the right-hand graph, despite the re-adsorption of the surfactant from the bulk to the interface, the interfacial concentration shows a sharp reduction between about  $z=10$  mm and  $z=30$  mm due to the rapid break-up of droplets in the highly turbulent mixing zone. After about  $z=30$  mm, the droplet break-up has essentially been completed and surfactant re-adsorption starts to increase the interfacial concentration. Note the steady rise in interfacial concentration towards the

pipe-mixer exit.

Figure 6.10 shows the profiles of the equilibrium surface tension, calculated from the Frumkin isotherm (Eqn (3.53)), and the mean diameter along the centreline of the pipe-mixer for Case 2. It can be seen that as the droplets break up between  $z=10$  and  $z=30$  mm, the surface tension increases rapidly due to the rapid reduction in the interfacial surfactant concentration. Beyond the  $z=30$  mm position, the surfactant begins to re-adsorb to the interface and the surface tension begins to fall again.

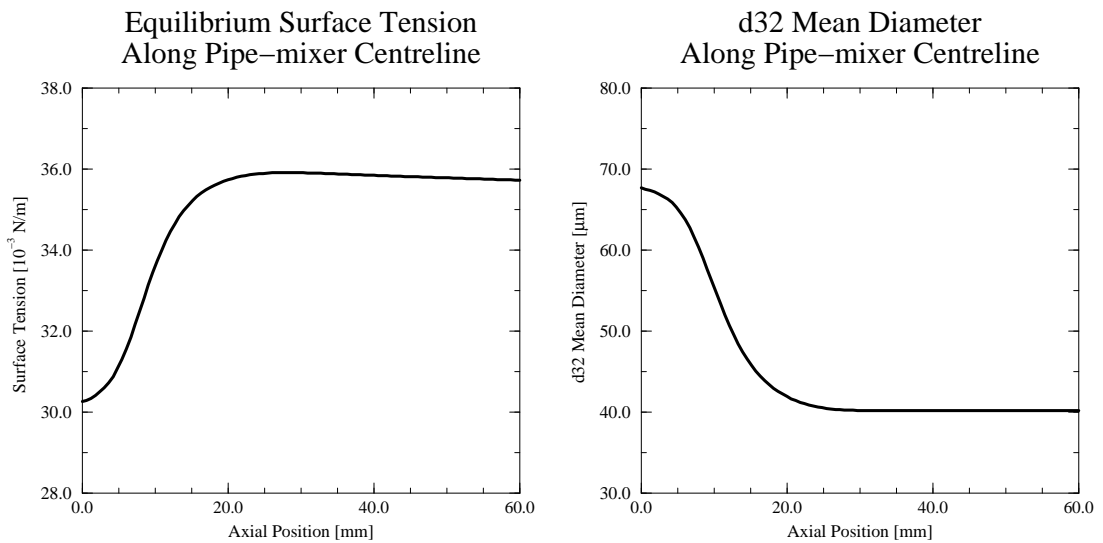


Figure 6.10: Equilibrium surface tension and mean diameter along centreline (Case 2).

#### 6.4.2.2 6/2.5 m/s Cases

These five two-phase cases also have surfactant concentrations ranging from 0% to 0.05%, as shown in Table 6.2. The comparisons between the predictions and experimental data are shown in Figures 6.30 to 6.39. Each figure shows the predicted and measured mean droplet diameter or the dispersed phase fraction for the  $z=10$ , 20, 40 and 60 mm measuring positions.

In general, the mean diameter predictions for the lower surfactant concentrations are reasonably close to the experimental data (see Figures 6.30, 6.32 and 6.34) although there are some discrepancies in the outer part of the pipe. In particular, the break-up rate at the centreline of the pipe is well captured with good agreement at all measuring stations. However, the droplet sizes at the higher surfactant concentrations (0.01% and 0.05%) are

significantly under-predicted at the  $z=60$  mm measuring station; see Figures 6.36 and 6.38.

It is interesting to note that the phase fraction profiles for these cases at this position show that the droplets have not been fully radially dispersed, although the droplet break-up has been completed by this stage. The phase fraction predictions compare quite reasonably with the experimental data, especially at the final measuring station. There are some discrepancies in the initial dispersion rate in all cases.

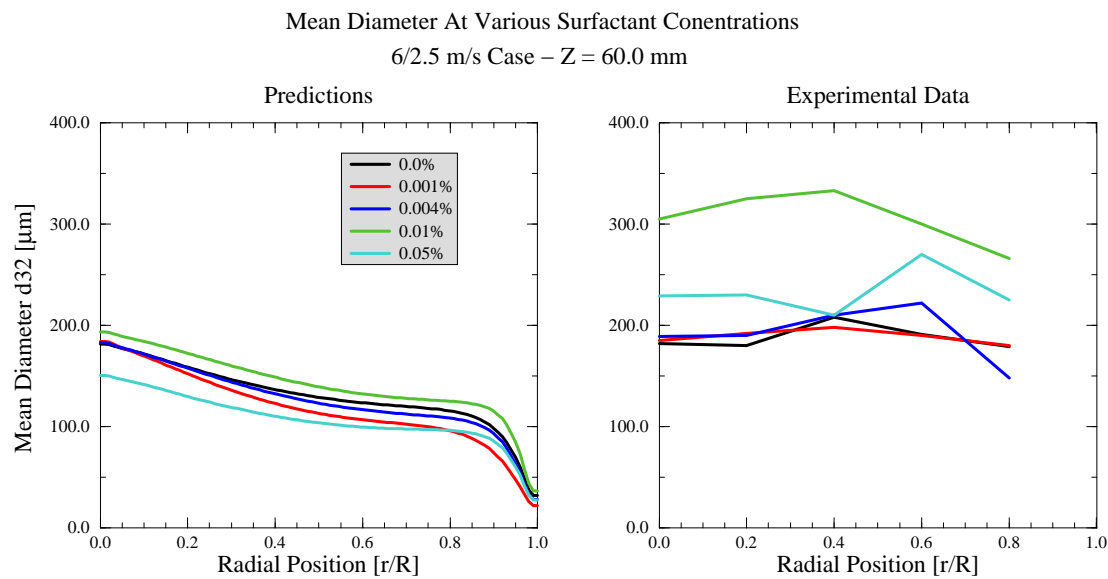


Figure 6.11: Mean diameter profiles for all surfactant concentrations, 6/2.5 m/s cases.

Figure 6.11 assembles the predicted and measured mean diameter profiles at  $z=60$  mm for all five surfactant concentrations. It can be seen that the case with a surfactant concentration of 0.01% produces the largest droplets in both the experiments and predictions; and the lower concentrations do not influence the final droplet size by much. However, the predicted effects of the surfactant for the high concentrations are not as marked as those observed experimentally. The 0.01% surfactant concentration experiment shows a significantly larger final droplet diameter than the other surfactant concentrations.

Figure 6.12 shows the predicted bulk and interfacial surfactant concentrations for Case 7 (0.001% surfactant concentration). Again, as the droplets begin to break up and their interfacial area increases rapidly, the surfactant begins to adsorb to the interface from the bulk. Here, as for the 15 m/s cases, the break-up rate of the droplets within the break-up zone is too rapid to allow significant re-adsorption to take place, resulting in the surface

tension deviating significantly from its initial value and approaching its surfactant-free value as shown in Figure 6.13.

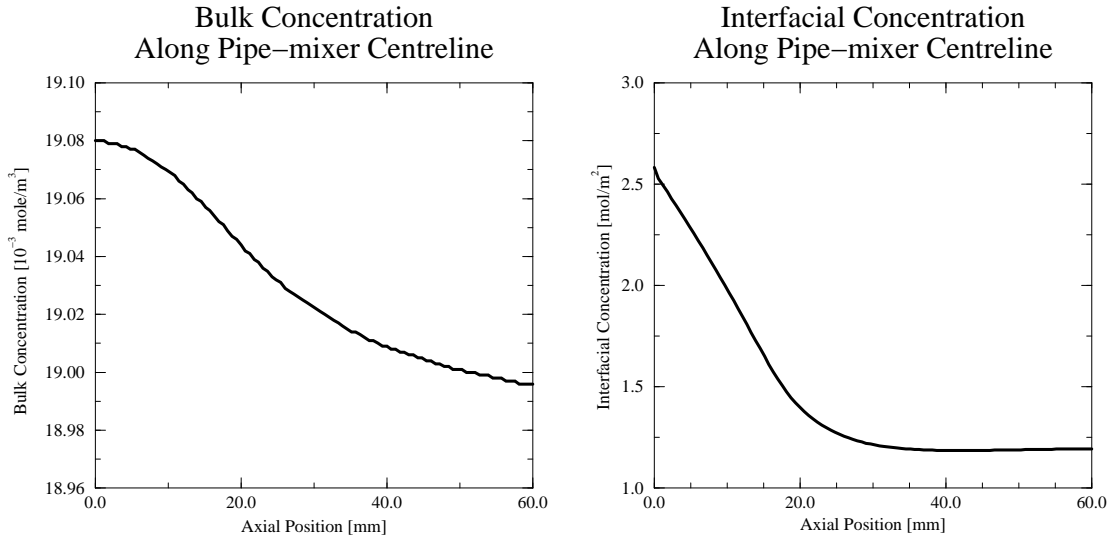


Figure 6.12: Bulk and interfacial surfactant concentration along centreline (Case 7).

The experimental data indicates that for the higher surfactant concentration cases, the final droplet size is larger than for the lower concentrations. Indeed, both the 6 m/s and the 15 m/s results show that the surfactant-free cases produce the smallest droplets. This result is somewhat surprising, since the higher surfactant concentration should result in faster re-adsorption to the interface and so reduce the surface tension making break-up more likely, resulting in a smaller final droplet size.

However, it is important to note that the break-up time-scale also is influenced by the surface tension, as shown by Eqn (3.39). Thus, although a smaller interfacial surface tension tends to reduce the critical diameter making break-up more likely, the time required for a deformation resulting in break-up to occur is lengthened. The final droplet size is governed by the complex interactions between the droplet's residence time in the highly turbulent region, the rate at which the droplet actually breaks up (and therefore the rate at which the surface area is increasing) and the rate at which the surfactant can re-adsorb to the interface.

The current model quite accurately predicts the trends in the influence of surfactants have on the break-up of droplets, even though the absolute magnitude of the final droplet size is not always well predicted. The coupling between the local droplet break-up and the transport of the surfactant and the dispersed phase is important in capturing these effects.

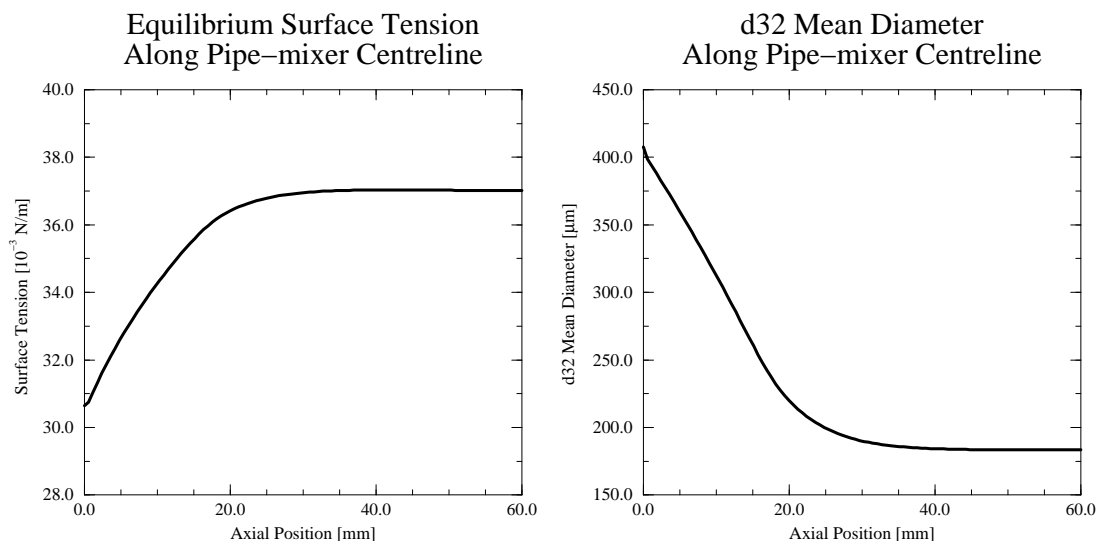


Figure 6.13: Equilibrium surface tension and mean diameter along centreline (Case 7).

It is not sufficient to perform the calculations using a ‘nominal’ equilibrium surface tension (ie, the surface tension at the nominal surfactant concentration) without accounting for the local variations due to surface area increase and re-adsorption. Figure 6.14 compares the predicted mean droplet diameter along the pipe centreline for Case 7 after excluding the transport of surfactant from the calculation with the ‘full model’ where the surfactant transport is properly accounted for.

In the reduced calculation, a constant surface tension of 30.6 Pa.s was specified corresponding to the equilibrium surface tension at a surfactant concentration of 0.001%. Since the transport of surfactant is not taken into account, the surface tension is not influenced by the surface area increase in the break-up zone leading to a lower surface tension than in the full model calculation. Consequently, the critical droplet diameter is reduced and the break-up rate is over-predicted. Figure 6.14 shows that the final droplet diameter is 16% below the experimental value which is well captured by the full model.



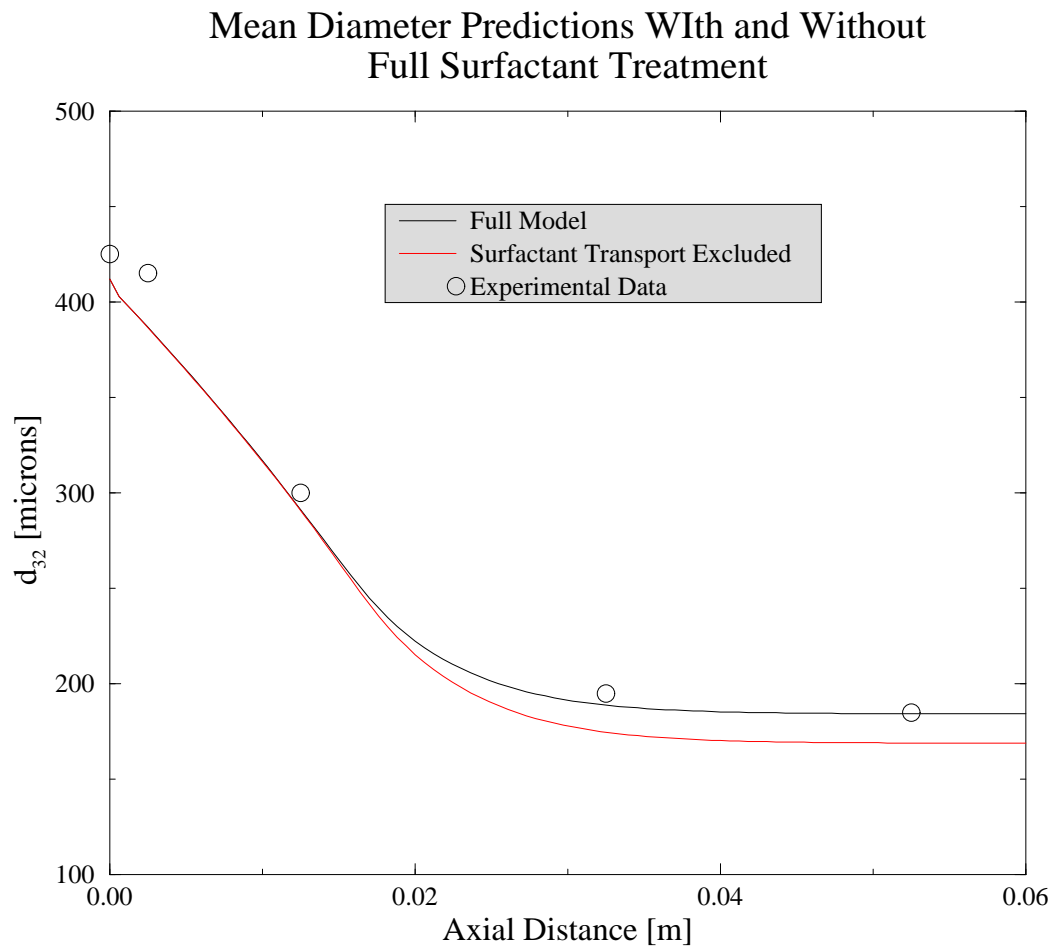


Figure 6.14: Effect of surfactant transport on the mean diameter predictions (Case 7).

### 6.4.2.3 Droplet Viscosity Variation Cases

Janssen *et al.* [138] performed three experiments with oil droplets of different viscosities to try to quantify the effects of the dispersed phase viscosity on the droplet break-up characteristics. The first of these cases, Case 11 in Table 6.2, uses Bayol 35 oil which has a viscosity of 3.5 mPas. Cases 12 and 13 employ Marcol 82 oil (with a viscosity of 30 mPas) and Marcol 172 (with a viscosity of 72 mPas) respectively.

Janssen *et al.* provided mean droplet size and phase fraction data for the  $z=20$  mm and  $z=60$  mm axial positions. Figures 6.40, 6.41 and 6.15 show the predicted and experimental data for these cases.

The first two cases show quite reasonable agreement at the last measuring station between the predictions and the experimental data for both the mean diameter and the phase fraction. However, there is a large discrepancy for the Marcol 82 case (Figure 6.41) for the mean diameter at the  $z=20$  mm case where the experimental data shows larger droplets in the outer part of the pipe. Again, the low phase fraction in this area may imply reduced accuracy in the mean diameter measurements.

Figure 6.15 shows the results for the Bayol 35 and Marcol 82 cases at the  $z=60$  mm position. The general trend that the final mean diameter falls as the droplet viscosity rises can be clearly seen. This trend has been successfully captured by the predictions.

However, the Marcol 172 case shows significant discrepancies between the predictions and measurements of the mean diameter. Indeed, the predictions imply that for this high dispersed-phase viscosity no break-up at all occurs, leading to significant over prediction of the mean droplet diameter at both the  $z=20$  and  $z=60$  measuring stations. On the other hand, despite the over-prediction of the dispersion rate at the  $z=20$  mm station, the final phase fraction profile is quite well predicted.

In order to understand why the predicted droplet size for the Marcol 172 case is so high, we have to examine the behaviour of the break-up model for high droplet viscosities. The dispersed phase viscosity is taken into account principally through the damping factor which is then used to calculate the local critical Weber number and thence the critical diameter, as discussed at length in Section 3.3.3.2. It should be recalled that the critical diameter is the diameter below which break-up will not occur and is used as the lower limit on the integral over the droplet size population; see Section 3.3.1 and Eqn (3.43).

The Marcol 172 case predictions suggest that the critical diameter is approximately constant down the entire length of the pipe-mixer tube at about 450 microns. The experimental droplet diameter is about 260 microns at the end of the pipe-mixer nozzle, reducing down to about 70 microns at the end of the pipe-mixer tube. Clearly, since the predicted

### Effect Of Viscosity Ratio On Droplet Break-up

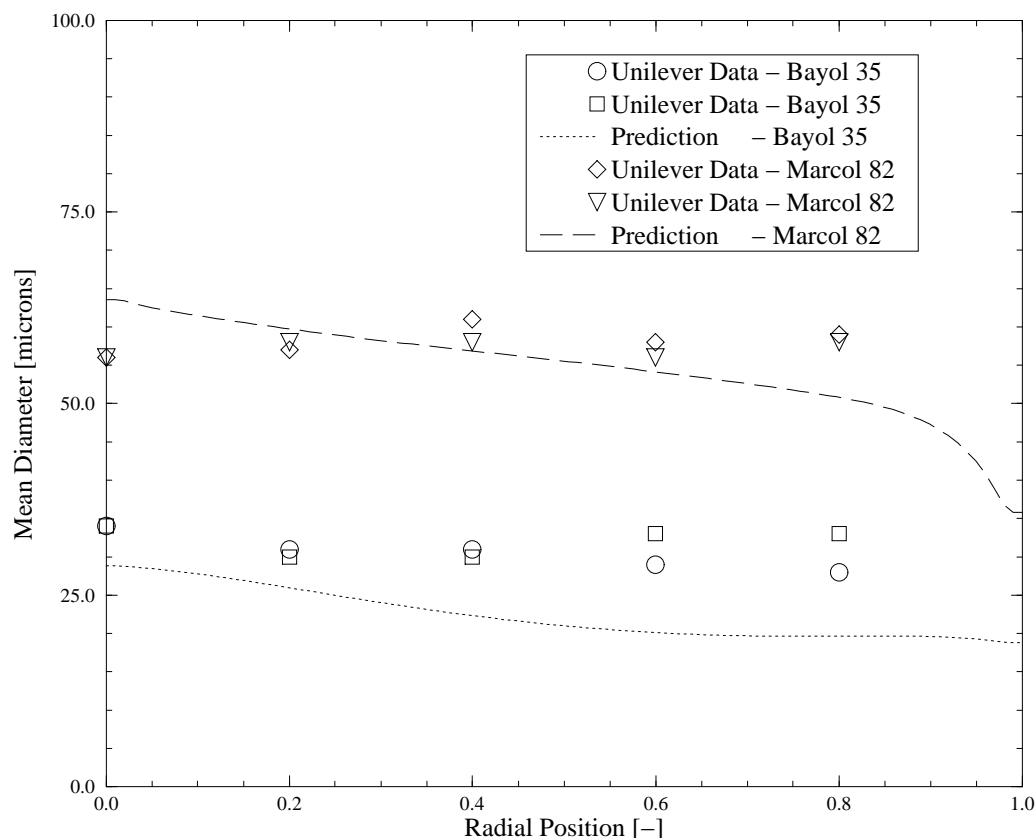


Figure 6.15: Mean diameter profiles for Bayol 35 and Marcol 82.

critical value is significantly above the actual mean droplet diameter, the model predicts very little break-up, consequently yielding high mean diameter droplets at the pipe-mixer exit.

Examination of the equation for the damping factor (Eqn (3.77)) shows that the damping factor increases with the viscosity ratio. This is illustrated in Figure 6.16. The left hand graph shows the damping factor as a function of the viscosity ratios for values between 1 and 100 and for mean droplet diameters of 50, 100 and 200  $\mu$  m. The other parameters in the damping factor equation (such as the dissipation rate, density ratio, etc) have been set to the conditions prevailing in Case 13 in the highly turbulent mixing region downstream of the nozzle exit. The graph clearly shows that the damping factor rises almost linearly with

the viscosity ratio with a slope which is inversely proportional to the droplet diameter.

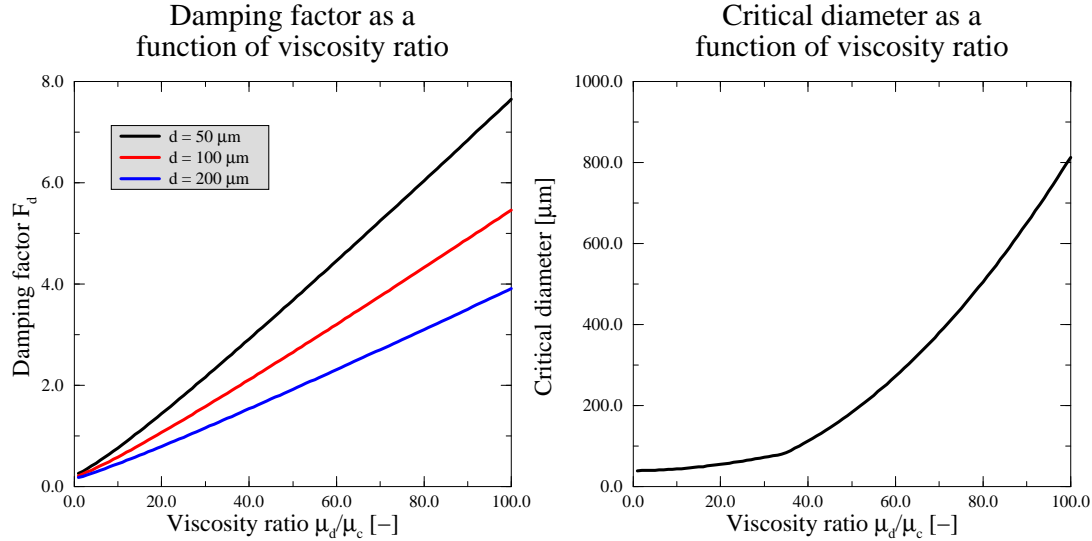


Figure 6.16: Damping factor and critical diameter as a function of viscosity ratio.

Figure 6.16 shows the calculated critical diameter for the conditions prevailing in Case 13 for viscosity ratio between 1 and 100. As described in Section 3.3.3.2, the calculation of the critical diameter from the damping factor has to be carried out iteratively because the damping factor is itself a function of diameter. The iterative solution first calculates the damping factor using the latest value for the critical diameter. The critical Weber number is then calculated using this damping factor, and is then used to calculate the new value for the critical diameter. The iterative sequence continues until the normalised difference in the critical diameter value between iterations is below a certain value.

The calculation of the critical diameter from the critical Weber number and the damping factor is complicated by the fact the damping factor has no physical significance beyond a certain value (see Section 3.3.3.2). For the present case, where the critical amplitude parameter  $K$  in Eqn (3.88) has a value of 0.54, the largest physically significant value for the damping factor is 2 which corresponds to the critical damping condition. If, after the iterative solution of  $d_c$ , the damping factor at the calculated critical diameter exceeds this physical limit then the critical diameter is given the value of the diameter at which this limiting value is reached.

Examination of the right-hand graph in Figure 6.16 shows that the critical diameter generally increases with viscosity ratio. Beyond a viscosity ratio of approximately 35, however, the critical diameter starts to rise sharply and the curve exhibits a discontinuity in its

gradient. This point corresponds to the point at which the critical diameter is limited by the damping factor reaching its maximum value, as outlined above. It can be seen that at this point the critical diameter has a value of approximately  $100\ \mu\text{m}$  which corresponds the diameter at which the damping factor attains a value of 2.0 in the left-hand graph. Further, it is this sharp rise in the critical diameter at higher viscosity ratios that leads to the discrepancies in the predictions for Case 13.

The behaviour of the model for high viscosity ratios is dominated by the fact that the damping factor at small droplet sizes is well above the maximum physical value. Physically, this means that the turbulence should not be able to induce destructive oscillations in the droplet because the inherent damping due to the droplets viscosity is too great. The experimental data, however, indicates that even at high viscosity ratios, small diameter droplets are still broken up by the turbulence. Hence, it can be concluded that the present modelling is not suitable for the prediction of high viscosity droplet break-up and may need to be extended to cover this case

As described in Section 3.3.3.2, the origin of this behaviour is due to the underlying modelling of turbulence as a harmonic disturbance whose frequency is directly coupled with its intensity [94]. Hence, large disturbances have a very short duration and their net effect is small. In reality, however, break up by such large disturbances may well be possible, although increasingly improbable. Chesters [94] has anticipated this situation and has stated that the way forward may be to abandon the critical Weber number approach and replace it with a probability-based approach. Here, the probability of break-up would be calculated for all droplet sizes and thus all would contribute to the overall break-up.

#### 6.4.2.4 Mesh Sensitivity Tests

Again, in order to gauge the effects of the mesh size on the accuracy of the two-phase calculations, the Case 6 (6/2.5 m/s, surfactant-free) calculations were repeated on all three meshes. Figure 6.17 shows the resulting profiles for the mean diameter and phase fraction at the  $z=60\ \text{mm}$  measuring position.

It can be seen that the results for all three meshes are very similar. Differences on the centreline are negligible, although small differences do appear for  $0.6 < r/R < 0.9$ . Here, the fine meshes produce slightly less dispersion leading to a reduction of about 2 to 3% in the phase fraction relative to the coarse mesh results. In this region the fine mesh results also imply that the droplet diameter profile is steeper next to the wall because of slightly less break-up in this region. This is due to the greater resolution of the turbulence region immediately adjacent to the wall.

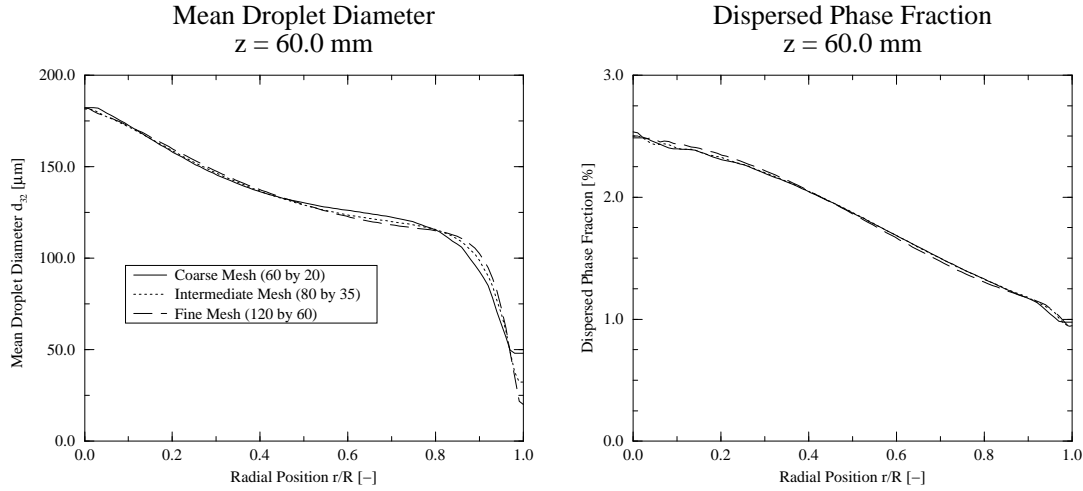


Figure 6.17: Mesh sensitivity results for Case 6 (6/2.5 m/s, surfactant-free).

#### 6.4.2.5 Turbulence Model Performance

The effects of the two-phase turbulence modelling on the results has been assessed by repeating the calculations for Case 1 (15/2.5 m/s, no surfactant) and Case 6 (6/2.5 m/s, no surfactant) with the additional two-phase turbulence source terms in the  $k$  and  $\epsilon$  equations excluded from the calculation. This reduces the turbulence model to a straightforward single-phase  $k$ - $\epsilon$  model. The effects of these terms on the calculations can be assessed by comparing these results with the previous calculations where the terms have been included.

Figure 6.18 shows the results for Case 1. All profiles relate to the centreline of the pipemixer. It can be seen that the results for both cases are very similar. The turbulent kinetic energy for the two-phase turbulence model is only at most 0.14% higher than the single-phase results (at the  $z=0.05$  position). This small increase over the single-phase turbulence is due to the drag-induced turbulence generation term (Eqn (2.89)). This effect is negligible when compared to the high shear-induced turbulence generation due to the high velocity difference between the nozzle and annulus streams in this case. The turbulent kinetic energy increases to a maximum at the point where the high shear zones converge on the centreline.

The small turbulence increase in the two-phase results is due to the drag between the phases, which is a consequence of the slip velocity. The droplets enter the calculation domain at a lower velocity than the continuous phase and so the slip velocity is relatively high in the inlet region. However, due to the small droplet sizes and the small density

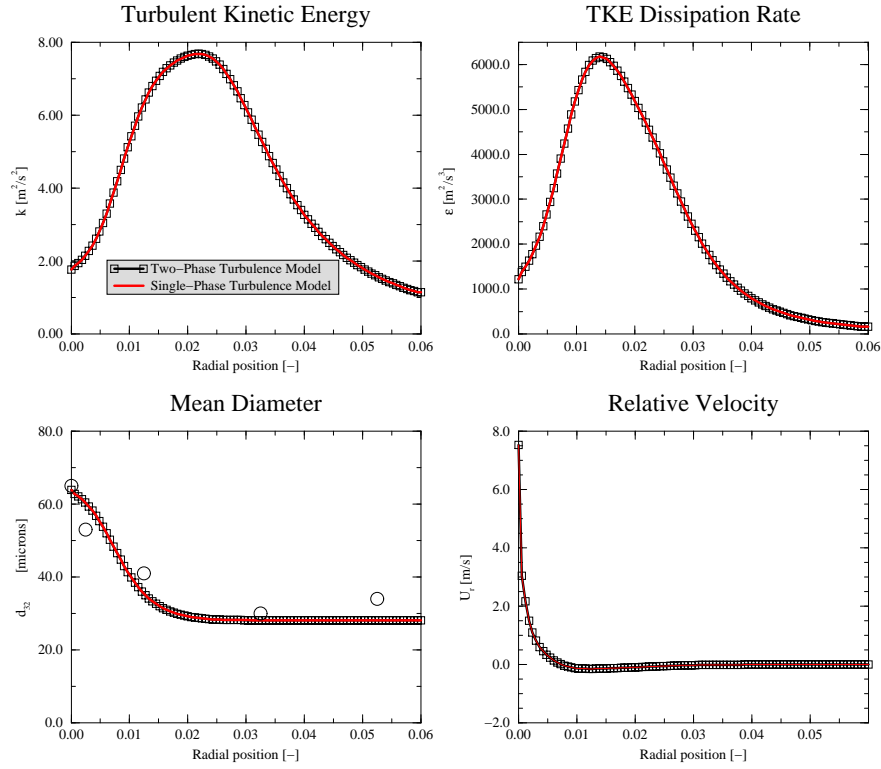


Figure 6.18: Turbulence model performance for Case 1 (15/2.5 m/s, surfactant-free).

difference between the phases, the droplets soon attain the velocity of the continuous phase as shown in the graph of the slip velocity in Figure 6.18. The drag-induced turbulence generation effect is therefore limited to the inlet region.

Since the differences between the single- and two-phase turbulent kinetic energy and the dissipation rate are small, the difference in the calculated droplet size is also small. The lower left-hand graph in Figure 6.18 shows the calculated and measured mean droplet size along the pipe centreline. It can be seen the development of the mean droplet size along the pipe centreline has been well captured.

Figure 6.19 shows similar comparisons for Case 6. It can be seen that the differences between the single- and two-phase turbulence models are more pronounced in this case. The turbulent kinetic energy from the two-phase model is approximately 7% higher than the single-phase model. Again, this increase is due to drag-induced turbulence generation. The difference is more pronounced in this case because the velocity difference between the nozzle and annulus is not as great as in the previous case and the shear-induced turbulence generation does not completely dominate.

The lower right-hand graph in Figure 6.19 shows the slip velocity between phases along the centreline. The initial slip velocity at the inlet plane reduces sharply downstream as

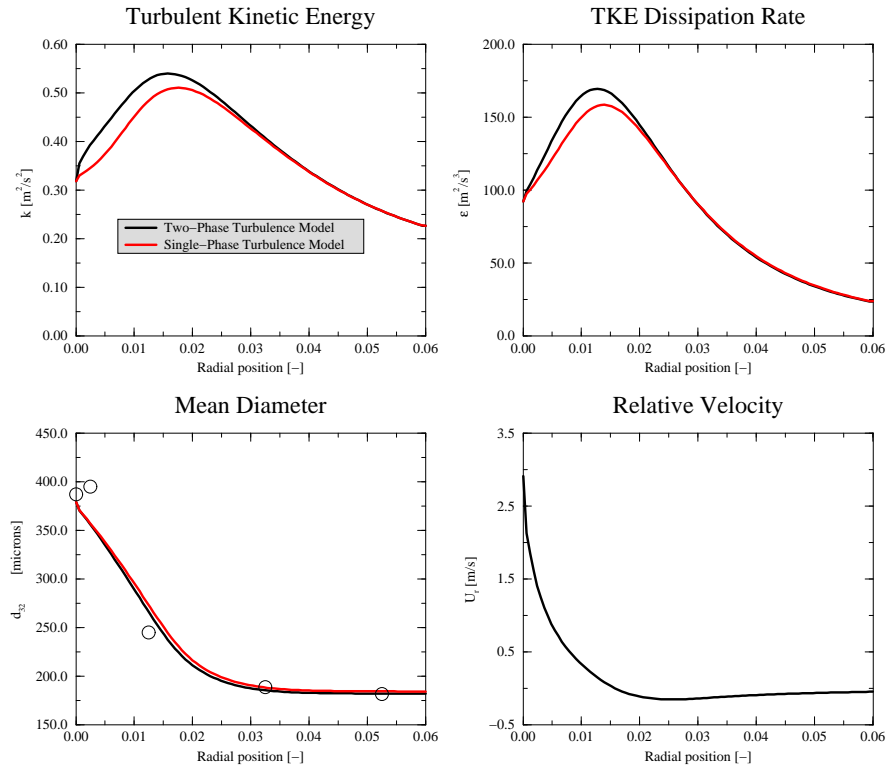


Figure 6.19: Turbulence model performance for Case 6 (6/2.5 m/s, surfactant-free).

the droplets accelerate to the continuous phase velocity. It can be seen that the increases in the turbulent kinetic energy and the dissipation rate are confined to the region where the slip velocity is large.

The predicted and measured mean droplet sizes are shown in the lower left-hand graph in Figure 6.19. The differences between the single- and two-phase models are small, despite the larger differences in  $k$  and  $\epsilon$ , due to the fact that the droplet break-up rate is a weak function of  $\epsilon$  (see Eqn (3.43)).

## 6.5 Discussion And Conclusions

Despite the unsatisfactory results of the current model at high viscosity ratios, its behaviour in the other regimes, especially those involving the influence of surfactants, has been very encouraging.

In particular, this study has highlighted the fact that the break-up characteristics of droplets are tightly coupled to the transport of the surfactant and the droplets, and to the dynamic nature of the interface. The results show that is not appropriate to simply calcu-



late the equilibrium surface tension at a particular surfactant concentration and perform a break-up calculation which does not account for local surfactant adsorption and desorption rate. It is especially important to account for the transport of the droplets through regions of high turbulence where the high break-up rate may lead to non-equilibrium conditions at the interface.

Further comparisons with accurate experimental data are necessary in order to accurately determine the appropriate value of the critical amplitude parameter  $K$  and to further investigate the re-adsorption rate to the droplet interface when the droplet residence time in the high turbulence zone is high. Most importantly, accurate data at the inlet plane for both phases is vitally important if drastic assumptions are to be avoided when prescribing the boundary and initial conditions.

The calculations have shown that the influence of the turbulence model is not of great importance in this study, where the small relative velocity between phases over the bulk of the calculation domain is small, at least in the prediction of the mean droplet diameter. Accurate experimental data relating to the turbulence properties in liquid-liquid two-phase systems is needed to determine the true performance of the two-phase turbulence model in these systems.

Finally, the lack of any numerical problems during the simulation of these cases is very pleasing. The drag model used in this particular study did not require the sub-iterative technique described in Section 4.5.2.1 to be used since, for the droplet diameters and slip velocities encountered, the drag law is essentially linear. However, it may be that for larger droplet sizes, or for cases where the influence of the surfactant on the drag force leads to a non-linear drag law, this technique may prove useful.

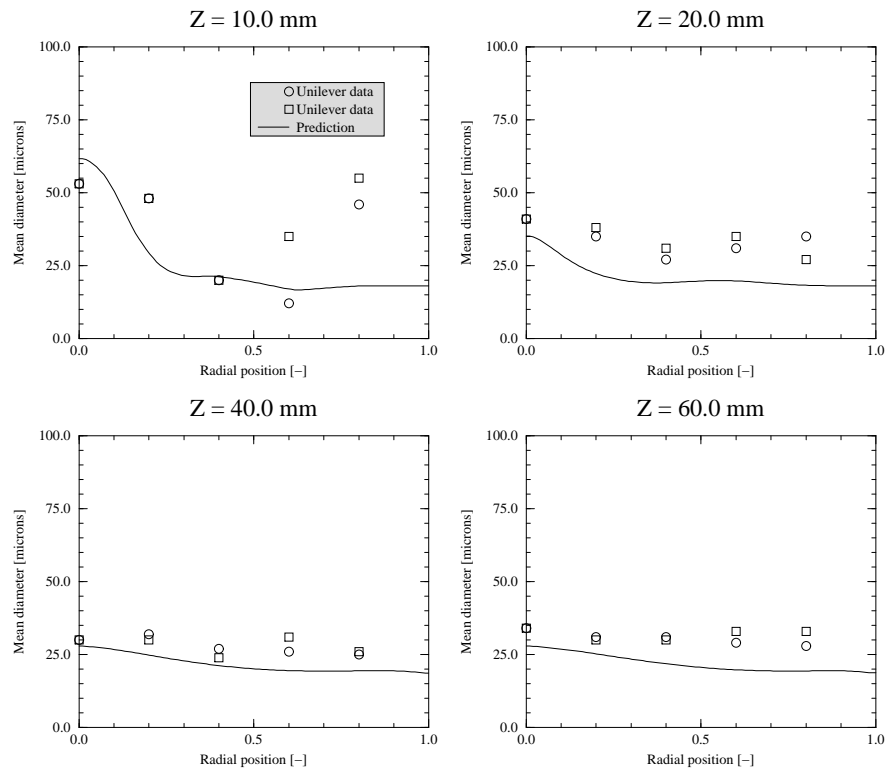


Figure 6.20: Case 1 (15/2.5 m/s) - Mean diameter profiles.

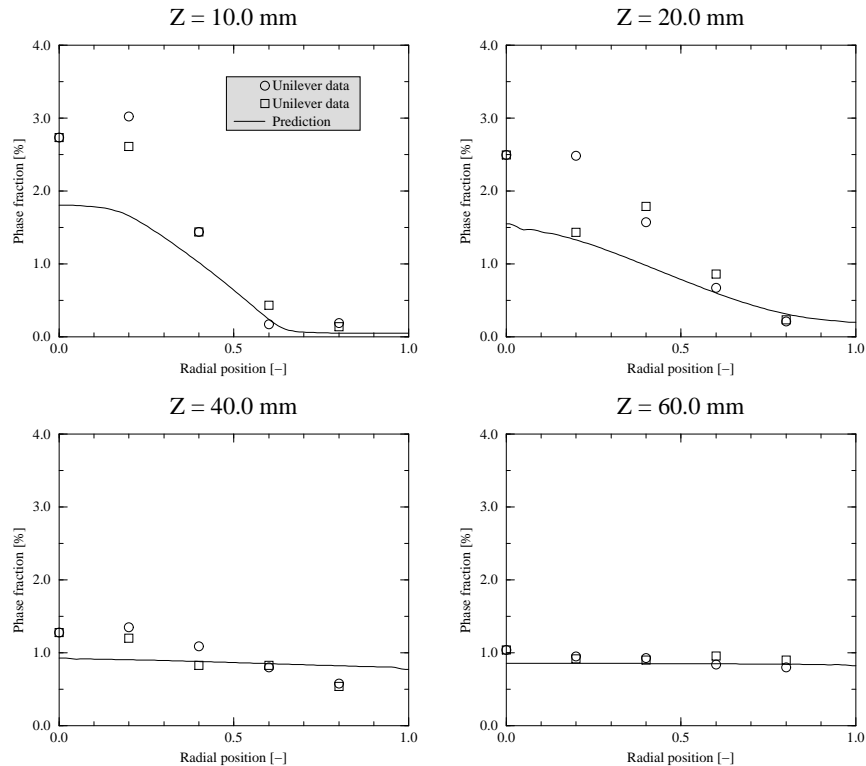


Figure 6.21: Case 1 (15/2.5 m/s) - Phase fraction profiles.

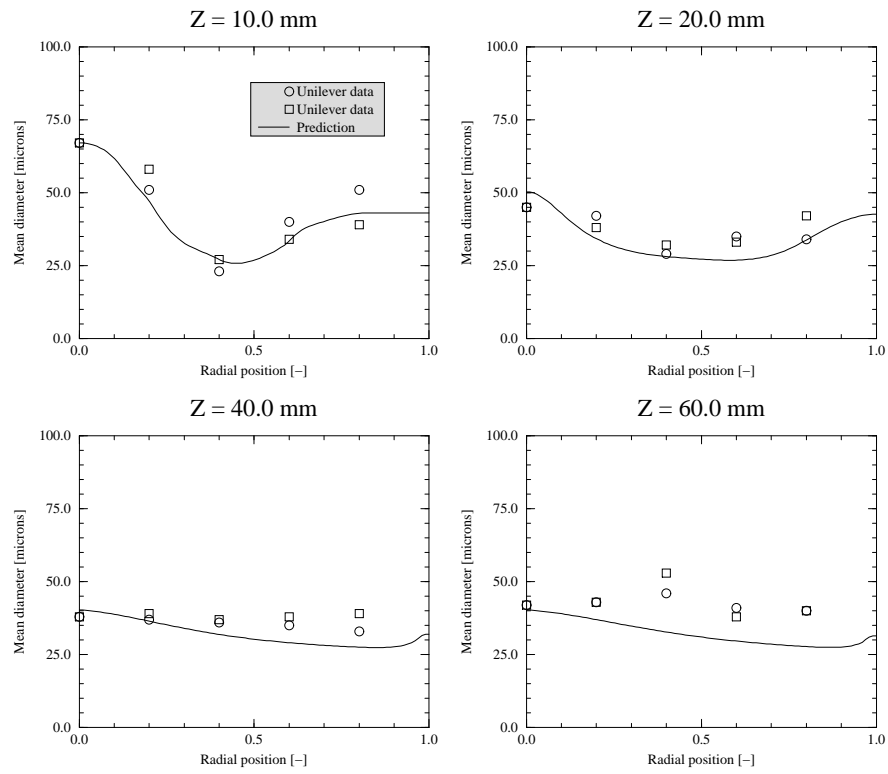


Figure 6.22: Case 2 (15/2.5 m/s) - Mean diameter profiles.

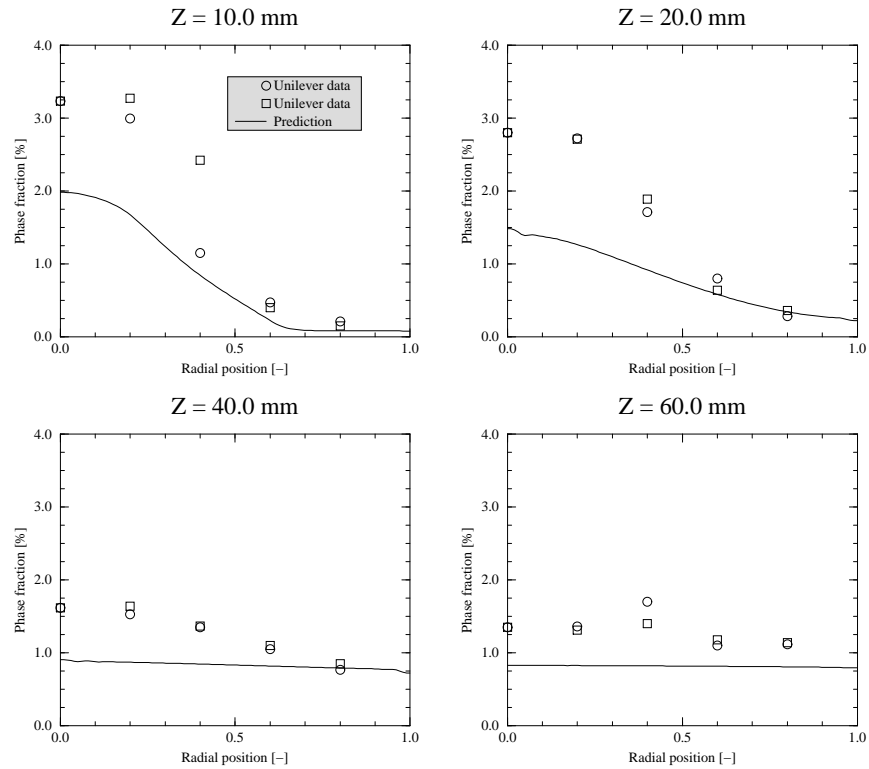


Figure 6.23: Case 2 (15/2.5 m/s) - Phase fraction profiles.

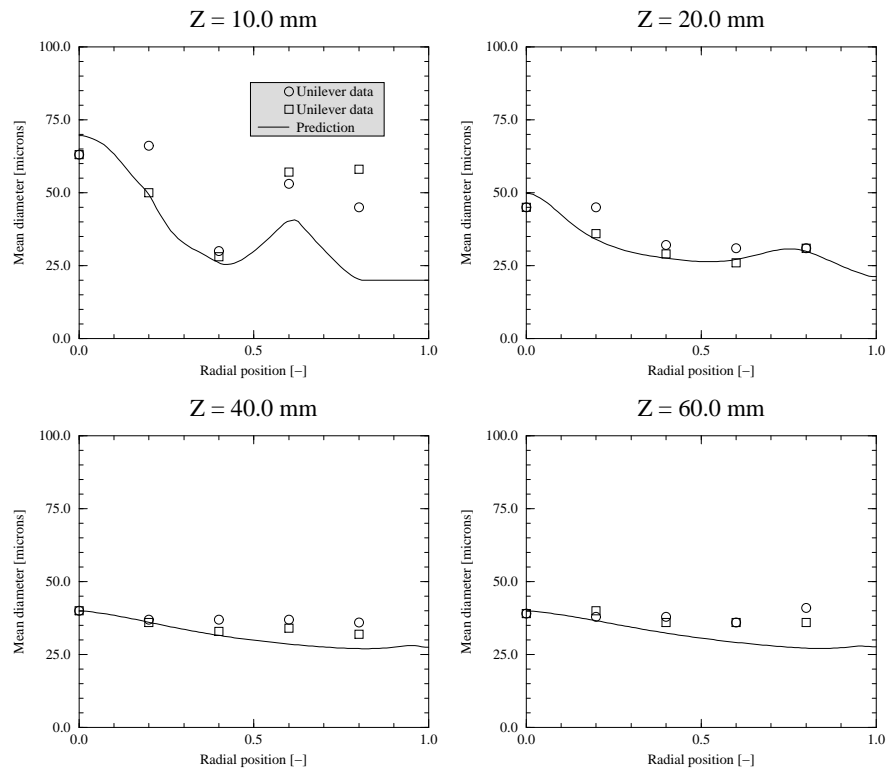


Figure 6.24: Case 3 (15/2.5 m/s) - Mean diameter profiles.

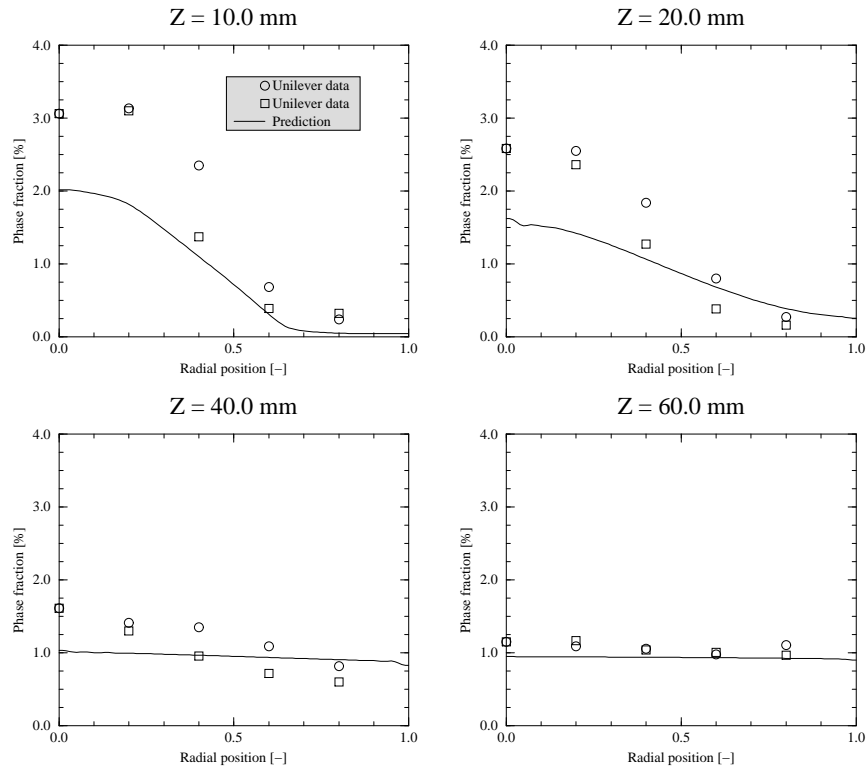


Figure 6.25: Case 3 (15/2.5 m/s) - Phase fraction profiles.

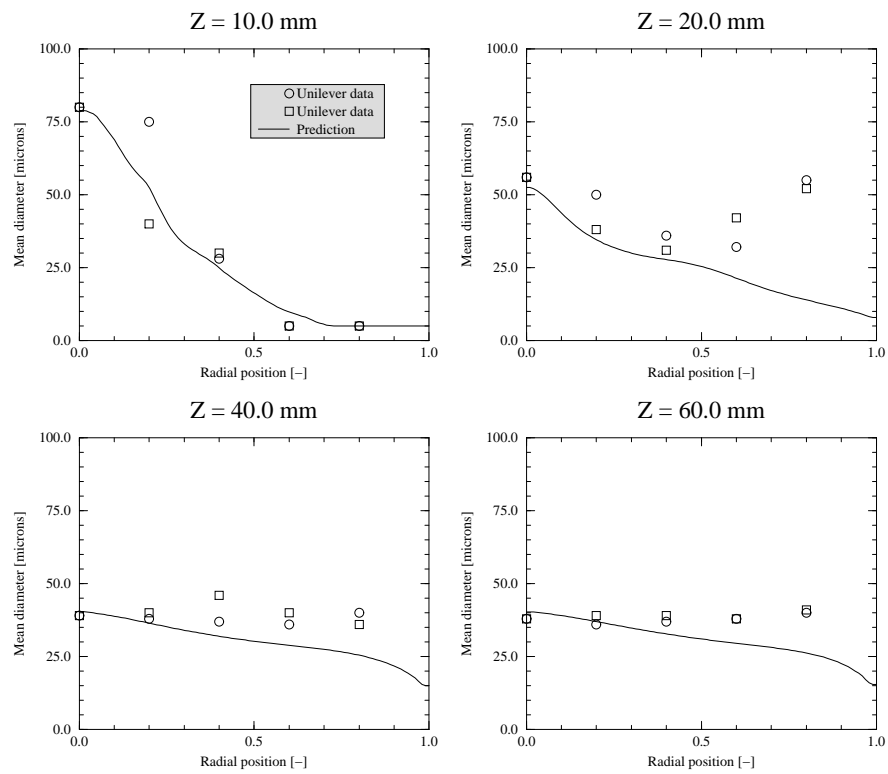


Figure 6.26: Case 4 (15/2.5 m/s) - Mean diameter profiles.

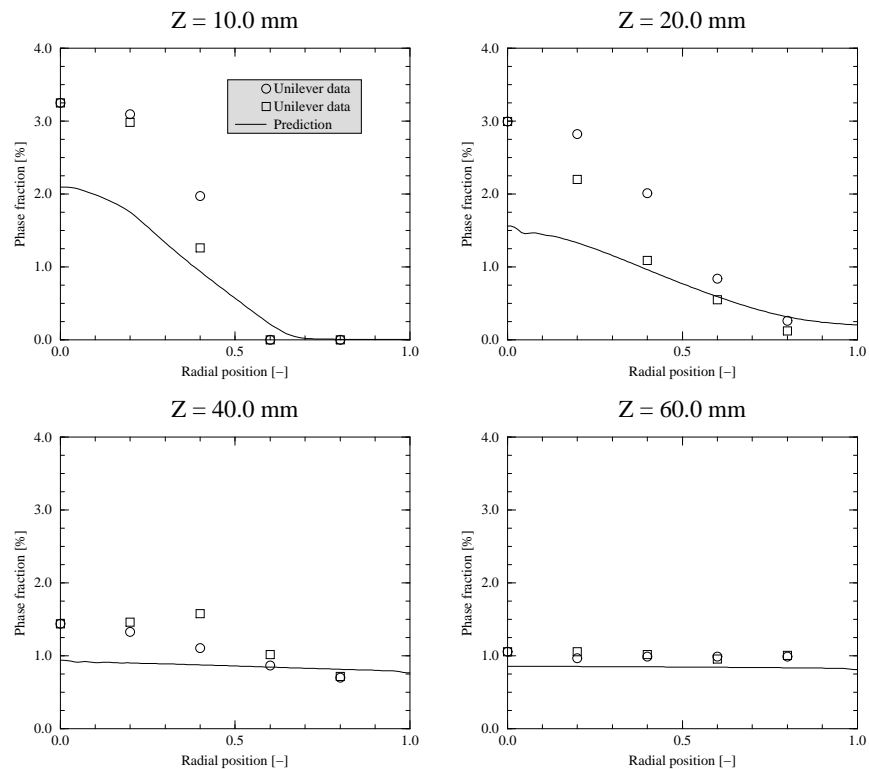


Figure 6.27: Case 4 (15/2.5 m/s) - Phase fraction profiles.

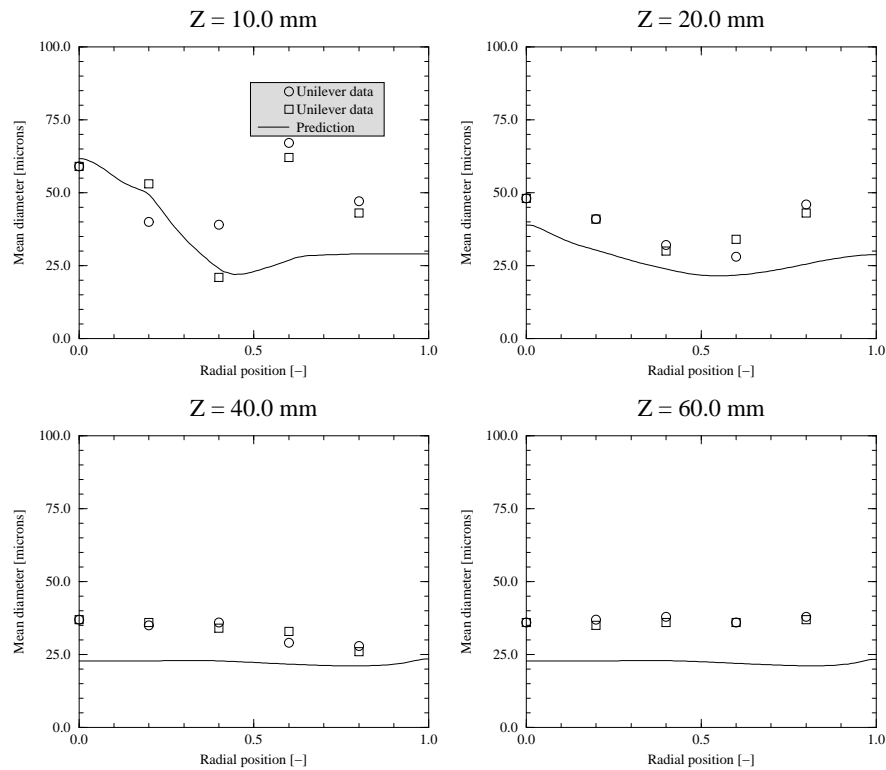


Figure 6.28: Case 5 (15/2.5 m/s) - Mean diameter profiles.

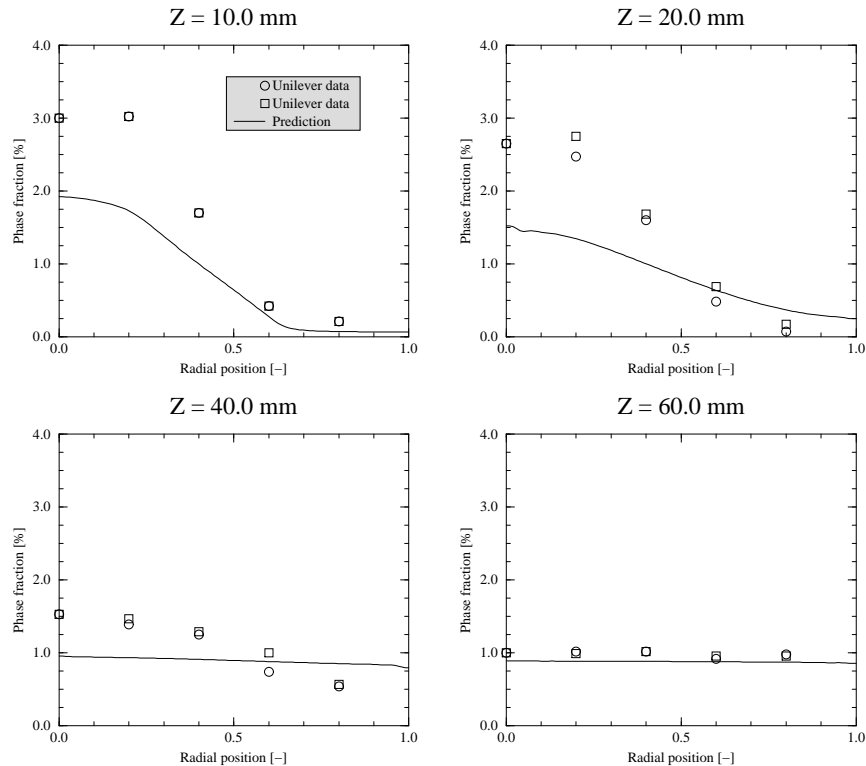


Figure 6.29: Case 5 (15/2.5 m/s) - Phase fraction profiles.

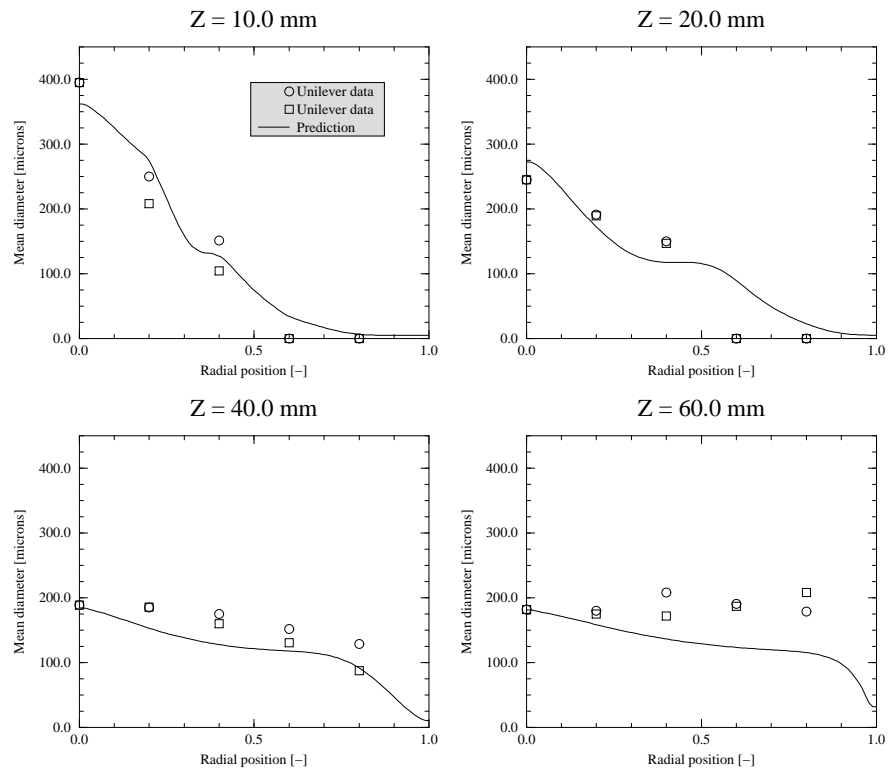


Figure 6.30: Case 6 (6/2.5 m/s) - Mean diameter profiles.

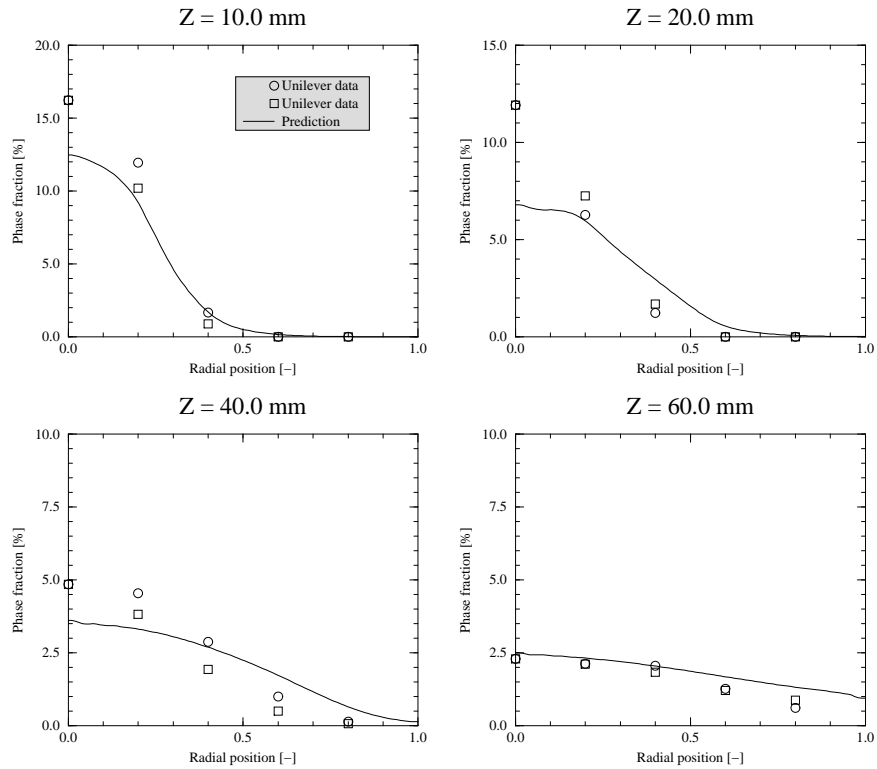


Figure 6.31: Case 6 (6/2.5 m/s) - Phase fraction profiles.

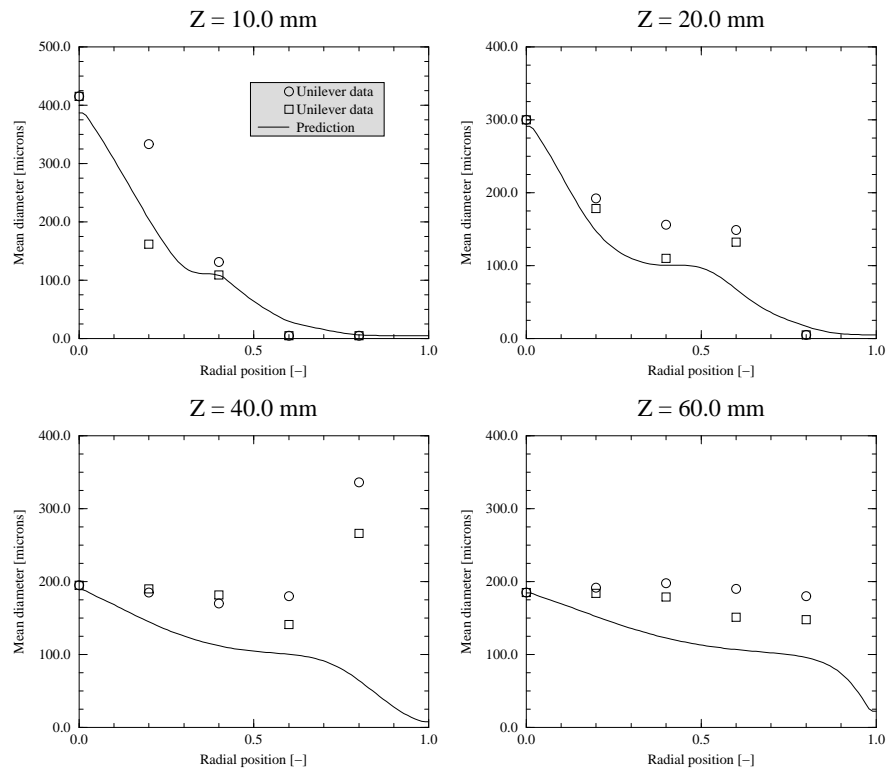


Figure 6.32: Case 7 (6/2.5 m/s) - Mean diameter profiles.

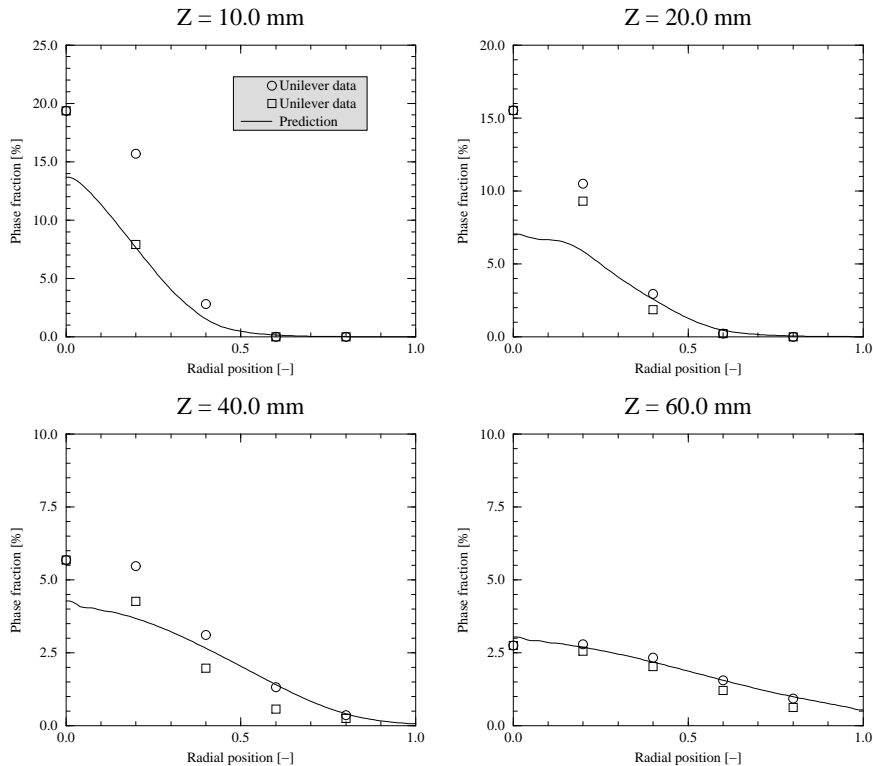


Figure 6.33: Case 7 (6/2.5 m/s) - Phase fraction profiles.



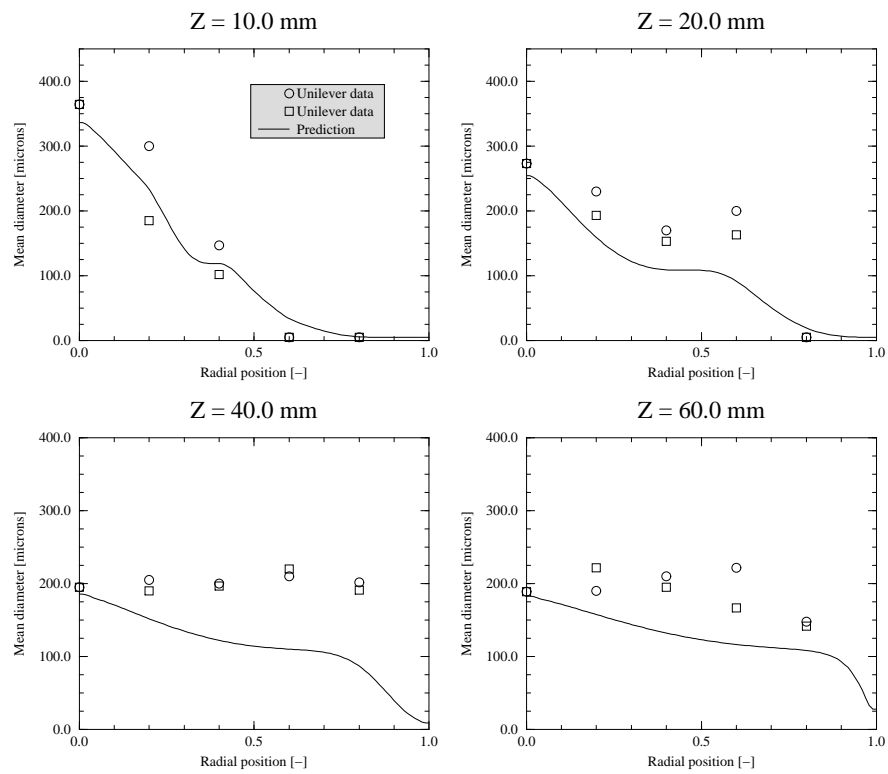


Figure 6.34: Case 8 (6/2.5 m/s) - Mean diameter profiles.

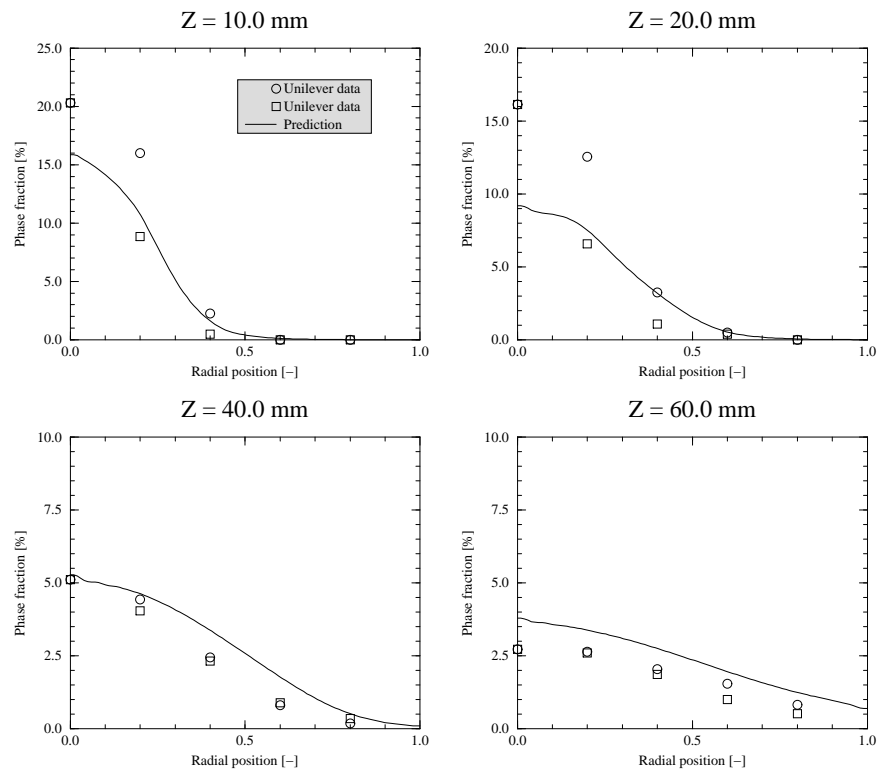


Figure 6.35: Case 8 (6/2.5 m/s) - Phase fraction profiles.

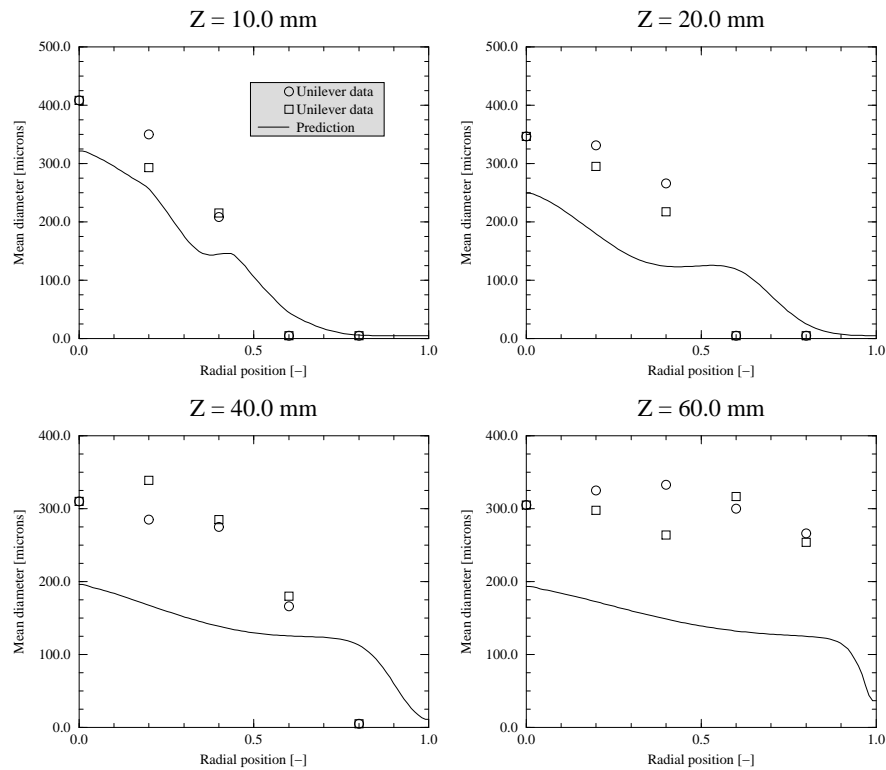


Figure 6.36: Case 9 (6/2.5 m/s) - Mean diameter profiles.

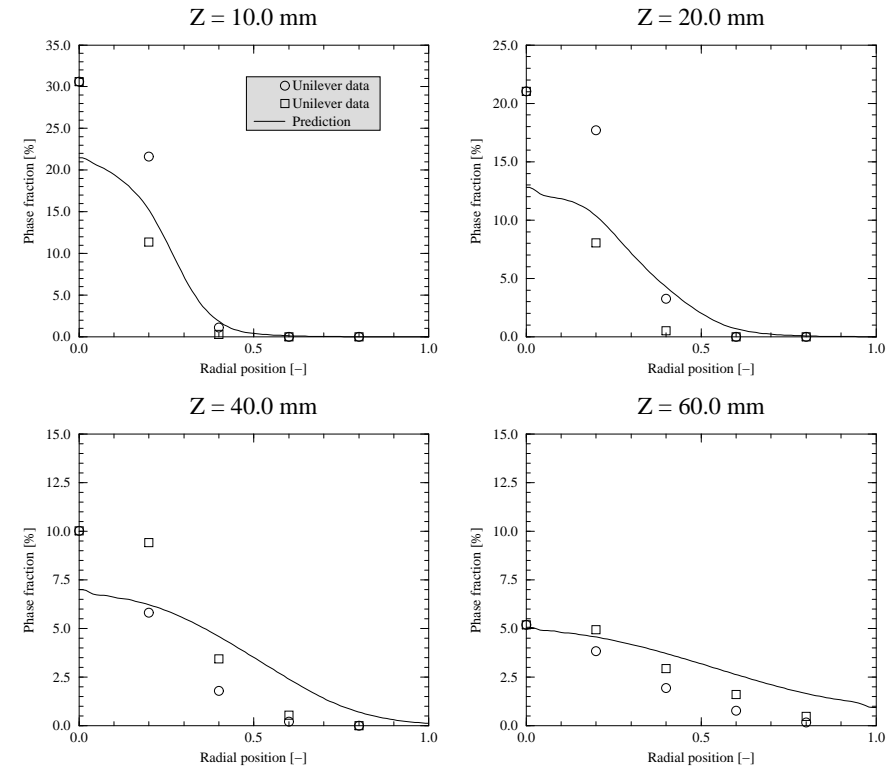


Figure 6.37: Case 9 (6/2.5 m/s) - Phase fraction profiles.

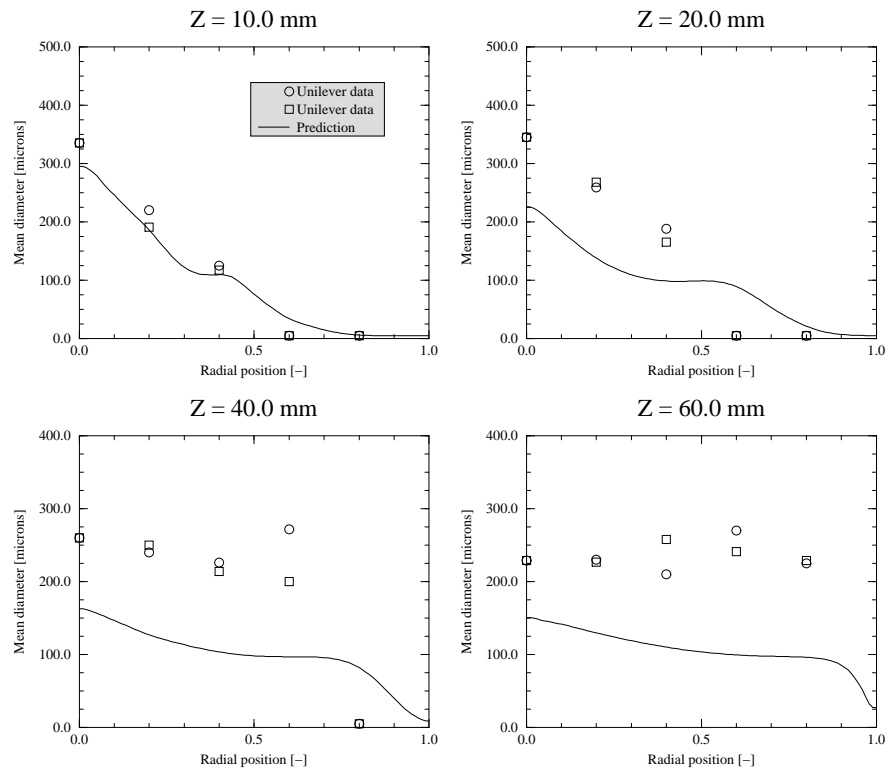


Figure 6.38: Case 10 (6/2.5 m/s) - Mean diameter profiles.

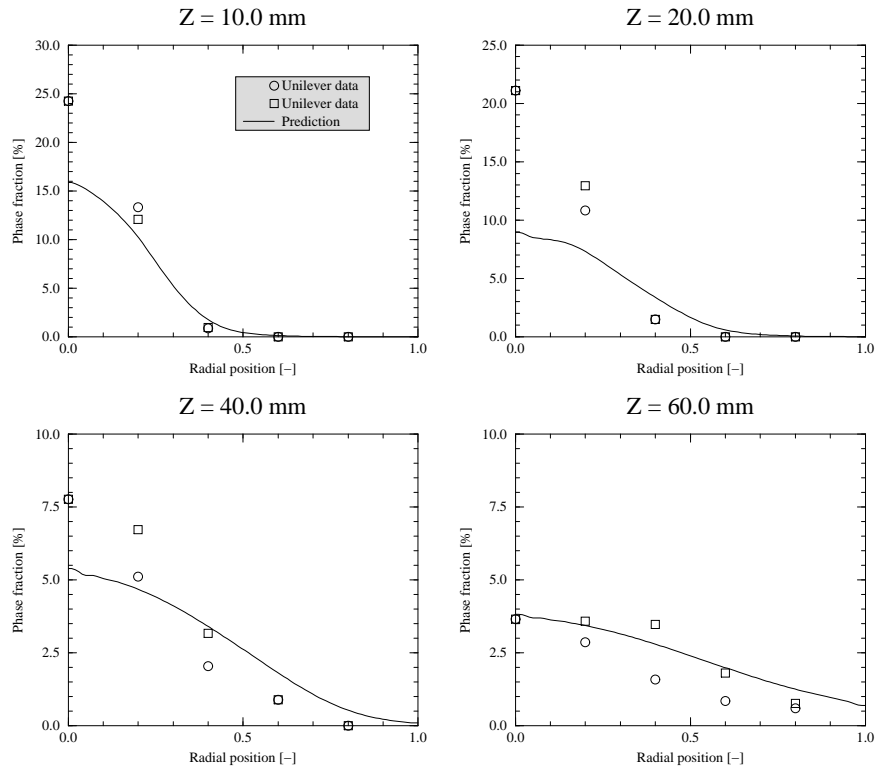


Figure 6.39: Case 10 (6/2.5 m/s) - Phase fraction profiles.

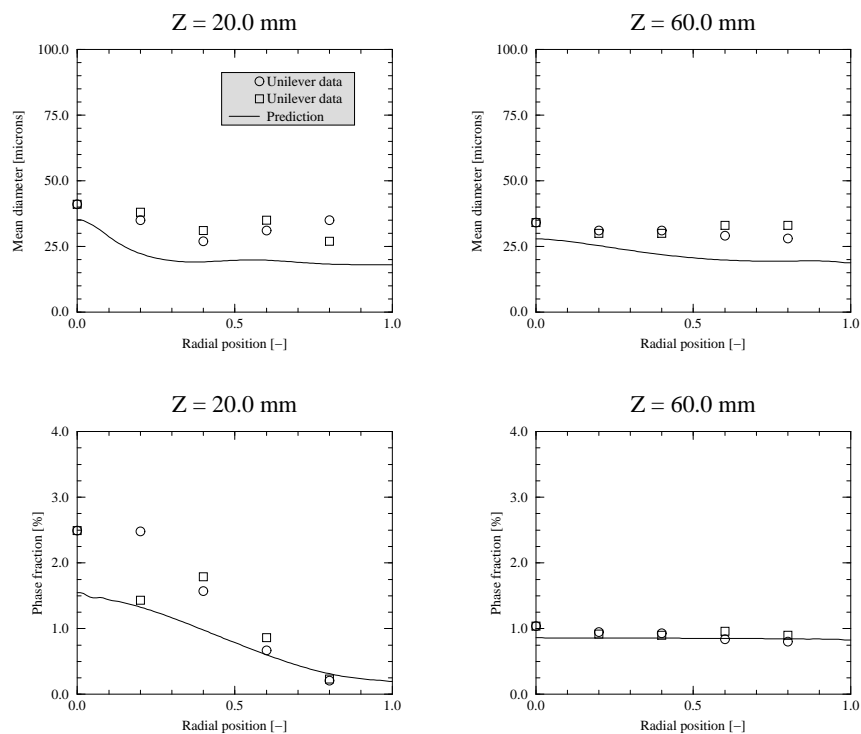


Figure 6.40: Case 11 (Bayol 35) - Mean diameter and phase fraction profiles.

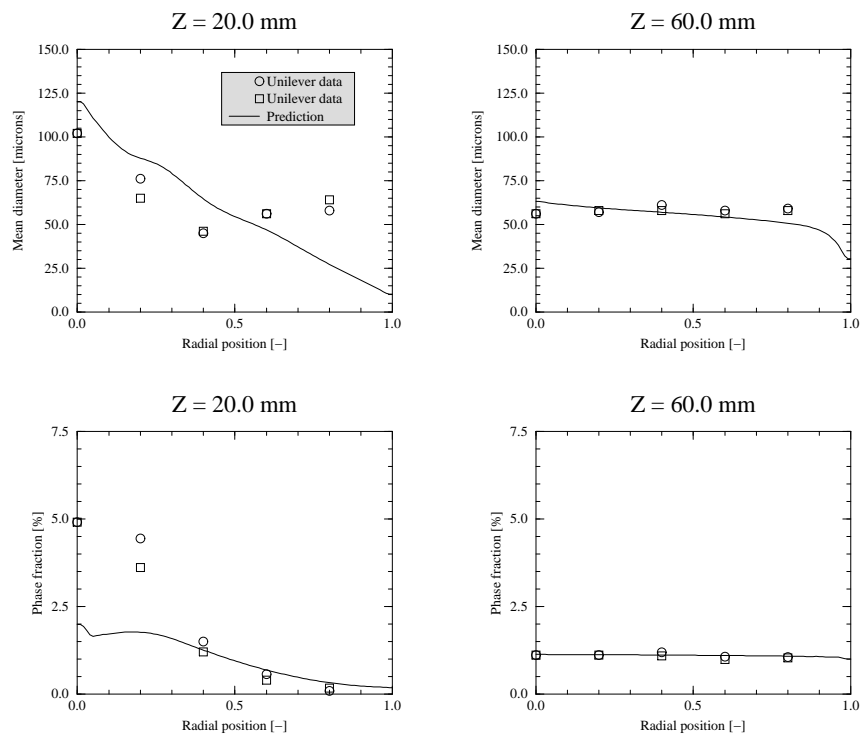


Figure 6.41: Case 12 (Marcol 82) - Mean diameter and phase fraction profiles.

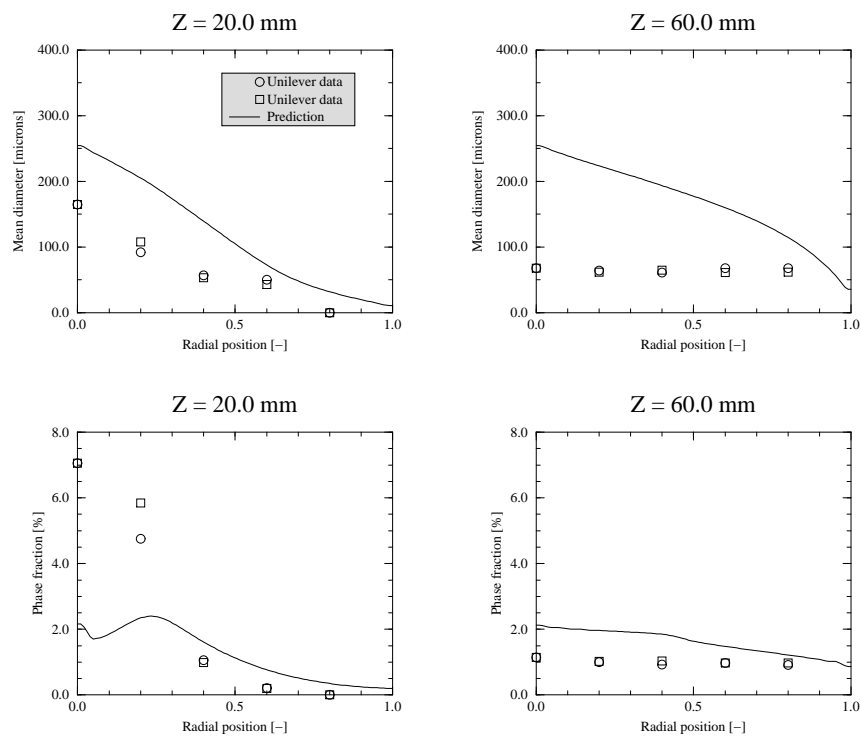


Figure 6.42: Case 13 (Marcol 172) - Mean diameter and phase fraction profiles.



## Chapter 7

# Two-Phase Flow In A Stirred Vessel

In this chapter the air-water two-phase flow in a sparged mixing vessel stirred by a six-bladed Rushton turbine is simulated and compared to the experimental data of Fischer [143]. The predictions are carried out using the general purpose commercial CFD code STAR-CD using an advanced technique which allows the impeller rotation to be simulated by using multiple reference frames in different regions of the tank. Reasonably good agreement is obtained for the dispersed phase fraction distribution and for the mean bubble velocity for the majority of the tank.

### 7.1 Introduction

The mixing together of two or more substances is one of the most common unit operations in the chemical process industries. Frequently, the mixing process is accompanied by chemical reaction, heat and mass transfer and break-up and coalescence of the dispersed phase. The device most commonly employed to perform this process is the Stirred Vessel, which essentially consists of a cylindrical tank containing a number of flat baffles attached to the inside periphery and a central shaft carrying one or more motor driven impellers, as shown in Figure 7.3. The presence of high shear regions caused by the impeller rotation and the existence of the baffles induces a high turbulence level in the fluid. Mixing and emulsification is achieved via the combined effects of the bulk motion and high local turbulence levels.

The design of such devices been mainly carried out in the past by empirical techniques and by trial-and-error experimentation (see for example Oldshue [144]). Such empirical

design methods have a number of disadvantages. Firstly, the information derived from such studies is usually global in nature (e.g. the power consumption of the impeller) and provide no information regarding the local physical processes within the flow. Secondly, the extrapolation of the data to new or novel processes or fluids is uncertain which could result in a sub-optimal design. These uncertainties are sometimes addressed by the construction of a pilot plant or by experiment, with a corresponding increase in the cost and time of the process design phase.

The application of CFD methods to stirred vessel flows can remove many of these uncertainties. CFD methods are able to provide extremely detailed local information, as well as the more traditional global parameters. They can be applied at relatively low cost to any number of cases involving any number of different geometrical configurations, operating conditions, fluid properties and at any level of detail.

The simulation of stirred vessel flows, however, has been hampered by the fact that the flow within the stirred vessel is inherently unsteady (periodic), three dimensional and involves a moving boundary geometry (i.e. the impeller). Until recently, a lack of computing power and suitable computational techniques have prevented the full simulation of even single-phase laminar flows within a stirred vessel. Despite this, many workers have been successful in applying approximate techniques which have proven to be very valuable. Recent advances in computer power and CFD techniques have now all but removed the 'geometrical' limitations and state-of-the-art CFD codes can now take into account the moving boundary and the periodic three dimensional nature of the flow on relatively affordable hardware.

The next major hurdle is concerned with the modelling of the physical processes and conditions within the stirred vessel. Many industrially important processes are two-phase, either solid-liquid, liquid-liquid or gas-liquid. The techniques required to provide accurate predictions of such systems in stirred vessels is still under development and have been the subject of numerous previous studies, most notably Politis [6] who proposed a technique to predict the solid-liquid flow in stirred vessels.

In this chapter the air-water bubbly flow in a sparged vessel stirred by a six-bladed Rushton turbine is simulated using a state-of-the-art computational technique. The system was studied experimentally by Fischer [143] using an Ultrasound Pulsed Doppler technique to provide local phase fraction and local dispersed phase velocity information. Despite these parameters being of significant importance in the understanding of the flow characteristics of two-phase systems, such experimental data is rarely found in the literature due to the difficulty in obtaining such measurements.

In the next section, some previous studies into stirred vessels are briefly examined and



their findings are summarised. Following this, details of Fischer's experimental studies are given. Then, in Section 7.4, the numerical simulations are discussed and finally, in Section 7.5, the experimental data and predictions are compared and some conclusions about the performance of the two-phase predictions are drawn.

## 7.2 Previous Stirred Vessel Studies

The majority of studies have been experimental and single-phase, although two-phase studies have appeared with increasing frequency in the last 10 years as experimental techniques have improved. Thorough reviews of the available literature have been reported by Bolour-Frousham [145], Politis [6] and Tabor [146].

### 7.2.1 Single-Phase Studies

The majority of single-phase flow studies have used a 'standard' stirred vessel configuration, where the relative proportions of the tank's principal dimensions are fixed, employing either a Rushton turbine or a pitched blade impeller. These studies have either been concerned with flow visualisation or with obtaining detailed measurements of the mean flow velocities and turbulence characteristics. The present case employs a six-bladed Rushton turbine in a cylindrical tank with four baffles. The main flow characteristics of such a configuration may be summarised as follows [6].

- The Rushton impeller rotation generates a radial, swirling stream of high velocity fluid which impinges on the tank walls forming upward and downward flowing wall jets.
- The jets induce a strong three dimensional vortical flow within the vessel, comprising two horizontal ring vortices above and below the impeller. The centres of these vortices are close to the impeller stream and the vessel wall. The lower vortex is stronger in standard vessels and causes the impeller stream to be diverted slightly upwards.
- Vertical vortices are formed behind the baffles.

Also, detailed measurements of the impeller stream have led to the discovery of two trailing vortices behind each of the impeller blades. These vortices are initially vertical but bend into a horizontal position as they leave the upper blade edge and extend well into the impeller discharge flow [147, 148], as shown in Figure 7.1.



Figure 7.1: Trailing vortices behind the Rushton impeller blades.

### 7.2.2 Two-Phase Studies

Two-phase experimental studies are not as common as those for single-phase flows due to the experimental difficulties in obtaining reliable data. The wide variety of possible flow configurations (different phase combinations, geometry, etc. ) and physical effects (mass transfer, break-up and coalescence, etc. ) has led to a dilution of the resources available for specific flow regimes.

Early two-phase experimental studies focused on solid-liquid flows, where the size distribution and properties of the dispersed phase could be accurately controlled and break-up and coalescence effects were absent. In these types of flows, the main issue is dispersion of the dispersed solids throughout the flow field and the minimum impeller speed or power input which will maintain the suspension. Thus, studies have tended to concentrate on the effects of geometry.

Reliable data has recently become available with the advent of modified LDA techniques such as phase Doppler discrimination or conductivity probes. Studies based on these techniques (e.g. Nouri [149]) have determined that the turbulence in the impeller stream is reduced with respect to the single-phase flow by about 13 to 28%, and that the velocity of the solid particles lags behind that of the continuous phase in upward flow and in the impeller stream and leads the continuous phase in downward flow.

Studies into gas-liquid flows have become more common in recent years. Many of these studies were concerned with the bubble size distribution throughout the vessel but most

do not give any data regarding the local dispersed phase fraction or local bubble velocities. Exceptions to this are Bakker [150], Bakker and Van Den Akker [151], Morud and Hjertager [152] and Fischer [143].

Many workers have reported the presence of gas filled cavities behind the impeller blades [147, 150, 153]. These cavities are caused by the reduced pressure in this region, and interact with the trailing vortices behind the impeller blades. The trailing vortices are thought to contribute significantly to break-up in emulsification systems [154].

Two-phase computational studies have tended to adopt a two-fluid approach [155, 156, 112, 157, 6, 152]. Most of the applications have been three dimensional, apart from Morud and Hjertager [152] who used a two dimensional cylindrical polar mesh where the impeller was modelled as a time averaged momentum source at the centre. Again, these two-phase studies used simplified impeller models which limited their usefulness as predictive tools but they did deliver encouraging results. Recent studies [158, 159, 160] have applied the more advanced multiple reference frame technique.

### 7.2.3 Impeller Modelling

Computational studies into stirred vessel flows have become more common as CFD techniques have improved. Early studies were inevitably single-phase and employed simplified, time-averaged models for the impeller, which removed the periodicity of the flow and rendered it time-independent.

One such technique was to obtain experimental or empirical information relating to a specific impeller at a number of points on an imaginary surface surrounding the impeller swept volume. The impeller region was then excluded from the simulation and the data applied as boundary conditions on the surface surrounding the impeller region [156, 145, 161]. Another technique was to impose empirically determined body forces and additional ‘sources’ of turbulence on the fluid within the impeller swept volume [6, 152]. These body forces and extra sources were again derived from studies of particular impeller designs.

These models have been successful in reproducing the gross features of the flow but their time-averaged nature means that they are incapable of predicting the periodic time-dependent behaviour of the flow and the flow features local to the impeller blades which may have a large effect on the performance of the vessel. In addition, their impeller-specific nature introduces an element of uncertainty when the models are used outside of their ‘derived’ ranges.

More advanced techniques are based on the full geometrical modelling of the impeller using either a ‘moving mesh’ or a ‘multiple reference frame’ approach [162]. Both techniques

are shown schematically in Figure 7.2. The moving mesh approach is the most general of the two and involves splitting the computational mesh into two concentric sections. Each section can move relative to the other whilst leaving the interface between the two mesh sections transparent to the solution of the flow equations. The geometry of the impeller is modelled exactly by the inner section of mesh which rotates with it, while the outer part of the tank (i.e. the section including the baffles) is modelled by a static mesh. Special techniques are applied to ensure numerical stability and accuracy while the mesh topology changes during the course of the calculation.

Such an approach is inherently time dependent but does allow the fully transient behaviour of the flow to be investigated. This may be essential in start-up or shut-down situations or when the flow is inherently unsteady. The drawback with this approach is the cost associated with performing three dimensional time dependent calculations which may be prohibitive for fine meshes or complex geometries.

The ‘multiple reference frame’ approach takes advantage of the fact that, when the distance between the impeller and the baffles is large enough, the flow within the impeller region is steady with respect to the impeller and the flow in the outer part of the tank is steady with respect to the baffles. Each region is simulated within an appropriate reference frame; for the outer part of the tank this is static, while for the impeller region it is rotating. The velocities at the interface are coupled by transforming the velocities between reference frames.

The advantages of this technique are that it does not require complex mesh motion and also the time independent nature of the flow in each region significantly reduces the overall computational cost. Even in cases where this approach is not strictly valid it can be used to great effect to provide the initial field for a true time dependent simulation using the moving mesh technique.

### 7.3 The Experiment of Fischer *et al.*

The experimental study by Fischer and co-workers [143, 153] into the air-water bubbly flow in a stirred vessel was motivated by the need for an understanding of the transfer of oxygen to micro-organisms in aerobic biochemical processes. Such processes have been described in the past by empirical correlations which describe the integral mass transfer of oxygen from the bubbles to the bulk fluid. Such studies do not yield any information on the non-uniform concentration distribution of the dissolved oxygen which occurs in industrial scale bioreactors and which can give rise to product quality problems in complex reactions. In order to provide accurate data to validate predictive models of such systems, Fischer *et*

*al.* [153] have provided detailed local information on the dispersed phase throughout the tank using a novel ultrasound pulse technique. The data reported includes the dispersed phase fraction, bubble size, bubble number density and bubble velocity.

The stirred vessel, illustrated in Figure 7.3, had three baffles and was stirred by a six-bladed Rushton turbine driven at 500 rpm. The air was introduced into the tank through a ring sparger situated towards the bottom of the tank at a rate of 0.93 vvm (volume gas per tank volume per minute).

All measurements were made on a vertical plane situated midway between a pair of baffles. The ultrasound pulsed doppler technique is based on the generation of ultrasound pulses which are reflected from the bubble's surface. The doppler shift resulting from the motion of the bubble relative to the probe enables its velocity to be deduced while the amplitude of the reflection and the number of returned pulses allows the interfacial surface area and the number density respectively to be determined. The Sauter mean diameter ( $d_{32}$ ) may then be deduced from these quantities by assuming that the bubbles are spherical. Fischer quotes errors of approximately 5% on the mean velocities and 15% on the phase fraction for this technique.

Fischer also employed a single point conductivity probe in order to validate the ultrasound technique. Fischer states that the two techniques have similar reliability. The phase fraction data obtained with this probe is also compared to the predictions in Section 7.5.

The measured mean diameter was approximately uniform over the majority of the tank at about 4 mm, although Fischer reports that in the impeller stream and adjacent to the sparger, the bubble diameters are approximately 1 mm and 8 mm respectively.

## 7.4 Numerical Simulations

The numerical simulations for this case were carried out using the commercial CFD code STAR-CD, which features a general purpose arbitrarily unstructured finite volume method and the multiple reference frame technique for the simulation of the impeller. It also has incorporated a two-fluid model very similar to the one proposed in Chapter 2. This model was implemented into STAR-CD as part of the same BRITE research project of which this thesis forms a part.

The principal difference between the present model and that implemented in STAR-CD lie in the treatment of the drag term and the neglect of the interfacial pressure term (Eqn (2.38)) in the phase momentum equations. STAR-CD adopts the drag model of Politis [6] which, in addition to the mean drag, has an extra component which takes account of the

fluctuations in the drag force induced by the surrounding turbulent eddies. Thus, in the STAR-CD formulation, Eqn (2.38) in the present formulation is replaced by

$$\mathbf{F}_d = A_d \bar{\mathbf{u}}_r - A_d \frac{\nu_c^t}{\alpha_d \alpha_c \sigma_\alpha} \nabla \alpha_d \quad (7.1)$$

where  $d$  is the bubble diameter,  $\nu_c^t$  is the turbulent viscosity,  $\bar{\mathbf{u}}_r$  is the mean relative velocity,  $\sigma_\alpha$  is the Schmidt number for the dispersed phase and  $A_d$  is given by Eqn (2.8).

The solution algorithm employed by STAR-CD is essentially the same as that of Oliveira [25] as outlined in Section 4.5.1.2.

The computational domain for this case, shown in Figure 7.4, corresponds to a 120 degree segment of the tank to take advantage of the periodicity of the geometry. Part of the shaft has been removed from Figure 7.4 to allow the impeller to be shown clearly. The position of the baffle is 30 degrees relative to the ‘upstream’ periodic plane while the positions of the impeller blades are positioned at 30 and 90 degrees. The sparger pipe has been modelled as a circular block of cells with the inlet on the inner face. The plane midway between the baffles coincides with the position of the second impeller blade. The impeller rotates anti-clockwise when viewed from above.

The total number of cells employed was 48252. The MRF approach requires that the section of the mesh surrounding the impeller, indicated in red in Figure 7.5, has a rotating frame of reference defined. This reference frame is defined to rotate with the angular velocity of the impeller. The outer radius of the impeller mesh region coincides with the midway point between the outer edge of the impeller blade and the inner edge of the baffles ( $2r/D = 0.59$ ). The impeller region extends 50 mm above and below the impeller.

Wall boundary conditions are applied to the bottom and sides of the tank and on the faces of the impeller blades and the baffles. The top surface of the tank is designated as an outlet for the dispersed phase and as a slip boundary for the continuous phase. The remaining two planes are designated as periodic flow surfaces. The upstream and downstream periodic planes are logically the same; flow into one plane is seen as flow out of the other. All co-ordinate transformations between the periodic planes are handled automatically.

The initial field for the calculations was obtained by solving the single-phase case for the same flow conditions. This yielded initial fields for the continuous phase velocity, turbulent kinetic energy and dissipation rate. Then, the two-phase calculation was started with the initial dispersed phase velocity set equal to that of the continuous phase, and the initial dispersed phase fraction set to a uniform value of 0.05. This practice was essential to the success of the calculation.

## 7.5 Results

Figure 7.6 shows radial profiles of the measured and predicted dispersed phase fraction on the plane midway between the impellers at eight different heights above the base of the tank. Both the ultrasound and conductivity probe measurements have been plotted, along with error bars denoting the 15% uncertainty quoted by Fischer.

It can be seen that the two measuring techniques produce quite different results in some regions of the tank, especially just under the impeller ( $z/H = 0.2$ ) where the ultrasound probe yields phase fraction measurements approximately 300-400 % higher than the conductivity probe. Despite these discrepancies, the two probes show the same trend in the data over most of the tank.

The peak in the phase fraction at  $r/R = 0.6$  at the lowest measuring station corresponds to the position of the gas injection point (i.e. the sparger pipe). The predictions in this region compare quite well to both probe measurements. Note that the sharp ‘spike’ in the predicted profile is due to the fact that the values for this profile have been taken directly from the calculation mesh; no interpolation or spline fitting has been applied. A finer mesh density in this region would be required in order to resolve this spike properly.

The profiles at the  $z/H = 0.20$  position (just below the impeller position) agree quite well with both probe data sets for  $r/R > 0.3$ . For  $r/R < 0.3$  the predictions are in agreement with the conductivity probe data only; the ultrasound probe data indicates much larger values for phase fraction in this region.

The results reflect the existence of the upper and lower ring vortices for both the continuous and dispersed phases. The peak in the phase fraction towards the wall at the  $z/H = 0.20$  position corresponds to the centre of the dispersed phase ring vortex, which can be clearly seen in Figure 7.8 which shows the bubble mean velocity vectors on the measuring plane. The peak in phase fraction at this position is caused by the migration of the bubbles into the low pressure region associated with the centre of the continuous phase vortex.

On the plane of the impeller ( $z/H = 0.31$ ) measured data is only available for  $r/R > 0.6$ , for which good agreement is obtained. The peak in the predicted phase fraction in the inner region corresponds to bubbles trapped in the wake of the impeller blade, while the trough is associated with the outer edge of the impeller blade where both phases experience rapid acceleration. The lower density of the dispersed phase causes the bubbles to accelerate faster in this region resulting in a reduction in the local gas phase fraction. These features are discussed in more detail below.

The remaining measuring stations show relatively flat profiles for the phase fraction. In general, the predictions agree reasonably well with the data although there is an over-

prediction of the phase fraction near to the top surface. These discrepancies may be due to differences between the measured and predicted gas velocities in this region, or due to some surface effect not accounted for in the simulations.

The measured and predicted profiles for the mean bubble velocity magnitude are shown in Figure 7.7. Figure 7.8 shows the predicted and measured bubble velocity vectors in the vertical measuring plane.

It can be seen that the profile at the  $z/H = 0.09$  position deviates somewhat from the measurements for  $0.2 < r/R < 0.6$ . The reason for this discrepancy is due to differences in the predicted velocity of the dispersed phase in this region, which is subject to the inward-flowing part of the lower ring vortex. The bubbles are seemingly carried further towards the tank centreline by the continuous phase in the predictions than indicated by the measurements. The peak in the phase fraction at  $r/R = 0.1$  is due to the bubbles rising up towards the impeller, again following the continuous phase lower ring vortex.

The velocity profile at the  $z/H = 0.2$  station shows interesting behaviour near to the wall in the form of a trough at about  $r/R = 0.8$ . It then rises sharply at the wall. This is due to the fact the continuous phase is flowing strongly downwards immediately adjacent to the wall and is carrying the bubbles down with it. Figure 7.8 shows this effect clearly. For  $r/R < 0.8$  the bubbles are travelling upwards towards the impeller.

The high bubble velocity magnitude shown in the profile at  $z/H = 0.31$  is due to the strong radial acceleration of the bubbles near the outer edge of the impeller blade. The experimental data shows a much smaller acceleration in this region as shown in the Figures 7.7 and 7.8.

The remaining profiles in Figure 7.7 show quite reasonable agreement for  $r/R > 0.4$ . Again, the high velocity magnitude near the wall is due to the co-current flow in this region due to the upper ring vortex. Discrepancies are apparent in the region  $r/R < 0.4$  where the predictions show a higher velocity magnitude.

The profiles of phase fraction and bubble velocity magnitude shown in Figures 7.6 and 7.7 reveal some interesting flow features within the tank. In order to see these features more clearly, Figure 7.9 shows the contours of phase fraction overlaid with the velocity vectors of the continuous phase. The regions of high phase fraction adjacent to the sparger, adjacent to the tank wall and on the inside edge of the impeller can be clearly seen.

Also, the upper and lower ring vortices formed by the continuous phase is clearly visible in Figure 7.9. It is interesting to note that the centres of the continuous phase and dispersed phase ring vortices (shown in Figure 7.8) are quite different. The centre of the lower bubble ring vortex is higher and closer to the wall than the continuous phase ring vortex



centre. The position of the upper bubble ring vortex is again higher than the continuous phase but is closer to the centre of the tank. These difference are due to the influence of buoyancy and lift forces acting on the dispersed phase.

The behaviour of the dispersed phase in the impeller region is shown more clearly in Figure 7.10 which shows contours of phase fraction on a plane 10 mm above the impeller position. The regions of high phase fraction immediately behind the impeller blades can be clearly seen. This phenomena has been observed experimentally by Fischer [143] and by others [147, 150] and is due to the low pressure region behind the blades trapping the bubbles. Also worthy of note is the regions of low phase fraction in front of the impeller blade and adjacent to the outer blade edge. The depletion of bubbles in these regions is caused by the strong acceleration of the gas bubbles there.

The region of high phase fraction behind the impeller blades can be more clearly visualised by plotting an isosurface of  $\alpha_d = 0.05$  in this region, as shown in Figure 7.11. It can be seen that the bubbles are mainly trapped near to the top edge of the impeller blade, possibly due to the effects of buoyancy. It is also apparent that bubbles are trapped just under the impeller plate, near to the centre of the tank.

Another flow interesting feature is the region of high phase fraction associated with the centre of the lower ring vortex. Figure 7.12 shows contours of phase fraction again but at a position 355 mm below the plane of the impeller. Two regions of high phase fraction can be clearly seen. The highest of these is behind the baffle in the centre of the vertical vortex formed in the baffle's wake. Again, the low pressure associated with the vortex centre attracts and holds the bubbles.

The region in front of the baffle also shows a region of high phase fraction. This is probably due to the existence of a near counter-current flow in this region where the continuous phase is flowing down at a rate nearly matching the rise velocity of the bubble due to its buoyancy. This effect causes the bubbles to crowd together. The circumferential position of the higher phase fraction region is probably due to the fact that the ring vortices are 'spiralling' due to the impeller motion. The baffle acts to halt the progress of the bubbles circumferentially leading to a high spot just in front of the baffle.

## 7.6 Discussion And Conclusions

The prediction of the two-phase flow within a stirred vessel represents a very challenging case for current CFD techniques. In this chapter we have shown that the current two-phase flow model coupled with the advanced features of a modern commercial CFD code is capable of predicting with a reasonable degree of accuracy the air-water bubbly flow in

a stirred vessel. Furthermore, the predictions have indicated the presence of a number of interesting flow features which would warrant further investigation.

Discrepancies in the prediction of the bubble mean velocity could be attributed to the assumption of a uniform bubble diameter of 4 mm in the prediction. The data indicates that the bubble diameter is approximately 1 mm in the impeller stream and 8 mm immediately adjacent to the sparger. It is in these regions where the predicted mean velocities deviate from the measurements.

Clearly, the variable bubble size within the tank, and the bubble break-up and coalescence could be simulated using the PDF approach outlined in Chapter 3. This case would serve as a good test of the break-up and coalescence models for gas-liquid systems. However, the models presented in Chapter 3 are strictly only valid for liquid-liquid systems and some development would be required before they could be applied to the gas-liquid case.

The motivation behind Fischer's experimental investigation into this case was to investigate the transfer of oxygen to micro-organisms in aerobic biochemical processes. Again, with some development of the models presented in Chapter 3, the simulations could be extended to include not only bubble break-up and coalescence but the mass transfer of oxygen into the continuous phase as well. Such a simulation would be extremely useful in the investigation of biochemical processes.

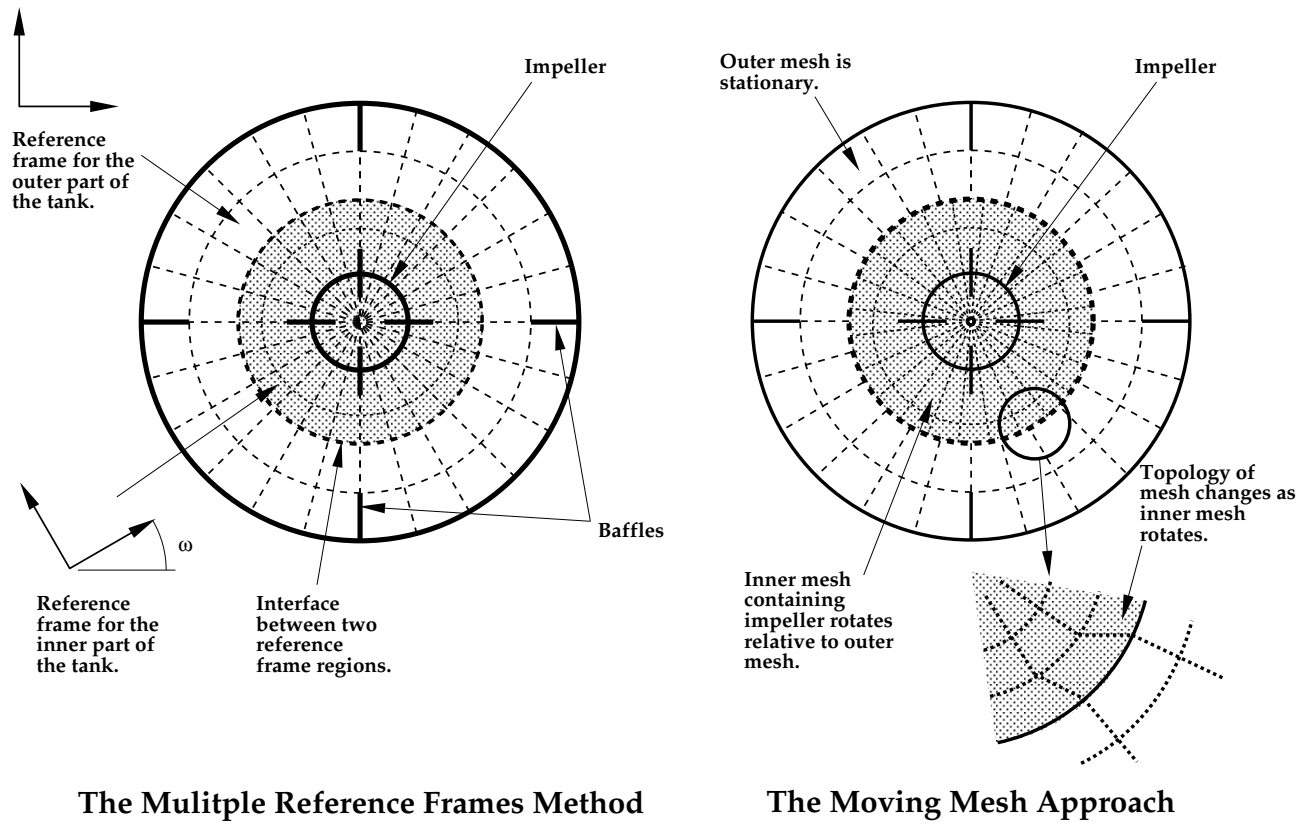


Figure 7.2: Multiple reference frames and moving mesh impeller model approaches.



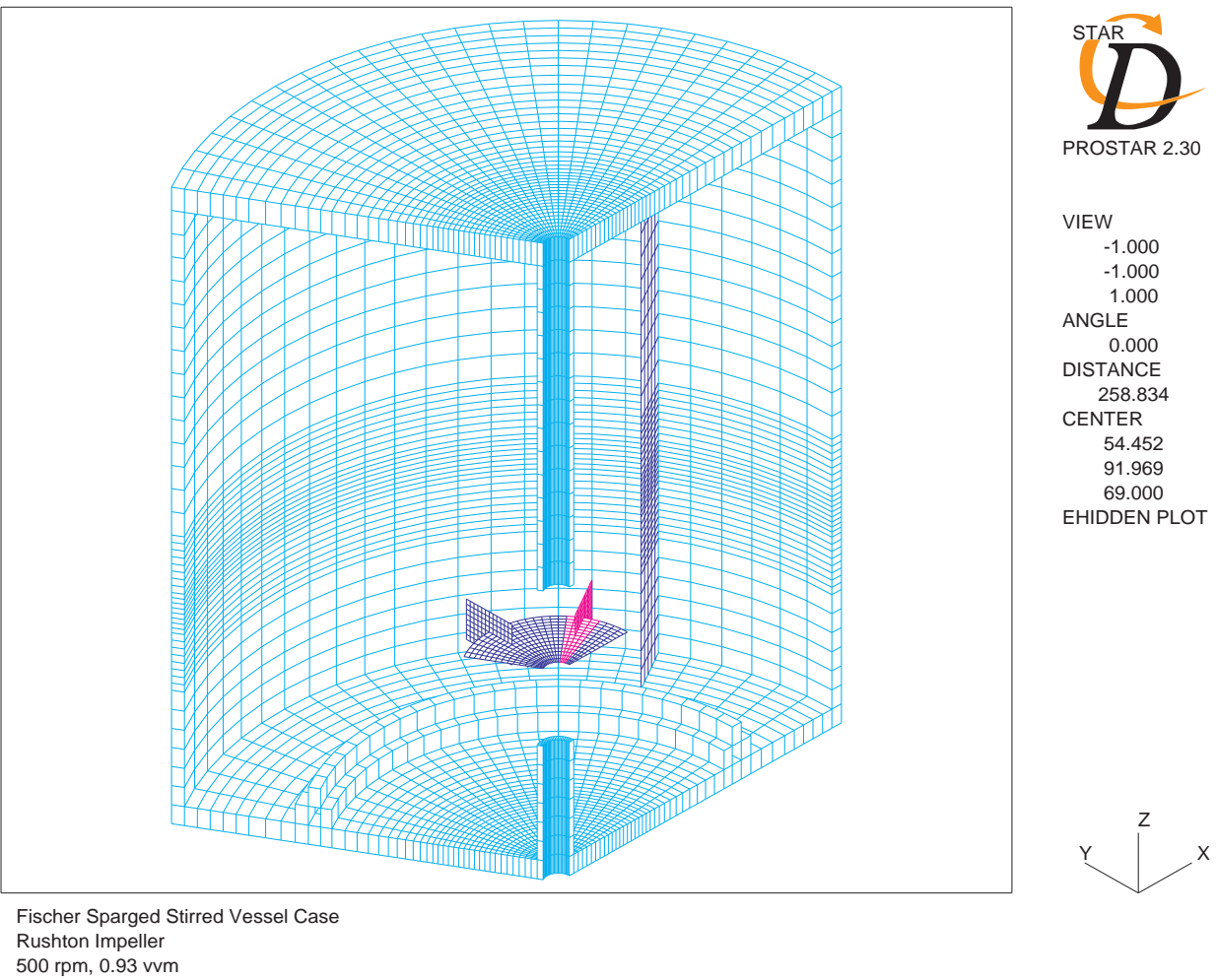
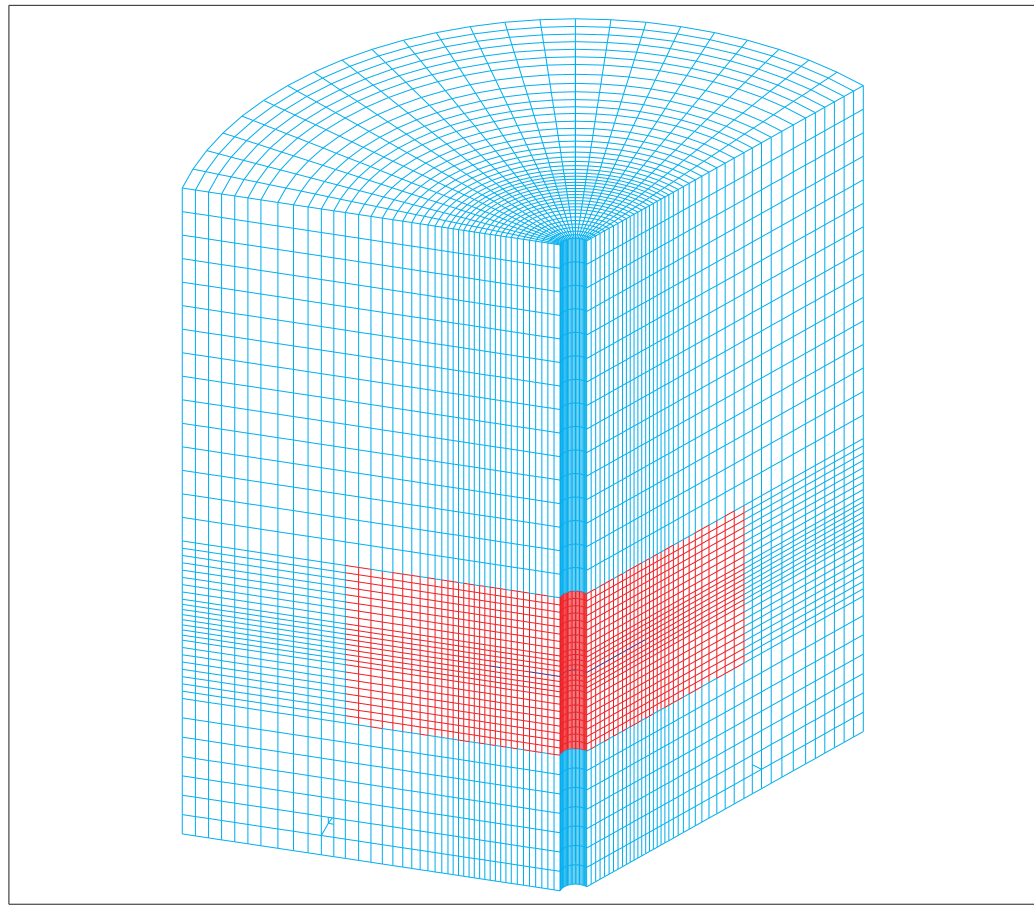
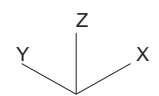


Figure 7.4: Overall layout of the stirred vessel computational mesh showing the impeller and baffles.



VIEW  
-1.000  
-1.000  
1.000  
ANGLE  
0.000  
DISTANCE  
258.834  
CENTER  
54.452  
91.969  
69.000  
EHIDDEN PLOT



Fischer Sparged Stirred Vessel Case  
Rushton Impeller  
500 rpm, 0.93 vvm

Figure 7.5: Location of the rotating reference frame section of the mesh.

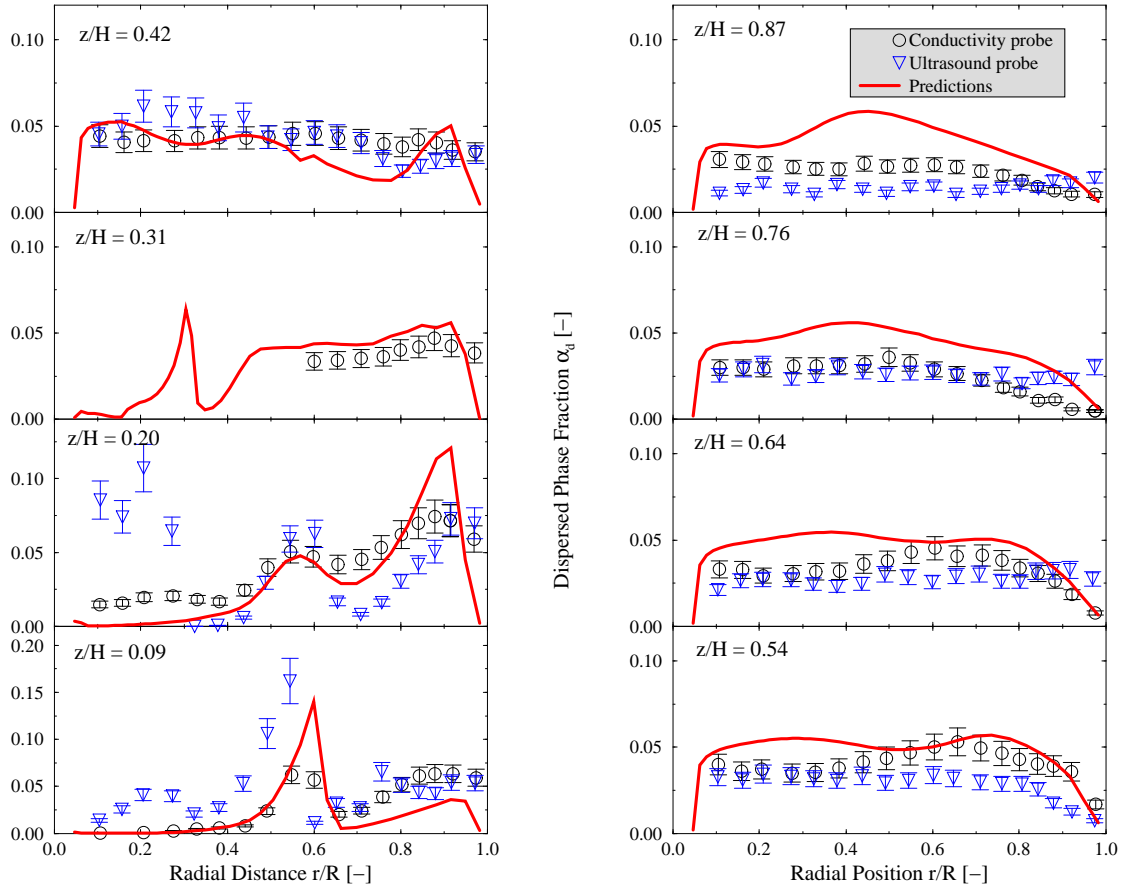


Figure 7.6: Predicted and measured dispersed phase fraction profiles.

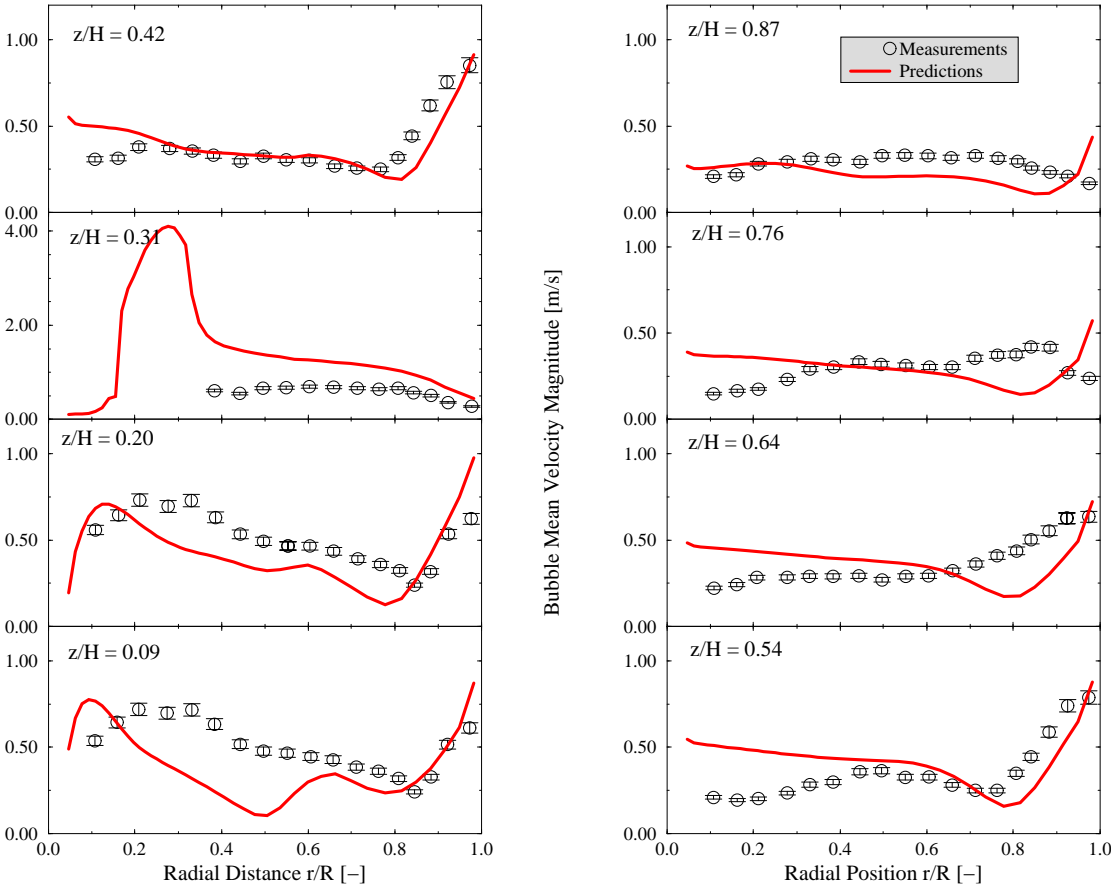


Figure 7.7: Predicted and measured bubble mean velocity profiles.



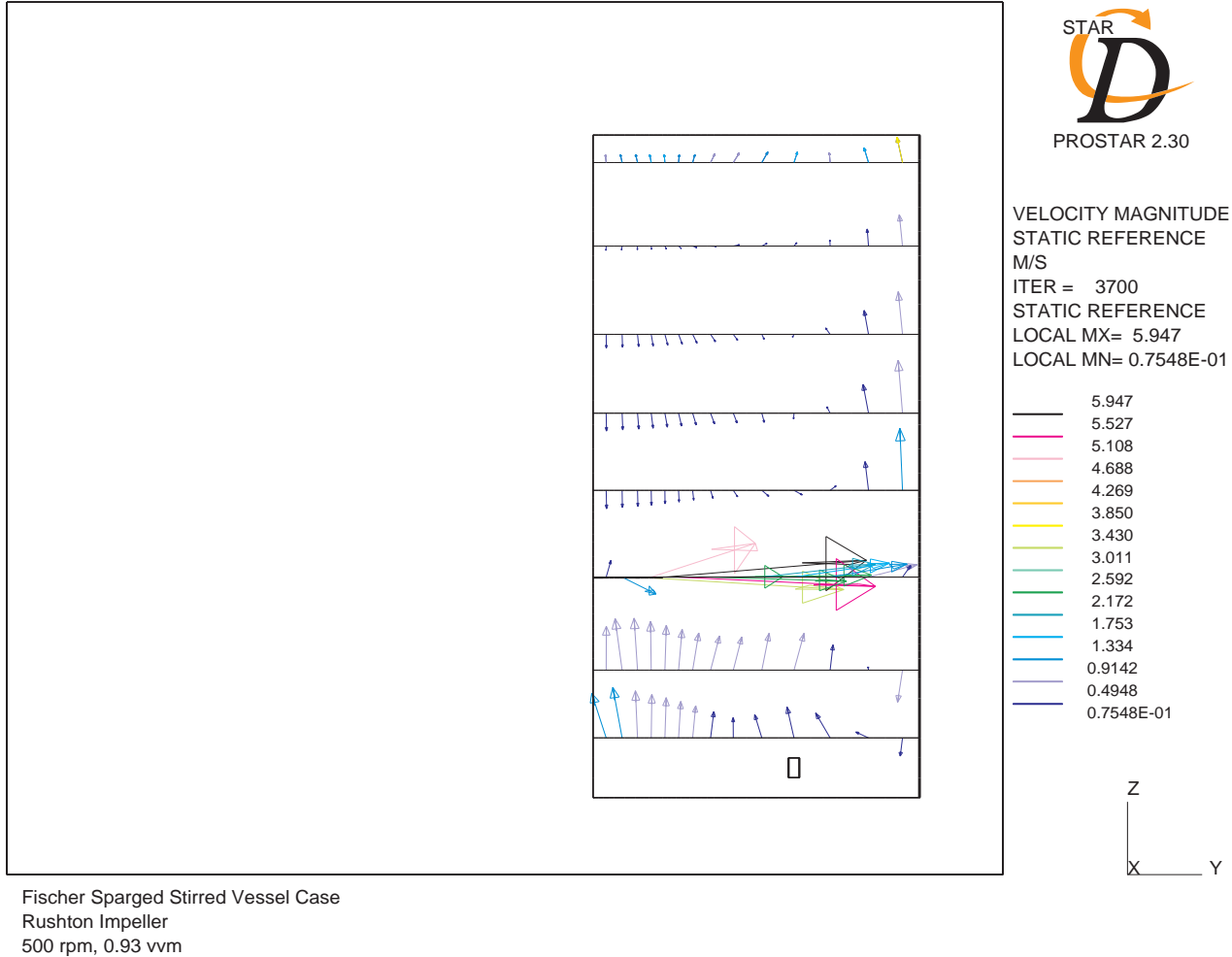


Figure 7.8: Predicted and measured bubble mean velocity vectors.

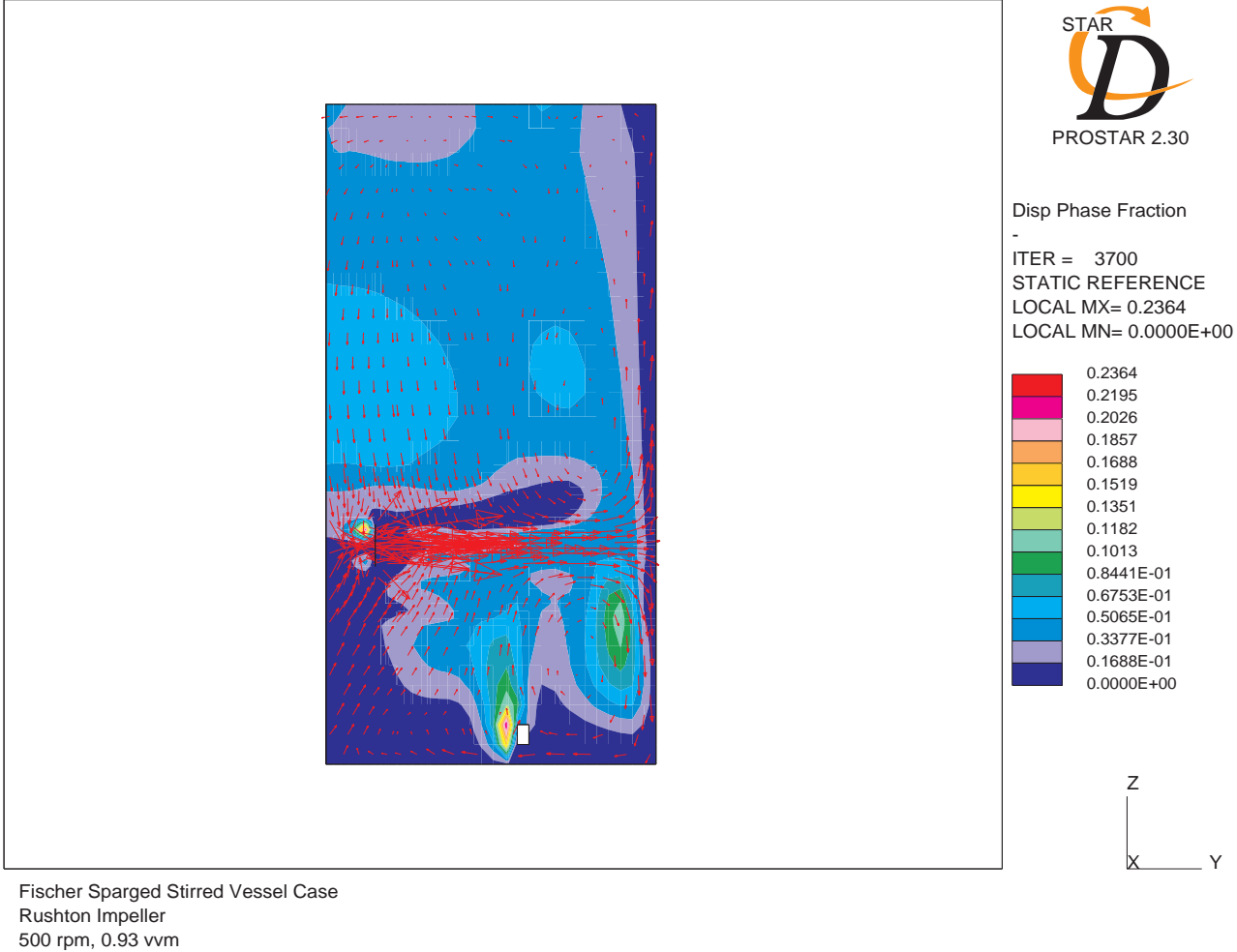


Figure 7.9: Phase fraction contours and continuous phase mean velocity vectors.

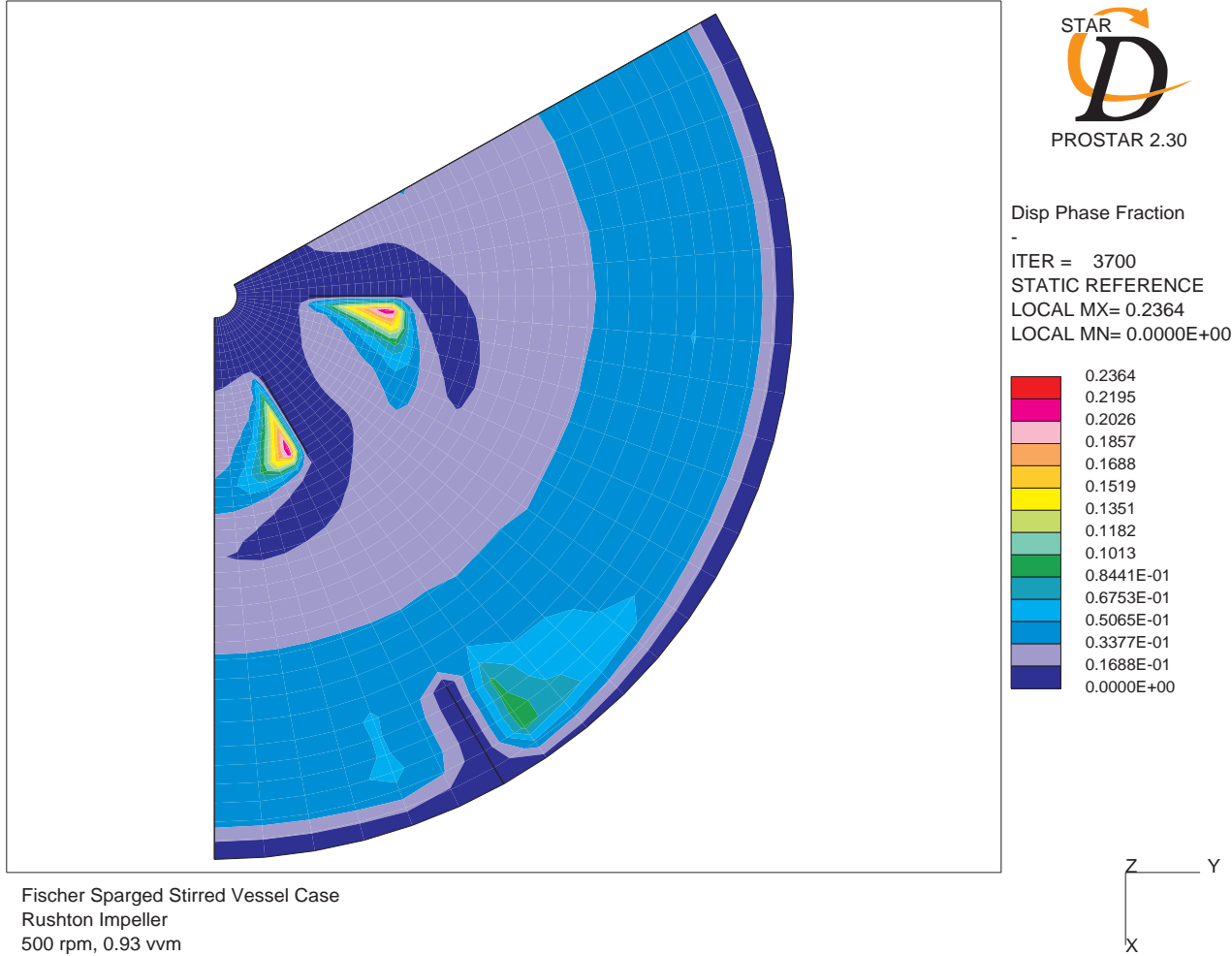


Figure 7.10: Phase fraction contours on a plane 10 mm above the impeller plane.

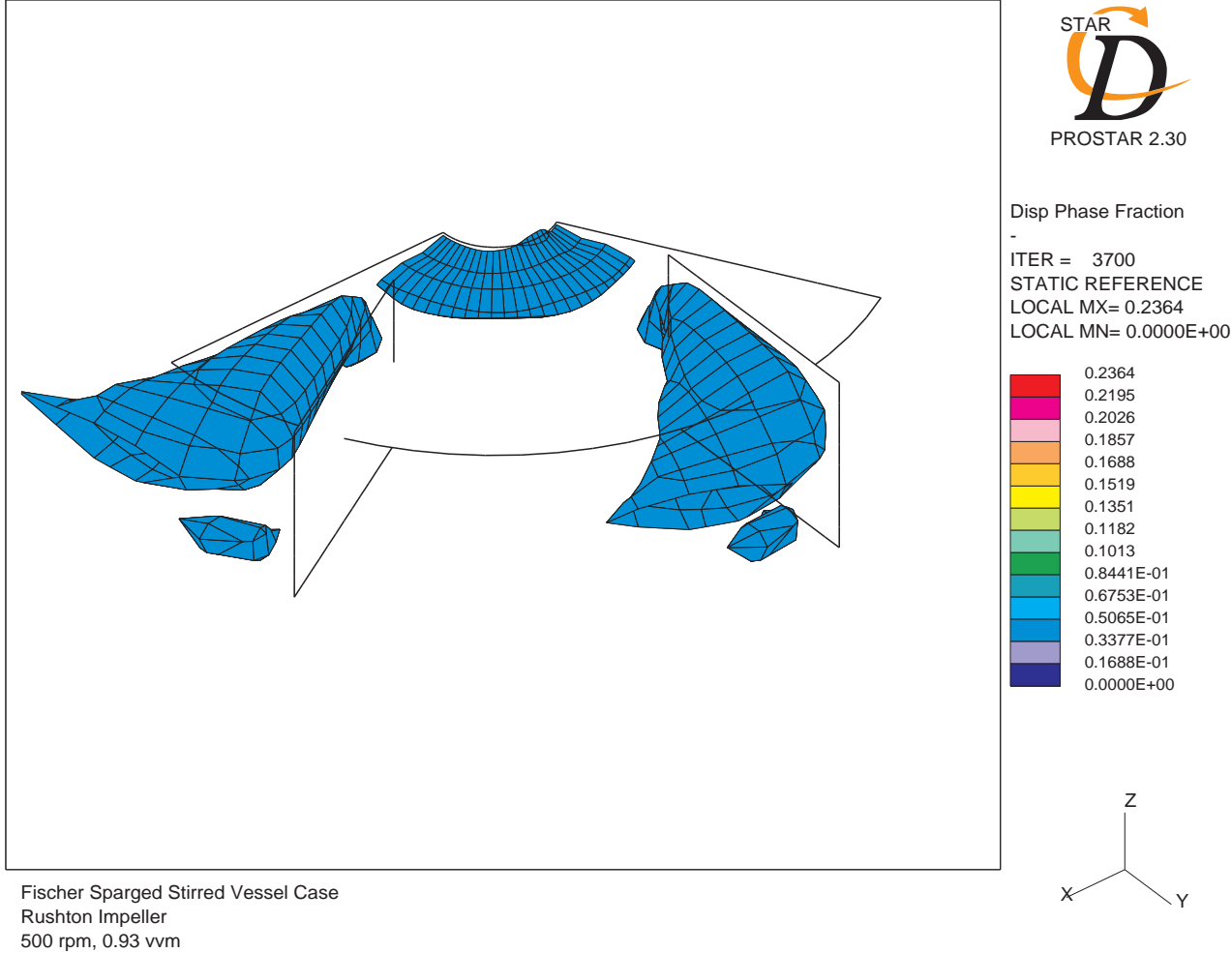


Figure 7.11: Phase fraction isosurface at  $\alpha_d = 0.05$  in the impeller region.

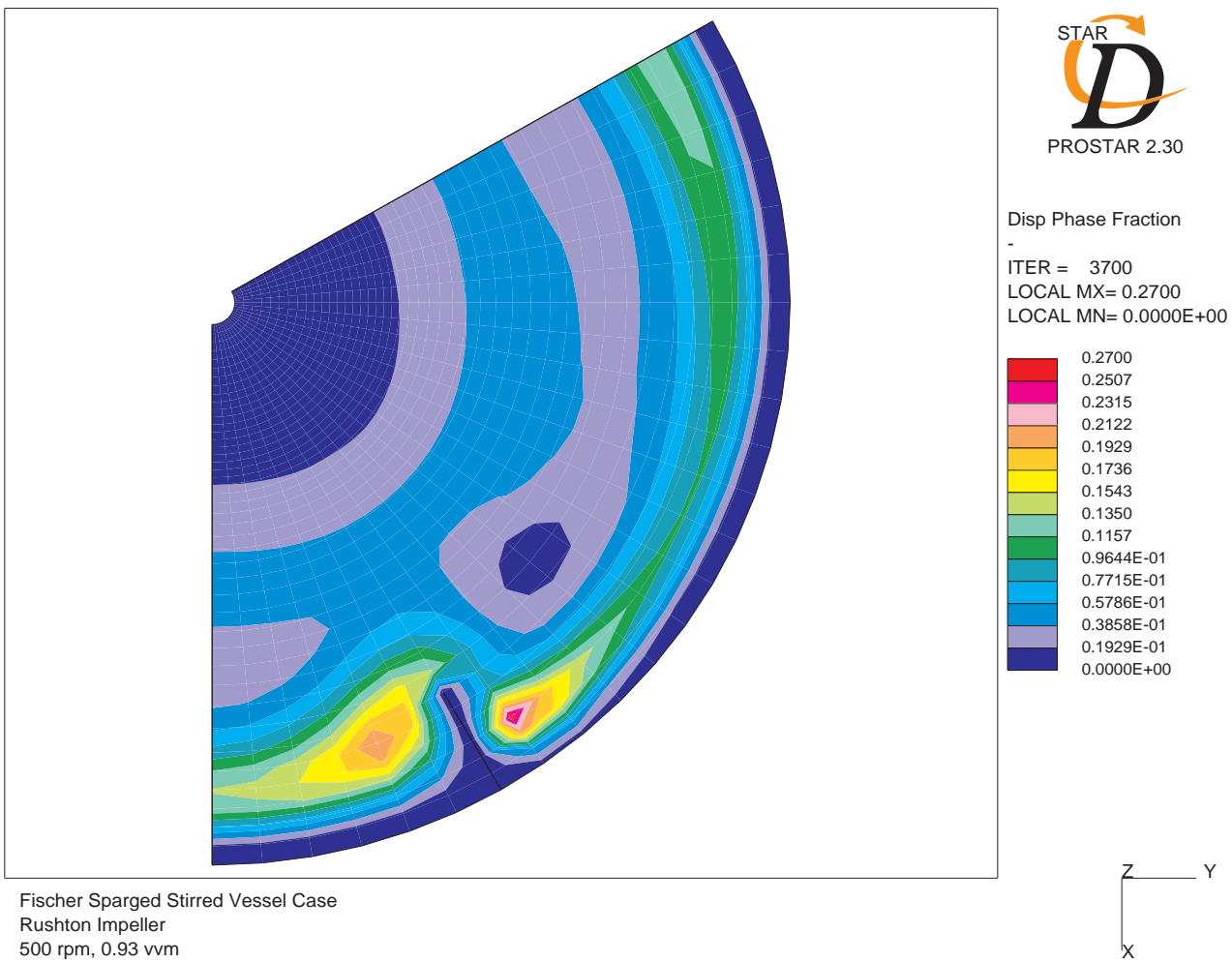


Figure 7.12: Phase fraction contours on a plane -35 mm below the impeller plane.



## Chapter 8

# Summary And Conclusions

### 8.1 Summary Of Achievements And Main Findings

This research has dealt with the development of a computational method for the prediction of dispersed gas-liquid, liquid-liquid and solid-liquid two-phase flows. The method has been developed in five distinct stages.

- The derivation of the fundamental mathematical model in the form of two-phase flow conservation equations for mass and momentum.
- The assembly of suitable physical models for the inter-phase forces and for the phase Reynolds stresses resulting in a closed equation set.
- The integration into the framework of a general method for taking into account droplet break-up and coalescence and a variable droplet size distribution.
- The development of a suitable numerical solution algorithm capable of providing stable and efficient solutions to the complete equation set.
- Validation of the method through comparison to detailed experimental data.

Each of these stages is summarised in turn below.

#### 8.1.1 Basic Mathematical Model

The Eulerian ‘two-fluid’ framework has been adopted as the basis for the derivation of the governing two-phase flow conservation equations. Here, the fundamental equations for the single-phase fluid flow within each phase, the so-called Navier-Stokes equations, are

averaged to produce Eulerian conservation equations pertaining to each phase but valid throughout the entire flow domain. Alternative approaches, such as the Lagrangian or Drift-Flux approaches, have been discarded in favour of the two-fluid approach on the basis that they are not as generally applicable to flows of engineering interest.

The present two-fluid conservation equations have been derived using a conditioned ensemble averaging technique where the equations are conditioned using a phase indicator function and then ensemble averaged once only. Early workers in the field have advocated the application of multiple time and volume averages in the belief that the spatial phase variations and the effects of turbulent velocity fluctuations are separable. Thus, the purpose of the first volume average is to remove the two-phase nature of the flow to yield 'instantaneous' flow equations which have smooth spatial derivatives but which still display velocity fluctuations due to turbulence. These equations are then time averaged to remove these velocity fluctuations and to produce smooth temporal derivatives.

In this work, it has been argued that in the general case the effects of phase variations and turbulent fluctuations are inter-woven and cannot be separated, except in a few limiting cases. For flows of general engineering interest, the temporal and spatial scales associated with the phase and turbulent variations overlap and it is not possible to devise an averaging approach which discriminates between the two. Equations derived using these techniques are strictly valid only when the constraints implicit in the applied averages are obeyed; for time and volume averaging, this means that the temporal and spatial resolution of the final equations is restricted.

Furthermore, workers who have adopted the multiple averaging approach have had to resort to redefining the dependent variables using phase fraction weighting in order to reduce the number of correlation terms appearing in the final equations. The experimental validation of such equations can be complex since experiments have to either measure phase fraction weighted values, or conditioned unweighted values have to be converted before meaningful comparison can take place. The resulting equations are therefore cumbersome and it is difficult to get a feel for the physical meaning underlying specific terms.

The single application of the more fundamental ensemble average has been shown to yield equations which are without the limitations on spatial or temporal resolution. In addition, since only a single average is applied, there is no need to resort to phase fraction weighting of the dependent variables resulting in a cleaner and somewhat simpler set of equations. The conditioned ensemble averaging technique has the added advantage of having a direct experimental analogue allowing direct comparison with experimental data produced via phase discrimination methods.



### 8.1.2 Physical Modelling

The averaging procedure introduces unknown correlation terms into the phase momentum equations which need to be modelled in terms of known quantities before they can be computed. These terms represent the effects of inter-phase momentum transfer and the effects of local velocity fluctuations on the mean phase velocities. For the former, models suitable for gas-liquid, liquid-liquid and solid-liquid dispersed two-phase flows have been assembled and include forces such as interphase drag, virtual mass and lift.

In the case of the interphase drag force, it has been shown by comparison with experimental data that the adoption of the more popular models for air-water systems may produce inaccurate results for medium to large bubble sizes. For the air-water case, a drag model based on curve fitting the actual experimental data for air bubbles rising through water has been adopted. It has been noted that for systems involving some form of surface contamination, the drag characteristic may be altered to such an extent that this approach represents the only way of obtaining a reliable drag model. Since the interphase drag is usually one of the dominant forces in a system, its accurate modelling is essential if an accurate, and numerically stable, solution is to be obtained.

The turbulence closure in the present work is based on the adoption of the eddy viscosity hypothesis coupled with a two equation  $k - \epsilon$  turbulence model. Here, the continuous phase Reynolds stress term is related to the mean shear rate by an eddy viscosity which is computed from local values for the continuous phase turbulent kinetic energy  $k$  and its dissipation rate  $\epsilon$ . The conditional averaged transport equations for these quantities have been formally derived, along with the more fundamental Reynolds stress transport equation. Again, these equations contain extra correlation terms which have to be modelled in order to obtain a closed equation set. The terms with single-phase counterparts are modelling in the same way as the ubiquitous single-phase  $k - \epsilon$  model. The modelling of the two-phase terms follows closely that of Kataoka and Serizawa [13], with suitable modifications to maintain consistency with the rest of the modelling. These terms account for the effects of drag induced turbulence generation, void wave propagation and surface energy changes.

The dispersed phase Reynolds stresses are modelled using the ‘Response Coefficient’ approach of Politis [6]. Here, the dispersed phase velocity fluctuations are related to those of the continuous phase by a scalar response coefficient  $C_t$ , which then allows the dispersed phase Reynolds stresses to be written in terms of the continuous phase Reynolds stresses. In this work, this approach has been generalised and the original approach of Politis has been identified as a limiting case. The conceptual difficulties in the original definition of  $C_t$  proposed by Politis have been removed by redefining it as the ratio of the phase RMS

velocities.

The introduction of the response coefficient allows the dispersed phase Reynolds stresses to be written in terms of the continuous phase Reynolds stresses, which in turn are modelled using the eddy viscosity approach described above. Sub-models for  $C_t$  for solid-liquid and gas-liquid system have been described.

### 8.1.3 Break-up and Coalescence Modelling

A generalised approach due to Ziman [83] and Chesters [81, 84, 85, 86] allowing droplet break-up, coalescence and variable size effects to be incorporated into the two-fluid framework has been described. This approach is based on a presumed droplet size PDF which is parameterised in terms of a series of conserved scalar quantities which are related to its moments. Transport equations for these quantities have been formally derived and include source and sink terms which account for the effects of droplet break-up and coalescence on the size distribution. Generic models for these terms have been provided by other researchers which rely on the specification of a small number of parameters, such as the break-up time-scale, the critical droplet diameter, the number of fragments, etc.

The various basic regimes for the break-up of droplets have been identified and include the ‘viscous’ regime where the droplets are smaller than the turbulent eddy size, and the ‘inertial’ regime where the droplets are larger than the turbulent eddy size. Basic models for each of these regimes have been assembled by specifying appropriate sub-models for each of the parameters in the generic form.

The effects of Surface-Active Agents (‘Surfactants’) on the break-up of droplets has been discussed at length. Surfactants are known to affect the break-up behaviour of droplets by altering the local surface tension. However, the dynamic behaviour of the surfactant and the droplet interface has been shown to have a significant effect at intermediate surfactant concentrations; the dilation and contraction of the interface due to rotation and deformation and the rate at which the surfactant can adsorb or desorb to or from the interface can result in break-up behaviour which is significantly different to that found by assuming an equilibrium surface tension value. Advanced break-up models for the viscous and inertial regimes have been proposed by Janssen [91, 92] and Chesters [94] which take surfactant effects and dispersed phase droplet viscosity into account.

Furthermore, for engineering applications, variations in the local bulk concentration and the local interfacial surface area available can also have a significant effect. To account for these, the conditional averaged transport equations for the bulk surfactant concentration and the interfacial surfactant concentration have been derived. These equations yield

important information on the changes in the local bulk and interface concentrations due to local changes in surface area due to the break-up and coalescence of the droplets.

#### 8.1.4 Numerical Solution Procedure

An existing numerical solution procedure, based on the finite volume discretisation of the two-phase equation set coupled with a fully implicit two-phase iterative solution algorithm has been substantially improved. The new algorithm addresses certain shortcomings identified in the algorithms proposed by previous workers with respect to the handling of the interphase drag and the imposition of continuity constraints. The coupling between the phase momentum equations due to the interphase term is handled by adopting the ‘partial elimination’ approach of Oliveira [25] and combining it with a new sub-iterative correction stage for the drag coefficient. This results in a solution algorithm which is both more efficient and stable than previous algorithms.

The partial elimination approach strengthens the coupling between the phase momentum equations by partially eliminating the drag terms in each equation by substituting for the entire momentum equation of the other phase. In addition, the resulting equations allow a significant portion of the drag-related terms to be treated implicitly, thus increasing the stability of the algorithm. The sub-iterative correction stage for the drag coefficient improves the stability of the algorithm even further by yielding an improved value for the drag coefficient which is used to calculate the magnitude of the drag-related terms in the momentum equations. The drag coefficient is calculated by deriving explicit expressions for the phase relative velocities from the phase momentum equations by using operator splitting. This approach reduces the instabilities caused by the lagging of information from one iteration to the other.

The efficacy of the new algorithm was demonstrated by applying it to a small one-dimensional test problem involving the air-water bubbly flow in a tapered duct. The algorithm was tested using a variety of under-relaxation factors and compared against the algorithm proposed by Oliveira [25]. The results show that the new algorithm outperforms the previous algorithm in two respects. Firstly, the new algorithm can obtain a converged solution without any difficulty for a wide range of under-relaxation factor values. The previous algorithm, on the other hand, could only obtain a solution for small under-relaxation values. Secondly, in cases where the previous algorithm could obtain a solution, the new algorithm is found to require far fewer iterations.

### 8.1.5 Experimental Validation Studies

The developed two-fluid model has been validated against data from three diverse experimental studies, involving air-water bubbly flow in a vertical ducted shear layer, the oil-water flow in an in-line pipe-mixer device involving droplet break-up in the presence of surfactants, and the air-water bubbly flow in a stirred vessel.

The experimental study of Roig [56] involved the vertical upward flow of two inlet streams with different velocities being brought together to form a plane shear layer within a square test section. In all, Roig studied a total of 8 cases with varying inlet stream velocity ratios and inlet phase fraction distribution, including 3 single phase cases. Measurements for the local phase fraction and the phase mean and RMS velocities were compared against predictions at various positions across the shear layer.

The predictions were found to be in generally good agreement with the experimental data. In particular, the lateral phase fraction distribution, which displays distinct peaks and troughs, was found to be well predicted. The influence of lateral lift forces caused by the presence of a velocity gradient was found to be of prime importance in the accurate prediction of this distribution. A lateral force balance for the dispersed phase demonstrated clearly the influence of the lateral lift force on the accuracy of the phase fraction predictions, and the relative unimportance of the dispersed phase Reynolds stresses.

The spreading rate of the two-phase shear layer, which was found to be much higher than in the single-phase case, was found to be well predicted. The predictions for the continuous RMS velocities, on the other hand, were found to be somewhat lower than the experimental data. Discrepancies of about 10% were found for the majority of cases. The reasons for these discrepancies were judged to stem from the assumptions made in the calculation of the inlet values for the turbulent kinetic energy and its dissipation rate, or due to the inherent inability of the  $k - \epsilon$  model to accurately predict flows involving relatively weak shear rates.

The performance of the proposed numerical solution algorithm was evaluated for this case by performing a series of calculations with different momentum equation under-relaxation factors, both with and without the sub-iterative correction to the drag coefficient. The results show that the sub-iterative correction stage to be essential if convergence is to be obtained at moderate under-relaxation factors. Without the sub-iterative correction stage, convergence could only be obtained. Furthermore, it was found that the number of iterations to convergence was relatively insensitive to the under-relaxation factor when the sub-iterative correction stage was used. An alternative approach, where different under-relaxation factors are used for the continuous and dispersed phase momentum equations,

a practice limited to steady state calculations, was evaluated and found to have comparable performance to the present algorithm.

Similarly, the performance of the present two-phase turbulence model for this case was evaluated by performing a series of calculations with and without the additional two-phase terms in the  $k$  and  $\epsilon$  equations. It was found that the bubble induced turbulence generation term in the  $k$  equation was very important in predicting the higher turbulence level indicated by the experimental data. Comparisons with predictions performed using a single-phase  $k - \epsilon$  model showed that the bubble induced turbulence term increased the turbulence level by about 20%.

In order to validate the variable droplet size approach and, in particular, the surfactant influenced break-up sub-models, the two-phase model was applied to the experimental case studied by Janssen *et al.* [138] who studied the break-up of oil droplets in an in-line pipe-mixer device. Janssen *et al.* measured the local phase fraction and mean droplet diameter across the diameter of the tube at various locations downstream of the inlet for 13 different cases involving different velocity ratios, surfactant concentrations and droplet viscosities.

The predictions for this case were very encouraging, with the effects of the different surfactant concentrations on the break-up rate of the droplets being well captured by the two-phase model. The predictions have shown that the presence of surfactants can have a significant, and sometimes unexpected, effect on the break-up of the droplets. Intuitively, it was thought that higher bulk surfactant concentrations would result in a higher break-up rate due to the significant reduction in the surface tension. However, the experimental data and the predictions have shown that the intermediate bulk surfactant concentrations result in a break-up rate which is much lower than expected.

The break-up rate was found to depend on the dynamic balance between the rate at which the interfacial surfactant concentration was reduced due to the rapid increase in the available surface area due to droplet break-up, and the rate at which the surfactant could re-adsorb to the newly generated surface area. At low and intermediate bulk surfactant concentrations, the surfactant could not re-adsorb to the interface fast enough to reduce the surface tension significantly while the droplet was in the high turbulence region. Higher bulk surfactant concentrations result in faster re-adsorption and have a more pronounced effect on the break-up rate.

This case has shown that it is not sufficient to account for surfactant effects in droplet break-up calculations by using assuming a constant and uniform ‘equilibrium’ surface tension. Calculations must take into account the dynamic nature of the system and account for the local transport of the surfactant both in the bulk and to and from the interface.

The predictions for the cases involving different droplet viscosities produced reasonably accurate results for low viscosity values only. At higher viscosities, the predictions indicate that droplet break-up does not occur, whereas the experimental data indicates that, while the break-up is much reduced compared to that for lower droplet viscosities, it is still finite. The behaviour of the predictions was attributable to the sub-model for the critical Weber number, which depends in turn on the calculation of the damping factor. The present model precludes all break-up when the damping factor is above a certain level, although in reality, break-up is evidently possible, though improbable.

The final validation case involved the air-water bubbly flow in a baffled stirred vessel as studied by Fischer [143], who measured the local phase fraction and dispersed phase mean velocity in a tank stirred by a six-blade Rushton turbine with three baffles attached to the outer wall. A ring sparger, located below the impeller, was used to generate air bubbles within the tank.

The predictions were carried out using a commercial CFD code with the ability to model complex geometries using an arbitrarily unstructured mesh. The impeller was modelled using an advanced Multiple Reference Frame approach where the flow in the inner impeller region and the outer baffled region can both be considered steady by defining an appropriate reference frame for each region.

The predictions were encouraging, although discrepancies in the predictions for the local phase fraction were sometimes relatively large. The profiles for the phase fraction in the impeller region was found to be quite well captured, as were the profiles in the region of the sparger. Larger discrepancies were observed near to the tank surface. Predictions for the bubble velocities were reasonably accurate in the majority of the tank, although discrepancies were evident again near the surface. The assumption of a constant and uniform bubble size of 4mm was thought to be a contributing factor to these discrepancies.

Overall, it can be concluded that the two-phase model presented in this work represents a very useful and reasonably accurate tool for the prediction of dispersed two-phase flows in a wide variety of geometries and flow configurations.

## 8.2 Suggestions For Further Work

The application of the present two-phase flow model to the three validation cases has highlighted certain areas which would benefit from further work. These areas cover the turbulence and physical effect modelling, the numerical solution algorithm and the application of the model to more experimental validations cases.

### 8.2.1 Turbulence And Physical Effect Modelling

The validation studies have shown the importance of the two-phase interaction terms in the phase momentum and turbulence equations. In particular, in the phase momentum equations, the drag, lift and interfacial pressure terms have proven to be crucial for the accurate prediction of many of the experimentally observed flow features. In addition, the bubble-induced turbulence term in the  $k$  equation has shown that turbulence predictions cannot be carried out using a single-phase turbulence model in flows with appreciable slip velocities. The physical understanding behind these crucial terms is not as complete as it should be and more research is required to remedy the situation.

Firstly, there are questions surrounding the applicability of the drag, virtual mass and lift force models at moderate to high phase fractions and, in particular, the appropriate values of the drag, virtual mass and lift coefficients for this case. Accurate experimental data pertaining to this situation needs to be used to gain more physical insight and to validate these sub-models extensively.

Secondly, the mechanisms by which bubbles and droplets can induce turbulence generation is not well understood. Again, accurate experimental data for this situation is required so that this effect can be more accurately modelled. The simplistic model presented in this work is unlikely to be adequate for the vast majority of cases, but it could serve as a starting point.

Another area which would benefit from further research is the Response Coefficient approach used to model the dispersed phase Reynolds stresses. The generalisation of this approach described in this work has shown that a large number of approximations and simplifications are possible. The presently adopted approach, where the phase Reynolds stresses are related using a single scalar coefficient, is the simplest of these. More research is required to determine whether any of the more complex models would be more appropriate.

The validation study for the break-up of oil droplets in an in-line pipe-mixer device has yielded very encouraging results. However, there is room for improvement in the modelling of the break-up effects, especially with respect to the break-up of droplet with a high viscosity. The approach suggested by Chesters [94] where the present damping factor approach is replaced by a probability-based approach should be pursued.

Finally, more work is required in the validation of the other break-up models, such as those for the viscous break-up with surfactants in turbulent and laminar flows, and for the coalescence models. Also, the range of available models should be extended to include non-binary break-up regimes, such as end-pinching and super-critical capillary break-up.

Again, accurate experimental data is required for these objectives to be achieved properly.

### 8.2.2 Numerical Solution Algorithm

The performance of the present numerical solution algorithm has been assessed with respect to the validation cases and has yielded very encouraging results. The algorithm has shown that it is more robust than previous algorithms and can produce converged results without the need to resort to very small under-relaxation factors. In terms of efficiency, the present algorithm has displayed some improvement over the previous algorithms, although the present sub-iterative solution technique used to calculate the updated value for the drag coefficient consumes more computing time. Alternative solution techniques, such as Newton-Raphson or Levenberg-Marquardt [163], should be investigated to assess their effect on the overall solution efficiency.

In the long term, improvements in the algorithm may be achieved by improving the imposition of individual phase continuity constraints by solving for the continuous and dispersed phase pressures separately. As each pressure is calculated, the corresponding individual phase continuity, and therefore global continuity, would be satisfied at each iteration. This approach, however, introduces two new problems. Firstly, the use of individual phase pressures may reduce the coupling between the phase momentum equations which are, at present, coupled through the common pressure as well as the interphase momentum transfer terms such as drag.

In addition, the concept of a dispersed phase pressure requires careful consideration since it is not simply the pressure within a single bubble but the conditional averaged pressure across a large number of bubbles. The adoption of individual phase pressures may require additional models to be introduced into the momentum equations to ensure that the final solution yields the correct pressure difference between phases, which will be due to the effects of surface tension.

Secondly, if the phase continuity equations are used to calculate the phase pressures, we cannot use the dispersed phase continuity equation as the basis for the calculation of the phase fraction. In this case we would need to use the topological, or interface transport, equation, as discussed in Appendix A. The use of this equation requires that the interfacial velocity be modelled in terms of the dispersed and continuous phase velocities thus introducing another element of uncertainty.

Finally, the move away from a single pressure system may have a large impact on the design of an appropriate solution algorithm and further research is needed to assess whether this approach would be beneficial.



### 8.2.3 Further Model Validation

The development of an accurate two-phase phase predictive model requires that its predictions be compared against as much experimental data as possible. To this end, more validation studies are required which cover a wide range of flow geometries and physical effects. In particular, the present model would benefit from direct comparison with data pertaining to the effects of bubble-induced turbulence, phase distribution in complex geometries such as ducts, pipes and stirred tanks and, if possible, involving droplet or bubble break-up or coalescence. The availability of accurate and suitable experimental data is the limiting factor here and more effort should be placed into producing experimental data specifically for the validation of predictive methods.



## Appendix A

# Conditional Averaging

### A.1 Introduction and Basic Definitions

Measurements at a fixed point in a multi-phase fluid flow need to be carefully considered since a fixed position measurement probe will, in general, encounter all phases. The measurement of a particular property of only one of the phases is achieved by making the measurement process ‘conditional’ on that phase being present at the measuring location at the time the measurement is taken. In experimental terms, this condition is determined by measuring some property of the flow which enables discrimination between the individual phases. For dispersed two-phase systems, phase discrimination may be based on temperature, conductivity, velocity or on the reflectivity of the interface between phases. Mathematically, the conditioning of a measured quantity  $\Phi$  is carried out by multiplying it by an appropriate indicator function which is defined to be unity within the phase of interest and zero elsewhere. For the present two-phase system, the phase indicator function is defined as

$$\chi_k(\mathbf{x}, t) = \begin{cases} 1 & \text{Phase } k \text{ present at } (\mathbf{x}, t). \\ 0 & \text{Otherwise.} \end{cases} \quad (\text{A.1})$$

where  $k$  takes the symbol  $c$  for the continuous phase, or  $d$  for the dispersed phase according to whichever phase is under consideration. The product  $\chi_k \Phi$  is called the conditioned quantity and is denoted  $\Phi^k$ . Note that  $\chi_k$  is piecewise continuous and therefore integrable, and that both  $\Phi$  and  $\Phi^k$  are defined throughout all space and time domains.

Figure A.1 shows the unconditioned and conditioned quantities  $\Phi$  and  $\Phi^k$  plotted against time as a bubble passes the measuring point. In this example the phase of interest is the

continuous phase and so we have used the continuous phase indicator function  $\chi_c$ .

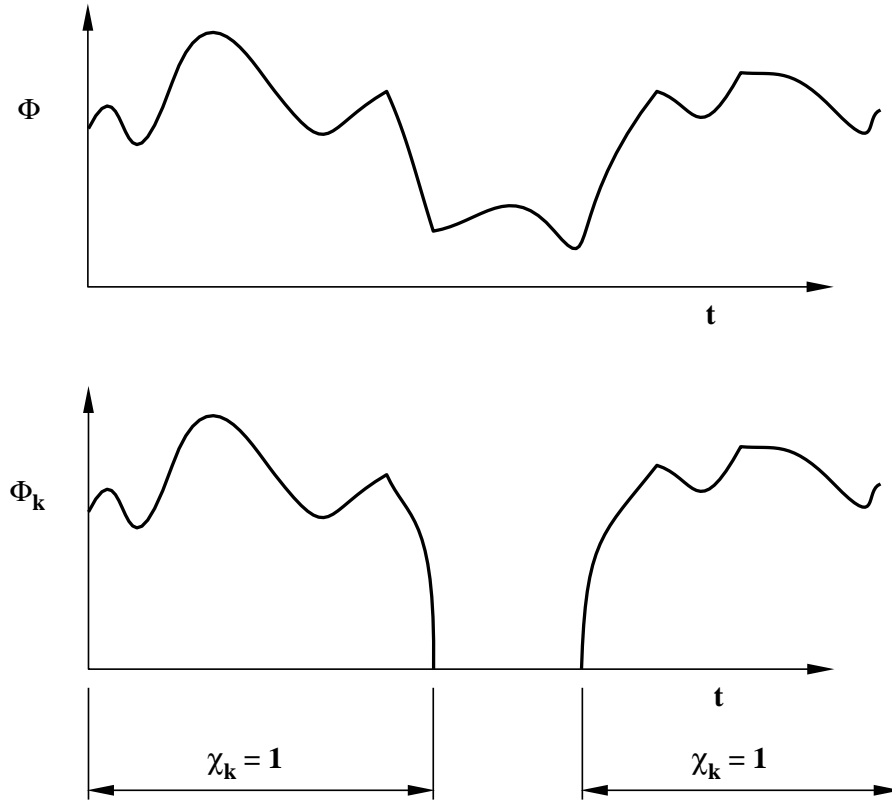


Figure A.1: Unconditioned and conditioned measurements.

The phase indicator function may be defined in terms of the Heaviside unit step function applied to a continuous scalar property known as the phase distribution function,  $f_k(\mathbf{x}, t)$ . The phase distribution function essentially describes the instantaneous position of the interfaces between the phases. In this work, it is defined as the signed distance from the interface such that it is positive within phase  $k$ , negative in the other phase(s) and zero at the interface; see Figure A.2.

The phase indicator function may be written in terms of the Heaviside unit step function and the phase distribution function as

$$\chi_k = \mathbb{H}\{f_k(\mathbf{x}, t)\} \quad (\text{A.2})$$

where  $\mathbb{H}\{\}$  denotes the Heaviside unit step function.

We note in passing that the phase distribution function is defined for each of the phases in the flow allowing the present framework to be applied to flows with an arbitrary number of phases. For the particular cases of two-phase flow, we note that we only need to consider the phase distribution function for one phase since

$$\chi_k = \mathbb{H}\{f_k(\mathbf{x}, t)\} \quad (\text{A.3})$$

$$\chi_k^\sim = \mathbb{H}\{-f_k(\mathbf{x}, t)\} \quad (\text{A.4})$$

where  $\chi_k^\sim$  represents the phase indicator function of the other phase.

The utility of defining the phase indicator function in terms of the Heaviside unit step function becomes apparent when we start to consider its temporal and spatial derivatives. The conservation equations of mass, momentum and energy involve temporal and spatial derivatives of the dependent variables. Conditioning these equations results in temporal and spatial derivatives of the phase indicator function.

The spatial derivative of the phase indicator function is found to be

$$\nabla \chi_k = \delta(f_k) \nabla f_k \quad (\text{A.5})$$

$$= \delta(f_k) |\nabla f_k| \mathbf{n}_k \quad (\text{A.6})$$

where  $\delta()$  is the Dirac delta function and  $\mathbf{n}_k$  is the unit normal interior to phase k.

It can be seen that the spatial derivative of the phase indicator function is zero except at the interface, where it has the absolute value of infinity in the direction normal to the interface pointing into phase k. Since the gradient of the phase distribution function  $f_k$  is unity at the interface, the above equation reduces to

$$\nabla \chi_k = \delta(f_k) \mathbf{n}_k \quad (\text{A.7})$$

The temporal derivative of the phase indicator function is intimately related to the motion of the interface. By considering the geometry of the interface, we see that

$$\frac{\partial \chi_k}{\partial t} = -\mathbf{v}_i \cdot \nabla \chi_k \quad (\text{A.8})$$

where  $\mathbf{v}_i$  is the velocity of the interface. By Eqn (A.7), we have

$$\frac{\partial \chi_k}{\partial t} = -\delta(f_k) \mathbf{v}_i \cdot \mathbf{n}_k \quad (\text{A.9})$$

## A.2 Conditional-Averaged Quantities

We now turn our attention to the averaging of the conditioned quantities defined in the previous section. In order to illustrate the technique, and also for consistency with the rest of this work, an ensemble average will be used, although these results are equally valid for any type of average. The ensemble average of a quantity  $\phi$  is defined as

$$\overline{\phi} = \lim_{N \rightarrow \infty} \frac{1}{N} \sum_N \phi \quad (\text{A.10})$$

Now, consider an unconditioned fluid dynamical quantity,  $\Phi$ , which may be a scalar, vector or tensor of any rank. In order to derive averaged information about the quantity  $\Phi$  in phase  $k$  we multiply it by the phase indicator function  $\chi_k$  and take the ensemble average.

$$\overline{\chi_k \Phi} = \lim_{N \rightarrow \infty} \frac{1}{N} \sum_N \chi_k \Phi \quad (\text{A.11})$$

Since the phase indicator function is zero except in phase  $k$ , the sum may be written

$$\begin{aligned} \overline{\chi_k \Phi} &= \lim_{N \rightarrow \infty} \frac{1}{N} \sum_{N_k} \Phi \\ &= \lim_{N \rightarrow \infty} \frac{N_k}{N} \frac{1}{N_k} \sum_{N_k} \Phi \\ &= \lim_{N_k \rightarrow \infty} \alpha_k \frac{1}{N_k} \sum_{N_k} \Phi \end{aligned} \quad (\text{A.12})$$

where  $N$  = total number of realisations, both phases present.

$N_k$  = total number of realisations, phase  $k$  present only.

$\alpha_k$  = phase fraction of phase  $k$  =  $N_k/N$ .

which leads to the important result

$$\overline{\chi_k \Phi} = \overline{\Phi^k} = \alpha_k \overline{\Phi_k} \quad (\text{A.13})$$

where  $\overline{\Phi}_k$  is the true ‘phasic’ average of  $\Phi_k$ , that is, the average of the quantity  $\Phi$  pertaining only to phase  $k$ .

By substituting for  $\Phi = 1$  in Eqn (A.13), we see that

$$\overline{\chi_k} = \alpha_k \quad (\text{A.14})$$

For the ensemble average used in this work,  $\alpha_k$  is defined as the number of realisations where phase  $k$  is present divided by the total number of realisations and is called the phase fraction. The phase fraction may be interpreted as the probability of that phase being present at a particular instant.

The application of other types of averages, however, will result in different physical interpretations for  $\alpha_k$ . A volume average, for instance, will result in  $\alpha_k$  being interpreted as a volume fraction, whilst for a time average  $\alpha_k$  is interpreted as a time fraction.

### A.3 Spatial and Temporal Derivatives

The unconditioned form of the conservation equations involve temporal and spatial derivatives of the dependent variable  $\Phi$ . When these equations are conditioned and then averaged, we obtain terms of the form  $\overline{\chi_k \nabla \Phi}$  and  $\overline{\chi_k \frac{\partial \Phi}{\partial t}}$ .

Taking the spatial derivative of  $\chi_k \nabla \Phi$  and applying an ensemble average, we have

$$\begin{aligned} \overline{\chi_k \nabla \Phi} &= \overline{\nabla \chi_k \Phi} - \overline{\Phi \nabla \chi_k} \\ &= \overline{\nabla \chi_k \Phi} - \overline{\Phi \nabla \chi_k} \end{aligned} \quad (\text{A.15})$$

since differentiation and ensemble averaging commute [38, 12]. The last term on the right hand side clearly represents the averaged influence of the interface since  $\nabla \chi_k$  is non-zero only at the interface.

In order to further analyse these terms, and following Dopazo [38], we integrate each term in Eqn (A.15) over an infinitesimal control volume,  $\delta V$ . For the first term on the right hand side this has no effect since  $\overline{\chi_k \Phi}$  can be considered constant over the infinitesimal control volume. The final term, however, may be transformed into a surface integral since it contains a delta function. It should be noted that integration over a volume and ensemble averaging commute, allowing the volume integral to be applied over one realisation of the interface. Thus, we have

$$\begin{aligned}
\overline{\chi_k \nabla \Phi} &= \nabla \overline{\chi_k \Phi} - \lim_{\delta V \rightarrow 0} \overline{\frac{1}{\delta V} \int_{\delta V(\mathbf{x},t)} \Phi \delta(f_k) \mathbf{n}_k dV} \\
&= \nabla \alpha_k \overline{\Phi}_k - \lim_{\delta V \rightarrow 0} \overline{\frac{1}{\delta V} \int_{\delta S(\mathbf{x},t)} \Phi \mathbf{n}_k dS}
\end{aligned} \tag{A.16}$$

where  $\delta S$  denotes an infinitesimal element of the interface and we have used Eqn (A.7).

Similarly, applying the same manipulations to the temporal derivative, we have

$$\begin{aligned}
\overline{\chi_k \frac{\partial \Phi}{\partial t}} &= \overline{\frac{\partial \chi_k \Phi}{\partial t}} - \overline{\Phi \frac{\partial \chi_k}{\partial t}} \\
&= \overline{\frac{\partial \chi_k \Phi}{\partial t}} - \overline{\Phi \frac{\partial \chi_k}{\partial t}} \\
&= \frac{\partial \alpha_k \overline{\Phi}_k}{\partial t} + \lim_{\delta V \rightarrow 0} \overline{\frac{1}{\delta V} \int_{\delta S(\mathbf{x},t)} \Phi \mathbf{v}_i \cdot \mathbf{n}_k dS}
\end{aligned} \tag{A.17}$$

#### A.4 Surface Average Notation

Following Weller [164], we define the surface average of a property,  $\widehat{\Phi}_k \Sigma$ , as the surface integral per unit volume divided by the surface area per unit volume,  $\Sigma$ .

$$\widehat{\Phi}_k = \frac{1}{\Sigma} \lim_{\delta V \rightarrow 0} \overline{\frac{1}{\delta V} \int_{\delta S(\mathbf{x},t)} \Phi dS} \tag{A.18}$$

where

$$\Sigma = \lim_{\delta V \rightarrow 0} \overline{\frac{1}{\delta V} \int_{\delta S(\mathbf{x},t)} dS} \tag{A.19}$$

The surface average of a quantity can be interpreted as the surface area weighted average value of  $\Phi_k$  at the interface.

Using Equations A.18 and A.19, Equations A.16 and A.17 become

$$\overline{\chi_k \nabla \Phi} = \nabla \alpha_k \overline{\Phi}_k - \widehat{\Phi_{k_i} \mathbf{n}_k} \Sigma \tag{A.20}$$

$$\overline{\chi_k \frac{\partial \Phi}{\partial t}} = \frac{\partial \alpha_k \overline{\Phi}_k}{\partial t} + \widehat{\Phi_{k_i} (\mathbf{v}_i \cdot \mathbf{n}_k)} \Sigma \tag{A.21}$$



where  $\Phi_{k_i}$  denotes the limiting value of  $\Phi_k$  at the interface.

It is instructive to consider the case when  $\Phi = 1$  is substituted into Equations A.20 and A.21.

$$\nabla \alpha_k = \widehat{\mathbf{n}_k} \Sigma \quad (\text{A.22})$$

$$\frac{\partial \alpha_k}{\partial t} = -\widehat{\mathbf{v}_i \cdot \mathbf{n}_k} \Sigma \quad (\text{A.23})$$

For homogeneous flows, the physical significance of Eqn (A.22) becomes readily apparent; values of  $\mathbf{n}_k$ , at the interface, in every direction are equally likely. Eqn (A.23) represents the rate of change of the phase fraction due to the motion of the interface. For statistically steady flows, Eqn (A.23) shows that positive and negative values of  $\mathbf{v}_i \cdot \mathbf{n}_k$  are equally likely.

## A.5 Interface Transport Equation

By considering the temporal derivative of the phase indicator function we see that

$$\begin{aligned} \frac{\partial \chi_k}{\partial t} + \mathbf{v}_i \cdot \nabla \chi_k &= 0 \\ \frac{D_i}{Dt} \chi_k &= 0 \end{aligned} \quad (\text{A.24})$$

which has the simple physical interpretation that the interface travels with the velocity of the interface  $\mathbf{v}_i$ . This equation is sometimes called the topological equation.

Averaging the topological equation gives

$$\frac{\partial \alpha_k}{\partial t} + \widehat{\mathbf{v}_i \cdot \mathbf{n}_k} \Sigma = 0 \quad (\text{A.25})$$

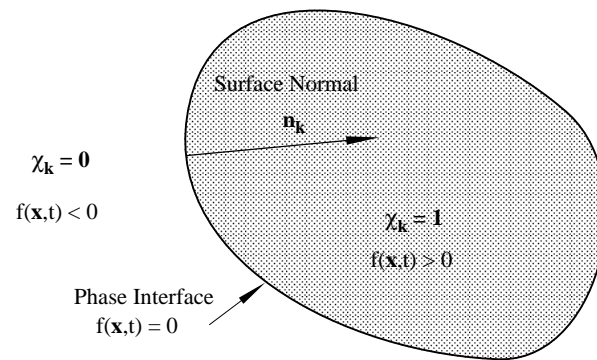


Figure A.2: Phase distribution function and surface normal definition.

## Appendix B

# Derivation of the $C_t$ model of Issa

This Appendix describes the detailed derivation of the  $C_t$  model of Issa [76] for gas-liquid flows. The derivation starts with the Lagrangian equation of motion for a bubble or particle of volume  $V$  which is given as

$$\rho_b V \frac{DU_b}{Dt} = -V \frac{\partial P}{\partial x} + \eta(U_c - U_b) + \frac{1}{2} \rho_c V \frac{D}{Dt}(U_c - U_b) \quad (\text{B.1})$$

where the subscripts  $b$  and  $c$  refer to the bubble and continuous phases respectively,  $P$  is the continuous phase pressure,  $U_c$  and  $U_b$  are the continuous phase and bubble velocities and  $\eta$  is the (assumed linear) drag coefficient. In the absence of viscous forces, the equation of motion of the continuous phase reduces to

$$\rho_c V \frac{DU_c}{Dt} = -\frac{\partial P}{\partial x} \quad (\text{B.2})$$

Note that the drag by the bubble/particle on the fluid is per unit volume of fluid and is therefore considered negligible by comparison with the other terms in Eqn (B.2).

Let the velocity fluctuation due to an eddy be denoted as  $u_c$  for the continuous phase and  $u_b$  for the bubble/particle and let the corresponding pressure fluctuation be denoted  $p$ . The equations governing the evolution of  $u$  and  $u_b$  may be derived from Equations B.1 and B.2 by a perturbation analysis which gives

$$\rho_b V \frac{Du_b}{Dt} = -V \frac{\partial p}{\partial x} + \eta(u_c - u_b) + \frac{1}{2} \rho_c V \frac{D}{Dt}(u_c - u_b) \quad (\text{B.3})$$

and

$$\rho_c V \frac{Du_c}{Dt} = -\frac{\partial P}{\partial x} \quad (\text{B.4})$$

The pressure derivative can be eliminated from Equations B.3 and B.4 to obtain

$$\rho_b V \frac{Du_b}{Dt} = \rho_c V \frac{Du_c}{Dt} + \eta(u_c - u_b) + \frac{1}{2} \rho_c V \frac{D}{Dt}(u_c - u_b) \quad (\text{B.5})$$

Introducing the assumption that  $u_b = C_t u_c$ , Eqn (B.5) becomes

$$\rho_b V C_t \frac{Du_c}{Dt} = \rho_c V \frac{Du_c}{Dt} + \eta u_c (1 - C_t) + \frac{1}{2} \rho_c V (1 - C_t) \frac{Du_c}{Dt} \quad (\text{B.6})$$

Introducing the approximation [165]

$$\frac{Du_c}{Dt} = \frac{u_c^2}{l_e} \quad (\text{B.7})$$

where  $l_e$  is the length scale of the energy containing eddies, Eqn (B.6) can be rearranged to yield

$$C_t = \frac{3 + \frac{2\eta l_e}{\rho_c V u_c}}{1 + \frac{2\eta l_e}{\rho_c V u_c} + 2\frac{\rho_b}{\rho_c}} \quad (\text{B.8})$$

Assuming that the bubble/particle is spherical of volume  $\pi d^3/6$ , and defining  $Re_t = (u_c l_e)/\nu$ , Eqn (B.8) becomes

$$C_t = \frac{3 + \beta}{1 + \beta + 2\frac{\rho_b}{\rho_c}} \quad (\text{B.9})$$

where  $\beta$  is given by

$$\beta = \frac{12\eta}{\pi d \mu} \left( \frac{l_e}{d} \right)^2 \frac{1}{Re_t} \quad (\text{B.10})$$

## Appendix C

# Turbulence Transport Equations

### C.1 Introduction

This appendix contains the detailed derivation of the conditional-averaged Reynolds stress, turbulent kinetic energy and turbulent kinetic energy dissipation rate transport equations. The derivation of these equations follows closely that of their single-phase counterparts, with suitable modifications due to the conditional-averaged framework.

Although the present work is based on a two equation eddy viscosity turbulence closure, the conditional-averaged Reynolds stress equation is derived here for completeness and also to serve as a convenient basis from which to derive the conditional-averaged turbulent kinetic energy equation. This equation may provide some insight into the mechanisms of turbulence generation in two-phase flow with which to guide the modelling in the turbulent kinetic energy and dissipation rate equations. In addition, future workers in this field may wish to attempt a two-phase second moment turbulence closure by taking this equation and modelling the additional interfacial terms.

Following this, the transport equations for the conditional-averaged turbulent kinetic energy and its dissipation rate are derived. The final equations are similar in form to the single-phase turbulence transport equations but with additional terms representing the effects of the two-phase nature of the flow. The physical significance of these extra terms, and their modelling, is discussed in detail in Chapter 3.

In order to derive the conditional-averaged Reynolds stress equation we first need to derive a transport equation for the fluctuating velocity. As discussed in Section 2.3.2.1, in order to maintain consistency with the conditional-averaged convection term in the momentum equations, the most appropriate definition for the fluctuating velocity is that given by

$$\begin{aligned} \mathbf{u}'_k &= \mathbf{U} - \frac{\chi_k \mathbf{U}}{\overline{\chi_k}} \\ &= \mathbf{U} - \overline{\mathbf{u}}_k \end{aligned} \quad (\text{C.1})$$

$$(\text{C.2})$$

where  $\mathbf{U}$  is the unconditioned velocity and  $\overline{\mathbf{u}}_k$  is the conditional-averaged velocity of phase  $k$ .

For clarity, the subscript  $k$  will henceforth be dropped from all properties; all mean and fluctuating velocities, densities and phase fractions are assumed to pertain to phase  $k$ .

From the above definition for the fluctuating velocity, we define the conditional-averaged Reynolds stress, turbulent kinetic energy  $k$  and its dissipation rate  $\epsilon$  for a particular phase as follows

$$\mathbb{R}_{ij} = \frac{\overline{\chi_k u'_i u'_j}}{\overline{\chi_k}} \quad (\text{C.3})$$

$$k = \frac{1}{2} \frac{\overline{\chi_k u'_i u'_i}}{\overline{\chi_k}} \quad (\text{C.4})$$

$$\epsilon = \frac{\overline{\chi_k \frac{\partial u'_i}{\partial x_j} \frac{\partial u'_i}{\partial x_j}}}{\overline{\chi_k}} \quad (\text{C.5})$$

where the Einstein summation convention applies on repeated indices.

The derivation of a transport for the Reynolds stress,  $k$  and  $\epsilon$  proceeds from a transport equation for the fluctuating velocity. The derivation of this equation is given in the next section.

## C.2 Fluctuating Velocity Transport Equation

The fluctuating velocity transport equation is derived via the manipulation of the instantaneous and conditional-averaged momentum equations. Under the assumptions of incompressible phases with no mass transfer these equations, in tensor notation, read

$$\frac{\partial U_i}{\partial t} + \frac{\partial}{\partial x_j} (U_i U_j) = g_i + \frac{\partial \sigma_{ij}}{\partial x_j} \quad (\text{C.6})$$

$$\frac{\partial \alpha \overline{u}_i}{\partial t} + \frac{\partial}{\partial x_j} (\alpha \overline{u}_i \overline{u}_j) = \alpha g_i + \frac{\partial \alpha \overline{\sigma}_{ij}}{\partial x_j} - \frac{\partial \alpha \overline{u'_i u'_j}}{\partial x_j} - \overbrace{\overline{\sigma}_{ij} n_j}^{\Sigma} \quad (\text{C.7})$$

where all symbols are as defined in Chapter 2.

Rearranging Eqn (C.7) and dividing through by  $\alpha$  gives

$$\begin{aligned} \frac{\partial \bar{u}_i}{\partial t} + \frac{\partial}{\partial x_j} (\bar{u}_i \bar{u}_j) - \bar{u}_i \frac{\partial \bar{u}_j}{\partial x_j} &= g_i + \frac{\partial \bar{\sigma}_{ij}}{\partial x_j} - \frac{\partial \overline{u'_i u'_j}}{\partial x_j} + \\ &\quad \frac{1}{\alpha} \{ \bar{\sigma}_{ij} - \sigma_{ij}^t \} \frac{\partial \alpha}{\partial x_j} - \frac{1}{\alpha} \overbrace{\sigma_{ij} n_j} \Sigma \end{aligned} \quad (C.8)$$

Subtraction of Eqn (C.8) from Eqn (C.6), noting Eqn (C.1), yields

$$\begin{aligned} \frac{\partial u'_i}{\partial t} + \frac{\partial}{\partial x_j} (U_i U_j - \bar{u}_i \bar{u}_j) + \bar{u}_i \frac{\partial \bar{u}_j}{\partial x_j} &= \frac{\partial}{\partial x_j} (\sigma_{ij} - \bar{\sigma}_{ij}) + \frac{\partial \overline{u'_i u'_j}}{\partial x_j} + \\ &\quad \frac{1}{\alpha} \{ \overline{u'_i u'_j} - \bar{\sigma}_{ij} \} \frac{\partial \alpha}{\partial x_j} + \frac{1}{\alpha} \overbrace{\sigma_{ij} n_j} \Sigma \end{aligned} \quad (C.9)$$

Since the phase mean and fluctuating velocities are defined in all space and time domains, the quantity  $U_i U_j$  may be decomposed into

$$U_i U_j = \bar{u}_i \bar{u}_j + \bar{u}_i u'_j + u'_i \bar{u}_j + u'_i u'_j \quad (C.10)$$

where all mean and fluctuating velocities are understood to pertain to phase  $k$ .

Similarly, the unconditioned laminar stress  $\sigma_{ij}$  may be decomposed into

$$\sigma_{ij} = \bar{\sigma}_{ij} + \sigma'_{ij} \quad (C.11)$$

whence Eqn (C.9) becomes

$$\begin{aligned} \frac{\partial u'_i}{\partial t} + \frac{\partial}{\partial x_j} (u'_i u'_j + \bar{u}_i u'_j + u'_i \bar{u}_j) + \bar{u}_i \frac{\partial \bar{u}_j}{\partial x_j} &= \frac{\partial \sigma'_{ij}}{\partial x_j} + \frac{\partial \overline{u'_i u'_j}}{\partial x_j} + \frac{1}{\alpha} \overline{u'_i u'_j} \frac{\partial \alpha}{\partial x_j} - \\ &\quad \frac{1}{\alpha} \bar{\sigma}_{ij} \frac{\partial \alpha}{\partial x_j} + \frac{1}{\alpha} \overbrace{\sigma_{ij} n_j} \Sigma \end{aligned} \quad (C.12)$$

Eqn (C.12) is the required transport equation for the fluctuating velocity component  $i$ .

### C.3 Derivation of the Conditional-Averaged Reynolds Stress Equation

The first stage in the derivation of the Reynolds stress equation is to take Eqn (C.12) and multiply through by  $u'_k$ . The resulting equation is then added to Eqn (C.12), written in terms of  $u'_k$  instead of  $u'_i$  and multiplied through by  $u'_i$ . After some rearrangement, we finally obtain

$$\begin{aligned}
& \frac{\partial u'_i u'_k}{\partial t} + \bar{u}_j \frac{\partial u'_i u'_k}{\partial x_j} + u'_k u'_j \frac{\partial \bar{u}_i}{\partial x_j} + u'_i u'_j \frac{\partial \bar{u}_k}{\partial x_j} + u'_i u'_k \frac{\partial \bar{u}_j}{\partial x_j} + \frac{\partial u'_i u'_j u'_k}{\partial x_j} + \\
& u'_i u'_k \left\{ \frac{\partial \bar{u}_j}{\partial x_j} + \frac{\partial u'_j}{\partial x_j} \right\} + \{ u'_k \bar{u}_i + u'_i \bar{u}_k \} \left\{ \frac{\partial u'_j}{\partial x_j} + \frac{\partial \bar{u}_j}{\partial x_j} \right\} = \\
& u'_k \frac{\partial \sigma'_{ij}}{\partial x_j} + u'_i \frac{\partial \sigma'_{kj}}{\partial x_j} + u'_k \frac{\partial \overline{u'_i u'_j}}{\partial x_j} + u'_i \frac{\partial \overline{u'_k u'_j}}{\partial x_j} + \\
& \frac{1}{\alpha} \{ u'_k \overline{u'_i u'_j} + u'_i \overline{u'_k u'_j} \} \frac{\partial \alpha}{\partial x_j} - \frac{1}{\alpha} \{ u'_k \bar{\sigma}_{ij} + u'_i \bar{\sigma}_{kj} \} \frac{\partial \alpha}{\partial x_j} + \\
& \frac{1}{\alpha} \left\{ u'_k \widehat{\sigma_{ij} n_j} \Sigma + u'_i \widehat{\sigma_{kj} n_j} \Sigma \right\} \quad (C.13)
\end{aligned}$$

The seventh and eighth terms in Eqn (C.13) are zero since

$$\frac{\partial \bar{u}_j}{\partial x_j} + \frac{\partial u'_j}{\partial x_j} = \frac{\partial}{\partial x_j} (\bar{u}_j + u'_j) = \frac{\partial U}{\partial x_j} = 0 \quad (C.14)$$

due to global continuity for incompressible phases.

Conditional averaging Eqn (C.13), using Equations A.21 and A.25 and rearranging, yields



$$\begin{aligned}
\frac{\partial \overline{\alpha u'_i u'_k}}{\partial t} + \frac{\partial}{\partial x_j} (\alpha \overline{u_j u'_i u'_k}) &= -\overline{\alpha u'_k u'_j} \frac{\partial \overline{u_i}}{\partial x_j} - \overline{\alpha u'_i u'_j} \frac{\partial \overline{u_k}}{\partial x_j} - \\
&\quad \frac{\partial}{\partial x_j} (\overline{\alpha u'_i u'_j u'_k}) - 2\alpha \epsilon_{ik} + \\
&\quad \frac{\partial}{\partial x_j} (\overline{\alpha u'_k \tau'_{ij}} + \overline{\alpha u'_i \tau'_{kj}}) - \\
&\quad \frac{1}{\rho} \left\{ \frac{\partial \overline{\alpha u'_i p'}}{\partial x_k} - \frac{\partial \overline{\alpha u'_k p'}}{\partial x_i} - \overline{\alpha p' \left( \frac{\partial u'_i}{\partial x_k} + \frac{\partial u'_k}{\partial x_i} \right)} \right\} + \\
&\quad \frac{1}{\rho} \left\{ \overbrace{u''_k p'' n_i} \Sigma + \overbrace{u''_i p'' n_j} \Sigma \right\} - \overbrace{u''_k \tau''_{ij} n_j} \Sigma + \overbrace{u''_i \tau''_{kj} n_j} \Sigma + \\
&\quad \overline{u_j} \overbrace{u''_i u''_k n_j} \Sigma + \overbrace{u''_i u''_j u''_k n_j} \Sigma - \overbrace{u''_i u''_k U_j n_j} \Sigma \quad (C.15)
\end{aligned}$$

where we have decomposed the laminar stress into the pressure plus shear stress components

$$\sigma_{ij} = -\frac{1}{\rho} p' \delta_{ij} + \tau'_{ij} \quad (C.16)$$

and  $\epsilon_{ik}$  is defined as

$$\epsilon_{ik} = \overline{\tau'_{ij} \frac{\partial u'_k}{\partial x_j}} + \overline{\tau'_{kj} \frac{\partial u'_i}{\partial x_j}} \quad (C.17)$$

Eqn (C.15) is the required conditional-averaged Reynolds stress equation for phase  $k$ .

## C.4 Conditional-Averaged Turbulent Kinetic Energy Equation

The conditional-averaged turbulent kinetic energy equation may be simply derived by contracting Eqn (C.14) about indices  $i$  and  $k$  and dividing by 2. Following this procedure we obtain

$$\begin{aligned}
\frac{\partial \alpha k}{\partial t} + \frac{\partial}{\partial x_j}(\alpha \bar{u}_j k) &= -\alpha \overline{u'_i u'_j} \frac{\partial \bar{u}_i}{\partial x_j} - \frac{\partial}{\partial x_j} \left\{ \alpha \frac{\overline{u'_i u'_i}}{2} u'_j + \frac{1}{\rho} \overline{p' u'_j} \right\} - \alpha \epsilon + \\
&\quad \frac{\partial}{\partial x_j}(\alpha \overline{u'_i \tau'_{ij}}) + \frac{1}{\rho} \overbrace{p'' u''_i n_i}^{\Sigma} - \overbrace{\tau''_{ij} u''_i n_j}^{\Sigma} - \\
&\quad \overbrace{k'' U_j n_j}^{\Sigma} + \bar{u}_j \overbrace{k'' n_j}^{\Sigma} + \overbrace{k'' u''_j n_j}^{\Sigma} \quad (C.18)
\end{aligned}$$

Where  $k''$  is defined as

$$k'' = \frac{u'_i u'_i}{2} \quad (C.19)$$

at the interface.

## C.5 Conditional-Averaged Dissipation Rate Equation

The first step in the derivation of the  $\epsilon$  equation is to differentiate the transport equation for the fluctuating velocity  $u'_i$  (Eqn (C.12)) with respect to  $x_k$  and multiply by  $\frac{\partial u'_i}{\partial x_k}$ . Neglecting terms which involve only averaged quantities (since these will soon disappear when the equation is conditional-averaged), this yields

$$\begin{aligned}
\frac{\partial}{\partial t} \left\{ \frac{1}{2} \frac{\partial u'_i}{\partial x_k} \frac{\partial u'_i}{\partial x_k} \right\} + \bar{u}_j \frac{\partial}{\partial x_j} \left\{ \frac{1}{2} \frac{\partial u'_i}{\partial x_k} \frac{\partial u'_i}{\partial x_k} \right\} &= -\frac{\partial u'_i}{\partial x_k} \frac{\partial u'_i}{\partial x_j} \frac{\partial \bar{u}_j}{\partial x_k} - \frac{\partial u'_i}{\partial x_k} \frac{\partial u'_j}{\partial x_k} \frac{\partial \bar{u}_i}{\partial x_j} - \\
&\quad u'_j \frac{\partial u'_i}{\partial x_k} \frac{\partial^2 \bar{u}_i}{\partial x_j \partial x_k} - \frac{1}{\rho} \frac{\partial u'_i}{\partial x_k} \frac{\partial^2 p'}{\partial x_i \partial x_k} + \frac{\partial u'_i}{\partial x_k} \frac{\partial^2 \tau'_{ij}}{\partial x_j \partial x_k} - \\
&\quad u'_j \frac{\partial}{\partial x_j} \left\{ \frac{1}{2} \frac{\partial u'_i}{\partial x_k} \frac{\partial u'_i}{\partial x_k} \right\} - \frac{\partial u'_i}{\partial x_k} \frac{\partial u'_i}{\partial x_j} \frac{\partial u'_j}{\partial x_k} - u'_i \frac{\partial u'_i}{\partial x_k} \frac{\partial^2 \bar{u}_j}{\partial x_k \partial x_j} - \\
&\quad \frac{\partial u'_i}{\partial x_k} \frac{\partial u'_i}{\partial x_k} \frac{\partial \bar{u}_j}{\partial x_j} - \bar{u}_i \frac{\partial u'_i}{\partial x_k} \frac{\partial^2 u'_j}{\partial x_k \partial x_j} - \frac{\partial \bar{u}_i}{\partial x_k} \frac{\partial u'_i}{\partial x_k} \frac{\partial u'_j}{\partial x_j} - \\
&\quad u'_i \frac{\partial u'_i}{\partial x_k} \frac{\partial^2 u'_j}{\partial x_k \partial x_j} - \frac{\partial u'_i}{\partial x_k} \frac{\partial u'_i}{\partial x_k} \frac{\partial u'_j}{\partial x_j} \quad (C.20)
\end{aligned}$$

The eighth and twelfth terms on the right hand side sum to zero due to global continuity. The sixth and thirteenth terms on the right hand side of Eqn (C.20) may be combined to yield

$$-\frac{\partial}{\partial x_j} \left\{ \frac{u'_j}{2} \frac{\partial u'_i}{\partial x_k} \frac{\partial u_i}{\partial x_k} \right\} \quad (\text{C.21})$$

and the tenth and eleventh terms combine to give

$$-\frac{\partial u'_i}{\partial x_k} \frac{\partial}{\partial x_k} (\bar{u}_i \frac{\partial u'_j}{\partial x_j}) \quad (\text{C.22})$$

Eqn (C.20) becomes

$$\begin{aligned} \frac{\partial}{\partial t} \left\{ \frac{1}{2} \frac{\partial u'_i}{\partial x_k} \frac{\partial u'_i}{\partial x_k} \right\} + \bar{u}_j \frac{\partial}{\partial x_j} \left\{ \frac{1}{2} \frac{\partial u'_i}{\partial x_k} \frac{\partial u'_i}{\partial x_k} \right\} = & -\frac{\partial u'_i}{\partial x_k} \frac{\partial u'_i}{\partial x_j} \frac{\partial \bar{u}_j}{\partial x_k} - \frac{\partial u'_i}{\partial x_k} \frac{\partial u'_j}{\partial x_k} \frac{\partial \bar{u}_i}{\partial x_j} - \\ & u'_j \frac{\partial u'_i}{\partial x_k} \frac{\partial^2 \bar{u}_i}{\partial x_j \partial x_k} - \frac{1}{\rho} \frac{\partial u'_i}{\partial x_k} \frac{\partial^2 p'}{\partial x_i \partial x_k} + \frac{\partial u'_i}{\partial x_k} \frac{\partial^2 \tau'_{ij}}{\partial x_j \partial x_k} - \\ & \frac{\partial}{\partial x_j} \left\{ \frac{u'_j}{2} \frac{\partial u'_i}{\partial x_k} \frac{\partial u'_i}{\partial x_k} \right\} - \frac{\partial u'_i}{\partial x_k} \frac{\partial u'_i}{\partial x_j} \frac{\partial u'_j}{\partial x_k} - \frac{\partial u'_i}{\partial x_k} \frac{\partial u'_i}{\partial x_k} \frac{\partial \bar{u}_j}{\partial x_j} - \\ & \frac{\partial u'_i}{\partial x_k} \frac{\partial}{\partial x_k} (\bar{u}_i \frac{\partial u'_j}{\partial x_j}) \end{aligned} \quad (\text{C.23})$$

The conditioning and averaging of Eqn (C.23) poses something of a problem since some of the terms contain more than one first order derivative or combinations of first and second order, or higher, derivatives. In this case, it is not clear which derivative is to absorb the indicator function leading to the appropriate interfacial term.

The intention here is to derive a conditional-averaged  $\epsilon$  equation which resembles as closely as possible its single phase counterpart, whilst still retaining mathematical rigour. In this way, it is hoped that the modelling of the conditional-averaged  $\epsilon$  equation may follow closely that of the single phase equation and so draw on the many years of experience in the application of  $k - \epsilon$  turbulence models to industrial flows.

To this end, the practice adopted here is to include the indicator function inside the derivative only if that term involves only one derivative (of first order). Following this practice, the conditional-averaged form of Eqn (C.23) reads

$$\begin{aligned}
\frac{\partial \alpha \epsilon}{\partial t} + \frac{\partial \bar{u}_j \alpha \epsilon}{\partial x_j} = & -2\nu\alpha \left\{ \frac{\partial \bar{u}_j}{\partial x_k} \overline{\frac{\partial u'_i}{\partial x_k} \frac{\partial u'_i}{\partial x_j}} + \frac{\partial \bar{u}_i}{\partial x_k} \overline{\frac{\partial u'_i}{\partial x_k} \frac{\partial u'_j}{\partial x_k}} + \frac{\partial^2 \bar{u}_i}{\partial x_j \partial x_k} \overline{u'_j \frac{\partial u'_i}{\partial x_k}} \right\} - \\
& \frac{2\nu\alpha}{\rho} \frac{\partial}{\partial x_i} \left( \overline{\frac{\partial p'}{\partial x_k} \frac{\partial u'_i}{\partial x_k}} \right) - \nu \frac{\partial}{\partial x_j} \left( \overline{u'_j \frac{\partial u'_i}{\partial x_k} \frac{\partial u'_i}{\partial x_k}} \right) + \nu\alpha \frac{\partial^2 \epsilon}{\partial x_j \partial x_j} - \\
& 2\nu\alpha \overline{\frac{\partial u'_i}{\partial x_k} \frac{\partial u'_i}{\partial x_j} \frac{\partial u'_j}{\partial x_k}} - 2\alpha \left\{ \nu \overline{\frac{\partial^2 u'_i}{\partial x_j \partial x_k}} \right\}^2 + \\
& \overline{u_j} \overbrace{\epsilon'' n_j} \Sigma - \overbrace{\epsilon'' \bar{u}_j n_j} \Sigma
\end{aligned} \tag{C.24}$$

Eqn (C.24) retains the major features of the single phase  $\epsilon$  equation. For example, the vortex stretching and viscous dissipation terms are present in essentially the same form. The conditional-averaged  $\epsilon$  equation contains only two extra terms due to the two-phase nature of the flow.

A detailed discussion of the modelling of this equation is given in Section 2.3.2.4

## Appendix D

# Overview Of The Single-Phase SIMPLE Algorithm

This appendix briefly describes the SIMPLE algorithm of Patankar [105] as applied to single-phase incompressible flows calculated on a co-located mesh.

The SIMPLE algorithm effectively addresses the coupling between the pressure and velocity fields and the imposition of the continuity constraints. The initial calculation of the velocity from the discretised momentum equations produces a velocity field which does not in general satisfy the continuity equation. The SIMPLE algorithm uses the continuity equation to calculate a new pressure field which when substituted back into the momentum equations yields a velocity field which does satisfy continuity. At the end of each iteration, new values for pressure and velocity have been obtained which satisfy the continuity equation. The sequence is repeated until the solution has converged.

The single-phase incompressible Navier-Stokes equations read

$$\nabla \cdot \mathbf{u} = 0 \quad (\text{D.1})$$

$$\frac{\partial \mathbf{u}}{\partial t} + \nabla \cdot \mathbf{u} \mathbf{u} = -\nabla p + \nabla \cdot \nu \nabla \mathbf{u} \quad (\text{D.2})$$

The first step in the SIMPLE algorithm is the initial prediction of the velocity field from the discretised momentum equation using the pressure and face flux fields from the previous iteration,  $p^o$  and  $\mathbb{F}^o$  respectively. Discretisation of Eqn (D.2) gives

$$\mathbb{A}_p \mathbf{u}_p^* = \mathbb{H}(\mathbf{u}^*) - \Delta p^o \quad (\text{D.3})$$

where

$$\mathbf{A}_p = \sum_n \mathbf{A}_n + S_p \quad (\text{D.4})$$

$$\mathbb{H}(\mathbf{u}) = \sum_n \mathbf{A}_n \mathbf{u}_n + \mathbf{S}_u \quad (\text{D.5})$$

and  $\mathbf{u}^*$  is the predicted velocity based on the previous iteration pressure field. The pressure gradient term has been taken out of  $\mathbf{S}_u$  to highlight the fact that it is calculated using the pressure values from the previous iteration. Eqn (D.3) is a vector equation which is solved by solving each of the scalar component equations in turn. The central coefficient and the neighbour coefficients are the same for each component. Eqn (D.3) is usually under-relaxed to promote stability using an under-relaxation factor of about 0.5 [166].

In general, the predicted velocity field  $\mathbf{u}^*$  will not satisfy the continuity equation (i.e.  $\nabla \cdot \mathbf{u}^* \neq 0$ ). A new pressure field  $p^*$  is postulated which will produce a velocity field which will does satisfy continuity. This new velocity field is denoted  $\mathbf{u}^{**}$  and we write the continuity equation as

$$\nabla \cdot \mathbf{u}^{**} = 0 \quad (\text{D.6})$$

In order to derive an equation for the new velocity  $\mathbf{u}^{**}$  we write Eqn (D.3) in operator split form [106] in terms of the new velocity  $\mathbf{u}_p^{**}$  and the updated pressure  $p^*$ .

$$\mathbf{A}_p \mathbf{u}_p^{**} = \mathbb{H}(\mathbf{u}^*) - \nabla p^* \quad (\text{D.7})$$

In the spirit of the Rhie and Chow procedure [167], the pressure gradient term in the above equation has been written in a ‘partially discretised’ form to signify that its evaluation has been deferred until later [107]. That is, we retain the ‘meaning’ of the pressure gradient term without actually calculating its value at this stage. It is this delay in the calculation of the pressure gradient term which allows a co-located mesh to be used without incurring the pressure-velocity de-coupling problem.

Since we have neglected the implicit coupling between the velocity at the point  $p$  and its neighbours, Eqn (D.7) is described as an ‘explicit’ equation for  $\mathbf{u}_p^{**}$  in terms of  $p^*$ . The physical meaning of this is that the correction required to make the velocity field conservative is assumed to be purely due to changes in the local pressure gradient. Rearranging,

$$\mathbf{u}_p^{**} = \frac{\mathbb{H}(\mathbf{u}^*)}{\mathbb{A}_p} - \frac{1}{\mathbb{A}_p} \nabla p^* \quad (\text{D.8})$$

Substitution of Eqn (D.8) into the continuity equation D.6 yields

$$\nabla \cdot \frac{1}{\mathbb{A}_p} \nabla p^* = \nabla \cdot \frac{\mathbb{H}(\mathbf{u}^*)}{\mathbb{A}_p} \quad (\text{D.9})$$

which is a Laplacian in  $p^*$ . Discretisation of Eqn (D.9) yields

$$\sum_f \mathbf{S}_f \cdot \left( \frac{1}{\mathbb{A}_p} \nabla p^* \right)_f = \sum_f \mathbf{S}_f \cdot \left( \frac{\mathbb{H}(\mathbf{u}^*)}{\mathbb{A}_p} \right)_f \quad (\text{D.10})$$

Rearranging the left hand side, we have

$$\sum_f \mathbf{S}_f \cdot \left( \frac{1}{\mathbb{A}_p} \right)_f (\nabla p^*)_f = \sum_f \mathbf{S}_f \cdot \left( \frac{\mathbb{H}(\mathbf{u}^*)}{\mathbb{A}_p} \right)_f \quad (\text{D.11})$$

The term  $(\nabla p^*)_f$  is the gradient of the pressure at the face and is calculated naturally from the two cell nodes on either side of the face via

$$(\nabla p^*)_f = \frac{p_p^* - p_n^*}{|\mathbf{d}_n|} \quad (\text{D.12})$$

All other terms at the face are to be evaluated using linear interpolation. If we had left the pressure gradient term in its discretised form (i.e., the gradient of pressure across the cell) and simply interpolated the gradient itself to the face, the pressure at  $p$  would not depend on the pressure within adjacent cells leading to the pressure-velocity de-coupling problem [105].

The solution of Eqn (D.11) yields the new pressure field  $p^*$  which is used to obtain the updated velocity field  $\mathbf{u}^{**}$  using Eqn (D.7). In the SIMPLE algorithm, the velocity field  $\mathbf{u}^{**}$  is the velocity field to be used in the next iteration and will therefore be denoted as  $\mathbf{u}^n$

$$\mathbf{u}_p^n = \frac{\mathbb{H}(\mathbf{u}^*)}{\mathbb{A}_p} - \frac{1}{\mathbb{A}_p} \nabla p^* \quad (\text{D.13})$$

Since the face fluxes are stored in addition to the velocities at the cell nodes, they are also required to be updated to obtain conservative fluxes for use in the next iteration. We use Eqn (D.13) to obtain an expression for the face velocity by linear interpolation.

$$\mathbf{u}_f^n = \left( \frac{\mathbb{H}(\mathbf{u}^*)}{\mathbb{A}_p} \right)_f - \left( \frac{1}{\mathbb{A}_p} \right) (\nabla p^*)_f \quad (\text{D.14})$$

Again, the pressure gradient term in the above equation is calculated using the two cell nodes on either side of the face using Eqn (D.12). The face flux is calculated simply by

$$\mathbb{F} = \mathbf{S}_f \cdot \mathbf{u}_f^n \quad (\text{D.15})$$

$$= \mathbf{S}_f \cdot \left( \frac{\mathbb{H}(\mathbf{u}^*)}{\mathbb{A}_p} \right)_f - \left( \frac{1}{\mathbb{A}_p} \right) (\nabla p^*)_f \quad (\text{D.16})$$

Once the velocity and flux corrections have been carried out, it is necessary to under-relax the pressure field  $p^*$  to obtain the new pressure field  $p^n$ . This is a consequence of assuming that the velocity corrections required to maintain conservation are purely due to the local pressure changes allowing the  $\mathbb{H}(\mathbf{u})$  term in Eqn (D.7) to be calculated explicitly. The new pressure field  $p^*$  is based on the local continuity requirement and, until convergence is obtained, deviates from the correct pressure. It is necessary to under-relax the pressure, once the velocities and fluxes have been corrected, to avoid instability in the solution [105]. The new pressure field is therefore given by

$$p^n = p^o + \lambda(p^* - p^o) \quad (\text{D.17})$$

where  $\lambda_p$  is an under-relaxation factor taken to be approximately 0.2 [166].

The final stage in the SIMPLE algorithm is the solution of the remaining scalar transport equations, such as those for  $k$  and  $\epsilon$ . All sources and coefficients for these equations are calculated using the latest values for pressure and velocity.



## Appendix E

# Break-up Source Term Evaluation

In order to evaluate the two integrals in Eqn (3.31) we may take advantage of the particular properties of the log-normal PDF [81, 83]. Each of these two integrals may be denoted by

$$\mathbb{I}_{d_c}^\lambda(\delta) = \int_{d_c}^\lambda n P(d) d^\delta d(d) \quad (\text{E.1})$$

where  $\delta$  takes the value  $\delta_1$  or  $\delta_2$  as given by Equations 3.32 and 3.33. Noting that  $S_\delta$  is defined as

$$S_\delta = n \int_0^\infty P(d) d^\delta d(d) \quad (\text{E.2})$$

Dividing and multiplying Eqn (E.1) by  $S_\delta$  we obtain

$$\mathbb{I}_{d_c}^\lambda(\delta) = \frac{\int_{d_c}^\lambda P(d) d^\delta d(d)}{\underbrace{\int_0^\infty P(d) d^\delta d(d)}_{\text{Active Population Term}}} S_\delta \quad (\text{E.3})$$

The first term on the right hand side of the above equation is the ‘active population term’ which represents the contribution of the droplet population involved in the break-up process as a fraction of the entire population. Noting that  $S_\delta$  may be rewritten in terms of the dispersed phase fraction and a mean diameter  $d_{3\delta}$  (Eqn (3.8)) and denoting the active population term as  $\mathbb{A}_{d_c}^\lambda(\delta)$ , Eqn (E.3) becomes

$$\mathbb{I}_{d_c}^\lambda(\delta) = \mathbb{A}_{d_c}^\lambda(\delta) \frac{6}{\pi} \alpha_d d_{3\delta}^{\delta-3} \quad (\text{E.4})$$

Now, for the log-normal PDF, the mean diameter  $d_{3\delta}$  may be determined from the distribution variance and the mean diameter  $d_{3\gamma}$  via Eqn (3.9). The evaluation of the active population term  $\mathbb{A}_{d_c}^\lambda$  is carried out by recasting it in terms of the error function  $\text{erf}(x)$  whence

$$\mathbb{A}_{d_c}^\lambda(\delta) = \frac{1}{2} \text{erf} \left\{ \frac{\ln(\lambda/d_{00})}{\sqrt{2\hat{\sigma}^2}} - \frac{\delta}{2} \sqrt{2\hat{\sigma}^2} \right\} - \frac{1}{2} \text{erf} \left\{ \frac{\ln(d_c/d_{00})}{\sqrt{2\hat{\sigma}^2}} - \frac{\delta}{2} \sqrt{2\hat{\sigma}^2} \right\} \quad (\text{E.5})$$

The mean diameter  $d_{00}$  is similarly determined from the local value of the dispersed phase fraction and  $S_\gamma$  via Eqn (3.9). The evaluation of the error function is performed using a numerical approximation [168].

$$\text{erf}(x) = 1 - (a_1 t + a_2 t^2 + a_3 t^3) e^{-x^2} \quad (\text{E.6})$$

$$t = \frac{1}{1 + px} \quad (\text{E.7})$$

The coefficients  $p, a_1, a_2$  and  $a_3$  are as shown in Table E.

Parameter	Value
$p$	0.47047
$a_1$	0.3480242
$a_2$	-0.0958798
$a_3$	0.7478556

Table E.1: Coefficients for the error function approximation.

The break-up source term, as given by Eqn (3.31), in terms of the active population term now reads

$$S_b = \frac{N'^{1-\gamma/3}}{\tau'_b} \mathbb{A}_{d_c}^\lambda(\delta_1) \frac{6}{\pi} \alpha_d d_{3\delta_1}^{\delta_1-3} - \frac{1}{\tau'_b} \mathbb{A}_{d_c}^\lambda(\delta_2) \frac{6}{\pi} \alpha_d d_{3\delta_2}^{\delta_2-3} \quad (\text{E.8})$$

## Appendix F

# Pseudo Turbulence Due To Bubble Size Variation

### F.1 Bubble Size Distribution Effects

For an arbitrary function of diameter of the form

$$f(d) = Ad^\gamma \quad (\text{F.1})$$

where  $d$  is the diameter and  $A$  is a constant coefficient, the mean value of the function in the presence of a distribution of bubble sizes is given by

$$\overline{f}(d) = A \int_0^\infty d^\gamma P(d) dd \quad (\text{F.2})$$

where  $P(d)$  is the bubble diameter probability density function (PDF). Eqn (F.2) shows that, in general, the mean of a function of diameter is only equal to the function of the mean diameter if the function is linear in the diameter  $d$  (ie,  $\gamma = 1$ ) and the PDF is symmetric about the mean diameter. Assuming that the PDF is of a log-normal form, which is defined as

$$P(d) = \frac{1}{d\hat{\sigma}\sqrt{2\pi}} \exp \left\{ -\frac{(\ln(\frac{d}{d_{00}}))^2}{2\hat{\sigma}^2} \right\} \quad (\text{F.3})$$

where  $\hat{\sigma}^2$  = Distribution variance.

$\hat{\sigma}$  = Standard deviation.

$d_{00}$  = Geometric mean diameter.

substitution into Eqn (F.2) gives

$$\overline{f(d)} = \frac{A}{\sqrt{2\pi\hat{\sigma}^2}} \int_0^\infty d^\gamma \exp \left\{ -\frac{(\ln(\frac{d}{d_{00}}))^2}{2\hat{\sigma}^2} \right\} \frac{dd}{d} \quad (\text{F.4})$$

The standardised random variable  $z$  is defined as

$$z = \frac{\ln(\frac{d}{d_{00}})}{\sqrt{2\hat{\sigma}^2}} - \frac{\gamma}{2}\sqrt{2\hat{\sigma}^2} \quad (\text{F.5})$$

so that we have

$$\frac{\left\{ \ln(\frac{d}{d_{00}}) \right\}^2}{2\hat{\sigma}^2} = z^2 + \gamma \ln(\frac{d}{d_{00}}) - \frac{\gamma^2}{2}\hat{\sigma}^2 \quad (\text{F.6})$$

and

$$dd = d\sqrt{2\hat{\sigma}^2} dz \quad (\text{F.7})$$

Substitution of the above into Eqn (F.4) gives

$$\overline{f(d)} = \frac{A}{\sqrt{\pi}} \int_{-\infty}^\infty d^\gamma \exp \left\{ -z^2 - \gamma \ln(\frac{d}{d_{00}}) + \frac{\gamma^2}{2}\hat{\sigma}^2 \right\} dz \quad (\text{F.8})$$

Rearranging,

$$\overline{f(d)} = \frac{A}{\sqrt{\pi}} \exp(\frac{\gamma^2\hat{\sigma}^2}{2}) d_{00}^\gamma \int_{-\infty}^\infty \exp(-z^2) dz \quad (\text{F.9})$$

The integral in the previous equation is related to the error function which is defined as

$$\text{erf}(x) = \frac{2}{\sqrt{\pi}} \int_0^x \exp(-z^2) dz \quad (\text{F.10})$$

In terms of the error function Eqn (F.9) becomes

$$\overline{f(d)} = \frac{A}{2} d_{00}^{\gamma} \exp\left(\frac{\gamma^2 \hat{\sigma}^2}{2}\right) \{\text{erf}(\infty) - \text{erf}(-\infty)\} \quad (\text{F.11})$$

$$= A d_{00}^{\gamma} e^{(\frac{\gamma^2 \hat{\sigma}^2}{2})} \quad (\text{F.12})$$

Note that for monodispersed system Eqn (F.12) reduces to the form of Eqn (F.1), since  $\hat{\sigma} = 0$ . Also, for a linear function in  $d$ , Eqn (F.12) shows that there is a bias towards the larger diameter bubbles, with respect to the geometric mean diameter, due to the log-normal distribution.

## F.2 Mean Terminal Velocity

Consider the terminal velocity of a distribution of bubble sizes steadily released into a quiescent and infinite fluid. The mean velocity of the dispersed phase at a point sufficiently far away from the inlet point so that all bubbles have reached their equilibrium terminal velocity will be given by

$$\overline{v_t}(d) = \int_0^{\infty} v_t(d) P(d) dd \quad (\text{F.13})$$

Given a function for the terminal rise velocity, which is of the form of Eqn (F.1), we can use Eqn (F.12) to calculate the apparent mean terminal velocity as measured in the ensemble or time averaged experiment.

For a distribution of bubbles with a mean diameter of 2 mm, a distribution variance of 0.03 (which implies that 99% of bubbles are within 0.5 mm of the mean size), and assuming that the terminal velocity is adequately described by the function proposed by Peebles and Garber [42],

$$v_t(d) = 0.136g^{0.76} \left\{ \frac{\rho_c}{\mu_c} \right\}^{0.52} d^{1.28} \quad (\text{F.14})$$

Eqn (F.12) gives a mean terminal velocity of 0.365 m/s. Compare this to the mean velocity using the mean diameter only in Eqn (F.14) of 0.356 m/s.

### F.3 Apparent RMS Velocity

Due to existence of a distribution of bubble sizes and terminal rise velocities, the measured apparent RMS velocity will be finite. The mean square velocity fluctuation is given by

$$\overline{v'^2} = \int_0^\infty (v_t(d) - \overline{v_t})^2 P(d) dd \quad (\text{F.15})$$

Rearranging,

$$\overline{v'^2} = \int_0^\infty v_t^2(d) P(d) dd - \overline{v_t}^2 \quad (\text{F.16})$$

Using Equations F.12 and F.14, we find that

$$\overline{v'^2} = \{0.136 g^{0.76} \left\{ \frac{\rho_c}{\mu_c} \right\}^{0.52} \}^2 d_{00}^\gamma e^{\left( \frac{\gamma^2 \sigma^2}{2} \right)} - \overline{v_t}^2 \quad (\text{F.17})$$

Substituting for  $\gamma = 2.56$  and  $\overline{v_t} = 0.365$  gives

$$\overline{v'^2} = 7.3 \times 10^{-3} \quad (\text{F.18})$$

The apparent RMS velocity is therefore 0.085 m/s, which implies an apparent turbulence intensity based on the mean terminal velocity of 24% (!). Based on the actual velocity of the bubbles ( $\approx 0.45 - 0.9$  m/s) in the INPT shear layer case the apparent turbulence intensity will be between 9 and 19%.

Note that the terminal velocity of a 2 mm bubble as measured by Haberman and Morton [21] is 0.3 m/s, implying that the above function for the terminal velocity over-predicts by approximately 20%. This over-prediction will have little effect on the calculation of the apparent RMS velocity.

# Bibliography

- [1] M Ishii. *Thermo-dynamic Theory of Two-phase Flow*. Eyrolles, Paris, 1975.
- [2] P B Whalley. *Two-Phase Flow and Heat Transfer : Oxford Chemistry Primers No.42*. Oxford Science Publications, 1996.
- [3] O Baker. Simultaneous flow of oil and gas. *Oil Gas J.*, 53, 1954.
- [4] G F Hewitt and D N Roberts. Studies of two-phase flow patterns by simultaneous flash and x-ray photography. *AERE-M2159*, 1969.
- [5] Y Taitel and A E Dukler. A model for predicting flow regime transitions in horizontal and near-horizontal gas-liquid flow. *AIChE J.*, 22:47–55, 1976.
- [6] S Politis. *Prediction of Two-phase Solid-liquid Turbulent Flow in Stirred Vessels*. PhD thesis, Imperial College of Science, Technology and Medicine, University of London, 1989.
- [7] O Ubbink. *Numerical prediction of two fluid systems with sharp interfaces*. PhD thesis, Imperial College of Science, Technology and Medicine, University of London, 1997.
- [8] A Tomiyama, I Zun, A Sou, and T Sakaguchi. Numerical analysis of bubble motion with the vof method. *Nuclear Engineering and Design*, 141:69–82, 1993.
- [9] H K Versteeg and W Malalasekera. *An Introduction to Computational Fluid Dynamics : The Finite Volume Method*. Longman Scientific and Technical, 1995.
- [10] D A Drew. Continuum modeling of two-phase flows. In R Meyer, editor, *Theory of dispersed multiphase flow*, pages 173–190. Academic Press, 1983b.
- [11] B E Launder and D B Spalding. *Lectures in Mathematical Models of Turbulence*. Academic Press, London, 1972.

- [12] D A Drew and G B Wallis. Fundamentals of two-phase flow modelling. In *Third International Workshop on Two-phase Flow Fundamentals*, pages 1–64, Imperial College, London, 1992.
- [13] A Serizawa and I Kataoka. Dispersed flow-i. In *Third International Workshop on Two-phase Flow Fundamentals*, Imperial College, London, 1992.
- [14] C M Tchen. *Mean value and correlation problems connected with the motion of small particles suspended in a turbulent fluid*. PhD thesis, University of Delft, 1947.
- [15] M R Maxey and J J Riley. Equation of motion for a small rigid sphere in a nonuniform flow. *Phys. Fluids A*, 26:883–889, 1983.
- [16] T R Auton. *The dynamics of bubbles, drops and particles in motion in liquids*. PhD thesis, Cambridge University, 1983.
- [17] S Elghobashi and G C Truesdell. Direct simulation of particle dispersion in a decaying isotropic turbulence. *J. Fluid Mech.*, 242:655–700, 1992.
- [18] F Durst, D Milojevic, and B Schonung. Eulerian and lagrangian predictions of particulate two-phase flows: A numerical study. *Appl. Math. Modelling*, 8:101–115, 1984.
- [19] A D Gosman and E Ioannides. Aspects of computer simulation of liquid-fueled combustors. *AIAA J. Energy*, 7:482–490, 1983.
- [20] C Kralj. *Numerical simulation of diesel spray*. PhD thesis, Imperial College of Science, Technology and Medicine, University of London, 1993.
- [21] G B Wallis. *One Dimensional Two-phase Flow*. McGraw Hill, New York, 1969.
- [22] X Zhang, Y Ra, and K Fukuda. A numerical analysis of two-phase flow by drift-flux model. In *Third International Symposium on Multiphase Flow and Heat Transfer*, Xi'an, China, 1994.
- [23] F J S Alhanati and S A Shirazi. Numerical simulation of gas-liquid flow inside a downhole centrifuge. *ASME: FED Numerical Methods In Multiphase Flows*, 185, 1994.
- [24] F Hermann, D Issler, and S Keller. Towards a numerical model of powder snow avalanches. In *Computational Fluid Dynamics '94*. John Wiley and Sons, 1994.
- [25] P de Oliveira. *Computer Modelling of Multidimensional Multiphase Flow and Applications to T-junctions*. PhD thesis, University of London, 1992.



- [26] R I Nigmatulin. Spatial averaging in the mechanics of heterogeneous and dispersed systems. *Int. J. Multiphase Flow*, 5, 1979.
- [27] S Whitaker. The transport equations for multiphase systems. *Chem. Eng. Sci.*, 28, 1973.
- [28] D A Drew. Mathematical modeling of two-phase flow. *Ann. Rev. Fluid Mech.*, 15:261–91, 1983a.
- [29] I Kataoka. Local instant formulation of two-phase flow. *International Journal of Multiphase Flow*, 12(5):745–758, 1986.
- [30] I Kataoka and A Serizawa. Basic equations of turbulence in gas-liquid two-phase flow. *Int. J. Multiphase Flow*, 15(5):843–855, 1989.
- [31] D A Drew. Averaged field equations for two-phase media. *Studies in applied Mathematics*, L(2):133–166, June 1971.
- [32] D A Drew. Averaged equations for two-phase flows. *Studies in applied Mathematics*, L(3):205–231, September 1971.
- [33] A Favre. Statistical equations of turbulent gases. In *Problems of Hydrodynamics and Statistical Mechanics*, SIAM, Philadelphia, PA, 1969.
- [34] W P Jones and J H Whitelaw. Calculation methods for reacting flows, a review. *Combustion and Flame*, 48(1), 1982.
- [35] M Lance and M L de Bertodano. Phase distribution phenomena and wall effects in bubbly two-phase flows. In *Third International Workshop on Two-phase Flow Fundamentals*, Imperial College, London, 1992.
- [36] O Simonin and P L Violet. Modeling of turbulent two-phase jets loaded with discrete particles. volume 259-270, pages 127–189. Hemisphere Publishing Corporation, NY, 1991.
- [37] O Simonin, F Poggi, and E Deutsch. Modelling of particle fluctuating motion and fluid turbulence modification in dilute liquid solid two-phase flow. In F.B. Serizwa, T. Fukano, and J Bataille, editors, *Proceedings of the Second International Conference on Multiphase Flow, Kyoto*, April 3-7 1995.
- [38] C Dopazo. On conditioned averages for intermittent turbulent flows. *J. Fluid Mech.*, 81(3):433–438, 1977.

- [39] Q Q Lu, J R Fontaine, and G Aubertin. Numerical study of the solid particle motion in grid-generated turbulent flows. *Int. J. Heat Mass Transfer*, 36(1):79–87, 1993.
- [40] B S Massey. *Mechanics of fluids*. Chapman and Hall, 1989.
- [41] R Clift and W H Gauvin. Motion of entrained particles in gas streams. *Canadian J. of Chemical Engineering*, 49:439, 1971.
- [42] F N Peebles and H J Garber. Studies on the motion of gas bubbles in liquids. *Chem. Eng. Prog.*, 49(2):88–97, 1953.
- [43] M Ishii and N Zuber. Drag coefficient and relative velocity in bubbly, droplet or particulate flows. *AIChE J.*, 25(5):843–854, 1979.
- [44] D M Wang. A curve-fitted drag coefficient model. Private Communication, 1994.
- [45] R Clift, J R Grace, and M E Weber. *Bubbles, Drops and Particles*. Academic Press, 1978.
- [46] L B Torobin and W H Gauvin. *Can. J. of Chem. Eng.*, 38, 1960.
- [47] L B Torobin and W H Gauvin. *A.I.Ch.E. J.*, 7, 1961.
- [48] J H Stuhmiller. The influence of interfacial pressure forces on the character of two-phase flow model equations. *Int. J. Multiphase Flow*, 3:551–560, 1977.
- [49] D A Drew, L Cheng, and R T Lahey Jr. The analysis of virtual mass effects in two-phase flow. *Int. J. Multiphase Flow*, 5:233–242, 1979.
- [50] D A Drew and R T Lahey Jr. The virtual mass and lift force on a sphere in rotating and inviscid flow. *Int. J. Multiphase Flow*, 13(1):113–121, 1987.
- [51] D A Drew and R T Lahey Jr. Some supplemental analysis concerning the virtual mass and lift force on a sphere in a rotating and straining flow. *Int. J. Multiphase Flow*, 16(6):1127–1130, 1990.
- [52] L M Milne-Thomson. *Theoretical Hydrodynamics*. McMillan and Co., 1968.
- [53] L Van Wijngaarden. Hydrodynamic interaction between gas bubbles in liquid. *J. of Fluids mechanics*, 77(1):27, 1976.
- [54] Y G Mokeyev. Effect of particle concentration on their drag and induced mass. *Fluid Mechanics - Soviet Research*, 6(1):161, 1977.

- [55] S K Wang, S J Lee, O C Jones Jr., and R T Lahey Jr. 3-D turbulence structure and phase distribution measurements in bubbly two-phase flows. *Int. J. Multiphase Flow*, 13(3), 1987.
- [56] V Roig. *Zone de Melange D'écoulements Diphasiques a Bulles*. PhD thesis, Institute National Polytechnique de Toulouse, 1993.
- [57] W P Jones and B E Launder. *Int. J. Heat and Mass Transfer*, 15:301, 1972.
- [58] A C Buckingham. Dusty gas influences on transport in turbulent erosive propellant flow. *AIAA J.*, 19(4):510, 1981.
- [59] A C Buckingham and W J Siekhaus. Interaction of moderately dense particle concentrations in turbulent flow. In *AIAA 19th Aerospace Sciences Meeting, St Louis, Missouri*, number AIAA-81-0346, 1981.
- [60] A C Buckingham and W J Siekhaus. Simulating interactions between turbulence and particles in erosive flow and transport. In C Taylor and B A Schrefler, editors, *Numerical methods in laminar and turbulent flows, Proc. 2nd international conference, Venice*. 1981.
- [61] F Pourahmadi. *Turbulence modelling of single and two-phase curved channel flows*. PhD thesis, University of California, Berkeley, 1982.
- [62] F Pourahmadi and J A C Humphrey. Modelling solid-fluid turbulent flows with application to predicting erosive wear. *Physico-Chemical Hydrodynamics*, 4(3):191, 1983.
- [63] S E Elghobashi and T W Abou-Arab. A two-equation turbulence model for two-phase flows. *Phys. Fluids*, 26(4):931–938, 1983.
- [64] S E Elghobashi, T W Abou-Arab, M Rizk, and A Mostafa. Prediction of the particle-laden jet with a two-equation turbulence model. *Int. J. Multiphase Flow*, 10(6):697, 1984.
- [65] C P Chen and P E Wood. A turbulence closure model for dilute gas-particle flows. *Canadian J. of Chemical Engineering*, 63, 1985.
- [66] C P Chen and P E Wood. Turbulence closure modelling of the dilute gas-particle axisymmetric jet. *AIChE J.*, 32(1):163, 1986.
- [67] R T Lahey Jr. The cfd analysis of multidimensional phenomena in multiphase flow. In *Second International Conference on Multiphase Flow*, Kyoto, Japan, 1995.

- [68] R L Peskin. The diffusivity of small suspended particles in turbulent fluids. In *AIChE National Meeting*, Baltimore, Maryland, 1962.
- [69] A Alajbegovic. *Phase distribution and turbulence structure for soli/fluid upflows in a pipe*. PhD thesis, Rensselaer Polytechnic Institute, NY, 1994.
- [70] W D McComb. *The Physics of Fluid Turbulence*. Clarendon Press, Oxford, 1990.
- [71] M L de Bertodano. *Turbulent bubbly two-phase flow in a triangular duct*. PhD thesis, Rensselaer Polytechnic Institute, 1992.
- [72] W Rodi. *Turbulence Models and Their Application in Hydraulics*. Int. Assoc. Hydraul. Res., 1979.
- [73] W Rodi. On the equation governing the rate of turbulent energy dissipation. Internal Report TM/TN/A/14, Imperial College of Science, Technology and Medicine, University of London, 1971.
- [74] M L de Bertodano, R T Lahey Jr., and O C Jones. Development of a  $k - \epsilon$  model for bubbly two-phase flow. *Transactions of the ASME*, 116:128–134, 1994.
- [75] A K Chesters. An approximate bubble-eddy interaction model. BRITE report II-15, BRITE II, 1992.
- [76] R I Issa. A simple model for  $C_t$ . Private Communication, December 1992.
- [77] M R Wells and D E Stock. The effects of crossing trajectories on the dispersion of particles in a turbulent flow. *J. Fluid Mech.*, 136, 1983.
- [78] K Eppinger, J Fabre, and C Suzanne. Bubble dispersion in homogeneous and isotropic turbulence. To be published, 1995.
- [79] W P Jones. Models for turbulent flows with variable density and combustion. In W Kollman, editor, *Prediction methods for turbulent flow*. Hemisphere Publishing Corp., 1980.
- [80] H J Ziman. A cfd framework for breakup and coalescence modelling. Brite report I-26, Brite-Euram project RIIB.0085.UK(H), January 1988.
- [81] A K Chesters. Source terms for drop coalescence and break-up in the transport equation for intensity of dispersion : First proposals. Brite report I-36, Brite-Euram project RIIB.0085.UK(H), July 1987.

- [82] R A de Bruijn. Emulsification in turbulent flows : Development of a computer code to predict drop sizes. Brite report I-30, Brite-Euram project RIIB.0085.UK(H), January 1988.
- [83] H J Ziman. Mixreact reference manual. Brite report I-72, Brite-Euram project RIIB.0085.UK(H), December 1989.
- [84] A K Chesters. Source terms due to mass transfer in the concentration equations for two-phase flows : First proposals. Brite report I-58, Brite-Euram project RIIB.0085.UK(H), may 1989.
- [85] A K Chesters. Source terms due to mass transfer in the concentration equations for two-phase flow : The effect of turbulence. Brite report I-59, Brite-Euram project RIIB.0085.UK(H), July 1989.
- [86] A K Chesters. The source term due to particle drift in the transport equation for intensity of dispersion. Brite report I-75, Brite-Euram project RIIB.0085.UK(H), October 1989.
- [87] M Alderliesten. *Anal. Proc.*, 21(167), 1984.
- [88] J J M Janssen, A K Chesters, and W G M Agterof. Formulation of source terms for break-up and coalescence : Status of tasks 1 and 2, october 1994. Brite report II-40, Brite-Euram project BE 4098, October 1994.
- [89] R A de Bruijn. Newtonian drop break-up in general laminar shear flows : Development of a computer code to predict drop sizes. Brite report I-15, Brite-Euram project RIIB.0085.UK(H).
- [90] A K Chesters. Viscous break-up in isotropic turbulence : Refined criteria based on the structure and intensity of the flow fields. Brite report I-42, Brite-Euram project RIIB.0085.UK(H), 1988.
- [91] J J M Janssen. Consequence of surfactant on the breakup of droplets I : Literature survey and approach assessment. Brite report II-8, Brite-Euram project BE 4098, May 1992.
- [92] J J M Janssen, A Boon, and W G M Agterof. Consequence of surfactant on the breakup of droplets II : Breakup in simple shear flow. Brite report II-9, Brite-Euram project BE 4098, February 1993.
- [93] H J Ziman. Inertial breakup of droplets and bubbles by shape oscillation. Brite report II-22, Brite-Euram project BE 4098, June 1993.

- [94] A K Chesters. The influence of surfactants on inertial break-up. Brite report II-55, Brite-Euram project BE 4098, August 1995.
- [95] C Gourdon and A K Chesters. Break-up in the presence of interphase mass transfer. Brite report II-15, Brite-Euram project BE 4098, January 1994.
- [96] H P Grace. Dispersion phenomena in high viscosity immiscible fluid systems and application of static mixers as dispersion devices in such systems. *Chem. Eng. Commun.*, 14, 1982.
- [97] J J M Janssen, A Boon, and W G M Agterof. Droplet behaviour at supercritical shear rates : Scaling laws for capillary break-up. Brite report II-21, Brite-Euram project BE 4098, November 1994.
- [98] H Lamb. *Hydrodynamics*. Cambridge University Press, 6'th edition, 1932.
- [99] H L Lu and R E Apfel. Shape oscillations of drops in the presence of surfactants. *J. Fluid Mech.*, 222:351, 1991.
- [100] A K Chesters. Local laws for coalescence rates in turbulent emulsions: a model for the collision and film thinning process when drop inertia dominates. Brite report I-31, Brite-Euram project RIIB.0085.UK(H), 1988.
- [101] J J M Janssen, J A Wieringa, F Groeneweg, A Boon, and W G M Agterof. Stirred vessel test cases. Brite report II-60, Brite-Euram project BE 4098, May 1995.
- [102] A K Chesters. Implementation of relations for damped inertial break-up : Further suggestions. Private Communication, September 1995.
- [103] A K Chesters. Surfactant concentration transport equations. Private Communication, February 1995.
- [104] H J Ziman. Extension of reaction extent framework to include mass transfer. Brite report I-54, Brite-Euram project RIIB.0085.UK(H), April 1989.
- [105] S V Panakar. *Numerical heat transfer and fluid flow*. McGraw-Hill, 1980.
- [106] R I Issa. Solution of the implicitly discretised fluid flow equations by operator-splitting. *J. Comp. Phys.*, 62(1):40–65, January 1986.
- [107] H Jasak. *Error analysis and estimation for finite volume method with applications to fluid flow*. PhD thesis, Imperial College of Science, Technology and Medicine, University of London, 1996.

- [108] S Muzaferija. *Adaptive finite volume method for flow prediction using unstructured meshes and multigrid approach*. PhD thesis, Imperial College of Science, Technology and Medicine, University of London, 1994.
- [109] J R Shewchuk. An introduction to the conjugate gradient method without the agonizing pain. Technical Report CMU-CS-94-125, School of Computer Science, Carnegie Mellon University, 1994.
- [110] B E Launder and D B Spalding. The numerical computation of turbulent flows. *Computer Methods In Applied Mechanics And Engineering*, 3:269–289, 1974.
- [111] S V Patankar and D B Spalding. A calculation procedure for heat, mass and momentum transfer in three-dimensional parabolic flows. *Inter. J. of Heat and Mass Transfer*, 15:1787, 1972.
- [112] M K Looney, A D Gosman, R I Issa, and S Politis. A two-phase flow numerical algorithm and its application to solid-liquid suspension flows. Technical Report FS/85/31, Imperial College of Science, Technology and Medicine, 1985.
- [113] F H Harlow and A A Amsden. Numerical calculation of multiphase fluid flow. *J. Comp. Phys.*, 17:19–52, 1975.
- [114] F H Harlow and A A Amsden. Flow of inter-penetrating material phases. *J. Comp. Phys.*, 18:440–464, 1975.
- [115] D B Spalding. Numerical computations of multiphase flow and heat transfer. In C Taylor and K Morgan, editors, *Recent advances in numerical methods in fluids*, volume 1. Pineridge Press, 1980.
- [116] P J Hartley and A Wynn-Evans. *A structured introduction to numerical mathematics*. Stanley Thornes (Publishers) Ltd, 1979.
- [117] G L Brown and A Roshko. On density effects and large structure in turbulent mixing layers. *J. Fluid Mech.*, 64:775–816, 1974.
- [118] C D Winant and F K Browand. Vortex pairing : the mechanism of turbulent mixing layer growth at moderate reynold’s number. *J. Fluid Mech.*, 63(2):237–255, 1974.
- [119] J P Hulin, C Fierfort, and R Coudol. Experimental study of vortex emission behind bluff obstacles in a gas liquid two-phase flow. *Int. J. Multiphase Flow*, 8(5):475–490, 1982.

- [120] R Chein and J N Chung. Effects of vortex pairing on particle dispersion in turbulent shear flows. *Int. J. Multiphase Flow*, 13(6):785–802, 1987.
- [121] K J Sene, J C R Hunt, and N H Thomas. The role of coherent structures in bubble transport by turbulent shear flows. *J. Fluid Mech.*, 259:219–240, 1994.
- [122] S N B Murthy. Turbulent mixing in nonreactive and reactive flows : A review. In S N B Murthy, editor, *Turbulent mixing in nonreactive and reactive flows*. Plenum Press, New York, 1974.
- [123] H W Liepmann and J Laufer.  $\Gamma$  Technical note 1257, NACA, 1947.
- [124] I Wygnanski and H E Fiedler. The two-dimensional mixing region. *J. Fluid Mech.*, 41(2):327–361, 1974.
- [125] H E Fiedler. On turbulence structure and mixing mechanism in free turbulent shear flows. In S N B Murthy, editor, *Turbulent mixing in nonreactive and reactive flows*. Plenum Press, New York, 1974.
- [126] P Bradshaw. Interacting shear layers in turbomachines and diffusers. In S N B Murthy, editor, *Turbulence in internal flows*. Hemisphere Publishing Corp., 1976.
- [127] M T Landahl and E Mollo-Christensen. *Turbulence and Random Processes in Fluid Mechanics*. Cambridge University Press, second edition, 1992.
- [128] K C Chang, M R Wang, W J Wu, and Y C Liu. Theoretical and experimental-study on 2-phase structure of planar mixing layer. *AIAA Journal*, 31(1), 1993.
- [129] L Poire. Boundary conditions for Mélodif calculations. Private Communication, 1993.
- [130] C M Ho and P Huerre. Perturbed free shear layers. *Ann. Rev. Fluid. Mech*, 16:365–424, 1984.
- [131] K A Stroud. *Engineering Mathematics*. Macmillan, 1982.
- [132] T J Liu and S G Bankoff. Structure of air water bubbly flow in a vertical pipe : I. Liquid mean velocity and turbulence measurements. *International Journal of Heat and Mass Transfer*, 36(4):1049–1060, 1993.
- [133] T J Liu and S G Bankoff. Structure of air water bubbly flow in a vertical pipe : II. Void fraction, bubble velocity and bubble-size distribution. *International Journal of Heat and Mass Transfer*, 36(4):1061–1072, 1993.



- [134] D M Wang. Bubbly flow in a backward-facing step flow. BRITE report II-34, BRITE II, 1994.
- [135] J O Hinze. *Turbulence*. McGraw Hill Inc., second edition, 1975.
- [136] O Leuchter. Effects of freestream turbulence and initial boundary layers on the development of turbulent mixing layers. In S N B Murthy, editor, *Turbulence in Internal Flows*. Hemisphere Publishing Corp., 1974.
- [137] J J M Janssen, A Boon, and W G M Agterof. Emulsification in a pipe mixer III : Modified set-up and lda analysis of flow conditions. Brite report II-38, Brite-Euram project BE 4098, April 1994.
- [138] J J M Janssen, A Boon, and W G M Agterof. Emulsification in a pipe mixer IV : Local mean drop size and local volume fraction. Brite report II-48, Brite-Euram project BE 4098, October 1994.
- [139] J J M Janssen, A Boon, and W G M Agterof. Emulsification in a pipe mixer V : Additional evaluation of lda measurements. Brite report II-52, Brite-Euram project BE 4098, January 1995.
- [140] J J M Janssen. Pipe-mixer experiments : Analysis of phase fraction and droplet size results. Private Communication, July 1995.
- [141] R Pal. *Colloids Surfaces A : Physiochem. Eng. Aspects*, 84:141–193, 1994.
- [142] J J M Janssen. Pipe-mixer experiments : Analysis of lda results. Private Communication, June 1994.
- [143] J Fischer. *Detaillierte Untersuchung der Gasphaseneigenschaften begaster Ruhrkessel*. PhD thesis, Institut fur Technische Chemie, Universitat Hannover, 1992.
- [144] J Y Oldshue. *Fluid Mixing Technology*. McGraw Hill, 1983.
- [145] A H Bolour-Frousham. *Prediction of Single-Phase Turbulent Flows in Agitated Mixing Vessels*. PhD thesis, Imperial College of Science, Technology and Medicine, University of London, 1986.
- [146] G Tabor. Literature survey : Stirred flows. Brite report II-41, Brite-Euram project BE 4098, September 1994.
- [147] K Van't Riet and J M Smith. The bahaviour of gas-liquid mixtures near rushton turbine blades. *Chemical Engineering Science*, 28:1031, 1973.

- [148] K Van't Riet and J M Smith. The trailing vortex system produced by a rushton turbine. *Chemical Engineering Science*, 30:1093, 1975.
- [149] J Nouri. PhD thesis, Imperial College of Science, Technology and Medicine, University of London, 1988.
- [150] A Bakker. *Hydrodynamics of Stirred Gas-Liquid Dispersions*. PhD thesis, Delft University of Technology, The Netherlands, 1992.
- [151] A Bakker and H E A van den Akker. A computational study on dispersing gas in a stirred reactor. In *Fluid Mechanics of Mixing : Proc. of the 7th European Congress on Mixing*, pages 37–45, 1992.
- [152] K E Morud and B H Hjertager. Lda measurements and cfd modelling of gas-liquid flow in a stirred vessel.
- [153] J Fischer, S Broring, and A Lubbert. Gas-phase properties in stirred tank bioreactors. *Chem. Eng. Technol*, 15:390–394, 1992.
- [154] A K Chesters. Viscous break-up of drops in impeller boundary layers. Brite report II-10, Brite-Euram project BE 4098, November 1992.
- [155] A D Gosman, R I Issa, C Lekakou, M K Looney, and S Politis. Multidimensional modelling of turbulent two-phase flows in stirred vessels. *AIChE Journal*, 38(12), 1992.
- [156] R I Issa and A D Gosman. The computation of three dimensional turbulent two-phase flows in mixer vessels. In *2nd Int. Conf Numerical Methods in Laminar and Turbulent Flow*, Venice, July 1981.
- [157] M K Looney, A D Gosman, R I Issa, and S Politis. Modelling of the turbulent flow of solid-liquid suspensions in stirred vessels. In *5th International Conference of Mathematical Modelling*, 1985.
- [158] M Z Liu, J Y Luo, G Tabor, R I Issa, and A D Gosman. Development of eulerian two-phase capability in star-cd and its application in chemical processing industries. In *CFD for process design section, Proceedings of CHEMPUTERS EUROPE III*, Frankfurt, Germany, October 1996. McGraw-Hill.
- [159] G Tabor, A D Gosman, and R I Issa. Numerical simulation of the flow in a mixing vessel stirred by a rushton turbine. In *Fluid Mixing V : UK Conference on Mixing*, number 140 in I.Chem.E. Symposium Series, pages 25–34, Bradford, 1996.

- [160] G Tabor. Validation of the two-phase model against experimental data. Brite report II-54, Brite-Euram project BE 4098, December 1995.
- [161] S M Kresta and P E Wood.  $\Gamma$  *AIChE J*,  $\Gamma(\Gamma)$ :448, 1991.
- [162] J Y Luo, R I Issa, and A D Gosman. Prediction of impeller induced flows in mixing vessels using multiple frames of reference. In *Eighth European Conference on Mixing*, 1994.
- [163] W H Press, S A Teulolsky, W T Vetterling, and B P Flannery. *Numerical recipes in C : The art of scientific computing*. Cambridge University Press, Cambridge, 1992.
- [164] H G Weller. The development of a new flame area combustion model using conditional averaging. Thermo-fluids section report TF/9307, Imperial College of Science, Technology and Medicine, 1993.
- [165] A K Chesters. An approximate bubble-eddy interaction model. Brite report II-5, Brite-Euram project BE 4098, August 1992.
- [166] M Peric. *A finite volume method for the prediction of three-dimensional fluid flow in complex ducts*. PhD thesis, Imperial College of Science, Technology and Medicine, University of London, 1985.
- [167] C M Rhie and W L Chow. A numerical study of the turbulent flow past an isolated airfoil with trailing edge separation. In *AIAA/ASME Third Joint Thermophysics, Fluids, Plasma and Heat Transfer Conference*, St. Louis, Missouri, 1982.
- [168] Abramowitz and Stegun. *Handbook of mathematical functions*. Dover, 1965.